Crops that grow in the dark, for astronauts' gardens p. 1004

Loss of amino acid taurine promotes aging pp. 1010 & 1028

How directed pressure speeds up chemistry pp. 1013 & 1053

Science

$15
9 JUNE 2023
science.org
AAAS



HITTING THE STREETS

Mammal movements during lockdowns pp. 1008 & 1059

EDITORIAL

Expelled from the mountain top?

In 1968, Martin Luther King Jr. professed, "We've got some difficult days ahead. But it really doesn't matter with me now, because I've been to the mountaintop.... And I've seen the Promised Land." Sadly, 55 years later, the United States may have future difficult days regarding fair access to higher education for peoples of diverse demographic backgrounds. Given the Supreme Court's conservative majority, all signs point to a decision that will make achieving racial diversity at all, especially at highly selective universities, impossible.

The specific cases now before the Court involve Harvard University and the University of North Carolina, Chapel Hill, and whether admission policies discriminate against Asian American and/or European American students. The Court could reverse its prior position that diversity considerations are constitutional as admission criteria. A reversal's impact will likely mimic the effects of California's Proposition 209. Since 1996, this amendment to the state constitution prohibits considerations of race, ethnicity, or sex for employment or enrollment in public institutions, including education. It resulted in about a 40% decrease in under-represented minority students in the state's most elite University of California public campuses.

> "The dark days... seem poised to return under a false banner of increasing fairness..."

Seven years ago, admission policies were on the Court's docket in *Fisher* v. *University of Texas*. It narrowly decided that such considerations of diversity factors were constitutional. On this page, I argued that diverse learning environments expose students to a broader range of perspectives, enhance education, and inculcate creativity and innovative habits of mind. Science, technology, engineering, and mathematics (STEM) demand creativity—their research needs diverse thinking. This can be enhanced with equitable opportunities for all populations to participate in all institutions of higher education. My own life experience attests to this need.

As a youth, I dreamed about becoming a scientist and eventually of attending the Massachusetts Institute of Technology (MIT). In 1965, this would have practically been impossible. I was attending a traditional "colored" high school in Florida and saw obvious disparities resulting from differential financial investments in my school versus other schools—desks in disrepair and the sharing of old textbooks often falling apart at the spine. I realized that society was betting against me and in favor of other kids because of race. The system was broken for students like me, and I lowered my expectations on achieving goals. In my mind, it was as if one group was taught the free-style stroke while another group was taught the backstroke in swimming. College admissions were akin to telling both groups to jump in a pool and compete with no regard for the structural unfairness of the training systems.

By 1969, MIT reexamined assumptions regarding its traditional metrics for the success of its students, and I was admitted. MIT's President Paul Gray said, "The conundrum, a problem that selective colleges and universities all wrestle with, is that they are pretty good at predicting success, predicting who will succeed, but they are pretty bad at predicting who will fail." After I graduated, he said of me, "on the record...was likely to be hanging on by his fingernails" at MIT, but "was evidently a star when he was here."

Einstein said, "Imagination is more important than knowledge... for knowledge is limited to all we now know and understand, while imagination embraces...all there ever will be to know and understand." This aligns with my experience in science and education. For example, in 2020, working with two doctoral physics students at Brown University, we presented a solution to a little studied and overlooked problem in string theory that had been unresolved since the 1990s. My background and experience contributed to imagining a different approach, and we created new mathematical and scientific knowledge. Decades later, MIT's awareness of diversity's value overcame the structural disadvantages of backgrounds such as my own and benefited science.

The dark days described by King and by MIT's president seem poised to return under a false banner of increasing fairness and meritocratic admissions to universities. If the Court continues to make it more difficult to progress toward a more perfect union and harder to "see the Promised Land," then an equitable future for all will become increasingly harder to reach.

–Sylvester James Gates Jr.



Sylvester James Gates Jr.
is a professor in the Department of Physics, University of Maryland, College Park, MD, USA.
gatess@umd.edu

PHOTO: JOHN CONSOLI/UNIVERSITY OF MARYLAND

10.1126/science.adj0265

> “We, too, are made of wonders, of great and ordinary loves, of small invisible worlds ...”
>
> **U.S. Poet Laureate Ada Limón** in “In Praise of Mystery: A Poem for Europa.” The text will be engraved on NASA’s Europa Clipper spacecraft before its 2024 launch to visit that moon of Jupiter.

IN BRIEF

Edited by **Jeffrey Brainard**

FORENSICS

Scientists help free imprisoned woman

Jailed 20 years on charges of killing her four children, Australian Kathleen Folbigg received a pardon this week and was set free, in large part thanks to recent genetics research, the lobbying of scientists, and the work of the Australian Academy of Science. Folbigg’s 2003 conviction stemmed from circumstantial evidence, such as ambiguous writings in her diary and the apparent unlikelihood of four children in one family dying naturally. But starting about 5 years ago, researchers recruited to reexamine Folbigg’s case identified a mutation that her two daughters inherited from their mother, and further studies indicated it most likely explains their sudden deaths. Another mutation, implicated in dangerous epilepsy, was found in both sons who died, prompting authorities to reconsider the criminal case. The academy, which served as an independent science adviser in the probe, applauded the pardon, issued by New South Wales’s state government.

NIH fellows move to unionize

LABOR RELATIONS | Early-career researchers at the U.S. National Institutes of Health (NIH) last week took a step toward forming a union, which would be the first to represent research fellows working at a federal agency. Organizers gathered signatures in support from roughly 3000 of the 4800 postdocs, graduate students, and other junior researchers who would be represented by the union and submitted the petition to the U.S. Federal Labor Relations Authority, which oversees federal employee unions. A majority of the 4800 would need to approve the union in an election. Researchers pushing for the union, NIH Fellows United, say they hope to obtain better pay and working conditions.

NSF funds better airborne radar

ATMOSPHERIC SCIENCE | The National Center for Atmospheric Research has been awarded $92 million to build a next-generation airborne radar to provide a sharper view of large storms, including hurricanes, the U.S. National Science Foundation announced last week. The Airborne Phased Array Radar (APAR) can scan in multiple directions at once, replacing existing instruments that record data in just one fixed direction. Mounted on a C-130 cargo airplane, APAR can distinguish between rain, ice, and snow—critical for understanding storm evolution in cooler climates—and it may improve predictions of a storm’s intensification. APAR will be a main instrument on the National Weather Service’s new fleet of hurricane-hunter planes, expected in 2030.

Defamation claim against NAS axed

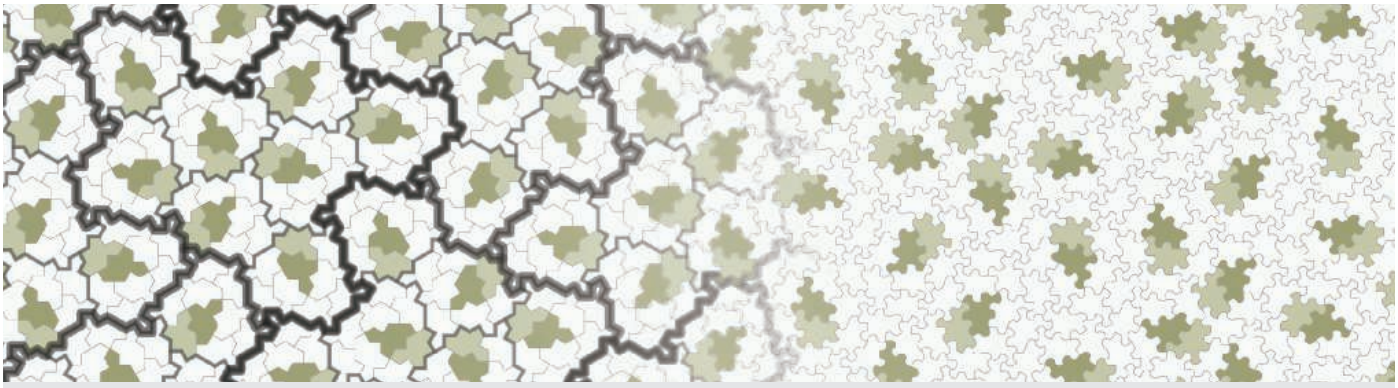
#METOO | A court last month dismissed a defamation lawsuit filed by Peruvian archaeologist Luis Jaime Castillo Butters against the U.S. National Academy of Sciences (NAS) and its president, Marcia McNutt. NAS ousted Castillo Butters in 2021 after an investigation at the Pontifical Catholic University of Peru found evidence of sexual harassment, charges Castillo Butters denies. However, when NAS ejected him, it stated only that he had breached its code of conduct and did not cite sexual harassment. A U.S. District Court in the District of Columbia concluded this undermined the defamation claim. In an email to *Science*, Castillo Butters said he intends to file a revised U.S. claim and to continue to fight in Peruvian courts, where he has sued one of his accusers. In January, an appeals court judge ordered a new trial in that case after a lower court convicted her of defamation.

Columbia co-worker’s suit settled

SCIENTIFIC COMMUNITY | A long-running gender discrimination lawsuit involving two Columbia University researchers has been settled out of court on undisclosed terms. It was filed in 2017 against virologist Ian Lipkin and Columbia by Lipkin’s former collaborator, Mady Hornig, a physician who, like Lipkin, studies the possible role of viruses in chronic fatigue syndrome/myalgic encephalopathy and other neurologic diseases at Columbia’s Mailman School of Public Health. Hornig told *Science* in an email: “I am very pleased with the resolution of this matter and look forward to continuing my research unimpeded.” Lipkin’s attorney and Columbia declined to comment.

Chaco Canyon sites protected

ARCHAEOLOGY | President Joe Biden’s administration last week banned new leases for oil and gas drilling in a 16-kilometer, archaeologically rich zone around New Mexico’s Chaco Culture National Historic Park. The action will safeguard 4700 archaeological sites outside the park, only some of which have been studied. The order is limited to 20 years and applies only to federal lands and mineral holdings in the 1419-square-kilometer zone, about two-thirds of which is owned by state, tribal, and private entities. A bigger challenge remains, advocates and archaeologists say: protecting sites in the 21,000-square-kilometer Greater Chaco region, of which the park and buffer zone are a small part. In February, a federal appeals court halted nearly 200 drilling permits in this larger region, calling the environmental reviews inadequate. Drilling continues under other permits.



MATH

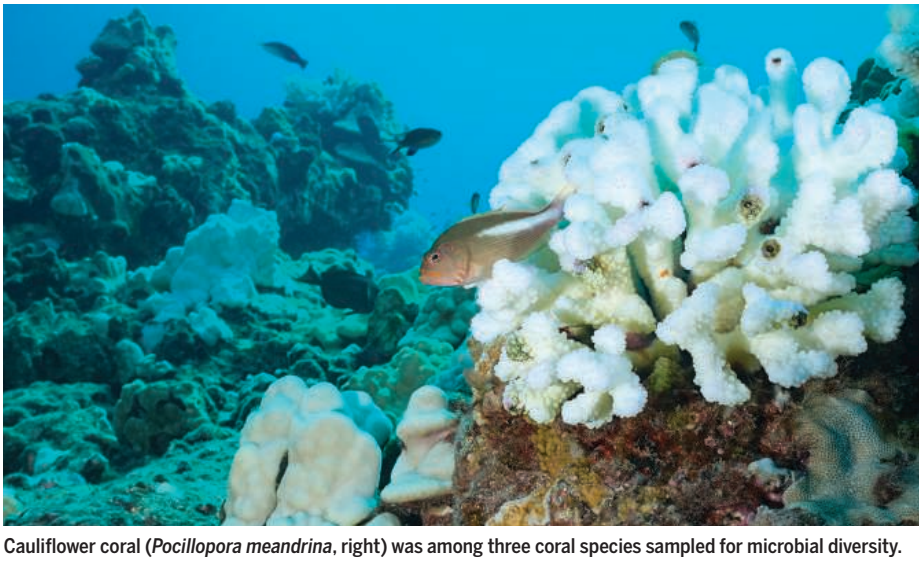
Tweak of shape clinches discovery of nonrepeating tiling

This time it's final: Mathematicians have found a single shape for an abstract 2D tile that, in theory, can cover an infinite plane without leaving any gaps and without producing a repeating pattern. The first such "aperiodic tiling" was discovered in the 1960s and comprised 104 different shapes. In 1977, famed British mathematician Roger Penrose discovered two shapes that could do the trick. Then in March, David Smith, a hobbyist in England, and colleagues produced an aperiodic tiling using a single 13-sided shape they called a "hat." But the proposed tiling contained some tiles that were mirror reflections of the hat—like puzzle pieces laid face side down—and some critics argued this meant two different tiles had been used. Now, Smith and colleagues have tweaked the shape to create one they call a "Spectre." It produces a tiling that includes no mirror images, they reported last week in a preprint posted on arXiv—leaving no space for objections.

A straight-edge shape (left) and its mirror image tile a plane with no repeating pattern; a "Spectre" shape with curved edges (right) does so with no mirror image.

Corals support vast microbiome

ECOLOGY | Coral reefs, bastions of marine biodiversity because of the abundant fish, invertebrates, and algae they support, are also home to Earth's greatest microbial diversity, according to a new estimate. From 2016 to 2018, an international team aboard the sailing ship *Tara* studied 99 reefs off 32 islands across the Pacific Ocean, sequencing DNA from more than 5000 samples of three coral species, two fish species, and plankton. The team then extrapolated the half-billion kinds of microbes, mostly bacteria, found off these islands to the entire Pacific, home to 80% of the world's coral species. This ocean's microbial diversity is equivalent to that previously estimated for all of Earth, they reported last week in *Nature Communications*. The researchers expect this high microbial diversity helps make the reefs more resilient in the face of heat waves and other stressors.



Cauliflower coral (*Pocillopora meandrina*, right) was among three coral species sampled for microbial diversity.

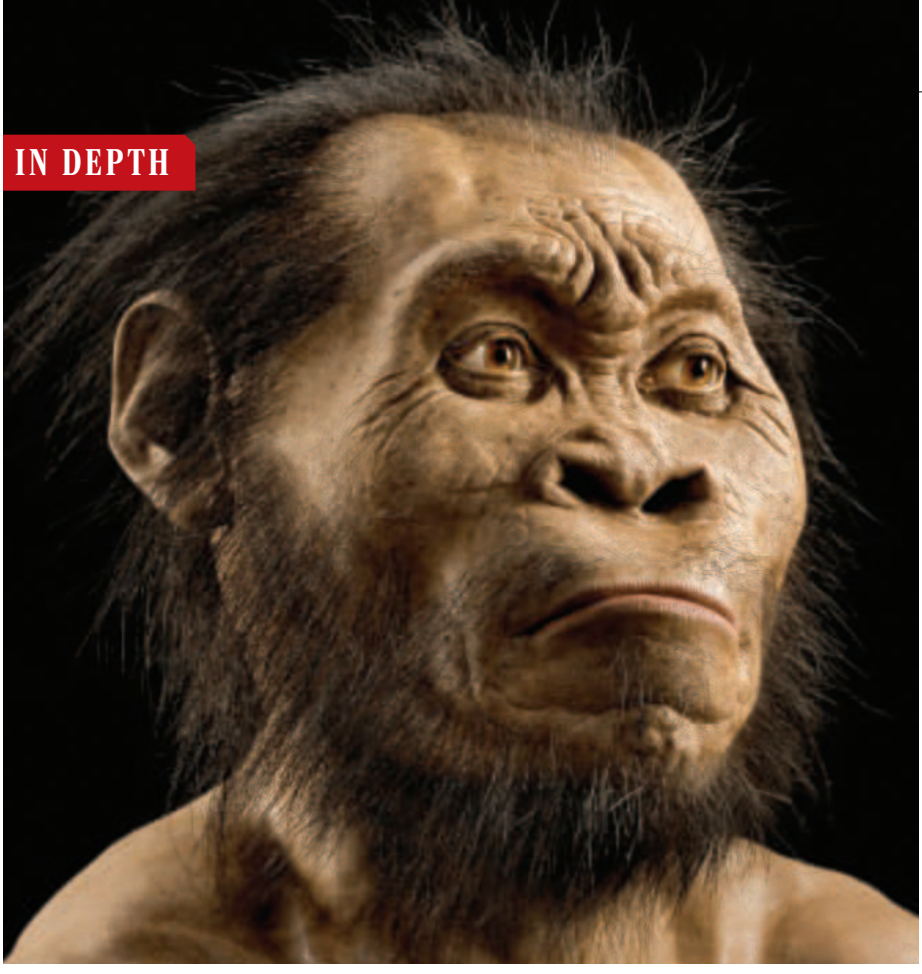
Chemist to lead Bulgaria

LEADERSHIP | Bulgaria's parliament this week approved a new government under a power-sharing agreement that will see two officials with science and research expertise serve as prime minister in succession. Under the agreement, Nikolai Denkov, a physical chemist at Sofia University and former minister of education and science, will serve initially. Mariya Gabriel, a politician who in May resigned as the European Commission's science chief, will be deputy prime minister. After 9 months, their roles will reverse. Despite the leaders' backgrounds, the government is not expected to prioritize science policy legislation.

Space solar power demonstrated

ENERGY | Researchers have taken a small step toward realizing a long-standing dream: harvesting solar energy in space and beaming it down to Earth. An experimental satellite launched in January has for the first time transmitted power in a microwave beam, steered the beam onto targets, and sent some of that power to a detector on Earth, the California Institute of Technology announced last week. By some recent estimates, giant orbiting generators will soon be competitive with earthbound nuclear plants, if launch costs continue to decrease.

IMAGES: (TOP TO BOTTOM) DAVID SMITH, JOSEPH SAMUEL MYERS, CRAIG S. KAPLAN, AND CHAIM GOODMAN-STRAUSS; DOUG PERRINE/NPL/MINDEN PICTURES



Researchers claim that *Homo naledi*, a small-brained human relative, buried its dead and made art long before our own species did.

PALEOANTHROPOLOGY

Was this extinct human the first gravedigger—and artist?

Anthropologists hail new *Homo naledi* fossils but doubt spectacular claims of intentional burial and art

By **Ann Gibbons**

A trio of papers posted online and presented at a meeting this week lays out an astonishing scenario. Roughly 240,000 years ago, they suggest, small-brained human relatives carried their dead through a labyrinth of tight passageways into the depths of a vast limestone cave system in South Africa. Working by firelight, these diminutive cave explorers dug shallow graves, sometimes arranging bodies in fetal positions and placing a stone tool near a child's hand. Some etched cave walls with crosshatches and others cooked small animals in what amounted to a subterranean funeral, more than 100,000 years before such behaviors emerged in modern humans.

If true, this scenario, based on a wealth of fossil finds in South Africa's Rising Star cave system, would have major implications for the dawn of human behavior as well as the abilities of our extinct cousins, *Homo naledi*. "We are facing a remarkable discovery here of hominids, nonhumans with brains a third of the size of [modern] humans … burying their dead, using symbols, and engaging in meaning-making activities," team leader Lee Berger of the University of the Witwatersrand said at a press conference. "Not only are [modern] humans not unique in their development of symbolic practices, but [we] may not have even invented such behaviors."

However, other researchers are overwhelmingly skeptical of the papers, which are in review at the online journal *eLife* and have been posted on bioRxiv. Researchers say they are wowed by the fossil finds, but the bodies could simply have fallen or been dumped into the pit and then been buried slowly by natural processes. Later hominins could have made the etchings, which are undated.

"I am more and more persuaded that something amazing happened here," given the wealth of skeletons, says paleoanthropologist María Martinón-Torres of the Spanish National Research Centre for Human Evolution. "But they have not met the test to show deliberate burial."

Berger's team made its first discovery in Rising Star in 2013: the bones of at least 15 individuals at the bottom of a chute 50 kilometers northwest of Johannesburg (*Science*, 11 September 2015, p. 1149). The team named the hominin a new species because it had a surprising mix of traits, such as a small brain and a globular skull. Researchers were also surprised by radiometric sediment dates showing how recently it lived: between 241,000 to 335,000 years ago—long after other human ancestors had evolved larger brains. As more bones emerged, Berger speculated they had been intentionally buried (*Science*, 12 May 2017, p. 571).

It was an explosive claim. The oldest widely accepted burial is of a modern human toddler dated to 78,000 years ago in a cave in Kenya, published in *Nature* in 2021 by Martinón-Torres and colleagues. Now, Berger says, he has evidence to prove his case.

In 2018, he was watching members of his team work in the caves, following the action by livestream because he was too big to crawl along the narrow passages to the chamber. Suddenly, the camera got bumped and went into infrared mode. In the black and white image, Berger could see the distinct edges of an "oval feature." "I think it's a grave," he told the excavators. "They said no."

Further excavation showed the oval to be a pit 8 centimeters deep and 50 by 25 centimeters in size, filled with 83 bone fragments and teeth from one *H. naledi* individual as well as a few fragments from other individuals. The bones were interspersed with orange-red stones, apparently from the layer below. Berger, who lost 20 kilograms to see the chamber himself, believes the stones show ancient gravediggers excavated the pit, digging up dirt and stones, setting them aside, and then using them to cover the body.

Elsewhere in the cave, the team found another set of very fragile bones. They removed two big chunks of sediment with bones inside, encased them in plaster, and took them to the lab. There, CT scans revealed 90 skeletal pieces and 51 dental pieces from three *H. naledi* individuals, including a child. The scans also revealed a tool-like stone object next to the child's hand. The researchers argue that the arrangement of the bones suggests the bodies were

carefully buried in a fetal or seated position.

They also discovered crosshatchings and other geometric shapes engraved on the cave walls; some were carved on top of others, indicating they were etched at different times. So far, the oldest undisputed symbolic art dates to 73,000 years at Blombos Cave in South Africa. But Berger, who presented the work this week at the Richard Leakey Memorial Conference at Stony Brook University, argues that the undated etchings must be the work of *H. naledi*, as no other hominin left traces in the caves.

He also says that in order to work in the dark, *H. naledi* had fire, although the papers include no evidence for this. But hominins controlled fire by at least 600,000 years ago. Berger has posted images online of charcoal and charred animal bones from the cave.

H. naledi had a brain of about 410 to 600 cubic centimeters, the size of a chimpanzee or *Australopithecus* brain. Taken together, the team's scenario suggests "that those of us that teach and write about the evolution of social behavior … need to step back and take humans off the pedestal," says co-author Agustín Fuentes of Princeton University. "Much of what we assumed was distinctly human, and distinctively caused by having a large brain, may not be [due to] either of those things."

Evolutionary biologist Clive Finlayson of the Gibraltar National Museum agrees. "It's not about brain size but how the brain is structured," he says. He thinks *H. naledi* "most likely" made the etchings because no remains of big-brained humans have been found in the cave. "It shows that *Homo naledi* had a level of self-awareness," Finlayson says.

But others say the team's evidence doesn't support such leaps. "The whole thing is unconvincing," says archaeologist João Zilhão of the University of Barcelona, who has proposed that Neanderthals made early cave art (*Science*, 23 February 2018, p. 852). He and others say natural processes could have positioned the *H. naledi* corpses. For example, the bodies could have been dumped into the chamber, or fallen or been washed in. Geologic movement and sedimentation, common in caves, could have moved the bones and covered them with dirt. The undated etchings, which resemble later carvings made by *H. sapiens* in South Africa, could have been made much later, adds archaeologist Paul Pettitt of Durham University.

At the moment, the data "sadly do not present a clear and unambiguous demonstration of a deliberate burial," says Pettitt, who is an expert on ancient burials. He says the team needs to finish excavating the pits and further scrutinize the bones and sediments to determine whether they were laid down simultaneously in a burial or at different times, and whether the bodies were disturbed later by geological movements. Martinón-Torres adds that it's unclear from the photos whether the bodies were laid down intact, as expected in a deliberate burial. "We don't have articulated bodies," she says.

Also missing is the wealth of fragmentary artifacts expected at a grave site, such as stone tools used to dig the pits. "There should be cultural debris that is typical of interments," says archaeologist Curtis Marean of Arizona State University. "They are going to have a terrific struggle making an iron clad case for pits and burials, given the extremely challenging work environment," he adds.

Researchers agree that by finding so many individuals of *H. naledi*, Berger and his team have uncovered a remarkable death scene. But without stronger evidence, *H. naledi* can't be given credit for inventing meaning-making behaviors, Pettitt and others say. "It's the hard science of excavation that's impressive here," Pettitt says. "We can and really should ignore speculation about *Homo naledi*'s apparent complex emotional intelligence and cognition." ■

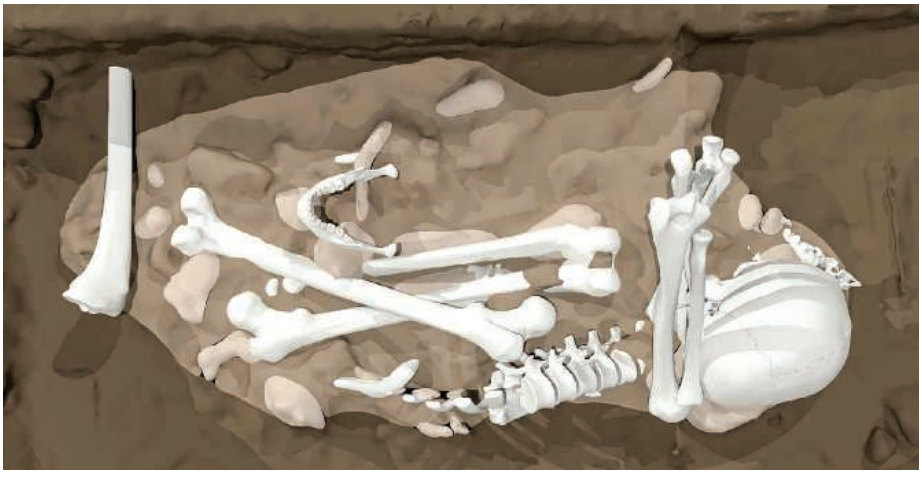


IMAGE: BERGER *ET AL.*, 2023

A digital reconstruction shows the positions of *Homo naledi* bones found in a shallow pit in a South African cave.

SCIENCE POLICY

Biden's pick for CDC wins praise

Former North Carolina health chief Mandy Cohen is also a Washington, D.C., veteran

By **Meredith Wadman**

Public health advocates are applauding the news that President Joe Biden intends to name Mandy Cohen, a physician and public health expert with broad government experience, to lead the U.S. Centers for Disease Control and Prevention (CDC).

Biden will appoint Cohen by the end of the month to replace current CDC Director Rochelle Walensky when she steps down, *The Washington Post* reported on 1 June. The White House did not respond to requests for comment and Cohen could not be reached.

Cohen, age 44, is an internist with an M.D. from Yale University and a master's in public health from Harvard University. She held increasingly high-level posts at the U.S. Centers for Medicare and Medicaid Services during former President Barack Obama's administration.

As North Carolina's secretary of health and human services from 2017 until 2022, Cohen won praise for steering the state's pandemic response with a transparent, bipartisan approach. She is now at Aledade, a company that works with primary health care practices.

Cohen is "savvy, courageous, passionate, and inspiring," says Nancy Messonnier, former head of CDC's respiratory diseases center who is now dean at the University of North Carolina's school of public health. In Washington, D.C., and North Carolina, "people really thought a lot of her," adds Georges Benjamin, executive director of the American Public Health Association.

A $9.2 billion, 13,000-employee agency, CDC took heat during the pandemic on everything from its rollout of COVID-19 tests to public communications. Walensky, an infectious disease physician who came to CDC from academia, launched an overhaul in August 2022 to improve communications and speed CDC's scientific publications. It's not clear whether Cohen, if appointed, would continue with those changes.

The CDC directorship does not currently require Senate confirmation. But the appointment is certain to be scrutinized by lawmakers from both parties. ■

carefully buried in a fetal or seated position.

They also discovered crosshatchings and other geometric shapes engraved on the cave walls; some were carved on top of others, indicating they were etched at different times. So far, the oldest undisputed symbolic art dates to 73,000 years at Blombos Cave in South Africa. But Berger, who presented the work this week at the Richard Leakey Memorial Conference at Stony Brook University, argues that the undated etchings must be the work of *H. naledi*, as no other hominin left traces in the caves.

He also says that in order to work in the dark, *H. naledi* had fire, although the papers include no evidence for this. But hominins controlled fire by at least 600,000 years ago. Berger has posted images online of charcoal and charred animal bones from the cave.

H. naledi had a brain of about 410 to 600 cubic centimeters, the size of a chimpanzee or *Australopithecus* brain. Taken together, the team's scenario suggests "that those of us that teach and write about the evolution of social behavior … need to step back and take humans off the pedestal," says co-author Agustín Fuentes of Princeton University. "Much of what we assumed was distinctly human, and distinctively caused by having a large brain, may not be [due to] either of those things."

Evolutionary biologist Clive Finlayson of the Gibraltar National Museum agrees. "It's not about brain size but how the brain is structured," he says. He thinks *H. naledi* "most likely" made the etchings because no remains of big-brained humans have been found in the cave. "It shows that *Homo naledi* had a level of self-awareness," Finlayson says.

But others say the team's evidence doesn't support such leaps. "The whole thing is unconvincing," says archaeologist João Zilhão of the University of Barcelona, who has proposed that Neanderthals made early cave art (*Science*, 23 February 2018, p. 852). He and others say natural processes could have positioned the *H. naledi* corpses. For example, the bodies could have been dumped into the chamber, or fallen or been washed in. Geologic movement and sedimentation, common in caves, could have moved the bones and covered them with dirt. The undated etchings, which resemble later carvings made by *H. sapiens* in South Africa, could have been made much later, adds archaeologist Paul Pettitt of Durham University.

At the moment, the data "sadly do not present a clear and unambiguous demonstration of a deliberate burial," says Pettitt, who is an expert on ancient burials. He says the team needs to finish excavating the pits and further scrutinize the bones and sediments to determine whether they were laid down simultaneously in a burial or at different times, and whether the bodies were disturbed later by geological movements. Martinón-Torres adds that it's unclear from the photos whether the bodies were laid down intact, as expected in a deliberate burial. "We don't have articulated bodies," she says.

Also missing is the wealth of fragmentary artifacts expected at a grave site, such as stone tools used to dig the pits. "There should be cultural debris that is typical of interments," says archaeologist Curtis Marean of Arizona State University. "They are going to have a terrific struggle making an iron clad case for pits and burials, given the extremely challenging work environment," he adds.

Researchers agree that by finding so many individuals of *H. naledi*, Berger and his team have uncovered a remarkable death scene. But without stronger evidence, *H. naledi* can't be given credit for inventing meaning-making behaviors, Pettitt and others say. "It's the hard science of excavation that's impressive here," Pettitt says. "We can and really should ignore speculation about *Homo naledi*'s apparent complex emotional intelligence and cognition." ■

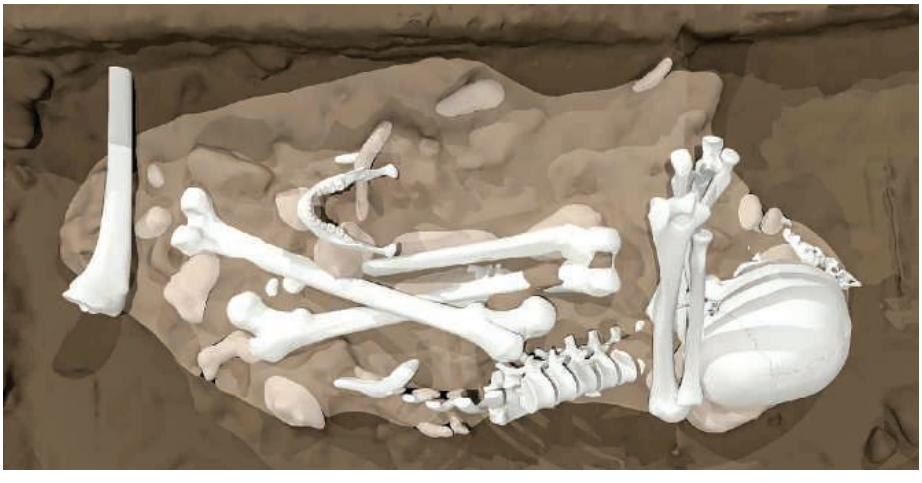


IMAGE: BERGER *ET AL.*, 2023

A digital reconstruction shows the positions of *Homo naledi* bones found in a shallow pit in a South African cave.

SCIENCE POLICY

Biden's pick for CDC wins praise

Former North Carolina health chief Mandy Cohen is also a Washington, D.C., veteran

By **Meredith Wadman**

Public health advocates are applauding the news that President Joe Biden intends to name Mandy Cohen, a physician and public health expert with broad government experience, to lead the U.S. Centers for Disease Control and Prevention (CDC).

Biden will appoint Cohen by the end of the month to replace current CDC Director Rochelle Walensky when she steps down, *The Washington Post* reported on 1 June. The White House did not respond to requests for comment and Cohen could not be reached.

Cohen, age 44, is an internist with an M.D. from Yale University and a master's in public health from Harvard University. She held increasingly high-level posts at the U.S. Centers for Medicare and Medicaid Services during former President Barack Obama's administration.

As North Carolina's secretary of health and human services from 2017 until 2022, Cohen won praise for steering the state's pandemic response with a transparent, bipartisan approach. She is now at Aledade, a company that works with primary health care practices.

Cohen is "savvy, courageous, passionate, and inspiring," says Nancy Messonnier, former head of CDC's respiratory diseases center who is now dean at the University of North Carolina's school of public health. In Washington, D.C., and North Carolina, "people really thought a lot of her," adds Georges Benjamin, executive director of the American Public Health Association.

A $9.2 billion, 13,000-employee agency, CDC took heat during the pandemic on everything from its rollout of COVID-19 tests to public communications. Walensky, an infectious disease physician who came to CDC from academia, launched an overhaul in August 2022 to improve communications and speed CDC's scientific publications. It's not clear whether Cohen, if appointed, would continue with those changes.

The CDC directorship does not currently require Senate confirmation. But the appointment is certain to be scrutinized by lawmakers from both parties. ■



Air samplers like this one at the U.K. National Physical Laboratory also capture nearby species' DNA.

ECOLOGY

Air pollution sensors can double as biodiversity monitors

Study points to cheap way to sniff out past and present species from DNA snagged in air filters

By **Elizabeth Pennisi**

Cyra Master • 6/6/23 5:28 PM
tweaked here and turned a line

Imagine being able to [illegible] that, based on tra[illegible] in the environme[illegible] and animals in th[illegible] weather forecast[illegible] wind, and temp[illegible] scientists might o[illegible] have said. But a paper published this week shows that routine, remote biodiversity monitoring may soon be a reality. By tapping into existing air quality monitoring sensors, researchers have discovered a cheap way to census nearby species.

"This paper is impressive because of its ingenuity," says Chris Jerde, an ecologist at the University of California, Santa Barbara who was not involved with the work. Julie Lockwood, an ecologist at Rutgers University, another outside expert, says the study "presents a very good opportunity to do large-scale biodiversity monitoring," something countries have agreed to perform as part of an international treaty called the Convention on Biological Diversity.

The new research builds on growing evidence that environmental DNA, or eDNA, is a powerful shortcut for cataloging species, reducing the need for labor-intensive traditional sampling methods such as trapping or directly observing individual plants or animals. "We are starting to see [that] eDNA is left everywhere," says Kristine Bohmann, a molecular ecologist at the [illegible]. Larger animals [illegible]les, and feathers, [illegible]letected eDNA in [illegible]tles, spiderwebs, [illegible]ts. Over the past [illegible]teams, including [illegible]rated they could [illegible]nts, insects, and mammals suspended in thin air.

James Allerton suspected that airborne DNA sampling might already be taking place as an accidental byproduct of pollution monitoring. A physicist at the National Physical Laboratory (NPL) in England, he helps oversee a 60-year-old effort by the U.K. government to monitor air quality by tracking heavy metals and other particles using hundreds of air samplers across the country. Allerton contacted Elizabeth Clare, a York University biologist whose team had shown that eDNA samples from air in a zoo captured the animal diversity within. Together with biologist Joanne Littlefair from Queen Mary University of London, the scientists agreed to see whether the country's air quality monitor filters had collected eDNA in addition to air pollutants.

The team extracted and sequenced DNA from a monitor at NPL in suburban London. They also gathered 8-month-old filters from a monitoring station in Scotland.

"We had no expectation that it would work," Clare recalls. And yet, the eDNA revealed the presence of 180 plants, fungi, insects, mammals, and amphibians, including 34 species of birds across the two sites, the team reports this week in *Current Biology*. The samples included DNA from threatened species such as hedgehogs and songbirds; ash, linden, and oak trees; and crops such as wheat and cabbage. "The fact that filters originally collected for other purposes can be repurposed for sensitive eDNA studies is astonishing," says Naiara Rodríguez-Ezpeleta, an eco-evolutionary geneticist at AZTI in Sukarrieta, Spain.

When it came to the number and kinds of species identified, "There was little difference at the two locations," Clare says, even though the Scottish samples had been in storage for 8 months. Researchers had thought the DNA would degrade over that period; its preservation "raises intriguing possibilities for eDNA analysis," Rodriguez-Ezpeleta says. Providing old filters are kept dry, which helps maintain the DNA's integrity, it might be possible to go back in time to track changes in biodiversity by looking at archived filters, Clare says.

That's exactly what Per Stenberg, a geneticist at Umeå University, has done in work yet to be published. His team has obtained DNA from 30 years' worth of archived air filters, removed weekly from sensors set up across Sweden during the Cold War to detect radioactive fallout from distant nuclear explosions. These samplers collected huge volumes of air and thus are very sensitive to low concentrations of contaminants, he explains. He and his colleagues found the DNA documented changes in the relative abundances of all types of organisms through time—trends that "correlate well with more traditional monitoring data," and could reflect the influence of climate change, he says.

Whether the many thousands of air filters monitoring pollution around the world can be a consistent and reliable way to detect changes in biodiversity isn't clear. "Detecting some species sometimes is not the same as detecting a signal of biodiversity change representative for a larger area," says Fabian Roger, an ecologist at ETH Zürich, who is testing the potential of air samplers to detect insects that may cause crop or tree damage. Researchers don't know how close to a sensor an organism needs to be for its DNA to be captured, or whether some organisms are easier to detect than others. "The devil is in the details," says Einar Eg Nielsen, a molecular ecologist at the Technical University of Denmark who was not involved with the study.

"The potential could be great," Roger adds. "But it's still to be demonstrated." ■

NEUROSCIENCE

No trip needed for psychedelics to lift mood?

LSD and psilocin molecules bind to antidepressant drug targets in the brain, study shows

By **Cathleen O'Grady**

Psychedelic drugs, best known for causing hallucinations, can also lift users' moods, preliminary results from clinical trials suggest. But the risks that come with the trip are an obstacle to using the drugs as antidepressants. Hallucinations might trigger psychosis in people with certain risk factors, and because of their unpredictable effects, clinicians have to closely monitor patients as they take the drugs.

Now, researchers think they may be able to take hallucinations out of the equation. LSD and psilocin—the psychedelic compound in magic mushrooms—can produce an antidepressant response in mice through a molecular mechanism that is completely separate from the one responsible for hallucinogenic effects, the team reported this week in *Nature Neuroscience*. The results, they say, pave the way to developing psychedelic-like drugs that could treat depression without hallucinations.

The work is rigorous and careful, says Revathy Chottekalapanda, a neuroscientist at Weill Cornell Medicine, and the results are intriguing. But Chottekalapanda and others emphasize that the path from demonstrating these kinds of effects in basic research to developing drugs that are effective in humans could be treacherous.

Research into the effects of psychedelics has focused heavily on the serotonin 2A receptor in the brain, because the drugs produce hallucinations by binding to this receptor. But psychedelics are "infamous for being superpromiscuous drugs" says Rafael Moliner, a neuroscience Ph.D. student at the University of Helsinki and lead author of the paper. "They interact with a lot of receptors."

In a 2021 paper in *Cell*, Moliner and his colleagues had shown that classical antidepressants work via the receptor for a signaling molecule called brain-derived neurotrophic factor (BDNF). When BDNF binds with this receptor, called TrkB, it sets off the cellular processes that drive neuroplasticity: the growth and reorganization of connections between brain cells. Antidepressant drugs also bind to TrkB, the researchers found—not taking the role of BDNF, but giving its signaling process a helping hand and boosting neuroplasticity, thought to be an important part of the antidepressant response.

In the new study, the researchers show that psychedelic drugs have a similar mechanism. First, they demonstrated that LSD and psilocin bind to TrkB in cells in a dish—and do so 1000 times more strongly than classical antidepressants. They also found the drugs spurred rat and mouse neurons to develop an increased number of neural connections, indicating increased neuroplasticity.



Psychedelic drugs such as psilocin, from magic mushrooms, act on a receptor involved in the growth and reorganization of connections between brain cells.

PHOTO: JAMES MACDONALD/BLOOMBERG/GETTY IMAGES

These findings suggested that psychedelics might have an antidepressant effect by acting on TrkB, even without triggering the serotonin receptor. So the team gave mice LSD alongside a compound that blocks the drug from binding to the serotonin 2A receptor, to see whether this would reduce depressionlike behavior without inducing hallucinations. With humans, you can simply ask whether someone experienced hallucinations, "but with mice, it's not that easy," Moliner says.

His team took advantage of the fact that rodents on a hallucinogenic drug normally twitch their heads as if they are shaking off a fly. Mice given LSD along with the serotonin 2A blocker did not display the head-twitch response. But they did show an improvement in the "freezing" behavior that researchers use as an analog of human depression, suggesting the drugs were still having an antidepressant effect.

These results may prompt more interest in finding drugs that exclusively target TrkB, says Gabriel Jacobs, a clinical pharmacologist at the Centre for Human Drug Research, and in investigating whether hallucinations are necessary for psychedelics' therapeutic effects in humans.

Others warn that animal studies of depression often do not translate well to humans. "Hundreds of papers" have found promising mechanisms for antidepressant treatment in mice, "none of which made it to the development of new pharmacological drugs that do better than gold-standard treatments for depression," says Eiko Fried, a clinical psychologist at Leiden University. And the promise of psychedelics in clinical trials is not clear-cut. They do seem to help people feel better, but it's not possible to conceal from patients whether they have taken a psychedelic or placebo, says Balázs Szigeti, a psychedelics researcher at Imperial College London.

Senior author Eero Castrén, a neuroscientist at Helsinki, believes his team's work may open up promising pathways for developing new, psychedelic-inspired antidepressants. But, he adds, "This will be quite a long journey." Even if such drugs seemed effective in animals, he says, extensive human tests would be needed to confirm that revamped psychedelics both relieve depression and are not hallucinogenic. "It's not something that is going to happen in the next 5 years." ■

SCHOLARLY PUBLISHING

How an Indian dental school climbed the ranks

Prodigious self-citation helps Saveetha Dental College top global lists, investigation finds

By **Frederik Joelving, Retraction Watch**

Each year, the 500 undergraduates at Saveetha Dental College in Chennai, India, participate in 4-hour exams that require them to write a 1500-word manuscript on research they have conducted. After faculty and students review and revise the papers, they use an online tool to add references to previously published work. Many of the papers are then submitted to and published by journals; the process contributed to the more than 1400 scholarly works the dental school published last year.

Saveetha, which calls itself a "pioneer in undergraduate publications," says the exercise is designed to help every student gain practical research experience—as well as at least 10 publications listed in Scopus, the vast literature database maintained by the publisher Elsevier. The college's website boasts that one Saveetha student published 24 papers.

But the torrent of undergraduate manuscripts—on topics including fruit intake by students and awareness of mental health among teenagers—also appears to serve a less savory purpose, an investigation by Retraction Watch has found. By systematically citing other papers published by Saveetha faculty—including papers on completely unrelated topics—the undergraduate publications have helped dramatically inflate the number of citations, a key measure of academic merit, linked to Saveetha.

This year, the college topped the global list of the most cited institutions in dentistry for the second straight year, according to QS World University Rankings. That metric helped secure the school's place "among the top 15 dental institutions in the world," Saveetha announced recently. It also propelled it to the top of India's national list of dental schools.

Self-citation has long been a popular—if controversial—shortcut for scientists looking to boost their academic standing. But the dental college, part of the larger Saveetha Institute of Medical and Technical Sciences (SIMATS), appears to have quietly pursued self-citation at an industrial scale, garnering thousands of mentions in the scientific literature in the process.

Dental college officials say they are unaware of any effort to systematically use self-citation to boost the institution's reputation. "We don't want anything to happen in an unethical way, that is our policy," says Sheeja Varghese, SIMATS's registrar and a professor at the dental school.



But others, including members of Saveetha's faculty, are skeptical. Adith Venugopal, an adjunct associate professor, has seen his own papers rack up more than 1000 citations since joining the dental school in 2020. Nearly all are from Saveetha. "I realized that this may be something like a university trying to cite itself more for gaining some rankings or something of that sort," he says, adding that he sees school officials "posting regularly that they are very highly published."

Outsiders say Saveetha's paper-writing strategy is specifically designed to make the self-citations appear legitimate. "It's meticulously done to mislead the reader and not to be identified by the system as self-citation," asserts Theodore Eliades, a professor of orthodontics at the University of Zürich and editor-in-chief of *The Korean Journal of Orthodontics*.

Saveetha's strategy involves inserting a single, relatively vague sentence into thousands of student papers, followed by references to up to two dozen articles written by Saveetha faculty, a review of publications indexed by Google Scholar suggests. For example, a 2022 paper about different techniques for machining steel—published by a student and a faculty member at the Saveetha School of Engineering in *Materials Today: Proceedings*—includes this seemingly benign language in its introduction: "Our team has a wider research knowledge and experience that has been converted into high impact publications." It is followed by more than a dozen citations of unrelated Saveetha publications.

It is not clear when the citations are added or who adds them. But they help each of the referenced papers climb the citation ranks. One cited paper, for example, is a 2019 study by two of the dental school's professors in the *Journal of Oral Biology and Craniofacial Research*, which describes a geometrical method for classifying the shapes of human faces—a topic with no obvious connection to machining steel. It has garnered 169 citations according to Google Scholar; all but four are from papers written by Saveetha authors.

Variants of the vague phrase—describing a research team with "a wealth of research and knowledge," "rich experience," "extensive knowledge," or "numerous original studies"—appear in at least 138 articles that cite the face study and whose text could be accessed by Google Scholar.

Varghese says she is "not aware" of the self-reinforcing citation pattern. But it appears to be benefiting her own work, too. Citations of her papers started to climb in 2019, mirroring a faculty-wide trend at the school. Her papers have now been cited 2310 times according to Scopus,

and more than 4300 times according to Google Scholar—nearly always by other Saveetha publications.

Venugopal, who is also an associate professor at the University of Puthisastra, says he first became aware of the widespread self-citation last year. He emailed Saveetha administrators asking for an explanation, but has received no reply. Meanwhile, he regularly gets alerts of new citations—"again another paper by Saveetha."

Elsevier says it is reviewing Saveetha's citation pattern. A different citation-tracking firm, Clarivate, is also paying attention to the school. David Pendlebury, head of research analysis at Clarivate's Institute for Scientific Information, which maintains the citation database Web of Science, declined to comment specifically on SIMATS. But in an email he noted that, over the past few years, the firm noticed a 17-fold increase in publications linked to the school, many in journals that Clarivate no longer includes in its database because of problematic editorial standards or other issues.

Self-citation has long been a concern in science, although its use appears to be declining in many nations, says Alberto Baccini of the University of Siena, an author of a recent preprint examining self-citation trends in 50 countries. He said the findings from Saveetha might help explain why one broad measure of self-citation is not dropping in India and China. "We cannot exclude that institutional self-citations are the source of the Indian anomaly in our data," Baccini said.

Academics in India say citation gaming can be an attractive way for an institution to boost its rankings, which can strengthen fundraising and enable schools to hike tuition. "It's all for fetching some good revenue," says a professor of orthodontics at an Indian university who requested anonymity for fear of reprisals. Saveetha is among India's most expensive dental schools, he notes, charging about $10,000 a year.

Some researchers say self-citation is not their only concern about Saveetha's practices. "I would worry much more about large numbers of low-quality papers" generated by its undergraduates, says Gautam Menon, a professor of physics and biology at Ashoka University. And Stuart Macdonald, a visiting professor at the University of Leicester who studies academic publishing, believes Saveetha's use of students to boost its standing is "coercive." The practice is "nasty," Macdonald says, "particularly if their degrees are dependent on it." ■

Frederik Joelving, based in Denmark, is an editor for Retraction Watch. This story was produced in collaboration with Retraction Watch.



PHOTO: PAUL SANCYA/GETTY IMAGES

Researchers developing next-generation COVID-19 vaccines want to test them against the existing ones (above), which are plentiful but unavailable for studies.

COVID-19

Companies hoard COVID-19 vaccines, stalling future research

Developing better products requires comparisons with existing shots that Pfizer and Moderna won't allow

By **Jon Cohen**

The U.S. government has tens of millions of unused doses of messenger RNA (mRNA) COVID-19 vaccines, regularly trashing shots as they pass their expiration dates. It's a dismal reflection on recent vaccine uptake, but it's also a serious roadblock for scientists testing and developing vaccines that could protect against future variants of SARS-CoV-2—and the next pandemic. Developers need existing vaccines as a benchmark to compare with new candidates. But government contracts with the vaccinemakers, and the companies' own policies, prohibit the use of the vaccines for research purposes.

"At this stage of the game, with millions of vaccines on the verge of being thrown away, this seems crazy," says Nicole Lurie, U.S. director of the Coalition for Epidemic Preparedness Innovations (CEPI). The situation is so dire that one startup has created mimics of the mRNA vaccines in use to help researchers improve their formulations.

Most researchers working on next-generation vaccines hope to create products that stimulate broader immunity to protect people from all sarbecoviruses, a group that includes variants of SARS-CoV-2, SARS-CoV-1, and related viruses found in bats and other wild animals that might spill over to humans. As part of the development process, researchers want to compare their candidates in animal models with the proven Moderna and Pfizer mRNA vaccines to see how immune responses to the candidate and existing vaccines stack up. They also want to give animals both kinds of vaccines and "challenge" them with different SARS-CoV-2 variants.

CEPI, which aims to speed the development of vaccines, has invested $230 million in 13 such vaccine candidates. The National Institute of Allergy and Infectious Diseases (NIAID) has committed nearly $60 million to seven other academic teams working on similar projects that aim to protect against a wide range of coronaviruses. Four groups receiving support from either CEPI or NIAID told *Science* that long-existing difficulties obtaining comparator vaccines have slowed their progress. "The acquisition of those direct comparators has been very difficult and challenging," says In-Kyu Yoon, a CEPI director.

Neither NIAID nor the Biomedical Advanced Research and Development Author-

and more than 4300 times according to Google Scholar—nearly always by other Saveetha publications.

Venugopal, who is also an associate professor at the University of Puthisastra, says he first became aware of the widespread self-citation last year. He emailed Saveetha administrators asking for an explanation, but has received no reply. Meanwhile, he regularly gets alerts of new citations—"again another paper by Saveetha."

Elsevier says it is reviewing Saveetha's citation pattern. A different citation-tracking firm, Clarivate, is also paying attention to the school. David Pendlebury, head of research analysis at Clarivate's Institute for Scientific Information, which maintains the citation database Web of Science, declined to comment specifically on SIMATS. But in an email he noted that, over the past few years, the firm noticed a 17-fold increase in publications linked to the school, many in journals that Clarivate no longer includes in its database because of problematic editorial standards or other issues.

Self-citation has long been a concern in science, although its use appears to be declining in many nations, says Alberto Baccini of the University of Siena, an author of a recent preprint examining self-citation trends in 50 countries. He said the findings from Saveetha might help explain why one broad measure of self-citation is not dropping in India and China. "We cannot exclude that institutional self-citations are the source of the Indian anomaly in our data," Baccini said.

Academics in India say citation gaming can be an attractive way for an institution to boost its rankings, which can strengthen fundraising and enable schools to hike tuition. "It's all for fetching some good revenue," says a professor of orthodontics at an Indian university who requested anonymity for fear of reprisals. Saveetha is among India's most expensive dental schools, he notes, charging about $10,000 a year.

Some researchers say self-citation is not their only concern about Saveetha's practices. "I would worry much more about large numbers of low-quality papers" generated by its undergraduates, says Gautam Menon, a professor of physics and biology at Ashoka University. And Stuart Macdonald, a visiting professor at the University of Leicester who studies academic publishing, believes Saveetha's use of students to boost its standing is "coercive." The practice is "nasty," Macdonald says, "particularly if their degrees are dependent on it." ■

Frederik Joelving, based in Denmark, is an editor for Retraction Watch. This story was produced in collaboration with Retraction Watch.

PHOTO: PAUL SANCYA/GETTY IMAGES



Researchers developing next-generation COVID-19 vaccines want to test them against the existing ones (above), which are plentiful but unavailable for studies.

COVID-19

Companies hoard COVID-19 vaccines, stalling future research

Developing better products requires comparisons with existing shots that Pfizer and Moderna won't allow

By **Jon Cohen**

The U.S. government has tens of millions of unused doses of messenger RNA (mRNA) COVID-19 vaccines, regularly trashing shots as they pass their expiration dates. It's a dismal reflection on recent vaccine uptake, but it's also a serious roadblock for scientists testing and developing vaccines that could protect against future variants of SARS-CoV-2—and the next pandemic. Developers need existing vaccines as a benchmark to compare with new candidates. But government contracts with the vaccinemakers, and the companies' own policies, prohibit the use of the vaccines for research purposes.

"At this stage of the game, with millions of vaccines on the verge of being thrown away, this seems crazy," says Nicole Lurie, U.S. director of the Coalition for Epidemic Preparedness Innovations (CEPI). The situation is so dire that one startup has created mimics of the mRNA vaccines in use to help researchers improve their formulations.

Most researchers working on next-generation vaccines hope to create products that stimulate broader immunity to protect people from all sarbecoviruses, a group that includes variants of SARS-CoV-2, SARS-CoV-1, and related viruses found in bats and other wild animals that might spill over to humans. As part of the development process, researchers want to compare their candidates in animal models with the proven Moderna and Pfizer mRNA vaccines to see how immune responses to the candidate and existing vaccines stack up. They also want to give animals both kinds of vaccines and "challenge" them with different SARS-CoV-2 variants.

CEPI, which aims to speed the development of vaccines, has invested $230 million in 13 such vaccine candidates. The National Institute of Allergy and Infectious Diseases (NIAID) has committed nearly $60 million to seven other academic teams working on similar projects that aim to protect against a wide range of coronaviruses. Four groups receiving support from either CEPI or NIAID told *Science* that long-existing difficulties obtaining comparator vaccines have slowed their progress. "The acquisition of those direct comparators has been very difficult and challenging," says In-Kyu Yoon, a CEPI director.

Neither NIAID nor the Biomedical Advanced Research and Development Author-

ity, which purchased and distributes the Pfizer and Moderna vaccines, responded to *Science*'s questions.

The original efficacy trials of the Pfizer and Moderna mRNA vaccines compared those vaccines with placebo shots. But when those products received emergency use authorizations in December 2020, they became the standard of comparison in any future efficacy trials. The initial push for comparators came from researchers developing COVID-19 vaccine candidates based on technologies other than mRNA, such as viral vectors or nasal delivery.

Now, groups aiming for more broadly protective vaccines need the comparators to improve the design of their own candidates. The first Pfizer and Moderna vaccines today have full approval from the Food and Drug Administration (FDA), a status that usually would allow researchers to purchase and study them. But because of the emergency pandemic response, the U.S. government owns all the product and, by contract with the companies, cannot provide it for research purposes. The contracts specify that the vaccines can only be used for immunizing humans; in theory, violations could create liability issues for the companies.

"This is an eminently solvable issue that must be addressed now."
***Science Held Hostage* report**, PrEP4All

The original doses of the Pfizer and Moderna vaccines, which contain the surface protein from the initial strain of SARS-CoV-2, are of limited value as comparators because the evolution of the virus has made them obsolete. The two companies now make "bivalent" products that mix in a surface protein from the Omicron variant. But they, too, are locked up under the government purchase agreements.

The companies could make their vaccines available. But Pfizer and Moderna would not discuss the issue with *Science*, although Pfizer did confirm that its bivalent vaccine is not for sale in any private market. "We are not currently providing it directly to other research organizations, with the exception of certain government-funded research organizations, outside of our own targeted clinical development program," the company stated.

Philip Krause, who for 11 years was deputy director of the FDA division that oversees vaccines, says he can understand why a company with vaccines on the market might look askance at sharing them with a potential competitor. "But obviously, it's something that works substantially against public health," says Krause, who left FDA in 2021 and now is a vaccine consultant. "If they're throwing doses away, or if those doses can't really be given to anyone anymore, that's all the worse."

PrEP4All, a nonprofit that advocates for improved public health responses to the COVID-19 pandemic, in April published a sharply critical report based on a 6-month investigation that involved many stakeholders and reviewed government contracts. "This an eminently solvable issue that must be addressed now—before [a] new crisis," concludes the report, titled *Science Held Hostage*.

Some have taken to workarounds. Duane Wesemann, an immunologist at Brigham and Women's Hospital who has one of the NIAID multiyear grants to develop a pan-sarbecovirus vaccine, says that "after many requests were denied on many fronts for many months" for comparators to use in mouse studies, his group resorted to using expired Pfizer mRNA vaccines. "It's not ideal, but in mice the vaccine works very well," Wesemann says.

In another compromise, Helix Biotech has helped frustrated pancoronavirus researchers by creating generic versions of the Pfizer and Moderna vaccines using publicly available formulas. Helix's clients include NIAID, which provides the comparators to researchers it funds. Graham Taylor, who started Helix last year, says labs have shown that their mimics trigger similar immune responses to the approved vaccines.

The Helix products cannot serve as comparators to help pan-sarbecovirus vaccines win FDA approval. Krause says regulators might be satisfied if human trials showed a pan-sarbecovirus vaccine triggered immune responses similar to those elicited by the best available approved products, a concept known as immunobridging. Or they might require developers to stage head-to-head clinical trials of proven products and experimental ones that use reduction in mild COVID-19 disease as the endpoint. Either way, at the moment, Moderna or Pfizer would have to allow the use of their bivalent vaccines.

Although animal studies could test the breadth of a pan-sarbecovirus vaccine's protection, delivering on its promise would require exposure to new variants or even new coronaviruses. That could only happen in real-world effectiveness studies that take place after a new virus starts to spread.

The boxes of unused COVID-19 vaccine now sitting in freezers point to one more hurdle for pan-sarbecovirus vaccines, Krause says: "Who will believe they need them?" ■

BIOMEDICINE

Can 'toxic' bilirubin be put to medical use?

New view of molecule's good side inspires plans to test it as treatment for a variety of illnesses

By **Mitch Leslie**

Generations of medical and biology students have been instilled with a dim view of bilirubin. Spawned when the body trashes old red blood cells, the molecule is harmful refuse and a sign of illness. High blood levels cause jaundice, which turns the eyes and skin yellow and can signal liver trouble. Newborns can't process the compound, and although high levels normally subside, a persistent surplus can cause brain damage.

Yet later this year up to 40 healthy Australian volunteers may begin receiving infusions of the supposedly good-for-nothing molecule. They will be participating in a phase 1 safety trial, sponsored by the South Korean company Bilix, that could pave the way for testing bilirubin as a treatment in organ transplant recipients and patients with conditions such as multiple sclerosis and stroke. The company's ambitions reflect a new view of bilirubin that emerged as researchers amassed lab, animal, and epidemiological data suggesting it plays a vital role in the body as a fierce antioxidant and anti-inflammatory.

"There's lots of levels of evidence that it's more than just a metabolic waste product," says molecular epidemiologist Laura Horsfall of University College London.

Bilirubin naturally arises when the spleen and other parts of the body dispose of heme, the core of the hemoglobin molecule in red blood cells. Heme is highly toxic; bilirubin, the breakdown product in mammals, is less so. Each week the average person generates about 2 grams of the yellowish substance, most of which the liver dumps into the intestines for elimination from the body.

There have been hints that bilirubin plays physiological roles. When birds and reptiles break down heme, Horsfall says, they produce a different molecule that is nontoxic and soluble in body fluids. That mammals

ity, which purchased and distributes the Pfizer and Moderna vaccines, responded to *Science*'s questions.

The original efficacy trials of the Pfizer and Moderna mRNA vaccines compared those vaccines with placebo shots. But when those products received emergency use authorizations in December 2020, they became the standard of comparison in any future efficacy trials. The initial push for comparators came from researchers developing COVID-19 vaccine candidates based on technologies other than mRNA, such as viral vectors or nasal delivery.

Now, groups aiming for more broadly protective vaccines need the comparators to improve the design of their own candidates. The first Pfizer and Moderna vaccines today have full approval from the Food and Drug Administration (FDA), a status that usually would allow researchers to purchase and study them. But because of the emergency pandemic response, the U.S. government owns all the product and, by contract with the companies, cannot provide it for research purposes. The contracts specify that the vaccines can only be used for immunizing humans; in theory, violations could create liability issues for the companies.

> **"This is an eminently solvable issue that must be addressed now."**
> ***Science Held Hostage* report**, PrEP4All

The original doses of the Pfizer and Moderna vaccines, which contain the surface protein from the initial strain of SARS-CoV-2, are of limited value as comparators because the evolution of the virus has made them obsolete. The two companies now make "bivalent" products that mix in a surface protein from the Omicron variant. But they, too, are locked up under the government purchase agreements.

The companies could make their vaccines available. But Pfizer and Moderna would not discuss the issue with *Science*, although Pfizer did confirm that its bivalent vaccine is not for sale in any private market. "We are not currently providing it directly to other research organizations, with the exception of certain government-funded research organizations, outside of our own targeted clinical development program," the company stated.

Philip Krause, who for 11 years was deputy director of the FDA division that oversees vaccines, says he can understand why a company with vaccines on the market might look askance at sharing them with a potential competitor. "But obviously, it's something that works substantially against public health," says Krause, who left FDA in 2021 and now is a vaccine consultant. "If they're throwing doses away, or if those doses can't really be given to anyone anymore, that's all the worse."

PrEP4All, a nonprofit that advocates for improved public health responses to the COVID-19 pandemic, in April published a sharply critical report based on a 6-month investigation that involved many stakeholders and reviewed government contracts. "This an eminently solvable issue that must be addressed now—before [a] new crisis," concludes the report, titled *Science Held Hostage*.

Some have taken to workarounds. Duane Wesemann, an immunologist at Brigham and Women's Hospital who has one of the NIAID multiyear grants to develop a pan-sarbecovirus vaccine, says that "after many requests were denied on many fronts for many months" for comparators to use in mouse studies, his group resorted to using expired Pfizer mRNA vaccines. "It's not ideal, but in mice the vaccine works very well," Wesemann says.

In another compromise, Helix Biotech has helped frustrated pancoronavirus researchers by creating generic versions of the Pfizer and Moderna vaccines using publicly available formulas. Helix's clients include NIAID, which provides the comparators to researchers it funds. Graham Taylor, who started Helix last year, says labs have shown that their mimics trigger similar immune responses to the approved vaccines.

The Helix products cannot serve as comparators to help pan-sarbecovirus vaccines win FDA approval. Krause says regulators might be satisfied if human trials showed a pan-sarbecovirus vaccine triggered immune responses similar to those elicited by the best available approved products, a concept known as immunobridging. Or they might require developers to stage head-to-head clinical trials of proven products and experimental ones that use reduction in mild COVID-19 disease as the endpoint. Either way, at the moment, Moderna or Pfizer would have to allow the use of their bivalent vaccines.

Although animal studies could test the breadth of a pan-sarbecovirus vaccine's protection, delivering on its promise would require exposure to new variants or even new coronaviruses. That could only happen in real-world effectiveness studies that take place after a new virus starts to spread.

The boxes of unused COVID-19 vaccine now sitting in freezers point to one more hurdle for pan-sarbecovirus vaccines, Krause says: "Who will believe they need them?" ■

BIOMEDICINE

Can 'toxic' bilirubin be put to medical use?

New view of molecule's good side inspires plans to test it as treatment for a variety of illnesses

By **Mitch Leslie**

Generations of medical and biology students have been instilled with a dim view of bilirubin. Spawned when the body trashes old red blood cells, the molecule is harmful refuse and a sign of illness. High blood levels cause jaundice, which turns the eyes and skin yellow and can signal liver trouble. Newborns can't process the compound, and although high levels normally subside, a persistent surplus can cause brain damage.

Yet later this year up to 40 healthy Australian volunteers may begin receiving infusions of the supposedly good-for-nothing molecule. They will be participating in a phase 1 safety trial, sponsored by the South Korean company Bilix, that could pave the way for testing bilirubin as a treatment in organ transplant recipients and patients with conditions such as multiple sclerosis and stroke. The company's ambitions reflect a new view of bilirubin that emerged as researchers amassed lab, animal, and epidemiological data suggesting it plays a vital role in the body as a fierce antioxidant and anti-inflammatory.

"There's lots of levels of evidence that it's more than just a metabolic waste product," says molecular epidemiologist Laura Horsfall of University College London.

Bilirubin naturally arises when the spleen and other parts of the body dispose of heme, the core of the hemoglobin molecule in red blood cells. Heme is highly toxic; bilirubin, the breakdown product in mammals, is less so. Each week the average person generates about 2 grams of the yellowish substance, most of which the liver dumps into the intestines for elimination from the body.

There have been hints that bilirubin plays physiological roles. When birds and reptiles break down heme, Horsfall says, they produce a different molecule that is nontoxic and soluble in body fluids. That mammals

opt for bilirubin even though it is toxic and insoluble suggests it may offer some benefits.

One may be its power to neutralize reactive oxygen species (ROS), destructive byproducts of metabolism that can injure DNA and other important cellular molecules. When mixed with lab-grown cells, bilirubin shields them from ROS, and mice lacking the molecule are more vulnerable to oxidative damage. "Bilirubin is the most potent antioxidant substance in the body," says hepatologist Claudio Tiribelli of the Italian Liver Foundation. It also tamps down damaging inflammation. For example, scientists have found that bilirubin may steer immune cells called macrophages to curtail their secretion of inflammatory molecules.

And research by drug designer Terry Hinds of the University of Kentucky and physiologist David Stec of the University of Mississippi Medical Center suggests bilirubin acts as a hormone. In cultured cells, it stimulates a key receptor called PPARalpha that helps control metabolism and body weight. Injections of the molecule slimmed down mice eating a high-fat diet, the scientists reported in 2016 in *PLOS ONE*.

"Nature puts almost everything to use, and even this 'waste product' is being used," says bilirubin biochemist David Stevenson of the Stanford University School of Medicine.

Some people might be reaping more benefits than others. About 10% of humans carry gene variants that result in slightly high bilirubin levels. For instance, people with a condition known as Gilbert syndrome don't make enough of a protein that helps prepare bilirubin for excretion. As a result, their blood concentrations of the molecule can be more than twice the upper limit of normal. But they don't have jaundice or any serious symptoms.

More striking, multiple studies suggest people who have moderately elevated bilirubin levels—whether because of Gilbert syndrome or other causes—are less likely to develop a plethora of illnesses, including heart disease, inflammatory bowel disease, diabetes, and many types of cancer. On the flip side, people with relatively low bilirubin levels are more vulnerable to these diseases. "The idea that bilirubin is protective is very well supported," Tiribelli says.

More evidence comes from Mendelian randomization studies, which compare the health of people who carry different gene variants to tease out cause and effect. In 2020, Horsfall and her colleagues analyzed data on more than 377,000 people from the UK Biobank, a national health registry. They discovered that people with two copies of a gene version that leads to higher bilirubin levels had a 17% lower risk of developing lung cancer, and the effect was even larger in smokers. Reactive oxygen molecules flood the lungs, and the extra bilirubin may help counteract their effects, Horsfall says.



Perhaps best known for producing jaundice, bilirubin is also a potent antioxidant and anti-inflammatory agent.

PHOTO: ARIF BISWAS/SHUTTERSTOCK

Suggestions that the molecule has a positive side have encouraged researchers to try to boost its levels in the past. One of the first was physician Philip Hench of the Mayo Clinic, who in the 1930s noticed that his rheumatoid arthritis (RA) patients improved when they developed jaundice. He tried to replicate the effect in several ways, including by injecting patients with bilirubin mixed with another molecule, but the results were inconsistent. (Hench later shared a Nobel Prize for identifying cortisone and treating RA with it.)

Such early efforts to turn bilirubin into a therapy faltered because of its balky nature. The molecule is insoluble and degraded by light, and injected doses are rapidly broken down or excreted.

Bilix's co-founder, chemist Sangyong Jon of the Korea Advanced Institute of Science and Technology, and colleagues overcame these problems by affixing the water-soluble molecule polyethylene glycol to one end of bilirubin. As they reported in 2016, in water the hybrid molecules huddle to form nanoparticles. These tiny spheres make the bilirubin soluble, protect it from light, and extend its life span in the blood from less than 20 minutes to several hours, says Myung Kim, Bilix's co-founder and CEO. They can also enter immune cells, allowing their bilirubin cargo to combat reactive oxygen species inside these cells and thereby fight inflammation.

A chemist at Bilix also figured out how to synthesize bilirubin, overcoming another hurdle. Slaughterhouse animals have provided most bilirubin for research, but this source contains three slightly different varieties of bilirubin and is not suitable for therapies, Kim says. "If you can't synthesize bilirubin, there is no company," he says.

Animal studies suggest bilirubin-toting nanoparticles are effective against a range of conditions. One is graft-versus-host disease (GVHD), a serious complication of organ and bone marrow transplants in which immune cells in the transferred tissue attack the recipient. "We are always looking for new therapies to prevent it," says Jin Seon Im, a clinician at the University of Texas MD Anderson Cancer Center. Because bilirubin eases inflammation, she and her colleagues decided to test the nanoparticles in mice that developed GVHD after bone marrow transplants. They found that the particles reduced tissue damage and more than doubled the animals' survival.

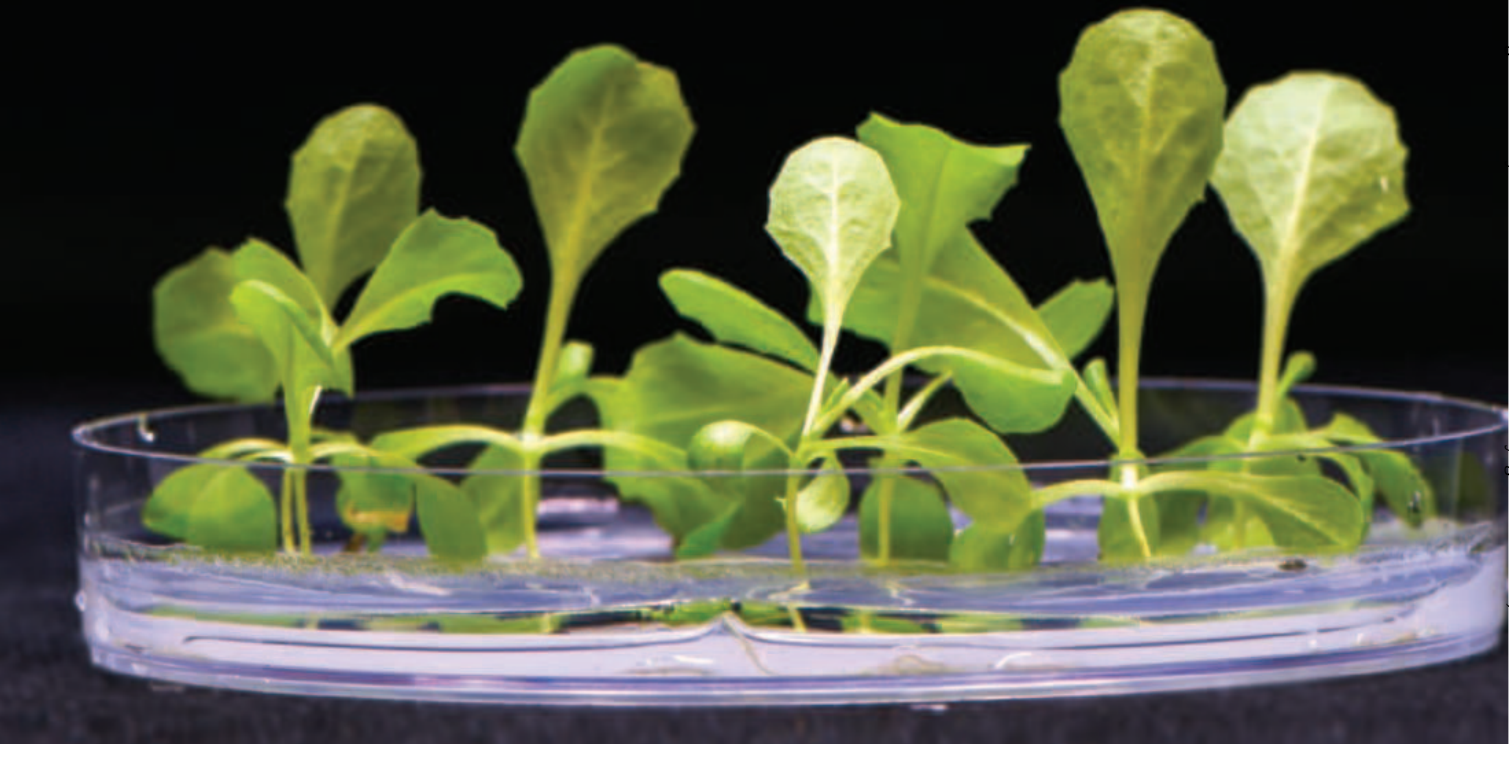
Bilix chose Australia for its phase 1 trial in part because the country's ethnic composition is similar to that of the United States, which would make it easier to get permission for future U.S. trials from the Food and Drug Administration. If the nanoparticles prove safe in the trial, due to launch in November, Kim says the company wants to test whether they can prevent tissue damage in transplanted kidneys, which are inundated by reactive oxygen species after their blood circulation resumes. Other potential targets include the skin condition atopic dermatitis, asthma, multiple sclerosis, and stroke.

Bilix's nanoparticles aren't the only way to boost bilirubin levels. Exercise, certain foods, and a number of drugs, including statins, can all have that effect. But the old view of bilirubin as molecular trash is still holding back research on how to take advantage of its salutary effects, Stec says. "There's an opportunity here we could be missing." ■

LET THERE BE DARK

Crops grown without sunlight could help feed astronauts bound for Mars, and someday supplement dinner plates on Earth

By **Robert F. Service**, *in Riverside, California*



Lettuce grown on acetate could be a step toward plants that can grow in the dark by thriving on chemical rather than solar energy.

For the first astronauts to visit Mars, what to eat on their 3-year mission will be one of the most critical questions. It's not just a matter of taste. According to one recent estimate, a crew of six would require an estimated 10,000 kilograms of food for the trip. NASA—which plans to send people to Mars within 2 decades—could stuff a spacecraft with prepackaged meals and launch additional supplies to the Red Planet in advance for the voyage home. But even that wouldn't completely solve the problem.

Micronutrients, including many vitamins, break down over months and will need to be synthesized en route. And food isn't just a source of calories, says Jennifer Fogarty, chief science officer at the Translational Research Institute for Space Health at Baylor College of Medicine. Taste, texture, freshness, and other factors all play major roles in maintaining our well-being. Simple survival "is not the goal," Fogarty says. Today's preserved food system, she concludes, "is completely inadequate for a Mars mission."

Robert Jinkerson, a chemical engineer at the University of California (UC), Riverside, thinks the answer is for astronauts to grow their own on-board garden—in the dark, with plant growth fueled by artificial nutrients rather than sunlight. It won't be easy; after all, plants evolved for hundreds of millions of years to extract energy from sunlight. But Jinkerson believes it can be done by reawakening metabolic pathways plants already possess—the same ones that power the germination of seeds buried in the ground and then shut off once a seedling's leaves start to reach for the Sun. In his vision of the future, electricity from solar panels could transform water and carbon dioxide (CO_2) exhaled by a spacecraft's crew into simple, energy-rich hydrocarbons that genetically modified plants could use to grow—even in the darkness of space or the dim light on Mars, which receives less than half as much sunlight as Earth.

His team has already shown that modified plants can survive, if not yet thrive, on a light-free regimen. If the UC Riverside researchers can get them to flourish, Jinkerson believes they'll be on a path to not only feeding astronauts, but also growing a wide variety of crops on Earth without land and abundant sunshine. "It could be implemented in places like the South Pole, in places where agriculture is not possible," says Jinkerson, whose team has already won two rounds of a NASA competition.

Others have tried to wean plants from light, and there's a reason why decades of attempts haven't worked. "They need light for everything," says Sue Rhee, a plant biologist at Carnegie Science. Light plays a role not just in photosynthesis, but also in germination, growth, flowering, and the ripening of fruit. But she thinks Jinkerson's vision is "bold" and worth trying, because it involves a combination of genetic tweaks and added nutrients that haven't been tried before. Patrick Shih, a plant molecular biologist at UC Berkeley, agrees. "They are trying to rethink how we do agriculture," Shih says. "It's a really out-of-the-box way of looking at it, which is refreshing."



Peppers grown on the International Space Station need light, but chemicals made from carbon dioxide exhaled by astronauts might sustain future space gardens.

PHOTO: NASA

JINKERSON'S ORIGINAL DREAM was to redesign fuel production, not food. As a postdoctoral researcher from 2014–17 he helped rewrite genes in photosynthetic algae to boost the production of oils that could be captured and converted into biofuels. At the time, chemists around the world had similar ambitions, backed by hundreds of millions of dollars from the likes of Shell and Exxon Mobil. Ultimately, the high cost of algal biofuels compared with petroleum, among other issues, doomed Jinkerson's project along with most of the others. But along the way he learned that some types of algae could grow in the dark when fed a simple liquid hydrocarbon called acetate.

In 2017, a few months after joining UC Riverside, Jinkerson found himself sitting in on a seminar by Feng Jiao, a chemist at the University of Delaware. Jiao was describing his team's experiments with an electrolyzer, a paperback book–size device that zaps CO_2 and water with electricity to create acetate and ethylene, a building block for plastics. Because of the massive market for ethylene, $176 billion annually at last count, most of the buzz around Jiao's electrolyzer centered on this compound. But it occurred to Jinkerson that if Jiao could make acetate from CO_2, his own team could feed it to algae, and one day perhaps food crops. "I thought it was a perfect match," Jinkerson says. "I pitched him in the parking lot and again 2 months later at a meeting."

The two teamed up. Jiao and his students revamped their electrolyzer to turn down ethylene production and turn up acetate. Last year, they reported in *Nature Catalysis* that they had shifted the output from 30% acetate to 99%, a purity high enough to feed directly to plants. The Delaware team has since carried out a technoeconomic analysis of its process, showing that producing acetate in an electrolyzer with regular grid power can be cheaper than the conventional process for producing acetate for use in textiles, among other things.

The milky-white pearl oyster mushrooms growing inside a stainless-steel refrigerator at UC Riverside's Plant Transformation Research Center illustrate what else can be done with that acetate. Each mushroom grows out of an oversize test tube packed with sand-like vermiculite bathed in liquid growth media, a mixture of acetate and inorganic nutrients including phosphorus and nitrogen. In work published last year in *Nature Food*, Jinkerson, Jiao, and colleagues fed acetate generated in their electrolyzer to mushrooms, yeast, and algae grown in the dark. Those organisms converted chemical energy into new biomass up to 18 times more efficiently than if they had been fed plants grown by photosynthesis.

The mushroom cultivation strategy was part of the team's entry in the Deep Space Food Challenge, a competition launched by NASA and the Canadian Space Agency in 2021 to come up with innovative ways to feed astronauts on extended deep space missions. The UC Riverside and Delaware collaborators call themselves Nolux (Latin for "no light"), and in October 2021 they were chosen out of more than 300 applicants as one of 18 U.S.-based finalists. (Other finalists include an outfit that feeds dried insect cells to a bioreactor to "emulate traditional meat products" and a project to create "meat" from pluripotent stem cells.)

In the next phase of the contest, teams put together prototype food production systems. Based on its results, Nolux calculates that acetate-fed mushrooms grown in a 2-cubic-meter reactor could provide about 8.5 kilograms of food per day, more than one-third of what a six-person crew on a deep space mission would need. Last month it was named one of five U.S. winners awarded a $150,000 prize.

Even a mushroom lover might balk at eating 1 kilogram or more of the fungi every day, however. And most plants will be harder to grow in the dark. Mushrooms, yeast, and some algae are heterotrophs, organisms that consume other plants or animals for their nutrition and are naturally able to grow in the dark. But nearly all plants are autotrophs, producing their own food from sunlight.

In the same *Nature Food* study, Jinkerson, Jiao, and their colleagues fed acetate to nine crop plants raised in the dark, including lettuce, tomatoes, and peppers. Although the plants survived, they didn't grow larger. Additional tests using acetate labeled with carbon-13, a heavy isotope of carbon, showed the plants could incorporate acetate into their tissues—an encouraging sign—but apparently not enough of it to support the growth of new tissue.

Further investigation revealed why. The acetate, it turns out, was processed through a metabolic cycle known as the Krebs cycle (see graphic, below). Plants normally use this pathway to break down sugar molecules built and stored during photosynthesis. They do so bit by bit, extracting energy in each step that can be used to synthesize proteins and other essential cellular building blocks. Leftover sugars can then be used for building plant tissue. But unlike sugar molecules, which have either five or six carbon atoms, acetate molecules only have two. And with each full turn of the Krebs cycle, plants release two molecules of CO_2, leaving no carbon atoms for the plant to build leaves, roots, or stems. It stays healthy but its growth stalls.

To create plants that can actually grow on acetate, and ultimately produce edible leaves and fruit, Jinkerson and his colleagues are now using CRISPR and other gene-editing tools to restart genes that are briefly active when seeds germinate. A metabolic pathway called the glyoxylate cycle allows seedlings to feed on the starches, proteins, and oils stored in seeds. The glyoxylate cycle bypasses steps in the Krebs cycle where carbon is lost as CO_2, so it should conserve carbon that could be used for growth. "They already have the pathway and already use it," Jinkerson says. But it shuts down as plants grow.

He notes that humans have a similar genetic switch that allows babies to process lactose, the sugar in milk, but then turns off in many adults, causing them to become lactose intolerant. Over the course of human evolution, that switch got turned back on for many, allowing them to drink milk. "Now, we're trying to do the same thing in plants," he says.

The initial results are promising. First, Jinkerson and his colleagues engineered *Arabidopsis*, a mustard plant commonly used for genetic studies to turn up a gene for an enzyme called acetyl-CoA synthetase (ACS) that chemically alters the acetate they consume. The change enabled the plants to grow normally when fed acetate at a high concentration, which would otherwise stunt growth. They are also now ramping up activity of two other genes—for isocitrate lyase (ICL) and malate synthase (MLS)—that enable germinating plants to bypass the Krebs cycle and metabolize acetate via the glyoxylate pathway. If that works, the UC Riverside team will test whether the engineered plants can flourish in the dark.

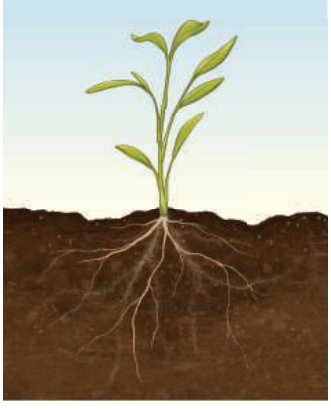
Rhee says the general strategy is a good one and notes that the modified *Arabidopsis*'s increased tolerance for acetate is a hopeful sign. But she notes that plants rely on light to trigger a host of other processes, including initiating signaling cascades that trigger flowering and ripening That could make it extremely difficult to coax them to grow completely in the dark. J. Clark Lagarias, a plant biochemist at UC Davis, agrees and points to additional challenges. These include a risk that fungi and algae might invade the growth medium and gobble up all the acetate before plants could consume it. That concern alone could be too much for NASA to stomach, says Adam Arkin, a bioengineer at UC Berkeley who also works on feeding astronauts on deep space missions. "We are very, very risk averse in space," Arkin says.

ACETATE ISN'T the only potential food source for dark-raised plants, however. Sugars are another attractive option, if they could somehow be supplied in space. Plants already make

Growing plants in the dark

Plants normally rely on photosynthesis to make sugars they use as fuel and to construct new tissue. Tweaking plant metabolism to allow them to grow in the dark could help feed astronauts on deep space missions and grow crops year-round on Earth.

Mature plant in sunlight



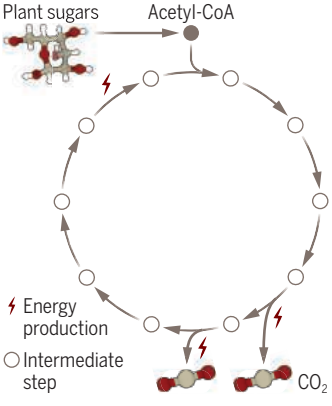
Seedling beneath ground



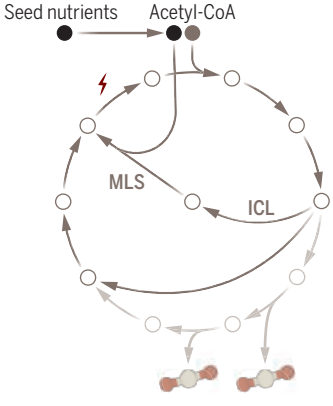
Mature plant in darkness



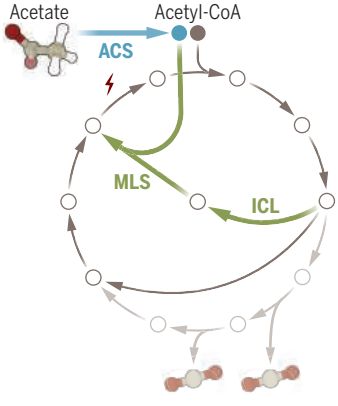
Krebs cycle
Plants use this metabolic cycle to extract energy from sugars made by photosynthesis, producing two carbon dioxide (CO_2) molecules in the process.



Glyoxylate cycle
Germinating plants use two enzymes, ICL and MLS, to bypass the Krebs cycle and harvest chemical energy stored in the seed. This cycle shuts off when photosynthesis takes over.



Modified glyoxylate cycle
Tweaking genes for key enzymes (blue and green) could restart the glyoxylate cycle in mature plants and enable them to grow on acetate in the absence of light.



sugars through photosynthesis and circulate them throughout their tissues to be metabolized in the Krebs cycle. Adapting plants to use sugars supplied artificially might not require the extensive rerouting of plant metabolism needed for acetate.

Soon after Jinkerson joined UC Riverside, he came across a paper by an international team of researchers showing cotton plants grew in the dark when fed sugar water and wondered whether the same could be done with food crops. He teamed up with Martha Orozco-Cárdenas, head of UC Riverside's Plant Transformation Research Center, to investigate. They started with tissue cultures from lettuce and showed these plants could grow in the dark when fed sucrose. Initial results showed only modest growth, but the taste was fine. "It tasted just like lettuce and was crispy," Jinkerson says. The team has also added genes for making vitamin B12 to the lettuce and shown that the dark-reared plants produce the vitamin—an advantage in space, where supplying this typically animal-derived vitamin will be a challenge.



Vertical farming is used today for some specialty crops, but the lighting required makes it an energy-intensive process.

The team is also trying to raise cherry tomatoes on sugar water, experimenting with dwarf plants they genetically modified to have almost no leaves or stems so that they channel the majority their energy into making fruit. Dubbed Small Plants for Space Exploration, or SPACE tomatoes, they're now scheduled for testing aboard the International Space Station to see how microgravity affects their growth and whether they can produce seeds that can be replanted. If so, they might offer astronauts an efficient way to produce fresh tomatoes, while minimizing inedible plant waste.

Lagarias thinks the sugar-fed dwarf tomatoes might thrive in the dark, particularly if the plants are given doses of light at select times. Previous work from his group and others, he says, shows that "plants can go through a complete life cycle in darkness with sugar." But they don't grow well. "To make this really effective you need light to turn on some aspects in development."

Jinkerson's group is working to tease apart the amount and timing of light needed to trigger signaling and other key processes. "It may only be important to give them light at certain times," Jinkerson says. He notes that only tiny amounts of light—1000 times less than is normally needed for plant growth—may be enough to trigger key developmental steps.

Even those dim flickers may not be essential. In the 27 April 2020 issue of *Plant Direct*, Lagarias and his colleagues reported that a particular mutation they discovered in rice plants alters a light-sensitive protein called phytochrome B, enabling it to trigger growth and development in the absence of light. "The plants develop in the dark as if in the light," he says.

Hauling tons of sugar into space as plant food may not make much sense, but recent advances in synthesizing sugars in electrolyzers may make that unnecessary. Compared with acetate, the molecular structures of sugars are more complex, making them more difficult to synthesize. But in the 19 October 2022 issue of *Joule*, researchers led by Peidong Yang, a chemist at UC Berkeley, reported using an electrolyzer to convert CO_2 and water to compounds called glycolaldehyde and formaldehyde. A metal catalyst then caused the molecules to react and form sugars, including glucose. And in the May 2022 issue of *Nature Catalysis*, researchers led by Tingting Zheng at the University of Electronic Science and Technology of China reported that they engineered yeast to convert electrolyzer-produced acetate to glucose at high yield. Though neither of these approaches yet matches the yield of Jiao's acetate electrolyzer, they raise hopes that future astronauts may be able to recycle their breath into plant food—and ultimately into fresh vegetables.

ON EARTH, light is free and plentiful, so there's no need for Jinkerson's metabolic wizardry in most agriculture. But for some high-priced vegetables, it might make sense. Dark rearing would allow growers to convert sugar, which currently costs just 45 cents per kilogram on the commodities market, into a product with far higher value. It also could enable those crops to be grown year-round anywhere in the world without worry about drought, storms, deep freezes, and long-distance transportation. "It allows us to reimagine what agriculture can be," Jinkerson says.

It might also save costs for vertical farming, a method already used to produce expensive fruits and vegetables (think artisanal greens) for restaurants and other high-end consumers. In today's vertical farms, plants are grown indoors on racks stacked floor to ceiling and illuminated with banks of high-efficiency LED lights. But the electricity needed to power those lights, among other energy demands, means vertical farms use on average seven times the energy of regular greenhouses. The added costs limit vertical farming's reach. "Our approach would eliminate the lights, and have stacks of plants growing in the dark," Jinkerson says.

"It's early days," says Lucas van der Zee, a plant biologist at Wageningen University who has also been trying to grow plants in the dark, but so far without success. "Since the beginning of agriculture, food production has been dependent on the Sun," he says. "But if you can find a way to separate growth from light that would be huge, and change food production around the world." Perhaps beyond our world as well. ■

PHOTO: AEROFARMS



ANIMAL BEHAVIOR

Mammals responded to reduced road traffic

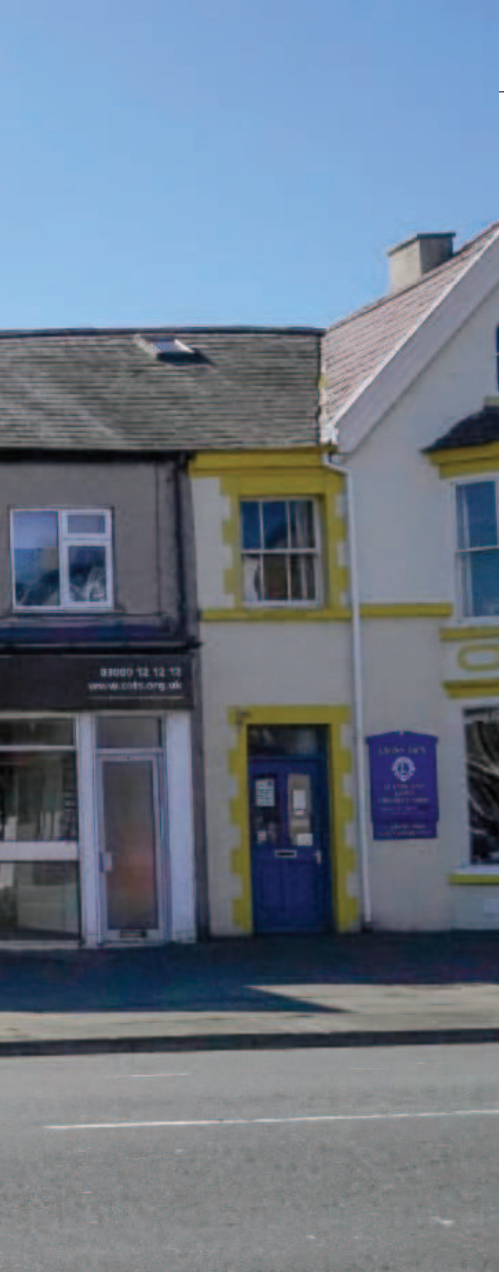
COVID-19 restrictions in 2020 reduced traffic worldwide and altered animal movement

By **Colleen Cassady St. Clair** and **Sage Raymond**

The frequency of animals crossing roadways is important to the conservation of countless species worldwide because roads cause mortality through vehicle collisions, reduce habitat, and limit movement of individuals (*1*). Road avoidance also limits dispersal, which increases isolation, inbreeding, and susceptibility of small populations to local extinction (*2*). Despite the global ubiquity of roads and their long-identified conservation implications (*3*, *4*), it has been difficult to determine whether road avoidance is caused by permanent road infrastructure or the day-to-day presence of vehicles. COVID-19 lockdowns during 2020 have provided an opportunity to answer this question. On page 1059 of this issue, Tucker *et al.* (*5*) report using data from other studies that tracked mammals both before and during COVID-19 lockdowns in 2020. They found that vehicle traffic alone appeared to change animal movement near roads with implications for population persistence and human-wildlife conflict.

Studies of mammals fitted with collars that track an animal's location every few hours using the global positioning system (GPS) are used to answer a range of questions about wildlife biology, conservation, and management (*6*). Tucker *et al.* incorporated data from 43 mammal species around the world and 2300 GPS-collared individ-

Department of Biological Sciences, University of Alberta, Edmonton, AB, Canada. Email: cstclair@ualberta.ca



Wild mountain goats roam the streets of Llandudno, Wales, on 31 March 2020, which was attributed to the lack of human activity and traffic owing to the COVID-19 lockdowns.

uals to assess whether the sudden reduction in vehicle traffic in the early COVID-19 lockdowns between 1 February and 28 April 2020 changed the way that animals moved near roads relative to the way that they moved in the same weeks 1 year earlier. The authors analyzed displacement between points (measured at 1-hour and 10-day scales) and proximity to roads for each animal. For each GPS data point, the authors also considered the extent of the adjacent human development (measured with a standardized index of human footprint), the strictness of the lockdown (measured with the Oxford COVID-19 Stringency Index), and between-year changes in the vegetative state of the habitat (measured by satellite imaging). For each animal, they analyzed the average distance traveled on an hourly scale, which could demonstrate fleeing responses, and a 10-day scale, which could demonstrate willingness to explore beyond their usual home ranges.

Tucker *et al.* observed substantial variation among individuals, species, and locations. Some studies have reported more uniform responses among different animals during the COVID-19 lockdowns in 2020, including mountain lions (*Puma concolor*) in California, USA (*7*), birds in Canada and the US (*8*), and Torresian crows (*Corvus orru*) in Australia (*9*), but the variability of the results presented by Tucker *et al.* is more consistent with other studies. For example, a pre–COVID-19 study in 2016 of 14 mammal species in India showed a range of responses to human activity (*10*), and a COVID-19–era study in 2022 of seven other mammal species in Slovenia showed that lockdowns in 2020 reduced roadkill for some species, such as roe deer (*Capreolus capreolus*) and wild boar (*Sus scrofa*), but increased it for others, especially badgers (*Meles meles*) (*11*). This variability suggests that even an experiment as widely synchronized and globally replicated as the COVID-19 lockdowns in dozens of countries did not affect animal movement in the same way.

However, Tucker *et al.* did find evidence for a few consistent effects. When and where the COVID-19 lockdowns were more strict, there was a 73% increase of the longest movements by individuals at the 10-day scale. This indicates that most animals were exploring more of the landscape when vehicle movement was more limited. However, in areas with greater human density, such as near an urban center, animals showed a 12% decline in the longest movements at the hourly scale during lockdowns. Tucker *et al.* suggested that this is because they were less frequently frightened by aversive stimuli, whether from road traffic or human presence, during the lockdowns and exhibited shorter fleeing distances. Their interpretation that roads caused less fearfulness when they had less traffic is supported by their observation of lesser avoidance of roads—animals were 36% closer to them than before the lockdowns. Changes in longest movements were contingent on the strictness of the lockdowns and human population density, showing that animals are both sensitive and responsive to human activity on and near roads.

Lesser road avoidance by animals during the lockdowns has implications for both wildlife and people that range from beneficial to potentially harmful. Conservation goals might be advanced with the greater movement of sensitive and rare species, such as the urban-avoiding mountain lions in the San Francisco Bay area of California, USA (*7*). However, closer proximity to roads by carnivores might increase the potential for conflict with people in highly populated areas. Proximity of people and wildlife may also affect disease dynamics. Greater sharing of space with people during the COVID-19 pandemic might be the reason that white-tailed deer (*Odocoileus virginianus*) in Ohio, USA, are now frequently infected with at least three lineages of severe acute respiratory syndrome coronavirus 2 (SARS-CoV-2) (*12*), which may produce variants that could evolve and be transmitted to people or livestock (*13*).

The COVID-19 lockdowns created a large unintentional experiment for the study of how human activities affect animal movements, including for species that are threatened, culturally important to people, or associated with human-wildlife conflict. Tucker *et al.* provided a comprehensive answer about the ability of some animals to make use of human-inhabited areas and even expand their habitats when human activity declines. Their results highlight the environmental impact of vehicle activity, which is discussed less often publicly than the effects of emissions, permanent road infrastructure, and habitat loss. This study shows the quantitative impact of vehicle presence on animal behavior, which has been much harder to measure. The authors also show how effectively and quickly some animals can take advantage of decreased traffic, which may offer support for traffic restrictions in protected areas (*14*) as well as greater appreciation for the cognitive flexibility of other species (*15*). ■

REFERENCES AND NOTES

1. T. Rytwinski, L. Fahrig, in *Handbook of Road Ecology*, R. van der Ree, D. J. Smith, C. Grilo, Eds. (Wiley, 2015), pp. 237–246.
2. A. Ceia-Hasse, L. M. Navarro, L. Borda-de-Água, H. M. Pereira, *Ecol. Modell.* **375**, 45 (2018).
3. S. C. Trombulak, C. A. Frissell, *Conserv. Biol.* **14**, 18 (2000).
4. P. L. Ibisch *et al.*, *Science* **354**, 1423 (2016).
5. M. A. Tucker *et al.*, *Science* **380**, 1059 (2023).
6. D. P. Seidel, E. Dougherty, C. Carlson, W. M. Getz, *Int. J. Geogr. Inf. Sci.* **32**, 2272 (2018).
7. C. C. Wilmers, A. C. Nisi, N. Ranc, *Curr. Biol.* **31**, 3952 (2021).
8. M. B. Schrimpf *et al.*, *Sci. Adv.* **7**, eabf5073 (2021).
9. B. L. Gilby *et al.*, *Biol. Conserv.* **253**, 108926 (2021).
10. A. Gangadharan, S. Vaidyanathan, C. C. St. Clair, *Anim. Conserv.* **19**, 451 (2016).
11. B. Pokorny, J. Cerri, E. Bužan, *J. Appl. Ecol.* **59**, 1291 (2022).
12. V. L. Hale *et al.*, *Nature* **602**, 481 (2022).
13. S. Mallapaty, *Nature* **604**, 612 (2022).
14. J. Whittington, P. Low, B. Hunt, *Sci. Rep.* **9**, 3772 (2019).
15. L. P. Barrett, L. A. Stanton, S. Benson-Amram, *Anim. Behav.* **147**, 167 (2019).

ACKNOWLEDGMENTS

The authors thank J. Cahill for helpful comments.

10.1126/science.add9662

AGING

Taurine linked with healthy aging

Reversing age-associated taurine loss improves mouse longevity and monkey health

By **Joseph McGaunn** *and* **Joseph A. Baur**

Taurine is an amino acid, but it contains a sulfonic acid and a β-amine that make it structurally and chemically distinct from the more familiar amino acids that form proteins. Although nearly absent in most plants, taurine makes up as much as 0.1% of the body weight of animals (*1*). Humans synthesize taurine but depend on exogenous sources in early life when production is insufficient to support development, making it semi-essential. In species with very low synthesis, such as cats, taurine remains essential throughout adulthood; inadequate intake leads rapidly to retinal damage, immunological issues, and cardiomyopathy (*2*). In humans, small clinical trials of taurine supplementation in adults have suggested benefits in metabolic and inflammatory diseases (*3, 4*). Yet, precisely what taurine does in most cases remains poorly understood. On page 1028 of this issue, Singh *et al.* (*5*) provide evidence that taurine maintains health in aged animal models.

Singh *et al.* demonstrate that a decline in circulating taurine is a feature of aging in multiple species, including humans, with levels falling by ~80% over the human life span. They further found that mice lacking the major taurine transporter had shorter adult life spans. Supplementing taurine from middle age increased median life span by 10 to 23% in wild-type *Caenorhabditis elegans* (nematode worms) and 10 to 12% in wild-type mice. In mice, administering taurine was also associated with improvements in strength, coordination, and memory, as well as attenuation of multiple hallmarks of aging, including cellular senescence, mitochondrial and DNA damage, and chronic inflammation ("inflammaging"). In middle-aged rhesus macaques, 6 months of taurine supplementation led to positive effects on bone health, metabolic phenotypes, and immunological profiles. The authors noted decreased circulating taurine in people with obesity and diabetes as well as its elevation by exercise, strengthening its correlation with general health.

What causes taurine deficiency during aging? One possibility is decreased calorie intake or changing food preference in aged individuals. However, prolonged intake of a vegan diet with negligible taurine content leads to a decline of only ~20% in circulating taurine in young healthy individuals (*6, 7*), suggesting that the ~80% decrease observed in older people by Singh *et al.* at least partly reflects a loss of capacity for endogenous synthesis. Most taurine synthesis has been thought to take place in the liver, and evidence from Fischer 344 rats indicates a decrease in hepatic taurine production with age (*8*). However, the final step in taurine synthesis—conversion of hypotaurine to taurine—was recently shown to be catalyzed by flavin-containing monooxygenase 1 (FMO1), which is expressed in rodent, but not human, liver (*9*). Thus, synthesis of taurine in other tissues or sharing of intermediates between tissues may play a greater role in humans.

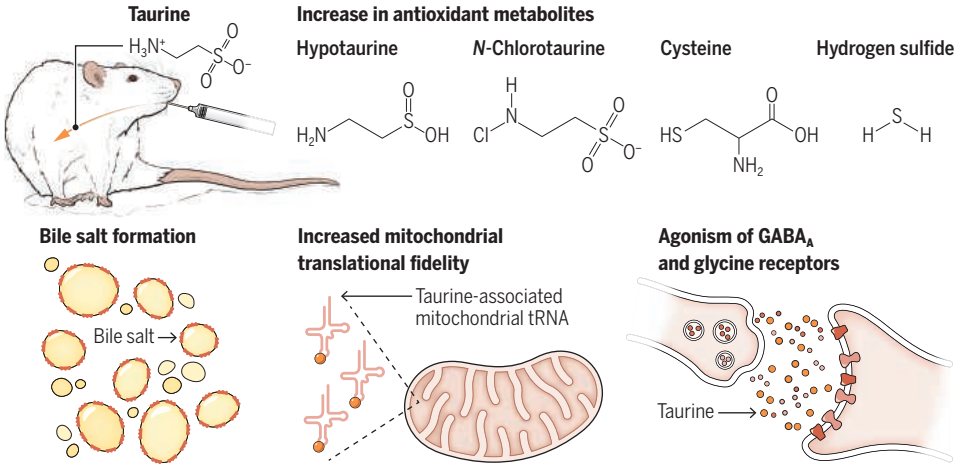
A key issue for any longevity intervention is whether it causes calorie restriction (which can extend life span) or acts through independent mechanisms. Singh *et al.* found that taurine supplementation did not affect food intake in mice but nonetheless caused a small decrease in body weight, indicating a calorie deficit. Energy expenditure was higher in taurine-treated mice and intestinal transit time was accelerated, although it is not clear if nutrient absorption was decreased. The change in intestinal behavior is intriguing, because taurine is conjugated to bile acids to form bile salts, which facilitate uptake of dietary lipids (*1*). It will be crucial to control for the effects of taurine on body composition and nutrient uptake in future studies.

One of the most studied mechanisms of action for taurine is an increase in antioxidant capacity (see the figure). Although oxidative damage is not clearly linked to mammalian life span, it plays a role in many age-associated pathologies (*10*). Taurine is a poor scavenger of reactive oxygen species, with the exception of hypochlorite, which it detoxifies to *N*-chlorotaurine (*11*). *N*-Chlorotaurine is anti-inflammatory and induces expression of antioxidant enzymes in mice and humans. Taurine supplementation might also cause an increase in levels of its precursors, including the antioxidants hypotaurine and cysteine. An interesting corollary is that up-regulating endogenous taurine synthesis would have the opposite result—consuming hypotaurine and cysteine. Taurine is also a substrate for the generation of hydrogen sulfide (H_2S), which can scavenge reactive oxygen and nitrogen species, and induce other antioxidant defenses (*12*). In support of a net antioxidant effect, Singh *et al.* found decreased oxidative damage to DNA and increased resistance to oxidative stress in taurine-treated mice.

Taurine is also incorporated into some mitochondrial transfer RNAs (tRNAs), where it is critical for maintaining codon specificity during translation (*13*). Singh *et al.* demon-

How might taurine increase health and longevity?

Supplemental taurine extends mouse life span, but the mechanism is unclear. Possible explanations include accumulation of multiple antioxidant and signaling metabolites, that taurine is a key component of bile acids and might therefore alter nutrient absorption, and that incorporation of taurine into mitochondrial transfer RNAs (tRNAs) can increase mitochondrial translational fidelity. Taurine is also an agonist of γ-aminobutyric acid type A ($GABA_A$) and/or glycine receptors and so might have effects on neurotransmission.



Department of Physiology and Institute for Diabetes, Obesity, and Metabolism, Perelman School of Medicine, University of Pennsylvania, Philadelphia, PA, USA.
Email: baur@pennmedicine.upenn.edu

strate that the taurine content of mitochondrial tRNAs decreases with age and is partially restored by taurine supplementation. The amount of NADH dehydrogenase subunit 6 (ND6), a mitochondrial protein that depends on taurine-modified tRNAs, also decreased with age and increased with taurine supplementation. Notably, causality remains to be tested.

Are there potential risks to taurine supplementation? Few have been suggested despite widespread supplementation of taurine in baby formula and energy drinks, and a good safety profile is anticipated given that millimolar concentrations are already present in tissues. However, potential risks still warrant consideration because large, long-term human safety trials are lacking, and the equivalent doses used in the study by Singh *et al.* would be very high in humans. Whether taurine supplementation influences human longevity is also unknown. Taurine can act as a γ-aminobutyric acid type A ($GABA_A$) and/or glycine receptor agonist to promote neuronal inhibition (*3*). Whether this might play a role in the beneficial effects of taurine on anxiety and memory in mice, observed by Singh *et al.*, or might have less desirable effects on neurotransmission remains unclear. There is also evidence for potential interactions of taurine with growth and sex hormone pathways (*3*). Although Singh *et al.* confirmed that taurine has positive effects on bone health, negative effects from taurine supplementation on bone microstructure have been observed in mice (*14*). Taurine is notably a source of energy for gut microbes and may influence, or be influenced by, microbiota composition. A singular focus on increasing dietary taurine risks driving poor nutritional choices, because plant-rich diets are associated with human health and longevity (*15*). Thus, like any intervention, taurine supplementation with the aim of improving human health and longevity should be approached with caution. ■

REFERENCES AND NOTES

1. R. J. Huxtable, *Physiol. Rev.* **72**, 101 (1992).
2. K. C. Hayes, E. A. Trautwein, *Vet. Clin. North Am. Small Anim. Pract.* **19**, 403 (1989).
3. J. J. Caine, T. D. Geracioti, *Cleve. Clin. J. Med.* **83**, 895 (2016).
4. C. J. Jong *et al.*, *Molecules* **26**, 4913 (2021).
5. P. Singh *et al.*, *Science* **380**, eabn9257 (2023).
6. S. A. Laidlaw *et al.*, *Am. J. Clin. Nutr.* **47**, 660 (1988).
7. S. K. Rana, T. A. Sanders, *Br. J. Nutr.* **56**, 17 (1986).
8. B. Eppler, R. Dawson Jr., *Biochem. Pharmacol.* **62**, 29 (2001).
9. S. Veeravalli *et al.*, *Drug Metab. Dispos.* **48**, 378 (2020).
10. A. B. Salmon *et al.*, *Free Radic. Biol. Med.* **48**, 642 (2010).
11. O. I. Aruoma *et al.*, *Biochem. J.* **256**, 251 (1988).
12. B. Murphy *et al.*, *FASEB J.* **33**, 13098 (2019).
13. T. Suzuki *et al.*, *EMBO J.* **21**, 6581 (2002).
14. M. Martiniakova *et al.*, *Physiol. Res.* **68**, 519 (2019).
15. V. D. Longo, R. M. Anderson, *Cell* **185**, 1455 (2022).

ACKNOWLEDGMENTS

J.A.B. is supported by National Institutes of Health grants DK098656 and HL165792.

10.1126/science.adi3025

IMMUNOTHERAPY

Cancer immunosurveillance by gut T cells

T cells primed in the gut influence immune responses to extraintestinal tumors

By **Brandon M. Pratt**[1] *and* **J. Justin Milner**[2,3]

The immune system has the ability to destroy aggressive malignancies when called into action by immunotherapy (*1*). Additionally, the gut microbiota critically influence systemic immune responses and the efficacy of cancer immunotherapies such as immune checkpoint blockade (ICB) (*2*, *3*). However, how gut microbiota or gut-primed immune cells regulate peripheral antitumor immune responses and ICB efficacy remains unclear. On page 1027 of this issue, Fidelle *et al.* (*4*), along with a study by Feliu *et al.* (*5*), reveal a critical role for gut-derived T cells in extraintestinal cancer immunosurveillance. These enterotropic T cells, which are primed in gut-draining lymph nodes, can migrate to distant tumors, where they substantially alter the tumor microenvironment (TME) and response to ICB. This unexpected extraintestinal role of gut T cells informs mechanisms of how antibiotics affect ICB responses, inspires therapeutic strategies to manipulate the TME, and may yield new biomarkers to guide ICB use.

The gut represents a distinct barrier site that is constantly exposed to microbes and dietary antigens, which requires a careful balancing of effector and suppressive immune responses to maintain intestinal homeostasis (*6*). Disruptions to the composition and homeostasis of the gut microbiota, referred to as dysbiosis, contribute to ICB resistance in tumor-bearing mice (*2*, *3*). Accordingly, several studies have reported that antibiotic treatment can negatively affect patient responses to ICB in diverse cancer types, including melanoma, renal cell carcinoma, and non–small cell lung cancer (*3*, *7*), emphasizing the systemic immunoregulatory role of the gut. Furthermore, gut-primed, enterotropic T cells that express the gut-homing α4β7 integrin influence extraintestinal immune responses in the context of inflammatory bowel disease (*8*). However, whether enterotropic T cells influence tumor immunosurveillance and whether gut microbiota are involved in this process remain unclear.

ICB boosts antitumor immune responses by interfering with regulatory immune checkpoints that restrain cancer immunosurveillance. Fidelle *et al.* investigated the mechanisms underpinning reduced ICB efficacy in mice after broad-spectrum antibiotic treatment. In a mouse model of fibrosarcoma, they found that after antibiotic treatment, gut recolonization by several species of the genus *Enterocloster* instigated ICB resistance. Moreover, they found that metabolites produced by *Enterocloster* species disrupt intestinal homing of α4β7 integrin–expressing T cells by reducing expression of the α4β7 ligand, mucosal addressin cell adhesion molecule 1 (MAdCAM-1), on gut endothelial cells that line intestinal vasculature. The loss of MAdCAM-1 expression triggered an exodus of α4β7 integrin–expressing T cells from the ileal lamina propria and gut-associated lymphoid tissues to tumor-draining lymph nodes of distant fibrosarcoma tumors that were implanted subcutaneously in mice.

Although diverse $CD4^+$ and $CD8^+$ T cell populations were found to move from the gut to tumors, Fidelle *et al.* identified a key role for interleukin-17A (IL-17A)–producing $CD4^+$ T regulatory 17 ($T_{reg}17$) cells in suppressing antitumor immune responses and ICB efficacy in antibiotic-treated mice. Notably, genetic or pharmacological disruption of the MAdCAM-1–α4β7 integrin interaction also interfered with ICB efficacy in mice, and the deleterious effects of antibiotic treatment could be abrogated by IL-17A neutralization in vivo or by steering enterotropic $T_{reg}17$ cells away from the tumor. Although the precise mechanisms by which enterotropic $T_{reg}17$ cells blunt systemic cancer immunosurveillance are unclear, enterotropic $T_{reg}17$ cells in the tumor and tumor-draining lymph nodes expressed genes encoding several canonical immunosuppressive molecules such as IL-10, CD39, and CD73, which likely contributed to an immunosuppressive TME.

Fidelle *et al.* also found that soluble MAdCAM-1 detected in the blood positively correlates with ileal MAdCAM-1 expression in mice and dysbiosis in non–small cell lung

[1]Department of Pharmacology, University of North Carolina, Chapel Hill, NC, USA. [2]Department of Microbiology and Immunology, University of North Carolina, Chapel Hill, NC, USA. [3]Lineberger Comprehensive Cancer Center, University of North Carolina, Chapel Hill, NC, USA.
Email: justin_milner@med.unc.edu

strate that the taurine content of mitochondrial tRNAs decreases with age and is partially restored by taurine supplementation. The amount of NADH dehydrogenase subunit 6 (ND6), a mitochondrial protein that depends on taurine-modified tRNAs, also decreased with age and increased with taurine supplementation. Notably, causality remains to be tested.

Are there potential risks to taurine supplementation? Few have been suggested despite widespread supplementation of taurine in baby formula and energy drinks, and a good safety profile is anticipated given that millimolar concentrations are already present in tissues. However, potential risks still warrant consideration because large, long-term human safety trials are lacking, and the equivalent doses used in the study by Singh *et al.* would be very high in humans. Whether taurine supplementation influences human longevity is also unknown. Taurine can act as a γ-aminobutyric acid type A ($GABA_A$) and/or glycine receptor agonist to promote neuronal inhibition (*3*). Whether this might play a role in the beneficial effects of taurine on anxiety and memory in mice, observed by Singh *et al.*, or might have less desirable effects on neurotransmission remains unclear. There is also evidence for potential interactions of taurine with growth and sex hormone pathways (*3*). Although Singh *et al.* confirmed that taurine has positive effects on bone health, negative effects from taurine supplementation on bone microstructure have been observed in mice (*14*). Taurine is notably a source of energy for gut microbes and may influence, or be influenced by, microbiota composition. A singular focus on increasing dietary taurine risks driving poor nutritional choices, because plant-rich diets are associated with human health and longevity (*15*). Thus, like any intervention, taurine supplementation with the aim of improving human health and longevity should be approached with caution. ■

REFERENCES AND NOTES

1. R. J. Huxtable, *Physiol. Rev.* **72**, 101 (1992).
2. K. C. Hayes, E. A. Trautwein, *Vet. Clin. North Am. Small Anim. Pract.* **19**, 403 (1989).
3. J. J. Caine, T. D. Geracioti, *Cleve. Clin. J. Med.* **83**, 895 (2016).
4. C. J. Jong *et al.*, *Molecules* **26**, 4913 (2021).
5. P. Singh *et al.*, *Science* **380**, eabn9257 (2023).
6. S. A. Laidlaw *et al.*, *Am. J. Clin. Nutr.* **47**, 660 (1988).
7. S. K. Rana, T. A. Sanders, *Br. J. Nutr.* **56**, 17 (1986).
8. B. Eppler, R. Dawson Jr., *Biochem. Pharmacol.* **62**, 29 (2001).
9. S. Veeravalli *et al.*, *Drug Metab. Dispos.* **48**, 378 (2020).
10. A. B. Salmon *et al.*, *Free Radic. Biol. Med.* **48**, 642 (2010).
11. O. I. Aruoma *et al.*, *Biochem. J.* **256**, 251 (1988).
12. B. Murphy *et al.*, *FASEB J.* **33**, 13098 (2019).
13. T. Suzuki *et al.*, *EMBO J.* **21**, 6581 (2002).
14. M. Martiniakova *et al.*, *Physiol. Res.* **68**, 519 (2019).
15. V. D. Longo, R. M. Anderson, *Cell* **185**, 1455 (2022).

ACKNOWLEDGMENTS

J.A.B. is supported by National Institutes of Health grants DK098656 and HL165792.

10.1126/science.adi3025

IMMUNOTHERAPY

Cancer immunosurveillance by gut T cells

T cells primed in the gut influence immune responses to extraintestinal tumors

By **Brandon M. Pratt**[1] *and* **J. Justin Milner**[2,3]

The immune system has the ability to destroy aggressive malignancies when called into action by immunotherapy (*1*). Additionally, the gut microbiota critically influence systemic immune responses and the efficacy of cancer immunotherapies such as immune checkpoint blockade (ICB) (*2*, *3*). However, how gut microbiota or gut-primed immune cells regulate peripheral antitumor immune responses and ICB efficacy remains unclear. On page 1027 of this issue, Fidelle *et al.* (*4*), along with a study by Feliu *et al.* (*5*), reveal a critical role for gut-derived T cells in extraintestinal cancer immunosurveillance. These enterotropic T cells, which are primed in gut-draining lymph nodes, can migrate to distant tumors, where they substantially alter the tumor microenvironment (TME) and response to ICB. This unexpected extraintestinal role of gut T cells informs mechanisms of how antibiotics affect ICB responses, inspires therapeutic strategies to manipulate the TME, and may yield new biomarkers to guide ICB use.

The gut represents a distinct barrier site that is constantly exposed to microbes and dietary antigens, which requires a careful balancing of effector and suppressive immune responses to maintain intestinal homeostasis (*6*). Disruptions to the composition and homeostasis of the gut microbiota, referred to as dysbiosis, contribute to ICB resistance in tumor-bearing mice (*2*, *3*). Accordingly, several studies have reported that antibiotic treatment can negatively affect patient responses to ICB in diverse cancer types, including melanoma, renal cell carcinoma, and non–small cell lung cancer (*3*, *7*), emphasizing the systemic immunoregulatory role of the gut. Furthermore, gut-primed, enterotropic T cells that express the gut-homing α4β7 integrin influence extraintestinal immune responses in the context of inflammatory bowel disease (*8*). However, whether enterotropic T cells influence tumor immunosurveillance and whether gut microbiota are involved in this process remain unclear.

ICB boosts antitumor immune responses by interfering with regulatory immune checkpoints that restrain cancer immunosurveillance. Fidelle *et al.* investigated the mechanisms underpinning reduced ICB efficacy in mice after broad-spectrum antibiotic treatment. In a mouse model of fibrosarcoma, they found that after antibiotic treatment, gut recolonization by several species of the genus *Enterocloster* instigated ICB resistance. Moreover, they found that metabolites produced by *Enterocloster* species disrupt intestinal homing of α4β7 integrin–expressing T cells by reducing expression of the α4β7 ligand, mucosal addressin cell adhesion molecule 1 (MAdCAM-1), on gut endothelial cells that line intestinal vasculature. The loss of MAdCAM-1 expression triggered an exodus of α4β7 integrin–expressing T cells from the ileal lamina propria and gut-associated lymphoid tissues to tumor-draining lymph nodes of distant fibrosarcoma tumors that were implanted subcutaneously in mice.

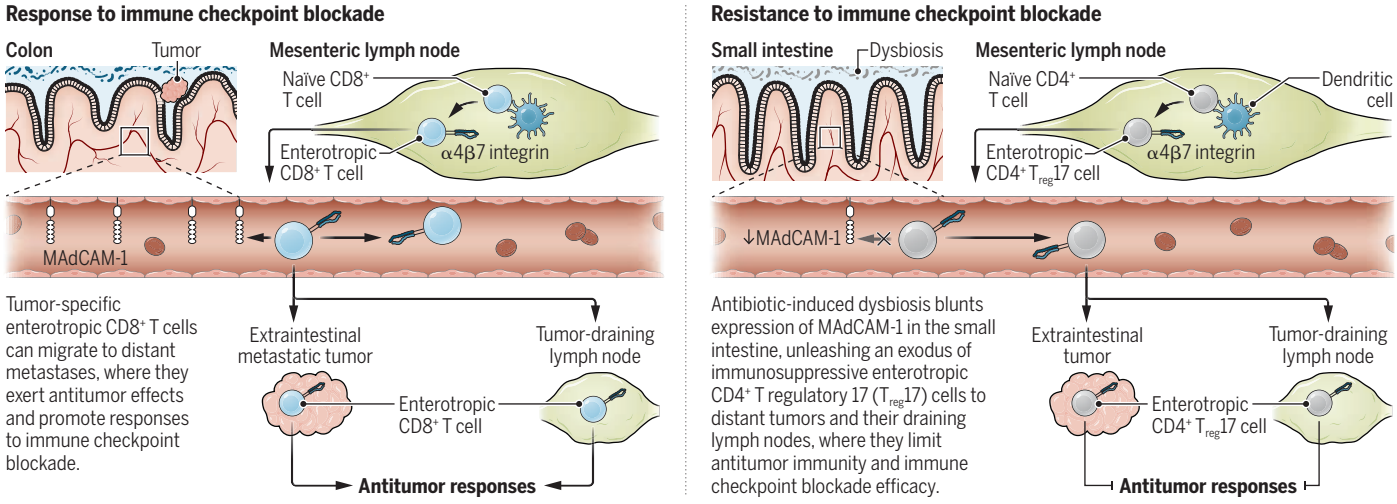
Although diverse $CD4^+$ and $CD8^+$ T cell populations were found to move from the gut to tumors, Fidelle *et al.* identified a key role for interleukin-17A (IL-17A)–producing $CD4^+$ T regulatory 17 ($T_{reg}17$) cells in suppressing antitumor immune responses and ICB efficacy in antibiotic-treated mice. Notably, genetic or pharmacological disruption of the MAdCAM-1–α4β7 integrin interaction also interfered with ICB efficacy in mice, and the deleterious effects of antibiotic treatment could be abrogated by IL-17A neutralization in vivo or by steering enterotropic $T_{reg}17$ cells away from the tumor. Although the precise mechanisms by which enterotropic $T_{reg}17$ cells blunt systemic cancer immunosurveillance are unclear, enterotropic $T_{reg}17$ cells in the tumor and tumor-draining lymph nodes expressed genes encoding several canonical immunosuppressive molecules such as IL-10, CD39, and CD73, which likely contributed to an immunosuppressive TME.

Fidelle *et al.* also found that soluble MAdCAM-1 detected in the blood positively correlates with ileal MAdCAM-1 expression in mice and dysbiosis in non–small cell lung

[1]Department of Pharmacology, University of North Carolina, Chapel Hill, NC, USA. [2]Department of Microbiology and Immunology, University of North Carolina, Chapel Hill, NC, USA. [3]Lineberger Comprehensive Cancer Center, University of North Carolina, Chapel Hill, NC, USA.
Email: justin_milner@med.unc.edu

Enterotropic T cells modulate responses to cancer immunotherapy in mice

Naïve T cells activated in the gut-draining lymph nodes differentiate into specialized T cell subsets that express the α4β7 integrin, which engages the mucosal addressin cell adhesion molecule 1 (MAdCAM-1) ligand that is expressed on intestinal endothelial cells. These enterotropic T cells can influence systemic antitumor immunity and responses to immunotherapy.



cancer patients. Low amounts of circulating soluble MAdCAM-1 were associated with ICB resistance in patients with advanced bladder, kidney, and lung cancer, potentially reflecting the mobilization of suppressive $T_{reg}17$ cells from the gut. These findings indicate that soluble MAdCAM-1 concentrations may be useful in guiding ICB treatment and point to the MAdCAM-1–α4β7 integrin axis as a potential target for improving ICB efficacy in the context of dysbiosis.

About 25% of colorectal cancer patients are diagnosed with aggressive metastatic disease, and there are limited effective treatment options (*9*). To investigate how local, gut-derived immune responses influence systemic immunosurveillance of distant metastases, Feliu *et al.* implemented a mouse model in which a mouse colorectal tumor cell line was grafted into both the colon and liver. They found that the presence of an intracolon tumor evoked rejection of an intrahepatic tumor in these mice compared with mice bearing solely intrahepatic tumors. Immunoprofiling and cell-tracking experiments revealed that α4β7 integrin–expressing enterotropic $CD8^+$ T cells that recognize tumor antigens trafficked from gut-draining lymph nodes of mice with intracolon tumors and accumulated in hepatic tumors. Treatment of mice with α4β7 integrin–depleting antibodies reversed this antimetastatic phenotype, implicating enterotropic α4β7-expressing $CD8^+$ T cells as key mediators of systemic cancer immunosurveillance. An intracolon tumor also favorably influenced immune responses in hepatic tumors after ICB treatment in mice.

Feliu *et al.* analyzed samples from 20 patients with microsatellite stable metastatic colorectal cancer and found that the frequency of patients with metastatic tumors expressing integrin β7 (*ITGB7*) and integrin α4 (*ITGA4*) genes was higher among ICB responders than in nonresponders. Moreover, in this same patient cohort, the authors found higher concentrations of circulating α4β7 integrin–expressing $CD8^+$ T cells in blood from ICB responders than in blood from nonresponders. Together, these data support a critical role for enterotropic α4β7-expressing $CD8^+$ T cells in systemic cancer immunosurveillance and their potential utility as predictive biomarkers of ICB responsiveness in patients with metastatic colorectal cancer.

The studies of Fidelle *et al.* and Feliu *et al.* highlight disparate roles for α4β7 integrin–expressing cytotoxic $CD8^+$ T cells and immunosuppressive $CD4^+$ $T_{reg}17$ cells in systemic cancer immunosurveillance (see the figure). Although Fidelle *et al.* show that metabolites produced by *Enterocloster* species may repress endothelial MAdCAM-1 expression in the gut, it remains to be determined what signals control the composition and degree to which protumorigenic enterotropic $T_{reg}17$ cells, antitumorigenic enterotropic $CD8^+$ T cells, and other enterotropic lymphocyte populations are mobilized from the gut to distant tumor sites. In addition to $T_{reg}17$ cells, Fidelle *et al.* demonstrate that antibiotic treatment induces an exodus of multiple subsets of enterotropic $CD4^+$ and $CD8^+$ T cells; however, enterotropic $CD8^+$ T cells that reached distant sarcomas exhibited features of exhaustion. Feliu *et al.* show that robust antimetastatic responses by enterotropic $CD8^+$ T cells were dependent on a vigorous antitumor immune response to the intracolon tumor, but the exact mechanisms that triggered the exodus of cytotoxic enterotropic T cells from the gut and the accompanying abscopal effect (whereby immune responses to one tumor can reject other related tumors) require further investigation. Uncovering the cues that control the kinetics and magnitude of enterotropic T cell trafficking may reveal new immunotherapy modalities or combinatorial strategies to boost existing approaches.

The work by Feliu *et al.* may also inspire new avenues for improving adoptive T cell therapies (whereby patient T cells are engineered to target tumors) through appropriation of attributes that confer potent antitumor activity to α4β7 integrin–expressing $CD8^+$ T cells. Indeed, they demonstrate that α4β7 integrin–expressing $CD8^+$ T cells may have a superior capacity for cytotoxic activity compared with $CD8^+$ T cells that lack α4β7 integrin. Deeper molecular profiling of gut-emigrating protumorigenic and antitumorigenic enterotropic T cell populations may further unveil key functional attributes of these cells, their relationship with other T cell subsets, and the drivers of their identity and trafficking behavior. ■

REFERENCES AND NOTES

1. A. D. Waldman *et al.*, *Nat. Rev. Immunol.* **20**, 651 (2020).
2. M. Vétizou *et al.*, *Science* **350**, 1079 (2015).
3. B. Routy *et al.*, *Science* **359**, 91 (2018).
4. M. Fidelle *et al.*, *Science* **380**, eabo2296 (2023).
5. V. Feliu *et al.*, *Sci. Immunol.* **8**, eadg8841 (2023).
6. S. Shalapour, M. Karin, *Annu. Rev. Immunol.* **38**, 649 (2020).
7. A. Elkrief *et al.*, *Ann. Oncol.* **30**, 1572 (2019).
8. D. H. Adams, B. Eksteen, *Nat. Rev. Immunol.* **6**, 244 (2006).
9. S. Vatandoust *et al.*, *World J. Gastroenterol.* **21**, 11767 (2015).

ACKNOWLEDGMENTS

The authors acknowledge members of the Milner lab and M. L. Mackichan for helpful input.

10.1126/science.adi3357

CHEMISTRY

A push for mechanochemistry

Chemical reactions can be accelerated by directional local pressure applied to molecules

By **Paul S. Weiss**[1,2,3,4]

A key goal of both synthetic chemistry and nanoscience is to manipulate specific bonds within molecules to drive reactions selectively. Nature performs this task with exquisite precision using enzymes that hold reactants and intermediates in place and even deforms them to drive reactions with great specificity, such as in DNA biosynthesis (*1*). On page 1053 of this issue, Zholdassov *et al.* (*2*) show that deforming molecules with uniaxial forces lowers the activation barrier to a particular synthetic reaction pathway, driving the reaction to occur more rapidly compared with either thermal activation or hydrostatic pressure. This mechanism inspires consideration of what other reactions could be accelerated in this way. Moreover, selectively bending or twisting one or more bonds to activate reactants and/or intermediates could potentially drive previously unfavorable reaction pathways. New synthetic strategies could be developed by leveraging this additional consideration in the design of chemical reactions.

Current synthetic tools that are used to deform molecules en masse remain rather blunt and include such techniques as ball milling (*3*) and hydrostatic pressure. For example, in ball milling, solvent is avoided (or largely avoided), often in order to make reactions more environmentally friendly, and force is applied to reactants by metal, ceramic, or polymer balls that drop onto them as the reaction container is rotated; the direction of the force on the molecules is thus random in each collision. At the nanoscale, scanning probe microscopes have been used to manipulate atoms on surfaces (*4*) and to induce reactions of single molecules with extraordinary specificity (*5*). The intra- and intermolecular potentials felt by molecules can be manipulated by applying electric fields or by supplying charge with the probe tip. Molecules can be isomerized through precise positioning of the atomically sharp probe tip and application of voltages between the tip and sample. Reactants can be positioned with respect to one another, and then reactions can be induced by using electric fields applied locally with the probe tip (*6*).

In polymer mechanochemistry, weak bonds called mechanophores are incorporated into the reactant systems. These bonds are designed to be reactive so as to drive further chemistry once activated by applied force, either by breaking or by becoming more reactive (*7*). They are not typically aligned, and so force along a specific direction is not required. Nevertheless, there have been tantalizing clues about the roles that directional force might have in polymer synthesis with the proper thought to molecular design. For example, polymer chains have been designed so that stretching the polymers weakens one set of bonds while strengthening another set (*8*).

"...selectively bending or twisting... bonds... could potentially drive previously unfavorable reaction[s]...."

In the mechanism described and demonstrated by Zholdassov *et al.*, reactions are driven—pushed—in a chemical direction. Bonds in the reactant molecules are bent directionally (strained) so as to become more reactive. The rates of intermolecular Diels-Alder cycloaddition reactions are accelerated by using pressure applied from reactants inked on a polymer stamp with co-reactants tethered to a surface to define pressure and direction and to maintain orientational control when the two are brought into controlled contact. In intermolecular Diels-Alder reactions, a six-membered ring is formed that links the reactants together; the reaction does not have intermediates. Zholdassov *et al.* found that the reaction rate acceleration depends on the substituents involved and reaches up to ~40-fold. The steric constraints and electronic structures of the reactants both play important roles, as elucidated by related calculations.

Implementing such reaction acceleration requires both the means to maintain the relative orientations of the reactant molecules and to apply pressure along the molecular direction that facilitates the desired reaction. The targeted result is that the activation barrier along a particular reaction coordinate is lowered, as in selective catalysis, but by manipulating the reactants and/or intermediates mechanically. This work could be extended by driving reactions along pathways that they would not otherwise proceed.

Isolating and orienting the reactants can play important roles in directing chemical reactions (*9*, *10*). This strategy is used in enzymatic reactions throughout nature but is less often applied in laboratory syntheses. Zholdassov *et al.* used a simple tool to apply directional pressure in their work. The inhomogeneity and gradients in their imaging data, related to the stamp pattern and contacts, indicate that the reactivity depends considerably on the applied pressure. Such pressure can be straightforwardly tuned by choice of materials and preparation of stamps; the resulting pressures, surface areas of contact, and other relevant parameters can be modeled accurately (*11*) and made uniform. Therefore, a "chemical press" can be envisioned that drives such reactions within a set pressure range or in spatial patterns across surfaces using soft lithographic methods (*12*, *13*).

Taking a page from the successes of polymer mechanochemistry, once the rules of pressure-induced reactions are elucidated, theory will play important roles in selecting and exposing functional groups and in designing bonds that are susceptible to reactions that yield targeted products with great selectivity. Zholdassov *et al.* have shown that the energetics are readily accessible and compare well with their experiments. Recent advances in soft lithography and parallel processing at the nanoscale will enable finer and more consistent means to "push" molecules into desired reactions. Alignment of the reactants and exposure of the key mechanically responsive bonds can be arranged by using chemical patterning and self-assembly methods for surface attachment. ■

[1]Department of Chemistry and Biochemistry, University of California, Los Angeles (UCLA), Los Angeles, CA, USA. [2]Department of Bioengineering, UCLA, Los Angeles, CA, USA. [3]Department of Materials Science and Engineering, UCLA, Los Angeles, CA, USA. [4]California NanoSystems Institute, UCLA, Los Angeles, CA, USA. Email: psw@cnsi.ucla.edu

REFERENCES AND NOTES

1. R. Rohs *et al.*, *Annu. Rev. Biochem.* **79**, 233 (2010).
2. Y. S. Zholdassov *et al.*, *Science* **380**, 1053 (2023).
3. J. L. Do, T. Friščić, *ACS Cent. Sci.* **3**, 13 (2017).
4. P. S. Weiss, D. M. Eigler, *Phys. Rev. Lett.* **69**, 2240 (1992).
5. F. Albrecht *et al.*, *Science* **377**, 298 (2022).
6. A. R. Kurland *et al.*, *J. Phys. Chem. Lett.* **1**, 2288 (2010).
7. J. Li *et al.*, *Acc. Chem. Res.* **48**, 2181 (2015).
8. S. Akbulatov *et al.*, *Science* **357**, 299 (2017).
9. M. Kim *et al.*, *Science* **331**, 1312 (2011).
10. S. A. Claridge *et al.*, *Chem. Soc. Rev.* **42**, 2725 (2013).
11. X. Xu *et al.*, *Nano Lett.* **17**, 3302 (2017).
12. W.-S. Liao *et al.*, *Science* **337**, 1517 (2012).
13. G. Liu *et al.*, *Chem. Rev.* **120**, 6009 (2020).

ACKNOWLEDGMENTS

P.S.W. thanks the National Science Foundation (grant #CHE-2004238) for support and A. M. Andrews for helpful discussions.

10.1126/science.adi3388

POLICY FORUM

CLIMATE POLICY

Credibility gap in net-zero climate targets leaves world at high risk

Looking at policies instead of promises shows that global climate targets may be missed by a large margin

By **Joeri Rogelj[1,2,3], Taryn Fransen[4,5], Michel G. J. den Elzen[6,7], Robin D. Lamboll[1], Clea Schumer[4], Takeshi Kuramochi[8,9], Frederic Hans[8], Silke Mooldijk[8], Joana Portugal-Pereira[10]**

Global climate policy is undergoing a rite of passage. What used to be a conversation about ambitious target setting now focuses increasingly on implementation and interventions to achieve these targets. This liminal transition from ambition to implementation is complex and presents deep ambiguities that are challenging for scientists to communicate and decision-makers to fathom. A critical question is whether we can believe that countries will deliver on the commitments they have made. By evaluating policy characteristics of countries' net-zero targets, we can assign the targets credibility ratings, then estimate how greenhouse gas (GHG) emissions and temperature are differentiated by our confidence in the targets. When we consider the credibility of current climate pledges, our assessment shows that the world remains far from delivering a safe climate future.

The drumbeat of climate impacts pounding vulnerable communities, the potential for further harm if climate change goes unchecked (*1*, *2*), and the incontrovertible scientific evidence of humanity's dominant contribution to these changes (*3*) have led the international community to adopt ambitious climate goals (*4*, *5*). These include holding global warming to well below 2°C compared to preindustrial levels while pursuing efforts to limit it to 1.5°C, and reducing global GHG emissions to net zero this century (*6*).

Policy roll-out at the country level is needed to deliver on these bold global targets. Under the Paris Agreement, countries pledge actions and emissions reductions that are to be achieved over the next decade (known as nationally determined contributions, or NDCs, currently targeting 2030) and long-term strategies toward net-zero GHG emissions "by or around midcentury" (*5*). Then—crucially—they must adopt and implement domestic policies to achieve them. Even the recent wave of updated NDCs and net-zero targets (*7*) leaves deep uncertainty about how much the world will actually warm (*8*). This uncertainty stems in large part from questions regarding the credibility of net-zero targets.

CREDIBILITY CREATES CLARITY

Communications about where global warming is heading have created a climate of confusion. More cautious analyses that only look at the current status of domestic policies and their influence on emissions in the medium term project global warming centering somewhere between 2.5° and 3°C in 2100—and continuing to increase thereafter (*8*, *9*) [see supplementary materials (SM) and table S1]. By contrast, analyses that factor in international commitments in NDCs and long-term pledges—taking them at face value regardless of how credible they are—suggest that global warming will stabilize between 1.5° and 2°C and even gradually reverse toward the end of the century (*8*–*10*).

The two outcomes could not contrast more sharply: a world where climate change continues toward levels that undermine sustainable development (*2*) versus a world where losses and damages are capped at potentially manageable levels. The implications for risk management and adaptation planning differ vastly between these two worlds.

Decision-makers and the general public alike need to understand where the tally is at, and which of these worlds current r and long-term policy is committing us to. Current analyses do not provide such clarity.

Projecting emissions trajectories decades into the future is an inherently uncertain exercise (*11*). However, this uncertainty can be clarified by assessing the reliability and quality of each target, and adjusting projected GHG emissions and global temperatures based on the current credibility of their achievement.

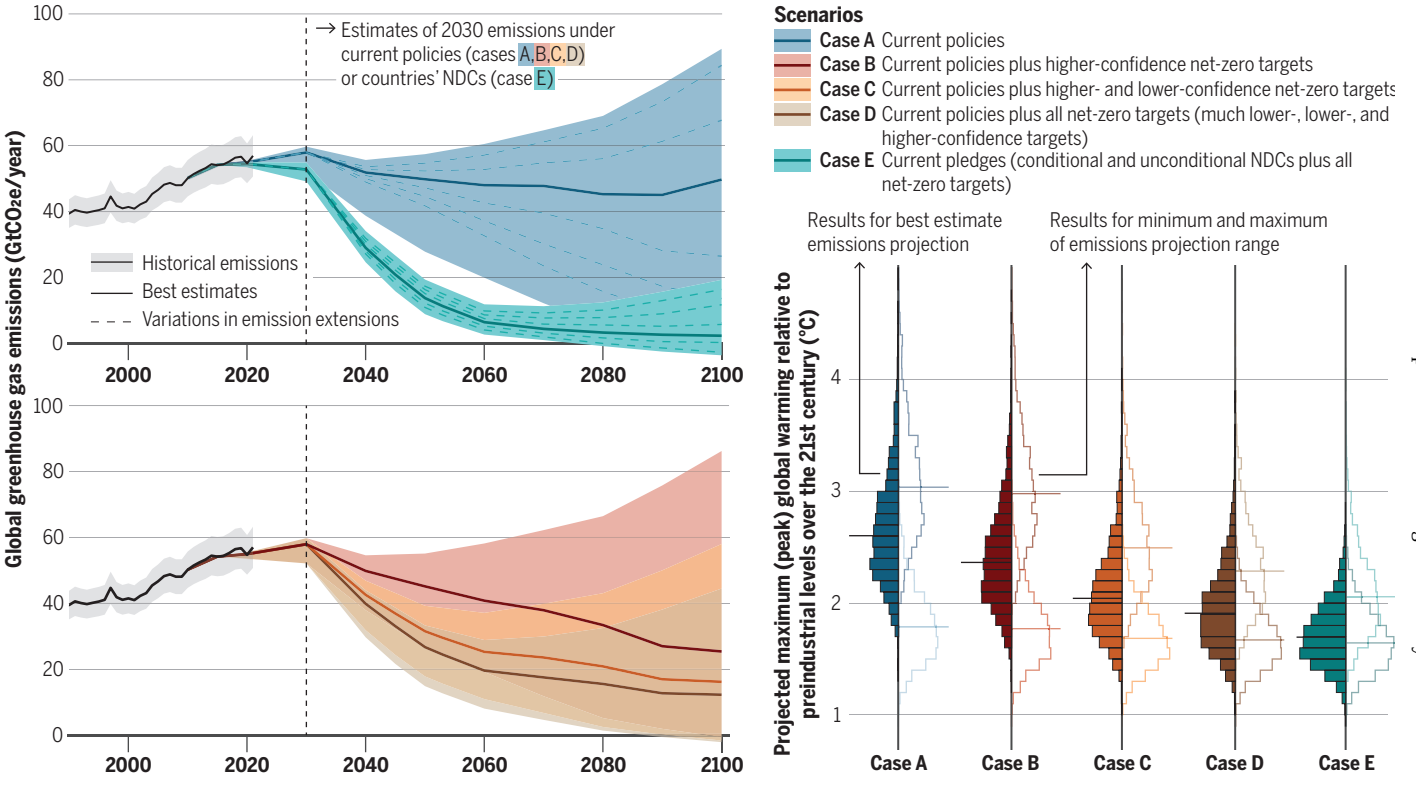
Here we identify and evaluate three characteristics of individual net-zero targets: whether the target is legally binding, whether there is a credible policy plan guiding its implementation, and whether a country's near-term policies already put emissions on a downward path over the next decade (SM and tables S3 to S5). We combine these metrics to produce a credibility rating of each country's net-zero target given current policy evidence. Each target is assigned a score of higher, lower, or much lower confidence. For example, the European Union has a legally binding target accompanied by a credible implementation plan, and its projected 2030 emissions are lower than their 2020 levels. Its net-zero target is therefore assigned a higher confidence score. A less favorable assessment in any of the three dimensions would result in a lower confidence score. Finally, these ratings are used to develop projections of global GHG emissions and temperature that are differentiated by the assessed confidence level. These projections cover an as yet unprobed gray area between the extremes that have been explored in the literature.

In total, we present five scenarios, in order of most conservative to most optimistic: (A) current policies, which considers only domestic policies and disregards both NDCs and net-zero and other long-term targets; (B) current policies plus higher-confidence net-zero targets; (C) current policies plus higher- and lower-confidence net-zero targets; (D) current policies plus all net-zero targets; and (E) current policies plus all (unconditional and conditional) NDC targets and all net-zero targets (see the figure). All except case E implicitly consider the credibility of NDCs by assuming reductions by 2030 through policies that are already on the books and are being implemented. Case E is the only one to assume that both NDCs and all net-zero targets are fully implemented. For all cases, emissions estimates for the year 2030 are

[1]Centre for Environmental Policy, Imperial College London, London, UK. [2]Grantham Institute for Climate Change and the Environment, Imperial College London, London, UK. [3]Energy, Climate and Environment Program, International Institute for Applied Systems Analysis, Laxenburg, Austria. [4]World Resources Institute, Washington, DC, USA. [5]Energy and Resources Group, University of California–Berkeley, Berkeley, CA, USA. [6]PBL Netherlands Environmental Assessment Agency, The Hague, Netherlands. [7]Institute for Environmental Studies (IVM), Vrije Universiteit Amsterdam, Amsterdam, Netherlands. [8]NewClimate Institute, Cologne, Germany. [9]Copernicus Institute of Sustainable Development, Utrecht University, Utrecht, Netherlands. [10]Centre for Energy and Environmental Economics (CENERGIA), Energy Planning Program, COPPE, Universidade Federal do Rio de Janeiro, Rio de Janeiro, Brazil. Email: j.rogelj@imperial.ac.uk

Emissions and peak temperature projections of five scenarios reflecting levels of target achievement

(Left panel) Historical and projected global greenhouse gas emissions (aggregated with 100-year global warming potential values, GWP-100, from the IPCC Sixth Assessment Report, based on the MESSAGE-GLOBIOM model). Best estimate emissions projections are shown as solid lines. Gray ranges show the 90% confidence interval for historical emissions. The shaded ranges reflect the full modeled spread due to uncertainty in near-term emissions by 2030 and ambiguity in their forward projections for each case. Each dashed line in the top-left panel illustrates an alternative assumption about how climate policy is continued after 2030; see supplementary materials (SM). (Right panel) Peak global warming outcomes for best estimate (solid histograms) and minimum and maximum (line histograms) emissions projections. Thin horizontal lines indicate the median estimate. Global warming outcomes for the year 2100 are shown in fig. S2 (see SM for data and methods).



$GtCO_2e$/year, gigatonnes of carbon dioxide equivalent per year; NDCs, nationally determined contributions.

based on the UN Environment Program Emissions Gap Report (*8*).

CREDIBLY OFF TRACK

Our results show a much more transparent picture of where we are heading, how policy targets narrow the cone of future climate projections, and which uncertainties remain because of assumptions analysts must still make. The most conservative scenario, case A, which considers only current policies, disregarding NDCs as well as net-zero and other long-term targets, produces both the highest emissions and warming estimates and the largest uncertainty. This case is estimated to lead to global emissions of ~58 (range: 52 to 60) gigatonnes of carbon dioxide equivalent per year ($GtCO_2e$/year) by 2030 (*8*), and the ambiguity about how they continue thereafter results in projected global GHG emissions in 2100 ranging from about zero to 90 $GtCO_2e$/year, with a best estimate of ~50 $GtCO_2e$/year (see SM for details). Global warming projections mirror this uncertainty, with best-estimate emissions leading to a median temperature projection for the year 2100 of 2.6°C, with a range of 1.7° to 3.0°C, depending on how policies are assumed to continue after 2030 (see the figure) (table S6).

In the most forgiving scenario, case E, in which all country promises regarding NDCs and net-zero targets (even those with much lower credibility) materialize, emissions, warming, and their uncertainties are all much smaller. Best-estimate future emissions in this case produce a median peak warming of 1.7°C over the course of the 21st century, with a much narrower uncertainty range due to smaller emission projection variations of 1.6° to 2.1°C. Although these figures may suggest that the Paris Agreement climate goals are well within reach, the fact that about 90% of assessed net-zero targets score a lower or much lower confidence of achievement confirms that, in reality, concrete and credible efforts to achieve these low temperature projections remain a long way off.

When only higher-confidence net-zero targets are included on top of current policies (case B), global warming is projected to increase to 2.4°C by 2100 (range due to emissions projection uncertainties: 1.7° to 3.0°C)—missing global climate goals by a long way. Warming is also projected to continue after 2100, as global emissions of long-lived GHGs would not yet have reached near-zero levels under these assumptions. Only when net-zero targets with lower (case C) or much lower (case D) confidence scores are also considered do median temperature projections become markedly lower, at 2.0°C and 1.9°C, respectively—still exceeding some or all of the global warming limits set out in the Paris Agreement (see the figure). Although our assessment builds on stylized modeling methods, the qualitative insights of our credibility assessment that shows that the world is still on a high-risk climate track are robust across a wide range of sensitivity cases that explore variations in model assumptions and structure (SM and tables S6 to S10).

Uncertainties in how strongly the climate will warm in response to humanity's past and future GHG emissions add a final

GRAPHIC: D. AN-PHAM/*SCIENCE* BASED ON J. ROGELJ *ET AL.*

level of uncertainty that we uncover here. The numbers reported above present the median estimate of the climate response. However, for risk assessments, it is essential to also consider how much warming can be expected at the tails of the distribution (*12, 13*) (tables S6 and S8). For example, case B, which assumes that only higher-confidence targets are met, results in a 1 in 3 chance of 2.6°C of warming (range: 1.9° to 3.2°C) and a 1 in 10 chance of 3.2°C (range: 2.3° to 3.8°C). Even for the most optimistic scenario, case E, the tails of the distributions illustrate the risk of warming exceeding 2°C.

Uncertainty about policy delivery and ambiguity about its continuation throughout the century are, together with the spread in the climate response, the main factors affecting projections of where global warming is heading. For example, the difference in median warming projections between the most conservative and most optimistic scenarios, cases A and E, is on the order of 1°C, and the difference between their 10th and 90th percentile warming estimates is 1.3°C for case A and 0.8°C for case E (tables S6 and S8). Further uncertainty contributions exist. For example, models can differ in their structure and socioeconomic assumptions, which in turn affect emissions and temperature projections (fig. S1). For example, median temperature projections based on four alternative model formulations can be 0.3° to 0.4°C higher than the results shown in the figure (table S10). In addition, many near- and long-term targets set a cap on total GHG emissions. In some cases, however, it is not clear which gases are covered, or what might happen to other gases when the target applies only to CO_2. This is an additional, yet second-order dimension causing variations in global warming projections of no more than 0.1°C globally (table S7).

PATHWAYS TO IMPROVEMENT

The lack of confidence in most net-zero targets today does not preclude an important role for them in climate policy. On the contrary, it is typical that targets precede implementation—there is no additional ambition in setting targets whose achievement is a foregone conclusion. What is imperative is that implementation does follow target setting and that decision-makers understand the degrees of warming at stake if it does not.

Our analysis shows that if only the highest-confidence net-zero targets are achieved, global temperature is expected to exceed the Paris Agreement limits. Reflecting net-zero targets in domestic legislation, formulating plans to implement them, and then translating those plans into policies and measures that drive emission reductions in the near term are critical steps to ensure the achievement of all net-zero targets and would therefore markedly improve the outcomes presented here.

Legally binding targets promote policy durability (e.g., as an insurance against political turnover), compliance, and cross-government coordination. Several countries, including the United Kingdom, Australia, Canada, Chile, Japan, and Nigeria, as well as the European Union, have already reflected their net-zero targets in law. Most, however, have not. When net-zero legislation accompanies net-zero target setting, national institutions will tend to support implementation, particularly in those countries with strong governance and institutions.

Implementation plans help to clarify which changes are needed at the sector and subsector level to achieve net-zero emissions, and can also identify necessary resources and assign responsibility for action. The Glasgow Climate Pact outlines a role for the long-term strategies that countries submit to the United Nations. It highlights that they can guide implementation and urges parties to develop long-term strategies "towards just transitions to net-zero emissions by or around mid-century" (*5*). To improve the credibility of their net-zero targets, countries should ensure that their long-term strategies lay out a clear pathway to net zero and accompany these with detailed domestic implementation plans as appropriate (*6*). The United States, for example, plans to release a National Climate Strategy focusing on "the immediate policies and actions" it needs to deliver the technology and infrastructure for achieving the net-zero-by-2050 target (*14*). Implementation plans should identify an emission pathway toward the target year, set key emission reduction measures to reach net zero, and include sector-specific details (*15*).

"Implementation plans should…include sector-specific details."

Neither legally binding targets nor implementation plans guarantee that targets will be achieved. It is therefore crucial that net-zero implementation plans are subsequently translated into domestic near-term policy targets and measures to ensure that emissions peak as soon as possible (in countries where they are still on the rise) and then rapidly decline across the board.

Irrespective of these improvements, climate risks will not be eliminated entirely (see the figure). Our results clearly illustrate that the best way to hedge against climate uncertainties and their potential disastrous impacts on nature and society is to set, implement, and achieve the promised near- and long-term targets. ■

REFERENCES AND NOTES

1. United Nations Framework Convention on Climate Change (UNFCCC), "FCCC/SB/2015/INF.1 - Report on the structured expert dialogue on the 2013–2015 review" (UNFCCC, 2015).
2. Intergovernmental Panel on Climate Change (IPCC), "Summary for Policymakers" in *Climate Change 2022: Impacts, Adaptation, and Vulnerability. Contribution of Working Group II to the Sixth Assessment Report of the Intergovernmental Panel on Climate Change* (Cambridge Univ. Press, 2022), pp. 3–33.
3. IPCC, "Summary for Policymakers" in *Climate Change 2021: The Physical Science Basis. Contribution of Working Group I to the Sixth Assessment Report of the Intergovernmental Panel on Climate Change* (Cambridge Univ. Press, 2021), pp. 3–32.
4. UNFCCC, *FCCC/CP/2015/L.9/Rev.1: Adoption of the Paris Agreement* (UNFCCC, 2015).
5. UNFCCC, *FCCC/PA/CMA/2021/10/Add.1 Decision 1/CMA.3 Glasgow Climate Pact* (UNFCCC, 2021).
6. J. Rogelj, O. Geden, A. Cowie, A. Reisinger, *Nature* **591**, 365 (2021).
7. UNFCCC, "FCCC/PA/CMA/2022/4: Nationally determined contributions under the Paris Agreement - Synthesis report by the Secretariat" (UNFCCC, 2022).
8. J. Rogelj, M. G. J. Den Elzen, J. Portugal-Pereira, "Chapter 4: The emissions gap" in *The UNEP Emissions Gap Report 2022: The Closing Window, Climate Crisis Calls for Rapid Transformation of Societies* (UNEP, 2022), pp. 26–37.
9. Climate Action Tracker, "Massive gas expansion risks overtaking positive climate policies. New CAT analysis shows LNG expansion plans threaten 1.5°C warming limit" (NewClimate Institute and Climate Analytics, 2022).
10. M. Meinshausen *et al*., *Nature* **604**, 304 (2022).
11. L. A. Smith, N. Stern, *Philos. Trans. - Royal Soc. Math. Phys. Eng. Sci.* **369**, 4818 (2011).
12. Z. Nicholls *et al*., "Cross-Chapter Box 7.1: Physical emulation of Earth System Models for scenario classification and knowledge integration in AR6" in *Climate Change 2021: The Physical Science Basis. Contribution of Working Group I to the Sixth Assessment Report of the Intergovernmental Panel on Climate Change* (Cambridge Univ. Press, 2021), pp. 962–967.
13. C. J. Smith *et al*., *Geosci. Model Dev.* **11**, 2273 (2018).
14. "The long-term strategy of the United States. Pathways to Net-Zero Greenhouse Gas Emissions by 2050" (United States Department of State and the United States Executive Office of the President, 2021), p. 65.
15. Climate Action Tracker, "Evaluation methodology for national net zero targets" (Climate Analytics and NewClimate Institute, 2021), p. 20.

ACKNOWLEDGMENTS

The authors thank the Integrated Assessment Modeling Consortium (IAMC) and the International Institute for Applied Systems Analysis (IIASA) for hosting the emission pathway data used in the IPCC SR15 and IPCC AR6 WG III and C. Smith for making the FaIR model and its IPCC AR6 calibration openly accessible and reusable. J.R. and R.D.L. acknowledge support from the European Union's Horizon 2020 research and innovation program under grant agreements no. 820829 (CONSTRAIN) and no. 101003687 (PROVIDE), and under no. 101003536 (ESM2025) for J.R. only. T.F. acknowledges support from the Link Foundation.

SUPPLEMENTARY MATERIALS

science.org/doi/10.1126/science.adg6248

10.1126/science.adg6248



BOOKS *et al.*

There is no single ideal climate that causes civilizations, such as the Roman empire—architectural artifacts of which are shown blanketed in snow in 2012—to rise, thrive, or fall.

PHOTO: ANDREAS SOLARO/AFP VIA GETTY IMAGES

ENVIRONMENTAL HISTORY

Empire and its environments

An ambitious "big history" of climate and civilization falls victim to the perils of the genre

By **Dagomar Degroot** *and* **Timothy Newfield**

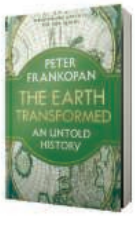
How have humans changed, and been changed by, Earth? That is the question that Peter Frankopan endeavors to answer in *The Earth Transformed*, a sweeping history that begins with the primordial oxidation of Earth's atmosphere and concludes in our current era of environmental crisis. In eloquent prose, the book offers some thought-provoking answers but cannot escape the limitations of its genre.

The book's subject is the long-standing focus of several academic fields of study, most notably environmental history, that today include the efforts of thousands of scholars. Its indebtedness to this scholarship accounts for its 200-page bibliography—a compendium that, evidently, was too big to publish in print. Readers must find it online and there browse it "at leisure."

The book's online bibliography exemplifies the problem with "big histories" that summarize the work of specialists in many disciplines and promise to, as the publisher's website puts it, "radically reframe the way we look at the world." Often, their authors do not fully understand how and why specialists make claims or why they disagree. As a result, they can easily leave readers with a distorted impression of an academic field, one that leans toward sensationalism.

More than other surveys, *The Earth Transformed* helpfully alerts readers when scholarship is not yet settled and acknowledges uncertainties that complicate its claims. It wisely recognizes that to find compelling links between environmental and social changes, evidence must be "handled carefully and put in contexts that are balanced, persuasive and appropriate."

Yet the book's claims frequently do not demonstrate familiarity with the sciences on which they depend. To argue that a volcanic eruption triggered the second-century Antonine Plague, for instance, Frankopan references a chronology of volcanic eruptions that was rendered obsolete some 15 years ago. He later references a revised eruption chronology but seems unaware that the new chronology differs from the old one or that there are multiple chronologies. The result is that an eruption portrayed in the book as preceding and provoking the plague actually followed it.



The Earth Transformed: An Untold History
Peter Frankopan
Knopf, 2023. 736 pp.

The Earth Transformed repeatedly conflates association with correlation, and correlation with causation, often by relying on flimsy evidence. It argues, for instance, that far-flung populations benefited from a "Roman Climatic Optimum" to such an extent that antiquity amounted to a global "time of empire." Given that there is no high-resolution climate data that span the Roman era or empire, however, the reader may wonder how we know that the period was indeed warm across much of the world.

The book also connects climatic changes after the purported Roman Climatic Optimum to the emergence and spread of diseases across the Roman Empire, despite admitting that "basic epidemiological details" about these diseases "are vague." Indeed, scholars do not know how such diseases were transmitted, where they emerged, or whether the climate changes that may have coincided with them manifested where they surfaced.

More than three decades after Michael Baillie cautioned scholars to avoid smearing together climatic and social changes that may in fact have unfolded in different places and at different times (*1*), *The Earth Transformed* offers plenty of examples of this tendency. Frankopan argues, for instance, that drought in northwestern China spurred the Huns westward in the fourth century, although they may have been nearly 2000 km removed from drought. Readers may likewise be confused to learn both that warm spring seasons "produced the sharp spikes in the prevalence of the bacterium that caused bubonic plague" in the sixth century and that the resulting plague pandemic took place in one of "the coldest decades" of the Holocene epoch.

Because *The Earth Transformed* skips so quickly through time, it cannot help but simplify complex histories to such an extent that they become unrecognizable. It argues, for example, that the differing competence of officials in Ming China and the Dutch Republic was the reason these societies fared differently in the 17th century, despite facing "similar climatic conditions" during the Little Ice Age. In fact, the Little Ice Age brought very different weather to these radically different societies, and few scholars believe that climate change was solely or even primarily responsible for their divergent trajectories.

The Earth Transformed regularly repeats the oldest, most simplistic narrative in scholarship of past climate change: that climatic "deterioration" caused empires to fall and climatic "improvement" allowed them to rise. Developed more than a century ago, this narrative depends on an assumption once used to justify European imperialism: that an ideal climate exists for civilization. It is hard to defend in light of newer, more sophisticated scholarship cited in the book's lengthy bibliography.

Do these flaws fatally undermine *The Earth Transformed*? Not quite. The book provides a survey that is sure to spark the imagination of nonexpert readers. We only hope that it will encourage, rather than dissuade, further reading. ■

The reviewers are at the Department of History, Georgetown University, Washington, DC 20057, USA. Email: dd865@georgetown.edu

REFERENCES AND NOTES

1. M. G. L. Baillie, *J. Theor. Archaeol.* **2**, 12 (1991).

10.1126/science.adh2717

SCIENCE LIVES

Thomas Young, 250 years later

A biographer reflects on the remarkable contributions of the prolific polymath

By **Andrew Robinson**

In 1931, Albert Einstein wrote a foreword to the fourth edition of Isaac Newton's 1704 *Opticks*, which described Newton's experiments with, and explanations of, phenomena associated with light, including his observations of the colors of thin films. These observations, wrote Einstein, were "the origin of the next great theoretical advance, which had to await, over a hundred years, the coming of Thomas Young."

Young's famous double-slit experiment, published in 1807, showed light passing through two neighboring slits and creating a diffraction pattern of bright and dark interference fringes—explicable by him only by assuming that light rays are waves, not streams of particles as stated by Newton. But in 1905, Einstein's quantum theory introduced the idea of wave–particle duality. Light somehow behaves as both wave and particle, depending on how you measure it, and the double-slit experiment can be used to demonstrate both types of behavior. In the 1960s, Richard Feynman declared the experiment "the heart of quantum mechanics" and its "only mystery." His comment remains apt.

The standard heritage plaque on Young's London house labels him simply as "Man of Science." It lacks space to mention that he was not only a physicist but also a true polymath, having made substantial contributions as a physician, physiologist, philologist, Egyptologist, and writer.

Trained as a physician in the 1790s, Young's investigations of the eye led him to explain its method of focusing on objects at varying distances, its astigmatism, and its perception of colors with three types of photoreceptors. Another key discovery in physics, elasticity—the ratio between stress and strain in materials—was formulated as Young's modulus in 1807. As for languages, Young—a remarkable linguist since childhood—compared the vocabulary and grammar of some 400 languages and coined the term "Indo-European" in 1813. This led to his pioneering attempt to decipher the Rosetta Stone's two ancient Egyptian scripts: hieroglyphic in 1814–19—which triggered Jean-François Champollion's full decipherment in 1822–24—and demotic in 1821–29. Young's numerous articles and books on all the preceding subjects, plus many others, included more contributions to the *Encyclopaedia Britannica* than were written by any other contributor in its history.



A satirical illustration by British caricaturist James Gillray published in 1802 portrays Thomas Young performing a demonstration of "the powers of air" at the Royal Institution.

Despite these achievements, Young had mixed feelings about polymathy. It certainly brought him no celebrity, such as a knighthood, either during his life or posthumously. Nonetheless, not long before he died in 1829 at age 55, Young reflected: "It is probably best for mankind that the researches of some investigators should be conceived within a narrow compass, while others pass more rapidly through a more extensive sphere of research."

Consider polymaths since the time of Young: for example, Charles Darwin, Hermann von Helmholtz, Florence Nightingale, Alfred Wegener, Erwin Schrödinger, Alan Turing, Linus Pauling, and Benoit Mandelbrot—each of whom worked in several disparate fields. Darwin contributed to zoology, botany, geology, paleontology, and philosophy, not to mention literature. Had he been required to complete a PhD in the biology of barnacles and then joined an academic life-sciences department rather than circumnavigating the planet on HMS *Beagle* in 1831–36, he would have lacked the varied experiences and exposure to different disciplines that led to his discovery of natural selection.

It is difficult today to be a polymath, but academic institutions have become more cognizant, in recent years, of the value of interdisciplinarity. In 2006, for example, a consortium of leading London universities united to form the Thomas Young Centre, a collaboration consisting of ~100 research groups within academic departments such as physics, materials, chemistry, Earth sciences, biology, and several branches of engineering that seeks to promote interdisciplinary study in materials science. In a recent statement to me, one of its cofounders, Imperial College physicist Michael Finnis, observed that "compartments" are not helpful in research and noted "Thomas Young seemed to represent the epitome of interdisciplinary thinking."

In 2023, the 250th anniversary of Young's birth, the chief lesson of his life for scientists is surely how Young made his greatest discovery, the double-slit experiment. It did not come from any formal training in physics. Instead, it emerged gradually from his fascination as a physician with human vision, which provoked his fascination with the physics of light. Polymathy is generally unpredictable—but curiosity and creativity are among its hallmarks. ■

Andrew Robinson is the author of *The Last Man Who Knew Everything* (Open Book Publishers, revised edition, 2023), a biography of Thomas Young.
Email: andrew@andrew-robinson.org

10.1126/science.adh9236



PHOTO: COPYRIGHT CARLOS GALLINGER. THE WAY OF THING

Green energy projects at odds with conservation

Protected areas and habitat connectivity have become global (*1*), national (*2*), and regional (*3*) conservation priorities, but protected areas alone do not ensure connectivity (*4*). For example, US federal legislation in 1994 designated millions of hectares as wilderness or otherwise protected areas in California's Mojave Desert, but without consideration for the importance of connectivity or the overall effect of that legislation on habitat fragmentation (*5*). Now, two green energy projects—a high-speed train (the Brightline High Speed Rail) and a solar generating facility (the Soda Mountain Solar Project)—are planned between proximate, albeit separate, protected areas, posing threats to the species the protected areas were intended to benefit (*6*). Habitat connectivity on public lands was not a consideration in 1994 (*5*), but it must be prioritized in future legislation (*2*).

Desert bighorn sheep (*Ovis canadensis nelsoni*), the largest native ungulate occupying the Mojave Desert, are habitat specialists that depend on interactions between populations occupying noncontiguous areas of suitable habitat (*7*). Fragmentation by human activity has disrupted those interactions, but restoration is possible (*8*–*10*). The planned solar facility, however, will complicate efforts to reconnect a fragmented metapopulation and will affect a variety of other species (*3*, *6*).

Desert bighorn sheep and other wildlife currently cross Interstate Highway 15 at several locations, but the high-speed rail will be continuous within the highway median, precluding their ability to cross at road level. Three overhead crossing structures will help maintain connectivity between wildlife populations on both sides of the highway (*10*). However, the proposed solar facility will be adjacent to one overcrossing and could negate its mitigatory benefit (*6*). A net gain in connectivity requires that the solar project does not impair existing movements or deter wildlife from using the overcrossing. Relocating the solar facility to a location farther from the overcrossing could help.

Protected areas and green energy projects have worthy goals but can also further fragment ecosystems (*6*, *9*). Instead of designating land to satisfy convenience, profit, or political expediency, legislators should protect landscapes in a way that safeguards ecological processes and habitat connectivity (*8*, *9*, *11*). Opportunities to develop proactive, rather than reactive, conservation strategies should not be wasted (*12*). An ecosystem-level approach to conservation planning will help ensure that one proposed project will not interfere with another project's ability to mitigate environmental impacts.

Vernon C. Bleich[1]*, Christina M. Aiello[2], Clinton W. Epps[2], John D. Wehausen[3]
[1]Department of Natural Resources and Environmental Science, University of Nevada Reno, Reno, NV, USA. [2]Department of Fisheries, Wildlife, and Conservation Sciences, Oregon State University, Corvallis, OR, USA. [3]Sierra Nevada Bighorn Sheep Foundation, Bishop, CA, USA.
*Corresponding author. Email: vcbleich@gmail.com

Desert bighorn sheep populations would be furth fragmented by planned renewable energy projects.

REFERENCES AND NOTES

1. P. Davidar *et al.*, *Science* **379**, 765 (2023).
2. L. C. Powers, A. E. Larsen, B. Leonard, A. J. Plantinga, *Biol. Conserv.* **270**, 109557 (2022).
3. California Department of Fish and Wildlife, "Restoring California's wildlife connectivity" (2022); https://nrm.dfg.ca.gov/FileHandler.ashx?DocumentID=204648.
4. B. A. Williams, C. Morgans, J. R. Rhodes, *Science* **379**, 1197 (2023).
5. US Congress, "S.21 - California Desert Protection Act of 1994" (1994); https://www.congress.gov/bill/103rd-congress/senate-bill/21/text.
6. L. Sahagun, "Can bighorns, a bullet train, and a huge solar farm coexist in the Mojave Desert?" *Los Angeles Times* (2023).
7. O. A. Schwartz, V. C. Bleich, S. A. Holl, *Biol. Conserv.* **37**, 179 (1986).
8. J. C. Whiting, V. C. Bleich, R. T. Bowyer, C. W. Epps, *Front. Ecol. Evol.* **11**, 1083350 (2023).
9. T. G. Creech, C. W. Epps, R. J. Monello, J. D. Wehausen, *Landsc. Ecol.* **29**, 605 (2014).
10. California Department of Fish and Wildlife, "Caltrans, California Department of Fish and Wildlife and Brightline agree to build wildlife overcrossings for rail project" (2023); https://wildlife.ca.gov/News/caltrans-california-department-of-fish-and-wildlife-and-brightline-agree-to-build-wildlife-overcrossings-for-rail-project#gsc.tab=0.
11. W. D. Newmark *et al.*, *Sci. Rep.* **13**, 474 (2023).
12. D. S. Wilcove, *Landsc. Ecol.* **7**, 23 (1987).

10.1126/science.adi0761

Obstacles to scientific input in global policy

The United Nations identifies the drivers of the planetary crisis as climate change, biodiversity loss, and pollution (*1*). Mitigation requires reliable science to inform decision-making. However, relevant research is often underutilized in policy planning and implementation because policy-making entities limit the ability of scientists to contribute to the process (*2*, *3*).

The United Nations Environment Programme (UNEP) welcomes the participation of independent scientists whose work is free of conflict of interest (*4*, *5*), but acquiring eligibility is difficult for many scientists (*6*). To be accredited by UNEP, organizations cannot receive any government funding, even if they are self-governed. Although some government-run institutions require scientists to abide by political messaging, which would present a true conflict of interest, scientists at independent institutions, such as universities, that accept government funding are free to make arguments based on scientific evidence. Because UNEP does not distinguish between these two scenarios, the nongovernmental requirement precludes government-funded universities from accreditation with UNEP. This limitation includes scientists from the majority of universities

in Europe and in many countries across the world, where most universities are public and faculty are state employees.

Scientists affiliated with government-funded institutions can seek other modes of entry to UNEP meetings, such as joining national delegations or nongovernmental organizations (NGOs). However, participating in this manner undermines scientists' ability to operate independently given that their true affiliations might be obscured. In addition, because some NGOs might be branded as activists (i.e., viewed as biased), the credibility of scientists' policy recommendations may be questioned (*7*).

A preferable option for scientists affiliated with government-funded institutions is to register through accreditation not directly with UNEP, but under multilateral environmental agreements, such as the Basel, Rotterdam, and Stockholm (BRS) Conventions. This option is available to everyone but underused. Because the requirements are less stringent, scientists are more likely to gain eligibility. Institutions can also register through this process. UNEP should make this option more visible and accessible.

Scientists with no conflicts of interest must be given the ability to participate in and contribute to effective, comprehensive, and equitable outcomes. To facilitate the admittance of such scientists, UNEP—with the support of member states—should accept universities as independent, self-governed entities that can be directly accredited. Academic institutions should support their employees in these processes. Improving the accessibility of global negotiating processes will allow independent scientists, whose trusted collective knowledge is essential in securing a path toward a sustainable future, to participate fully in policy negotiations.

Bethanie Carney Almroth[1]*, Amila Abeynayaka[2], Miriam L. Diamond[3], Trisia Farrelly[4], Marina Fernandez[5], Sedat Gündoğdu[6], Ibrahim Issifu[7], Idun Rognerud[8], Andreas Schäffer[9], Martin Scheringer[10], Patricia Villarrubia-Gómez[11], Rufino Varea[12], Penny Vlahos[13], Martin Wagner[14], Marlene Ågerstrand[15]
[1]Department of Biological and Environmental Sciences, University of Gothenburg, Göteborg, Sweden. [2]Institute for Global Environmental Strategies, Hayama, Japan. [3]Department of Earth Sciences and School of the Environment, University of Toronto, Toronto, ON, Canada. [4]Political Ecology, Research Centre, Massey University, Aotearoa New, Zealand. [5]Laboratorio de Neuroendocrinología, Instituto de Biología y Medicina Experimental, Consejo Nacional de Investigaciones Científicas y Técnicas (IBYME-CONICET), Buenos Aires, Argentina. [6]Faculty of Fisheries, Cukurova University, Adana, Turkey. [7]Fisheries Economics Research Unit, Institute for the Oceans and Fisheries, University of British Columbia, Vancouver, Canada. [8]Norwegian Institute for Water Research, Oslo, Norway. [9]Institute for Environmental Research, North Rhine-Westphalia Technical University of Aachen (RWTH) Aachen University, 52074 Aachen, Germany. [10]Eidgenössische Technische Hochschule (ETH) Zürich, Zürich, Switzerland. [11]Stockholm Resilience Centre, Stockholm University, Stockholm, Sweden. [12]School of Agriculture, Geography, Environment, Ocean and Natural Sciences, The University of the South Pacific, Suva, Fiji. [13]Department of Marine Sciences, University of Connecticut, Avery Point, CT, USA. [14]Department of Biology, Norwegian University of Science and Technology, Trondheim, Norway. [15]Department of Environmental Science, Stockholm University, Stockholm, Sweden.
*Corresponding author.
Email: bethanie.carney@bioenv.gu.se

REFERENCES AND NOTES

1. United Nations Framework Convention on Climate Change, "What is the triple planetary crisis?" (2022); https://unfccc.int/blog/what-is-the-triple-planetary-crisis.
2. J. Claudet *et al*., *One Earth* **2**, 34 (2020).
3. J. C. Young *et al*., *Biodivers. Conserv.* **23**, 387 (2014).
4. UNEP, "Resumed first session of the ad hoc open-ended working group on a science-policy panel to contribute further to the sound management of chemicals and waste and to prevent pollution (OEWG 1.2)" (2023); https://wedocs.unep.org/bitstream/handle/20.500.11822/41396/OWEG_1.2.pdf?sequence=1&isAllowed=y.
5. UNEP, "Registration information for INC1" (2023); https://wedocs.unep.org/bitstream/handle/20.500.11822/41310/Registration_INC1.pdf.
6. UNEP, Accreditation (2023); https://www.unep.org/civil-society-engagement/accreditation.
7. K. Rietig, *Pol. Sci.* **47**, 141 (2014).

COMPETING INTERESTS

T.F. is on the UNEP Scientific Advisory Committee.

10.1126/science.adi1103

Evaluating peer review at NIH

The National Institutes of Health (NIH), in an effort to ensure equity and reduce bias, has proposed a plan to change how grant proposals are peer reviewed (*1*). However, the proposed changes do not address previous evidence about bias in the peer review process, and the agency has not specified how it plans to evaluate progress. NIH should ensure that the policies and practices that control the conduct and communication of grant reviews are informed by evidence and subject to accountability.

The NIH's Center for Scientific Review (CSR) has published research showing that Black applicants are less likely than white applicants to receive funding for comparable proposals because of bias in peer scoring (*2*). CSR then designed and implemented a randomized experimental study demonstrating that double-blinding the review process would reduce that bias (*3*). An independent analysis of NIH grant funding over the past 30 years also shows persistent inequities related to gender, race, and ethnicity in the awarding of grants (*4*). However, the proposed grant review policy does not mention race or diversity, equity, and inclusion. Instead, it aims to reduce reputational bias and enable reviewers to focus on scientific merit through a modest reorganization of scoring criteria.

Neither the proposal nor its accompanying report (*5*) provides a rationale for the specific changes or plans for future evaluation. The report identifies persistent racial disparities in funding but does not explain how the changes will alleviate them. It cites no external research and describes no internal evidence that supports the proposed policies. Although NIH committed to "continuous review" of peer review after making policy changes in 2012, the evaluation consisted only of satisfaction surveys and ceased after 3 years (*6*).

We should not expect NIH's system to be optimal, nor that all changes to its operational science policies will succeed. However, the scientific community should expect NIH to build on scientific research, communicate its aims and rationale, and include (and fund) assessment mechanisms. The community should understand the changes' goals and how NIH will accumulate knowledge about what does and does not work.

Micah Altman[1]* and Philip N. Cohen[2]
[1]Center for Research on Equitable and Open Scholarship, MIT Libraries, Massachusetts Institute of Technology, Cambridge, MA, USA. [2]Department of Sociology, University of Maryland, College Park, College Park, MD, USA.
*Corresponding author. Email: escience@mit.edu

REFERENCES AND NOTES

1. NIH Grants and Funding, "A proposed simplified framework for NIH peer review criteria" (2022); https://grants.nih.gov/policy/peer/Proposed-Framework/index.htm.
2. E. A. Erosheva *et al*., *Sci. Adv.* **6**, eaaz4868 (2020).
3. R. K. Nakamura *et al*., *eLife* **10**, e71368 (2021).
4. M. Nguyen *et al*., *JAMA Network Open* **6**, e230855 (2023).
5. Simplifying Review Criteria Working Groups to the CSR Advisory Council, "Recommendations for Simplifying R01 Review Criteria" (NIH, 2021); https://public.csr.nih.gov/sites/default/files/2021-04/Recommendations_of_the_CSRAC_Working_Group_on_Simplifying_Review-non-CT_and_CT.pdf.
6. NIH Grants and Funding, "Continuous review of peer review" (2017); https://grants.nih.gov/policy/peer/continuous-review.htm.

10.1126/science.adi1570

ERRATA

Erratum for the Report "Synthetic transcription elongation factors license transcription across repressive chromatin" by G. S. Erwin *et al*., *Science* 380, eadi0634 (2023). Published online 7 April 2023.

10.1126/science.adi0634

Erratum for the Report "Geometric deep learning of RNA structure" by R. J. L. Townshend *et al*., *Science* 379, eadg6616 (2023). Published online 27 January 2023.

10.1126/science.adg6616

RESEARCH

IN *SCIENCE* JOURNALS

Edited by **Michael Funk**



BIOGEOGRAPHY

Climate underlies major African biomes

The distribution of vegetation types across the globe is determined by climate, but at the local or regional scale, very different vegetation can occur depending on past disturbances and species interactions. Higgins *et al.* investigated how well climate alone can predict the distribution of forest and savanna across tropical and subtropical Africa. Using vegetation plot data, the authors created niche projections for more than 9000 plant species and climate suitability estimates for major growth forms. The resulting model predicted forest versus savanna occurrence with high accuracy, suggesting that spatial variation in climate drives both large-scale and relatively fine-scale vegetation patterns. The effects of climate change on the distribution of African forest and savanna may thus be more predictable than has previously been recognized. —BEL

Science, add5190, this issue p. 1038

In Africa, dominance of C4 grasses, such as in the savanna of Botswana pictured above, or of tropical evergreen trees is largely determined by climate.

PALEOECOLOGY

Losing giants

Mammal faunas in the past were rich, with very large species on all continents, but the vast majority of these species are now extinct. It is reasonably well accepted that the arrival of humans led to extinction of these megafauna in many regions. However, humans evolved in Africa and have coexisted there with some megafauna into the present despite evidence for extinctions going back to earlier than 4 million years ago. Bibi and Cantalapiedra looked at fossil species with respect to a size-abundance model from the late Miocene through the present. Testing three different hypotheses describing drivers of decline, the authors concluded that a changing environment led to patterns of large mammal loss during this period. —SNV

Science, add8366, this issue p. 1076

QUANTUM PHYSICS

A beam splitter for phonons

Phonons are the fundamental quantum vibrations within materials, with individual phonons representing the collective motion of many trillions of atoms. Efforts are underway to determine whether these mechanical vibrations can be developed into a quantum-computing architecture just like their optical cousin, photons. Qiao *et al*. demonstrate a beam splitter for single phonons and controlled two-phonon interference. Adding to the ability to launch and detect single phonons, a beam splitter now provides the final piece in the toolbox to develop a mechanically based platform for quantum computing. —ISO

Science, adg8715, this issue p. 1030

INORGANIC CHEMISTRY

Bismuth hides its triplet

Bismuth conventionally coordinates to at least three other atoms. Pang *et al.* report the synthesis and crystallization of an unusual compound in which a monovalent bismuth center is bonded to just a single bulky carbon ligand. Although theory predicts that this bonding motif should leave two electrons unpaired in a triplet state, the compound did not exhibit a paramagnetic response. The authors attribute this observation to thermal isolation of the lowest magnetic sublevel by the large spin-orbit coupling intrinsic to heavy elements. —JSY

Science, adg2833, this issue p. 1043

DEVELOPMENTAL BIOLOGY

Rewiring chromosomes in development

Whether changes in the three-dimensional (3D) structures of chromosomes regulate gene expression during development has been hotly debated. A major challenge to studying these systems is how to relate a long-range chromatin interaction thousands of base pairs away to its target gene. Liu *et al*.

developed a multi-omics sequencing approach to profile 3D genome structures and gene expression at the same time in single cells, which enables a direct linkage between chromatin conformation and gene expression. Leveraging this new tool, the authors identified widespread chromatin interactions, especially between loci enriched for active enhancers, and found that they were rewired before gene activation during mouse embryonic development. This observation suggests that dynamic chromatin organization plays a critical role in the control of gene expression. —DJ

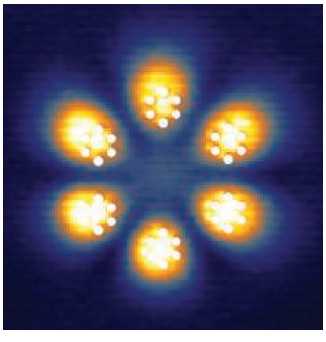
Science, adg3797, this issue p. 1070

QUANTUM CHEMISTRY

Emulating molecular orbitals

There is considerable interest in developing tunable quantum simulators of many-body Hamiltonians that use weakly conducting or insulating surfaces. Using patterned cesium atoms and surface confinement of electrons on indium–tin surfaces, Sierda *et al*. created artificial molecular orbitals that were strongly decoupled from the bulk bands, emulating a series of well-known planar organic molecules. This system serves as a versatile platform with which to emulate quantum chemistry on a surface and provides new ways to look at the interplay between structure and molecular orbitals. This will have relevance for quantum and organic chemistry, solid-state physics, and many-body physics. —YS

Science, adf2685, this issue p. 1048



Conductance imaging reveals artificial hybrid molecular orbitals for clusters of cesium atoms arranged in a benzene structure.

CREDITS: (LEFT TO RIGHT) SIERDA *ET AL.*; WILDLIFE GMBH/ALAMY STOCK PHOTO

FERROELECTRICS

Reducing barriers to polarization

Nitride-based ferroelectric wurtzites are an emerging family of crystals that are highly attractive as switching materials for modern microelectronics. The chemistry of these materials is a good match for current semiconductor platforms. Calderon *et al*. used an array of characterization tools to determine exactly how a representative wurtzite composed of aluminum, boron, and nitrogen undergoes polarization switching. A more detailed understanding of this process is vital for lowering the electric field under which these materials switch, because this is a limiting factor in moving them into applications. —BG

Science, adh7670, this issue p. 1034

CANCER

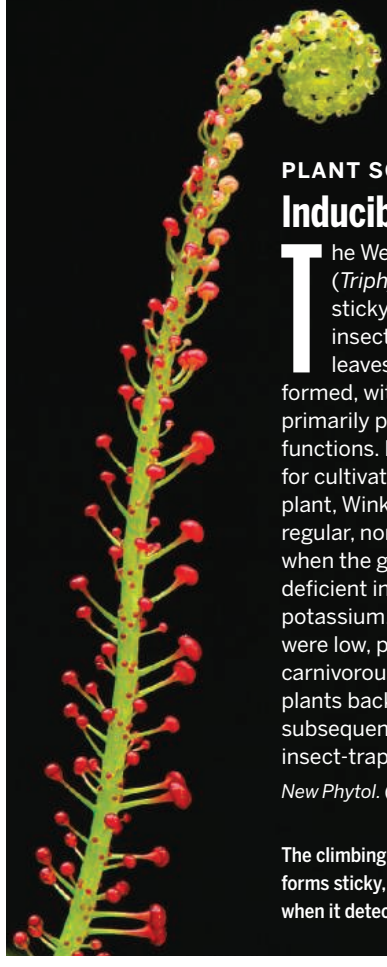
Fighting fibrosis

Treatment for non–small cell lung cancer (NSCLC) has improved considerably since the development of immune checkpoint blockade therapies, but many tumors still fail to respond. Herzog *et al*. found that tumor-associated fibrosis, which is common in patients but is not found in murine models, impaired antitumor immune responses. The authors modeled fibrosis in murine models of NSCLC and found that targeting fibrosis by inhibition of transforming growth factor β signaling could sensitize tumors to immune checkpoint blockade when used in combination with chemotherapy. These results highlight a potential path forward to increasing the sensitivity of NSCLC tumors to immunotherapy. —CSM

Sci. Transl. Med. (2023) 10.1126/scitranslmed.adh8005

IN OTHER JOURNALS

Edited by **Caroline Ash** *and* **Jesse Smith**



PLANT SCIENCE

Inducible carnivory

The West African liana (*Triphyophyllum peltatum*) uses sticky glandular leaves to trap insect prey. However, these leaves are only sometimes formed, with other leaves performing primarily photosynthetic or climbing functions. By developing a protocol for cultivation of this tricky-to-grow plant, Winkelmann *et al.* found that regular, noncarnivorous leaves formed when the growth medium was normal, deficient in nitrogen, or deficient in potassium. But when phosphate levels were low, plants formed glandular carnivorous leaves. Transferring plants back to full nutrients caused subsequent leaves to develop without insect-trapping glands. —MRS

New Phytol. (2023) 10.1111/nph.18960

The climbing plant *Triphyophyllum peltatum* forms sticky, glandular, carnivorous leaves when it detects low phosphate levels.

COGNITION

Learn a new language ASAP

Being bilingual is associated with better cognitive performance and reduced risk of developing dementia. However, some studies have not found any protective effects of bilingualism. Ballarini *et al.* hypothesized that becoming bilingual at different stages in life could have different effects on cognition, potentially explaining these discrepancies. In a cohort of more than 700 older individuals, the authors found that the earlier participants became bilingual, the better they performed on cognitive tests. For individuals that became bilingual late in life (at more than 65 years of age), cognitive performance was similar to that in age-matched monolingual individuals. For long-lasting cognitive benefits, learning a second language early in life is the key. —MMa

Neurobiol. Aging (2023) 10.1016/j.neurobiolaging.2022.12.005

GLYCAN SYNTHESIS

Living polymerization of sugars

Biological polysaccharides are highly complex, with many potential monomers and linkages that determine both physical properties and biological function. Assembling large polymers precisely can be a challenge for chemists. Wu *et al*. developed a chemical synthesis of large glycans through living cationic ring-opening polymerization using 1,6-anhydrosugars as

ALSO IN *SCIENCE* JOURNALS

Edited by **Michael Funk**

CANCER IMMUNOTHERAPY

Dysbiosis redirects gut Tr17 cells to tumors

Immune checkpoint blockade therapy for the treatment of cancer can have reduced efficacy when antibiotics are administered and then discontinued before the start of therapy. Fidelle *et al*. investigated whether bacteria that rebound may affect the treatment response (see the Perspective by Pratt and Milner). *Enterocloster* species that recolonized the guts of mice treated with antibiotics down-regulated the expression of MAdCAM-1, the ligand for integrin α4β7 that helps to retain an immunosuppressive subset of T cells (Tr17 cells) within the gut. This leads to transit of Tr17 cells to tumors and tumor-draining lymph nodes, where they compromise immune checkpoint blockade therapy. In cancer patients undergoing immunotherapy, low levels of serum-soluble MAdCAM-1 correlated with intestinal dysbiosis and poor clinical outcomes for renal, bladder, and lung tumors. —PNK & STS

Science, abo2296, this issue p. 1027; see also adi3357, p. 1011

AGING

Slowing aging with taurine

Aging is associated with physiological changes that range in scale from organelles to organ systems, but we are still working to understand the molecular basis for these changes. Studying various animals, Singh *et al.* found that the amount of the semi-essential amino acid taurine in circulation decreased with age (see the Perspective by McGaunn and Baur). Supplementation with taurine slowed key markers of aging such as increased DNA damage, telomerase deficiency, impaired mitochondrial function, and cellular senescence. Loss of taurine in humans was associated with aging-related diseases, and concentrations of taurine and its metabolites increased in response to exercise. Taurine supplementation improved life span in mice and health span in monkeys. —LBR

Science, abn9257, this issue p. 1028; see also adi3025, p. 1010

COSMOLOGY

Lensing measures the Hubble constant

The Hubble constant measures the expansion rate of the Universe, but different methods give inconsistent values. Kelly *et al*. studied a supernova that had its light split into multiple images by the gravitational lensing of a foreground galaxy cluster. They combined measurements of the time delay between the multiple images with predictions made by multiple lensing models of the cluster. This approach allowed the authors to make a blinded measurement of the Hubble constant, finding a value that is more consistent with that derived from the cosmic microwave background than with the cosmic distance ladder. —KTS

Science, abh1322, this issue p. 1029

ANIMAL MOVEMENT

Freed by lockdowns

Policies to reduce human movement during the early months of the COVID-19 pandemic produced a kind of natural experiment to observe how human activities affect animal behavior. Using GPS tracking data from 2300 individual mammals of 43 species, Tucker *et al*. documented changes in mammal movement patterns during the spring of 2020 compared with the previous year (see the Perspective by St. Clair and Raymond). In locations with strict lockdown policies, animals traveled longer distances during the lockdown period. In highly populated areas, mammals moved less frequently and were closer to roads than they were before the pandemic. These results demonstrate how human activities constrain animal movement and what happens when those activities cease. —BEL

Science, abo6649, this issue p. 1059; see also add9662, p. 1008

MECHANOCHEMISTRY

Pressure points for Diels-Alder reactions

Using ball mills to conduct chemical reactions in solid state has the potential to eliminate vast quantities of solvent waste. However, the energetics of these reactions are much harder to discern and optimize than reactions in the solution phase. Zholdassov *et al*. used a modified atomic force microscope to study in a more precise, controlled fashion how the forces squeezing molecules together in a ball mill might influence the Diels-Alder cycloaddition reaction (see the Perspective by Weiss). The authors observed much greater acceleration through mechanical distortion than hydrostatic pressure would deliver. —JSY

Science, adf5273, this issue p. 1053; see also adi3388, p. 1013

STROKE

Stopping the swelling after stroke

Stroke often causes cerebral edema, brain swelling caused by fluid accumulation. Water uptake through aquaporin 4 (AQP4) channels in perivascular astrocytes results in blood vessel compression and cerebral edema. Stokum *et al*. investigated the pathways in astrocyte end feet, cellular extensions that wrap around cerebral blood vessels and contribute to these processes in mice. The authors found a cation-dependent cascade that induced the acute translocation of AQP4 channels to the cell membrane. Blocking this cascade reduced brain swelling and improved functional recovery from ischemic stroke in these mice. —LKF

Sci. Signal. (2023) 10.1126/scisignal.add6364

CLIMATE ECONOMICS

The costs of ENSO

The El Niño–Southern Oscillation (ENSO) affects weather globally and thus has many important socioeconomic impacts. How might possible changes to ENSO caused by anthropogenic climate change affect the economies of individual countries and the global economy? Callahan and Mankin show that El Niño persistently reduces economic growth and that national economies are sensitive to El Niño even when warming is taken into account. Future global economic growth could decline because of anthropogenic intensification of ENSO variability. —HJS

Science, adf2983, this issue p. 1064

T CELLS

Bladder T cells protect against UTIs

Urinary tract infections (UTIs) resulting primarily from uropathogenic *E. coli* are often recurrent, but the reason for the incomplete development of immune memory remains unclear. Using a mouse model of recurrent UTIs, Rousseau *et al*. demonstrated that immune memory against UTIs is mediated by tissue-resident memory T (T_{RM}) cells that require antigen persistence for their development. UTIs induced a strong, mixed T helper cell response in the bladder mucosa and subsequently established T_{RM} cells. Protection against recurrent UTIs was maintained after depletion of circulating T cells that left local T_{RM} cells intact, whereas early antibiotic treatment decreased protection against recurrent UTIs. These results identify bladder T_{RM} cells as key mediators of protection against recurrent UTIs and as a potential target for future vaccine development. —CO

Sci. Immunol. (2023) 10.1126/sciimmunol.abn4332

developed a multi-omics sequencing approach to profile 3D genome structures and gene expression at the same time in single cells, which enables a direct linkage between chromatin conformation and gene expression. Leveraging this new tool, the authors identified widespread chromatin interactions, especially between loci enriched for active enhancers, and found that they were rewired before gene activation during mouse embryonic development. This observation suggests that dynamic chromatin organization plays a critical role in the control of gene expression. —DJ

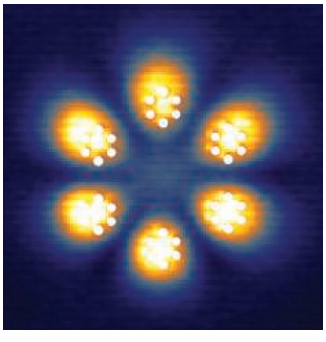
Science, adg3797, this issue p. 1070

QUANTUM CHEMISTRY

Emulating molecular orbitals

There is considerable interest in developing tunable quantum simulators of many-body Hamiltonians that use weakly conducting or insulating surfaces. Using patterned cesium atoms and surface confinement of electrons on indium–tin surfaces, Sierda *et al*. created artificial molecular orbitals that were strongly decoupled from the bulk bands, emulating a series of well-known planar organic molecules. This system serves as a versatile platform with which to emulate quantum chemistry on a surface and provides new ways to look at the interplay between structure and molecular orbitals. This will have relevance for quantum and organic chemistry, solid-state physics, and many-body physics. —YS

Science, adf2685, this issue p. 1048



Conductance imaging reveals artificial hybrid molecular orbitals for clusters of cesium atoms arranged in a benzene structure.

CREDITS: (LEFT TO RIGHT) SIERDA *ET AL.*; WILDLIFE GMBH/ALAMY STOCK PHOTO

FERROELECTRICS

Reducing barriers to polarization

Nitride-based ferroelectric wurtzites are an emerging family of crystals that are highly attractive as switching materials for modern microelectronics. The chemistry of these materials is a good match for current semiconductor platforms. Calderon *et al*. used an array of characterization tools to determine exactly how a representative wurtzite composed of aluminum, boron, and nitrogen undergoes polarization switching. A more detailed understanding of this process is vital for lowering the electric field under which these materials switch, because this is a limiting factor in moving them into applications. —BG

Science, adh7670, this issue p. 1034

CANCER

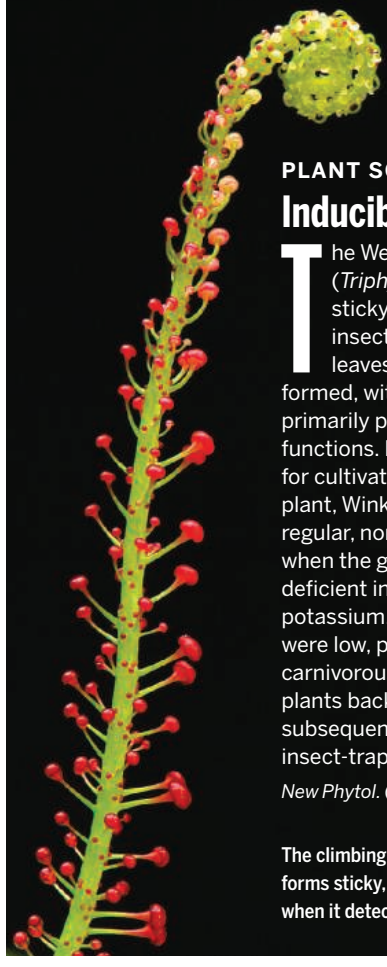
Fighting fibrosis

Treatment for non–small cell lung cancer (NSCLC) has improved considerably since the development of immune checkpoint blockade therapies, but many tumors still fail to respond. Herzog *et al*. found that tumor-associated fibrosis, which is common in patients but is not found in murine models, impaired antitumor immune responses. The authors modeled fibrosis in murine models of NSCLC and found that targeting fibrosis by inhibition of transforming growth factor β signaling could sensitize tumors to immune checkpoint blockade when used in combination with chemotherapy. These results highlight a potential path forward to increasing the sensitivity of NSCLC tumors to immunotherapy. —CSM

Sci. Transl. Med. (2023) 10.1126/scitranslmed.adh8005

IN OTHER JOURNALS

Edited by **Caroline Ash** *and* **Jesse Smith**



PLANT SCIENCE

Inducible carnivory

The West African liana (*Triphyophyllum peltatum*) uses sticky glandular leaves to trap insect prey. However, these leaves are only sometimes formed, with other leaves performing primarily photosynthetic or climbing functions. By developing a protocol for cultivation of this tricky-to-grow plant, Winkelmann *et al.* found that regular, noncarnivorous leaves formed when the growth medium was normal, deficient in nitrogen, or deficient in potassium. But when phosphate levels were low, plants formed glandular carnivorous leaves. Transferring plants back to full nutrients caused subsequent leaves to develop without insect-trapping glands. —MRS

New Phytol. (2023) 10.1111/nph.18960

The climbing plant *Triphyophyllum peltatum* forms sticky, glandular, carnivorous leaves when it detects low phosphate levels.

COGNITION

Learn a new language ASAP

Being bilingual is associated with better cognitive performance and reduced risk of developing dementia. However, some studies have not found any protective effects of bilingualism. Ballarini *et al.* hypothesized that becoming bilingual at different stages in life could have different effects on cognition, potentially explaining these discrepancies. In a cohort of more than 700 older individuals, the authors found that the earlier participants became bilingual, the better they performed on cognitive tests. For individuals that became bilingual late in life (at more than 65 years of age), cognitive performance was similar to that in age-matched monolingual individuals. For long-lasting cognitive benefits, learning a second language early in life is the key. —MMa

Neurobiol. Aging (2023) 10.1016/j.neurobiolaging.2022.12.005

GLYCAN SYNTHESIS

Living polymerization of sugars

Biological polysaccharides are highly complex, with many potential monomers and linkages that determine both physical properties and biological function. Assembling large polymers precisely can be a challenge for chemists. Wu *et al*. developed a chemical synthesis of large glycans through living cationic ring-opening polymerization using 1,6-anhydrosugars as

CONSERVATION

Satellites to watch the killing



The hen harrier is specifically endangered in the UK because of illegal activities associated with moorland management for red grouse hunting.

Despite protection, top predators often become victims of wildlife crime because of clashes with human interests. Ewing *et al.* documented illegal killing of a protected avian predator in the UK, the hen harrier (*Circus cyaneus*). This highly endangered bird occurs on upland ericaceous heaths that are intensively managed for the hunting of red grouse (*Lagopus lagopus scotica*). The authors used satellite tagging to track the fate of 148 individuals between 2014 and 2021 and found up to 75% mortality in young tagged birds (<2 years old) caused by illegal killing, when 90% survival would otherwise be expected. Killing localities tended to overlap with areas of grouse moor, especially in northern England and northeastern Scotland. Most tellingly, the authors found that peak deaths coincided with the shooting season. Although satellite tagging provides a valuable tool for conservationists to use to reveal the extent of covert wildlife killing, the authors also noted 43 harriers with previously well-performing satellite tags that inexplicably stopped transmitting. —CA

Biol. Cons. (2023) 10.1016/j.biocon.2023.110072

a starting material. Although limited to alpha-1,6 linkages, this approach is reversible, accepts a range of monomer units, and can produce polysaccharides with an adjustable and relatively narrow molecular weight range. Such glycans will be of potential use in materials and biotechnology applications. —MAF

Nat. Chem. (2023)
10.1038/s41557-023-01193-2

ORGANIC CHEMISTRY

Carbon–carbon bonds forged from phosphorus

Modern chemistry makes frequent use of metals to help form carbon–carbon bonds. Peng *et al.* report an alternative approach that relies on phosphorus as the matchmaker. Specifically, they used phosphonates to bridge acid chlorides with alcohols or amines. Blue light excitation then counterintuitively couples those fragments through both carbons (rather than forming carbon–oxygen or carbon–nitrogen bonds) to produce α-hydroxy or α-amino ketones. Mechanistic studies and simulations support an intramolecular radical hydrogen atom transfer process. —JSY

Chem (2023)
10.1016/j.chempr.2023.04.011

STELLAR EVOLUTION

Simulating supermassive stars

Stars that form from pristine gas (made in the Big Bang) are expected to have extreme masses because of their lack of elements heavier than lithium. These supermassive stars evolve so quickly that they are still accreting material when they end their lives. Herrington *et al.* simulated supermassive stars at a range of accretion rates, finding two regimes of behavior. Above an accretion rate threshold, the star was red and collapsed before running out of fuel because of the intense pulsations. Below the threshold, the star was blue and followed the main sequence, completing fusion before collapsing. Both types left behind a black hole with sufficient mass to power the quasars observed in the early Universe. —KTS

Mon. Not. R. Astron. Soc. (2023)
10.1093/mnras/stad572

GENETICS

Conserving a cadre of Canadian canids

Conservation of threatened species is increasingly reliant on an understanding of the genomes of those species. In North America, the status of several canids as species or hybrids is being revisited. Vilaça *et al.* analyzed the genomes of 68 canids from North America, including eight species of coyotes and wolves, to elucidate the hybridization history and status of the highly debated eastern wolf. Analyses of these genomes revealed multiple ancient and recent hybridization events among these species, but showed that eastern wolves have their own private ancestry components, indicating that they did not originate through hybridization alone. These results hint at the complexities inherent in defining species and the possible ramifications of those complexities on conservation. —CNS

Mol. Biol. Evol. (2023)
10.1093/molbev/msad055

RESEARCH ARTICLE SUMMARY

COSMOLOGY

Constraints on the Hubble constant from supernova Refsdal's reappearance

Patrick L. Kelly*, Steven Rodney, Tommaso Treu, Masamune Oguri, Wenlei Chen, Adi Zitrin, Simon Birrer, Vivien Bonvin, Luc Dessart, Jose M. Diego, Alexei V. Filippenko, Ryan J. Foley, Daniel Gilman, Jens Hjorth, Mathilde Jauzac, Kaisey Mandel, Martin Millon, Justin Pierel, Keren Sharon, Stephen Thorp, Liliya Williams, Tom Broadhurst, Alan Dressler, Or Graur, Saurabh Jha, Curtis McCully, Marc Postman, Kasper Borello Schmidt, Brad E. Tucker, Anja von der Linden

INTRODUCTION: The Hubble constant (H_0) quantifies the rate at which the Universe is expanding. It has been predicted that observations of a supernova (SN) that is multiply imaged by a foreground gravitational lens could, in principle, be used to measure H_0. The time delays between the SN's multiple images are expected to be inversely proportional to the value of H_0.

In late 2014, a SN was found that was strongly lensed by the galaxy cluster MACS J1149.5+2223. Dubbed SN Refsdal, it appeared in four images around a galaxy that was a member of the cluster. Models of the gravitational lens predicted that a fifth image of SN Refsdal would appear within the next year. Multiple teams made blind predictions for the timing and relative brightness of the SN's reappearance.

RATIONALE: The two most precise previous measurements of the Hubble constant are inconsistent with each other (at >5σ significance), which is known as the Hubble tension. Measurements of thermonuclear supernovae (SNe) in the nearby Universe have yielded $H_0 = 73$ 1.0 km s^{-1} Mpc^{-1}. Observations of the cosmic microwave background (CMB) have led to a lower value of $H_0 = 67.4 \pm 0.6$ km s^{-1} Mpc^{-1}, assuming standard cosmology. If this tension is confirmed using independent measurements, it could indicate problems with standard cosmology. An alternative cosmology, such as those involving an additional early dark energy or more species of particles, might be required to reconcile the measurements.

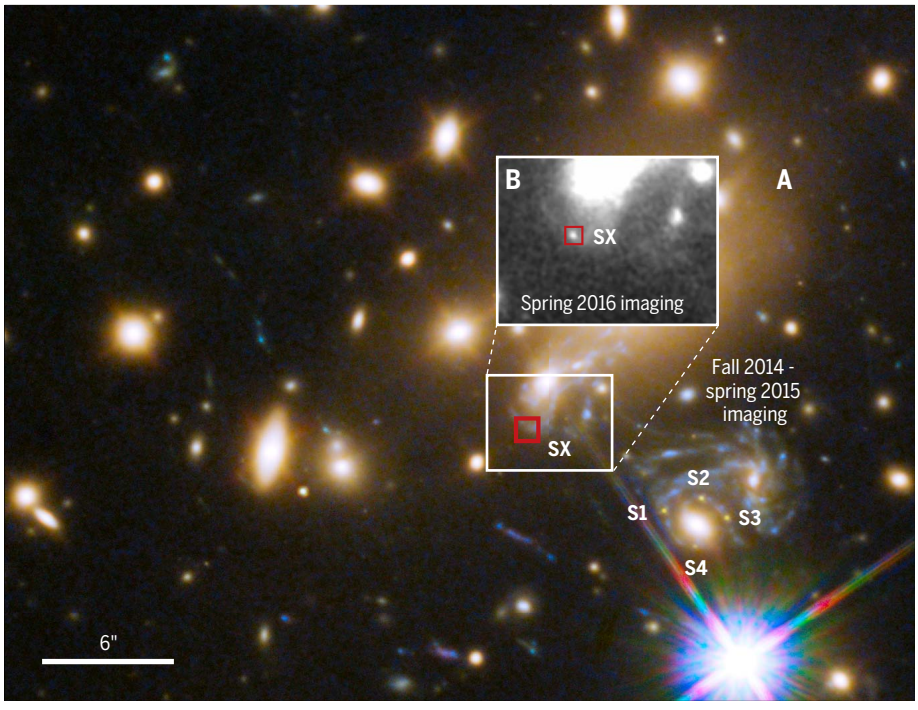
The predicted additional image of SN Refsdal appeared in 2015. Follow-up observations have allowed the time delays and magnification ratios between the multiple images to be determined. We combine those measurements with the pre-reappearance model predictions to perform a blinded calculation of the value of H_0.

RESULTS: We compute the likelihood of the time delay, magnification, and position measurements given each lens model's predictions after rescaling the time delay predictions for different values of H_0. This approach weights each model's contributions in a combined constraint on H_0. Weights are assigned according to each model's ability to reproduce the observations that are independent of H_0 (location of the reappearance, magnification ratios, and ratios of time delays).

We perform two estimates of H_0: (i) from all lens models that made published predictions before the reappearance was observed and (ii) using a subset of those models, by selecting those that are most consistent with the observations and dominate the weights.

CONCLUSION: We infer a value of H_0 of $64.8^{+4.4}_{-4.3}$ km s^{-1} Mpc^{-1} using the full set of eight pre-reappearance models and of $66.6^{+4.1}_{-3.3}$ km s^{-1} Mpc^{-1} from the two preferred models. Our results are most consistent with the H_0 value measured from the CMB but do not exclude the higher value from nearby SNe.

We used a simulation of a galaxy cluster lens to verify that the uncertainty on our measurement of H_0 is consistent with expectations. The ability of the lens models to reproduce the positions of the SN images also implies an expected uncertainty on H_0, which we find agrees with our constraints. The best agreement between lens models and observations that are independent of H_0 is achieved by the models that were constructed by assigning dark-matter halos to both the cluster and to individual galaxies in the cluster. ■



Appearance and reappearance of SN Refsdal, strongly lensed by the galaxy cluster MACS J1149.5+2223. Both panels were taken with the Hubble Space Telescope. (**A**) Images S1 to S4 (labeled) of SN Refsdal appear in an Einstein cross configuration in 2014. Models predicted the appearance of an additional image SX in the region denoted by the red box. (**B**) Observation of SX in spring 2016 after its appearance in late 2015. In (A), colors were assigned to coadded images taken in these filters: blue, F606W (*V*-band) and F814W (*I*-band); green, F105W (*Y*-band) and F125W (*J*-band); and red, F140W (between the *J*- and *H*-bands) and F160W (*H*-band). The image in (B) used only the F125W filter, so it is shown in grayscale.

The list of author affiliations is available in the full article online.
*Corresponding author. Email: plkelly@umn.edu
Cite this article as P. L. Kelly *et al.*, *Science* **380**, eabh1322 (2023). DOI: 10.1126/science.abh1322

READ THE FULL ARTICLE AT
https://doi.org/10.1126/science.abh1322

RESEARCH ARTICLE

COSMOLOGY

Constraints on the Hubble constant from supernova Refsdal's reappearance

Patrick L. Kelly[1]*, Steven Rodney[2], Tommaso Treu[3], Masamune Oguri[4,5,6], Wenlei Chen[1], Adi Zitrin[7], Simon Birrer[8,9], Vivien Bonvin[10], Luc Dessart[11], Jose M. Diego[12], Alexei V. Filippenko[13,14], Ryan J. Foley[15], Daniel Gilman[16,3], Jens Hjorth[17], Mathilde Jauzac[18,19,20,21], Kaisey Mandel[22,23], Martin Millon[10,8], Justin Pierel[24,2], Keren Sharon[25], Stephen Thorp[26,22], Liliya Williams[1], Tom Broadhurst[27], Alan Dressler[28], Or Graur[29,30], Saurabh Jha[31], Curtis McCully[32,33], Marc Postman[24], Kasper Borello Schmidt[34], Brad E. Tucker[35,36,37], Anja von der Linden[9]

The gravitationally lensed supernova Refsdal appeared in multiple images produced through gravitational lensing by a massive foreground galaxy cluster. After the supernova appeared in 2014, lens models of the galaxy cluster predicted that an additional image of the supernova would appear in 2015, which was subsequently observed. We use the time delays between the images to perform a blinded measurement of the expansion rate of the Universe, quantified by the Hubble constant (H_0). Using eight cluster lens models, we infer $H_0 = 64.8^{+4.4}_{-4.3}$ kilometers per second per megaparsec. Using the two models most consistent with the observations, we find $H_0 = 66.6^{+4.1}_{-3.3}$ kilometers per second per megaparsec. The observations are best reproduced by models that assign dark-matter halos to individual galaxies and the overall cluster.

Strong gravitational lensing occurs when the gravitational influence of a foreground mass, such as a galaxy cluster, produces multiple images of a well-aligned background source. In principle, the time delays between the images of a strongly lensed supernova (SN) directly determine the geometric distance, which enables a measurement of the Hubble constant H_0 (*1*). Although originally proposed for supernovae (SNe), this technique, known as time-delay cosmography (*2*), has only been applied to quasars strongly lensed by single-galaxy foreground lenses (*3*–*5*). The strongly lensed SN Refsdal appeared in late 2014 in four resolved images, designated S1 to S4 (coordinates listed in table S1), arranged in a cross-like configuration (known as an Einstein cross) around an early-type member of the galaxy cluster MACS J1149.5+2223 (right ascension $11^h49^m35.8^s$, declination +22°23′55″, all coordinates are J2000 equinox; hereafter referred to as MACS J1149) (fig. S1A) (*6*). Models of the gravitational lens predicted that an additional image would appear, designated SX (table S1), which was observed in 2015 (fig. S1B) (*7*). A companion paper (*8*) has measured the relative time delay between the images S1 to S4 and image SX as $376.0^{+5.6}_{-5.5}$ days, a precision of 1.5%, using Hubble Space Telescope (HST) observations in the near-infrared F125W (*J*-band) and F160W (*H*-band) broadband filters. If the matter distribution in the foreground MACS J1149 cluster lens were known exactly, time-delay cosmography could provide a measurement of H_0 with equivalent 1.5% precision.

The value of H_0 is currently debated because of a tension between early-time and late-time probes of the expansion rate of the Universe. Assuming a standard cosmological model with flat geometry, a cosmological constant Λ, and cold dark matter (CDM), the cosmic microwave background (CMB) measurements using the *Planck* satellite imply $H_0 = 67.4 \pm 0.6$ km s^{-1} Mpc^{-1} (*9*). By contrast, the alternative local distance ladder method, used by the Supernova H0 for the Equation of State (SH0ES) team, yields $H_0 = 73.04 \pm 1.04$ km s^{-1} Mpc^{-1} (*10*). This tension between the SH0ES and *Planck* H_0 measurements has >5σ statistical significance, indicating a potential problem with standard cosmology (*11*).

Measurements of H_0 using independent techniques are needed to confirm or refute the apparent tension. A local distance ladder measurement using the tip of the red giant branch (TRGB) method yields $H_0 = 69.8 \pm 0.8(\text{stat}) \pm 1.7(\text{sys})$ km s^{-1} Mpc^{-1} (*12*). Time-delay cosmography using quasar systems, multiply imaged by foreground galaxy-scale lenses, find $H_0 = 73.7^{+1.4}_{-1.5}$ km s^{-1} Mpc^{-1} (*13*) or $H_0 = 74.5^{+5.6}_{-6.1}$ km s^{-1} Mpc^{-1} (with broader assumptions) for time-delay lenses and $H_0 = 68.4^{+4.1}_{-3.2}$ km s^{-1} Mpc^{-1} when combining time-delay lenses with non–time-delay lenses at lower redshift, assuming that both are drawn from the same parent population (*14*). The appearance of the final image of SN Refsdal provides an opportunity to make an independent measurement of H_0 using models of MAC J1149 (*15*, *16*). The systematic uncertainties of cluster-scale models (*17*) differ from the galaxy-scale models used for quasar time-delay measurements.

Lensed SNe (*18*) are predicted to provide more precise time-delay measurements than quasar observations and require shorter observations spanning months or years (*19*–*21*). Time delays of months or years are expected to be unusual among SNe that are strongly lensed by clusters with extensive preexisting observations (*22*). The massive galaxy cluster MACS J1149 [total mass $(1.4 \pm 0.3) \times 10^{15}$ $M_\odot$ (*23*–*25*)] was observed numerous times before

[1]Minnesota Institute for Astrophysics, University of Minnesota, Minneapolis, MN 55455, USA. [2]Department of Physics and Astronomy, University of South Carolina, Columbia, SC 29208, USA. [3]Department of Physics and Astronomy, University of California, Los Angeles, CA 90095, USA. [4]Center for Frontier Science, Chiba University, Chiba 263-8522, Japan. [5]Research Center for the Early Universe, University of Tokyo, Tokyo 113-0033, Japan. [6]Kavli Institute for the Physics and Mathematics of the Universe, University of Tokyo, Kashiwa, Chiba 277-8583, Japan. [7]Physics Department, Ben-Gurion University of the Negev, Beer-Sheva 8410501, Israel. [8]Kavli Institute for Particle Astrophysics and Cosmology, Stanford University, Stanford, CA 94305, USA. [9]Department of Physics and Astronomy, Stony Brook University, Stony Brook, NY 11794, USA. [10]Laboratoire d'Astrophysique, Ecole Polytechnique Federale de Lausanne, Observatoire de Sauverny, CH-1290 Versoix, Switzerland. [11]Institut d'Astrophysique de Paris, Centre National de la Recherche Scientifique–Sorbonne Université, F-75014 Paris, France. [12]Instituto de Física de Cantabria, Consejo Superior de Investigaciones Científicas y la Universidad de Cantabria, 39005 Santander, Spain. [13]Department of Astronomy, University of California, Berkeley, CA 94720, USA. [14]Miller Institute for Basic Research in Science, University of California, Berkeley, CA 94720, USA. [15]Department of Astronomy and Astrophysics, University of California Observatories, Lick Observatory, University of California, Santa Cruz, CA 95064, USA. [16]Department of Astronomy and Astrophysics, University of Toronto, Toronto, ON, M5S 3H4, Canada. [17]Dark Cosmology Centre, Niels Bohr Institute, University of Copenhagen, DK-2100 Copenhagen, Denmark. [18]Centre for Extragalactic Astronomy, Department of Physics, Durham University, Durham DH1 3LE, UK. [19]Institute for Computational Cosmology, Durham University, Durham DH1 3LE, UK. [20]Astrophysics Research Center, University of KwaZulu-Natal, Durban 4041, South Africa. [21]School of Mathematics, Statistics, and Computer Science, University of KwaZulu-Natal, Durban 4041, South Africa. [22]Institute of Astronomy and Kavli Institute for Cosmology, Cambridge CB3 0HA, UK. [23]Statistical Laboratory, Department of Pure Mathematics and Mathematical Statistics, University of Cambridge, Cambridge CB3 0WB, UK. [24]Space Telescope Science Institute, Baltimore, MD 21218, USA. [25]Department of Astronomy, University of Michigan, Ann Arbor, MI 48109, USA. [26]The Oskar Klein Centre, Department of Physics, Stockholm University, AlbaNova, 10691 Stockholm, Sweden. [27]Ikerbasque Foundation, University of the Basque Country, Donosita International Physics Center, Donostia, Spain. [28]The Observatories of the Carnegie Institution for Science, Pasadena, CA 91101, USA. [29]Institute of Cosmology and Gravitation, University of Portsmouth, Portsmouth PO1 3FX, UK. [30]Department of Astrophysics, American Museum of Natural History, New York, NY 10024, USA. [31]Department of Physics and Astronomy, Rutgers, The State University of New Jersey, Piscataway, NJ 08854, USA. [32]Las Cumbres Observatory, Goleta, CA 93117, USA. [33]Department of Physics, University of California, Santa Barbara, CA 93106, USA. [34]Leibniz-Institut fur Astrophysik Potsdam, 14482 Potsdam, Germany. [35]The Research School of Astronomy and Astrophysics, Mount Stromlo Observatory, Australian National University, Canberra, ACT 2611, Australia. [36]National Centre for the Public Awareness of Science, Australian National University, Canberra, ACT 2611, Australia. [37]The Australian Research Council Centre of Excellence for All-Sky Astrophysics in 3 Dimensions, ACT 2611, Australia.
*Corresponding author. Email: plkelly@umn.edu

the appearance of SN Refsdal, placing strong constraints on its mass distribution (*26*–*28*). Numerous teams have used lens models to predict the reappearance of SN Refsdal, before the observation of SX (*29*, *30*). These models used several different assumptions, so the appearance of SX can also be used to test those assumptions.

The reappearance of SN Refsdal, in image SX, was detected in HST observations taken on 11 December 2015 universal time (UT) (*6*) and was reported to the community the next day (*31*). This initial observation was used to estimate the relative time delay between SX and S1 as 320 to 380 days (*32*).

Each lens model yielded predictions $\Delta t_{\mathrm{X,1}}^{\mathrm{pred,70}}$ for the relative time delay between images SX and S1 (designated by the subscripts X and 1, respectively) as well as between other image pairs, assuming $H_0 = 70\ \mathrm{km\ s^{-1}\ Mpc^{-1}}$ (denoted by the superscript 70). For fixed values of the cosmological matter density parameter Ω_M and the dark energy density Ω_Λ, the predicted time delay $\Delta t_{\mathrm{X,1}}^{\mathrm{pred}}(H_0)$ for a given value of H_0 depends inversely on the value of H_0

$$\Delta t_{\mathrm{X,1}}^{\mathrm{pred}}(H_0) = \Delta t_{\mathrm{X,1}}^{\mathrm{pred,70}} \times \frac{70\ \mathrm{km\ s^{-1}\ Mpc^{-1}}}{H_0} \quad (1)$$

which allows the predicted time delay to be computed for a given value of H_0 for each model. The uncertainty associated with this rescaling of the predictions is smaller than ~0.7 km $\mathrm{s^{-1}}$ $\mathrm{Mpc^{-1}}$, given the weak dependence of H_0 on Ω_M and Ω_Λ. Using a simulation of a galaxy cluster (*33*), we calculate that the single model that receives the greatest weight in our analysis can recover H_0 with at least 5% accuracy (*34*). We also determine that our error budget is consistent with the model's astrometric errors (*35*).

We use two sets of lens models to compute parallel estimates of the value of H_0, using our observations of SN Refsdal. We first obtain an estimate of the value of H_0 using a set of predictions from eight models—which we refer to as the Diego-a free-form model (*29*); the Zitrin-c* light-traces-mass (LTM) model (*29*); and the Grillo-g (*29*), Oguri-a* and Oguri-g* (*29*), Jauzac-15.2* (*30*), and Sharon-a* and Sharon-g* (*29*) simply parameterized models. Models that are simply parameterized use easy-to-compute parametric forms to describe the distribution of dark matter, using priors inferred from the luminous tracers and cosmological simulations. They include one or more cluster-scale halos and assign a dark-matter halo to each luminous galaxy-cluster member after scaling the halo mass according to the galaxies' properties, such as stellar mass or velocity dispersion. The second, parallel estimate includes only the Grillo-g and Oguri-a* models, which we selected before unblinding the time delay, as explained below. In both cases, each model's contribution to the H_0 inference is weighted according to its ability to reproduce H_0-independent observables.

Blinded analysis

To avoid human bias, we carried out our analysis without knowledge of the time-delay measurements and the implied value of H_0. For the light curve (flux as a function of time) of each of the images S1 to SX, we selected a random number, whose value was stored but kept hidden, which was added to the dates associated with the flux measurements, shifting the light curve in time by an unknown amount (*8*). Before unblinding the time delay, we were only aware that the relative delay of SX and S1 was in the range of 320 to 380 days (68% confidence level) from a previously published analysis of two epochs of imaging (*36*). This range corresponds to ~17% in H_0 before unblinding.

Observables used for likelihood functions

We use constraints on the time delay between images A and B from the observed light curves (LCs) expressed as a probability $P(\Delta t_{\mathrm{A,B}}|\mathrm{LC})$. The prediction for the time delay, $\Delta t_{\mathrm{A,B}}^{\mathrm{pred,70}}$, from each lens model M_l is then used with Bayes' theorem to constrain H_0

$$P(H_0;M_l|\mathrm{LC}) \propto P(H_0)P(M_l) \int P(\Delta t_{\mathrm{A,B}}|M_l;H_0)P(\Delta t_{\mathrm{A,B}}|\mathrm{LC})d\Delta t_{\mathrm{A,B}} \quad (2)$$

where $P(H_0)$ is a prior probability for H_0, $P(M_l)$ is a prior probability for model l, and $P(\Delta t_{\mathrm{A,B}}|M_l;H_0)$ is the likelihood of $\Delta t_{\mathrm{A,B}}$, given the model prediction and a value of H_0.

We include in our likelihood function the relative time delays between four image pairs, S2 and S1, S3 and S1, S4 and S1, and SX and S1, and magnification ratios of three image pairs, S2/S1, S3/S1, and SX/S1 (the exclusion of the magnification ratio S4/S1 is discussed below), and the position of the reappearance. For the set of observables $\mathcal{O}$, we find

$$P(H_0|\mathrm{LC}) \propto P(H_0)\sum_l P(M_l) \int P(\mathcal{O}|M_l;H_0)P(\mathcal{O}|\mathrm{LC})d\mathcal{O}_1 \ldots d\mathcal{O}_n \quad (3)$$

Including these observables, in addition to the SX to S1 time delay, allows us to weight each model's contribution to the H_0 inference according to its ability to reproduce the observables (*15*). We only include observables in the likelihood function if their values were not available to lens modelers before they made their pre-reappearance predictions.

Figure 1 shows the predicted position of the final image (SX) from each lens model, overlaid on a difference image showing the detected position of SX. We use the SX position in the likelihood calculation because it was not known when the pre-reappearance models were constructed.

The HST F125W and F160W light curves of image S4 have very strong evidence (>5σ) that the SN overlaps a region of high magnification because of one or more stars (or stellar remnants) in the foreground cluster lens (microlensing) (*8*). The apparent F125W-F160W color of S4 is bluer than the other four images of the SN by 0.28 ± 0.05 mag in the first 150 days after its peak brightness (in the observer frame) and 1.8 ± 0.4 mag after 150 days [figure 12 of (*8*)]. This bluer color implies that (i) the SN does not have a uniform color and (ii) it overlaps a region, called a caustic, where the magnification due to stars changes abruptly, which causes differential magnification (*8*). Simulations of lensing of an azimuthally symmetric synthetic SN, with properties similar to those of SN Refsdal (*37*), by objects in the foreground cluster lens do not predict microlensing events with color differences as large as that observed for S4 [figure 6 of (*8*)]. Therefore, we exclude the magnification ratio of S4 to S1 because we cannot model accurately the extreme microlensing event, cannot correct its magnification, or assign an uncertainty.

The observables $\mathcal{O}$ we use to compute likelihoods are a set inferred from the light curve

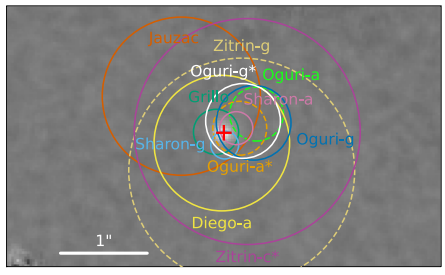


Fig. 1. Comparison between the predicted and actual positions of the reappearance of SN Refsdal image SX in late 2015. Grayscale shows the difference between a coaddition of HST F125W images taken after the appearance of SX (December 2015 through May 2016) and a coaddition of F125W imaging acquired before the reappearance of SX (before July 2015). SX appears as a white source in this presentation, at coordinates listed in table S1. Overlain are colored circles indicating the positions predicted by each model (labeled next to each circle). The radius of each circle indicates the root mean square (RMS) of the offsets between the predicted and observed positions of all multiply imaged galaxies used as constraints on the lens model (*29*, *30*). The pre-reappearance Oguri-a prediction is dashed bright green, and the revised position of the Oguri-a* model, after including SX's position as a constraint, is dashed light orange. The location of the circle shown for Zitrin-c* in solid purple was not computed before the reappearance.

$$\mathcal{O}_{1,j} = [\Delta t_{2,1}, \Delta t_{3,1}, \Delta t_{4,1}, \Delta t_{X,1}, \mu_2/\mu_1, \mu_3/\mu_1, \mu_X/\mu_1] \quad (4)$$

where $\Delta t_{j,1}$ is the relative time delay between the jth image and S1, and μ_j/μ_1 is the ratio of the magnifications of image jth and image S1. Two additional observables describe SX's position

$$\mathcal{O}_p = [\alpha_X, \delta_X] \quad (5)$$

where α_X and δ_X are (respectively) the right ascension and declination coordinates of SX. The measured ratios of the relative time delays of the images, magnification ratios, and relative positions of the images are all independent of H_0.

Lens models

Table S2 lists the lens models of MACS J1149 that were published before the appearance of SX: There are eight models from six research groups (*29*, *30*). We use these models, with updates described below, to constrain H_0. The Bradac and Merten models were not used to make predictions and were excluded from the time-delay calculations (*34*).

Several of the published pre-reappearance calculations have required revisions. The first Zitrin calculation was amended to address an issue affecting the time-delay surface (*29*). Although their underlying mass models have remained the same, the Sharon-a, Sharon-g, and Jauzac15.1 time-delay predictions required revisions by ~20% because of technical issues affecting their time-delay calculations (*30*, *34*). The observed location of SX differed by >1σ from that predicted by the Oguri-a and Oguri-g models (Fig. 1), so we also updated the Oguri-a and Oguri-g models by adding SX's position as a constraint. To preserve blinding, the direction of the ~1σ shift in the SX to S1 time delay was not disclosed until after we unblinded the time-delay measurement. We use an asterisk to denote models whose predictions were updated or first made after the reappearance. When computing the likelihood of each model, we use pre-reappearance Oguri predictions for SX's position.

For the first of our parallel estimates of H_0, we use the full set of eight pre-reappearance models, after the corrections above. The Diego-a and Zitrin-c* models were not able to reproduce the Einstein cross. The second parallel estimate for the value of H_0 uses only the Grillo-g and Oguri-a* models because their time-delay calculations did not require large corrections (~20%), and they reproduced the positions of the four images S1 to S4 with <0.1″ precision. These two models were selected before unblinding the time-delay measurement. With the exception of the Jauzac model, all other model predictions were published as part of an organized effort (*29*). These models were given the choice to use only the images of

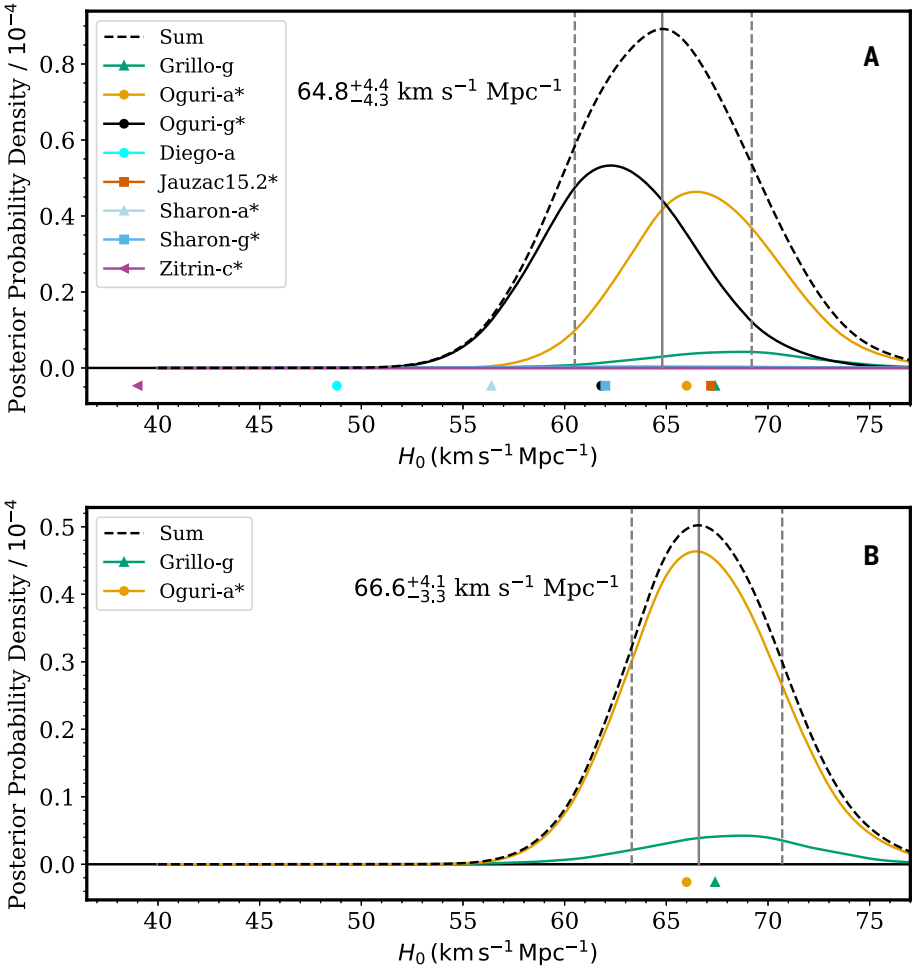


Fig. 2. Constraints on H_0 from SN Refsdal. (**A**) Constraints using the full set of eight models constructed before the reappearance, some with subsequent updates. (**B**) Parallel constraints using the subset of two pre-appearance models: the Grillo-g and the Oguri-a* model, with the latter only updated using the reappearance's position. Both panels show the posterior probability densities for each model as colored lines (see legend), and their sum (dashed black line), assuming a uniform prior. The colored markers beneath each plot show the most probable value of H_0 for each of the models, calculated from their predicted SX to S1 time delays. The vertical gray lines show the most likely value from the summed distribution, with the pair of dashed vertical lines marking the 16th and 84th percentile confidence intervals. Models were weighted by their ability to describe the data (Table 2), so for most models in (A), the probability densities are very small with the lines overlapping zero. The purple arrow for Zitrin-c* in (B) points toward the model's most probable value of H_0, which is smaller than 39 km s^{-1} Mpc^{-1}.

Table 1. H_0 constraints and weights determined by posterior probabilities for each set of lens-model predictions. The first column lists the most probable value of H_0 and our 16th, 84th, and 99.7th percentile confidence levels. Other columns list the weights (out of 1.0) we calculated using the constraints from SN Refsdal. The first and second rows are our parallel estimates of the value of H_0 using all eight models and our two preferred models, respectively. The relative weights are proportional to the models' posterior probabilities. Dashes indicate not applicable.

H_0 (km s^{-1} Mpc^{-1})		Weight of each model							
Confidence levels		Diego-a	Grillo-g	Jauzac15.2*	Oguri-a*	Oguri-g*	Sharon-a*	Sharon-g*	Zitrin-c*
16-50-84	99.7								
$64.8^{+4.4}_{-4.3}$	73.6	7.1×10^{-6}	0.044	1.0×10^{-5}	0.44	0.51	0.00072	0.0062	3×10^{-9}
$66.6^{+4.1}_{-3.3}$	74.8	–	0.091	–	0.91	–	–	–	–

strongly lensed galaxies with spectroscopic redshifts (referred to as the gold sample) or all the images of strongly lensed galaxies. We label models using the gold sample with a "g" suffix and those that used all images with an "a" suffix. The Grillo team only produced a model using the gold set of images. The Oguri models were created with both sets, but its authors preferred the Oguri-a* model over the Oguri-g* model (*28*). We therefore chose to adopt the Oguri-a* model.

Table S2 also lists several models that were produced after the reappearance, which could therefore not make pre-reappearance predictions for SX. For completeness, we also calculated a value of H_0 that includes these models without using SX's position, but we do not regard it as a blinded result.

Likelihood calculation

We used light-curve simulations to compute the likelihood of the data, given a value of H_0. In total, 1000 sets of simulated light curves of S1 to SX were produced (*8*) for random relative magnifications and time delays. These light curves have noise characteristics and measurement cadences that closely approximate the SN Refsdal observations and include the lensing effects of the expected population of dark-matter subhalos and stars in the foreground cluster (*8*). The simulated light curves are used to measure and correct the bias associated with the four light-curve fitting algorithms (*8*) and construct a Gaussian mixture model for the likelihood of the observations that accounts for the covariance among the measurements (*34*).

H_0 constraints

For the two parallel estimates of H_0, table S3 lists the values of our unblinded measurements of the relative time delays and magnification ratios, including the companion paper's constraint on the SX to S1 time delay of $376.0^{+5.6}_{-5.5}$ days (*8*). Gravitational lensing magnification has a sign (positive or negative) associated with it, but only the absolute value of the magnification can be measured directly through observations of images' brightnesses. When we unblinded the revised Oguri-a* and Oguri-g* model predictions, by analyzing Markov chain Monte Carlo (MCMC) chains of lens model parameters, we did not anticipate that the predicted magnification values (which we had not inspected) included the magnification's sign. After unblinding, the

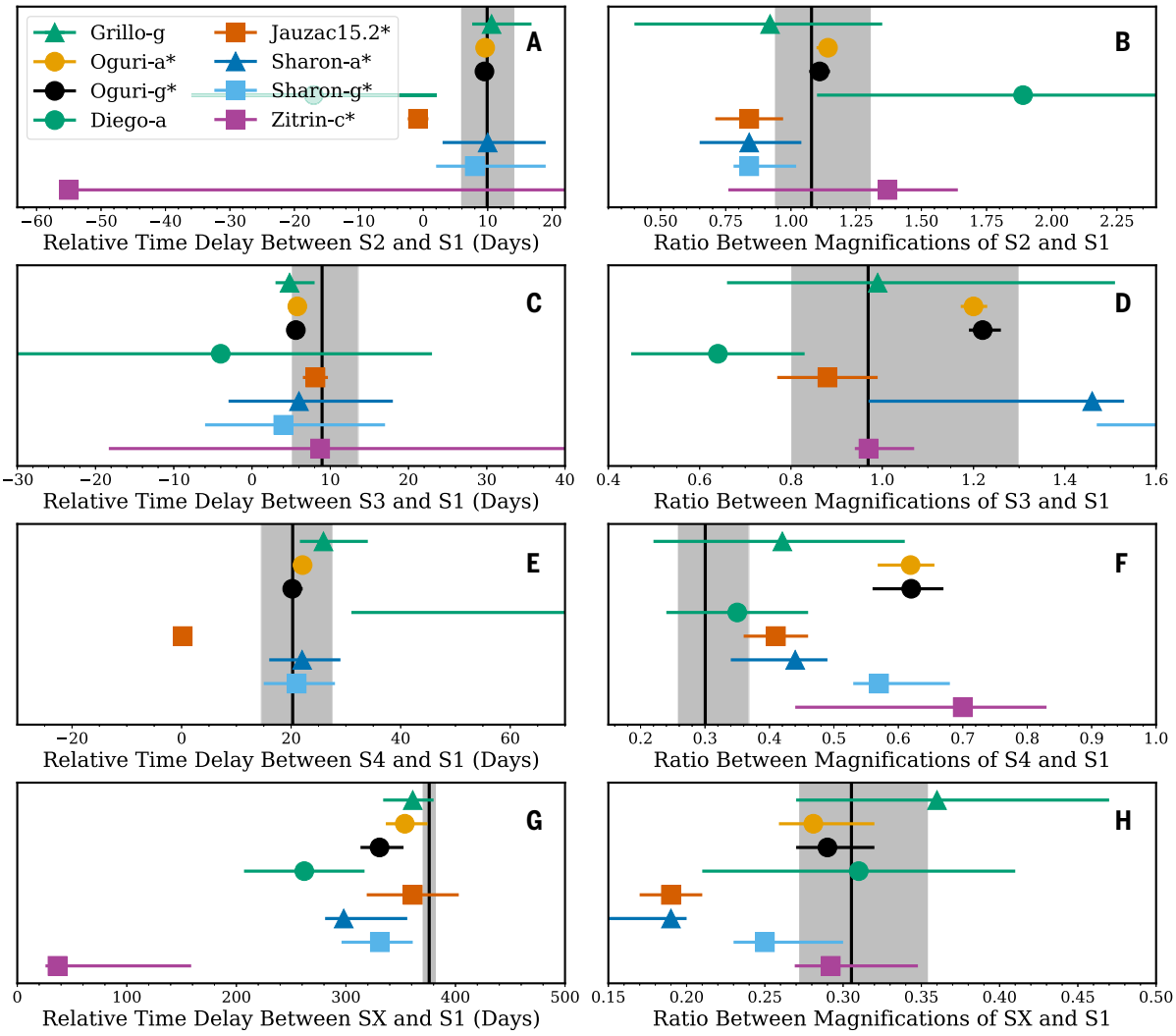


Fig. 3. Model predictions and measured relative time delays and magnification ratios between images S2 to SX and S1. (**A**, **C**, **E**, and **G**) Relative time delays between images S2 to SX and S1. Colored bars indicate the model predictions (see legend), with dots at the median value and bars extending to the 16th and 84th percentiles (*8*). (**B**, **D**, **F**, and **H**) Same, but for the ratios of the magnification of images S2 to SX and S1. (A) and (B) compare S1 with S2, (C) and (D) compare S1 with S3, (E) and (F) compare S1 with S4, and (G) and (H) compare S1 with SX. Models with an asterisk were revised after SX was observed. The predicted time delays shown were computed for $H_0 = 70$ km s^{-1} Mpc^{-1}.

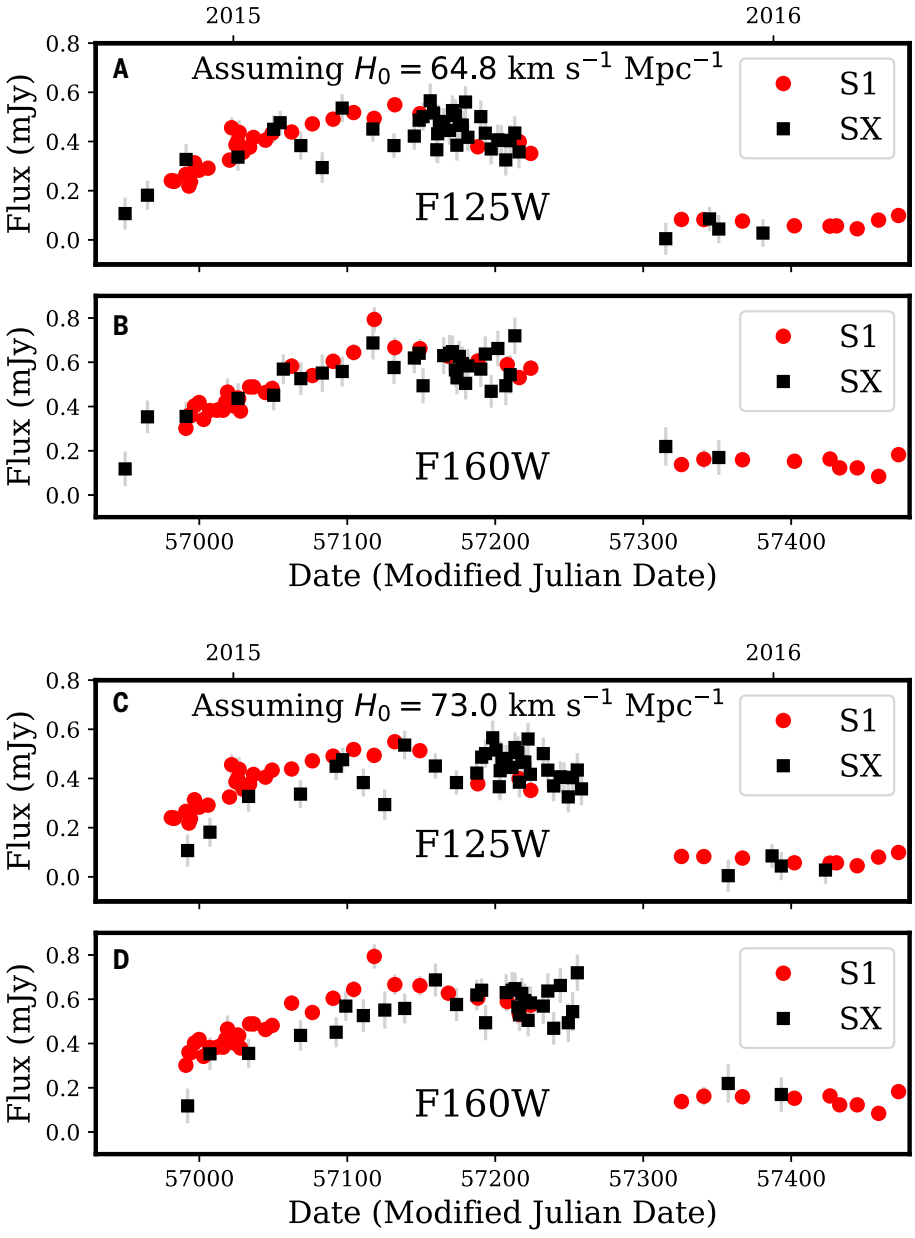


Fig. 4. Shifted light curves of images S1 and SX. (**A** and **B**) Fluxes of the images S1 (red circles) and SX (black squares) in the F125W filter (A) and the F160W filter (B), shown as a function of time after removing the measured 376.0-day delay (*8*), which corresponds to a constraint on the value of H_0 of $64.8^{+4.4}_{-4.3}$ km s^{-1} Mpc^{-1}. mJy, millijansky. (**C** and **D**) The same light curves but using the delay of 333.8 days expected for $H_0 = 73.04$ km s^{-1} Mpc^{-1}, the value inferred from the SN distance ladder (*10*) given the eight pre-reappearance models weighted according to their ability to reproduce the H_0-independent observables. While we fixed the SX to S1 time delay, we allow the magnification ratio of SX and S1 to vary in our model fitting. The ratios of the magnifications of SX and S1 that minimize the χ^2 value between a piecewise polynomial model of the light curve (*8*) and the measured photometry are 0.31 and 0.32, respectively. Error bars show 1σ uncertainties. The χ^2 difference between the calculations for the two time delays is 58.1 with 178 degrees of freedom, favoring (A) and (B) over (C) and (D).

negative magnifications affected the weights of the Oguri-a* and Oguri-g* models, but the issue was immediately apparent. We report it for transparency; we addressed it by applying an absolute value function to the magnification used in the weighting process. The only other postblinding changes to our analysis were choosing to present an additional estimate of H_0 that includes all pre-reappearance models (not just the preferred models) and to use SX's position instead of the SX to S1 angular separation to weigh models, which changed the results by 0.1 km s^{-1} Mpc^{-1}.

When we consider all eight pre-reappearance models, we find $H_0 = 64.8^{+4.4}_{-4.3}$ km s^{-1} Mpc^{-1} (Fig. 2). The weights for all eight models, listed in Table 1, show that the Oguri-a* and Oguri-g* models receive weights of 0.44 and 0.51, respectively, whereas the Grillo-g model receives 0.044 (from a total of 1.0). Figure 3, A to H, shows a comparison between the constraints on the observables and the model predictions. The Oguri models are the best match to the observations, which is why they received higher weights. When we consider only the Grillo-g and Oguri-a* models, we find $H_0 = 66.6^{+4.1}_{-3.3}$ km s^{-1} Mpc^{-1}. In this sample, Grillo-g receives a weight of 0.091, and Oguri-a* receives a weight of 0.91. For all models listed in table S2 that can be used to make time-delay calculations, even those produced after the appearance of SX, we find $H_0 = 64.6^{+4.4}_{-4.2}$ km s^{-1} Mpc^{-1} (fig. S3). The latter calculation does not use the position of SX to weight models because it was already known when some of those models were produced.

The measured value of the delay is $376.0^{+5.6}_{-5.5}$ days (*8*), which yields $H_0 = 64.8^{+4.4}_{-4.3}$ km s^{-1} Mpc^{-1} considering the eight pre-reappearance models. We next calculate the time delay expected if H_0 is equal to the value found by the SH0ES local distance ladder. For $H_0 = 73.04$ km s^{-1} Mpc^{-1}, the weighted combination of the eight pre-reappearance models yields a delay between SX and S1 of 333.8 days.

While holding the time delay between SX and S1 fixed but allowing the ratio of their magnifications to vary, we fitted the F125W and F160W light curves of SX and S1 using a piecewise polynomial model (*8*). This model describes the light curve in each filter as two polynomials. The first, a third order polynomial, applies before 150 days after peak brightness, and the second, a second-order polynomial, applies at later epochs. We first fix the SX to S1 time delay to 333.8 days (corresponding to $H_0 = 73$ km s^{-1} Mpc^{-1}) and then to 376.0 days ($H_0 = 64.8^{+4.4}_{-4.3}$ km s^{-1} Mpc^{-1}). The fixed 333.8-day SX to S1 delay yields a worse χ^2 greater by 58.1 for 178 degrees of freedom. We conclude that a shorter time delay of 333.8 days for $H_0 = 73$ km s^{-1} Mpc^{-1} and a flexible model provide a substantially worse match to the observations of SN Refsdal. Figure 4 shows the light curves of images S1 and SX shifted by 376.0 days (Fig. 4, A and B) and 333.8 days (Fig. 4, C and D). The ratios of the magnifications of SX and S1 that minimize the χ^2 value between a piecewise polynomial model of the light curve (*8*) and the measured photometry are 0.31 and 0.32, respectively.

Figure 5A compares our measurements of H_0 from SN Refsdal with previous results using both the late-time and early-time Universe constraints. The posterior probability

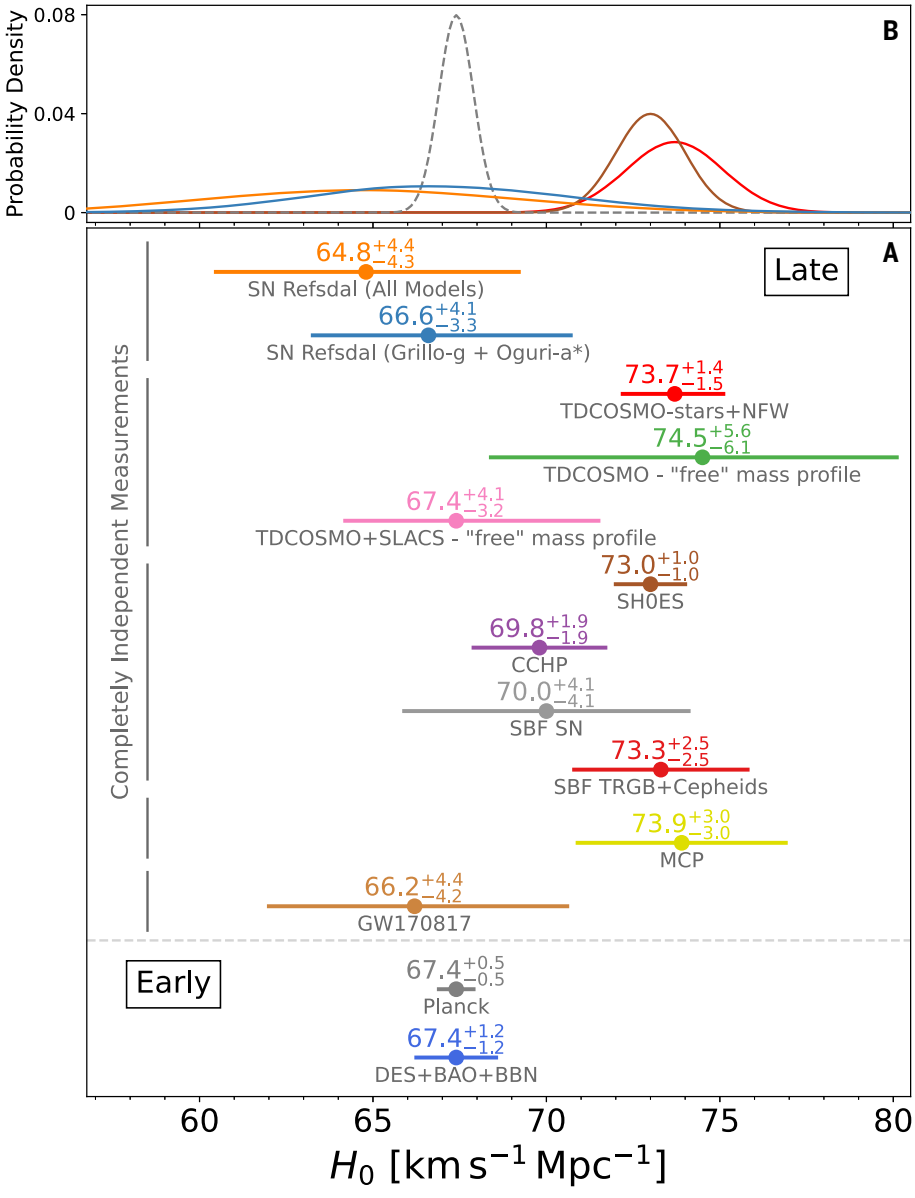


Fig. 5. Comparison of the H_0 measurement using SN Refsdal with previous measurements. (**A**) Constraints from our measurements of SN Refsdal for the full set of eight models (orange) and our preferred subset of the two best models (blue). These are compared with previous constraints from SH0ES + Gaia (*10*), the Carnegie-Chicago Hubble Program (CCHP) (*12*), H0 Lenses in COSMOGRAIL's Wellspring (HOLICOW) (*13*), STRong lensing Insight into DES (STRIDES) (*40*), surface brightness fluctuations (SBF) SN (*41*), SBF Tip of the Red Giant Branch (TRGB)+Cepheids (*42*), Megamaser Cosmology Project (MCP) (*43*), gravitational wave event GW 170817 (*44*), Planck (*9*), and Dark Energy Survey (DES) + Baryon Acoustic Oscillation (BAO) + Big Bang nucleosynthesis (BBN) (*45*). (**B**) posterior probability densities for SN Refsdal (orange and blue), Planck [(*9*), dashed gray], SH0ES (*10*), and HOLICOW (*13*). Error bars show the 16th, 50th, and 84th percentile confidence levels. Dashed horizontal line separates measurements from observations of the early Universe from the late Universe. H_0 measurements bracketed by different vertical gray bars are entirely independent of each other. Figure generated using a previous comparison (*46*).

Table 2. Posterior probability for each set of lens-model predictions.

Diego-a	Grillo-g	Jauzac15.2*	Oguri-g*	Oguri-a*	Sharon-a*	Sharon-g*	Zitrin-c*
7×10^{-9}	4.3×10^{-5}	9.9×10^{-9}	0.00043	0.0005	7.1×10^{-7}	6.1×10^{-6}	3×10^{-12}

distributions from our H_0 measurement are shown in Fig. 5B along with several previous measurements of the expansion rate. Our two estimates of H_0 using SN Refsdal favor values for H_0 that are smaller than the SH0ES estimate (*10*) by 8.2 km s^{-1} Mpc^{-1} and 6.4 km s^{-1} Mpc^{-1}, which correspond to 1.8σ and 1.5σ, respectively. Our most probable values of H_0 are smaller by 2.6 km s^{-1} Mpc^{-1} and 0.8 km s^{-1} Mpc^{-1}, corresponding to differences of 0.6σ and 0.2σ, respectively, from the value of H_0 inferred from early-Universe observations (*9*).

Systematic uncertainties and error budget

We considered two sets of models for our parallel estimates of H_0, but every model separately prefers smaller values of H_0 than 68 km s^{-1} Mpc^{-1} given the SX to S1 time delay (Fig. 2). We check whether our measurement of H_0 is robust to the assumptions of the simply parameterized models using a model produced after the appearance of SX. The Chen2020 model (*38*) makes only minimal assumptions about the distribution of matter at the cluster scale; it calculates an SX to S1 time delay of 332.35 ± 9.32 days assuming $H_0 = 70$ km s^{-1} Mpc^{-1} (*38*), consistent with those of the simply parameterized models (table S4). The Chen2020 model also reproduces the Einstein cross.

The closely related Oguri-a* and Oguri-g* models account for 95% of the weight for our primary estimate of H_0, whereas the Oguri-a* model accounts for 91% of the weight of our parallel estimate (Table 1). Given the model's weights, we use the MCMC chain for the Oguri-a* model to construct an error budget for the model. We split the Oguri-a* model parameters (*28*) into six sets of related parameters and construct a second-order model of the predicted SX to S1 time delay in terms of these variables, after subtracting the mean value of each parameter from the values of the parameters (*34*). We next compute the reduction in the variance of the predicted SX to S1 time delay when we add each group of model parameters in succession.

There is covariance among the groups of model parameters, so we compute the mean of the reduction of the variance after repeating the calculation for all permutations of the groups of parameters. The resulting error budget (fig. S4) shows that the cluster's principal dark-matter halo, which dominates its mass, has the largest contribution to the uncertainty in H_0.

We used the Hera galaxy cluster simulation (*33*) to assess the ability of the Oguri models to recover the value of H_0 by applying the same modeling code [GLAFIC (*28*, *39*)] to the simulation. In fig. S5, we compare the time delays and uncertainties estimated from the Hera simulation (*33*) with those estimated using the GLAFIC code. This comparison assumes the same cosmological parameters that were

used to construct the Hera simulations ($H_0 = 72\ \mathrm{km\ s^{-1}\ Mpc^{-1}}$ and $\Omega_M = 0.24$). We find that the recovered and actual time delays in fig. S5 are correlated, with a best-fitting slope of 1.046 ± 0.021. We infer that GLAFIC can be used to infer H_0 within ~5%, consistent with the error budget calculated for SN Refsdal.

Both the Grillo and Oguri teams performed their time-delay calculations using the positions of images S1 and SX as predicted by their models. We examined whether the models' SX to S1 time delays would shift if the images' observed positions instead are used (*34*); we find differences of <2 days (table S4), less than the precision of the measured time delay. An independent investigation by the Grillo team into the accuracy of H_0 estimated using SN Refsdal found that a 3% constraint on the relative S1 to SX time delay corresponds to 6% uncertainty in H_0 (*17*), which is consistent with our uncertainty calculations.

Analytical expectation for H_0 uncertainty

The change in H_0 due to an overprediction or underprediction of the separation of two images of a strongly lensed object can be described by a simple differential equation (*35*). We use this relationship, and the predicted image positions for S1 and SX in the MCMC chain for the Oguri-a* model, to compute the expected uncertainty in H_0. We find that the precision with which the Oguri-a* model reproduces the separation of SX and S1 corresponds to a 5.5% uncertainty in H_0. We also find that ~92% of the variance in the relative time delay of SX and S1 can be accounted for by the predicted separation of the two images. Therefore, we conclude that our ~5% error budget for the Oguri-a* model is consistent with the analytic expectation.

SN cosmography with a cluster lens

We have used observations of SN Refsdal to perform cosmography and measure the cosmic expansion rate. Using two sets of models, we derived constraints on H_0 of $64.8^{+4.4}_{-4.3}\ \mathrm{km\ s^{-1}\ Mpc^{-1}}$ and $66.6^{+4.1}_{-3.3}\ \mathrm{km\ s^{-1}\ Mpc^{-1}}$.

We expect that our results have different systematic uncertainties compared with other methods for measuring H_0, including time-delay cosmography using quasars, which instead use galaxy-scale lenses. The dominant source of uncertainty in our H_0 measurement is the cluster lens model. The 1.5% uncertainty in the measurement of the SX to S1 time delay (*8*) is sufficiently small that it would provide an equally precise constraint on the value of H_0 if the cluster model were perfect.

Our analysis uses lens models that were blind to the time-delay measurement. The models that account for almost all of the weight in our estimate of H_0 are consistent with the observations (Fig. 3), with the exception of the relative magnification of image S4, which appears to have experienced a microlensing event. The simply parameterized models best reproduce the observables, even when the CMB and SN constraints on H_0 are used as priors (see supplementary text). We analyzed our error budget using the Oguri-a* model, finding that our ~5.5% uncertainty on H_0 is consistent with analytic expectations (*35*) given the model's astrometric accuracy. Further tests using a simulated galaxy cluster also indicated an expected uncertainty of ~5%.

REFERENCES AND NOTES

1. S. Refsdal, On the Possibility of Determining Hubble's Parameter and the Masses of Galaxies from the Gravitational Lens Effect. *Mon. Not. R. Astron. Soc.* **128**, 307–310 (1964). doi: 10.1093/mnras/128.4.307
2. T. Treu, P. J. Marshall, Time delay cosmography. *Astron. Astrophys. Rev.* **24**, 11 (2016). doi: 10.1007/s00159-016-0096-8
3. M. Tewes *et al.*, COSMOGRAIL: The COSmological MOnitoring of GRAvItational Lenses. *Astron. Astrophys.* **556**, A22 (2013). doi: 10.1051/0004-6361/201220352
4. S. H. Suyu *et al.*, Cosmology from gravitational lens time delays and Planck data. *Astrophys. J. Lett.* **788**, L35 (2014). doi: 10.1088/2041-8205/788/2/L35
5. S. Birrer *et al.*, TDCOSMO - IV. Hierarchical time-delay cosmography – joint inference of the Hubble constant and galaxy density profiles. *Astron. Astrophys.* **643**, A165 (2020). doi: 10.1051/0004-6361/202038861
6. P. L. Kelly *et al.*, Multiple images of a highly magnified supernova formed by an early-type cluster galaxy lens. *Science* **347**, 1123–1126 (2015). doi: 10.1126/science.aaa3350; pmid: 25745167
7. P. L. Kelly *et al.*, Deja vu all over again: The reappearance of supernova Refsdal. *Astrophys. J. Lett.* **819**, L8 (2016). doi: 10.3847/2041-8205/819/1/L8
8. P. L. Kelly *et al.*, The Magnificent Five Images of Supernova Refsdal: Time Delay and Magnification Measurements. *Astrophys. J.* **948**, 93 (2023). doi: 10.3847/1538-4357/ac4ccb
9. Planck Collaboration, *Planck* 2018 results - VI. Cosmological parameters. *Astron. Astrophys.* **641**, A6 (2020). doi: 10.1051/0004-6361/201833910
10. A. G. Riess *et al.*, A Comprehensive Measurement of the Local Value of the Hubble Constant with 1 km s^{-1} Mpc^{-1} Uncertainty from the Hubble Space Telescope and the SH0ES Team. *Astrophys. J. Lett.* **934**, L7 (2022). doi: 10.3847/2041-8213/ac5c5b
11. L. Verde, T. Treu, A. G. Riess, Tensions between the early and late Universe. *Nat. Astron.* **3**, 891–895 (2019). doi: 10.1038/s41550-019-0902-0
12. W. L. Freedman *et al.*, The Carnegie-Chicago Hubble Program. VIII. An Independent Determination of the Hubble Constant Based on the Tip of the Red Giant Branch. *Astrophys. J.* **882**, 34 (2019). doi: 10.3847/1538-4357/ab2f73
13. M. Millon *et al.*, TDCOSMO - I. An exploration of systematic uncertainties in the inference of H_0 from time-delay cosmography. *Astron. Astrophys.* **639**, A101 (2020). doi: 10.1051/0004-6361/201937351
14. S. Birrer *et al.*, HOLiCOW – IX. Cosmographic analysis of the doubly imaged quasar SDSS 1206+4332 and a new measurement of the Hubble constant. *Mon. Not. R. Astron. Soc.* **484**, 4726–4753 (2019). doi: 10.1093/mnras/stz200
15. J. Vega-Ferrero, J. M. Diego, V. Miranda, G. M. Bernstein, The Hubble Constant from SN Refsdal. *Astrophys. J. Lett.* **853**, L31 (2018). doi: 10.3847/2041-8213/aaa95f
16. C. Grillo *et al.*, Measuring the Value of the Hubble Constant "à la Refsdal." *Astrophys. J.* **860**, 94 (2018). doi: 10.3847/1538-4357/aac2c9
17. C. Grillo *et al.*, On the Accuracy of Time-delay Cosmography in the Frontier Fields Cluster MACS J1149.5+2223 with Supernova Refsdal. *Astrophys. J.* **898**, 87 (2020). doi: 10.3847/1538-4357/ab9a4c
18. M. Oguri, Strong gravitational lensing of explosive transients. *Rep. Prog. Phys.* **82**, 126901 (2019). doi: 10.1088/1361-6633/ab4fc5; pmid: 31634885
19. M. Oguri, Y. Kawano, Gravitational lens time delays for distant supernovae: Breaking the degeneracy between radial mass profiles and the Hubble constant. *Mon. Not. R. Astron. Soc.* **338**, L25–L29 (2003). doi: 10.1046/j.1365-8711.2003.06290.x
20. G. Dobler, C. R. Keeton, Microlensing of Lensed Supernovae. *Astrophys. J.* **653**, 1391–1399 (2006). doi: 10.1086/508769
21. A. Goobar *et al.*, iPTF16geu: A multiply imaged, gravitationally lensed type Ia supernova. *Science* **356**, 291–295 (2017). doi: 10.1126/science.aal2729; pmid: 28428419
22. X. Li, J. Hjorth, J. Richard, The rates and time-delay distribution of multiply imaged supernovae behind lensing clusters. *J. Cosmol. Astropart. Phys.* **2012**, 015 (2012). doi: 10.1088/1475-7516/2012/11/015
23. A. von der Linden *et al.*, Weighing the Giants – I. Weak-lensing masses for 51 massive galaxy clusters: Project overview, data analysis methods and cluster images. *Mon. Not. R. Astron. Soc.* **439**, 2–27 (2014). doi: 10.1093/mnras/stt1945
24. P. L. Kelly *et al.*, Weighing the Giants – II. Improved calibration of photometry from stellar colours and accurate photometric redshifts. *Mon. Not. R. Astron. Soc.* **439**, 28–47 (2014). doi: 10.1093/mnras/stt1946
25. D. E. Applegate *et al.*, Weighing the Giants – III. Methods and measurements of accurate galaxy cluster weak-lensing masses. *Mon. Not. R. Astron. Soc.* **439**, 48–72 (2014). doi: 10.1093/mnras/stt2129
26. H. Ebeling, A. C. Edge, J. P. Henry, MACS: A Quest for the Most Massive Galaxy Clusters in the Universe. *Astrophys. J.* **553**, 668–676 (2001). doi: 10.1086/320958
27. A. Zitrin, T. Broadhurst, Discovery of the largest known lensed images formed by a critically convergent lensing cluster. *Astrophys. J.* **703**, L132–L136 (2009). doi: 10.1088/0004-637X/703/2/L132
28. R. Kawamata, M. Oguri, M. Ishigaki, K. Shimasaku, M. Ouchi, Precise strong lensing mass modeling of four *Hubble* Frontier Field clusters and a sample of magnified high-redshift galaxies. *Astrophys. J.* **819**, 114 (2016). doi: 10.3847/0004-637X/819/2/114
29. T. Treu *et al.*, "Refsdal" meets Popper: Comparing predictions of the re-appearance of the multiply images supernova behind MACSJ1149.5+2223. *Astrophys. J.* **817**, 60 (2016). doi: 10.3847/0004-637X/817/1/60
30. M. Jauzac *et al.*, Hubble Frontier Fields: Predictions for the return of SN Refsdal with the MUSE and GMOS spectrographs. *Mon. Not. R. Astron. Soc.* **457**, 2029–2042 (2016). doi: 10.1093/mnras/stw069
31. P. L. Kelly *et al.*, Detection of a SN near the center of the galaxy cluster field MACS1149 consistent with predictions of a new image of Supernova Refsdal. *Astron. Telegr.* **8402**, 1 (2015).
32. S. A. Rodney *et al.*, SN Refsdal: Photometry and time delay measurements of the first Einstein Cross supernova. *Astrophys. J.* **820**, 50 (2016). doi: 10.3847/0004-637X/820/1/50
33. M. Meneghetti *et al.*, The Frontier Fields lens modelling comparison project. *Mon. Not. R. Astron. Soc.* **472**, 3177–3216 (2017). doi: 10.1093/mnras/stx2064
34. Materials and methods are available as supplementary materials.
35. S. Birrer, T. Treu, Astrometric requirements for strong lensing time-delay cosmography. *Mon. Not. R. Astron. Soc.* **489**, 2097–2103 (2019). doi: 10.1093/mnras/stz2254
36. P. L. Kelly *et al.*, Hubble Space Telescope Discovery of a Probable Caustic-Crossing Event in the MACS1149 Galaxy Cluster Field. *Astron. Telegr.* **9097**, 1 (2016).
37. L. Dessart, D. J. Hillier, Supernovae from blue supergiant progenitors: What a mess! *Astron. Astrophys.* **622**, A70 (2019). doi: 10.1051/0004-6361/201833966
38. W. Chen, P. L. Kelly, L. L. R. Williams, Blind Prediction of the Returning Image of Supernova Refsdal from a New Lens Model of the Galaxy Cluster MACS J1149.5+2223. *Res. Notes AAS* **4**, 215 (2020). doi: 10.3847/2515-5172/abcf2b
39. M. Oguri, The Mass Distribution of SDSS J1004 + 4112 Revisited. *Publ. Astron. Soc. Jpn.* **62**, 1017–1024 (2010). doi: 10.1093/pasj/62.4.1017
40. A. J. Shajib *et al.*, STRIDES: A 3.9 per cent measurement of the Hubble constant from the strong lens system DES J0408 −5354. *Mon. Not. R. Astron. Soc.* **494**, 6072–6102 (2020). doi: 10.1093/mnras/staa828
41. N. Khetan *et al.*, A new measurement of the Hubble constant using Type Ia supernovae calibrated with surface brightness fluctuations. *Astron. Astrophys.* **647**, A72 (2021). doi: 10.1051/0004-6361/202039196
42. J. P. Blakeslee, J. B. Jensen, C.-P. Ma, P. A. Milne, J. E. Greene, The Hubble Constant from Infrared Surface Brightness Fluctuation Distances. *Astrophys. J.* **911**, 65 (2021). doi: 10.3847/1538-4357/abe86a
43. D. W. Pesce *et al.*, The Megamaser Cosmology Project. XIII. Combined Hubble Constant Constraints. *Astrophys. J. Lett.* **891**, L1 (2020). doi: 10.3847/2041-8213/ab75f0

44. T. Dietrich *et al*., Multimessenger constraints on the neutron-star equation of state and the Hubble constant. *Science* **370**, 1450–1453 (2020). doi: 10.1126/science.abb4317; pmid: 33335061
45. T. M. C. Abbott *et al*., Dark Energy Survey Year 1 Results: A Precise H_0 Estimate from DES Y1, BAO, and D/H Data. *Mon. Not. R. Astron. Soc.* **480**, 3879–3888 (2018). doi: 10.1093/mnras/sty1939
46. V. Bonvin, M. Millon, HOLiCOW H0 tension plotting notebook, v1.0, Zenodo (2020); https://doi.org/10.5281/zenodo.3635517.
47. P. Kelly, Constraints on the Hubble constant for Supernova Refsdal's reappearance, Zenodo (2023); https://doi.org/10.5281/zenodo.7818787.

ACKNOWLEDGMENTS

We thank program coordinators B. Periello and T. Royle as well as contact scientists N. Pirzkal, I. Momcheva, and K. Sahu of the Space Telescope Science Institute (STScI) for their help carrying out the HST observations. We also appreciate useful discussions with P. Rosati, C. Grillo, S. Suyu, and M. Meneghetti. We used the HFF Lens Model website, hosted by the Mikulski Archive for Space Telescopes (MAST) at STScI. **Funding:** P.L.K., A.V.F., T.T., J.P., and S.R. received financial support from NASA/STScI grants GO-14041, 14199, 14208, 14528, 14872, 14922, 15050, 15791, and 16134. P.L.K. is supported by NSF grant AST-1908823. M.O. acknowledges support by the WPI Initiative (MEXT, Japan) and by JSPS KAKENHI grants JP18K03693, JP20H00181, JP20H05856, and JP22H01260. T.T. acknowledges the support of NSF grant AST-1906976. S.T. was supported by the Cambridge Centre for Doctoral Training in Data-Intensive Science funded by the UK Science and Technology Facilities Council (STFC). J.P. was supported by the NASA FINESST award 80NSSC19K1414. J.M.D. acknowledges the support of project PGC2018-101814-B-100 (MCIU/AEI/MINECO/FEDER, UE) Ministerio de Ciencia, Investigación y Universidades. J.M.D. was funded by the Agencia Estatal de Investigación, Unidad de Excelencia María de Maeztu, ref. no. MDM-2017-0765. M.J. is supported by the United Kingdom Research and Innovation (UKRI) Future Leaders Fellowship (grant MR/S017216/1). M.M. and V.B. acknowledge support from the European Research Council (ERC) under the Horizon 2020 Research and Innovation Program (COSMICLENS: grant agreement 787886). A.V.F. is grateful for funding from the Christopher R. Redlich Fund, the TABASGO Foundation, the UC Berkeley Miller Institute for Basic Research in Science (as a Miller Senior Fellow), and financial contributions from many additional individual donors. R.J.F. is supported in part by NASA grant NNG17PX03C, NSF grants AST-1518052 and AST-1815935, the Gordon and Betty Moore Foundation, the Heising-Simons Foundation, and the David and Lucile Packard Foundation. J.H. acknowledges support from VILLUM FONDEN investigator grant 16599. S.J. is supported by NSF CAREER award AST-0847157 as well as by NASA/Keck JPL RSA 1508337 and 1520634. K.M. acknowledges funding from the European Union's Horizon 2020 Research and Innovation Program under ERC grant agreement no. 101002652 and Marie Skłodowska-Curie grant agreement no. 873089. A.Z. acknowledges support by grant no. 2020750 from the United States–Israel Binational Science Foundation (BSF), by grant no. 2109066 from the US NSF, and by the Ministry of Science and Technology, Israel. **Author contributions:** P.L.K. measured the SN photometry, developed the statistical framework and analysis code, and drafted the manuscript. P.L.K., S.R., T.T., A.V.F., R.J.F., J.H., T.B., O.G., S.J., C.M., M.P., K.B.S., B.E.T., and A.v.d.L. obtained follow-up HST imaging. P.L.K., S.R., T.T., S.B., V.B., L.D., D.G., K.M., M.M., J.P., K.S., and S.T. contributed to the time-delay measurement. P.L.K., S.R., T.T., V.B., A.V.F., K.M., and S.T. helped prepare the manuscript. S.R., T.T., L.W., T.B., and A.D. aided the interpretation. M.O., W.C., A.Z., J.M.D., and M.J. modeled the galaxy cluster. **Competing interests:** The authors declare no competing interests. **Data and materials availability:** The HST imaging is available from https://mast.stsci.edu/search/ui/#/hst under proposal IDs 14041, 14199, 14208, 14528, 14872, and 14922. The measured time delays and magnifications are listed in table S3, and the predicted values are listed in tables S4 and S5. Our analysis code is archived on Zenodo (*47*).
License information: Copyright © 2023 the authors, some rights reserved; exclusive licensee American Association for the Advancement of Science. No claim to original US government works. https://www.science.org/about/science-licenses-journal-article-reuse

SUPPLEMENTARY MATERIALS

science.org/doi/10.1126/science.abh1322
Materials and Methods
Supplementary Text
Figs. S1 to S6
Tables S1 to S15
References (*48*–*67*)

Submitted 22 February 2021; accepted 24 April 2023
Published online 11 May 2023
10.1126/science.abh1322

RESEARCH ARTICLE SUMMARY

AGING

Taurine deficiency as a driver of aging

Parminder Singh†*, Kishore Gollapalli†, Stefano Mangiola‡, Daniela Schranner‡, Mohd Aslam Yusuf‡, Manish Chamoli‡ *et al.*

INTRODUCTION: Aging is an inevitable multifactorial process. Aging-related changes manifest as the "hallmarks of aging," cause organ functions to decline, and increase the risk of disease and death. Aging is associated with systemic changes in the concentrations of molecules such as metabolites. However, whether such changes are merely the consequence of aging or whether these molecules are drivers of aging remains largely unexplored. If these were blood-based drivers of aging, then restoring their concentration or functions to "youthful" levels could serve as an antiaging intervention.

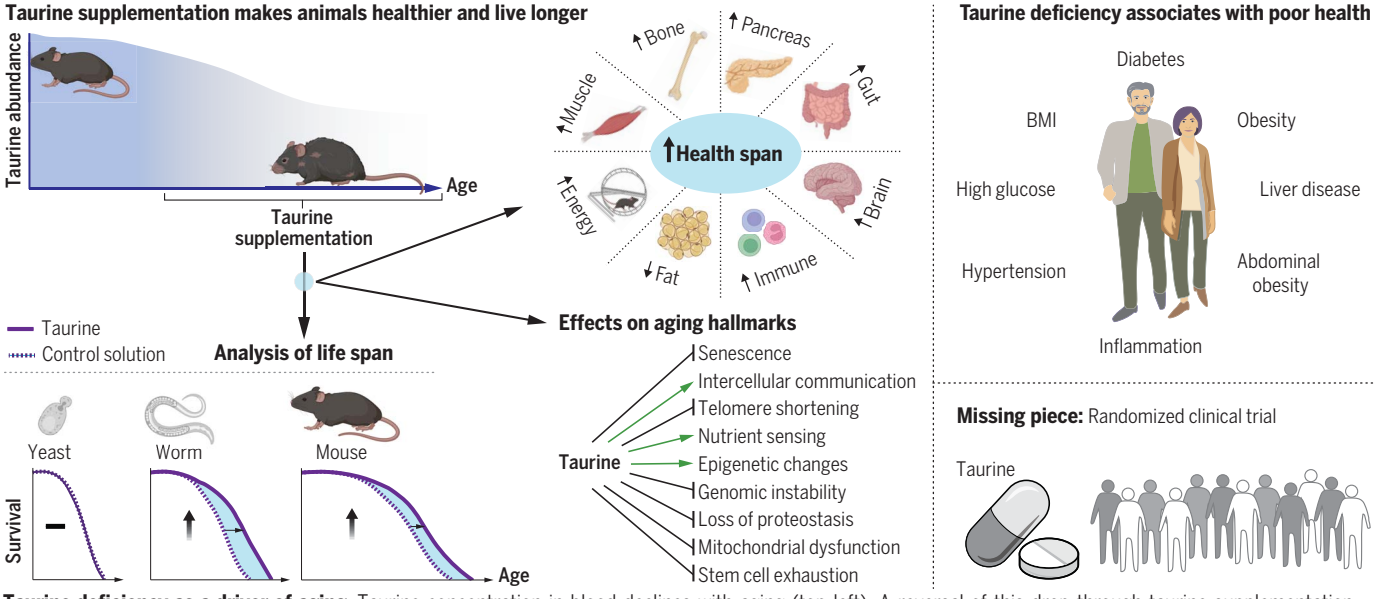
RATIONALE: Taurine, a semiessential micronutrient, is one of the most abundant amino acids in humans and other eukaryotes. Earlier studies have shown that the concentration of taurine in blood correlates with health, but it is unknown whether blood taurine concentrations affect aging. To address this gap in knowledge, we measured the blood concentration of taurine during aging and investigated the effect of taurine supplementation on health span and life span in several species.

RESULTS: Blood concentration of taurine declines with age in mice, monkeys, and humans. To investigate whether this decline contributes to aging, we orally fed taurine or a control solution once daily to middle-aged wild-type female and male *C57Bl/6J* mice until the end of life. Taurine-fed mice of both sexes survived longer than the control mice. The median life span of taurine-treated mice increased by 10 to 12%, and life expectancy at 28 months increased by about 18 to 25%. A meaningful antiaging therapy should not only improve life span but also health span, the period of healthy living. We, therefore, investigated the health of taurine-fed middle-aged mice and found an improved functioning of bone, muscle, pancreas, brain, fat, gut, and immune system, indicating an overall increase in health span. We observed similar effects in monkeys. To check whether the observed effects of taurine transcended the species boundary, we investigated whether taurine supplementation increased life span in worms and yeast. Although taurine did not affect the replicative life span of unicellular yeast, it increased life span in multicellular worms. Investigations into the mechanism or mechanisms through which taurine supplementation impro[illegible] the health span and life span revealed [illegible] taurine positively affected several hallmarks of aging. Taurine reduced cellular senescence, protected against telomerase deficiency, suppressed mitochondrial dysfunction, decreased DNA damage, and attenuated inflammation. An association analysis of metabolite clinical risk factors in humans showed that lower taurine, hypotaurine, and *N*-acetyltaurine concentrations were associated with adverse health, such as increased abdominal obesity, hypertension, inflammation, and prevalence of type 2 diabetes. Moreover, we found that a bout of exercise increased the concentrations of taurine metabolites in blood, which might partially underlie the antiaging effects of exercise.

CONCLUSION: Taurine abundance decreases during aging. A reversal of this decline through taurine supplementation increases health span and life span in mice and worms and health span in monkeys. This identifies taurine deficiency as a driver of aging in these species. To test whether taurine deficiency is a driver of aging in humans as well, long-term, well-controlled taurine supplementation trials that measure health span and life span as outcomes are required. ■

The list of author affiliations is available in the full article online.
*Corresponding author. Email: vky2101@cumc.columbia.edu
†These authors contributed equally to this work.
‡These authors contributed equally to this work.
Cite this article as P. Singh *et al.*, *Science* **380**, eabn9257 (2023). DOI: 10.1126/science.abn9257

READ THE FULL ARTICLE AT
https://doi.org/10.1126/science.abn9257



Taurine deficiency as a driver of aging. Taurine concentration in blood declines with aging (top left). A reversal of this drop through taurine supplementation increased healthy life span in mice and worms but not in yeast (bottom left and top middle). Taurine supplementation affected several hallmarks of aging (middle). In humans, lower taurine concentrations were associated with multiple diseases (top right). A randomized controlled clinical trial in humans is warranted to assess the antiaging effects of taurine (bottom right). BMI, body mass index.

RESEARCH ARTICLE

AGING

Taurine deficiency as a driver of aging

Parminder Singh[1]†‡, Kishore Gollapalli[2]†§, Stefano Mangiola[3,4,5,6]¶, Daniela Schranner[7,8]¶, Mohd Aslam Yusuf[9]¶, Manish Chamoli[10]¶, Sting L. Shi[2]#, Bruno Lopes Bastos[11], Tripti Nair[12], Annett Riermeier[7], Elena M. Vayndorf[13], Judy Z. Wu[13], Aishwarya Nilakhe[1], Christina Q. Nguyen[13], Michael Muir[13], Michael G. Kiflezghi[13], Anna Foulger[10], Alex Junker[14], Jack Devine[14], Kunal Sharan[15], Shankar J. Chinta[10], Swati Rajput[16], Anand Rane[10], Philipp Baumert[7], Martin Schönfelder[7], Francescopaolo Iavarone[17], Giorgia di Lorenzo[17], Swati Kumari[1], Alka Gupta[1], Rajesh Sarkar[1], Costerwell Khyriem[18,19], Amanpreet S. Chawla[20,21], Ankur Sharma[18,19], Nazan Sarper[22], Naibedya Chattopadhyay[16], Bichitra K. Biswal[1], Carmine Settembre[17,23], Perumal Nagarajan[24,25], Kimara L. Targoff[26], Martin Picard[14], Sarika Gupta[1], Vidya Velagapudi[27], Anthony T. Papenfuss[3,4], Alaattin Kaya[28], Miguel Godinho Ferreira[11], Brian K. Kennedy[29,30,31], Julie K. Andersen[10], Gordon J. Lithgow[10], Abdullah Mahmood Ali[32], Arnab Mukhopadhyay[12], Aarno Palotie[27,33,34], Gabi Kastenmüller[8], Matt Kaeberlein[13], Henning Wackerhage[7], Bhupinder Pal[3,4,5,6], Vijay K. Yadav[1,2,15,35]*

Aging is associated with changes in circulating levels of various molecules, some of which remain undefined. We find that concentrations of circulating taurine decline with aging in mice, monkeys, and humans. A reversal of this decline through taurine supplementation increased the health span (the period of healthy living) and life span in mice and health span in monkeys. Mechanistically, taurine reduced cellular senescence, protected against telomerase deficiency, suppressed mitochondrial dysfunction, decreased DNA damage, and attenuated inflammaging. In humans, lower taurine concentrations correlated with several age-related diseases and taurine concentrations increased after acute endurance exercise. Thus, taurine deficiency may be a driver of aging because its reversal increases health span in worms, rodents, and primates and life span in worms and rodents. Clinical trials in humans seem warranted to test whether taurine deficiency might drive aging in humans.

According to the World Population Prospects of the United Nations, the number of people aged 65 and older will increase from 1 in 11 in 2019 to 1 in 6 in 2050 (*1*). Although this is a success of modern medicine and of government policies, it is vital to ensure that the elderly also remain healthy, because this will increase the quality of life and reduce the costs associated with societal aging (*2*–*5*). Over the past two decades, efforts to identify antiaging interventions that reduce morbidity and increase life span have intensified (*2*–*11*). This has led to the identification of compounds that may increase healthy life span (the period of life span spent in good health) such as rapamycin, metformin, nicotinamide adenine dinucleotide (NAD) precursors, and senolytics (*2*–*6*, *12*).

Aging is a complex process that affects all organs (*13*, *14*). The age-induced decline in organ functions involves several cell-autonomous events termed "hallmarks of aging." The central hallmarks include genomic instability, deregulated nutrient sensing, mitochondrial dysfunction, stem cell exhaustion, and accumulation of senescent cells (*13*). Aging-associated decline in organ functions also results from changes in the concentrations of endogenous metabolites, hormones, and micronutrients in blood (*15*–*17*). However, it is unclear whether these changes are passengers or drivers of aging. If a molecule in blood is a driver of aging, then a correction to its youthful levels would delay aging and increase healthy life span.

Taurine (2–aminoethanesulfonic acid), a semiessential micronutrient, is one of the most abundant amino acids found in organisms across eukaryotic phyla (*18*–*22*). In mammalian cells, taurine is produced from cysteine through the action of cysteine sulfinic acid decarboxylase (CSAD) (*20*). Taurine can also be obtained from the diet and is taken up by cells through taurine transporters (*20*). Taurine deficiency during early life causes functional impairments in skeletal muscle, eye, and the central nervous system (*23*–*26*) that are related to aging-associated disorders. Moreover, concentrations of taurine and its metabolites decline in some tissues with age, and acute taurine supplementation in young animals enhances the functions of several organs (*27*–*35*). Given the decline in taurine abundance during aging and its known health effects, we aimed to find out whether taurine deficiency is a driver of aging and affects healthy life span.

Results

Decline of serum concentrations of taurine with age in mice, monkeys, and humans

To comprehensively study whether taurine abundance influences healthy life span, we measured blood taurine concentrations at different ages in mice, monkeys, and humans. In *C57Bl/6J* wild-type (WT) mice, serum taurine concentrations declined from 132.3 ± 14.2 ng/ml at 4 weeks to 40.2 ± 7.1 ng/ml at 56 weeks, which correlates negatively with age (slope = −25.7; $p < 2 \times 10^{-16}$) (Fig. 1A). In 15-year-old monkeys, serum taurine concentrations were 85% lower than in 5-year-old monkeys (Fig. 1B). Likewise, taurine concentrations in elderly humans were decreased by more than 80% compared with the concentration in serum of younger individuals (Fig. 1C).

Taurine supplementation increases the life span of mice

To determine whether the observed drop in taurine concentration contributes to aging, we

[1]Metabolic Research Laboratories, National Institute of Immunology, New Delhi, India. [2]Vagelos College of Physicians and Surgeons, Columbia University, New York, NY, USA. [3]The Walter and Eliza Hall Institute of Medical Research, Parkville, VIC, Australia. [4]Department of Medical Biology, University of Melbourne, Melbourne, VIC, Australia. [5]School of Cancer Medicine, La Trobe University, Bundoora, VIC, Australia. [6]Olivia Newton-John Cancer Research Institute, Heidelberg, VIC, Australia. [7]Exercise Biology Group, Technical University of Munich, Munich, Germany. [8]Institute of Computational Biology, Helmholtz Zentrum München, Neuherberg, Germany. [9]Department of Bioengineering, Integral University, Lucknow, India. [10]Buck Institute for Research on Aging, Novato, CA, USA. [11]Institute for Research on Cancer and Aging of Nice (IRCAN), Nice, France. [12]Molecular Aging Laboratory, National Institute of Immunology, New Delhi, India. [13]Department of Laboratory Medicine and Pathology, University of Washington, Seattle, WA, USA. [14]Department of Neurology, Columbia University, New York, NY, USA. [15]Mouse Genetics Project, Wellcome Sanger Institute, Cambridge, UK. [16]Division of Endocrinology, CSIR-Central Drug Research Institute, Lucknow, India. [17]Telethon Institute of Genetics and Medicine (TIGEM), Pozzuoli, Italy. [18]Harry Perkins Institute of Medical Research, Perth, WA, Australia. [19]Curtin Medical School, Curtin University, Perth, WA, Australia. [20]Immunobiology Laboratory, National Institute of Immunology, New Delhi, India. [21]MRC-Protein Phosphorylation and Ubiquitination Unit, University of Dundee, Dundee, UK. [22]Pediatrics and Pediatric Hematology, Kocaeli University Hospital, Kocaeli, Turkey. [23]Department of Clinical Medicine and Surgery, Federico II University, Naples, Italy. [24]Primate Research Facility, National Institute of Immunology, New Delhi, India. [25]Small Animal Research Facility, National Institute of Immunology, New Delhi, India. [26]Division of Cardiology, Department of Pediatrics, Columbia University, New York, NY, USA. [27]Institute for Molecular Medicine Finland FIMM, University of Helsinki, Helsinki, Finland. [28]Department of Biology, Virginia Commonwealth University, Richmond, VA, USA. [29]Healthy Longevity Translational Research Program, Yong Loo Lin School of Medicine, National University of Singapore, Singapore, Singapore. [30]Centre for Healthy Longevity, National University Health System, Singapore, Singapore. [31]Departments of Biochemistry and Physiology, Yong Loo Lin School of Medicine, National University of Singapore, Singapore, Singapore. [32]Department of Medicine, Columbia University Irving Medical Center, New York, NY, USA. [33]Broad Institute of Harvard and MIT, Cambridge, MA, USA. [34]Analytic and Translational Genetics Unit, Massachusetts General Hospital, Boston, MA, USA. [35]Department of Genetics and Development, Columbia University, New York, NY, USA.
*Corresponding author. Email: vky2101@cumc.columbia.edu
†These authors contributed equally to this work. ‡Present address: Buck Institute for Research on Aging, Novato, CA, USA. §Present address: Department of Microbiology and Immunology, Columbia University, New York, NY, USA. ¶These authors contributed equally to this work. #Present address: Department of Molecular, Cellular, and Developmental Biology, University of California Santa Barbara, Santa Barbara, CA, USA.

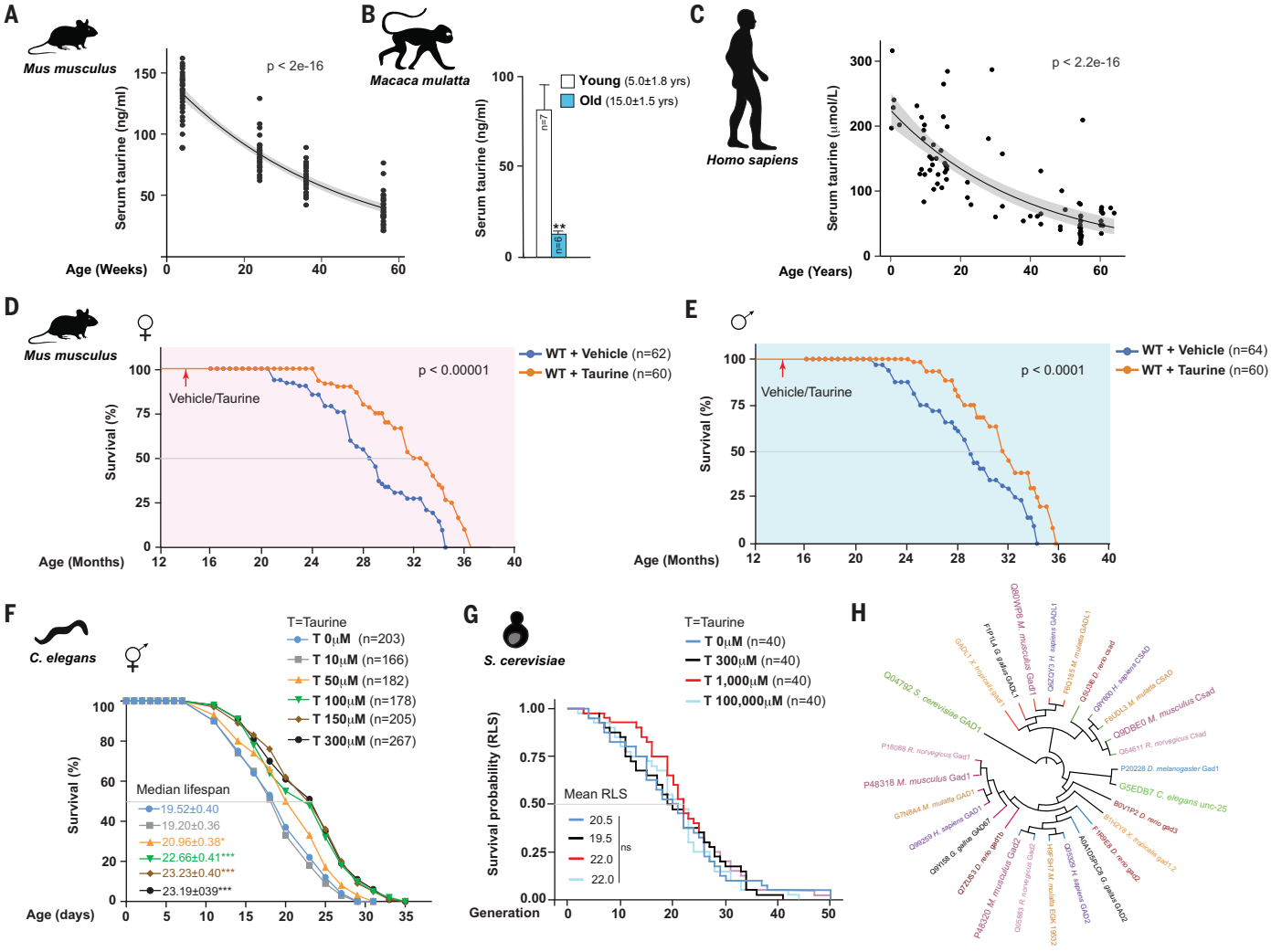


Fig. 1. Taurine deficiency is a driver of aging in evolutionarily divergent species. (**A** to **C**) Serum taurine levels in female mice at different ages (A), in young (5-year-old) and old (15-year-old) female monkeys (B), and in humans at different ages (C). In (A) and (C), shaded regions indicate standard error. (**D** and **E**) Life-span assay of middle-aged (14-month-old) WT female (D) and male (E) *C57Bl/6J* mice orally fed taurine (1000 mg per kg body weight per day) at 10:00 am until the end of life. (**F**) Life-span assay of WT nematodes that were fed diet supplemented with different concentrations of taurine (0, 10, 50, 100, 150, and 300 μM). (**G**) RLS assay in yeast cultured on YPD plates with different concentrations of taurine (0, 300, 1000, and 100,000 μM). (**H**) Phylogenetic analysis of taurine biosynthesis enzymes in eukaryotes. Statistical analysis details are as follows: The OASIS software (https://sbi.postech.ac.kr/oasis) was used to calculate *p* values using a log rank test (the Mantel-Cox method) in mice and worm experiments, and a Wilcoxon rank-sum test was used to calculate *p* values in yeast RLS assays. *N* values are shown within the panels. All values are means ± SEM. ns indicates not significant. ***$p \leq 0.001$, **$p \leq 0.01$, and *$p \leq 0.05$* are versus WT or control.

orally administered control solution or taurine at 1000 mg per kg body weight (T1000), once daily at 10:00 am, to 14-month-old (middle-aged) *C57Bl/6J* WT female and male mice until the end of life. The dose and frequency of taurine administration was selected based on a pilot study, which showed that when given once daily to middle-aged WT mice, this regimen increased the peak blood taurine concentrations to baseline concentrations in young (4-week-old) mice (see materials and methods and fig. S1, A to D, for a description of these studies). Regardless of their sex, taurine-fed mice survived longer than control mice (Fig. 1, D and E). The median life-span increase was 10 to 12%, and life expectancy at 28 months increased by 18 to 25% (Fig. 1, D and E). Median life-span estimates for control female and male mice were consistent in two independent cohorts (females: 871 to 885 days; males: 785 to 815 days). In these experiments, both control and taurine-fed mice had ad libitum access to the same chow (Teklad Irradiated 18% protein and 6% fat diet-2918). Thus, the improved survival of taurine-fed mice was not a consequence of low survival of control animals or differences in diet. Collectively, these results indicate that taurine deficiency is a driver of aging in mice because its reversal increases life span.

Taurine supplementation increases the life span of worms but not yeast

The taurine biosynthetic pathway is evolutionarily conserved among multicellular eukaryotes (*21*, *36*). To find out whether taurine also affects aging in species other than mice, we conducted taurine supplementation experiments in lower species. First, we tested the effect of taurine in worms, which also exhibit an age-associated decline in taurine (*37*). Taurine supplementation significantly extended both the median and maximum life spans of *Caenorhabditis elegans* in a dose-dependent manner (Fig. 1F). Longevity, calculated using the median life span of untreated and taurine-treated worms,

was extended by 10 to 23% in worms treated with higher taurine concentrations in four independent worm cohorts and in two independent laboratories (University of Washington, Seattle, WA, USA, and the National Institute of Immunology, New Delhi, India) (Fig. 1F and fig. S1, E to G). We also investigated the effect of taurine on replicative life span (RLS) in budding yeast, *Saccharomyces cerevisiae*, which is a unicellular eukaryote. In contrast to mice and worms, taurine supplementation did not affect the RLS (*38*) of yeast cultured on nutrient-rich yeast extract–peptone–dextrose (YPD) plates or on a synthetic medium (Fig. 1G and fig. S1, H to J). These results may be explained by organismal differences in taurine metabolism. For example, the taurine metabolism enzymes yeast glutamate decarboxylase (GAD) and mammalian CSAD diverged early during evolution (Fig. 1H) (*39*). Thus, although taurine may not affect the RLS in unicellular eukaryotes, its effect on life span is conserved in invertebrates and mammals.

Taurine supplementation increases health span in aged WT female mice

A meaningful antiaging therapy should improve health span, or the period of healthy living (*2*–*5*, *40*). To assess the effects of taurine supplementation on health span, we orally administered taurine at 500 (T500) and 1000 (T1000) mg per kg body weight per day to female mice once daily for 10 to 12 months, starting at the age of 14 months, and analyzed the health of bone, muscle, brain, pancreas, fat, gut, and the immune system through functional assays or tissue analysis of deceased animals (fig. S2A).

Reduced age-associated body-weight gain and improved bone mass in female mice treated with taurine

Taurine treatment suppressed age-associated body-weight gain by ~10% in the T1000 group compared with controls (Fig. 2A). Fat-pad weight divided by body weight percentage was dose-dependently reduced in taurine-treated mice (Fig. 2B). Taurine-administered mice did not differ in body length and food consumption (in weight-stable mice) or suffer obvious toxic effects (as evidenced by a blinded histopathological scoring of tissue sections by a trained histopathologist) in multiple tissues compared with controls (fig. S2, B to D). Bone structure analysis through histology and microcomputed tomography (μCT) showed that taurine treatment increased bone mass (bone volume divided by total volume percentage) in both the spine and femur compared with that in controls (Fig. 2C). A three-point bending test showed that femur maximal load and stiffness—two surrogates of bone quality—improved in taurine-treated mice compared with controls (Fig. 2D). Taurine also cured osteoporosis and suppressed ovariectomy-induced body-weight gain in a rodent model of menopause (fig. S2, E to G). This latter evidence indicates that the effect of taurine on health parameters in females might be linked to its effect on body weight in other conditions of aging, such as menopause.

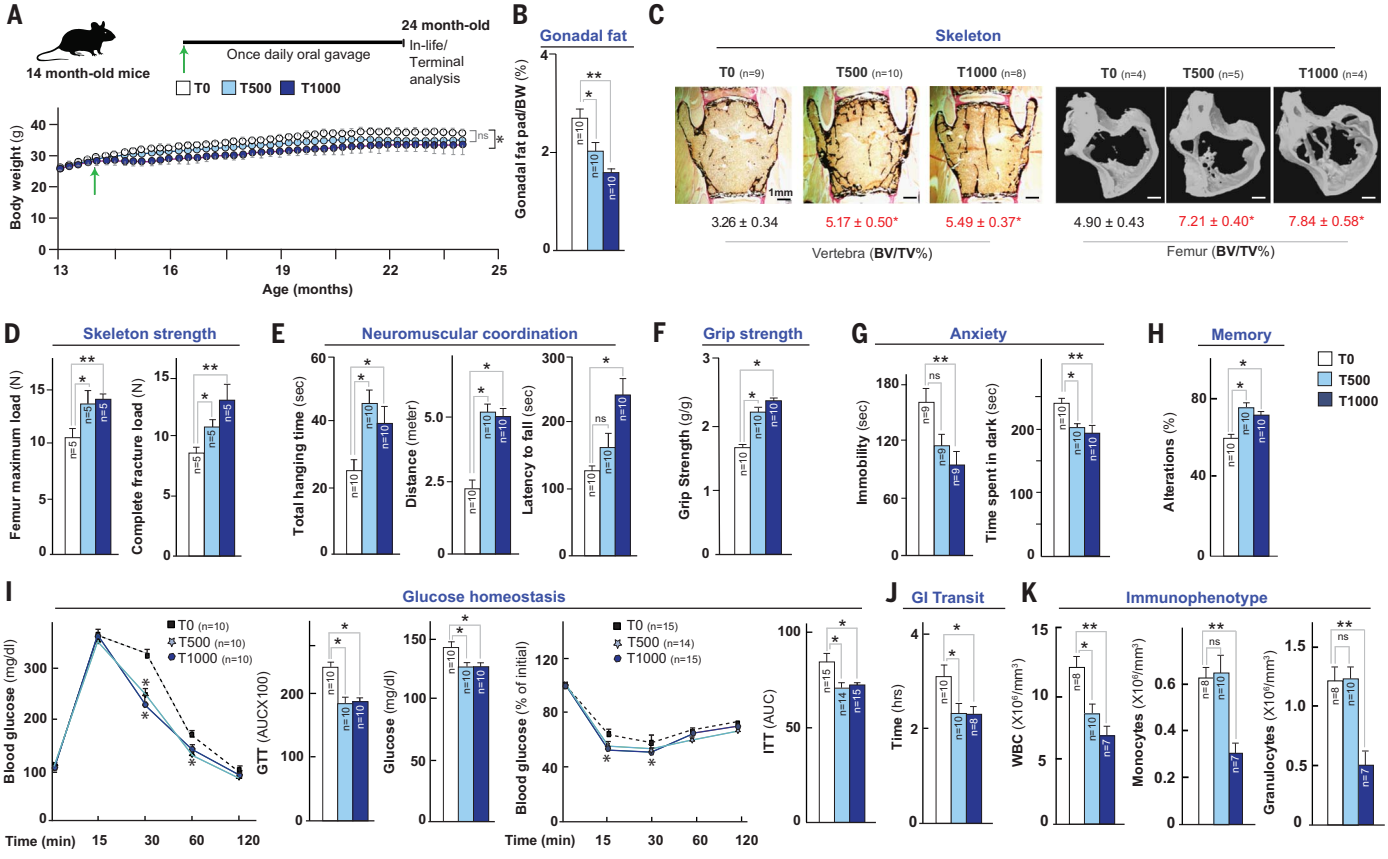


Fig. 2. Taurine supplementation increases health span in aged mice. (**A** to **K**) Changes in body weight (A), fat percentage (B), bone structure, strength parameters in spine and femur [(C) and (D)], neuromuscular and muscle strength [(E) and (F)] (rotarod, wire hang, and grip-strength tests), anxiety (G) (tail suspension and dark-light tests), memory (H) (Y maze test), pancreas function (I) (glucose and insulin tolerance tests), GI transit (J) (oral carmine dye test), and immunophenotyping (K) (immune cell parameters in blood) in 24-month-old WT *C57Bl/6J* female mice orally fed once daily with taurine (0, 500, or 1000 mg per kg body weight per day) beginning at middle age (14 months). In (C), histology (left) and μCT (right) images are shown. A statistical analysis was performed using Graph Pad Prism 7. Data were considered statistically significant at $p \leq 0.05$ calculated by using Student's *t* test, one-way analysis of variance (ANOVA), or two-way ANOVA. *n* values are shown within the panels. All values are means ± SEM. ns indicates not significant. $^{**}p \leq 0.01$, and $^{*}p \leq 0.05$ are versus WT or control. BV, bone volume; BW, body weight; GTT, glucose tolerance test; ITT, insulin tolerance test; TV, total volume.

Increased muscle endurance, coordination, and strength in taurine-treated female mice

An analysis of the effect of taurine treatment on neuromuscular functions showed that total hanging time and distance run in the rotarod test was increased in the T500 and T1000 groups, whereas latency to fall in the wire hang test was increased in the T1000 group (Fig. 2E). Grip strength tests revealed that both doses of taurine increased muscle strength compared with controls (Fig. 2F).

Reduced depression-like behavior and anxiety and enhanced exploratory behavior and memory in taurine-treated female mice

Increased anxiety and decreased exploration are common age-induced behavioral changes (*41*). In the tail suspension test (*42*), taurine-treated mice showed less depression-like behavior compared with controls (Fig. 2G). The light-dark box test (*43*) revealed that taurine-treated mice spent less time in the dark area, which is indicative of lesser anxiety (Fig. 2G). The Y maze test (*44*) showed that taurine-treated mice had a higher natural curiosity for exploration compared with control mice (Fig. 2H).

Improved glucose homeostasis and gastrointestinal transit time in taurine-treated female mice

Analysis of glucose homeostasis using an intraperitoneal glucose tolerance test showed that taurine-treated mice metabolized oral glucose more efficiently than control mice and had lower glucose concentrations when fed ad libitum (Fig. 2I). Likewise, taurine-treated mice had improved insulin sensitivity in the insulin tolerance test (Fig. 2I). These improvements in glucose homeostasis might be a consequence of the reduced adiposity in taurine-treated mice. Gastrointestinal (GI) transit time increases with age (*45*). An analysis of intestinal transit time using nonabsorbable red carmine dye administered by oral gavage (*46*) showed a faster transit in taurine-treated mice, which could contribute to the observed weight loss in these mice (Fig. 2J).

Ameliorated myeloid-leukocyte prominence in taurine-treated aged female mice

Aging alters immune cell numbers in the blood, resulting in increased susceptibility to infection (*47*). A complete blood count showed that taurine treatment decreased the number of white blood cells (WBCs), monocytes, and granulocytes but not the number of red blood cells (Fig. 2K and fig. S2H). Although there was no difference in the efficacy of T500 and T1000 doses on the WBC numbers, the numbers of monocytes and granulocytes were only decreased at the T1000 dose (Fig. 2K). These results show that the myeloid-leukocyte prominence associated with aging-related inflammatory states is ameliorated by high-dose taurine treatment.

Improved health-span metrics in middle-aged male WT mice after taurine administration

To assess whether taurine affects the health span of male mice, as it does in female mice, we treated 14-month-old WT male mice with or without T1000 for 8 to 16 weeks and measured fat, bone, muscle, pancreas, and brain health (fig. S3A). Taurine did not affect bodyweight gain in males up to 16 weeks but significantly reduced fat-pad weight divided by body weight percentage compared to controls (fig. S3, B and C). To identify the cause of the reduced adiposity of taurine-treated mice, we analyzed energy expenditure. Taurine-treated mice consumed more oxygen, generated more carbon dioxide, and had higher respiratory exchange ratios and energy expenditures even though their total activity was decreased compared with that of controls (fig. S3, D to H). Taurine-treated male mice also showed greater muscle strength, neuromuscular coordination, bone density, glucose tolerance, and memory as well as reduced anxiety compared with controls (fig. S3, I to N). Thus, taurine supplementation improved the function of every organ investigated in middle-aged female and male mice and likely increased overall health span.

Effects of taurine on cellular mechanisms in increasing healthy life span

What are the mechanisms through which taurine affects cellular functions to increase healthy life span? To address this question, we performed an RNA-sequencing (RNA-seq) analysis in taurine-deficient and control osteoblasts from mice. These bone-forming cells were chosen because they abundantly express a taurine transporter (encoded by *Slc6a6*), whose deletion impairs differentiation and function of mutant cells in culture and in mice (fig. S4, A to E). Conversely, numbers and function of WT osteoblasts were increased by taurine treatment in vitro and in vivo. (fig. S4, A to E). RNA-seq analysis (*48*) of taurine-deficient osteoblasts showed that the top biological functions identified in the gene-set enrichment analysis (GSEA) are related to aging mechanisms (*13*) such as telomere function, oxidative stress, immune system function, protein translation, and stem cell maintenance (Fig. 3A and figs. S4, F to M). A search for the term "aging" in the GSEA pathways output showed significant alterations in six gene signatures (see table S1 for details). All six signatures showed the expected direction of change (up- or down-regulation) for a pro-aging effect (fig. S4N). Together, these results imply that taurine deficiency generates an aging-related transcriptomic signature in cells.

Suppression of senescence by taurine

A network analysis of taurine-regulated genes showed that senescence-associated secretory phenotype (SASP) genes, such as *p16* and *p21*, which encode inhibitors of cyclin-dependent kinases and promote cell cycle arrest, formed the highest number of genetic interactions (fig. S4O). Consistent with the idea that taurine suppresses senescence, irradiation-induced increase in senescence-associated β-galactosidase (SA β-gal) staining in osteoblasts cultured with taurine was about one-fourth of that in cells cultured without taurine (fig. S4P). In neuronal culture experiments, taurine supplementation increased neuronal survival after treatment with paraquat, a DNA damaging agent that induces senescence (*49*) (fig. S4Q). Moreover, taurine supplementation decreased an age-associated increase in senescence in mice (Fig. 3, B and C, and fig. S5A). To test whether taurine deficiency causes accumulation of senescent cells, we used mice lacking the taurine transporter Slc6a6 (*23*). Lack of Slc6a6 compromises taurine entry into embryonic cells, rendering embryos deficient in taurine. The phenotypes observed postnatally in 0.5- to 3-month-old *Slc6a6* mutant mice (*23*) could be due to taurine deficiency affecting these phenotypes during development or postnatally (hereafter, we refer to these mice as congenitally taurine-deficient mice). Adult *Slc6a6*$^{-/-}$ mice showed accelerated aging-related phenotypes, including decreased bone density, poor neuromuscular coordination, compromised muscle strength, increased anxiety, and decreased memory (fig. S5, C to L). Analysis of bone, muscle, brain, fat, and liver showed increased senescence in taurine-deficient mice compared with controls (fig. S5, A and B). To investigate whether accumulation of senescent cells in these organs contributes to the compromised health span of taurine-deficient mice, we treated 8-month-old *Slc6a6*$^{-/-}$ mice with or without a combination of senolytics—dasatinib (D) (*50*) and quercetin (Q) (D+Q treatment)—bimonthly for 4 months. Relative to controls, D+Q-treated *Slc6a6*$^{-/-}$ mice had a lower abundance of SASP markers (fig. S5M). D+Q treatment also improved bone-, muscle-, anxiety-, and memory-related parameters in *Slc6a6*$^{-/-}$ mice (fig. S5, N to Q). Taurine-deficient mice had shorter lives than WT mice, and the median life span of mutant mice that received senolytic treatment until the end of life increased by ~21% (Fig. 3D). The finding that senolytic treatment did not rescue the shorter life span of taurine-deficient mice suggests that taurine also affects other factors besides senescence. We therefore assessed molecular and cellular features of other aging hallmarks in taurine-supplemented middle-aged mice and in taurine-deficient mice.

Taurine suppresses adverse consequences of telomerase deficiency

Replication-based telomere shortening triggers cellular senescence and affects aging (*51*). Taurine supplementation in mice or zebrafish or its deficiency in mice did not affect telomerase

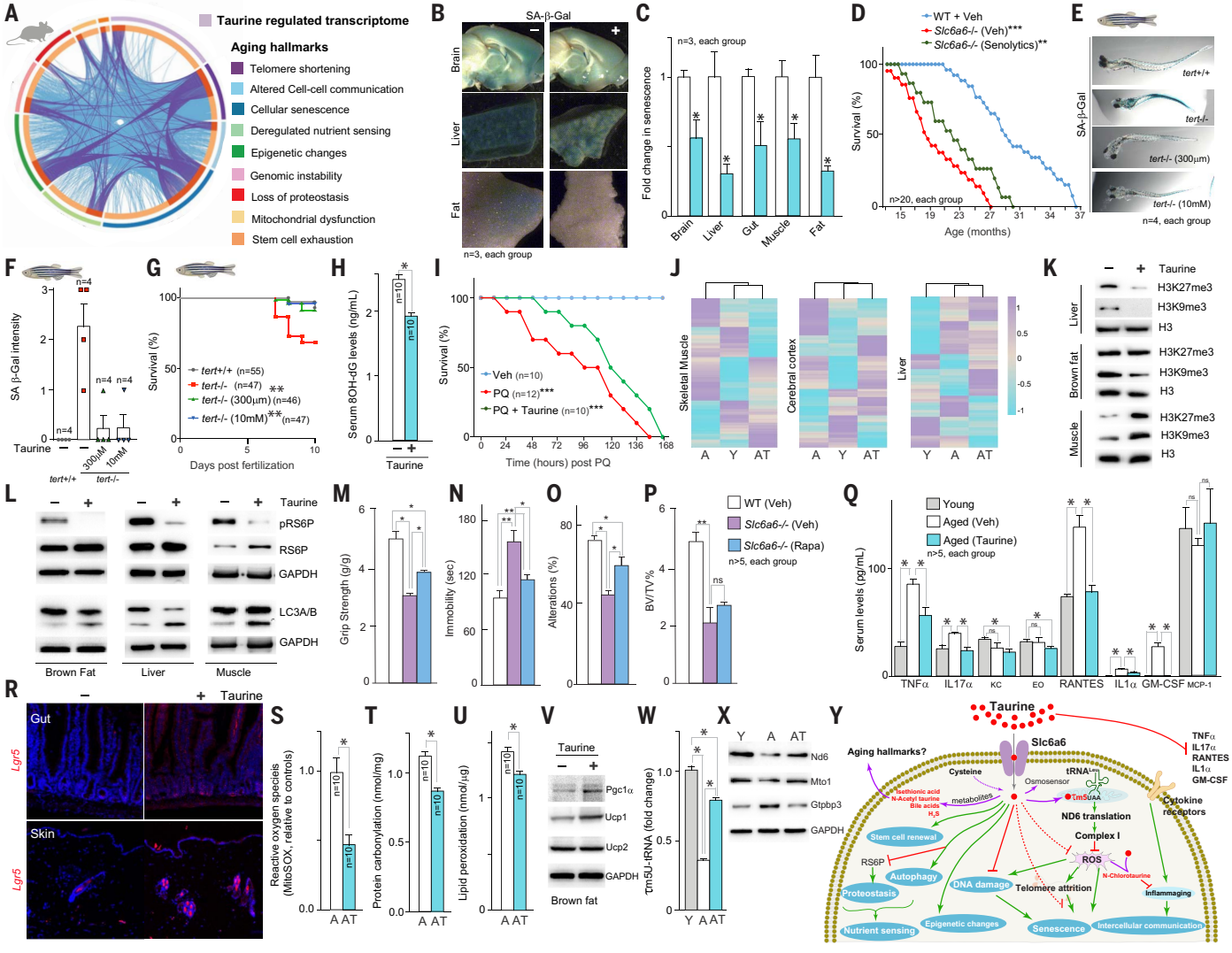


Fig. 3. Taurine regulation of healthy life span is associated with alterations in multiple aging hallmarks. (**A**) Circos plot representing a comparative analysis of a taurine-deficient transcriptome with the core gene signatures of nine aging hallmarks. (**B** and **C**) SA β-Gal staining (blue-stained cells) (B) and relative quantification of staining (C) in tissues collected from mice with or without taurine supplementation, as viewed with whole-mount imaging. (**D**) Life-span assay of congenitally taurine-deficient (*Slc6a6*$^{-/-}$) mice and littermate controls that received either vehicle or senolytics (D+Q treatment) biweekly until the end of life. (**E** to **G**) SA β-Gal staining photomicrographs (E), relative quantification of staining (F), and survival analysis (G) of telomerase-deficient [*tert*$^{-/-}$(G2)] zebrafish embryos with or without taurine supplementation (300 μm or 10 mM) beginning at 2 dpf. (**H**) Serum 8-OH-dG concentrations in vehicle-treated (−) or taurine-treated (+) mice. (**I**) Kaplan-Meier survival curves for mice after paraquat (PQ) treatment, with or without prior taurine supplementation (T1000 for 1 month). Veh, vehicle. (**J** and **K**) Comparative DNA methylation levels of 2045 age-related CpG sites in the muscle, cerebral cortex, and liver (J) and changes in histone H3K27me3, H3K9me3, and H3 levels in the liver, brown fat, and muscle (K) of 4-month-old WT (young, Y), 16-month-old vehicle-treated WT (aged, A), and 16-month-old taurine-treated WT (aged-taurine, AT) mice. (**L**) Changes in phosphoribosomal S6 protein (pRS6P) and LC3A/B levels in the brown fat, liver, and muscle of vehicle- or taurine-treated aged mice. GAPDH, glyceraldehyde phosphate dehydrogenase. (**M** to **P**) Changes in muscle function (grip-strength test) (M), anxiety (tail suspension test) (N), memory (Y maze test) (O), and bone mass [bone volume divided by total volume percentage (BV/TV%)] (P) in 6-month-old *Slc6a6*$^{-/-}$ mice and littermate controls that received either vehicle or rapamycin (once daily for 6 weeks). (**Q**) Serum levels of various cytokines in young mice, aged mice, and aged mice treated with taurine. EO, eotaxin; KC, keratinocyte cytokine. (**R** to **V**) In situ hybridization analysis of *Lgr5* expression in the gut and skin (R), levels of mitochondrial ROS (superoxide anion radicals, MitoSOX assay) in skeletal muscle mitochondria (S), protein carbonyl levels in the liver (T), lipid peroxidation levels in the liver (U), and Pgc1α, Ucp1, and Ucp2 levels in the brown fat (V) of aged mice treated without or with taurine. (**W** and **X**) Changes in τm5U tRNA modification (W) and Nd6, Mto1, and Gtpbp3 protein levels in the liver (X) of young mice, aged mice, and aged mice treated with taurine. In (W), $n \geq 6$ mice in each group. (**Y**) Schematic representation of the effect of taurine and taurine-derived biomolecules (in red) on classical hallmarks of aging. For (K), (L), (V), and (X), Western blots are representative of at least three independent biological replicates. Statistical analysis details are as follows: For (D), (G), and (I), the OASIS software (https://sbi.postech.ac.kr/oasis) was used to calculate p values using a log rank test (the Mantel-Cox method), and for other panels, statistical analysis was performed with Graph Pad Prism 7 using Student's t test or one-way or two-way ANOVA. All values are means ± SEM. ns indicates not significant. ***$p \leq 0.001$, **$p \leq 0.01$, and *$p \leq 0.05$ are versus WT or control.

gene expression (fig. S5, R and S). To investigate whether taurine affects telomerase deficiency–induced deterioration in organismal health, we used a zebrafish model of telomerase deficiency (*52*). *tert*$^{-/-}$(G2) fish show an increase in senescence, and ~40% of them die within 10 days postfertilization (dpf) (*52*). Supplementing the medium used for *tert*$^{-/-}$(G2) fish with taurine, starting at 2 dpf, suppressed senescence (Fig. 3, E and F). Moreover, at concentrations of 300 μM and 10 mM, taurine rescued lethality in *tert*$^{-/-}$(G2) zebrafish embryos (Fig. 3G).

Taurine suppresses DNA damage and improves the survival of mice after oxidative DNA damage

Aging is associated with genomic DNA lesions in multiple cell types (*53*). Taurine supplementation reduced serum 8-hydroxydeoxyguanosine (8-OH-dG) abundance, a measure of oxidative DNA damage (*54*), in aged mice (Fig. 3H). Conversely, DNA damage [measured as the abundance of phospho-γ-H2A histone family member X (H2Ax)] was increased in the muscle of taurine-deficient mice (fig. S5T). In a paraquat model of DNA damage–induced lethality, mice administered with paraquat without prior taurine supplementation died within 150 hours, but mice treated with taurine lived slightly longer (Fig. 3I). Thus, taurine supplementation suppressed DNA damage and improved the survival of mice after oxidative DNA damage.

Taurine affects epigenetic changes in the genome

Methylation at CpG sites and of histones changes with age and affects the state of chromatin, which affects DNA packaging and gene expression (*55*, *56*). We therefore analyzed changes in methylation of 2045 CpG sites and measured two histone modifications [histone 3 lysine 9 trimethylation (H3K9me3) and histone 3 lysine 27 trimethylation (H3K27me3)] in multiple tissues obtained from untreated or taurine-treated middle-aged mice and compared them with those in tissues from young mice. Clustering analysis showed that the CpG methylation pattern in the muscle and cerebral cortex of taurine-treated old mice was more similar to that in young mice than to that in untreated old mice (Fig. 3J). However, the pattern in liver from taurine-supplemented mice was more similar to that in old mice than to that in young mice (Fig. 3J). Conversely, muscles from taurine-deficient mice showed changes in the amount of CpG site methylation, and the DNA methylation pattern of muscles in 70-week-old taurine-deficient mice was similar to that in 206-week-old WT mice (fig. S5U). Taurine treatment decreased the abundance of H3K9me3 in brown fat and liver but increased it in skeletal muscle; H3K27me3 abundance was suppressed in the liver, increased in muscle, and unaffected in brown fat (Fig. 3K). The varied changes in DNA and histone methylation indicate that taurine may affect chromatin conformation, which could contribute to altered transcription during aging.

Taurine modulates nutrient sensing and proteostasis pathways

Aging cells have a reduced ability to sense nutrients and maintain proteostasis (*57*). We assessed changes in nutrient sensing by measuring the phosphorylation of ribosomal S6 protein (RS6P), a key regulator of ribosomal function, and proteostasis by measuring changes in abundance ratio of isoforms A and B of the light chain 3 (LC3A/B), an autophagy marker. Taurine supplementation decreased phosphorylation of RS6P in the liver, brown fat, and skeletal muscle (Fig. 3L). Phosphorylation of RS6P was increased in the muscle of taurine-deficient mice (fig. S5V). Taurine-supplemented mice had more autophagy (as judged by LC3A/B abundance) in the liver, brown fat, and skeletal muscle, whereas it was decreased in taurine-deficient mice (Fig. 3L and fig. S5V). To test whether an increase in phosphorylation of RS6P and a decrease in autophagy contribute to the compromised health span in taurine-deficient mice, we treated *Slc6a6*$^{-/-}$ mice with or without rapamycin [8 mg per kg body weight intraperitoneally once daily (*58*) for 6 weeks], which inhibits phosphorylation of RS6P and increases autophagy. Compared with control mice, rapamycin-treated taurine-deficient mice showed improved muscle-, anxiety-, and memory-related parameters but not increased bone mass (Fig. 3, M to P). Thus, the effects of taurine supplementation on nutrient sensing and proteostasis pathways contribute to its beneficial effects on several health parameters.

Taurine effects on inflammatory cytokines

Intercellular communication is compromised with age (*59*). One example is the accumulation of proinflammatory and other cytokines (*59*). Serum concentrations of tumor necrosis factor–α (TNFα), interleukin-17α (IL-17α), RANTES (regulated upon activation, normal T cell expressed and presumably secreted), IL-1α, and granulocyte-macrophage colony-stimulating factor (GM-CSF) were increased in middle-aged mice compared with young mice, but taurine-treated middle-aged mice had amounts of these cytokines that were similar to those in young control animals (Fig. 3Q). These results, together with the observation that the ratio of myeloid cells to lymphoid cells was significantly decreased in taurine-supplemented mice (Fig. 2K), indicates that sustained taurine concentrations help prevent the proinflammatory state that is observed during aging.

Positive effects of taurine on the health of stem cells or their renewal

Aging reduces the ability of tissues to regenerate after injury. This is linked to defects in tissue-specific stem cells (*60*). We analyzed changes in the number of stem cell populations in the gut epithelium and hair follicles obtained from untreated and taurine-treated middle-aged mice through staining for the gene encoding leucine-rich repeat–containing G protein–coupled receptor 5 (*Lgr5*), which is a wingless-related integration site (Wnt) target gene expressed in the stem or progenitor cells (*61*). The numbers of *Lgr5*$^{+}$ cells in these two tissues were increased by taurine supplementation (Fig. 3R). Conversely, the numbers of *Lgr5*$^{+}$ cells in the gut epithelium and hair follicles were decreased in taurine-deficient mice compared with control mice (fig. S5W). Thus, taurine supplementation may increase the regenerative capacity of some tissues by increasing the number of resident stem cells.

Taurine promotion of mitochondrial health

Compromised mitochondrial biogenesis and oxidative capacity leads to progressive accumulation of reactive oxygen species (ROS)–mediated damage that contributes to aging (*62*). ROS accumulation in mitochondria isolated from the muscle of taurine-treated middle-aged mice was decreased compared with that in the muscle of control mice (Fig. 3S), whereas it was increased in the muscle of taurine-deficient mice (fig. S6A). Measurement of lipid peroxidation and protein carbonylation, two indirect markers of ROS-induced molecular damage, in the liver showed a decrease (of ~22 and ~11%, respectively) in taurine-supplemented mice compared with control mice (Fig. 3, T and U). Assessment of the abundance of peroxisome proliferator–activated receptor–gamma coactivator 1 alpha (Pgc1α), a key regulator of mitochondrial biogenesis, and uncoupling protein 1 (Ucp1), which uncouples mitochondrial fuel oxidation and respiration from adenosine triphosphate (ATP) production (*63*), in brown fat showed increased amounts in taurine-treated middle-aged mice, and their abundance was decreased in taurine-deficient mice (Fig. 3V and fig. S6B). These results indicate that taurine promotion of mitochondrial homeostasis may contribute to its effect on health.

We next investigated how taurine affects cellular mechanisms during aging (*24*). One pool of cytosolic taurine is actively transported into mitochondria, where it is conjugated to the uridine residue at the wobble position of tRNA^{Leu}(UUA), forming 5-taurinomethyluridine-tRNA^{Leu}(UUA) (τm5U-tRNA) (*64*). τm5U modification is specific to mitochondrial tRNAs (*64*) and promotes the translation of NADH-ubiquinone oxidoreductase chain 6 protein (ND6), an electron transport chain complex I subunit (*64*). We therefore measured whether

τm5U tRNA modification changed during aging in mice. The τm5U content of tRNAs was reduced by >60% in aged liver compared with young liver; in taurine-supplemented mice, the τm5U content of tRNAs was reduced by only about 20% (Fig. 3W and fig. S6C). Consistent with the role of τm5U-tRNA^{Leu} in promoting the translation of ND6, amounts of this protein were decreased in aged mice compared with young mice and were increased by taurine supplementation (Fig. 3X and fig. S6D). Taurine supplementation, however, did not affect the translation of nuclear DNA–encoded mitochondrial oxidative phosphorylation (OXPHOS) proteins in aged mice (fig. S6E). We conducted experiments on worms to test whether regulation of organismal health by taurine requires complex I activity. Taurine increased the motility of control worms, which is indicative of better health status (*65*), but failed to do so in rotenone-treated worms (fig. S6F), suggesting that increasing mitochondrial complex I activity is a mechanism by which taurine promotes health. The aforementioned analyses of molecular and cellular features of aging hallmarks show that during aging, taurine supplementation may impart health benefits by affecting such features in various cells or tissues (Fig. 3Y).

Lower circulating taurine and its metabolites in humans are associated with multiple age-associated pathologies

To determine whether blood levels of taurine-pathway metabolites (taurine, hypotaurine, and *N*-acetyltaurine) are associated with health variables in humans, we performed an association analysis of circulating taurine metabolite levels with >50 clinical risk factors in 11,966 subjects of the EPIC-Norfolk study (fig. S7, A and B) (*66*). We found that higher blood taurine and hypotaurine levels were associated with lower body mass index (BMI) and waist-to-hip ratio as well as less abdominal obesity (Fig. 4A). Furthermore, higher levels of taurine metabolites were associated with a lower prevalence of type 2 diabetes and lower glucose levels (Fig. 4A). Also, higher taurine and hypotaurine levels were associated with lower levels of the inflammation marker C-reactive protein (CRP). For liver- and lipid-related traits such as aspartate aminotransferase (AST) and blood cholesterol, we found positive associations with taurine levels but negative associations with those of its precursor hypotaurine (Fig. 4A). Blood cell parameters like hemoglobin, platelets, and WBC count correlated positively with the three taurine metabolites (Fig. 4A). Association does not establish causation, but these results are consistent with taurine deficiency contributing to human aging.

A bout of exercise increases abundance of taurine and its metabolites

We next investigated whether blood levels of taurine-pathway metabolites respond to exercise, which improves many health- and aging-related variables (*67*, *68*). Specifically, we analyzed concentrations of taurine-pathway metabolites in serum before and after a graded exercise test in male athletes (sprinters, endurance runners, and natural bodybuilders) and sedentary individuals (fig. S7C). Taurine levels significantly increased (1.16-fold) in response to a graded cycle exercise test in all the investigated athlete groups ($p_{bodybuilding}$ = 0.046, $p_{endurance}$ = 0.0021, p_{sprint} = 0.0017) (Fig. 4B) and tended to be higher in the sedentary subjects, although the change was not significant ($p_{sedentary}$ = 0.067) (Fig. 4B). Levels of hypotaurine were significantly increased 1.36-fold in response to exercise in all subjects (Fig. 4C). Levels of *N*-acetyltaurine were significantly increased by 1.18- and 1.28-fold in endurance athletes (p = 0.027) and sprinters (p = 0.0016), respectively, and tended to be elevated in bodybuilders and sedentary subjects, although the change was not significant ($p_{bodybuilders}$ = 0.054, $p_{sedentary}$ = 0.067) (Fig. 4D). These results are consistent with the notion that an increase in taurine and taurine-related metabolites might mediate some of the health benefits of exercise.

Taurine supplementation improves health parameters in middle-aged nonhuman primates

To test whether taurine has health and anti-aging effects in nonhuman primates, we fed aged rhesus monkeys (15 ± 1.5 years old, equivalent to 45 to 50 years old in humans) control solution or taurine [250 mg per kg body weight (T250), equivalent to T1000 in mice] at 10:00 am once daily for 6 months and then measured the health variables (fig. S7D). Before the start of taurine supplementation, body weight and bone density were not significantly different in the two groups of aged monkeys (fig. S7, E and F). Three hours after oral feeding, serum taurine concentrations in taurine-fed monkeys were about twice (65.4 ± 10.1 ng/ml) that in controls (35.1 ± 7.3 ng/ml). Monkeys that received taurine gained 0.75 kg less body weight, and their fat percentage tended to be lower compared with that of controls (Fig. 4E). In-life dual-energy x-ray absorptiometry (DEXA) analysis after 6 months of taurine treatment showed that taurine increased bone density and content in the lumbar spine (L1 to L4) and legs, but not in the head, in taurine-treated monkeys compared with control monkeys (Fig. 4F and fig. S7, G and H). Serum markers of bone formation (osteocalcin) increased, whereas those of resorption [C-terminal telopeptide of type 1 collagen (Ctx)] decreased about 16 weeks after the start of treatment; these levels were maintained until the end of the dosing period (fig. S7, I and J). Taurine treatment reduced fasting blood glucose concentrations by 19% (Fig. 4G). Taurine also reduced the serum concentrations of liver damage markers AST and alanine transaminase (ALT) by ~36 and 20%, respectively (Fig. 4, H and I). Numbers of WBCs, monocytes, and granulocytes, which increase with age, were decreased by ~50% in taurine-treated monkeys compared with control monkeys (Fig. 4, J to L). Consistent with the beneficial effect of taurine on the mitochondrial health observed in worms and mice, indirect markers of ROS-induced molecular damage—DNA 8OH-dG, lipid peroxide, and protein carbonyl concentrations—were decreased by ~36, 11, and 20%, respectively, in the sera of taurine-supplemented monkeys (Fig. 4, M to O). Thus, taurine has beneficial effects on most tested health parameters (body weight, bone, glucose, liver, and immunophenotype) in nonhuman primates.

Discussion

Taurine abundance decreases in blood and tissues during aging. We found that a reversal of this decline through taurine supplementation increased markers of healthy life span in worms and mice as well as health span in monkeys, which identifies taurine deficiency as a driver of aging in these species. In mice, the effect of taurine supplementation on healthy life span was greater in females than in males, indicating that sex-specific pathways may mediate taurine action. The optimal dose of taurine to maximize its efficacy differed depending on the physiological functions tested, which was possibly due to a wide variation in the uptake rate, synthesis, and metabolism of taurine in different biological fluids and tissues (*24*, *69*–*76*).

Taurine appeared to affect all the established hallmarks of aging. Although we do not yet know the initial events that taurine elicits, we provide evidence for the suppressed taurinylation of mitochondrial tRNAs during aging in mitochondrial dysfunction, a prominent feature of aging. It is also possible that other taurine-derived biomolecules besides τm5U-tRNA may directly or indirectly affect mitochondrial homeostasis or other aging features. Indeed, taurine contributes to the production of several other biomolecules, depending on the cell type or types that affect, or can potentially affect, aging (*24*). These molecules include *N*-chlorotaurine (*77*), hydrogen sulfide (H_2S) (*78*), isethionic acid (*24*), *N*-acetyltaurine (*79*), and 5-taurinomethyl-2-thiouridine (τm5s2U)-tRNA^{Lys} (*24*). We propose that a combination of taurine and taurine-derived biomolecules may delay aging by affecting various aging hallmarks in distinct cells and tissues.

The effects of taurine intervention on aging and congenital taurine deficiency in a mouse model are largely consistent, except for body weight accrual and glucose homeostasis (Fig. 2 and fig. S5). The concentrations of taurine in the serum and tissues of congenitally taurine-deficient mice are more severely reduced than in the biological fluids and tissues of aged

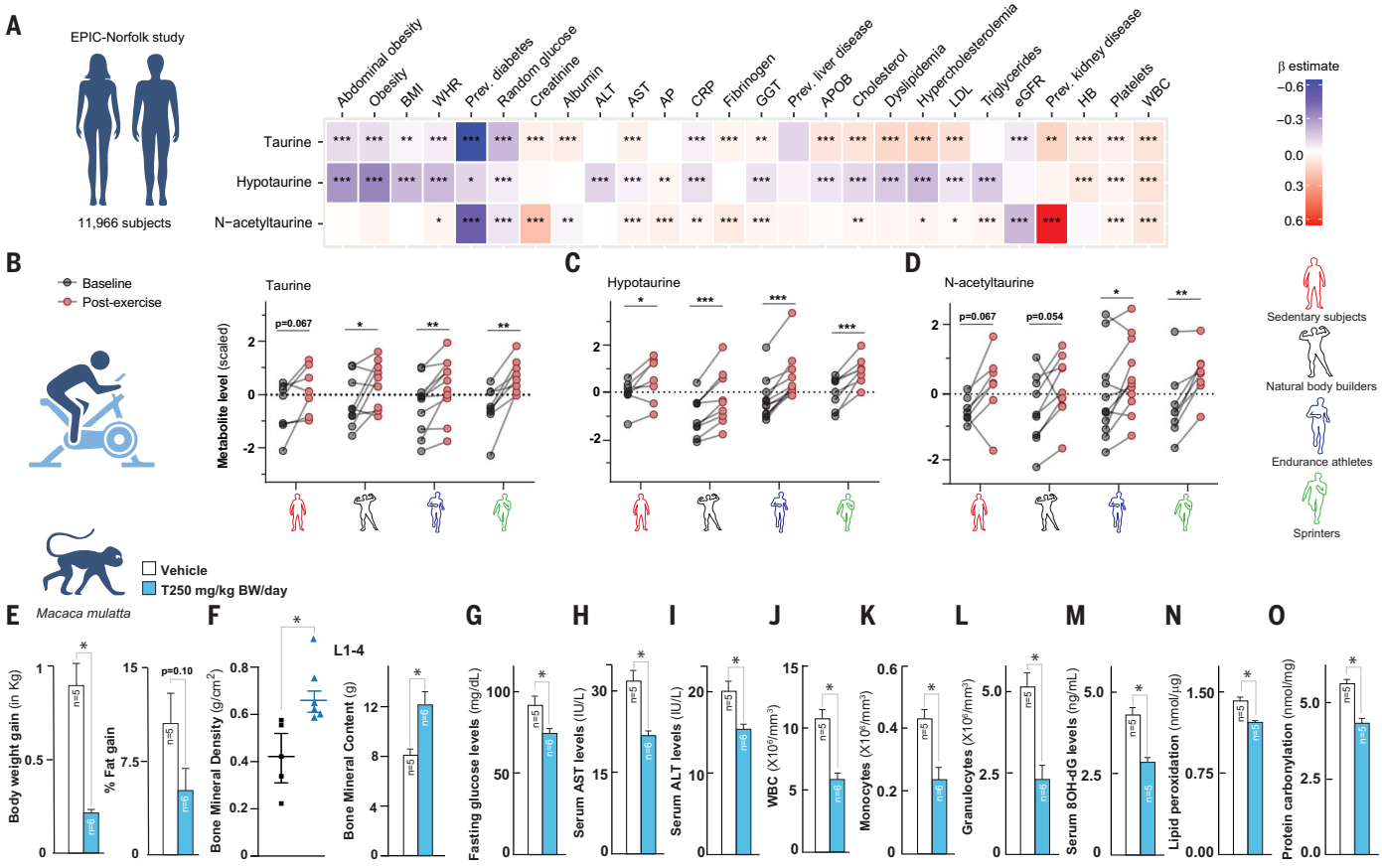


Fig. 4. Taurine pathway affects health span in primates. (**A**) Heatmap showing the results from linear regression models for assessing the associations between clinical risk factors and taurine-related metabolites (taurine, hypotaurine, and *N*-acetyltaurine) in blood from 11,966 subjects in the EPIC-Norfolk study. Effect size and direction of these associations are given by the β estimates resulting from these regression models. A negative β estimate (blue color) indicates an inverse association, where higher levels of a metabolite correlated with lower levels of a clinical parameter. A positive β estimate (red color) indicates a positive association, where higher levels of a metabolite correlated with higher levels of a clinical parameter. For example, as shown in blue, higher levels of taurine correlated with a lower prevalence of type 2 diabetes. Taurine-related metabolites were measured using an untargeted metabolomics approach (Metabolon HD4 platform). Data were extracted from the open-access web server located at https://omicscience.org/apps/mwasdisease/. AP, alkaline phosphatase; APOB, apolipoprotein B; eGFR, estimated glomerular filtration rate; GGT, γ-glutamyl transferase; HB, hemoglobin; LDL, low-density lipoprotein; WHR, waist-to-hip ratio. (**B** to **D**) Serum taurine (B), hypotaurine (C), and *N*-acetyltaurine (D) levels at fasted rest (baseline) and 5 min after a maximum graded exercise test (postexercise) in three groups of competitive athletes and healthy sedentary subjects. Metabolite levels are provided as *z*-scores, that is, relative to the mean of measured levels with mean = 0 and standard deviation = 1. (**E** to **O**) Body-weight gain in kilograms and percent fat gain (E); bone mineral density and content in the lumbar spine (L1 to L4) (bone) (F); fasting glucose levels (pancreas function) (G); serum AST and ALT levels (liver dysfunction markers) [(H) and (I)]; WBC, monocyte, and granulocyte numbers (immunophenotyping in blood) [(J) to (L)]; and serum 8-OH-dG, lipid peroxide, and protein carbonyl levels (indirect markers of ROS-induced molecular damages) [(M) to (O)] in 15-year-old monkeys orally fed once daily with vehicle (TO) or taurine (T250) for 6 months. Statistical analysis details are as follows: For (A), summary statistics, including standardized regression coefficients (β estimates) and nominal *p* values, on a relevant subset of 26 clinical traits and three taurine-related metabolites were extracted from a web server. Regression coefficients and nominal *p* values were plotted in a heatmap using R version 4.1.0. For the exercise cohort in [(B) to (D)], differences between baseline and postexercise metabolite levels were analyzed per subject group using a paired-sample *t* test. Batch corrections were done using R version 4.1.0; the graphs were prepared using GraphPad Prism. For [(E) to (O)], statistical analysis was performed with Graph Pad Prism 7 using Student's *t* test or one-way or two-way ANOVA. All values are means ± SEM. $p \le 0.001$***, $p \le 0.01$**, and $p \le 0.05$* are versus WT or control.

rodents and humans (*23*, *27*, *80*). However, in the liver, the concentrations of τm5U, a downstream conjugate of taurine, were similarly affected. Thus, during early life, taurine appears to be essential for homeostasis in several organ systems, and its deficiency during development may compromise these functions postnatally. Consistent with this hypothesis, organisms have a three- to fourfold higher taurine concentration in embryonic tissues than in adult tissues; moreover, taurine deficiency during development leads to growth retardation, blindness, and osteoporosis (*25*, *81*), and its supplementation during gestation increased bone mass postnatally (fig. S5X). This role of taurine in embryonic tissues that affects postnatal phenotypes would be consistent with the theory of the developmental origin of aging phenotypes (*82*, *83*). It is possible that developmental or postnatal changes in taurine metabolism might affect the rate of aging during late life, and adjusting this endogenous machinery might extend healthy life span.

In humans, lower levels of taurine-pathway metabolites were associated with multiple age-associated diseases, such as obesity, diabetes, and inflammation (Fig. 4A). In the FinnGen database (Freeze R5), polymorphisms in the taurine biosynthesis gene, *CSAD*, are associated with hypertension (fig. S7K), and *SLC6A6*

mutations cause retinal degeneration and cardiomyopathy (*26*, *84*). However, taurine supplementation in subjects with metabolic abnormalities does not affect BMI (*85*). Furthermore, our results, together with those of previous studies (*86*, *87*), show that taurine concentrations increase in healthy men after acute endurance exercise and after 24 weeks of exercise training in obese individuals. Although the mechanisms that increase blood taurine concentrations after exercise are unclear, these results suggest that some of the health benefits of exercise may be explained by an increase in blood taurine concentrations.

A limitation of our study is that we have not tested the effect of taurine in male monkeys, and our association studies in humans did not distinguish between sexes. Nevertheless, together with our supplementation studies in 15-year-old monkeys, the results presented in this work suggest that an increase in taurine concentrations or its actions may have the potential to suppress the decline in biological functions that occurs during human aging.

Reversal of taurine deficiency during aging may be a promising antiaging strategy. Given that taurine has no known toxic effects in humans (though rarely used in concentrations used here), can be administered orally, and affects all the major hallmarks of aging, human trials are warranted to examine whether taurine supplementation increases healthy life span in humans.

Methods summary

Life-span analysis

Mice

Life-span analysis was performed in middle-aged mice that were administered once-daily oral taurine supplementation with or without other interventions.

Yeast

RLS of yeast was assessed on nutrient-rich YPD plates or on a synthetic medium with or without taurine.

Worms

The life span of worms was assessed on agar plates supplemented with taurine or without.

Health-span analysis

The functions and health of various organs in middle-aged mice and monkeys were assessed after taurine supplementation and included the following: body weight; fat-pad weight; bone histology and μCT or DEXA measurements of bone; rotarod, wire-hang, and grip-strength tests of neuromuscular strength; glucose and insulin tolerance tests of glucose homeostasis; tail suspension, light-dark box, and Y maze tests of behavior; GI transit tests; energy expenditure tests; and blood counts of immune cells. Aging hallmarks were assessed in WT middle-aged mice supplemented with taurine, taurine-deficient mice, telomerase-deficient zebrafish, and worms. This analysis included assessments of senescence through SA β-Gal staining, SASP markers, irradiation, and senolytic intervention in taurine-deficient mice; DNA damage by using molecular markers and paraquat-induced lethality assays; telomere function by using telomerase expression in mice and zebrafishes and in telomerase-deficient zebrafishes; epigenetic changes based on CpG and histone methylations; nutrient sensing and proteostasis through phospho-RS6P measurements, autophagy marker analysis through LC3A/B abundance, and rapamycin intervention in taurine-deficient mice; and mitochondrial function through ROS measurements. In addition, electron transport chain assessments, Western blotting of OXPHOS proteins, and rotenone assays were performed in worms; stem cells were assessed using *Lgr5* in situ hybridization; and cytokine levels were measured in the blood. A human association analysis of taurine-pathway metabolites with health variables was performed in individuals from the EPIC-Norfolk study. Effect size and direction of these associations are given by the β estimates resulting from these regression models. A negative β estimate indicates an inverse association, where higher levels of a metabolite correlated with lower levels of a clinical parameter. A positive β estimate indicates a positive association, where higher levels of a metabolite correlated with higher levels of a clinical parameter. The effect of exercise on serum levels of taurine-pathway metabolites in humans was assessed before and after an endurance exercise test in athletes (sprinters, body builders, and marathon runners) and sedentary individuals. A detailed account of the methods and statistical analyses used in this study is provided in the supplementary materials.

REFERENCES AND NOTES

1. Department of Economic and Social Affairs of the United Nations, Population Division, "World population ageing 2019: Highlights" (ST/ESA/SER.A/430, United Nations, 2019); https://www.un.org/en/development/desa/population/publications/pdf/ageing/WorldPopulationAgeing2019-Highlights.pdf.
2. G. V. Mkrtchyan *et al*., ARDD 2020: From aging mechanisms to interventions. *Aging* **12**, 24484–24503 (2020). doi: 10.18632/aging.202454; pmid: 33378272
3. D. Gems, L. Partridge, Genetics of longevity in model organisms: Debates and paradigm shifts. *Annu. Rev. Physiol.* **75**, 621–644 (2013). doi: 10.1146/annurev-physiol-030212-183712; pmid: 23190075
4. J. Campisi *et al*., From discoveries in ageing research to therapeutics for healthy ageing. *Nature* **571**, 183–192 (2019). doi: 10.1038/s41586-019-1365-2; pmid: 31292558
5. K. Meyer, B. A. Yankner, Slowing down aging. *Cell Metab.* **26**, 592–593 (2017). doi: 10.1016/j.cmet.2017.09.012; pmid: 28978424
6. H. Pan, T. Finkel, Key proteins and pathways that regulate lifespan. *J. Biol. Chem.* **292**, 6452–6460 (2017). doi: 10.1074/jbc.R116.771915; pmid: 28264931
7. M. C. Haigis, B. A. Yankner, The aging stress response. *Mol. Cell* **40**, 333–344 (2010). doi: 10.1016/j.molcel.2010.10.002; pmid: 20965426
8. T. A. Rando, H. Y. Chang, Aging, rejuvenation, and epigenetic reprogramming: Resetting the aging clock. *Cell* **148**, 46–57 (2012). doi: 10.1016/j.cell.2012.01.003; pmid: 22265401
9. E. H. Blackburn, C. W. Greider, J. W. Szostak, Telomeres and telomerase: The path from maize, Tetrahymena and yeast to human cancer and aging. *Nat. Med.* **12**, 1133–1138 (2006). doi: 10.1038/nm1006-1133; pmid: 17024208
10. D. W. Lamming, L. Ye, D. M. Sabatini, J. A. Baur, Rapalogs and mTOR inhibitors as anti-aging therapeutics. *J. Clin. Invest.* **123**, 980–989 (2013). doi: 10.1172/JCI64099; pmid: 23454761
11. W. A. Cabral *et al*., Genetic reduction of mTOR extends lifespan in a mouse model of Hutchinson-Gilford progeria syndrome. *Aging Cell* **20**, e13457 (2021). doi: 10.1111/acel.13457; pmid: 34453483
12. L. J. Niedernhofer, P. D. Robbins, Senotherapeutics for healthy ageing. *Nat. Rev. Drug Discov.* **17**, 377 (2018). doi: 10.1038/nrd.2018.44; pmid: 29651106
13. C. López-Otín, M. A. Blasco, L. Partridge, M. Serrano, G. Kroemer, The hallmarks of aging. *Cell* **153**, 1194–1217 (2013). doi: 10.1016/j.cell.2013.05.039; pmid: 23746838
14. T. B. Kirkwood, Understanding the odd science of aging. *Cell* **120**, 437–447 (2005). doi: 10.1016/j.cell.2005.01.027; pmid: 15734677
15. S. I. Imai, L. Guarente, It takes two to tango: NAD^+ and sirtuins in aging/longevity control. *NPJ Aging Mech. Dis.* **2**, 16017 (2016). doi: 10.1038/npjamd.2016.17; pmid: 28721271
16. Y. Zhang *et al*., The starvation hormone, fibroblast growth factor-21, extends lifespan in mice. *eLife* **1**, e00065 (2012). doi: 10.7554/eLife.00065; pmid: 23066506
17. A. Asadi Shahmirzadi *et al*., Alpha-ketoglutarate, an endogenous metabolite, extends lifespan and compresses morbidity in aging mice. *Cell Metab.* **32**, 447–456.e6 (2020). doi: 10.1016/j.cmet.2020.08.004; pmid: 32877690
18. H. Ripps, W. Shen, Review: taurine: a "very essential" amino acid. *Mol. Vis.* **18**, 2673–2686 (2012). pmid: 23170060
19. L. L. Spriet, J. Whitfield, Taurine and skeletal muscle function. *Curr. Opin. Clin. Nutr. Metab. Care* **18**, 96–101 (2015). doi: 10.1097/MCO.0000000000000135; pmid: 25415270
20. I. H. Lambert, D. M. Kristensen, J. B. Holm, O. H. Mortensen, Physiological role of taurine—From organism to organelle. *Acta Physiol.* **213**, 191–212 (2015). doi: 10.1111/apha.12365; pmid: 25142161
21. A. Hébert *et al*., New insights into sulfur metabolism in yeasts as revealed by studies of *Yarrowia lipolytica*. *Appl. Environ. Microbiol.* **79**, 1200–1211 (2013). doi: 10.1128/AEM.03259-12; pmid: 23220962
22. F. G. Tiedemann, Einige neue Bestandtheile der Galle des Ochsen. *Ann. Physik. Chem* **9**, 326–337 (1827).
23. U. Warskulat *et al*., Phenotype of the taurine transporter knockout mouse. *Methods Enzymol.* **428**, 439–458 (2007). doi: 10.1016/S0076-6879(07)28025-5; pmid: 17875433
24. J. G. Jacobsen, L. H. Smith, Biochemistry and physiology of taurine and taurine derivatives. *Physiol. Rev.* **48**, 424–511 (1968). doi: 10.1152/physrev.1968.48.2.424; pmid: 4297098
25. K. C. Hayes, R. E. Carey, S. Y. Schmidt, Retinal degeneration associated with taurine deficiency in the cat. *Science* **188**, 949–951 (1975). doi: 10.1126/science.1138364; pmid: 1138364
26. M. N. Preising *et al*., Biallelic mutation of human *SLC6A6* encoding the taurine transporter TAUT is linked to early retinal degeneration. *FASEB J.* **33**, 11507–11527 (2019). doi: 10.1096/fj.201900914RR; pmid: 31345061
27. B. Eppler, R. Dawson Jr., Dietary taurine manipulations in aged male Fischer 344 rat tissue: Taurine concentration, taurine biosynthesis, and oxidative markers. *Biochem. Pharmacol.* **62**, 29–39 (2001). doi: 10.1016/S0006-2952(01)00647-5; pmid: 11377394
28. H. J. Stuerenburg, B. Stangneth, B. G. Schoser, Age related profiles of free amino acids in human skeletal muscle. *Neuroendocrinol. Lett.* **27**, 133–136 (2006). pmid: 16648814
29. L. M. Suárez, M. D. Muñoz, R. Martín Del Río, J. M. Solís, Taurine content in different brain structures during ageing: Effect on hippocampal synaptic plasticity. *Amino Acids* **48**, 1199–1208 (2016). doi: 10.1007/s00726-015-2155-2; pmid: 26803657
30. T. Yoshimura *et al*., Age-related decline in the taurine content of the skin in rodents. *Amino Acids* **53**, 429–434 (2021). doi: 10.1007/s00726-021-02956-2; pmid: 33608821
31. E. M. Carneiro *et al*., Taurine supplementation modulates glucose homeostasis and islet function. *J. Nutr. Biochem.* **20**, 503–511 (2009). doi: 10.1016/j.jnutbio.2008.05.008; pmid: 18708284
32. K. Fukuda, Y. Nishi, T. Usui, Free amino acid concentrations in plasma, erythrocytes, granulocytes, and lymphocytes in

umbilical cord blood, children, and adults. *J. Pediatr. Gastroenterol. Nutr.* **3**, 432–439 (1984). doi: 10.1097/00005176-198406000-00022; pmid: 6737189
33. M. Jeevanandam, D. H. Young, L. Ramias, W. R. Schiller, Effect of major trauma on plasma free amino acid concentrations in geriatric patients. *Am. J. Clin. Nutr.* **51**, 1040–1045 (1990). doi: 10.1093/ajcn/51.6.1040; pmid: 2349917
34. B. N. Ames, Prolonging healthy aging: Longevity vitamins and proteins. *Proc. Natl. Acad. Sci. U.S.A.* **115**, 10836–10844 (2018). doi: 10.1073/pnas.1809045115; pmid: 30322941
35. T. Ito *et al*., Tissue depletion of taurine accelerates skeletal muscle senescence and leads to early death in mice. *PLOS ONE* **9**, e107409 (2014). doi: 10.1371/journal.pone.0107409; pmid: 25229346
36. L. S. Yilmaz *et al*., Modeling tissue-relevant Caenorhabditis elegans metabolism at network, pathway, reaction, and metabolite levels. *Mol. Syst. Biol.* **16**, e9649 (2020). doi: 10.15252/msb.20209649; pmid: 33022146
37. Q. L. Wan *et al*., Metabolomic signature associated with reproduction-regulated aging in *Caenorhabditis elegans*. *Aging* **9**, 447–474 (2017). doi: 10.18632/aging.101170; pmid: 28177875
38. M. A. McCormick *et al*., A comprehensive analysis of replicative lifespan in 4,698 single-gene deletion strains uncovers conserved mechanisms of aging. *Cell Metab.* **22**, 895–906 (2015). doi: 10.1016/j.cmet.2015.09.008; pmid: 26456335
39. S. T. Coleman, T. K. Fang, S. A. Rovinsky, F. J. Turano, W. S. Moye-Rowley, Expression of a glutamate decarboxylase homologue is required for normal oxidative stress tolerance in *Saccharomyces cerevisiae*. *J. Biol. Chem.* **276**, 244–250 (2001). doi: 10.1074/jbc.M007103200; pmid: 11031268
40. S. J. Olshansky, From lifespan to healthspan. *JAMA* **320**, 1323–1324 (2018). doi: 10.1001/jama.2018.12621; pmid: 30242384
41. H. Shoji, K. Takao, S. Hattori, T. Miyakawa, Age-related changes in behavior in C57BL/6J mice from young adulthood to middle age. *Mol. Brain* **9**, 11 (2016). doi: 10.1186/s13041-016-0191-9; pmid: 26822304
42. L. Steru, R. Chermat, B. Thierry, P. Simon, The tail suspension test: A new method for screening antidepressants in mice. *Psychopharmacology* **85**, 367–370 (1985). doi: 10.1007/BF00428203; pmid: 3923523
43. M. Bourin, M. Hascoët, The mouse light/dark box test. *Eur. J. Pharmacol.* **463**, 55–65 (2003). doi: 10.1016/S0014-2999(03)01274-3; pmid: 12600702
44. E. Pavlopoulos *et al*., Molecular mechanism for age-related memory loss: The histone-binding protein RbAp48. *Sci. Transl. Med.* **5**, 200ra115 (2013). doi: 10.1126/scitranslmed.3006373; pmid: 23986399
45. N. Dey *et al*., Regulators of gut motility revealed by a gnotobiotic model of diet-microbiome interactions related to travel. *Cell* **163**, 95–107 (2015). doi: 10.1016/j.cell.2015.08.059; pmid: 26406373
46. J. M. Yano *et al*., Indigenous bacteria from the gut microbiota regulate host serotonin biosynthesis. *Cell* **161**, 264–276 (2015). doi: 10.1016/j.cell.2015.02.047; pmid: 25860609
47. R. H. Cho, H. B. Sieburg, C. E. Muller-Sieburg, A new mechanism for the aging of hematopoietic stem cells: Aging changes the clonal composition of the stem cell compartment but not individual stem cells. *Blood* **111**, 5553–5561 (2008). doi: 10.1182/blood-2007-11-123547; pmid: 18413859
48. S. Mangiola, R. Molania, R. Dong, M. A. Doyle, A. T. Papenfuss, tidybulk: An R tidy framework for modular transcriptomic data analysis. *Genome Biol.* **22**, 42 (2021). doi: 10.1186/s13059-020-02233-7; pmid: 33482892
49. S. J. Chinta *et al*., Cellular senescence is induced by the environmental neurotoxin paraquat and contributes to neuropathology linked to Parkinson's disease. *Cell Rep.* **22**, 930–940 (2018). doi: 10.1016/j.celrep.2017.12.092; pmid: 29386135
50. J. S. Yi *et al*., Low-dose dasatinib rescues cardiac function in Noonan syndrome. *JCI Insight* **1**, e90220 (2016). doi: 10.1172/jci.insight.90220; pmid: 27942593
51. M. J. McEachern, A. Krauskopf, E. H. Blackburn, Telomeres and their control. *Annu. Rev. Genet.* **34**, 331–358 (2000). doi: 10.1146/annurev.genet.34.1.331; pmid: 11092831
52. C. M. Henriques, M. C. Carneiro, I. M. Tenente, A. Jacinto, M. G. Ferreira, Telomerase is required for zebrafish lifespan. *PLOS Genet.* **9**, e1003214 (2013). doi: 10.1371/journal.pgen.1003214; pmid: 23349637
53. A. Y. Maslov *et al*., DNA damage in normally and prematurely aged mice. *Aging Cell* **12**, 467–477 (2013). doi: 10.1111/acel.12071; pmid: 23496256
54. M. L. Hamilton *et al*., Does oxidative damage to DNA increase with age? *Proc. Natl. Acad. Sci. U.S.A.* **98**, 10469–10474 (2001). doi: 10.1073/pnas.171202698; pmid: 11517304
55. R. E. Marioni *et al*., DNA methylation age of blood predicts all-cause mortality in later life. *Genome Biol.* **16**, 25 (2015). doi: 10.1186/s13059-015-0584-6; pmid: 25633388
56. E. M. Michalak, M. L. Burr, A. J. Bannister, M. A. Dawson, The roles of DNA, RNA and histone methylation in ageing and cancer. *Nat. Rev. Mol. Cell Biol.* **20**, 573–589 (2019). doi: 10.1038/s41580-019-0143-1; pmid: 31270442
57. L. Bettedi, L. C. Foukas, Growth factor, energy and nutrient sensing signalling pathways in metabolic ageing. *Biogerontology* **18**, 913–929 (2017). doi: 10.1007/s10522-017-9724-6; pmid: 28795262
58. A. Bitto *et al*., Transient rapamycin treatment can increase lifespan and healthspan in middle-aged mice. *eLife* **5**, e16351 (2016). doi: 10.7554/eLife.16351; pmid: 27549339
59. L. Ferrucci, E. Fabbri, Inflammageing: Chronic inflammation in ageing, cardiovascular disease, and frailty. *Nat. Rev. Cardiol.* **15**, 505–522 (2018). doi: 10.1038/s41569-018-0064-2; pmid: 30065258
60. J. Oh, Y. D. Lee, A. J. Wagers, Stem cell aging: Mechanisms, regulators and therapeutic opportunities. *Nat. Med.* **20**, 870–880 (2014). doi: 10.1038/nm.3651; pmid: 25100532
61. N. Barker *et al*., Identification of stem cells in small intestine and colon by marker gene *Lgr5*. *Nature* **449**, 1003–1007 (2007). doi: 10.1038/nature06196; pmid: 17934449
62. T. E. S. Kauppila, J. H. K. Kauppila, N. G. Larsson, Mammalian mitochondria and aging: An update. *Cell Metab.* **25**, 57–71 (2017). doi: 10.1016/j.cmet.2016.09.017; pmid: 28094012
63. J. Lin *et al*., Defects in adaptive energy metabolism with CNS-linked hyperactivity in *PGC-1α* null mice. *Cell* **119**, 121–135 (2004). doi: 10.1016/j.cell.2004.09.013; pmid: 15454086
64. T. Suzuki, T. Suzuki, T. Wada, K. Saigo, K. Watanabe, Taurine as a constituent of mitochondrial tRNAs: New insights into the functions of taurine and human mitochondrial diseases. *EMBO J.* **21**, 6581–6589 (2002). doi: 10.1093/emboj/cdf656; pmid: 12456664
65. J. T. Pierce-Shimomura *et al*., Genetic analysis of crawling and swimming locomotory patterns in *C. elegans*. *Proc. Natl. Acad. Sci. U.S.A.* **105**, 20982–20987 (2008). doi: 10.1073/pnas.0810359105; pmid: 19074276
66. M. Pietzner *et al*., Plasma metabolites to profile pathways in noncommunicable disease multimorbidity. *Nat. Med.* **27**, 471–479 (2021). doi: 10.1038/s41591-021-01266-0; pmid: 33707775
67. D. E. Warburton, C. W. Nicol, S. S. Bredin, Prescribing exercise as preventive therapy. *CMAJ* **174**, 961–974 (2006). doi: 10.1503/cmaj.1040750; pmid: 16567757
68. B. K. Pedersen, B. Saltin, Exercise as medicine—Evidence for prescribing exercise as therapy in 26 different chronic diseases. *Scand. J. Med. Sci. Sports* **25**, 1–72 (2015). doi: 10.1111/sms.12581; pmid: 26606383
69. J. Bergström, P. Fürst, L. O. Norée, E. Vinnars, Intracellular free amino acid concentration in human muscle tissue. *J. Appl. Physiol.* **36**, 693–697 (1974). doi: 10.1152/jappl.1974.36.6.693; pmid: 4829908
70. C. E. Wright, H. H. Tallan, Y. Y. Lin, G. E. Gaull, Taurine: Biological update. *Annu. Rev. Biochem.* **55**, 427–453 (1986). doi: 10.1146/annurev.bi.55.070186.002235; pmid: 3527049
71. I. H. Lambert, Regulation of the cellular content of the organic osmolyte taurine in mammalian cells. *Neurochem. Res.* **29**, 27–63 (2004). doi: 10.1023/B:NERE.0000010433.08577.96; pmid: 14992263
72. I. Holopainen, P. Kontro, Taurine and hypotaurine transport by a single system in cultured neuroblastoma cells. *Acta Physiol. Scand.* **122**, 381–386 (1984). doi: 10.1111/j.1748-1716.1984.tb07522.x; pmid: 6516887
73. K. Takahashi *et al*., Taurine transporter in primary cultured neonatal rat heart cells: A comparison between cardiac myocytes and nonmyocytes. *Biochem. Pharmacol.* **65**, 1181–1187 (2003). doi: 10.1016/S0006-2952(03)00003-0; pmid: 12663053
74. S. S. Oja, I. Lehtinen, P. Lähdesmäki, Taurine transport rates between plasma and tissues in adult and 7-day-old mice. *Q. J. Exp. Physiol. Cogn. Med. Sci.* **61**, 133–143 (1976). doi: 10.1113/expphysiol.1976.sp002344; pmid: 1047457
75. G. Lee, H. Lee, J. Hong, S. H. Lee, B. H. Jung, Quantitative profiling of bile acids in rat bile using ultrahigh-performance liquid chromatography-orbitrap mass spectrometry: Alteration of the bile acid composition with aging. *J. Chromatogr. B Analyt. Technol. Biomed. Life Sci.* **1031**, 37–49 (2016). doi: 10.1016/j.jchromb.2016.07.017; pmid: 27450898
76. R. Calvani *et al*., Fecal and urinary NMR-based metabolomics unveil an aging signature in mice. *Exp. Gerontol.* **49**, 5–11 (2014). doi: 10.1016/j.exger.2013.10.010; pmid: 24184118
77. M. Barua, Y. Liu, M. R. Quinn, Taurine chloramine inhibits inducible nitric oxide synthase and TNF-alpha gene expression in activated alveolar macrophages: Decreased NF-κB activation and IκB kinase activity. *J. Immunol.* **167**, 2275–2281 (2001). doi: 10.4049/jimmunol.167.4.2275; pmid: 11490015
78. J. J. DiNicolantonio, J. H. OKeefe, M. F. McCarty, Boosting endogenous production of vasoprotective hydrogen sulfide via supplementation with taurine and *N*-acetylcysteine: A novel way to promote cardiovascular health. *Open Heart* **4**, e000600 (2017). doi: 10.1136/openhrt-2017-000600; pmid: 28674632
79. X. Shi, D. Yao, C. Chen, Identification of *N*-acetyltaurine as a novel metabolite of ethanol through metabolomics-guided biochemical analysis. *J. Biol. Chem.* **287**, 6336–6349 (2012). doi: 10.1074/jbc.M111.312199; pmid: 22228769
80. T. Ito *et al*., Cardiac and skeletal muscle abnormality in taurine transporter-knockout mice. *J. Biomed. Sci.* **17**, S20 (2010). doi: 10.1186/1423-0127-17-S1-S20; pmid: 20804595
81. P. Roman-Garcia *et al*., Vitamin B_{12}-dependent taurine synthesis regulates growth and bone mass. *J. Clin. Invest.* **124**, 2988–3002 (2014). doi: 10.1172/JCI72606; pmid: 24911144
82. J. P. de Magalhães, G. M. Church, Genomes optimize reproduction: Aging as a consequence of the developmental program. *Physiology* **20**, 252–259 (2005). doi: 10.1152/physiol.00010.2005; pmid: 16024513
83. A. V. Shindyapina *et al*., Rapamycin treatment during development extends lifespan and healthspan. bioRxiv 2022.2002.2018.481092 [Preprint] (2022); doi: 10.1101/2022.02.18.481092
84. M. Ansar *et al*., Taurine treatment of retinal degeneration and cardiomyopathy in a consanguineous family with SLC6A6 taurine transporter deficiency. *Hum. Mol. Genet.* **29**, 618–623 (2020). doi: 10.1093/hmg/ddz303; pmid: 31903486
85. L. Guan, P. Miao, The effects of taurine supplementation on obesity, blood pressure and lipid profile: A meta-analysis of randomized controlled trials. *Eur. J. Pharmacol.* **885**, 173533 (2020). doi: 10.1016/j.ejphar.2020.173533; pmid: 32871172
86. A. M. Brennan *et al*., Plasma metabolite profiles in response to chronic exercise. *Med. Sci. Sports Exerc.* **50**, 1480–1486 (2018). doi: 10.1249/MSS.0000000000001594; pmid: 29509640
87. C. Cuisinier *et al*., Role of taurine in osmoregulation during endurance exercise. *Eur. J. Appl. Physiol.* **87**, 489–495 (2002). doi: 10.1007/s00421-002-0679-0; pmid: 12355187
88. S. Mangiola, P. Singh, K. Gollapalli, V.K. Yadav, Transcriptome changes in taurine deficient cells. *Zenodo* (2023); https://doi.org/10.5281/zenodo.770045.

ACKNOWLEDGMENTS

We thank D. Renn for histology, H. Liu for genotyping, S. Surender for monkey experiments, and G. Karsenty and V. Mahajan for facilities. V.K.Y. dedicates this study to the memory of his mother, Bhagwanti Devi, for showing the path of perseverance. **Funding:** This work was funded by a Nathan Shock Center of Excellence in the Basic Biology of Aging Project Grant (V.K.Y.); National Institutes of Health (NIH) R01HD107574 (V.K.Y.); Wellcome 098051 (V.K.Y.); Deutsche Forschungsgemeinschaft (DFG) 450149205-TRR333/1 (P.B., H.W.); NIH P30AG013280 (M.K.); NIH T32AG066574 (M.G.K.); Institut National Du Cancer (INCa) PLBIO21-228 (M.G.F.); Science and Engineering Research Board (SERB) STR/2019/00064 (A.M.); Department of Biotechnology (DBT) BT/PR40325/BTIS/137/1/2020 (B.K.B.); a Longevity Impetus Grant (A.K.); Academy of Finland Center of Excellence in Complex Disease Genetics grant nos. 312074, 336824, and 352793 (A.P.); The Sigrid Juselius Foundation (A.P.); a Larry L. Hillblom Foundation Fellowship (M.C.); Victorian Cancer Agency (VCA) Fellowship nos. ECRF21036 (S.M.) and MCRF21002 (B.P.); and a DBT Ramalingaswamy Fellowship (V.K.Y.). **Author contributions:** Conceptualization: V.K.Y.; Investigation: P.S., K.G., S.M., D.S., M.A.Y., M.C., B.L.B., A.N., S.L.S., A.Ri., E.M.V., A.F., T.N., A.J., J.D., J.Z.W., C.Q.N., M.M., M.G.K., K.S., S.J.C., S.R., S.K., A.Ra., P.B., M.S., F.I., G.d.L., A.G., R.S., C.K., A.S.C., A.S., N.C., B.K.B., P.N., V.V., A.M.A., V.K.Y.; Analysis and interpretation: D.S., P.S., M.C., K.G., S.M., M.A.Y., B.L.B., A.N., S.L.S., A.Ri., E.M.V., A.F., T.N., A.J., J.D., J.Z.W., C.Q.N., M.M., M.G.K., K.S., S.J.C., S.R., A.Ra., P.B., M.S., F.I., G.d.L., A.G., R.S., C.K., A.S.C., A.S., N.C., B.K.B., S.G., P.N., A.M., N.S., V.V., A.P., B.K.K., C.S., K.L.T., M.P., A.T.P., A.K., M.G.F., J.K.A., G.J.L., A.M.A., G.K., M.K., H.W., B.P., V.K.Y.; Funding acquisition: V.K.Y.; Project administration: V.K.Y., H.W., B.P., M.K., G.K.; Supervision: V.K.Y., H.W., G.K., B.P., M.K., A.M., B.K.B., S.G., M.G.F., M.C.; Writing – original draft: V.K.Y.;

Writing – review and editing: V.K.Y., H.W., M.A.Y., B.P., G.K., M.K., D.S., A.M., P.S., M.C., K.G., S.M. **Competing interests:** Columbia University has filed provisional patent applications on which V.K.Y. is listed as an inventor. The remaining authors declare no competing interests. **Data and materials availability:** All data are available in the main text or the supplementary materials. The codes used for data analysis are stored publicly at github main_taurine.R at https://github.com/stemangiola/singh_et_al_taurine_bone/blob/master/main_taurine.R. Sequencing scaled counts have been deposited at Zenodo (*88*).

License information: Copyright © 2023 the authors, some rights reserved; exclusive licensee American Association for the Advancement of Science. No claim to original US government works. https://www.sciencemag.org/about/science-licenses-journal-article-reuse

SUPPLEMENTARY MATERIALS

science.org/doi/10.1126/science.abn9257
Materials and Methods
Figs. S1 to S7
Table S1
References (*89*–*130*)
MDAR Reproducibility Checklist

View/request a protocol for this paper from *Bio-protocol*.

Submitted 1 January 2022; resubmitted 20 September 2022
Accepted 14 April 2023
10.1126/science.abn9257

RESEARCH ARTICLE SUMMARY

CANCER IMMUNOTHERAPY

A microbiota-modulated checkpoint directs immunosuppressive intestinal T cells into cancers

Marine Fidelle *et al.*

INTRODUCTION: Resistance of cancers to immune checkpoint inhibitors (ICIs) can result from antibiotic (ABX) treatment, likely as a result of a deviated gut microbiota. ABX compromise clinical outcome when administered before, rather than during, ICI administration, suggesting that bacterial recolonization following ABX discontinuation may be deleterious. Gut commensals induce the differentiation of an immunosuppressive subset of FoxP3$^+$ retinoic acid receptor–related orphan receptor-γt (RORγt$^+$) regulatory ($T_{reg}17$) cells. Lymphocytes primed in the mesenteric lymph nodes (mLNs) or homing to the intestinal lamina propria express the α4β7 integrin interacting with its counter-receptor, mucosal addressin cell adhesion molecule-1 (MAdCAM-1), which is expressed in high endothelial venules (HEVs).

RATIONALE: We hypothesized that disruption of the MAdCAM-1–α4β7 interaction that retains $T_{reg}17$ cells might cause their migration from the gut to tumors and thereby compromise the anticancer effects of ICIs. We used two complementary methods to visualize the exodus of intestinal T cells to subcutaneous tumors and tumor-draining lymph nodes (tdLNs): (i) Kaede mice expressing a fluorescent protein that is photoconverted upon ultraviolet light illumination of the ileum and (ii) the injection of carboxyfluorescein succinimidyl ester into mLNs. Moreover, we used transgene-enforced *Madcam1* expression in the liver to locally intercept $T_{reg}17$ cells during their migration.

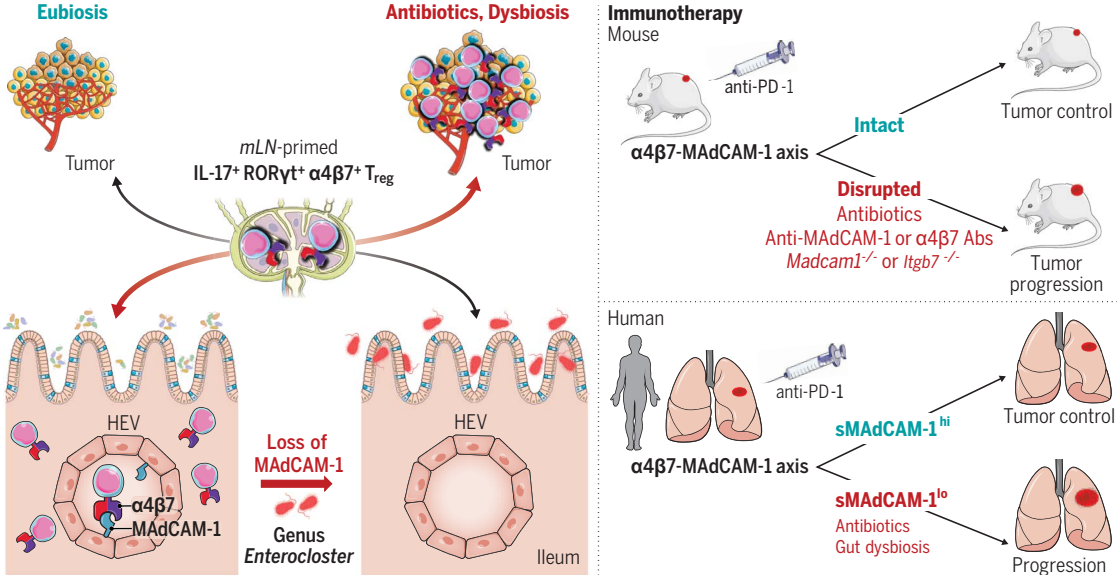
RESULTS: Several classes of ABX down-regulated *Madcam1* expression in ileal venules, Peyer's patches and mLNs, coinciding with the ileal exodus of α4β7$^+$ T helper (T_H17) and $T_{reg}17$ cells toward extraintestinal tumors and tdLNs. This ABX-induced reduction in MAdCAM-1 could be explained by the recolonization of the gut by the genus *Enterocloster* (encompassing the *E. clostridioformis* species), because its oral administration was sufficient to down-regulate MAdCAM-1 expression through its effects on bile acid metabolism. Genetic or antibody-mediated neutralization of MAdCAM-1 or α4β7 integrin phenocopied the immunosuppressive effects of ABX, promoting resistance to ICIs targeting programmed cell death protein 1 (PD-1) and inducing a surge in gut-derived α4 $T_{reg}17$ cells in tdLNs and tumors. Restoration of MAdCAM-1 on ileal HEV by fecal microbial transplantation or blockade of IL-17A reversed the inhibitory effects of ABX. Ectopic expression of MAdCAM-1 in the liver caused the local retention of enterotropic α4β7$^+$ $T_{reg}17$ cells, reducing their accumulation in tumor beds and improving immunotherapy outcomes in mice. Finally, low-serum-soluble MAdCAM-1 was identified as a proxy of intestinal dysbiosis and a robust predictor of shorter overall and progression-free survival of renal, bladder, and lung cancer patients under immunotherapy with antibodies targeting PD-1 or PD-L1. In non-small-cell lung cancer patients, the prognostic value of soluble MAdCAM-1 was independent of PD-L1 expression.

CONCLUSION: The relocation of enterotropic and immunosuppressive $T_{reg}17$ cells to cancerous tissue (tumors and tdLNs) is repressed by the molecular interaction between the HEV addressin MAdCAM-1 and the integrin α4β7 expressed by $T_{reg}17$ cells. Disruption of the MAdCAM-1 expression by ABX or gut dysbiosis causes the relocation of $T_{reg}17$ cells into tumors, consequently compromising cancer immunosurveillance and the therapeutic efficiency of ICIs in mice and patients. ■

The complete list of authors and their affiliations is available in the full article online.
Corresponding author. Email: Laurence Zitvogel, laurence.zitvogel@gustaveroussy.fr; Guido Kroemer, kroemer@orange.fr; Conrad Rauber, conrad.rauber@gmx.de
Cite this article as M. Fidelle *et al.*, *Science* 380, eabo2296 (2023). DOI: 10.1126/science.abo2296

READ THE FULL ARTICLE AT
https://doi.org/10.1126/science.abo2296

MAdCAM-1 as a gut immune checkpoint for cancer immunosurveillance. Bacteria from the genus *Enterocloster*, for example, after discontinuation of ABX, induce the down-regulation of MAdCAM-1 in the ileal lamina propria and mLNs, inducing the exodus of the immunosuppressive α4β7$^+$ $T_{reg}17$ cells from the gut to cancers and tdLNs. Disruption of the MAdCAM-1–α4β7 axis compromises the efficacy of immunotherapy in mice and patients.



RESEARCH ARTICLE

CANCER IMMUNOTHERAPY

A microbiota-modulated checkpoint directs immunosuppressive intestinal T cells into cancers

Marine Fidelle[1,2,3]†, Conrad Rauber[1,2,3,4]*†, Carolina Alves Costa Silva[1,2,3]†, Ai-Ling Tian[1,2, 5,6], Imran Lahmar[1,2,3], Anne-Laure Mallard de La Varende[1,2,3], Liwei Zhao[1,5,6], Cassandra Thelemaque[1,3], Isabelle Lebhar[1,3], Meriem Messaoudene[7], Eugenie Pizzato[1,3], Roxanne Birebent[1,2,3], Maxime Descartes Mbogning Fonkou[1,3], Silvia Zoppi[1,2,8], Anna Reni[1,2,9], Cécile Dalban[10], Marion Leduc[1,5,6], Gladys Ferrere[1,3,11], Sylvère Durand[1,5,6], Pierre Ly[1,3,12], Aymeric Silvin[1,3], Kevin Mulder[1,2,3], Charles-Antoine Dutertre[1,3], Florent Ginhoux[1,3], Satoru Yonekura[1,2,3], Maria Paula Roberti[1,3,13,14], Maryam Tidjani-Alou[1,3], Safae Terrisse[1,2,3], Jianzhou Chen[1,3], Oliver Kepp[1,5,6], Angela Schippers[15], Norbert Wagner[15], Javier Suárez-Gosálvez[16], Sebastian Kobold[16,17], Jean-Eudes Fahrner[1,2,3], Corentin Richard[7], Jacques Bosq[18], Leonardo Lordello[1,3], Giacomo Vitali[19], Nathalie Galleron[19], Benoît Quinquis[19], Emmanuelle Le Chatelier[19], Lucas Blanchard[20], Jean-Philippe Girard[20], Anne Jarry[21], Nadine Gervois[21], Emmanuelle Godefroy[21], Nathalie Labarrière[21,22], Ronald Koschny[4], Romain Daillère[11], Benjamin Besse[1,2], Caroline Truntzer[23], François Ghiringhelli[23], Nicolas Coatnoan[24,25], Vanessa Mhanna[24,25], David Klatzmann[24,25], Damien Drubay[1,26,27], Laurence Albiges[1,2], Andrew Maltez Thomas[28], Nicola Segata[28,29], François-Xavier Danlos[1,2,3,12,30], Aurélien Marabelle[1,2,3,12,30], Bertrand Routy[7,31], Lisa Derosa[1,2,3,12]†, Guido Kroemer[5,6,32]*†, Laurence Zitvogel[1,2,3,12]*†

Antibiotics (ABX) compromise the efficacy of programmed cell death protein 1 (PD-1) blockade in cancer patients, but the mechanisms underlying their immunosuppressive effects remain unknown. By inducing the down-regulation of mucosal addressin cell adhesion molecule 1 (MAdCAM-1) in the ileum, post-ABX gut recolonization by *Enterocloster* species drove the emigration of enterotropic $\alpha4\beta7^{+}CD4^{+}$ regulatory T 17 cells into the tumor. These deleterious ABX effects were mimicked by oral gavage of *Enterocloster* species, by genetic deficiency, or by antibody-mediated neutralization of MAdCAM-1 and its receptor, $\alpha4\beta7$ integrin. By contrast, fecal microbiota transplantation or interleukin-17A neutralization prevented ABX-induced immunosuppression. In independent lung, kidney, and bladder cancer patient cohorts, low serum levels of soluble MAdCAM-1 had a negative prognostic impact. Thus, the MAdCAM-1–$\alpha4\beta7$ axis constitutes an actionable gut immune checkpoint in cancer immunosurveillance.

Immune checkpoint inhibitors (ICIs) targeting the immunosuppressive interaction between programmed cell death protein 1 (PD-1) and programmed death-ligand 1 (PD-L1) are used in the clinical management of many cancer types (*1*, *2*). Primary resistance to ICIs has been attributed to various molecular or cellular cues (*3*–*5*). In addition, several studies confirmed the deleterious effect of antibiotics (ABX) on clinical benefit in patients receiving ICIs (*6*–*8*). Meta-analyses have revealed that ABX uptake is more harmful on clinical outcome when administered before, rather than during, ICI administration, suggesting that bacterial recolonization after an ABX course may be particularly deleterious (*9*–*11*). How these new bacterial compositions interfere with the reprogramming of the tumor microenvironment (TME) remains a conundrum.

The α4 (CD49d) and β7 integrin subunits interact to form the α4β7 heterodimer. By interacting with its counter-receptor, mucosal addressin cell adhesion molecule 1 (MAdCAM-1), α4β7 integrin mediates lymphocyte adhesion and diapedesis from the circulation across the vascular endothelial barrier into gut-associated secondary lymphoid tissue (GALT) or the lamina propria (LP). MAdCAM-1 is constitutively expressed in LP venules, as well as in GALT high endothelial venules, and up-regulated by inflammatory cytokines (*12*–*14*). By preventing the migration of inflammatory $\beta7^{+}$ T cells from the circulation to the gut, antibodies (Abs) targeting α4β7 or MAdCAM-1 reduce the severity of colitis in patients with inflammatory bowel disease (*15*–*17*).

The intestinal microbiota plays a role in maintaining the homeostatic functions of gut regulatory T (T_{reg}) and interleukin-17 (IL-17)–producing T helper (T_H17) cells (*18*, *19*). Gut T_H17 cells also control extra-intestinal inflammation (*20*–*24*). T_H17 cells and a lineage-related $FoxP3^{+}ROR\gamma t^{+}$ regulatory subset ($T_{reg}17$ cells) blunt antitumor immunosurveillance during carcinogenesis (*25*). In humans and mice, the expression of the transcription factor retinoic acid–related orphan receptor-γt (RORγt) is characteristic of a subpopulation of tumor-infiltrating T_{reg} cells that are induced by gut commensals (*26*–*28*). Thus, we hypothesized that ABX-induced overgrowth of selected species (*11*, *29*) might affect the trafficking of T_{reg} cells between the intestinal and tumoral compartments, thereby aggravating cancer immunosuppression and resistance to PD-1 blockade.

ABX down-regulate MAdCAM-1 ileal expression in mice and patients

The use of a cocktail of broad-spectrum ABX [ampicillin, colistin, and streptomycin (ACS)] to sterilize the gastrointestinal tracts of mice attenuates the anticancer effects of PD-1 blockade

[1]Gustave Roussy Cancer Campus, Villejuif Cedex, France. [2]Université Paris-Saclay, Faculté de Médecine, Le Kremlin-Bicêtre, France. [3]Institut National de la Santé Et de la Recherche Médicale (INSERM) U1015, Équipe Labellisée - Ligue Nationale contre le Cancer, Villejuif, France. [4]Department of Gastroenterology and Infectious Diseases, University Hospital Heidelberg, Heidelberg, Germany. [5]Centre de Recherche des Cordeliers, INSERM U1138, Équipe Labellisée - Ligue Nationale contre le Cancer, Université Paris Cité, Sorbonne Université, Paris, France. [6]Metabolomics and Cell Biology Platforms, Gustave Roussy Cancer Campus, Villejuif, France. [7]Centre de Recherche du Centre Hospitalier de l'Université de Montréal (CRCHUM), Montréal, Quebec, Canada. [8]Department of Medicine and Surgery, University of Parma, Parma, Italy. [9]Section of Oncology, Department of Medicine, University of Verona School of Medicine and Verona University Hospital Trust, Verona, Italy. [10]Clinical Research Department, Centre Léon Bérard, Lyon, France. [11]EverImmune, Gustave Roussy Cancer Campus, Villejuif Cedex, France. [12]Center of Clinical Investigations in Biotherapies of Cancer (BIOTHERIS), Villejuif, France. [13]Clinical Cooperation Unit Applied Tumor Immunity, German Cancer Research Center (DKFZ), Heidelberg, Germany. [14]Department of Medical Oncology, National Center for Tumor Diseases (NCT), Heidelberg University Hospital (UKHD), Heidelberg, Germany. [15]Department of Pediatrics, University Hospital RWTH Aachen, Aachen, Germany. [16]Center of Integrated Protein Science Munich (CIPS-M) and Division of Clinical Pharmacology, Department of Medicine IV, Klinikum der Universität München, LMU Munich, Germany. [17]German Cancer Consortium (DKTK), partner site Munich, Munich, Germany. [18]JBO Consultant, Paris, France. [19]MetaGenoPolis, INRAe, Université Paris-Saclay, Jouy en Josas, France. [20]Institut de Pharmacologie et de Biologie Structurale, IPBS, Université de Toulouse, CNRS, UPS, Toulouse, France. [21]Nantes Université, Université d'Angers, INSERM, CNRS, Immunology and New Concepts in ImmunoTherapy, INCIT, UMR 1302/EMR6001, Nantes, France. [22]LabEx IGO, Université de Nantes, Nantes, France. [23]Université de Bourgogne Franche-Comté, Plateforme de Transfert de Biologie du Cancer, Centre Georges-François Leclerc, Equipe Labellisée Ligue Nationale Contre le Cancer, Centre de Recherche INSERM LNC-UMR1231, Institut Médical de Génétique et d'Immunologie, Dijon, France. [24]AP-HP, Hôpital Pitié-Salpêtrière, Clinical Investigation Center for Biotherapies (CIC-BTi) and Immunology-Inflammation-Infectiology and Dermatology Department (3iD), Paris, France. [25]Sorbonne Université, INSERM, UMRS959 Immunology-Immunopathology-Immunotherapy Laboratory, Paris, France. [26]Office of Biostatistics and Epidemiology, Gustave Roussy Cancer Campus, Université Paris-Saclay, Villejuif, France. [27]Inserm, Université Paris-Saclay, CESP U1018, Oncostat, labeled Ligue Contre le Cancer, Villejuif, France. [28]Department of Computational, Cellular and Integrative Biology, University of Trento, Trento, Italy. [29]Istituto Europeo di Oncologia (IEO), National Cancer Institute (IRCCS), Milan, Italy. [30]Drug Development Department, Gustave Roussy Cancer Campus, Villejuif Cedex, France. [31]Hematology-Oncology Division, Department of Medicine, Centre Hospitalier de l'Université de Montréal (CHUM), Montréal, Quebec, Canada. [32]Institut du Cancer Paris CARPEM, Department of Biology, Hôpital Européen Georges Pompidou, Assistance Publique – Hôpitaux de Paris (AP-HP), Paris, France.
***Corresponding author. Email: laurence.zitvogel@gustaveroussy.fr (L.Zi.); kroemer@orange.fr (G.K); conrad.rauber@gmx.de (C.Ra.)**
†These authors contributed equally to this work.

(7). ACS reduced the expression of most ileal chemokines and *Madcam1* (Fig. 1A and fig. S1A). These effects were specific for the ileum, because they were not observed in the colon or in MCA205 fibrosarcomas (Fig. 1A and fig. S1A). Ileal *Madcam1* mRNA and protein levels were decreased as determined by quantitative reverse transcription polymerase chain reaction (RT-qPCR) (Fig. 1A), immunohistochemistry (Fig. 1B), flow cytometry of ileal CD45$^-$ LP cells (Fig. 1C and fig. S1B), and enzyme-linked immunosorbent assay (ELISA) of ileal tissue lysates (Fig. 1D). The integrity of the intestinal architecture and vasculature was notably preserved after ACS administration without any alteration in the density of CD31$^+$ capillaries (fig. S1C). Levels of MAdCAM-1 began to decrease on day 3 of ACS administration and did not recover on day 4 (ACS+4d) or even on day 12 after ACS cessation (Fig. 1, C and D). The ACS cocktail also down-regulated *Madcam1* gene expression in Peyer's patches and in mesenteric lymph nodes (mLNs) (fig. S1, D and E). Other ABX regimens using β-lactams (ceftazidime and cefepime cephalosporins), aminoglycosides (streptomycin), polymyxins (colistin), and macrolides (erythromycin) also down-regulated ileal *Madcam1* (fig. S1, E and F). By contrast, piperacillin plus tazobactam, rifaximin, and vancomycin had no effect on *Madcam1* expression in two distinct animal facilities located in France (fig. S1E) and Canada (fig. S1F). *Madcam1*, but not vascular cell adhesion protein (*Vcam1*), mRNA levels were 10 times lower in tumor-draining LNs (tdLNs) than in mLNs (fig. S1G). Mass spectrometry of ileal bacteria cultured from animals treated with various ABX regimens under aerobic and anaerobic conditions identified several species belonging to the genus *Enterocloster* (e.g., *Enterocloster clostridioformis* and *Enterocloster bolteae*) (29) that prevailed 4 or 7 days after ACS or erythromycin cessation but not in any other experimental condition (table S1). These *Enterocloster* spp. were previously identified in the stools of cancer patients resistant to PD-1 blockade (10, 11), as well as in chronic inflammatory disorders (30), and mediate resistance to cancer immunotherapy with PD-1 blockade in mice (31). Whereas oral gavage of *E. clostridioformis* reduced ileal *Madcam1* mRNA (Fig. 1E), administration of immunostimulatory *Akkermansia* strain p2261 (*Akk.* p2261) (7, 10) or *Enterococcus hirae* (32) increased

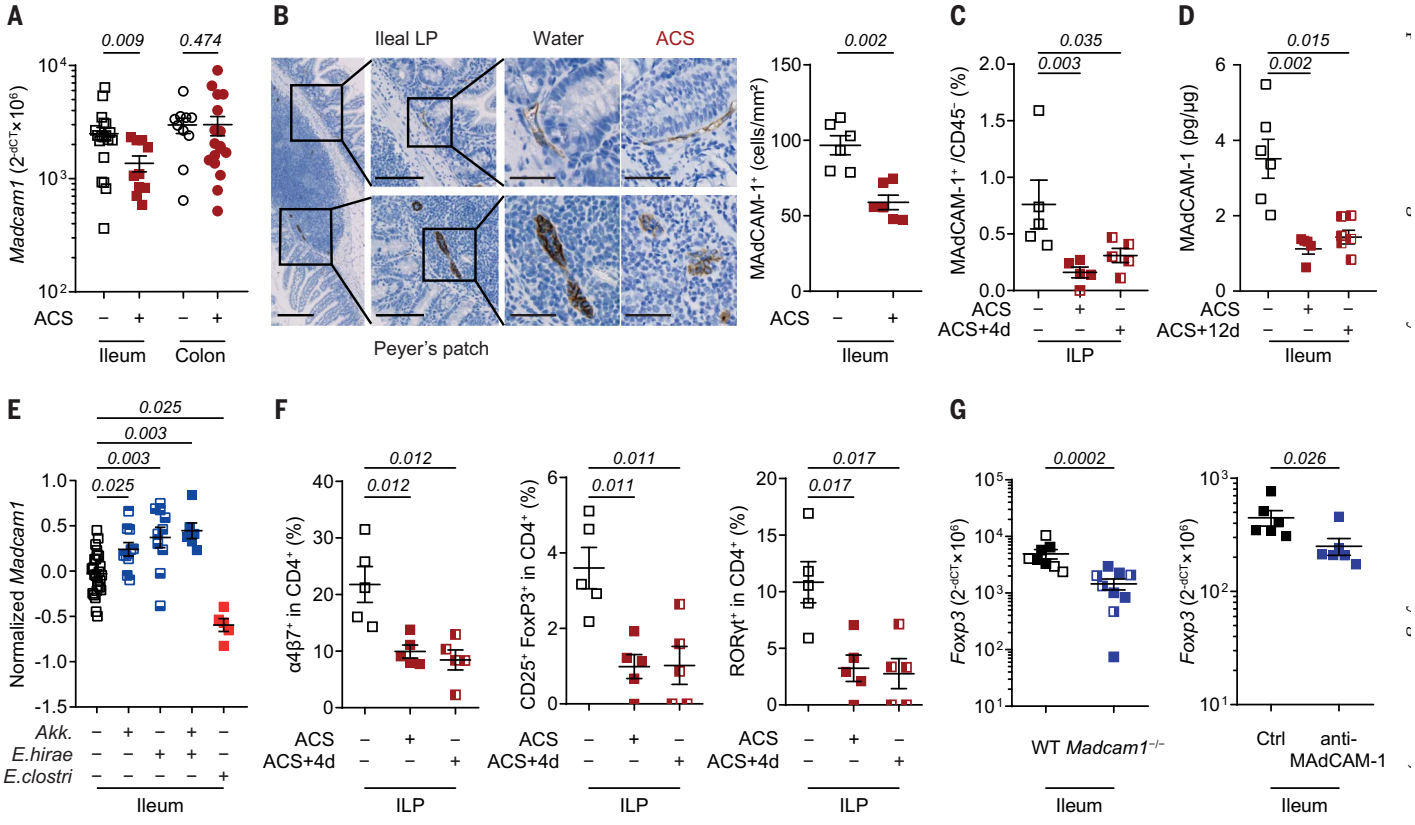


Fig. 1. Broad-spectrum ABX down-regulate MAdCAM-1 expression in the murine ileal vasculature. (**A** to **D**) Relative transcription (A) and protein (B to D) levels of *Madcam1* gene product obtained with RT-qPCR (A), immunohistochemistry staining of MAdCAM-1 in ileal lamina propria (ILP) venules and high endothelial venules in Peyer's patches in ACS-treated and untreated mice (as indicated above micrograph pictures; scale bars, 200 μm, 100 μm, and 40 μm, respectively) (B), flow cytometry gating on CD45$^-$ cells of ILP (C), or ELISA (D) of ileal (A to D) or colonic (A) tissues in C57BL/6 mice after continuous ACS, ACS+4d, or ACS+12d spontaneous recolonization, or after cessation of ACS. Each dot represents one ileum [(A) to (D)] or colon (A). n = 2 in (A) and n = 3 in (B) to (D). (**E**) RT-qPCR of relative *Madcam1* gene expression normalized on the naive SPF mice group in ileal mucosae of C57BL/6 mice reared in SPF conditions (no ABX conditioning) that underwent oral gavage with bacteria species aligned on the x axis (n = 4). *Akk.*, *Akkermansia strain p2261; E. clostri*, *E. clostridioformis*. (**F**) Same experiments as in (C) performing flow cytometric analysis of ILP CD4$^+$ T cell subsets (α4β7$^+$ versus CD25$^+$ FoxP3$^+$ T_{reg} cells versus RORγt$^+$ CD4$^+$ T_H17 cells) during continuous ACS or at the ACS+4d phase, with each dot representing one ileum. (**G**) Ileal expression levels of *Foxp3* in *Madcam1* gene-deficient mice (left) or phenocopied with an anti–MAdCAM-1 Ab (right) treated (full dots) or not with anti–PD-1 Ab that did not affect ileal *Madcam1* expression levels (not shown) without ACS conditioning. Each dot represents the RT-qPCR data of one ileum (n = 6 mice per group per experiment). (A), (E), and (G) depict a pool of two to three independent experiments. Results from a representative experiment are shown in (B), (C), (D), and (F). Comparisons between groups were analyzed using nonparametric Mann–Whitney U test (two groups) or Kruskal–Wallis H test (more than two groups) followed by multiple-comparisons test by controlling the FDR. Error bars indicate means ± SEM.

basal *Madcam1* expression in ileal tissues from eubiotic mice reared in specific-pathogen-free (SPF) conditions (Fig. 1E). Moreover, ACS-induced down-regulation of ileal *Madcam1* mRNA correlated with a decrease in regulatory cytokines and transcription factors (e.g., *Foxp3*, *Il17a*, *Il22*, and *Rorc*) (fig. S1, A, H, and I). Consistent with this, ACS depleted mucosal T_{reg} and T_H17 cells from the ileal LP (Fig. 1F and fig. S2A). Finally, ACS phenocopied the ileal immunomodulatory effects of *Madcam1* knockout or antibody neutralization of MAdCAM-1 (Fig. 1G).

We confirmed the coordinated inhibitory effects of several class of ABX on the ileal, but not cecal nor colonic, expression of *MADCAM1* and *RORC* in 31 patients who were treated with ABX (n = 10) compared with nontreated patients (n = 21) while they underwent intestinal endoscopy and biopsies for various indications (Fig. 2, A and B, and table S2). As in mice, we found a correlation between *MADCAM1* and *IL17A* ileal mRNA levels (Fig. 2C). In clinical trials, fecal microbial transfer (FMT) from melanoma patients who benefited from PD-1 blockade circumvents primary resistance to ICIs in one-third of metastatic melanoma recipients (*33*, *34*). Moreover, FMT from some human donors fails to improve ICI responses (*7*, *35*). We tested whether random FMT from non-small-cell lung cancer (NSCLC) patients to ABX-preconditioned mice would modulate ileal *Madcam1* gene expression. Three of six FMTs down-regulated *Madcam1* mRNA (Fig. 2D and table S3). Shotgun metagenomics-based analyses of these three human stools revealed an overrepresentation of *Enterocloster* spp., including *E. clostridioformis*, as well as that of *Hungatella hathewayi*, which is phylogenetically close to *Enterocloster* spp. (*29*), in two out of three of these stools compared with the three other human fecal samples (Fig. 2D). Mice orally gavaged with stools that down-regulated *Madcam1* expression exhibited a relative over-representation of *E. clostridioformis* (Fig. 2D). Finally, the longitudinal follow-up of cancer patients >60 days after ABX cessation revealed significant decreases of the

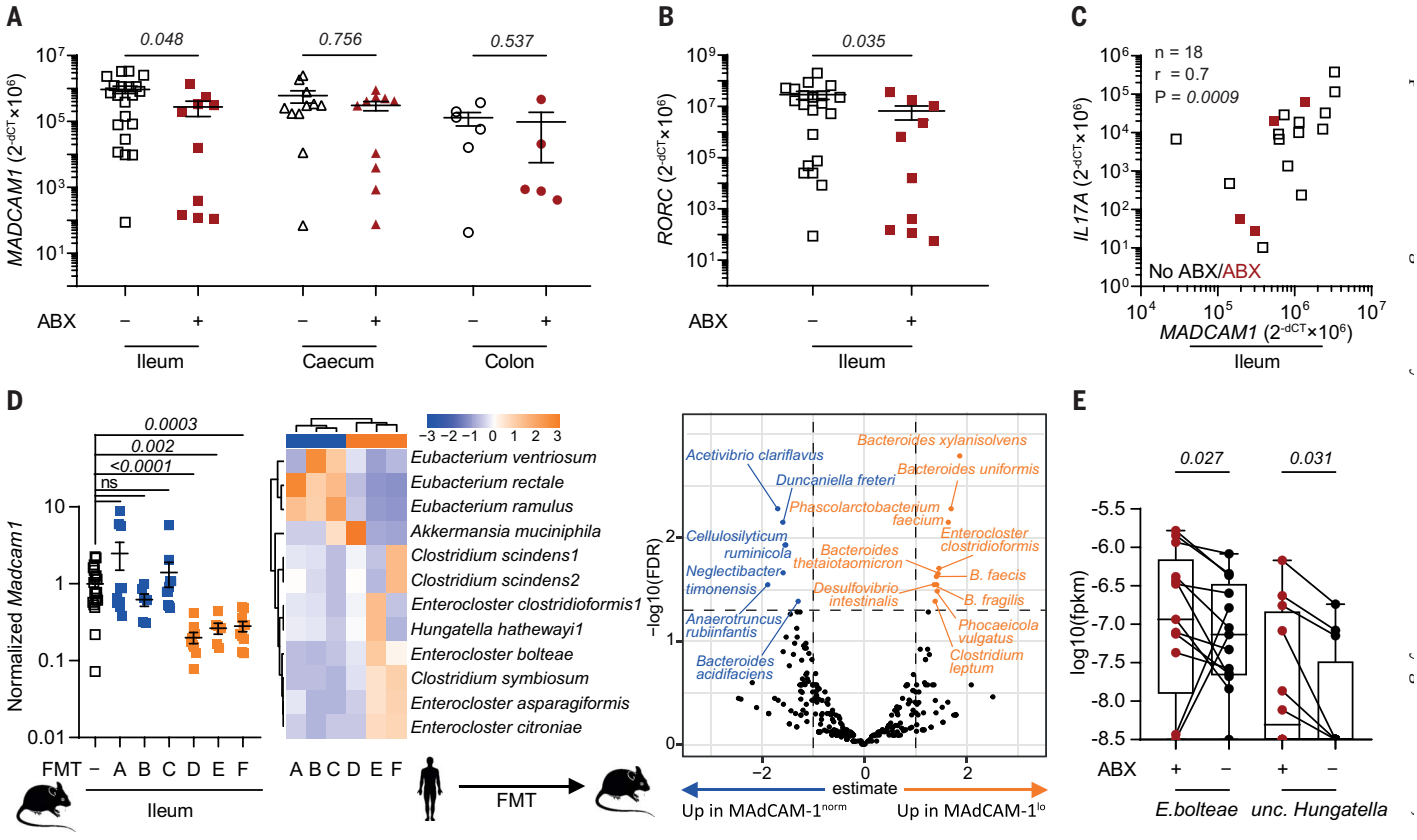


Fig. 2. Down-regulation of ileal *Madcam1* gene expression in patients taking ABX. (**A** and **B**) RT-qPCR–based transcriptional levels of human *MADCAM1* (A) and *RORC* genes (B) in intestinal biopsies collected during endoscopic intervention in 21 control (ABX-free) patients and 10 ABX-treated patients (table S2). Each dot represents one biopsy from ileum, cecum, or colon, with a single patient being represented one to three times. (**C**) Spearman's correlation between ileal *IL17A* and *MADCAM1* gene expressions in ABX-treated or untreated patients. (**D**) Impact of FMT in ABX-treated (3 days) recipient mice using feces from NSCLC patients at diagnosis (before PD-1 blockade) (table S3) on ileal *Madcam1* gene expression normalized on the SPF (FMT−) mice group [log10 axis (D), left panel]. Each experiment used a different FMT donor six times independently and comprised six to 10 animals per group. Each dot represents one ileum. Nonsupervised hierarchical clustering of the taxonomic composition of human donor feces (defined using shotgun MG sequencing), selecting bacteria of high prevalence >25% and clinically relevant (*10*) [(D), middle panel], and volcano plot contrasting significantly different stool taxa of FMT-recipient mice, as assessed using 16*S* rRNA-seq, selecting bacteria of high prevalence and, according to ileal expression levels of *Madcam1* (right panel). Norm, normal levels of MAdCAM-1 (in SPF controls). (**E**) Shotgun metagenomics-based determination of the relative abundance of fecal species significantly affected by the ABX uptake in lung cancer patients during ABX versus >60 days after ABX discontinuation in a paired analysis including n = 13 individuals. fpkm, fragments per kilo base of transcript per million mapped fragments (gene expression unit). Comparisons between groups were analyzed using nonparametric Mann–Whitney U test (two groups) or Kruskal–Wallis H test (more than two groups) followed by multiple-comparisons test by controlling the FDR. For (C), nonparametric Spearman's correlation was performed. For the volcano plot in (D), a linear regression was performed to assess *Madcam1* expression as a function of bacteria prevalence in mouse feces and FDR correction was applied. For (E), nonparametric Wilcoxon matched-pairs signed-rank test was performed. Error bars indicate means ± SEM.

abundance of *Enterocloster* and *Hungatella* spp. (Fig. 2E). Thus, broad-spectrum ABX down-regulate the expression of the ileal mucosal addressin MAdCAM-1, correlating with reduced ileal *Foxp3*, *Il17a*, and *Rorc*.

To further elucidate potential molecular cues explaining MAdCAM-1 loss after relative dominance of ileal *E. clostridioformis*, we performed mass spectrometric metabolomics of murine ileal contents 7 days after gavage with this bacterium. There were significant changes in biliary acid levels (fig. S3A), consistent with a previous report (*36*). We screened the effects of various biliary acid (*37*, *38*) and bacteria on *Madcam1* expression in vitro using two murine endothelial cell lines, transformed endothelial sinusoidal cells (TSECs) and brain endothelial cells (bEnd.3), engineered to express green fluorescent protein (GFP) under the control of the *Madcam1* promoter (fig. S3B). Live *E. clostridioformis* directly reduced expression of GFP, whereas the immunogenic *Akk.* failed to do so (fig. S3C). Lithocholic acid (LCA), as well as two synthetic farnesoid X receptor (FXR) agonists, significantly decreased GFP expression in TSEC and bEnd.3 exposed to IL-1β plus tumor necrosis factor-α (TNF-α) in a dose-dependent manner (fig. S3D). Distinct LCA isoforms reduced GFP expression levels at different dose levels (fig. S3E). RT-qPCR confirmed that LCA down-regulated *Madcam1* mRNA expression levels in TSEC cells (fig. S3F). Moreover, LCA (fig. S3, G and H) and ursodeoxycholic acid (UDCA) (fig. S3I) dampened *Madcam1* gene expression levels in ileum and ileal Peyer's patches and in mLNs in vivo, consistent with a prior report (*39*). Thus, one of the mechanisms by which *Enterocloster* spp. may down-regulate MAdCAM-1 in GALT is through the accumulation of distinct biliary acids.

ABX induce the exodus of enterotropic α4β7$^+$ CD4$^+$ T cell subsets to tdLNs

We hypothesized that the loss of ileal MAdCAM-1 might affect the trafficking of enterotropic T cells expressing the MAdCAM-1 receptor α4β7. We used Kaede mice, which express a fluorescent protein (*40*) that is photoconverted (PC) upon ultraviolet light (UV) illumination to study the exodus of intestinal cells (*20*, *22*, *23*). To track the fate of ileal, cecal, and mLN cells (henceforth referred to as "intestine") 24 hours after photoconversion of tumor bearers, we analyzed PC leukocytes in various organs by flow cytometry (fig. S4A). Up to 22.8 ± 2.6% of mLNs cells remained PC$^+$ and PC$^+$ cells became detectable in the spleen (5.1 ± 0.5%) and tdLNs (4.0 ± 0.3%) (fig. S4A). UV illumination of the ileum also enabled the visualization of gut leukocyte emigration to tdLNs or tumors, albeit to a lower extent than intestine illumination (fig. S4B). As a second method of cell tracking, we directly injected carboxyfluorescein succinimidyl ester (CFSE) into the mLNs (*41*) and then followed the emigration of CFSE-labeled cells to distant sites at 24 hours (fig. S4C). Up to 1.0 ± 0.2% of splenocytes, 0.8 ± 0.1% of tdLN cells, and 0.2 ± 0.02% of tumor-infiltrating leukocytes were replaced by mLN-derived leukocytes (fig. S4C). Both methods revealed the selective enrichment of PC$^+$ or CFSE$^+$ α4β7$^+$ CD4$^+$ T cells in the spleen, tdLN, and tumor at 24 hours (Fig. 3, A and B, and fig. S4, D and E). Ab-mediated inhibition of MAdCAM-1 in mice led to a more pronounced migration of PC$^+$ or CSFE-labeled cells from the mLNs to the tdLNs than in control animals (fig. S4, F and G). By contrast, the migration of mLNs cells to the contralateral LNs (cLNs) was not affected (fig. S4G).

Bulk-RNA sequencing (RNA-seq) of α4β7^{hi} CD4$^+$ T cells compared with α4β7$^-$ CD4$^+$ T cells purified from mLNs of tumor-bearing mice revealed that α4β7^{hi} CD4$^+$ T cells overexpressed not only the *Itga4* subunit of α4β7 but also genes involved in T_{reg} cell functions and T_H17 cell polarization. However, these cells down-regulated *Tnfrsf9* (Fig. 3C and data S1).

We investigated how ACS-induced dysbiosis affected the exodus of CSFE-labeled mLNs cells to tdLNs (Fig. 3D). Transient ACS treatment for 14 days, followed by discontinuation of ACS for 4 days, facilitated the mLN to tdLN migration of α4β7$^+$ $T_{reg}17$ cells, but not that of IL-17A$^+$ α4β7$^+$ FoxP3$^-$ CD4$^+$ conventional T cells or α4β7$^-$ T_{reg} cells (Fig. 3E, fig. S5A). ACS did not increase the bona fide T_{reg} cell pool of the tdLNs constituted by the locally expanded (extraintestinal, CFSE$^-$) cells (fig. S5B). $T_{reg}17$ cells, which represent up to 40% of intestinal T_{reg} cells, constituted the most mobile α4β7$^+$ CFSE$^+$ fraction, accounting for 0.2 ± 0.1% of all CSFE$^+$ CD4$^+$ cells reaching the tdLNs 24 hours after injection of CSFE into mLNs and after cessation of ACS (fig. S5B). These originally enterotropic $T_{reg}17$ cells not only produced IL-17A but also IL-22 (fig. S5B). *Madcam1*$^{-/-}$ mice also manifested a similar mLN to tdLN, but not cLN, migration of CFSE-labeled T_{reg} cells (Fig. 3F and fig. S5C). Similarly, in Kaede-transgenic mice subjected to UV illumination of the intestine (fig. S4A), a neutralizing anti–MAdCAM-1 Ab promoted the gut to tdLN migration of PC$^+$ CD25^{hi} α4β7$^+$ CD4$^+$ T cells (Fig. 3G). Because recolonization after ACS is accompanied by the emergence of *Enterocloster* spp. (table S1) that down-regulated ileal *Madcam1* (Fig. 1E), we investigated whether oral gavage with *E. clostridioformis* would be sufficient to trigger this mLN to tdLN migration. Indeed, this bacterium facilitated the selective intestinal translocation of PC$^+$, but not PC$^-$, CD25^{hi} (but not CD25$^-$) T_H17 cells (CCR6$^+$CXCR3$^-$) (Fig. 3H). These findings suggest that the migrating enterotropic T cells do not use MAdCAM-1–expressing high endothelial venules to enter distal tissues. Instead, we observed a role for L/P-selectins in T cell homing to tumor beds during MAdCAM-1 down-regulation (fig. S6), as previously described (*42*, *43*).

We next performed Rhapsody-based single-cell RNA-seq of CFSE$^+$ CD4$^+$ T cells recovered from tdLNs at 24 hours after CFSE injection into mLNs in mice treated with ACS and oral *E. clostridioformis* (fig. S7, A and B). Unsupervised clustering of the CFSE$^+$ CD4$^+$ T cells from tdLNs partitioned the data into four cellular clusters (fig. S7C and data S2) (*44*). A small cluster featured the prototypic effector T_{reg} cell phenotype (*26*) (fig. S7D). This T_{reg} cell subset overexpressed the genes, *Nrp1*, *Cd39*, and *Cd73*, which are involved in tumor immunosuppression (fig. S7D), and differed from all the other emigrating cells by the overexpression of genes associated with the $T_{reg}17$ cell program (*26*) (fig. S7D). Another distinctive cluster harbored a follicular T helper/regulatory cell (TFH/TFR)-like transcriptional profile with proliferative/exhaustion hallmarks (*45*) (fig. S7E). Two other subsets were characterized by a type I interferon (IFN) fingerprint (fig. S7F) and a CD8-like regulatory profile defined by immunosuppressive signaling pathways (*46*–*51*) (fig. S7G and data S2).

Most of the mLNs emigrating cells to tdLNs were T cells, although some B cells were also observed (Fig. 4A). To address the clonality of T_{reg} cells that emigrated from the mLNs, we performed single-cell and deep T cell receptor (TCR) sequencing of CFSE$^+$ T cells harvested from various locations at 24 hours after mLNs CFSE injection. Unsupervised clustering of the CFSE$^+$ T cells partitioned the data into four cellular clusters, one composed of T_{reg} cells, one of conventional T cells, and two of CD8$^+$ T cells (Fig. 4B and fig. S8, A and B). On the basis of the TCR repertoire (*52*), tumor-infiltrating T_{reg} cells, but not conventional T cells, exhibited higher clonal expansion in mice gavaged with *E. clostridioformis* compared with control mice (Fig. 4C). There was a 10-fold increase of TCRs from clusters composed of tumor and tdLN TCRs in mice gavaged with *E. clostridioformis* compared with controls, with a concomitant decrease of TCRs from clusters restricted to mLNs (Fig. 4D). This recirculation affected preferentially T_{reg} cells over conventional T cells (Fig. 4C). Similar clonal expansions were observed in the CD8$^+$ population (fig. S8C). The functional profile of mLN T_{reg} cells that reached the tumor differed from that of its origin, with an up-regulation of genes involved in immunosuppression, cytolysis, and type I IFN responses (Fig. 4E and fig. S8A). Oral gavage with *E. clostridioformis* significantly increased the proliferative potential of migratory T_{reg} cells with the up-regulation of genes implicated in the cell cycle, chromatin silencing, and H3K27 trimethylation, as well as regulatory functions (*Il10*) within tumor beds (Fig. 4, E

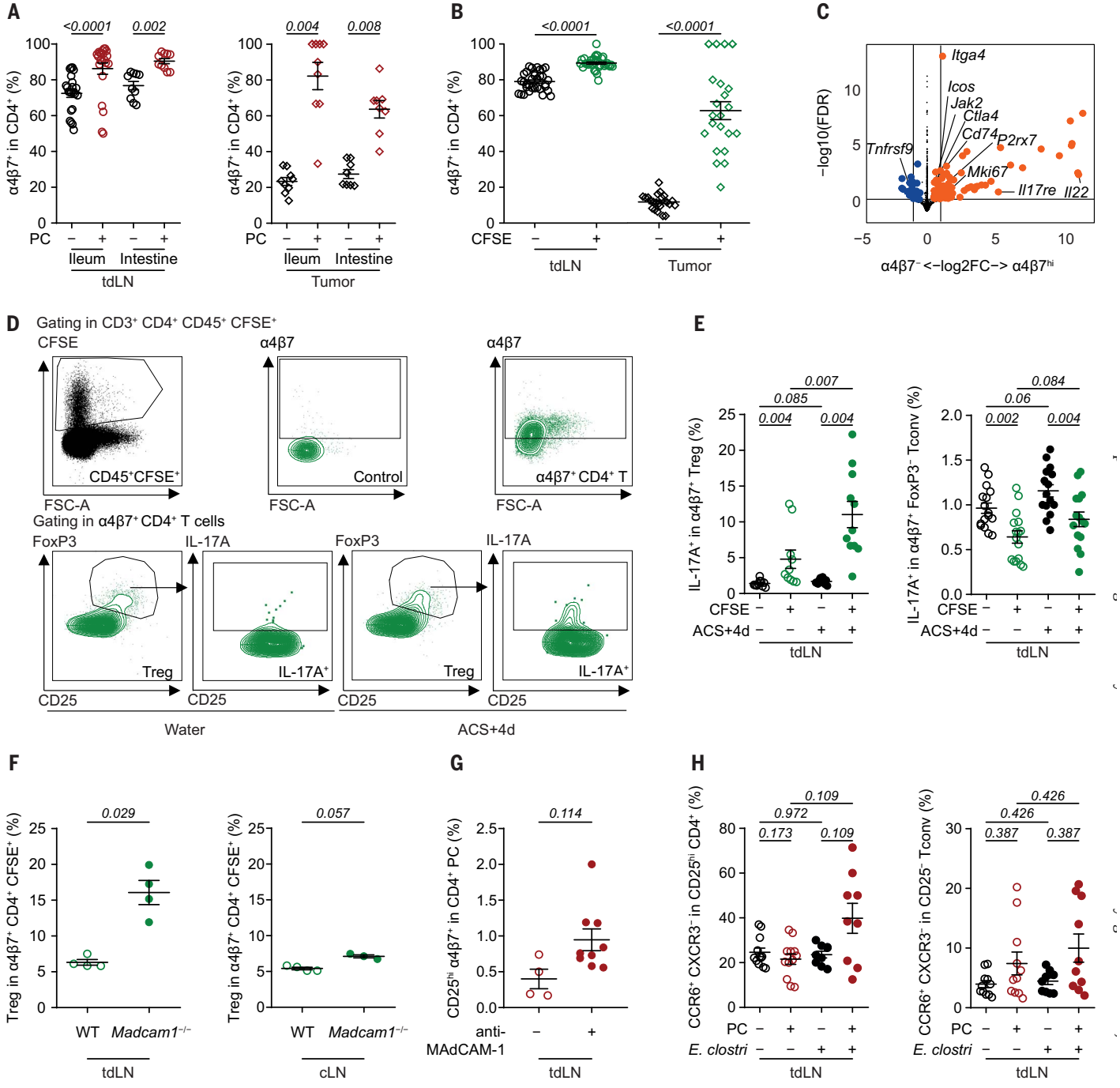


Fig. 3. ABX-induced exodus of enterotropic α4β7⁺ T_{reg}17 cells toward tumor beds. (**A**) Flow cytometric analysis of α4β7 expression in PC⁻ or PC⁺ CD4⁺ T cells residing in the tdLNs or tumor bed in Kaede mice UV illuminated in the ileum or the "intestine" (ileum + cecum + mLNs). (**B**) Same as in (A) but in WT mice subjected to CFSE injection in the mLNs and gating on CFSE⁻ or CFSE⁺ CD4⁺ T cells. (**C**) Volcano plot depicting the differential gene transcription in bulk RNA-seq of α4β7ʰⁱ versus α4β7⁻ CD4⁺ lymphocytes cell sorted from mLNs in four MCA205 tumor-bearing animals. Volcano plot was generated computing the log2 FC ratio of the mean relative abundances of transcripts in α4β7ʰⁱ versus α4β7⁻ CD4⁺ lymphocytes (*x* axis) with the co-log10 of *P* values deriving from Mann–Whitney *U* test for each transcript followed by multiple-comparisons test by controlling the FDR. Blue and orange dots are considered significant ($P < 0.05$), whereas back dots are not ($P > 0.05$) (data S1). (**D** to **F**) Representative gating strategy and dot plots in flow cytometric analyses of the IL-17A–secreting α4β7⁺ T_{reg} cells (FoxP3⁺ CD25⁺), α4β7⁺ conventional T cells (FoxP3⁻), CD4⁺ T cells within CFSE⁺ (originating from the mLNs, green dots), or CFSE⁻ cells (tdLNs resident cells, black dots) reaching the tdLNs during the ACS+4d phase ($n = 10$ to 16 mice per group) [(D) and (E)]. (F) Flow cytometric determination of CFSE⁺ T_{reg} cells reaching the tdLNs (left) or cLNs (right) in day 7 established MCA205 bearing WT versus *Madcam1*$^{-/-}$ mice (not treated with ACS) 24 hours after CFSE injection in mLNs. Each dot represents one mouse. (**G**) Same as in (F) but in Kaede tumor–bearing mice treated or not with anti–MAdCAM-1 Ab (day 8 after tumor inoculation), photoconverted at day 10. Flow cytometry at day 11 could identify T_{reg}-like cells using membrane staining for CD25ʰⁱ. Each dot represents one mouse. (**H**) Flow cytometric phenotyping of T cells from tdLNs in tumor-bearing mice at day 11 after MCA205 inoculation, gavaged with *E. clostridioformis* (*E. clostri*) at day 8, and photoconverted in the ileum at day 10. The percentages of CXCR6⁺CXCR3⁻

cells in CD4$^+$ T cells expressing high levels of CD25 (T_{reg}17-like, left) or CD25$^-$ (right) in Kaede mice within PC$^+$ (originating from the mLNs) or PC$^-$ cells (tdLN-resident cells) reaching the tdLNs during the colonization phase with *E. clostridioformis*. (A), (B), (E), and (H) show a pool of three to five independent experiments containing five mice per group. Results from a representative experiment are shown in (C), (D), and (F). Each dot represents one mouse. Comparisons between groups were analyzed using nonparametric Mann–Whitney *U* test (two groups) or Kruskal–Wallis *H* test (more than two groups) followed by multiple-comparisons test by controlling the FDR. For the PC$^+$ versus PC$^-$ or CFSE$^+$ versus CFSE$^-$ comparisons, Wilcoxon matched-pairs signed-rank test was performed. Error bars indicate mean ± SEM.

and F). The most noticeable commonality between mLNs emigrating CD8$^+$ and CD4$^+$ T cells reaching the sarcoma was the shutdown of the translation machinery, as previously reported in exhausted CD8$^+$ T cells in chronic infection and cancer (*53*–*56*) (Fig. 4E, fig. S8, D and E, and data S2). Thus, the enterotropic α4β7$^+$ CD4$^+$ T cells that translocate from the mLNs and Peyer's patches to the tdLNs comprise T_{reg} and T_{reg}17 cells that exhibit immunosuppressive functions. These immunosuppressive programs further increased when the cells reached the tumor bed, in conditions where the MAdCAM-1–α4β7 axis is compromised by neutralization or knockout of MAdCAM-1, recolonization after ABX, or *E. clostridioformis*–induced dysbiosis.

The anticancer efficacy of PD-1 blockade relies on the MAdCAM-1–α4β7 axis

Given the immunosuppressive role of T_{reg}17 cells during cancer immunosurveillance (*27*, *28*, *57*), disruption of the MAdCAM-1–α4β7 interaction may interfere with ICI-mediated anticancer effects. Loss of ileal *Madcam1* expression correlated with increased tumor size in tumor-bearing animals regardless of PD-1 blockade (fig. S9A). PD-1 blockade also reduced MCA205 fibrosarcoma growth in wild-type (WT) C57BL/6 mice, but failed to do so in *Madcam1*$^{-/-}$ mice and *Itgb7*$^{-/-}$ animals, which lack the β7 chain required for the formation of the α4β7 heterodimer (Fig. 5A). Similarly, MCA205 fibrosarcoma, 4T1 breast, and orthotopic TC-1 lung cancers normally reduced their growth in response to PD-1 blockade but failed to do so after injection of neutralizing anti–MAdCAM-1 or anti–α4β7 Abs (Fig. 5B, C and D). In *Madcam1*$^{-/-}$ mice, there was a constitutive increase of α4β7$^+$ CD4$^+$ T cells in the spleen and in the tumor, where they represented ~3% of tumor-infiltrating lymphocytes (TILs) (Fig. 5E), as previously described (*58*). Injection of a neutralizing anti–MAdCAM-1 Ab during spontaneous tumor progression reshaped the TME and led to a threefold increase in the intratumoral accumulation of T_{reg}17 cells expressing intestinal T cell markers such as α4β7, CCR6, and CCR9 (fig. S9, B and C). Although only 17 ± 0.9% of all MCA205 TILs were α4β7$^+$, and 76 ± 1.5% of T_{reg}17 cells were α4β7$^+$ (fig. S9C). In subcutaneous tumors (MCA205, 4T1), T_{reg} cells represented 11.7 ± 1.6% of α4β7$^+$ CD4$^+$ TILs and, among these T_{reg} cells, 44.5 ± 5.3% were RORγt$^+$ (table S4). Bacterial recolonization of the gut 4 days after ACS phenocopied *Madcam1* gene deficiency, inducing a threefold to fivefold increase in the proportion of T_{reg}17 cells in tumor beds (Fig. 5, F and G). The tumor-homing behavior of T_{reg}17 cells was transient and no longer observed by 12 days after ACS, except when anti–PD-1 Ab was coadministered (Fig. 5H and fig. S9D). Indeed, anti–PD-1 Abs facilitated the priming and/or expansion of T_{reg}17 cells in the mLNs in MCA205 tumor-bearing mice (fig. S9E) and contributed to the accumulation of T_{reg}17 cells within tumors (Fig. 5H, fig. S9, F and G). In this context, intratumoral T_{reg} represented 19.1 ± 2.8% of α4β7$^+$ CD4$^+$ TIL and, among these, T_{reg}, 51.1 ± 7.7% and 61.3 ± 7% were RORγt$^+$ and IL-17A$^+$, respectively (table S4).

The recruitment of T_{reg}17 cells promoted by PD-1 inhibition was further increased when *E. clostridioformis*, but not *Lactobacillus reuteri*, was supplemented by oral gavage after ACS discontinuation (fig. S9H). Blockade of the MAdCAM-1–α4β7 axis during PD-1–targeted immunotherapy impaired the infiltration of tumors by effector CCR5$^+$ CD8$^+$ T cells (*59*, *60*) (Fig. 5I). Given that the antimicrobial and pro-inflammatory properties of IL-17, alone or with IL-22 (*57*, *61*), neutralizing these cytokines may circumvent the harmful effects of bacterial recolonization after ABX and during PD-1 inhibition. Indeed, neutralization of IL-17A, but not IL-22RA, counteracted the deleterious effects of ACS on PD-1 blockade (Fig. 5J). Thus, IL-17A plays a role in the immunosuppressive effects of ABX.

MAdCAM-1 liver expression reduces the tumoral accumulation of enterotropic T_{reg} cells

To strengthen the cause–effect relationship between MAdCAM-1 gut expression and emigration of enterotropic suppressive T cells to tumors, we enforced MAdCAM-1 expression in the liver by hydrodynamic injection of *Madcam1*-encoding cDNA inserted into a vector (*62*). Liver-specific overexpression of the transgene was verified by RT-qPCR and immunohistochemistry (Fig. 6, A and B). Liver expression of MAdCAM-1 correlated with recirculation of the soluble form of MAdCAM-1 (sMAdCAM-1) (fig. S9I). There was a positive correlation between liver *Madcam1* and *Foxp3* mRNA expression or the local presence of FoxP3$^+$ T cells (Fig. 6C). In ACS-treated mice, enforced hepatic MAdCAM-1 expression reduced the frequency of tumoral α4β7$^+$, but not α4β7$^-$, T_{reg} cells (Fig. 6, D and E). Moreover, high hepatic *Foxp3* expression correlated with a reduction of tumor size (Fig. 6F). Anti–PD-1 Ab significantly increased liver *Rorc* expression, even more so upon ACS (Fig. 6G), with a positive correlation with liver *Madcam1* (Fig. 6H). Moreover, ACS-induced resistance to anti–PD-1 Abs could be circumvented when mice ectopically expressed *Madcam1* in the liver to locally retain T_{reg} cells (Fig. 6I). There was a negative correlation between tumor size and liver *Madcam1* mRNA levels in these conditions (Fig. 6J). Thus, MAdCAM-1 acts as an immune checkpoint controlling the retention of T_{reg} cells.

Soluble MAdCAM-1 is a strong prognostic factor of cancer patient responses

To investigate the clinical relevance of these findings, we first analyzed TIL infiltrates for the presence of enterotropic α4β7$^+$ T cells in fresh human tumors and ex vivo propagated TILs. The α4β7$^+$ fraction of T_{reg} and CD8$^+$ T cells represented up to 8.3 ± 2.1% and 24.5 ± 6.9%, respectively, expressed inhibitory receptors and could electively produce IL-17 (fig. S10, A and B). RORγt$^+$ FoxP3^{hi} cells represented 4.5 ± 0.8% of CD4$^+$ cells in TILs in expansion and expressed the enterotropic marker α4β7$^+$ (fig. S10C). On the basis of previous reports (*63*) and given the correlation between liver or ileal MAdCAM-1 and circulating sMAdCAM-1 levels in mice (fig. S9, I and J), we analyzed the clinical significance of serum sMAdCAM-1 at diagnosis in two independent cohorts of 115 and 187 patients with advanced NSCLC treated with anti–PD-1/PD-L1 antibodies (table S5). Patients treated with ABX exhibited lower sMAdCAM-1 levels than ABX-free patients (Fig. 7A). Baseline serum sMAdCAM-1 was a strong independent prognostic factor of survival in NSCLC patients who did not take ABX and to a lesser extent in those who took ABX before ICIs (Fig. 7B), with high baseline levels associated with prolonged overall survival and progression-free survival (Fig. 7C and fig. S10D). Low sMAdCAM-1 levels identified the subset of PD-1 antibody-refractory patients within PD-L1^{hi} (≥50%) NSCLC tumors (Fig. 7D and fig. S10E). Using multivariate Cox regression analysis that took clinical variables into consideration revealed that sMAdCAM-1 is an independent prognostic factor in NSCLC patients (table S5 and table S6). Neither tumor mutational burden nor MER4 retrotransposon elements correlated with sMAdCAM-1 levels (*64*) (fig. S10F). We validated the clinical significance of serum sMAdCAM-1 as a biomarker of overall survival in 212 metastatic renal cell

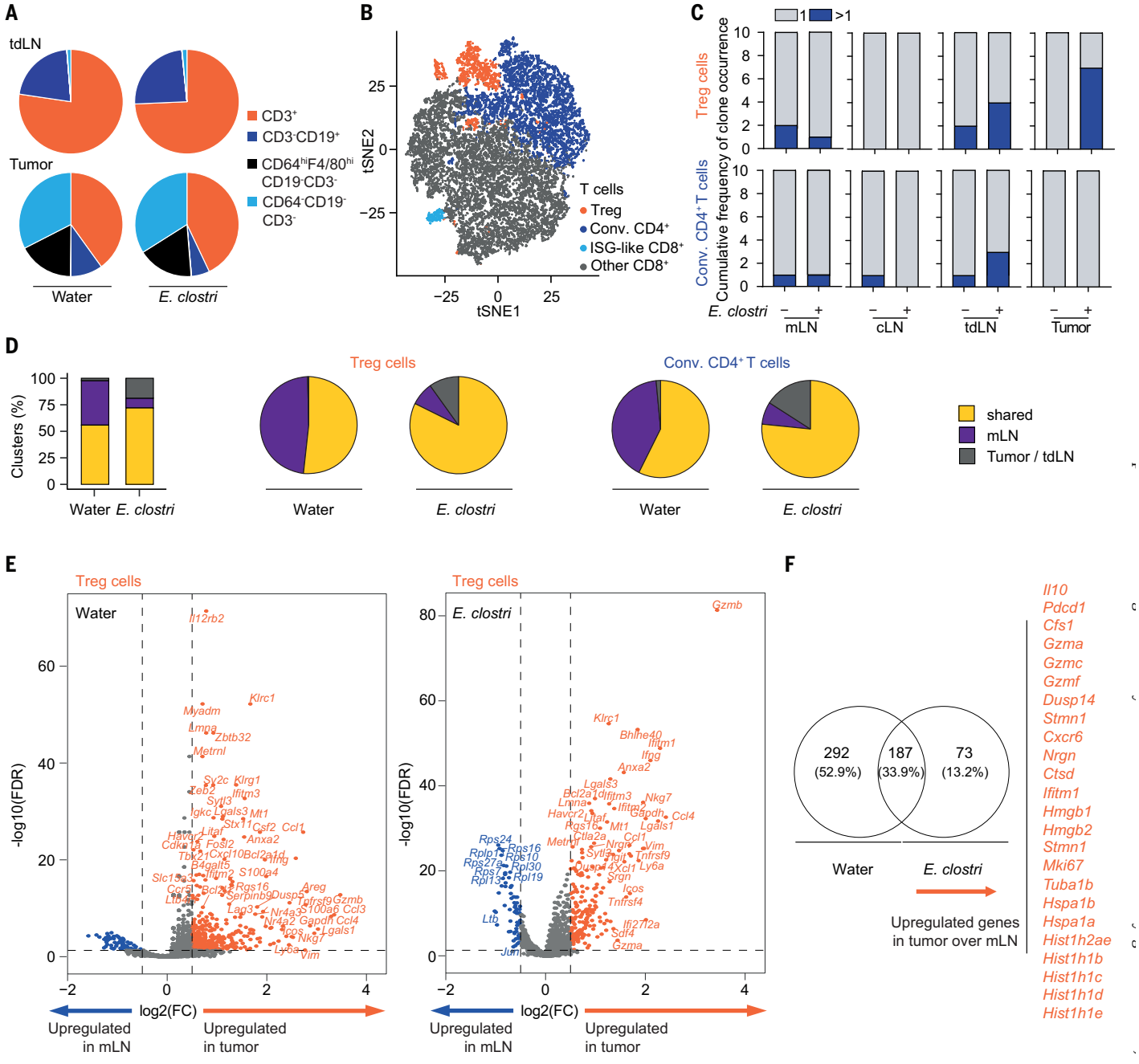


Fig. 4. Clonal and functional patterns of emigrating T_{reg} cells according to locations. (**A**) Single-cell sorting and RNA-seq in tumor bearers 11 days after MCA205 implantation using 10X Genomics technology to characterize phenotypic traits of CFSE$^+$ CD4$^+$ and CD8$^+$ T cell subsets emigrating from mLNs (CFSE injection at day 10) and reaching tdLNs, cLNs, or tumor beds, or recovered in mLNs after oral gavage with water or *E. clostridioformis* at day 5 and day 7. Determination of CFSE$^+$ mLNs cells emigrating from the gut to the tdLNs (top) or tumor beds (bottom) by flow cytometry, according to oral gavage with *E. clostridioformis*, depicted in proportions of all CFSE$^+$ cells. (**B**) Single-cell RNA-seq and cell clustering by mean of *t*-distributed stochastic neighbor embedding (tSNE) of CFSE$^+$ mLNs T cells recovered in mLNs, cLNs, tdLNs, and tumor bed 24 hours after inoculation of CFSE in mLNs according to transcriptomics patterns. (**C**) Single-cell TCR sequencing was performed on CFSE-stained lymphocytes sampled from the mLNs, cLNs, tdLNs, or the tumor. Clones were divided into fractions on the basis of their occurrence in the repertoire. Clones with an occurrence of one are represented in gray, and those with counts higher than one are shown in blue. The cumulative frequency of each fraction was calculated within the repertoire of each sample. Cumulative frequencies in FoxP3$^+$CD127$^-$ (top) and FoxP3$^-$ (bottom) CD4$^+$ T cells according to location are depicted. (**D**) TCRs from mLNs or pooled tumor and tdLNs (tumor/tdLNs) were clustered with DeepTCR, generating clusters of paired TRA-TRB clonotypes with shared specificities. Clusters were assigned as being mLNs (purple), tumor/tdLNs (gray), or shared (yellow) on the basis of the percentage of clonotypes composing them. Proportion of mLNs, tumor/tdLNs, and shared clusters in control (water) and *E. clostridioformis*–gavaged mice (left) and within T_{reg} and conventional CD4$^+$ T cells (middle and right). (**E**) Volcano plot of differentially expressed genes in CFSE$^+$ FoxP3$^+$ CD127$^-$ CD4$^+$ T cells in tumors versus mLNs (orange versus blue in *x* axis), in water-treated (left) versus *E. clostridioformis*–treated (right) groups (data S2). (**F**) Venn diagram comparing control and *E. clostridioformis*–treated groups for genes up-regulated in the tumor (versus mLNs), highlighting in orange only those up-regulated in *E. clostridioformis*–treated mice (data S2). Also refer to fig. S8A for detailed CD4$^+$ T cell phenotypes and subsets and to fig. S8, B, D, and E, for CD8$^+$ T cell counterparts. (A) depicts a pool of two independent experiments containing six mice per group. Sequencing data [(B) to (F)] were collected once.

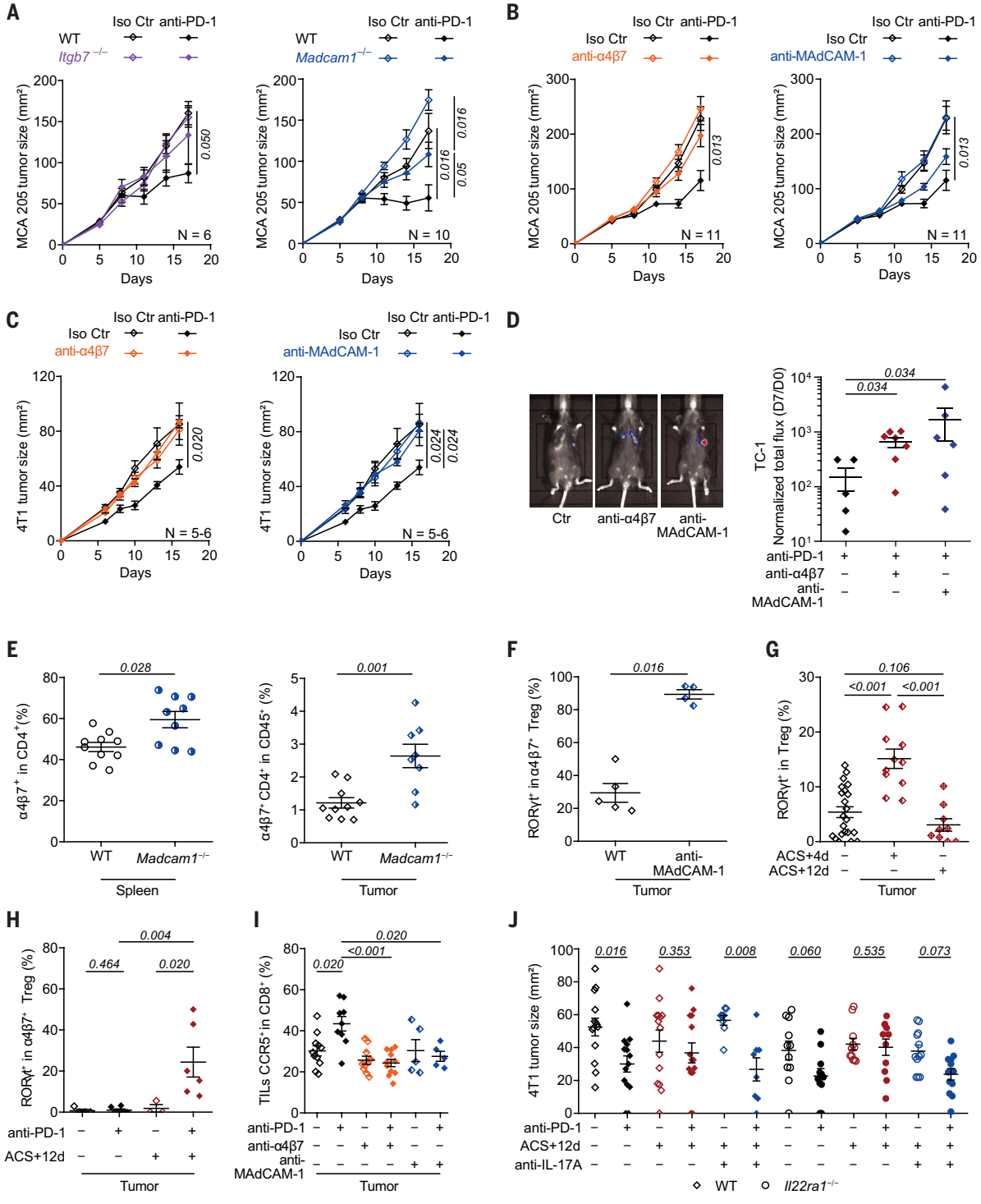


Fig. 5. Disruption of the MAdCAM-1–α4β7 axis induced maladaptive responses to anti–PD-1 Abs in mice. (**A**) Tumor growth kinetics of subcutaneous MCA205 (syngeneic of C57BL/6) implanted in WT versus *Itgb7*- or *Madcam1*-deficient mice. (**B** to **D**) Tumor growth kinetics or whole-body luminescence-based imaging after implantation of subcutaneous (s.c) MCA205 syngeneic of C57BL/6 (B), mammary 4T1 syngeneic of BALB/c (C), and orthotopic luciferase-expressing lung TC-1-luc cancer syngeneic of C57BL/6 (D) in animals treated with isotype control, anti–α4β7 mAb, or anti–MAdCAM-1 mAb while receiving anti-PD-1 therapeutic antibodies (or isotype control Abs). For D, ratios between pre– and post–PD-1 blockade with isotype control mAb, anti–α4β7 mAb, or anti–MAdCAM-1 mAb were calculated. Shown are means ± SEM of tumor sizes among five to six mice per group overtime in two treatment groups: anti–PD-1 versus isotype control Ab. (**E**) Flow cytometric analysis of α4β7 expression on $CD4^+$ T cell splenocytes and TILs in WT versus *Madcam1*-deficient mice. Each dot represents one mouse. (**F** to **H**) Intracellular flow cytometric analysis of RORγt expression in $\alpha4\beta7^+$ or total $CD25^+$ $FoxP3^+$ T_{reg} TILs in anti–MAdCAM-1 or isotype control Ab-treated mice (F) or in WT MCA205 tumor-bearing mice receiving the ACS conditioning regimen (ACS+4d or ACS+12d) treated or not with anti–PD-1 Abs (G and H). (**I**) Flow cytometric analyses of TILs for $CCR5^+$ $CD8^+$ effector T cells in subcutaneous MCA205 tumor-bearing mice treated with isotype control mAb, anti–α4β7 mAb, or anti–MAdCAM-1 mAb in the setting of PD-1 blockade.

(**J**) 4T1 WT or 4T1 *Il22ra1*$^{-/-}$ tumor cell lines were inoculated subcutaneously 3 days after starting ACS for 4 days. At ACS discontinuation (after 7 days), neutralizing anti–PD-1 and anti–IL-17A Abs (or isotype control Abs) were injected intraperitoneally five times every 3 days until day 12. Tumor sizes of subcutaneous 4T1 WT or 4T1 *Il22ra1*$^{-/-}$ tumors at euthanization. In each experiment, four or five anti–PD-1 intraperitoneal injections were administered every 3 days during the ACS+12d phase. Results from a representative experiment are depicted in (A) to (D), (F), and (H). Graphs in (E), (I), and (J) contain pooled data of two experiments. Each experiment comprised five to eight mice per group and was performed independently two to four times, leading to similar conclusions. Each dot represents one mouse. Comparisons between groups were analyzed using nonparametric Mann–Whitney *U* test (two groups) or Kruskal–Wallis *H* test (more than two groups), followed by multiple-comparisons test by controlling the FDR. Error bars indicate mean ± SEM.

carcinoma patients under second-line nivolumab (*65*) (Fig. 7E and table S5) and in 79 patients diagnosed with metastatic bladder cancer treated with durvalumab (anti–PD-L1) (*66*) (Fig. 7F and table S5).

To demonstrate the relationship between sMAdCAM-1 and gut dysbiosis in advanced NSCLC patients, we performed supervised hierarchical clustering of metagenomics species (MGS) defining the taxonomic composition of the intestinal microbiota using shotgun MG according to the median of sMAdCAM-1 serum levels (199 ng/ml) in 95 NSCLC patients (table S7). MGS richness and Shannon indices were reduced in sMAdCAM-1^{lo} (<median) compared with sMAdCAM-1^{hi} (greater than or equal to median) patients (Fig. 8A). Moreover, the gut composition diverged between sMAdCAM-1^{lo} versus sMAdCAM-1^{hi} patients, as indicated by the ANCOM-based beta-diversity (Fig. 8B). Supervised MG analysis revealed two clusters of MGS that were significantly different in relative abundance between the two patient groups (Fig. 8C). Low circulating sMAdCAM-1 levels were associated with an increase in MGS from the genus *Enterocloster* (*E. clostridioformis*), which reduced ileal *Madcam1* expression in mice (Fig. 1E), and *E. bolteae*; both of these species are associated with chronic inflammatory disorders including cancer (*30*, *31*) and poor prognosis in patients treated with immunotherapy (*10*) (Fig. 8D). Thus, sMAdCAM-1 is a surrogate marker of intestinal dysbiosis and is associated with patient overall survival in advanced bladder, lung, and kidney cancer.

Discussion

To decipher the mechanisms involved in the immunosuppressive effects of ABX, we studied the emigration of T cells from the gut to distal tumors. We found that the relocation of enterotropic and immunosuppressive $T_{reg}17$ cells to cancer-relevant compartments is at least partially controlled by the molecular interaction between MAdCAM-1 and α4β7. This demonstration follows prior evidence that gut-derived T_H17 cells control extraintestinal autoimmunity (*20*–*24*) and inflammation (*67*, *68*). $T_{reg}17$ cells harbor an exacerbated immunosuppressive phenotype compared with conventional T_{reg} cells (*26*). Recent intestinal $T_{reg}17$ emigrants found in tdLNs exhibit gut-specific T_{reg} cell features (*69*, *70*), T_H17 cell–related gene expression patterns (*71*), as well as immunosuppressive traits such as *Dusp2*/PCA1 (*47*) and *Pik3ip1* (*72*). In tumors or tdLNs, gut T cell emigrants shut down protein translation and acquire features of exhaustion or lytic functions, perhaps reflecting chronic TCR stimulation (*56*). These data collected in tumor-bearing hosts may be interpreted in the context of inflammatory bowel disease, in which the anti–α4β7 Ab vedolizumab increases the recirculation of extraintestinal α4β7$^+$ T_{reg} cells and central memory T_H17 cells (*73*–*75*). However, on the basis of our results, α4β7 neutralization may have undesirable systemic immunosuppressive effects in the context of intestinal dysbiosis. Thus, prospective studies should monitor circulating sMAdCAM-1 and α4β7$^+$ T_{reg}, $T_{reg}17$, and T_H17 cells in cancer patients treated with ICIs alone or in combination with FMT or vedolizumab to correlate these parameters with efficacy and toxicity.

Materials and Methods

Patient characteristics and clinical description

Medical centers and regulatory approvals for translational research

For feces and serum collection, ancillary studies were conducted at Gustave Roussy Cancer Campus (GRCC), France according to the ethical guidelines and approval of the local Committees for the Protection of Persons in Biomedical Research (CCPPRB). The ONCOBIOTICS trial (www.clinicaltrials.gov, NCT04567446, ID-RCB no. 2017-A02010-53), a multicentric prospective observational study, was designed to evaluate the impact of the microbiome composition in the clinical outcome of patients with advanced NSCLC treated with anti–PD-(L)1 (*10*). We enrolled patients across 12 academic centers in France and two centers in Canada. Adult patients with pathologically confirmed advanced nonsquamous or squamous NSCLC and an Eastern Cooperative Oncology Group (ECOG) performance status score of 0 to 2 amenable to ICI as standard of care and willing to provide a stool sample were eligible. Eligible patients received ICI after progression on platinum-based chemotherapy regimens either with nivolumab or atezolizumab regardless of PD-L1 expression or with pembrolizumab if PD-L1 ≥ 1%. Given the subsequent approval of first-line ICI during the study accrual period, patients who received pembrolizumab monotherapy or in combination with platinum-based chemotherapy, depending on PD-L1 expression, were also included. Standard of care treatment was continued until disease progression, unacceptable adverse effects, or completion as per protocol (2 years of ICI). Full eligibility criteria are listed in the trial protocol (available at www.clinicaltrials.gov, NCT04567446). Baseline characteristics, including a detailed listing of concurrent medications received over the past 2 months before ICI initiation and the date of last follow-up, were entered at each center in an electronic case report form. Feces were collected according to the International Human Microbiome Standards (IHMS) guidelines (SOP 03 V1) before the first injection. Serum samples were prospectively collected after prior anti–PD(L)1 immunotherapy within the Gustave Roussy Cancer Campus–sponsored PREMIS study (www.clinicaltrials.gov, NCT03984318). Patients enrolled in PREMIS were ≥18 years of age, with histologically proven solid malignancy and at least one tumor evaluation by imaging after immunotherapy onset. The PREMIS study was approved by an ethical committee (Comité de Protection des Personnes Sud-Ouest et Outre Mer I; ID-RCB: 2018-A01257-48) and the institutional review board (CSET no. 2018/2728). All enrolled patients provided a signed informed consent. Furthermore, we disposed of one cohort of 45 patients with NSCLC receiving treatment with anti–PD-1/PD-L1 checkpoint inhibitors between 2014 and 2020. Patients were treated in the Georges François Leclerc Cancer Center. For all patients, abundance of transcripts from RNA-seq data was available, and for some patients, PD-L1 protein expression in tumor cells assessed using immunohistochemistry was also available, as well as tumor mutational burden estimated from whole-exome sequencing. We had access to a cohort of patients with advanced renal cell carcinoma treated with an anti–PD-1 enrolled in the NIVOREN trial (www.clinicaltrials.gov, NCT03013335; EudraCT: 2015-004117-24). Finally, an additional cohort of patients with bladder cancer treated with an anti–PD-(L)1 alone or together with anti–CTLA-4 and enrolled in the IOPREDI study (EudraCT 2016-005068-33) was studied. For tumor flow cytometric analyses of fresh or cultivated TILs, all tumor tissues were processed according to the Helsinki Declaration and the guidelines of the French ethics Committee for Research on Human Tissues. Tissue biocollection was registered with the French Ministry for Higher Education and Research (DC-2014-2206) with approval from the ethics committee (CPP Ouest IV, Nantes).

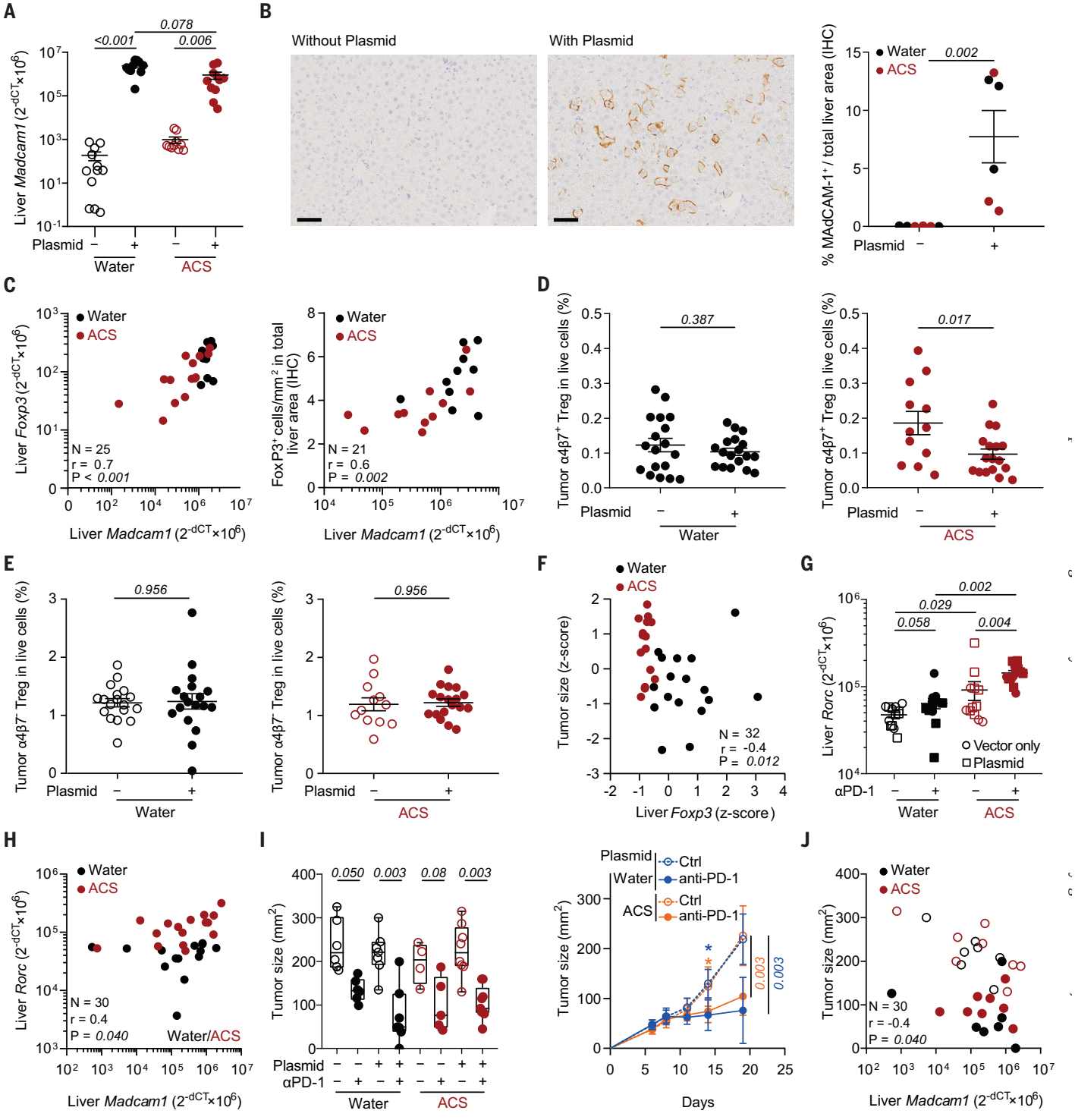


Fig. 6. Interception of immunosuppressive T cells by transfection-enforced overexpression of MAdCAM-1 in the liver. The experiment involved rapid hydrodynamic intravenous injection of *Madcam1*-encoding cDNA subcloned into a pLIVE plasmid vector (plasmid+) or vector alone (plasmid−) into day 5 tumor-bearing mice preconditioned with ACS for 3 to 4 days (or with water from day −3 to day +5) and treated [(G) to (J)] or not [(A) to (F)] with four intraperitoneal inoculations of anti–PD-1 Ab from day 6 to day 14. (**A** and **B**) Liver expression of *Madcam1* mRNA (A) or MAdCAM-1 protein (B) as assessed by RT-qPCR (A) or immunohistochemistry (IHC) (B) according to plasmid inoculation and ACS treatment. One representative micrograph is shown for immunohistochemistry [(B), left]. Scale bar, 40 μm. (**C**) Spearman's correlations between liver *Foxp3*/FoxP3 in RT-qPCR (left), immunohistochemistry (right), and *Madcam1* mRNA (RT-qPCR) relative expression in plasmid-treated mice. (**D** and **E**) Flow cytometric analysis of $\alpha4\beta7^+$ (D) or $\alpha4\beta7^-$ (E) T_{reg} cells in water or ACS-treated mice according to *Madcam1*-encoding cDNA plasmid injection (or control vector). Shown are concatenated mean ± SEM percentages of stained T cells. (**F**) Spearman's correlation between liver *Foxp3* in RT-qPCR after normalization of relative expression (*z* score), and tumor size at euthanization (day 14). (**G** and **H**) Liver expression of *Rorc* and *Madcam1* relative gene expression in RT-qPCR according to PD-1 blockade and *Madcam1*-encoding cDNA

plasmid injection (or control vector) as well as ACS (or water). (H) Spearman's correlation between liver *Rorc* and *Madcam1* relative gene expression in RT-qPCR in plasmid-treated mice. (**I** and **J**) Tumor size in MCA205-bearing animals treated with anti–PD-1 Abs in water or ACS-treated mice according to *Madcam1*-encoding cDNA plasmid injection (or control vector) [(I), left]. Tumor growth kinetics in MCA205-bearing animals treated with anti–PD-1 Abs with or without ACS in animals inoculated with the vector alone or the *Madcam1*-encoding cDNA plasmid [(I), right]. (J) Spearman's correlation between liver *Madcam1* relative expression in RT-qPCR and tumor size at euthanization (day 19) in plasmid-treated mice. Except for (B), which shows a representative experiment, graphs depict the data pooled from two independent experiments containing six to 10 mice per group. Each dot represents one mouse. Black and red dots represent water- and ACS-treated animals, respectively. Comparisons between groups were analyzed using nonparametric Mann–Whitney *U* test (two groups) or Kruskal–Wallis *H* test (more than two groups) followed by multiple-comparisons test for controlling the FDR and nonparametric Spearman's correlations. Error bars indicate means ± SEM.

Each patient included in this study signed an informed consent form. For the four fresh NSCLC tumors examined by flow cytometry, ≥18-year-old patients from Gustave Roussy Cancer Campus, Marie Lannelongue, Cochin, Tenon, Foch, Kremlin-Bicêtre, and Saint Joseph hospitals with primary resectable tumors provided written informed consent according to the protocols reviewed and approved by institutional ethics committee, including the investigator-sponsored, study "mAb in sitro test" (ID-RCB: 2016-A00732-49). The experiments conformed to the principles set out in the Declaration of Helsinki and the Department of Health and Human Services Belmont Report. For collection of endoscopic and blood samples, a clinical study, "Einfluss von Antibiotika auf das Darm-Chemokinnetzwerk bei Patienten mit soliden Tumoren," was conducted at University Clinics Heidelberg, Germany, according to the ethical guidelines and approval of the Regierungspräsisium Karlsruhe.

Collection of endoscopic samples and blood samples

Eligible patients underwent ileocolonoscopy according to clinical standard protocols for non-study-related indications (table S2) between July 2018 and November 2019. When feasible, endoscopic biopsies of the mucous membranes of the terminal ileum, cecum, and right and left colons were performed in each patient. Tissue samples were either snap frozen in liquid nitrogen and stored at −80°C or immersed into 2% paraformaldehyde (PFA) for histology. In addition, two blood samples (10 ml in EDTA tubes) were collected before ileocolonoscopy. All included patients responded to a questionnaire to assess dietary history, and baseline clinical data were retrieved from the local clinical information system.

Metagenomic analysis of patient stools

Fecal samples were prospectively collected at different time points (V1, before ICI; V2, before the second ICI injection; V3, 3 months after ICI; and V4, 6 months after ICI) at each center following the International Human Microbiome Standards (IHMS) guidelines, but only the baseline V1 sample was considered for this analysis. For metagenomic analysis, the stools were processed for total DNA extraction and sequencing with Ion Torrent technology following MetaGenoPolis (INRAE) France, as previously reported (*7*, *10*, *11*). The gene abundance table was processed using the MetaOMineR (momr R) package. We conducted PERMANOVA using the function adonis from the vegan R package (v2.5-7) with the Atchinson distance on centered log ratios using species-level abundances and 1000 permutations. We used an ensemble of univariate and multivariate differential abundance methods that included age, gender, and cohort in the models, using either species-level relative abundances or count data, where absolute raw counts were estimated from species-level relative abundances by multiplying these values by the total number of reads for each sample. These differential abundance methods included; DESeq2 (v.1.30.0) (*76*) with the poscounts estimator (DESeq2_poscounts); DESeq2 with the poscounts estimator and a zero-inflated negative binomial model (DESeq2_poscounts_zb); DESeq2 with trimmed mean of M values (TMM; DESeq2_TMM); limma (v3.46.0) (*77*) with TMM values (limma_voom_TMM); limma with TMM values and a zero-inflated negative binomial model (limma_voom_TMM_zb); ANCOM-BC (v.1.0.1) (*78*); and Maaslin2 (v.1.4.0) (*79*) and LeFsE (*80*).

sMAdCAM-1 quantification in patients

sMAdCAM-1 was quantified in patient sera with the Bio-Plex 200 systems (Bio-Rad) and sMAdCAM-1 kit from R&D Systems (Human Luminex Discovery Assay LXSAHM).

Cell culture, reagents, and tumor cell lines

MCA205 fibrosarcoma cells (syngeneic from C57BL/6 mice) and 4T1 WT and 4T1-*Il22ra1*$^{-/-}$ breast cancer cell lines [syngeneic from BALB/c, kindly provided by Dr. S. Kobold (*57*), LMU Klinikum, Germany] were cultured at 37°C in the presence of 5% CO_2 in RPMI 1640 containing 10% fetal calf serum (FCS), 2 mM L-glutamine, 100 IU/ml penicillin–streptomycin, 1 mM sodium pyruvate, and minimum essential medium nonessential amino acids (henceforth referred to as complete RPMI 1640). Luciferase-transfected TC-1 cell lines syngeneic for C57BL/6 mice [kindly provided by E. Deutsch, GRCC] were cultured at 37°C in the presence of 5% CO_2 in complete RPMI 1640 and 1 mM Hepes buffer. Cell lines were regularly tested for mycoplasma contamination and were not used after 10 passages.

Mice

All animal experiments were performed in compliance with French and European laws and regulations. The local institutional animal ethics board and French Ministère de la Recherche approved all mouse experiments (permission numbers: 2016-049-4646, 2017_049_99741, 2019_036_21124, and 2022_064_40164). Experiments were performed in accordance with Government and institutional guidelines and regulations. Female C57BL/6 and BALB/c mice were purchased from Harlan or Envigo (France). Mice were used between 7 and 12 weeks of age. *Madcam1*$^{-/-}$ and *Itgb7*$^{-/-}$ mice were a kind gift from A. Schippers (University Hospital Aachen, Aachen, Germany). *Madcam1*$^{-/-}$ and *Itgb7*$^{-/-}$ mice and control littermates were backcrossed on the C57BL/6 background and were obtained from an in-house breeding at the local animal care facility at the University Hospital Aachen. The Kaede mice were a kind gift from M. Tomura (Kyoto University, Kyoto, Japan) and were backcrossed and maintained on the C57BL/6 background. All mouse experiments were performed at the animal facility at the GRCC, where animals were housed in SPF conditions.

Antibiotic treatments

If not otherwise indicated, mice were treated with a broad-spectrum ABX solution containing ampicillin (1 mg/ml), streptomycin (5 mg/ml), and colistin (1 mg/ml) (Sigma-Aldrich) (ACS) added to sterile drinking water. In experiments in which single antibiotics were used, the concentrations were identical as stipulated above for ampicillin (A), colistin (C), or streptomycin (S), and were 1 mg/ml for erythromycin, 0.25 mg/ml for vancomycin, 6.15 mg/ml for ceftazidime, 4.1 mg/ml for cefepime, 16.4/2.05 mg/ml for piperacillin/tazobactam, and 1.13 mg/ml for rifaximin. Solutions and bottles were changed three times weekly. In the experiments in which the antibiotic mixture was used, antibiotic activity was confirmed by cultivating fecal pellets for 48 hours at 37°C in aerobic and anaerobic conditions. To evaluate the impact of antibiotics on MAdCAM-1 expression in the intestine, ACS were administered during 7 to 14 days and discontinued for 4 days (ACS+4d) or for 12 days (ACS+12d) or were continued until the end of the experiment in the drinking water of naive or MCA205 tumor-bearing mice.

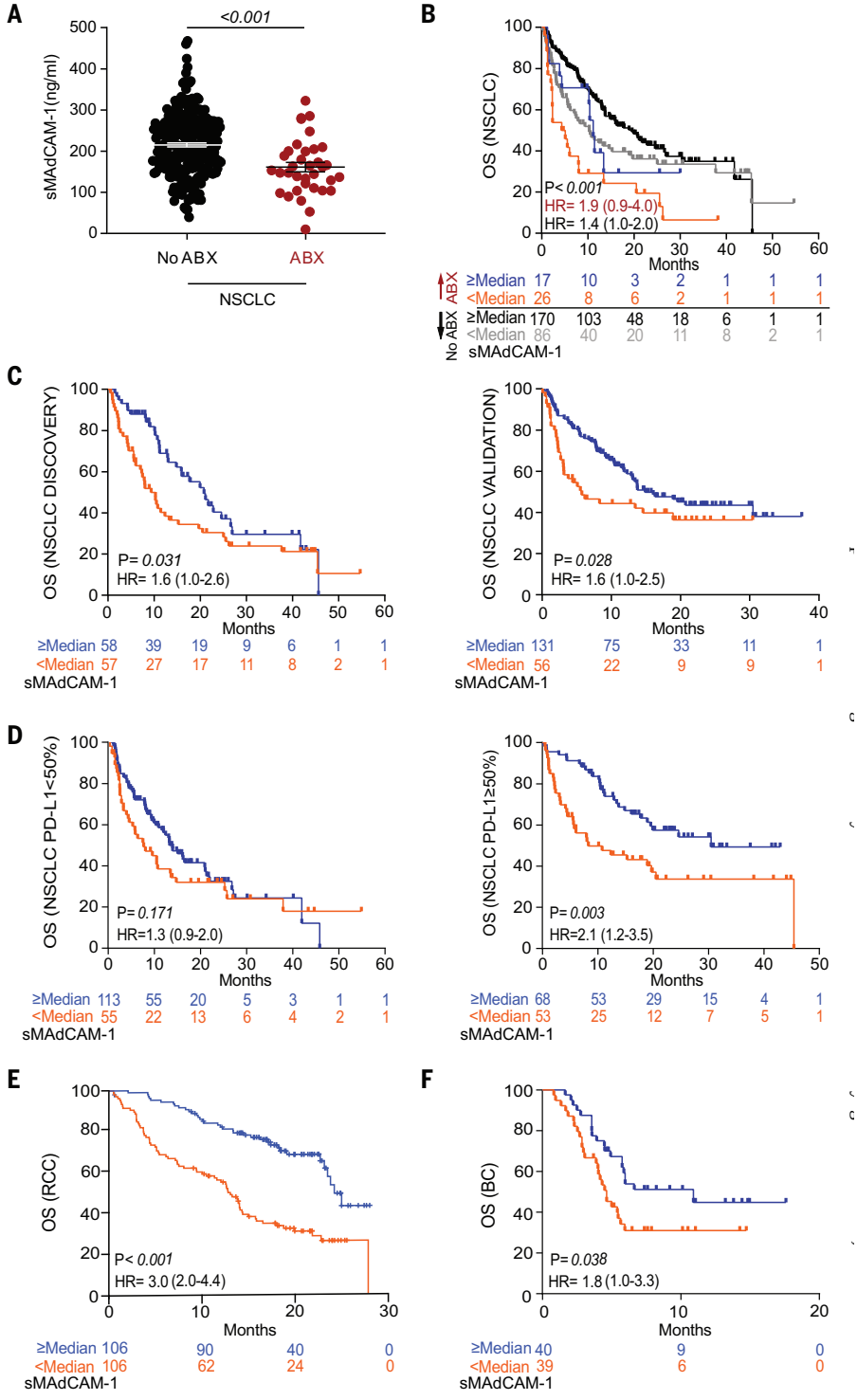


Fig. 7. Serum-soluble MAdCAM-1 is a robust prognosis parameter in cancer patients. (**A**) Luminex immunoassay monitoring of serum levels of sMAdCAM-1 in 299 NSCLC patients belonging to two independent cohorts according to history of recent ABX uptake (tables S5 and S7). Each dot represents one patient's serum. Error bars represent means ± SEM. (**B** to **D**) Overall survival (OS) analysis using the Kaplan Meier estimator and Cox regression to assess the prognostic value of serum levels of sMAdCAM-1, split using the median of the NSCLC patient discovery cohort amenable to PD-1 blockade, according to ABX uptake history (B). This cut-off determined from the discovery cohort allowed us to split the patients into two groups of different prognosis in the validation cohort (C). (D) Idem as in (C) combining both cohorts of NSCLC and segregating patients according to tumor PD-L1 expression and the cut-off value of sMAdCAM-1 (median of the discovery cohort) (see table S5 for patient descriptions, table S6 for multivariable analysis, and fig. S10, D and E, for progression-free survival). (**E**) Same as in (C) but overall survival in 212 in second- or third-line metastatic renal cell carcinoma (RCC) patients amenable to nivolumab. (**F**) Same as in (C) but overall survival in 79 patients diagnosed with metastatic bladder cancer (BC) treated with durvalumab (anti–PD-L1). Kaplan–Meier overall survival curves were generated, and hazard ratios (HRs) are indicated.

FMT experiments

In FMT experiments, mice received 3 to 7 days of ACS before undergoing FMT the next day by oral gavage. FMT was performed by thawing fecal material. Mice were placed in a new cage after the procedure. Two hundred microliters of the suspension was then transferred by oral gavage into each ACS-pretreated recipient using animal-feeding needles. In addition, another 100 µl was applied to the fur of each animal.

Oral bacterial gavage with commensal species

Akk. p2261 was provided by everImmune (Villejuif, France). *E. hirae* 13144 isolates were originally isolated from spleens or mLNs of SPF mice treated with cyclophosphamide at GRCC. *E. clostridioformis* was isolated from the ileum of mice that received ACS in drinking water for 7 days followed by 4 days ABX-free at GRCC. *Akk.* p2261, *E. clostridioformis*, and *L. reuteri* were grown on Columbia agar with 5% sheep blood (COS) plates in an anaerobic atmosphere created using three anaerobic generators (Biomerieux) at 37°C for at least 72 hours. *E. hirae*

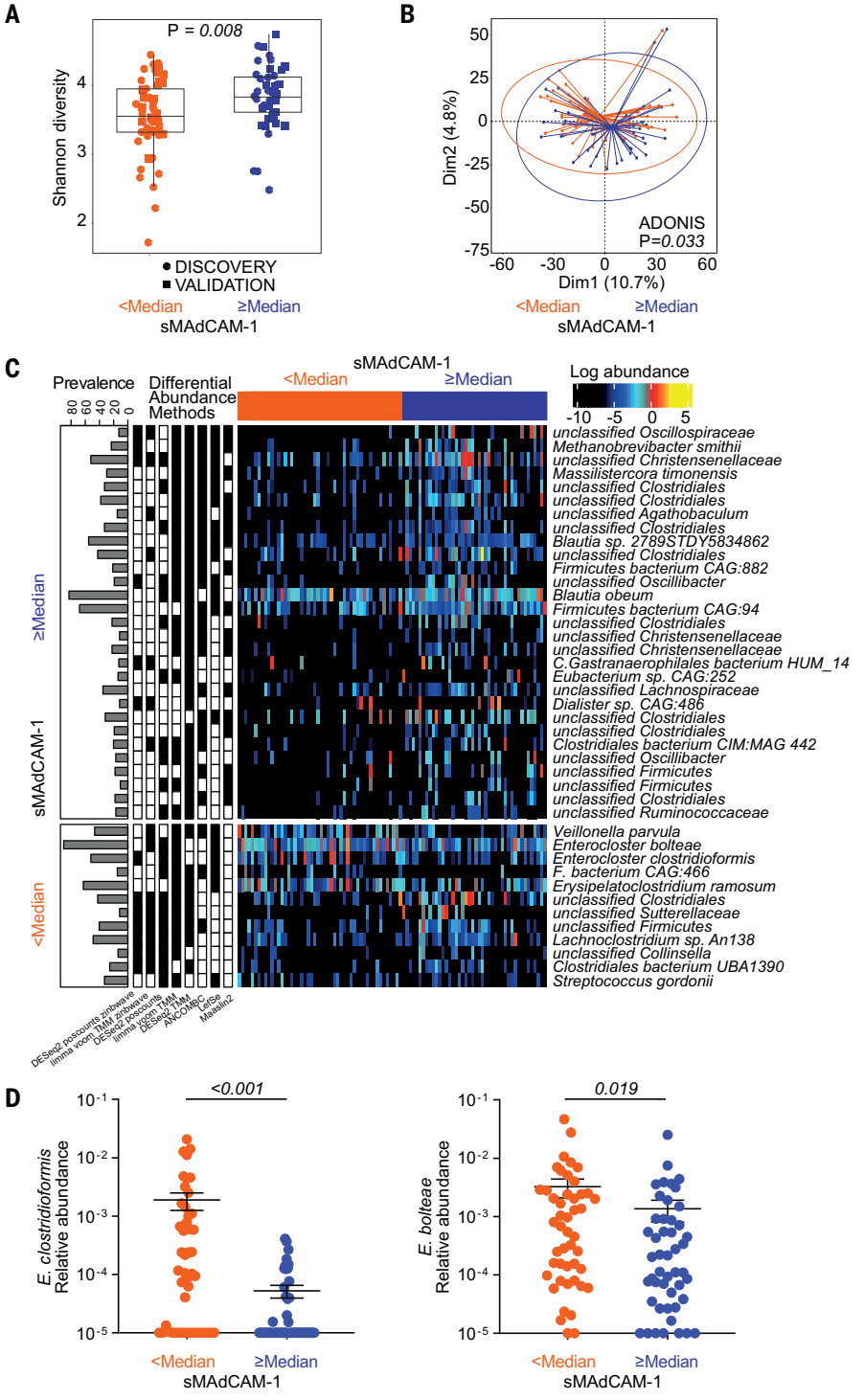


Fig. 8. Serum sMAdCAM-1 is a proxy for gut dysbiosis. (**A** and **B**) Alpha (A) and beta (B) diversity of the taxonomic content of the intestinal microbiota according to the serum sMAdCAM-1 levels in 95 NSCLC patients. (A) MGS Shannon diversity evaluation in shotgun MG sequencing according to the median of sMAdCAM-1 in the whole population composed of 95 NSCLC patients (refer to table S7 for patient description). The *P* value was calculated by a Wilcoxon test blocking for cohort. (B) Principal-component analysis of species-level centered log-ratio–transformed relative abundance. The *P* value was calculated using ADONIS and 999 permutations. (**C**) Differentially abundant species according to sMAdCAM-1 serum levels (<, low; ≥, high according to median) color coded according to the relative abundance of each species detected by at least three different methods. (**D**) Relative abundances of two distinct species from the genus *Enterocloster*, categorizing the patients according to the median of sMAdCAM-1. Each dot represents each patient's stool. Comparisons between groups were analyzed using the nonparametric Mann–Whitney *U* test (two groups). Error bars indicate means ± SEM.

13144 was grown in 5% sheep blood enriched Columbia agar for 24 hours at 37°C in aerobic conditions. Colonization of SPF C57BL/6 mice was performed by oral gavage with 100 µl of suspension containing 1×10^8 to 1×10^9 bacteria. Bacteria concentrations were calculated using a fluorescence spectrophotometer (Eppendorf) at an optical density of 600 nm in 0.9% NaCl. Mice were gavaged one to four times. In applicable experiments, oral gavages were performed concomitantly with anti–PD-1 Ab treatment four times. The identification of specific bacteria was accomplished using a matrix-assisted laser desorption/ionization–time-of-flight (MALDI-TOF) mass spectrometry (Brucker, France).

Oral gavage with biliary acids

Mice were gavaged four times every 2 days with 120 mg/kg body weight LCA (ThermoFisher Scientific, 229090050) or UDCA (Delursan, Teva Santé) diluted in corn oil.

Subcutaneous cancer mouse models

MCA205 sarcoma and 4T1 WT and Il22ra1$^{-/-}$ breast cancer

Syngeneic C57BL/6 mice were implanted with 0.8×10^6 MCA205 sarcoma cells subcutaneously and treated intraperitoneally when tumors reached 20 to 40 mm^2 in size with anti–PD-1 mAb (250 µg/mouse; clone RMP1-14) or isotype control (clone 2A3). Syngeneic BALB/c mice were implanted with 0.5×10^5 4T1 WT or *Il22ra1*$^{-/-}$ breast cancer cells subcutaneously and treated intraperitoneally with anti–PD-1 or isotype control mAbs. Mice were injected four times at 3-day intervals with anti–PD-1 (Bio X Cell, clone RPMI-14, 250 µg per mouse) or isotype control (Bio X Cell, clone 2A3, 250 µg per mouse) mAbs. Tumor length and width were routinely monitored three times a week by means of a caliper. In experiments using anti-α4β7 mAb (DATK32, 200 µg per mouse), anti–MAdCAM-1 mAb (MECA-367, 200 µg per mouse), or their isotype controls (clone 2A3 in both cases), monoclonal Abs were injected intraperitoneally every 3 days starting from day 0 until the final anti–PD-1 injection. In the experiment using anti–IL-17A mAb (clone IL-17F, 100 µg per mouse), mice were injected intraperitoneally concomitantly with anti–PD-1 treatment. All antibodies were purchased from Bio X Cell. In the experiment using anti-CD62L or anti–PSGL-1 mAbs (clones Mel-14 and 4RA10, respectively, 100 µg per mouse), mice were injected intraperitoneally concomitantly with anti–MAdCAM-1 treatment.

Orthotopic luciferase engineered-TC-1

C57BL/6 mice were anesthetized with isoflurane. Under sterile conditions, a lateral incision was made on the chest wall of each mouse, and 6×10^5 TC-1-Luc cells in 10 µl of Matrigel

(Corning) were injected into the lung. The skin incision was closed with a surgical skin clip. To monitor tumor growth twice weekly, mice received a percutaneous injection of luciferase substrate (beetle luciferin, potassium salt; Promega) at a dose of 150 mg/kg body weight. Eight minutes after luciferin inoculation, photons were acquired on a Xenogen IVIS 50 bioluminescence in vivo imaging system (Caliper Life Sciences Inc., Hopkinton, MA, USA).

Construction of liver-specific overexpression vector

The plasmid pLIVE vector was purchased from Mirus (catalog no. MIR 5420, Madison, WI, USA), and Madcam1 (NM_013591) mouse-tagged ORF clone from OriGene (catalog no. MR226268, Rockville, MD, USA). pLIVE vector, which is designed for liver-specific expression and uses a chimeric promoter composed of the mouse minimal albumin promoter and the mouse alpha fetoprotein enhancer II, was selected to construct the liver-specific Madcam1 overexpression vector.

The gene encoding mouse Madcam1 was amplified from Madcam1 (NM_013591) mouse tagged ORF clone (pCMV6-Entry-Madcam1) with primers listed below by RT-PCR with OneTaq hot start DNA polymerase (catalog no. M0481, NEB, Ipswich, MA, USA). For more effective expression of Madcam1, Kozak sequences (underlined) were selected and added in forward primer (Madcam1-F-Kozak: 5′-GGCGCGCCGCCACCATGGAATCCATCCTGGCC-3′; Madcam1-R:5′-CTCGAGTCATAGGTGTGT ACATGAGC-3′). The Madcam1 cDNA was then cloned into the AscI and Xho I sites of the pLIVE vector, yielding the pLIVE-Madcam1 plasmid. The large amount of vector DNAs were prepared by an PureLink expi endotoxin-free maxi plasmid purification kit (catalog no. A31231, Invitrogen, Carlsbad, CA, USA) for further hydrodynamic tail vein injection.

Generation of a liver-specific overexpression mouse model

Six-week-old female WT C57BL/6 mice were purchased from Envigo (Huntingdon, UK). All mice were maintained in a temperature-controlled and pathogen-free environment with 12-hour light–dark cycles with food and water ad libitum. The constructs of pLIVE as a control and pLIVE-Madcam1 vector DNA (250 μg per mouse) were delivered to the mouse liver using the hydrodynamic tail vein injection procedure by using the TransIT-QR hydrodynamic delivery solution (catalog no. MIR 5240, Mirus, Madison, WI, USA) according to the manufacturer's instructions.

Flow cytometry

Mouse

Tumors, mLNs, tdLNs, cLNs, ilea, and spleens were harvested at different time points as indicated in the individual experiments. Excised tumors were cut into small pieces and digested in RPMI medium containing Liberase at 25 μg/ml (Roche) and DNase1 at 150 IU/ml (Roche) for 30 min at 37°C, and then crushed and filtered twice using 100-μm and 70-μm cell strainers (Becton & Dickinson). Lymph nodes and spleens were crushed in RPMI medium and subsequently filtered twice through a 100-μm cell strainer. Ilea were collected and fat tissue, Peyer's patches, and feces were removed. Intestines were cut longitudinally and then cut transversally into small pieces into a tube. Pieces were transferred into a new 50-ml tube with 20 ml of IEC washing medium [phosphate-buffered saline (PBS), 5% FCS, 5 mM EDTA, and 1 mM dithiothreitol), vortexed, and shaken at 37°C for 20 min. Tissue and cell suspension were filtered with a cell strainer (100 μm). The filtered cell suspension was discarded. The remaining tissue was incubated for 30 min in LPC medium (RPMI, 5% FCS, 0.25 mg/ml collagenase VIII, and 10 U/ml of DNAse I) and then dissociated through a 100-μm cell strainer. The cells obtained from the lamina propria in cell suspension were washed twice with PBS and kept on ice for subsequent analysis. Four million cells from each sample were preincubated with purified anti-mouse CD16/CD32 (clone 93; eBioscience) for 30 min at 4°C before membrane staining. For intracellular staining, the FoxP3 staining kit (eBioscience) was used. Dead cells were excluded using the Live/Dead Fixable Yellow dead cell stain kit (Life Technologies) or LIVE/DEAD Fixable Aqua Dead Cell Stain Kit (Biolegend). For IL-17 and IL-22 staining, cells were stimulated at 37°C during 4 hours with phorbol 12-myristate 13-acetate (PMA)/ionomycin and Golgi stop cocktail. Information on the antibodies used to stain murine cells is found in table S8. Stained samples were acquired on CytoFLEX S 13 colors (Beckman Coulter), and analyses were performed with Kaluza software 2.1 (Beckmann Coulter). T_H17 cell gating depended on the mouse model that was used. The Kaede fluorochrome could not retain its photoconverted state upon fixation with PFA. For Kaede mice, T_H17 cells were identified as $CXCR3^-$ and $CCR6^+$ $CD4^+$ T cells and T_{regs} as $CD127^-CD25^{hi}$ $CD4^+$ T cells. In other mouse models, T_H17 and $T_{reg}17$ cells were defined after gating on $ROR\gamma t^+$ $CD4^+$ or $ROR\gamma t^+$ and/or $IL\text{-}17A^+$ $CD25^+$ $FoxP3^+$ $CD4^+$ cells, respectively.

Human

Information on the antibodies (clones, sources, and concentrations) used to stain human cells is provided in table S9. For IL-17 and IL-22 staining, cells were stimulated at 37°C for 4 hours with PMA, ionomycin, and brefeldin A (Invitrogen, catalog no. 00-4975). Dead cells were excluded using the LIVE/DEAD Fixable Aqua Dead Cell Stain Kit (Biolegend). Stained samples were acquired on BD LSRFortessa X-20 Cell Analyzer and analyzed with FlowJo v10.8.1 software.

Immunohistochemistry and quantification of MAdCAM-1 in ilea

Mice ilea "Swiss rolls" were prepared from the experiments and fixed in buffered formalin for 24 to 48 hours and then sent for conventional histological processing. For morphological analysis, hematoxylin, eosin, and saffron staining (HES) slides were generated. Bond Leica automated immunostainer instruments were used to perform immunohistochemistry. Three-micrometer-thick paraffin sections were processed for heat-induced antigen retrieval (ER2 corresponding EDTA buffer, pH 9) for 20 min at 100°C. Slides were incubated with the antibody for 1 hour at room temperature. For MAdCAM-1 staining, slides were incubated with MAdCAM-1 antibody (Abcam, AP-MAB0842, rat, 1:100) for 1 hour at room temperature. Slides were incubated with a Polink rat kit as secondary antibodies and revealed with diamino-benzidine-peroxidase (DAB, ThermoFisher, ready for use solution, 1 ml), after incubation for 5 min at room temperature.

For image analysis and MAdCAM-1 quantification, QuPath software was used (*81*). ROIs were defined first by "simple tissue detection" function and modified by hand in each whole slide image (WSI). To quantify the cell density of biomarker-positive cells, "Positive cell detection" was used.

Histological processing of MAdCAM-1–expressing liver

Murine livers were obtained from the experiments and fixed in buffered formalin for 24-48 hours and then cut vertically in parallel sections, which were sent for conventional histological processing. For morphological analysis, hematoxylin, eosin, and saffron staining (HES) slides were generated. Bond Leica automated immunostainer instruments were used to perform immunohistochemistry. Three-micrometer-thick paraffin sections were processed for heat-induced antigen retrieval (ER2 corresponding EDTA buffer, pH 9) for 20 min at 100°C. Slides were incubated with the antibody for 1 hour at room temperature. The following antibodies were used: anti-FoxP3 (Cell Signaling Technology, D608R, rabbit, 1:200, ER2) and anti-RORγt (Abcam, EPR20006, rabbit, 1:3000, ER2). The antibodies were detected with DAB (ThermoFisher, ready-for-use solution, 1 ml), after incubation for 5 min at room temperature. Finally, the sections were counterstained by hematoxylin (Leica Biosystems).

Quantification of FoxP3 and MAdCAM-1 in MAdCAM-1–expressing liver

Images for analysis were acquired as WSIs with a slide scanner (Zeiss Axio Scan.Z1) and

Olympus VS120 whole-slide imaging system. Image analysis was performed using QuPath, version 0.3.2 (*81*). WSI for FoxP3 were evaluated through multiple steps: (i) simple tissue detection was performed (threshold 220, requested pixel size 20 μm, minimum area 100,000 μm^2, max fill area 100,0000 μm^2, smooth image, cleanup with median filter, smooth coordinates, single annotation); (ii) fast cell counts (cell detection channel DAB, Gaussian sigma 1.5 μm, background radius 15 μm, use difference of Gaussians, cell detection threshold 0.5, DAB threshold 0.5); (iii) exclusion of detections corresponding to artifacts (folded tissue, dark pigment sedimented, hemorrhage, intravascular lymphocytes) was performed by a pathologist (L.L.); (iv) create density map; and (v) select the region of interest (ROI) with 1 mm^2, representing the highest density in the tissue (hotspot). Hotspot density was then normalized for each experiment based on the control group, and then pooled (n = 2). WSIs for RORγt were evaluated for hotspot compared with the same ROI as indicated for FoxP3. The RORγt$^+$ nuclei were then counted manually, based on morphology, because many nuclei from hepatocytes were also stained in some of the evaluated conditions.

Tracing migration of leukocytes from the gut to the TME

Kaede experiments

Kaede transgenic mice were anesthetized with 2 to 2.5% isoflurane and administered buprenorphine (0.01 mg/kg body weight) intraperitoneally for analgesia. For photoconversion of ilea, abdominal skin and peritoneum were cut at the midline to access the intraperitoneal terminal ileum. For photoconversion of the cecum, ileum, and mLNs, the cecal pole was first identified. Then, the cecal pole, including the terminal ileum, the mLNs, and proximal colon, was gently mobilized through the midabdominal incision onto a sterile plastic-coated surgical drape. Nontarget structures were covered with aluminum foil. The ventral and dorsal parts of the targeted structures were exposed to ultraviolet light emitted from a 395-nm wavelength emitting diode (Winzwon) light for 30 s each. After illumination, the tissue was moistened with sterile isotonic sodium chloride and gently repositioned into the peritoneal cavity. The peritoneal membrane was closed by continuous stitch with a 5-0 monofil nylon suture (Ethicon). The skin was closed with two 9-mm wound clips (EZ Clip Kit).

CFSE staining of mLN cells up to TME or tdLNs

C57BL/6 mice were anesthetized with 2 to 2.5% isoflurane and administered buprenorphine (0.01 mg/kg body weight) intraperitoneally for analgesia. Abdominal skin and peritoneum were cut at the midline to access the mLNs. The mLNs were gently mobilized through the midabdominal incision onto a sterile plastic-coated surgical drape. Ileum draining mLNs were visually identified according to their vasculature. The two most prominent mLNs were injected with 100 μM CFSE diluted in 5 μl of PBS using a 30-Ga insulin syringe. After repositioning the mLNs, the peritoneal membrane was closed by continuous stitch with a 5-0 monofil nylon suture (Ethicon).

RNA extraction and RT-qPCR

Lysis and extraction protocols were identical for human and mouse samples. Tumor or intestinal samples were snap-frozen in liquid nitrogen in RLT Plus buffer containing 0.1% beta mercaptoethanol. On the day of extraction, samples were thawed at 4°C and homogenized in a microtube homogenizer (Benchmark Scientific) in RNA-free glass bead tubes (Dutscher). Total RNA extraction and genomic DNA removal were performed with the RNeasy Mini kit (Qiagen) following the manufacturer's recommendations. A maximum of 1 μg of RNA, measured using a NanoDrop Spectrophotometer (ThermoFisher Scientific), was reverse-transcribed into cDNA with a mixture composed of SuperScript III Reverse Transcriptase (Life Technologies), RNaseOUT^M Recombinant Ribonuclease Inhibitor (Life Technologies), random primers (Promega), and Deoxynucleoside Triphosphate Set, PCR grade (Roche Diagnostics).

Quantitative gene expression assay

The expression of mouse and human *B2M*, *FOXP3*, *IFNG*, *IL10*, *IL17A*, *IL22*, *MADCAM1*, *VCAM1*, *PPIA*, *RORC*, *IL18*, and *TBX21* genes (all from Life Technologies) was analyzed with the TaqMan Gene Expression Assay using the Universal Master Mix II on a StepOnePlus Real-Time PCR System (Life Technologies). Amplifications were performed using the following ramping profile: one cycle at 95°C for 10 min, followed by 45 cycles of 95°C for 30 s, and 60°C for 1 min. RT-qPCR data were normalized to the expression levels of the housekeeping genes *B2M* or *Ppia*, as indicated in each figure, by means of the $2^{-\Delta Ct}$ method multiplied by 10^6.

Tissue lysis and chemokine analyses

Intestinal and tumoral samples were snap-frozen in liquid nitrogen in a nondenaturing cell lysis buffer containing 50 mM Tris HCl, pH 7.4, 150 mM NaCl, 300 mM sucrose, 10 mM EDTA, 0.1% Triton X-100, and Complete, Mini, EDTA-free Protease Inhibitor Cocktail (Roche). For subsequent lysis, samples were thawed at 4°C and lysed on a tube homogenizer (Precellys) in ceramic beads lysis tubes (Precellys). Tissue homogenate was centrifuged at 4000*g* for 5 min. The supernatant was used for subsequent analysis. Chemokine concentrations in the tissue lysate were determined according to the manufacturer's recommendations using the CCL2, CCL3, CCL4, CCL5, CCL25, and MAdCAM-1 Duoset ELISA kits (R&D Systems) or using Legendplex Mouse proinflammatory chemokine panel (BioLegend) with cytometric analysis performed on a CytoFLEX S (Beckman Coulter).

Ileal tissue sample preparation and bile acid detection by UHPLC-MS

Approximately 30 mg of collected tissue was weighed and placed in a 2-ml homogenizer tube with ceramic beads (Precellys, Bertin Technologies, France) with 1 ml of ice-cold extraction mixture (9:1 methanol–water, −20°C, with labeled ^{13}C-glycocholic acid as internal standard). To facilitate the extraction of endogenous metabolites, samples were then completely homogenized (3 cycles of 20 s/ 2380*g*; Precellys 24, Bertin Technologies, Montigny-le-Bretonneux, France) and centrifuged (10 min at 15,000*g*, 4°C). To detect bile acids, 300 μl of supernatant was collected and treated following a previously described protocol (*82*). Bile acids were analyzed by LC-MRM (Multiple Reaction Monitoring) with a 1290 UHPLC (Ultra-High Performance Liquid Chromatography, Agilent Technologies) coupled to a mass spectrometer 6470 TQ (Triple Quadrupole, Agilent Technologies), as previously described (*83*). Targeted data were cleaned with a R (version 4.0) dedicated package (https://github.com/kroemerlab/GRMeta).

Bulk RNA sequencing of $\alpha4\beta7^{+/-}$ CD4$^+$ mesenteric T cells

α4β7$^+$ and α4β7$^-$ CD4$^+$ T cells were isolated from mLNs by flow cytometry. Preparation of mRNA-seq libraries and nextseq 75SE run deep sequencing were performed at GeneCore EMBL (Heidelberg, Germany).

Single-cell RNA sequencing by BD Rhapsody

After isolation of CFSE$^+$ CD4$^+$ T cells by flow cytometry, 10,000 cells were washed in cold PBS and loaded onto a BD Rhapsody cartridge and processed according to the manufacturer's instructions for targeted single-cell RNA-seq using the predesigned Immune Response Panel (Mouse). The library was clustered at 1.75 pM on a NextSeq500 system (Illumina) to generate ~40,000 paired-end reads per cell using High Output v2 chemistry. Sequenced single-cell data was demultiplexed using bcl2fastq2 v2.20.

Single-cell TCR and RNA library construction and sequencing by 10X Genomics Chromium

After isolation of CFSE$^+$CD4$^+$ and CD8$^+$ T cell by flow cytometry from mLNs, cLNs, tdLNs, and tumors, single-cell-library construction was performed using Chromium Next GEM

Single Cell 5′ Kit v2 (PN-1000263), Chromium Next GEM Chip K Single Cell Kit (PN-1000287), Single Cell VDJ 5′ Gel Bead, Chromium Single Cell Mouse TCR Amplification Kit, 16 rxns (reactions) (PN-1000254), Library Construction Kit (16 rxns) (PN-1000190), and Dual Index Kit TT Set A (96 rxns) (PN-1000215) kits according to the manufacturer's protocol. Briefly, single-cell suspensions from a total of 500 to 20,000 cells with barcoded gel beads and partitioning oil were loaded to Chromium Next GEM Chip K to generate single-cell gel bead-in-emulsion. Full-length cDNA along with cell barcode identifiers were PCR-amplified to generate 5′Gene Expression (GEX) libraries and V(D)J libraries. Libraries were sequenced using a NovaSeq 6000 (Illumina) to achieve a minimum of 23,000 paired-end reads per cell for GEX and 7000 paired-end reads per cell for V(D)J. Reads were aligned using Cell Ranger v6.1.1 to the GRCm38 mouse references.

Repertoire clonality

TCR sequencing data were processed using the "immunarch" R package. Clonotypes within each population and compartments were then divided into fractions with an occurrence of 1 or >1. The cumulative frequency of each fraction was calculated within the repertoire of each sample.

Sequence similarity analysis

DeepTCR was used to cluster paired TRA-TRB clonotypes on the basis of sequence similarity, using a train variational autoencoder. This generates clusters composed of sequences with a likelihood of shared specificities. The clusters were assigned as being mLNs, tumor/dLN or shared based on the percentage of clonotypes composing them. A cluster was considered as specific to a compartment if the log2 fold change (FC) was equal to or higher than 1.5. Otherwise, clusters were considered as shared between the compartments (*52*).

Single-cell RNA-seq analysis

Expression matrices were analyzed using the R environment (version 4.2.1) with the Seurat package (v4.2.1). High-quality cells characterized by <10% of mitochondrial genes, >200 unique molecular identifier (UMI) features, and <15,000 unique UMIs were selected for further analysis. Count matrix was normalized with regularized negative binomial regression based on the 3000 most variable genes using the SCTransform function. Principal component analysis was used for dimensionality reduction using the RunPCA on the 3000 most variable genes. Contributive components were identified visually using an elbow plot. Nearest neighbors were determined with the FindNeigbhors function using contributive PCA components, and cells were clustered using the Louvain clustering algorithm with the FindClusters function. Resolution of the clustering algorithm was chosen based on a bootstrapping procedure, the resolution giving rise to the maximum number of clusters with co-assignment probabilities superior to 5% was chosen. Differential gene expression analysis was performed using the FindMarkers function and *P* values were corrected using the p.adj base function with the FDR procedure. Volcano plot visualization was performed using the ggplot2(v3.4.0) R package, Heatmap visualization was performed using the ComplexHeatmap (v2.14.0) R package, and Venn Diagram visualization was performed using the ggven R package (v0.1.9).

Cell lines and treatment

Culture media and supplements for cell culture were obtained from Life Technologies (Carlsbad, CA, USA), and plastic material was obtained from Greiner BioOne (Kremsmünster, Austria) and Corning (Corning, New York, USA). Mouse TSECs were a generous gift from B. P. Fennimore (University of Colorado Anschutz Medical Campus, Aurora, CO, USA) and bEnd.3 cells were purchased from the ATCC. TSECs were cultured in Dulbecco's modified Eagle's medium/nutrient mixture F-12 (DMEM/F-12) plus endothelial growth supplement (catalog no. 1052, ScienCell, Carlsbad, CA, USA), supplemented with 10% fetal bovine serum (FBS), 10 U/ml of penicillin sodium, and 10 μg/ml of streptomycin sulfate. bEnd.3 cells were cultured in DMEM with 2.5 mM L-glutamine, supplemented with 10% FBS, 10 U/ml penicillin sodium, and 10 μg/ml of streptomycin sulfate. Both cell lines were cultured in the presence of 5% CO_2 at 37°C. Transfected TSECs (TSEC::MAdCAM-1-GFP) and bEnd.3 cells (bEnd.3::MAdCAM-1-GFP) were selected with 500 μg/ml G418 sulfate (50 mg/ml, catalog no. 10131027, Gibco), and stable transformants were maintained under G418 selection pressure. Recombinant murine TNF-α (catalog no. 315-01A, PeproTech) and IL-1β (catalog no. 211-11B, PeproTech) were diluted in culture media from a stock of 40 μg/ml at the time of treatment. Bile acids (lithocholic acid (LCA) (catalog no. 700218P-10MG, Sigma-Aldrich), dehydrolithocholic acid (3-oxo-LCA) (catalog no. 700217P-10MG, Sigma-Aldrich), allolithocholic acid (allo-LCA) (catalog no. 700330P-5MG, Sigma-Aldrich), isoallo-LCA (catalog no. R203424-1MG, Sigma-Aldrich), taurolithocholic acid sodium salt (tauro-LCA) (catalog no. 700252P-10MG, Sigma-Aldrich), sodium chenodeoxycholate (CDCA) (catalog no. C8261-1G, Sigma-Aldrich), sodium taurochenodeoxycholate (TCDCA) (catalog no. T6260-100MG, Sigma-Aldrich), deoxycholic acid (DCA) (catalog no. 30960-25G, Sigma-Aldrich), UDCA (catalog no. 208590250, Thermoscientific), tauroursodeoxycholic acid (TUDCA) (catalog no. 580549-1GM, Millipore), glycoursodeoxycholic acid (GUDCA) (catalog no. 06863-1G, Sigma-Aldrich), and taurodeoxycholic acid (TDCA) (catalog no. 580221-5GM, Millipore) and FXR agonists/antagonists (GW4064 (catalog no. G5172-5MG, Sigma-Aldrich), cilofexor (catalog no. HY-109083, MCE), tropifexor (catalog no. HY-107418, MedChemExpress (MCE), and (Z)-guggulsterone (catalog no. G5168-25MG, Sigma-Aldrich)) dissolved in DMSO were diluted 1:1000, 1:10,000, and 1:100,000 in culture media to a final concentration of 100 μM, 10 μM, and 1 μM, respectively. Bacteria were cultured (and in some instances pasteurized) before being diluted in culture media to a working concentration with an optical density of 0.5, 0.25, and 0.1, reespectively (*Akk.* p2261 everImmune strain, *E. clostridioformis*).

Construction of MAdCAM-1 promoter plasmid

The MAdCAM-1 promoter construct is a PCR product from mouse genomic DNA amplified using 5′-GGAATTCTACCCCCACAGGCCTGCC-3′ as forward primer (EcoRI site is underlined, Eurofins, Nantes, France) and 5′-AGGCCGCGGGGGCCGGCAGCTTCCTAC-3′ as the reverse primer (SacII site is underlined, Eurofins). After digestion by EcoRI-HF and SacII (NEB, Ipswich, MA, USA), the MAdCAM-1 promoter DNA fragment was extracted using a Monarch DNA gel extraction kit (NEB, Ipswich, MA, USA). The purified fragments were subcloned into the promoterless pAcGFP1-1 vector (Clontech, Mountain View, CA, USA).

Establishment of MAdCAM-1 promoter reporter cell lines

TSECs and bEnd.3 cells were transfected with the recombinant expression vector pAcGFP1-1-MAdCAM-1 using FuGENE HD transfection reagent (catalog no. E2312, Promega). Twenty-four hours after transfection, stable transfectants were isolated by selection with 500 μg/ml G418. The transfectants (TSEC::MAdCAM-1-GFP and bEnd.3::MAdCAM-1-GFP) were maintained in culture medium containing 500 μg/ml of G418 for 2 weeks. The G418-resistant cells were selected and single-cell clones were isolated to establish TSEC::MAdCAM-1-GFP and bEnd.3::MAdCAM-1-GFP stable cell lines expressing GFP under the control of the MAdCAM-1 promoter.

High-content microscopy

TSEC::MAdCAM-1-GFP and bEnd.3::MAdCAM-1-GFP cells were seeded in 384-well/96-well μclear imaging plates (Greiner BioOne) and allowed to adapt overnight. Cells were treated with the indicated agents, then fixed with 3.7% PFA (w/v in PBS) (catalog no. F8775, Sigma-Aldrich) containing 2 μg/ml of Hoechst 33342 at 4°C overnight. Subsequently, the fixative was exchanged with PBS and the plates were analyzed by automated microscopy. Image acquisition was performed using an ImageXpress

Micro C automated confocal microscope (Molecular Devices, Sunnyvale, California, USA) equipped with a 20× PlanApo objective (Nikon, Tokyo, Japan), followed by automated image processing with R software using the EBImage package (available from the Bioconductor repository https://www.bioconductor.org) and the MorphR package (available from the GitHub repository https://github.com/kroemerlab/MorphR) In short, cytoplasm and nucleus were segmented and fluorescence intensities were assessed. After exclusion of cellular debris and dead cells, data were normalized, statistically evaluated, and graphically depicted. Images were also extracted and pixel intensities scaled (to the same extent for all images of a given experiment) using R software. At least four view fields were analyzed per well, and each experiment was assessed at least four times.

Statistics

In vitro and in vivo

Data analyses were performed either with the statistical environment R (http://www.R-project.org/) or Prism 6 (GraphPad, San Diego, CA, USA). The standardization of each marker was performed using the z score (difference of each sample value from the mean and/or standard deviation). When a control group was available, the data were standardized by dividing the value by the mean of the control group. Nonparametric Mann-Whitney U test was used for comparison of two unpaired groups. The Wilcoxon matched-pairs signed-rank test was used to compare two groups of paired samples. Kruskal-Wallis H test was used to compare more than two groups, correcting the statistical significance for multiple comparisons and FDR using the two-stage step-up method of Benjamini, Krieger, and Yekutieli. All reported tests are two-tailed and were considered significant at $P < 0.05$.

Patients

sMAdCAM-1 was a prognostic factor of the patient response in NSCLC, renal cell carcinoma, and bladder cancer patients. For each cohort, two groups of patients were defined by the sMAdCAM-1 median. Overall survival and progression-free survival analyses were performed using the Kaplan-Meier estimator, and the patient groups were compared using the log-rank (Mantel-Cox) test.

REFERENCES AND NOTES

1. C. Robert *et al*., Ipilimumab plus dacarbazine for previously untreated metastatic melanoma. *N. Engl. J. Med.* **364**, 2517–2526 (2011). doi: 10.1056/NEJMoa1104621; pmid: 21639810
2. J. Brahmer *et al*., Nivolumab versus docetaxel in advanced squamous-cell non-small-cell lung cancer. *N. Engl. J. Med.* **373**, 123–135 (2015). doi: 10.1056/NEJMoa1504627; pmid: 26028407
3. S. Spranger, R. Bao, T. F. Gajewski, Melanoma-intrinsic β-catenin signalling prevents anti-tumour immunity. *Nature* **523**, 231–235 (2015). doi: 10.1038/nature14404; pmid: 25970248
4. J. Gao *et al*., Loss of IFN-γ pathway genes in tumor cells as a mechanism of resistance to anti-CTLA-4 therapy. *Cell* **167**, 397–404.e9 (2016). doi: 10.1016/j.cell.2016.08.069; pmid: 27667683
5. N. J. Neubert *et al*., T cell-induced CSF1 promotes melanoma resistance to PD1 blockade. *Sci. Transl. Med.* **10**, eaan3311 (2018). doi: 10.1126/scitranslmed.aan3311; pmid: 29643229
6. A. Elkrief, L. Derosa, G. Kroemer, L. Zitvogel, B. Routy, The negative impact of antibiotics on outcomes in cancer patients treated with immunotherapy: A new independent prognostic factor? *Ann. Oncol.* **30**, 1572–1579 (2019). doi: 10.1093/annonc/mdz206; pmid: 31268133
7. B. Routy *et al*., Gut microbiome influences efficacy of PD-1-based immunotherapy against epithelial tumors. *Science* **359**, 91–97 (2018). doi: 10.1126/science.aan3706; pmid: 29097494
8. J. J. Mohiuddin *et al*., Association of antibiotic exposure with survival and toxicity in patients with melanoma receiving immunotherapy. *J. Natl. Cancer Inst.* **113**, 162–170 (2021). doi: 10.1093/jnci/djaa057; pmid: 32294209
9. L. Derosa *et al*., Microbiota-centered interventions: The next breakthrough in immuno-oncology? *Cancer Discov.* **11**, 2396–2412 (2021). doi: 10.1158/2159-8290.CD-21-0236; pmid: 34400407
10. L. Derosa *et al*., Intestinal *Akkermansia muciniphila* predicts clinical response to PD-1 blockade in advanced non-small cell lung cancer patients. *Nat. Med.* **28**, 315–324 (2022). doi: 10.1038/s41591-021-01655-5; pmid: 35115705
11. L. Derosa *et al*., Gut bacteria composition drives primary resistance to cancer immunotherapy in renal cell carcinoma patients. *Eur. Urol.* **78**, 195–206 (2020). doi: 10.1016/j.eururo.2020.04.044; pmid: 32376136
12. G. Gorfu, J. Rivera-Nieves, K. Ley, Role of beta7 integrins in intestinal lymphocyte homing and retention. *Curr. Mol. Med.* **9**, 836–850 (2009). doi: 10.2174/156652409789105525; pmid: 19860663
13. M. Briskin *et al*., Human mucosal addressin cell adhesion molecule-1 is preferentially expressed in intestinal tract and associated lymphoid tissue. *Am. J. Pathol.* **151**, 97–110 (1997). pmid: 9212736
14. H. Ogawa *et al*., Mechanisms of MAdCAM-1 gene expression in human intestinal microvascular endothelial cells. *Am. J. Physiol. Cell Physiol.* **288**, C272–C281 (2005). doi: 10.1152/ajpcell.00406.2003; pmid: 15483224
15. B. G. Feagan *et al*., Vedolizumab as induction and maintenance therapy for ulcerative colitis. *N. Engl. J. Med.* **369**, 699–710 (2013). doi: 10.1056/NEJMoa1215734; pmid: 23964932
16. M. Hassan-Zahraee *et al*., Anti-MAdCAM antibody increases β7 + T cells and CCR9 gene expression in the peripheral blood of patients with Crohn's disease. *J. Crohns Colitis* **12**, 77–86 (2018). doi: 10.1093/ecco-jcc/jjx121; pmid: 28961803
17. W. Reinisch *et al*., Long-term safety and efficacy of the anti-MAdCAM-1 monoclonal antibody ontamalimab [SHP647] for the treatment of ulcerative colitis: The open-label study TURANDOT II. *J. Crohns Colitis* **15**, 938–949 (2021). doi: 10.1093/ecco-jcc/jjab023; pmid: 33599720
18. D. R. Littman, A. Y. Rudensky, Th17 and regulatory T cells in mediating and restraining inflammation. *Cell* **140**, 845–858 (2010). doi: 10.1016/j.cell.2010.02.021; pmid: 20303875
19. P. Pandiyan *et al*., Microbiome dependent regulation of Tregs and Th17 cells in mucosa. *Front. Immunol.* **10**, 426 (2019). doi: 10.3389/fimmu.2019.00426; pmid: 30906299
20. C. F. Krebs *et al*., Autoimmune renal disease is exacerbated by S1P-receptor-1-dependent intestinal Th17 cell migration to the kidney. *Immunity* **45**, 1078–1092 (2016). doi: 10.1016/j.immuni.2016.10.020; pmid: 27851911
21. Y. K. Lee, J. S. Menezes, Y. Umesaki, S. K. Mazmanian, Proinflammatory T-cell responses to gut microbiota promote experimental autoimmune encephalomyelitis. *Proc. Natl. Acad. Sci. U.S.A.* **108** (Suppl 1), 4615–4622 (2011). doi: 10.1073/pnas.1000082107; pmid: 20660719
22. A. M. Magnuson *et al*., Population dynamics of islet-infiltrating cells in autoimmune diabetes. *Proc. Natl. Acad. Sci. U.S.A.* **112**, 1511–1516 (2015). doi: 10.1073/pnas.1423769112; pmid: 25605891
23. A. M. Morton *et al*., Endoscopic photoconversion reveals unexpectedly broad leukocyte trafficking to and from the gut. *Proc. Natl. Acad. Sci. U.S.A.* **111**, 6696–6701 (2014). doi: 10.1073/pnas.1405634111; pmid: 24753589
24. H.-J. Wu *et al*., Gut-residing segmented filamentous bacteria drive autoimmune arthritis via T helper 17 cells. *Immunity* **32**, 815–827 (2010). doi: 10.1016/j.immuni.2010.06.001; pmid: 20620945
25. M. R. I. Young, Th17 cells in protection from tumor or promotion of tumor progression. *J. Clin. Cell. Immunol.* **7**, 431 (2016). doi: 10.4172/2155-9899.1000431; pmid: 27453801
26. E. Sefik *et al*., MUCOSAL IMMUNOLOGY. Individual intestinal symbionts induce a distinct population of RORγ$^+$ regulatory T cells. *Science* **349**, 993–997 (2015). doi: 10.1126/science.aaa9420; pmid: 26272906
27. N. R. Blatner *et al*., Expression of RORγt marks a pathogenic regulatory T cell subset in human colon cancer. *Sci. Transl. Med.* **4**, 164ra159 (2012). doi: 10.1126/scitranslmed.3004566; pmid: 23241743
28. A. Rizzo *et al*., RORγt-expressing Tregs drive the growth of colitis-associated colorectal cancer by controlling IL6 in dendritic cells. *Cancer Immunol. Res.* **6**, 1082–1092 (2018). doi: 10.1158/2326-6066.CIR-17-0698; pmid: 29991500
29. K. N. Haas, J. L. Blanchard, Reclassification of the *Clostridium clostridioforme* and *Clostridium sphenoides* clades as *Enterocloster* gen. nov. and *Lacrimispora* gen. nov., including reclassification of 15 taxa. *Int. J. Syst. Evol. Microbiol.* **70**, 23–34 (2020). doi: 10.1099/ijsem.0.003698; pmid: 31782700
30. R. Gacesa *et al*., Environmental factors shaping the gut microbiome in a Dutch population. *Nature* **604**, 732–739 (2022). doi: 10.1038/s41586-022-04567-7; pmid: 35418674
31. S. Yonekura *et al*., Cancer induces a stress ileopathy depending on β-adrenergic receptors and promoting dysbiosis that contributes to carcinogenesis. *Cancer Discov.* **12**, 1128–1151 (2022). doi: 10.1158/2159-8290.CD-21-0999; pmid: 34930787
32. A.-G. Goubet *et al*., Multifaceted modes of action of the anticancer probiotic *Enterococcus hirae*. *Cell Death Differ.* **28**, 2276–2295 (2021). doi: 10.1038/s41418-021-00753-8; pmid: 33976389
33. E. N. Baruch *et al*., Fecal microbiota transplant promotes response in immunotherapy-refractory melanoma patients. *Science* **371**, 602–609 (2021). doi: 10.1126/science.abb5920; pmid: 33303685
34. D. Davar *et al*., Fecal microbiota transplant overcomes resistance to anti-PD-1 therapy in melanoma patients. *Science* **371**, 595–602 (2021). doi: 10.1126/science.abf3363; pmid: 33542131
35. B. Routy *et al*., The gut microbiota influences anticancer immunosurveillance and general health. *Nat. Rev. Clin. Oncol.* **15**, 382–396 (2018). doi: 10.1038/s41571-018-0006-2; pmid: 29636538
36. R. Y. Gao *et al*., Bile acids modulate colonic MAdCAM-1 expression in a murine model of combined cholestasis and colitis. *Mucosal Immunol.* **14**, 479–490 (2021). doi: 10.1038/s41385-020-00347-6; pmid: 33004979
37. D. V. Guzior, R. A. Quinn, Review: Microbial transformations of human bile acids. *Microbiome* **9**, 140 (2021). doi: 10.1186/s40168-021-01101-1; pmid: 34127070
38. Y. Sato *et al*., Novel bile acid biosynthetic pathways are enriched in the microbiome of centenarians. *Nature* **599**, 458–464 (2021). doi: 10.1038/s41586-021-03832-5; pmid: 34325466
39. J. B. J. Ward *et al*., Ursodeoxycholic acid and lithocholic acid exert anti-inflammatory actions in the colon. *Am. J. Physiol. Gastrointest. Liver Physiol.* **312**, G550–G558 (2017). doi: 10.1152/ajpgi.00256.2016; pmid: 28360029
40. M. Tomura *et al*., Monitoring cellular movement in vivo with photoconvertible fluorescence protein "Kaede" transgenic mice. *Proc. Natl. Acad. Sci. U.S.A.* **105**, 10871–10876 (2008). doi: 10.1073/pnas.0802278105; pmid: 18663225
41. V. Singh *et al*., Microbiota dysbiosis controls the neuroinflammatory response after stroke. *J. Neurosci.* **36**, 7428–7440 (2016). doi: 10.1523/JNEUROSCI.1114-16.2016; pmid: 27413153
42. C. M'Rini *et al*., A novel endothelial L-selectin ligand activity in lymph node medulla that is regulated by alpha(1,3)-fucosyltransferase-IV. *J. Exp. Med.* **198**, 1301–1312 (2003). doi: 10.1084/jem.20030182; pmid: 14597733
43. J. Mitoma *et al*., Critical functions of N-glycans in L-selectin-mediated lymphocyte homing and recruitment. *Nat. Immunol.* **8**, 409–418 (2007). doi: 10.1038/ni1442; pmid: 17334369
44. E. Cano-Gamez *et al*., Single-cell transcriptomics identifies an effectorness gradient shaping the response of CD4$^+$ T cells to cytokines. *Nat. Commun.* **11**, 1801 (2020). doi: 10.1038/s41467-020-15543-y; pmid: 32286271
45. Z. T. Freeman *et al*., A conserved intratumoral regulatory T cell signature identifies 4-1BB as a pan-cancer target. *J. Clin. Invest.* **130**, 1405–1416 (2020). doi: 10.1172/JCI128672; pmid: 32015231
46. Y. Gao *et al*., Transcriptional profiling identifies caspase-1 as a T cell-intrinsic regulator of Th17 differentiation. *J. Exp. Med.* **217**, e20190476 (2020). doi: 10.1084/jem.20190476; pmid: 31967646
47. D. Lu *et al*., The phosphatase PAC1 acts as a T cell suppressor and attenuates host antitumor immunity. *Nat. Immunol.* **21**, 287–297 (2020). doi: 10.1038/s41590-019-0577-9; pmid: 31932812
48. J.-H. Kim *et al*., Molecular networks of FOXP family: Dual biologic functions, interplay with other molecules and clinical implications in cancer progression. *Mol. Cancer* **18**, 180 (2019). doi: 10.1186/s12943-019-1110-3; pmid: 31815635

49. L. Li, N. Patsoukis, V. Petkova, V. A. Boussiotis, Runx1 and Runx3 are involved in the generation and function of highly suppressive IL-17-producing T regulatory cells. *PLOS ONE* **7**, e45115 (2012). doi: 10.1371/journal.pone.0045115; pmid: 22984619
50. L. Belarif *et al*., IL-7 receptor influences anti-TNF responsiveness and T cell gut homing in inflammatory bowel disease. *J. Clin. Invest.* **129**, 1910–1925 (2019). doi: 10.1172/JCI121668; pmid: 30939120
51. Y. Chen *et al*., Pik3ip1 is a negative immune regulator that inhibits antitumor T-cell immunity. *Clin. Cancer Res.* **25**, 6180–6194 (2019). doi: 10.1158/1078-0432.CCR-18-4134; pmid: 31350312
52. J.-W. Sidhom, H. B. Larman, D. M. Pardoll, A. S. Baras, Author Correction: DeepTCR is a deep learning framework for revealing sequence concepts within T-cell repertoires. *Nat. Commun.* **12**, 2309 (2021). doi: 10.1038/s41467-021-22667-2; pmid: 33850137
53. T. C. Wirth *et al*., Repetitive antigen stimulation induces stepwise transcriptome diversification but preserves a core signature of memory CD8(+) T cell differentiation. *Immunity* **33**, 128–140 (2010). doi: 10.1016/j.immuni.2010.06.014; pmid: 20619696
54. T. Wu *et al*., The TCF1-Bcl6 axis counteracts type I interferon to repress exhaustion and maintain T cell stemness. *Sci. Immunol.* **1**, eaai8593 (2016). doi: 10.1126/sciimmunol.aai8593; pmid: 28018990
55. E. J. Wherry *et al*., Molecular signature of CD8+ T cell exhaustion during chronic viral infection. *Immunity* **27**, 670–684 (2007). doi: 10.1016/j.immuni.2007.09.006; pmid: 17950003
56. K. Araki *et al*., Translation is actively regulated during the differentiation of $CD8^+$ effector T cells. *Nat. Immunol.* **18**, 1046–1057 (2017). doi: 10.1038/ni.3795; pmid: 28714979
57. C. Voigt *et al*., Cancer cells induce interleukin-22 production from memory $CD4^+$ T cells via interleukin-1 to promote tumor growth. *Proc. Natl. Acad. Sci. U.S.A.* **114**, 12994–12999 (2017). doi: 10.1073/pnas.1705165114; pmid: 29150554
58. T. L. Denning, G. Kim, M. Kronenberg, Cutting edge: CD4+CD25+ regulatory T cells impaired for intestinal homing can prevent colitis. *J. Immunol.* **174**, 7487–7491 (2005). doi: 10.4049/jimmunol.174.12.7487; pmid: 15944246
59. D. Dangaj *et al*., Cooperation between constitutive and inducible chemokines enables T cell engraftment and immune attack in solid tumors. *Cancer Cell* **35**, 885–900.e10 (2019). doi: 10.1016/j.ccell.2019.05.004; pmid: 31185212
60. A. González-Martín, L. Gómez, J. Lustgarten, E. Mira, S. Mañes, Maximal T cell-mediated antitumor responses rely upon CCR5 expression in both CD4(+) and CD8(+) T cells. *Cancer Res.* **71**, 5455–5466 (2011). doi: 10.1158/0008-5472.CAN-11-1687; pmid: 21715565
61. A. M. Cooper, IL-17 and anti-bacterial immunity: Protection versus tissue damage. *Eur. J. Immunol.* **39**, 649–652 (2009). doi: 10.1002/eji.200839090; pmid: 19283706
62. T. Yokoo *et al*., Liver-targeted hydrodynamic gene therapy: Recent advances in the technique. *World J. Gastroenterol.* **22**, 8862–8868 (2016). doi: 10.3748/wjg.v22.i40.8862; pmid: 27833377
63. A. K. Holmer *et al*., Biomarkers are associated with clinical and endoscopic outcomes with vedolizumab treatment in Crohn's disease. *Therap. Adv. Gastroenterol.* **13**, 1756284820971214 (2020). doi: 10.1177/1756284820971214; pmid: 33240396
64. J. Lecuelle *et al*., MER4 endogenous retrovirus correlated with better efficacy of anti-PD1/PD-L1 therapy in non-small cell lung cancer. *J. Immunother. Cancer* **10**, e004241 (2022). doi: 10.1136/jitc-2021-004241; pmid: 35277462
65. L. Albiges *et al*., Safety and efficacy of nivolumab in metastatic renal cell carcinoma (mRCC): Final analysis from the NIVOREN GETUG AFU 26 study. *J. Clin. Oncol.* **37** (7_suppl), 542 (2019). doi: 10.1200/JCO.2019.37.7_suppl.542
66. G. P. Sonpavde *et al*., Primary results of STRONG: An open-label, multicenter, phase 3b study of fixed-dose durvalumab monotherapy in previously treated patients with urinary tract carcinoma. *Eur. J. Cancer* **163**, 55–65 (2022). doi: 10.1016/j.ejca.2021.12.012; pmid: 35042068
67. A. Liesz *et al*., Regulatory T cells are key cerebroprotective immunomodulators in acute experimental stroke. *Nat. Med.* **15**, 192–199 (2009). doi: 10.1038/nm.1927; pmid: 19169263
68. C. Benakis *et al*., Commensal microbiota affects ischemic stroke outcome by regulating intestinal γδ T cells. *Nat. Med.* **22**, 516–523 (2016). doi: 10.1038/nm.4068; pmid: 27019327
69. R. J. Miragaia *et al*., Single-cell transcriptomics of regulatory T cells reveals trajectories of tissue adaptation. *Immunity* **50**, 493–504.e7 (2019). doi: 10.1016/j.immuni.2019.01.001; pmid: 30737144
70. A. R. Muñoz-Rojas, D. Mathis, Tissue regulatory T cells: Regulatory chameleons. *Nat. Rev. Immunol.* **21**, 597–611 (2021). doi: 10.1038/s41577-021-00519-w; pmid: 33772242
71. N. Yosef *et al*., Dynamic regulatory network controlling TH17 cell differentiation. *Nature* **496**, 461–468 (2013). doi: 10.1038/nature11981; pmid: 23467089
72. U. U. Uche *et al*., PIK3IP1/TrIP restricts activation of T cells through inhibition of PI3K/Akt. *J. Exp. Med.* **215**, 3165–3179 (2018). doi: 10.1084/jem.20172018; pmid: 30429249
73. A. Fischer *et al*., Differential effects of α4β7 and GPR15 on homing of effector and regulatory T cells from patients with UC to the inflamed gut in vivo. *Gut* **65**, 1642–1664 (2016). doi: 10.1136/gutjnl-2015-310022; pmid: 26209553
74. G. D'Haens *et al*., Effect of PF-00547659 on central nervous system immune surveillance and circulating β7+ T cells in Crohn's disease: Report of the TOSCA study. *J. Crohns Colitis* **12**, 188–196 (2018). doi: 10.1093/ecco-jcc/jjx128; pmid: 28961770
75. G. Calenda *et al*., Integrin α4β7 blockade preferentially impacts CCR6+ lymphocyte subsets in blood and mucosal tissues of naive Rhesus macaques. *J. Immunol.* **200**, 810–820 (2018). doi: 10.4049/jimmunol.1701150; pmid: 29196458
76. M. I. Love, W. Huber, S. Anders, Moderated estimation of fold change and dispersion for RNA-seq data with DESeq2. *Genome Biol.* **15**, 550 (2014). doi: 10.1186/s13059-014-0550-8; pmid: 25516281
77. M. E. Ritchie *et al*., limma powers differential expression analyses for RNA-sequencing and microarray studies. *Nucleic Acids Res.* **43**, e47 (2015). doi: 10.1093/nar/gkv007; pmid: 25605792
78. H. Lin, S. D. Peddada, Analysis of compositions of microbiomes with bias correction. *Nat. Commun.* **11**, 3514 (2020). doi: 10.1038/s41467-020-17041-7; pmid: 32665548
79. H. Mallick *et al*., Multivariable association discovery in population-scale meta-omics studies. *PLOS Comput. Biol.* **17**, e1009442 (2021). doi: 10.1371/journal.pcbi.1009442; pmid: 34784344
80. N. Segata *et al*., Metagenomic biomarker discovery and explanation. *Genome Biol.* **12**, R60 (2011). doi: 10.1186/gb-2011-12-6-r60; pmid: 21702898
81. P. Bankhead *et al*., QuPath: Open source software for digital pathology image analysis. *Sci. Rep.* **7**, 16878 (2017). doi: 10.1038/s41598-017-17204-5; pmid: 29203879
82. C. Grajeda-Iglesias *et al*., Oral administration of *Akkermansia muciniphila* elevates systemic antiaging and anticancer metabolites. *Aging (Albany NY)* **13**, 6375–6405 (2021). doi: 10.18632/aging.202739; pmid: 33653967
83. S. Durand, C. Grajeda-Iglesias, F. Aprahamian, N. Nirmalathasan, O. Kepp, G. Kroemer, "The intracellular metabolome of starving cells," in *Methods in Cell Biology*, O. Kepp, L. Galluzzi, Eds. (Academic, 2021), vol. 164 of *Monitoring Vesicular Trafficking in Cellular Responses to Stress - Part A*, pp. 137–156; ; https://www.sciencedirect.com/science/article/pii/S0091679X21000431.

ACKNOWLEDGMENTS

We would like to particularly thank the animal facility and the Flow Cytometry and Pathology Platforms of Gustave Roussy, especially P. Gonin, L. Touchard, C. Metereau, A. Noel, and O. Bawa, and the PREMIS operational team, especially S. Farhane (project leader), S. Messayke (pharmacovigilance), L. Bedouda (clinical research associate), R. Chaabane (clinical research associate), C. Mohamed-Djalim (clinical research associate), and all investigators. Some figure items were partly generated using Servier Medical Art, provided by Servier, licensed under a Creative Commons Attribution 3.0 unported license. **Funding:** This work was supported by the SEERAVE Foundation, European Union Horizon 2020, Project Number 825410 and Project Acronym ONCOBIOME, Institut National du Cancer (INCa), ANR Ileobiome – 19-CE15-0029-01, ANR RHU5 ANR-21-RHUS-0017 IMMUNOLIFE, MAdCAM INCA_ 16698, ANR-IHU Méditerranée-Infections, Ligue contre le cancer, LABEX OncoImmunology, la direction generale de l'offre de soins (DGOS), SIRIC SOCRATE (INCa/DGOS/INSERM 6043), and PACRI network. G.K. was supported by the Ligue contre le Cancer (équipe labelisée); Agence National de la Recherche (ANR) – Projets blancs; AMMICa US23/CNRS UMS3655; Cancéropôle Ile-de-France; Fondation pour la Recherche Médicale (FRM); Equipex Onco-Pheno-Screen; European Joint Programme on Rare Diseases (EJPRD); European Research Council (ICD-Cancer), European Union Horizon 2020 program Crimson; Institut National du Cancer (INCa); Institut Universitaire de France; LabEx Immuno-Oncology (ANR-18-IDEX-0001); a Cancer Research ASPIRE Award from the Mark Foundation; SIRIC Stratified Oncology Cell DNA Repair and Tumor Immune Elimination (SOCRATE); SIRIC Cancer Research and Personalized Medicine (CARPEM); the Prism project funded by the Agence Nationale de la Recherche under grant number ANR-18-IBHU-0002; and the TriPoD European Research Council Advanced EU (322856) and Recherche Hospitalo-Universitaire iMAP (ANR-16-RHUS-0001) grants to D.K. O.K. was funded by INCA and the DIM Elicit. The PREMIS study was funded by Gustave Roussy fondation & Malakoff Humanis. The Bladder cohort from IOPREDI ancillary study / STRONG study (NCT03084471) was funded by AstraZeneca. This study contributes to the IdEx Université de Paris ANR-18-IDEX-0001. M.F. was funded by SEERAVE Foundation. C.Ra. received a fellowship from Immuntrain within the Marie-Slodowska Curie Training network of the European Union (LMU Klinikum). L.D., B.R., S.Y., and F.X.D. were supported by Philantropia at Gustave Roussy Foundation. I.La. was funded by Fondation pour la Recherche Médicale (FRM). A.Sc. and N.W. were funded by DFG (German Research Foundation) – Project-ID 403324012 – SFB 1382. **Author contributions:** Conceptualization: L.Zi., G.K., C.Ra., M.F.; Data curation: I.La., K.M., G.V., V.M., A.M.T.; Formal analysis: M.F., C.Ra., C.A.C.S., I.La., C.D., M.L., S.D., K.M., S.Y., J.E.F., C.Ri., L.L., G.V., E.L.C., R.D., V.M., D.D., A.M.T., L.D.; Funding acquisition: L.Zi., G.K., L.D.; Investigation: M.F., C.Ra., C.A.C.S., A.L.T., I.La., A.L.M.L.V., L.Zh., C.Th., I.Le., M.M., E.P., R.B., M.D.M.F., S.Z., A.R., M.L., G.F., P.L., A.Si., K.M., C.A.D., M.P.R., M.T.A., J.C., J.B., L.L., R.D., C.Tr., N.C., V.M., L.D., G.K., L.Zi.; Methodology: M.F., C.Ra., A.L.T., I.La., L.Zh., I.Le., A.Si., F.Gi., S.Y., O.K., A.Sc., N.W., J.S.G., S.K., J.B., L.L., N.Ga., B.Q., E.L.C., L.B., J.P.G., R.D., C.Tr., F.Gh., V.M., D.K., A.M.T., N.S., G.K., L.Zi.; Resources: A.Si., K.M., C.A.D., F.Gi., M.P.R., S.T., A.Sc., N.W., J.S.G., S.K., E.L.C., L.B., J.P.G., A.J., N.Ge., E.G., N.L., R.K., R.D., B.B., C.Tr., F.Gh., N.C., V.M., D.K., L.A., A.M.T., N.S., F.X.D., A.M., B.R., L.D., G.K., L.Zi.; Software: M.F., I.La., C.D., K.M., C.Ri., G.V., V.M., D.D., A.M.T.; Supervision: L.Zi., G.K., M.F., C.Ra., L.D., F.Gi., O.K., E.L.C., N.L., D.K., N.S.; Validation: M.F., C.Ra., C.A.C.S., L.D.; Visualization: M.F., C.Ra, C.A.C.S., A.L.T., I.La., A.L.M.L.V., R.B., L.D.; Writing – original draft: L.Zi., G.K., C.Ra., M.F.; Writing – review & editing: L.Zi., G.K., C.Ra, M.F., C.A.C.S., D.D., A.L.T., M.P.R., O.K., E.G., N.L., V.M., L.D. **Competing interests:** L.Zi. founded and is the SAB president of everImmune. L.Zi. had grant support from Daichi Sankyo, Kaleido, 9 m, and Pileje. G.K. holds research contracts with Daiichi Sankyo, Eleor, Kaleido, Lytix Pharma, PharmaMar, Osasuna Therapeutics, Samsara Therapeutics, Sanofi, Tollys, and Vascage. G.K. has consulted for Reithera. G.K. is on the board of directors of the Bristol Myers Squibb Foundation France. G.K. is a scientific cofounder of everImmune, Osasuna Therapeutics, Samsara Therapeutics, and Therafast Bio. G.K. is in the scientific advisory boards of Hevolution, Institut Servier, and Longevity Vision Funds. G.K. is the inventor of patents covering therapeutic targeting of aging, cancer, cystic fibrosis, and metabolic disorders. Among these, patents were licensed to Bayer (WO2014020041-A1, WO2014020043-A1), Bristol-Myers Squibb (WO2008057863-A1), Osasuna Therapeutics (WO2019057742A1), PharmaMar (WO2022049270A1 and WO2022048775-A1), Raptor Pharmaceuticals (EP2664326-A1), Samsara Therapeutics (GB202017553D0), and Therafast Bio (EP3684471A1). R.D filed the WO2022/268841 A1 patent. O.K. is a scientific cofounder of Samsara Therapeutics. L.D. is member of the SAB of everImmune. L.A. is an advisor or consultant for Astellas, BMS, Ipsen, Janssen, MSD, Pfizer, EISAI, and Roche. Gustave Roussy filed a patent with registration number EP21305846.4 and reference number B210162EPA/VEM/CPO, "Methods for diagnosing a cancer-induced ileopathy and their use for improving cancer treatment by immunotherapy" licensed to everImmune. The remaining authors declare no competing interests. **Data and materials availability:** All data are available in the main text or the supplementary materials. Patient data are available to vetted researchers and not to the broader public through a data transfer agreement. A materials transfer agreement will be necessary to access to intestinal species from everImmune or Gustave Roussy. Bulk RNA-Seq data (E-MTAB-12787), single-cell Rhapsody RNA-Seq data (E-MTAB-12784), 16S rRNA sequencing data (E-MTAB-12812), 10X single-cell RNA and TCR sequencing data (E-MTAB-12846), metagenomics data (bioprojects PRJNA944152 and PRJNA751792), and metabolomics data (Elsevier/Mendeley data DOI: 10.17632/4b76mz87r6.1) are all publicly available. **License information:** Copyright © 2023 the authors, some rights reserved; exclusive licensee American Association for the Advancement of Science. No claim to original US government works. https://www.science.org/about/science-licenses-journal-article-reuse

SUPPLEMENTARY MATERIALS

science.org/doi/10.1126/science.abo2296
Figs. S1 to S10
Tables S1 to S9
Data S1 and S2
MDAR Reproducibility Checklist

View/request a protocol for this paper from *Bio-protocol*.

Submitted 21 January 2022; resubmitted 12 December 2022
Accepted 14 April 2023
10.1126/science.abo2296

RESEARCH ARTICLE

QUANTUM PHYSICS

Splitting phonons: Building a platform for linear mechanical quantum computing

H. Qiao[1], É. Dumur[1,2]†, G. Andersson[1], H. Yan[1], M.-H. Chou[1,3], J. Grebel[1], C. R. Conner[1], Y. J. Joshi[1], J. M. Miller[1,3], R. G. Povey[1,3], X. Wu[1], A. N. Cleland[1,2]*

Linear optical quantum computing provides a desirable approach to quantum computing, with only a short list of required computational elements. The similarity between photons and phonons points to the interesting potential for linear mechanical quantum computing using phonons in place of photons. Although single-phonon sources and detectors have been demonstrated, a phononic beam splitter element remains an outstanding requirement. Here we demonstrate such an element, using two superconducting qubits to fully characterize a beam splitter with single phonons. We further use the beam splitter to demonstrate two-phonon interference, a requirement for two-qubit gates in linear computing. This advances a new solid-state system for implementing linear quantum computing, further providing straightforward conversion between itinerant phonons and superconducting qubits.

Linear optical quantum computing (LOQC) presents a scalable approach to quantum computing that relies only on relatively simple optical elements such as beam splitters, phase shifters, and single-photon sources and detectors (*1*). The similarity between photons and phonons poses the question as to whether linear mechanical quantum computing (LMQC) might be achieved using phonons.

Prior experiments with phonons in solid systems have included the quantum control of mechanical motion (*2*–*4*), entanglement between macroscopic mechanical objects (*5*–*8*), coupling between surface acoustic waves and qubits (*9*–*13*), the deterministic emission and detection of individual surface acoustic wave (SAW) phonons (*14*, *15*), and the transmission of quantum information (*14*–*18*), among other demonstrations (*19*, *20*).

Here, we explore the potential for linear quantum computing by demonstrating a phonon beam splitter for SAW phonons, first showing that the beam splitter deterministically converts a single incident phonon to a superposition output state, with one phonon in either of the two output channels. This is a phase-coherent process, which we further exploit to demonstrate a single-phonon interferometer, using qubits to control the phonon phase. We further explore two-phonon interference through the Hong-Ou-Mandel (HOM) effect (*21*), central to a controlled-phase gate in LOQC (*1*, *22*), using two SAW phonons whose simultaneous arrival suppresses the output of coincident phonons in the two output channels, in favor of a superposed two-phonon-per-channel output, with a suppression visibility of 0.910 ± 0.013.

These results demonstrate the basic toolset to begin exploring linear mechanical quantum computing, which is perhaps unexpected given that in our system, a single phonon represents the collective motion of a large number ($\sim 10^{15}$) of atoms.

[1]Pritzker School of Molecular Engineering, University of Chicago, Chicago, IL 60637, USA. [2]Center for Molecular Engineering and Material Science Division, Argonne National Laboratory, Lemont, IL 60439, USA. [3]Department of Physics, University of Chicago, Chicago, IL 60637, USA.
*Corresponding author. Email: anc@uchicago.edu
†Present address: Univ. Grenoble Alpes, CEA, Grenoble INP, IRIG, PHELIQS, 38000 Grenoble, France.

Device description

Our device comprises two superconducting Xmon qubits, Q_1 and Q_2 (*23*, *24*), coupled via two tunable couplers G_1 and G_2 (*25*) to two unidirectional interdigitated transducers, UDT_1 and UDT_2 (*15*). These are linked by a 2-mm-long SAW phonon channel, interrupted by a phonon beam splitter BS (Fig. 1, A to C). The beam splitter, comprising a set of 16 parallel metal fingers, is designed to reflect approximately half of the acoustic signal, while transmitting the remainder. Details for the qubit, UDT, and BS designs appear in (*26*). The beam splitter is intentionally positioned 300 nm closer to UDT_1 than UDT_2, resulting in 214- and 290-ns travel times from each transducer to the beam splitter. The variable coupler between each qubit and its associated UDT allows us to shape the phonon emission, with typical emission times ranging from 14 ns (maximum coupling) to more than 10 μs (minimum, "off" coupling), which we characterize from the couplers' time-dependent emission rates $\kappa_{1,2}(t)$ (fig. S2) (*14*).

The qubits, variable couplers, and their associated control and readout lines are fabricated on a sapphire substrate, whereas the acoustic elements (UDTs and BS) are fabricated on a separate lithium niobate substrate. After fabrication, the two dies are aligned and attached to one another using a flip-chip assembly (*27*). The device is operated in a dilution refrigerator with a base temperature of about 10 mK.

Single-phonon beam splitter

We first characterize the system by measuring the response to single phonons with both qubits set to the operating frequency of 3.925 GHz. One qubit (either Q_1 or Q_2) is excited to its $|e\rangle$ state and a phonon is emitted, where we shape the emission to have a hyperbolic secant waveform, $\phi_{1,2}(t) \propto \mathrm{sech}(t/2\sigma_{1,2})$, through the calibrated time-dependent modulation of the qubit's variable coupling rate $\kappa_{1,2}(t)$ (*14*); the characteristic wave packet width is $\sigma_{1,2} = 17.9$ ns. The phonon released from Q_1 (Q_2) interacts with the beam splitter, ideally resulting in the output state $(i|10\rangle + |01\rangle)/\sqrt{2}((|10\rangle + i|01\rangle)/\sqrt{2})$; see also fig. S1, B and C. We use the notation $|\mathrm{ph}_1\mathrm{ph}_2\rangle$, where $\mathrm{ph}_{1,2}$ denotes the phonon number in the output channel directed toward $Q_{1,2}$, respectively. The beam splitter output is then captured by both qubits, through a calibrated time-dependent variation of each qubit's coupling rate. In Fig. 1, D and E, we display the excited-state probability $P_{Q1,2}(t)$ for each qubit and their joint excitation probability $P_{ee}(t)$ as a function of measurement time t. The joint excitation probability $P_{ee}(t)$ remains very small, consistent with the expectation of no joint qubit excitation in this measurement, as each experiment involves only one phonon at a time. From these data, we extract a beam splitter reflectivity $\eta = 0.61$ and effective itinerant phonon lifetime $\tau_{ph} = 1.3$ μs, in agreement with a separate characterization of the BS design (fig. S1D) and previous measurements of phonon propagation loss in similar systems (*14*, *15*). The effective lifetime includes loss from phonon scattering during transits between the UDTs and the BS, and from the UDT and BS elements themselves, as well as any losses during qubit release or capture.

We perform two-qubit state tomography for the final joint qubit state generated in Fig. 1D, displaying the absolute value of the density matrix ρ in Fig. 1F. We find a Bell state fidelity $\mathcal{F} = \sqrt{\mathrm{Tr}(\rho_{\mathrm{Bell}} \cdot |\rho|)} = 0.816 \pm 0.004$ to the ideal Bell state ρ_{Bell}, indicating that the phonon beam splitter maintains quantum coherence; the uncertainties here and elsewhere represent one standard deviation. Decay in the principal density matrix elements is consistent with phonon propagation and scattering loss, included via the effective phonon lifetime in the simulations that generate the dashed frames.

Single phonon interferometry

We further demonstrate the coherence of the BS element by performing a Mach-Zehnder–like interference experiment using a single itinerant phonon. In Fig. 2A, we display the

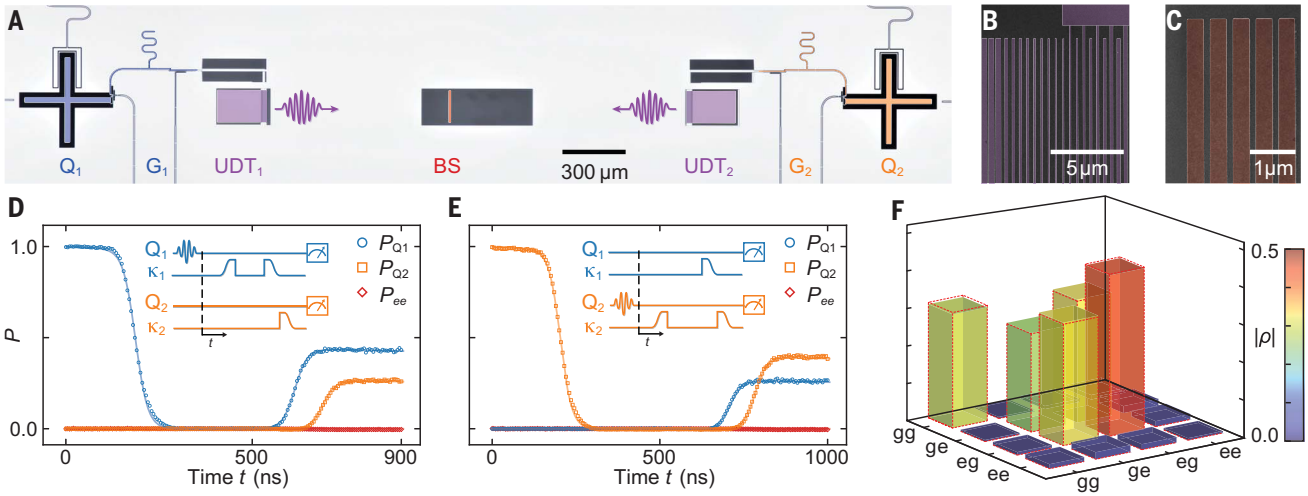
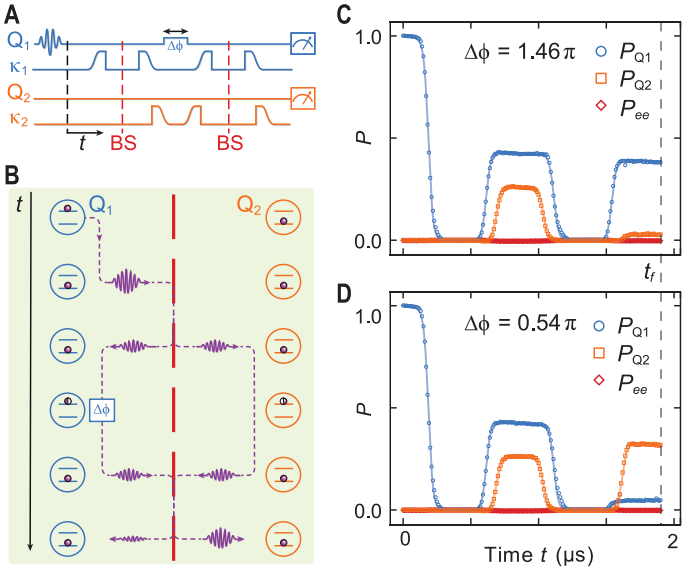


Fig. 1. Device description and characterization. (**A**) False-color optical micrograph of two superconducting qubits (Q_1 and Q_2) coupled to unidirectional transducers (UDT_1 and UDT_2) via tunable couplers (G_1 and G_2), on either side of a phonon beam splitter (BS). Qubits and couplers are fabricated on a sapphire die, with UDTs and BS on a separate, smaller lithium niobate die; micrograph taken from the backside of the flip-chip assembled device. (**B**) False-color scanning electron micrograph of transducer-mirror UDT combination, and (**C**) top-left corner of BS. (**D** and **E**) A single phonon is sent from Q_1 (Q_2) to the BS and "split" by it, and the output is subsequently captured by each qubit. Measurements of both qubits are made at time t, yielding the excited-state populations P_{Q1} (blue circles), P_{Q2} (orange squares), and the joint excitation probability P_{ee} (red diamonds). Solid-color lines are numerical simulations (*26*). Insets: Control pulse sequences. (**F**) After the qubits capture the phonon emitted in (D), we perform two-qubit state tomography yielding the two-qubit density matrix ρ, with Bell state fidelity $\mathcal{F} = 0.816 \pm 0.004$. The tomography measurement is repeated 10 times, and the density matrix is reconstructed in each repetition and constrained to be Hermitian. Bars represent measured |ρ|, and red dashed frames are simulated values.



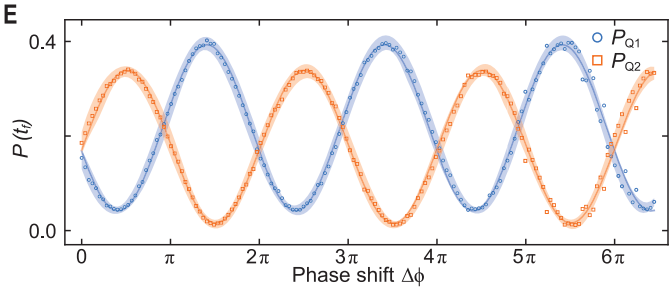


Fig. 2. Single-phonon interferometry. (**A**) Control pulse sequence. (**B**) Schematic representation: A single phonon is emitted by Q_1, split by the BS, and captured by both qubits, a process identical to the Bell state generation shown in Fig. 1D. A brief frequency change of Q_1 adds a phase shift Δϕ, followed by a phonon release from each qubit, timed to give coincident signals at the BS and thus generating interference. (**C** and **D**) Deterministic routing of the BS interference output to either Q_1 or Q_2, respectively, for phase shifts $\Delta\varphi = 1.46\pi$ or 0.54π. Solid blue, orange, and red lines are simulations. (**E**) Excitation probability for Q_1 and Q_2 as a function of the control phase Δφ, showing an interference pattern with visibility $\mathcal{V}_{Q1} = 0.806 \pm 0.004$ and $\mathcal{V}_{Q2} = 0.910 \pm 0.005$. The relative phase Δφ is varied by changing Q_1's frequency for a variable length of time, as illustrated in the pulse sequence. Light blue and orange shaded areas denote one standard deviation calculated from 34 repeated scans. Solid blue and orange lines are cosine fits.

control pulse sequence, in Fig. 2B a schematic representation of the experiment, and in Fig. 2, C to E, the results from this experiment. A single phonon is emitted from Q_1 with the same waveform as in Fig. 1D, and the beam-split phonon is captured by Q_1 and Q_2. The phase of Q_1 relative to Q_2 is then changed by Δφ, and the excitations are reemitted through a timed release from each qubit, resulting in a zero-delay interference at the BS. The phase-dependent interference allows control of which channel receives the output phonon, shown by plotting the excited-state probabilities $P_{Q1,2}$, as well as the joint excitation probability P_{ee}, for two choices of phase $\Delta\varphi = 1.46\pi$ and 0.54π in Fig. 2, C and D; these choices of phase result in routing the maximal output phonon population to Q_1 or Q_2, respectively. In Fig. 2E, we display the resulting high-visibility interference fringes for the final excitation probabilities $P_{Q1,2}(t_f)$ as a function of Δφ. The interference fringe visibility for Q_1 is $\mathcal{V}_{Q1} = 0.806 \pm 0.004$ and for Q_2, $\mathcal{V}_{Q2} = 0.910 \pm 0.005$, where the visibilities are defined as $\mathcal{V}_{Q1,2} = (P_{Q1,2,\max} - P_{Q1,2,\min})/(P_{Q1,2,\max} + P_{Q1,2,\min})$. There is a slight misalignment in the interference pattern for P_{Q1} compared to P_{Q2}, so that, e.g., the phases

for Fig. 2, C and D, do not differ by exactly π. This is possibly because the phase difference between reflected and transmitted phonons is not exactly π/2 [see fig. S1C and discussion in (*28*)].

Hong-Ou-Mandel effect

We next study two-phonon interference, shown in Fig. 3, with the schematic process shown in the inset to Fig. 3A. One phonon is emitted by each qubit, timed so that the phonons arrive at the beam splitter with a relative delay τ; the beam splitter output is then captured by the two qubits. The probability P_{11} of having coincident single phonons in the outputs of a lossless beam splitter with reflectivity η is (*26*)

$$P_{11}(\tau) = 1 - 2\eta + 2\eta^2 + (2\eta^2 - 2\eta)\left[\int \phi_1(t-\tau)\phi_2(t)dt\right]^2 \quad (1)$$

For large delays, the integral is zero, so $P_{11}(\tau \gg \sigma_{1,2}) \rightarrow 1 - 2\eta + 2\eta^2 = 0.524$, using the measured beam splitter reflectivity η. For zero relative delay and identical time-matched waveforms, the integral is unity, giving $P_{11}(0) = (1 - 2\eta)^2 = 0.048$. The coincident probability P_{11} is thus strongly suppressed for zero delay compared to large delays, with a theoretical visibility $\mathcal{V}_{th} \equiv [P_{11}(\tau \gg \sigma_{1,2}) - P_{11}(0)]/P_{11}(\tau \gg \sigma_{1,2}) = 0.908$.

We cannot directly measure the coincident phonon probability P_{11}, but the qubit joint excitation probability P_{ee} serves as a proxy: The probability for both qubits to be excited is closely related to the probability of having a phonon in each output channel. The two probabilities are not in general simply related, owing in part to the nonzero probability of the two-phonon state in each output channel, as well as the different phonon loss rates and imperfect phonon capture by the qubits in the two channels. However, we find experimentally that P_{ee} and P_{11} are closely proportional, with $P_{ee} \approx \alpha P_{11}$ with an empirical scale factor $\alpha = 0.265$. The experimental P_{ee} is also in good agreement with simulations for large and for zero delay (Fig. 3, A to C).

We show the experimental pulse sequence in the inset to Fig. 3B: The qubits are calibrated to emit phonons at 3.925 GHz, and the variable couplers are tuned to release phonons with a hyperbolic secant shape, with fit wave packet widths $\sigma_{1,2} = 8.4$ and 8.3 ns, respectively, timed so the phonons arrive at the beam splitter with relative time delay τ. After emission, the qubits are in their ground states $|g\rangle$. The phonons output from the beam splitter are captured by the two qubits, using the reverse process to emission (*14*, *15*), and the two qubits are measured simultaneously. The capture process is timed so that each qubit catches its own beam-split phonon, with an efficiency very similar to the single-phonon experiment in Fig. 1, D and E.

In Fig. 3, A to C, we show the excited-state probabilities for the two qubits for three different relative delays, $\tau = -150$ ns, $\tau = 0$ ns, and $\tau = 150$ ns, including data taken during the phonon emission and capture processes. In Fig. 3D, we show the corresponding joint excitation probability P_{ee} as a function of delay time τ, directly extracted from the joint two-qubit state measurements. When the delay $\tau \gg \sigma_{1,2}$, phonons pass independently through the beam splitter, yielding a joint qubit excitation probability $P_{ee,max} = P_{Q1} \times P_{Q2} = 0.139 \pm 0.003$. However, when the two phonons arrive at the beam splitter with zero delay τ, two-phonon interference suppresses the coincident phonon output state $|11_{ph}\rangle$, and similarly suppresses P_{ee}, with a minimum at zero delay of $P_{ee,min} = 0.0125 \pm 0.0018$. The visibility of the dip in P_{ee}, $\mathcal{V}_{exp} \equiv (P_{ee,max} - P_{ee,min})/P_{ee,max} = 0.910 \pm 0.013$, agrees well with the visibility calculated for P_{11}. In the "catch" portion of this experiment, the qubits do not capture the entire phonon signal; this can be seen in Fig. 3A, where the transmitted portion of the phonon from Q_1 briefly excites Q_2 at $t \sim 670$ ns. As Q_2's coupler is left on, this excitation is subsequently reemitted. As in this process, the two qubits are detecting the same phonon emitted by Q_1;

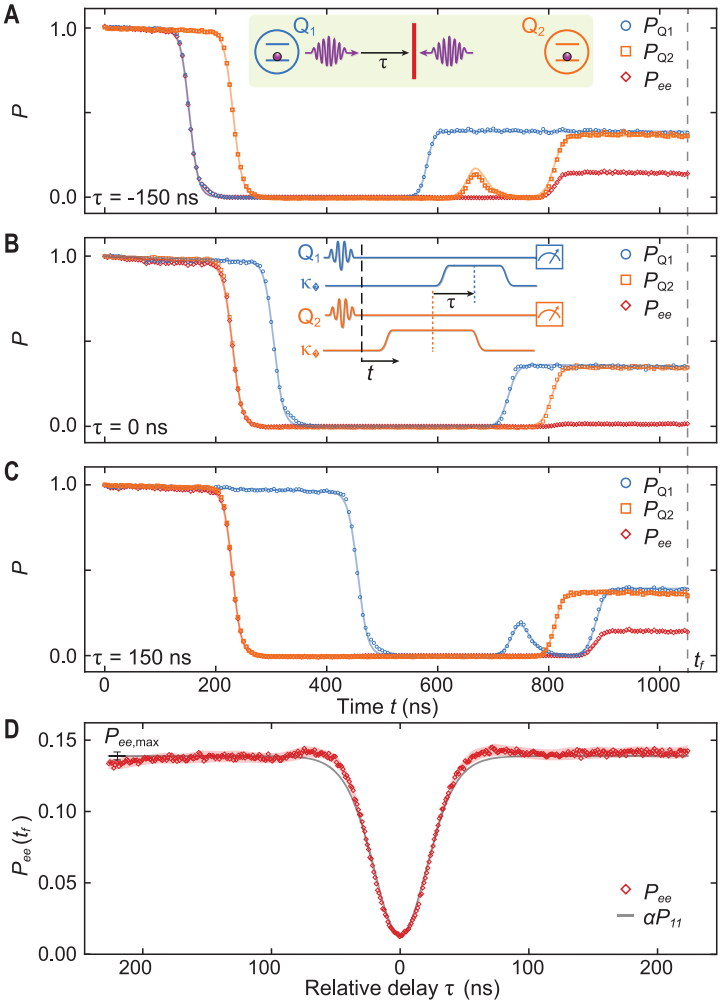


Fig. 3. Two-phonon interference. Each qubit is initialized to its excited state $|e\rangle$, and the qubit coupling rates $\kappa_{1,2}$ controlled to emit a single phonon from each qubit, timed so that the centers of the phonon wave packets reach the center of the beam splitter with a relative delay of (**A**) $\tau = -150$ ns, (**B**) 0 ns, and (**C**) 150 ns, with extracted phonon wave packet widths of $\sigma_1 = 8.4$ ns (Q_1) and $\sigma_2 = 8.3$ ns (Q_2). The output waveforms from the beam splitter are subsequently captured by the qubits via a tuned variation of their coupling rates, and simultaneous measurements of the qubits made at time *t*. Solid lines are numerical simulations (*26*). A schematic of the process appears in the inset to panel (A), and a pulse sequence in the inset to panel (B). The coupling remains on between release and catch. Blue and orange dashed lines in the pulse sequence denote phonon-arrival times at the BS. (**D**) Two-qubit joint excitation probability P_{ee} measured at time t_f as a function of relative delay τ, showing a pronounced Hong-Ou-Mandel dip for coincident phonons. The visibility of the dip is $\mathcal{V} = 0.910 \pm 0.013$, with $P_{ee,max} = 0.139 \pm 0.003$ marked in the upper-left corner (black error bar). Gray line is αP_{11}, calculated from Eq. 1 with parameters extracted from panels (A) to (C) (see main text). Light-red shaded area denotes 1 SD, calculated from 10 repeated scans for each delay τ.

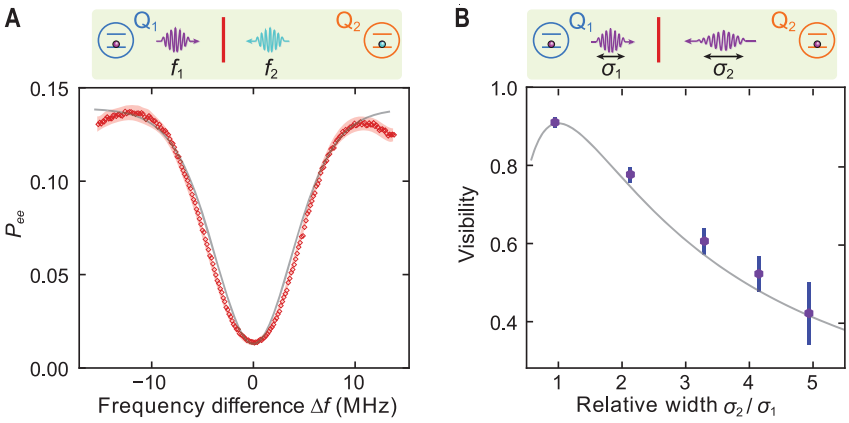


Fig. 4. Frequency and wave packet dependence of two-phonon interference. (**A**) Top: Schematic of phonons released with different frequencies $f_{1,2}$. Main panel: After setting the frequency of Q_1 to f_1 = 3.925 GHz, we vary the relative frequency of Q_2 (horizontal axis) with zero relative delay τ while monitoring the joint excitation probability P_{ee} after phonon capture (vertical axis). Wave packet widths are fixed at $\sigma_{1,2} = 16.0$ and 16.7 ns. A high-visibility dip $\mathcal{V} = 0.899 \pm 0.013$ is observed at zero frequency difference. Gray line represents αP_{11} from frequency-domain theoretical model in (*26*). (**B**) Top: Schematic of phonons released with different wave packet widths $\sigma_{1,2}$. Main panel: We fix both phonon center frequencies at 3.925 GHz, as well as the width $\sigma_1 = 8.8$ ns for Q_1, while varying that for Q_2 over the values $\sigma_2 = 18.7$, 28.9, 36.4, and 43.3 ns, and perform the two-phonon interference experiment. We plot the relative phonon wave packet width σ_2/σ_1 (horizontal axis) and show the resulting HOM dip visibility (vertical axis). The measured visibility is maximal when the wave packets have equal widths, then falls with increasing relative width. First data point is from Fig. 3D, and the other data are from fig. S4. Gray line is calculated from Eq. 1.

only one qubit can be excited at a time, so P_{ee} remains small in this portion of the measurement. There is a similar behavior at $t \sim 750$ ns in Fig. 3C, involving the phonon emitted by Q_2. For zero delay, the two-phonon signal is only partially captured by the receiving qubits, as each qubit can only catch a single phonon; this is similar to the response of non–number-resolving photon detectors (see fig. S3, showing a variation of this measurement process).

We also study the indistinguishability of the two phonons by varying their relative center frequencies and wave packet widths. While fixing the phonon wave packet widths $\sigma_{1,2} = 16.0$ ns and 16.7 ns, setting the delay τ to zero, and fixing Q_1's frequency to $f_1 = 3.925$ GHz, we systematically vary Q_2's frequency f_2 using the qubit flux control. In Fig. 4A, we display the resulting measured joint excitation probability P_{ee} as a function of relative frequency detuning $\Delta f = f_1 - f_2$. We observe a clear dip in P_{ee} with frequency Δf, with visibility $\mathcal{V} = 0.899 \pm 0.013$. The full width at half maximum of the dip is 9.5 MHz, close to the bandwidth of the phonon wave packets. A similar experiment has been done with optical photons (*29*), with similar results. Next, to study the waveform width dependence, we vary the wave packet width σ_2 of Q_2 while fixing that of Q_1 to $\sigma_1 = 8.8$ ns. With a pulse sequence similar to that shown in Fig. 3B, we perform a two-phonon interference experiment, with results displayed in Fig. 4B. The observed variation in visibility is in excellent agreement with the prediction of Eq. 1. This experiment can also be performed while arbitrarily varying the functional dependence of the phonon waveform; we show an example of this in fig. S5.

Conclusion and outlook

Together, these experiments demonstrate a quantum-coherent beam splitter, operated with single-phonon sources and detectors, and the ability to control phonon phase through a qubit. These provide all the elements needed to explore the implementation of linear mechanical quantum computing in this system. An outstanding question is whether phonon loss can be made sufficiently small to enable scaling to useful computational systems. Certainly, gigahertz-frequency bulk acoustic systems, as well as mechanically suspended optomechanical resonators, have much longer phonon lifetimes than we demonstrate here (*3*, *30*), providing some optimism for better performance. It is unlikely that this acoustic approach to linear quantum computing will compete with optical approaches, in which recent implementations have somewhat smaller size elements operating at much higher speeds (*31*, *32*). However, the straightforward integration of phononic circuits with superconducting qubits might provide important opportunities for hybrid computing systems and will further support the development of phononic communication networks (*33*–*38*), possibly integrating computational capabilities.

REFERENCES AND NOTES

1. E. Knill, R. Laflamme, G. J. Milburn, *Nature* **409**, 46–52 (2001).
2. A. D. O'Connell *et al.*, *Nature* **464**, 697–703 (2010).
3. Y. Chu *et al.*, *Science* **358**, 199–202 (2017).
4. K. J. Satzinger *et al.*, *Nature* **563**, 661–665 (2018).
5. T. A. Palomaki, J. D. Teufel, R. W. Simmonds, K. W. Lehnert, *Science* **342**, 710–713 (2013).
6. R. Riedinger *et al.*, *Nature* **556**, 473–477 (2018).
7. C. F. Ockeloen-Korppi *et al.*, *Nature* **556**, 478–482 (2018).
8. E. A. Wollack *et al.*, *Nature* **604**, 463–467 (2022).
9. M. V. Gustafsson *et al.*, *Science* **346**, 207–211 (2014).
10. R. Manenti *et al.*, *Nat. Commun.* **8**, 975 (2017).
11. A. Noguchi, R. Yamazaki, Y. Tabuchi, Y. Nakamura, *Phys. Rev. Lett.* **119**, 180505 (2017).
12. B. A. Moores, L. R. Sletten, J. J. Viennot, K. W. Lehnert, *Phys. Rev. Lett.* **120**, 227701 (2018).
13. A. N. Bolgar *et al.*, *Phys. Rev. Lett.* **120**, 223603 (2018).
14. A. Bienfait *et al.*, *Science* **364**, 368–371 (2019).
15. É. Dumur *et al.*, *NPJ Quantum Inf.* **7**, 173 (2021).
16. A. Bienfait *et al.*, *Phys. Rev. X* **10**, 021055 (2020).
17. A. Zivari, R. Stockill, N. Fiaschi, *Nat. Phys.* **18**, 789 (2022).
18. A. Zivari *et al.*, *Sci. Adv.* **8**, eadd2811 (2022).
19. U. Delić *et al.*, *Science* **367**, 892–895 (2020).
20. L. Shao *et al.*, *Nat. Electron.* **5**, 348–355 (2022).
21. C. K. Hong, Z. Y. Ou, L. Mandel, *Phys. Rev. Lett.* **59**, 2044–2046 (1987).
22. P. Kok *et al.*, *Rev. Mod. Phys.* **79**, 135–174 (2007).
23. J. Koch *et al.*, *Phys. Rev. A* **76**, 042319 (2007).
24. R. Barends *et al.*, *Phys. Rev. Lett.* **111**, 080502 (2013).
25. Y. Chen *et al.*, *Phys. Rev. Lett.* **113**, 220502 (2014).
26. Materials and methods are available as supplementary materials.
27. K. J. Satzinger *et al.*, *Appl. Phys. Lett.* **114**, 173501 (2019).
28. R. Uppu, T. A. W. Wolterink, T. B. H. Tentrup, P. W. H. Pinkse, *Opt. Express* **24**, 16440–16449 (2016).
29. P. Imany *et al.*, *Opt. Lett.* **43**, 2760–2763 (2018).
30. G. S. MacCabe *et al.*, *Science* **370**, 840–843 (2020).
31. W. Bogaerts *et al.*, *Nature* **586**, 207–216 (2020).
32. L. S. Madsen *et al.*, *Nature* **606**, 75–81 (2022).
33. S. J. M. Habraken, K. Stannigel, M. D. Lukin, P. Zoller, P. Rabl, *New J. Phys.* **14**, 115004 (2012).
34. W. Fu *et al.*, *Nat. Commun.* **10**, 2743 (2019).
35. J. C. Taylor, E. Chatterjee, W. F. Kindel, D. Soh, M. Eichenfield, *NPJ Quantum Inf.* **8**, 19 (2022).
36. M. C. Kuzyk, H. Wang, *Phys. Rev. X* **8**, 041027 (2018).
37. M.-A. Lemonde *et al.*, *Phys. Rev. Lett.* **120**, 213603 (2018).
38. W. Chen *et al.*, *Nat. Phys.* 10.1038/s41567-023-01952-5 (2023).

ACKNOWLEDGMENTS

We thank A. Bienfait and P. Duda for helpful discussions.
Funding: Devices and experiments were supported by the Air Force Office of Scientific Research and the Army Research Laboratory. Results are in part based on work supported by the US Department of Energy Office of Science National Quantum Information Science Research Centers. É.D. was supported by LDRD funds from Argonne National Laboratory. This work was partially supported by UChicago's MRSEC (NSF award DMR-2011854) and by the NSF QLCI for HQAN (NSF Award 2016136). We made use of the Pritzker Nanofabrication Facility, which receives support from SHyNE, a node of the National Science Foundation's National Nanotechnology Coordinated Infrastructure (NSF grant no. NNCI ECCS-2025633).
Author contributions: H.Q. designed and fabricated the devices, performed the measurements, and analyzed the data. É.D. contributed to UDT design and measurement techniques. G.A., H.Y., M.H.C., and J.G. provided suggestions with measurement and data analysis. A.N.C. advised on all efforts. All authors contributed to the discussions and production of the manuscript. **Competing interests:** The authors declare no competing interests. **Data and materials availability:** All data are available, in both the manuscript and the supplementary materials. **License information:**

Copyright © 2023 the authors, some rights reserved; exclusive licensee American Association for the Advancement of Science. No claim to original US government works. https://www.sciencemag.org/about/science-licenses-journal-article-reuse

SUPPLEMENTARY MATERIALS

science.org/doi/10.1126/science.adg8715
Materials and Methods
Supplementary Text
Figs. S1 to S5
Table S1
References (*39*–*43*)

Submitted 26 January 2023; accepted 28 April 2023
10.1126/science.adg8715

FERROELECTRICS

Atomic-scale polarization switching in wurtzite ferroelectrics

Sebastian Calderon V[1], John Hayden[2], Steven M. Baksa[2], William Tzou[1], Susan Trolier-McKinstry[2], Ismaila Dabo[2], Jon-Paul Maria[2], Elizabeth C. Dickey[1]*

Ferroelectric wurtzites have the potential to revolutionize modern microelectronics because they are easily integrated with multiple mainstream semiconductor platforms. However, the electric fields required to reverse their polarization direction and unlock electronic and optical functions need substantial reduction for operational compatibility with complementary metal-oxide semiconductor (CMOS) electronics. To understand this process, we observed and quantified real-time polarization switching of a representative ferroelectric wurtzite ($Al_{0.94}B_{0.06}N$) at the atomic scale with scanning transmission electron microscopy. The analysis revealed a polarization reversal model in which puckered aluminum/boron nitride rings in the wurtzite basal planes gradually flatten and adopt a transient nonpolar geometry. Independent first-principles simulations reveal the details and energetics of the reversal process through an antipolar phase. This model and local mechanistic understanding are a critical initial step for property engineering efforts in this emerging material class.

Between 2019 and 2021, researchers worldwide demonstrated unexpected ferroelectricity in solid solutions in the AlN-ScN (*1*), AlN-BN (*2*), GaN-ScN (*3*), and ZnO-MgO (*4*) composition families. These reports disrupted the more than 100-year-old perspective that wurtzite crystals are pyroelectric and piezoelectric but cannot be ferroelectric because the polarization cannot be switched with an electric field. The important scientific and technological consequences that accompanied this understanding were that (i) we have a previously unknown class of ferroelectrics that violates the long-standing relationship linking polarization and ferroelectric transition temperature (*5*)—that is, they are likely not soft-mode ferroelectrics; (ii) the new physical mechanisms that enable ferroelectricity will almost certainly impart different manifestations of physical scaling trends and different property dependencies on temperature, pressure, and time; and (iii) these materials can be processed at or near room temperature with a robust property response, and in some cases (for example, $Al_{1-x}B_xN$) they consist exclusively of elements that are already common and essential in the silicon complementary metal-oxide semiconductor (CMOS) front end.

This emerging ability to directly integrate a strongly hysteretic nonlinear dielectric is transformational for future logic, memory, high-power, acoustic, or electro-optic devices (*6*–*8*). These ferroelectrics, however, bring their own challenges, the most notable being that the margin between the coercive field and breakdown field is uncomfortably small at room temperature. Consequently, devices are operated in close proximity to their failure thresholds, which invariably erodes electrical endurance and can induce degradation pathways.

Lowering the energetic switching barriers is a principal goal necessary to realize the full potential of ferroelectric wurtzites in electr… optical, and acoustic devices. Empirically, … know that epitaxial tensile strain and an increased dopant concentration can reduce coercive fields in $Al_{1-x}Sc_xN$ (*9*, *10*) and $Al_{1-x}B_xN$ (*2*), presumably by reducing the energy barriers that regulate the polarity switch, and that increasing temperature also reduces the coercive field by thermally activating the nucleation and switching processes (*11*). These trends are based on macroscopic observations—that is, on measuring millimeter-scale capacitors—and although the trends demonstrate possibilities to reduce the coercive field, they do not provide local mechanistic insight.

Understanding these trends and phenomena at global and local-length scales is essential so that the property response of wurtzite ferroelectrics can be further developed for practical use. We addressed this challenge by measuring in situ the polarization reversal process at the atomic scale. Our experimental approach takes advantage of local electrostatic sample charging occurring during the illumination of dielectric materials in the electron microscope, which can induce the necessarily large local electric fields (*12*, *13*) for polarization switching in ferroelectrics (*14*, *15*). We used scanning transmission electron microscopy (STEM) in differentiated differential phase contrast mode (dDPC) to observe in situ polarization inversion in thin films of the composition $Al_{0.94}B_{0.06}N$ [(Al,B)N]. Materials in this composition space have remanent polarization (P_r) values exceeding 125 μC cm^{-2} while maintaining bandgaps above 5.8 eV; this is a substantial advantage relative to other wurtzite-based ferroelectrics, albeit the coercive fields are also larger (*2*). Our experimental analysis documents polarization switching with quantitative information at the atomic scale that is coinformed with first-principles calculations of the same composition. The first-principles simulation analyses provide an atomic-scale understanding of the switching pathways and energetics in these emerging ferroelectric materials. Covalidation

[1]Department of Materials Science and Engineering, Carnegie Mellon University, Pittsburgh, PA 15213, USA. [2]The Pennsylvania State University, Department of Materials Science and Engineering and Materials Research Institute, University Park, PA 16802, USA.
*Corresponding author. Email: ecdickey@cmu.edu

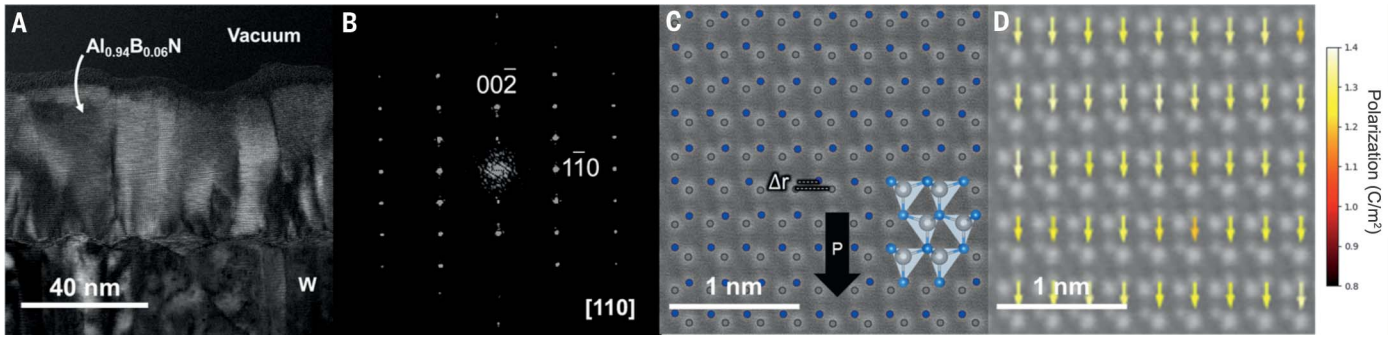


Fig. 1. Structure of (Al,B)N. (**A**) dDPC-STEM images for (Al,B)N film. (**B**) Fast Fourier transform calculated from the (Al,B)N region of image in (A). (**C**) dDPC-STEM image of an (Al,B)N grain oriented along the [110] direction, where the location of the atomic columns has been highlighted with blue (N) and gray (Al) circles after Gaussian fitting. "P" with arrow shows the direction of polarization. (**D**) dDPC image overlapped with a vector map indicating the calculated polarization at each unit cell.

of STEM imaging and density functional theory support a switching mechanism in which a transient antipolar structure mediates the switching process; the transient structure is similar to long-standing models for inversion domain boundaries in III-nitrides.

Effect of boron and wake-up process on the structure

We show a dDPC-STEM image of an (Al,B)N film grown by means of reactive pulsed dc sputtering on a W electrode, showing a columnar grain structure with a nominal epitaxial relation of (Al,B)N <001> // W <110> // growth direction (Fig. 1). The W electrode is faceted, and we observed small variations in the orientation of (Al,B)N grains, leading to the low density of dislocations that are observed in the image. We detected the out-of-plane crystalline mosaicity in the rocking curves of the 002 reflection of the (Al,B)N films, with full width at half-maximum (FWHM) values of 1.44° (fig. S1).

From the STEM images, we made structural polarization measurements to compare with macroscopic measurements. To quantify the spontaneous polarization, we acquired dDPC images along the <110> zone axis (Fig. 1C), where the growth direction points from the bottom to the top of the image along the $[00\bar{1}]$ direction of (Al,B)N. We determined the polarization orientation from the images by establishing the nitrogen tetrahedral orientation (Fig. 1C, inset). This orientation is polarization down—that is, the positive end of the permanent dipole points to the substrate, which is commonly referred to as an "N-polar" growth direction. Among the observed regions, the N-polar orientation is uniform with no evidence of Al-polar orientations, which is consistent with prior studies that show uniformly N-polar-oriented films (*16*). The atomic-column positions of both Al(B) and N were determined with a Gaussian fitting process on the dDPC images, which allows precise location of the atomic-column positions and thus an accurate quantification of the polarization, as previously reported (*17*). The polarization was quantified by using the Born effective charges calculated from density-functional perturbation theory (*18*). We show a vector-map representation of the calculated polarization per unit cell for an as-deposited (Al,B)N film (Fig. 1D), which we discuss in comparison with other samples.

We constructed a summary comparison of the calculated polarization per unit cell for as-deposited pure AlN film (Fig. 2A), an as-deposited (Al,B)N film (Fig. 2B), and a field-cycled (Al,B)N film left in the opposite polarity from the as-deposited film (Fig. 2C). The sputtered AlN film (Fig. 2A) exhibits an average polarization magnitude of 1.13 ± 0.07 C m^{-2}. The standard deviation is close to the measurement uncertainty arising from the atomic-column fitting process. The average measured polarization magnitude is 6.6% less than that of the ideal AlN structural model (1.21 C m^{-2}). The as-deposited (Al,B)N film (Fig. 2B) exhibits an average spontaneous polarization of 1.30 C m^{-2}, 13% larger than the undoped film, which is in agreement with the trend predicted by first principles (*2*). The (Al,B)N film exhibits peak-to-peak variations of 1.13 to 1.36 C m^{-2} and a standard deviation of 0.10 C m^{-2} within the measured area. These variations, which exceed the measurement error, are consistent with the chemical and structural inhomogeneities associated with the 6% B substitution—for example, FWHM x-ray peak widths of ~1° in ω and 2θ circles and a large radial misfit of B for Al.

Electric field–induced polarization switching from the as-deposited unipolar state can be highly frequency dependent. For kilohertz pulses just above the coercive field, full reversal per cycle may take many tens of cycles. For slow cycling (for example, 0.1 Hz), one sweep can be sufficient. This "wake-up" process that precedes fast polarization reversal is ascribed to low initial domain-wall density and mobility (*16*). To better understand this wake-up phenomenon, we completed the same STEM polarization analysis on a field-cycled sample and compared those results against bulk electrical

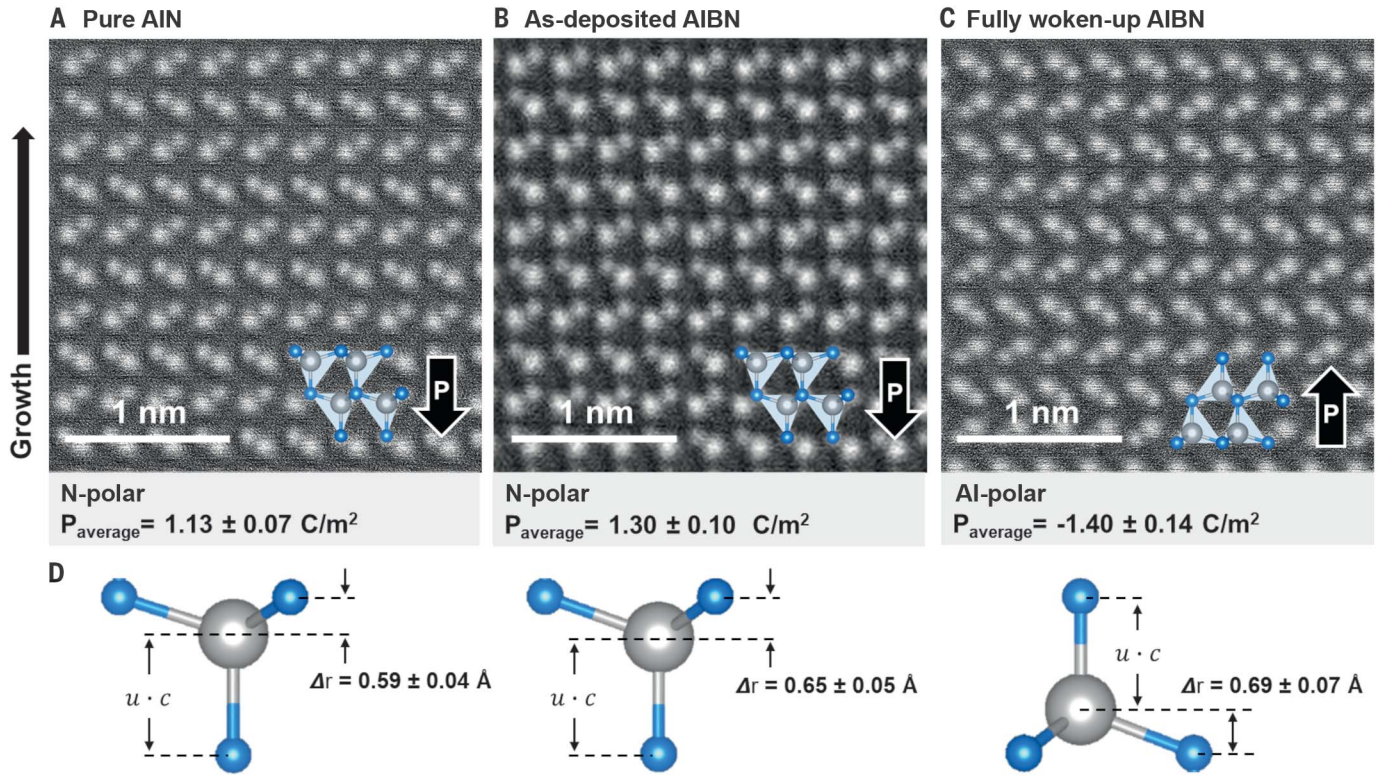


Fig. 2. Polarization evolution. (**A** to **C**) dDPC images for (A) pure AlN, (B) (Al,B)N as-deposited, and (C) field-cycled (Al,B)N. (**D**) Schematic of the structure modification after boron incorporation and field cycling. dDPC-STEM images showing the full field of view are presented in fig. S2.

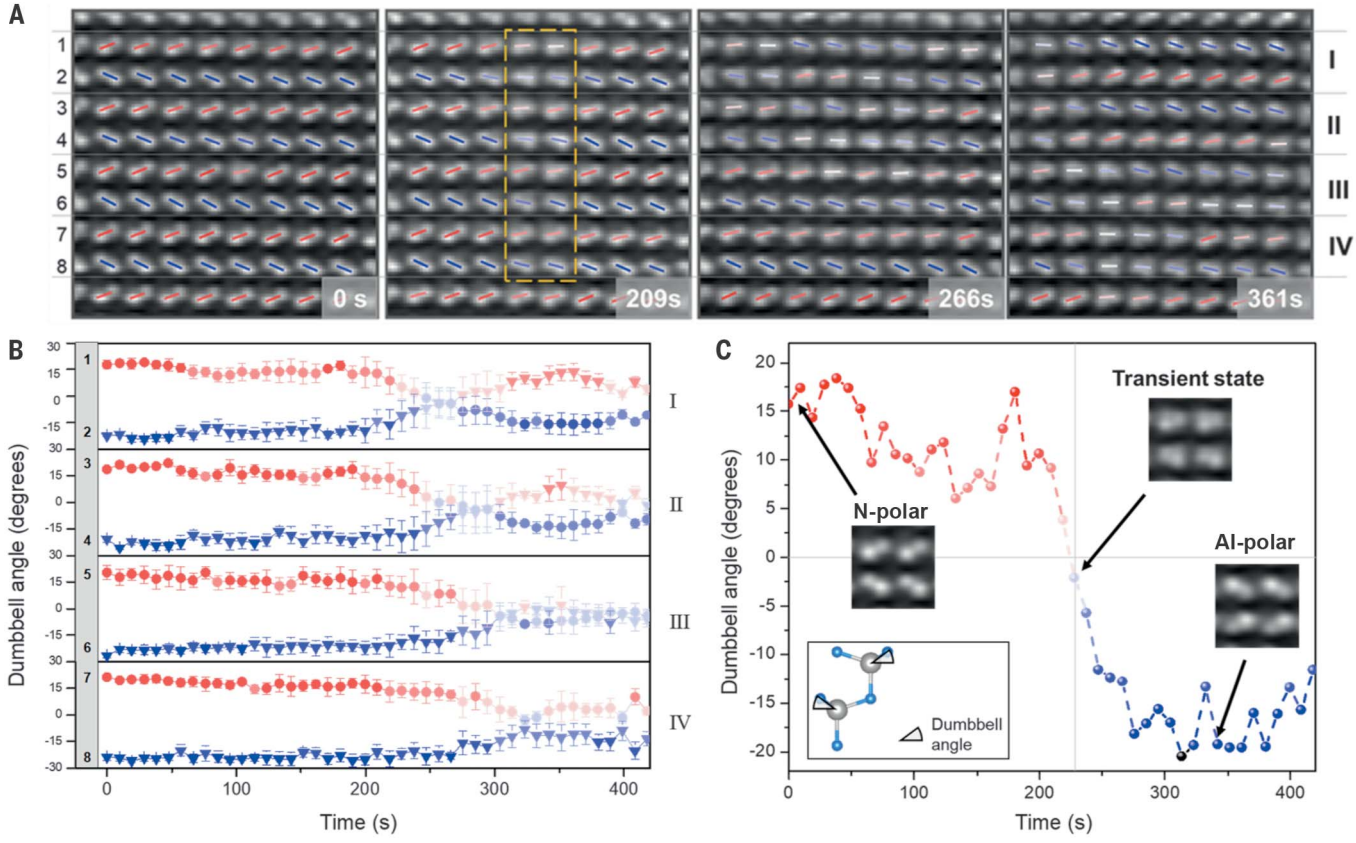


Fig. 3. In situ polarization switching. (**A**) dDPC-STEM frames at 0, 209, 266, and 361 s for in situ polarization switching. (**B**) AlN dumbbell-angle evolution as a function of time for the corresponding frames in (A). The Roman numerals in (A) and (B) indicate the different regions in the images going from the top of the frame (I) to the bottom (IV). The rows of AlN dumbbells in the images are numbered from 1 to 8 for reference between (A) and (B). (**C**) Dumbbell-angle evolution as a function of time for one unit cell. (Inset) The schematics of the dumbbell angle and the dDPC images at specific times.

measurements. For a fully woken-up sample, hysteresis loops yield P_r of 1.38 ± 0.01 C m^{-2}, whereas dDPC-STEM imaging yields 1.40 ± 0.14 C m^{-2}. Furthermore, the STEM-based polarization measurements allow us to compare the intrinsic spontaneous polarization in the as-deposited and field-cycled states (Fig. 2, B and C). The similarity of these STEM-quantified polarization magnitudes (average values within ~7%) suggests that the wake-up process does not substantially alter the bulk material structure.

To further explore this possibility, we analyzed the average local structure evolution using two-dimensional vector pair correlation functions (vPCF) calculated from dDPC-STEM images that can be found in the supplementary materials (fig. S3) (*19*). The relevant parameter extracted from vPCF is Δr (Fig. 2D), which describes the distance between the nearest (Al,B) basal-plane layers and N layers, also referred to as the "puckering" of the wurtzite basal planes. Whereas the average Δr increases 10% on alloying AlN with 6% B, the Δr in as-deposited and field-cycled (Al,B)N states are the same within one standard deviation of the measurement distribution, supporting the conclusion of no major structural phase transitions during the wake-up process. We therefore infer that the wake-up phenomenon is more likely associated with interfacial or nucleation site–based mechanisms than bulk crystal-structure changes.

In situ switching observations

Electron microscopy can visualize ferroelectric polarization reversal at length scales that reveal local atomic and domain structures (*15*, *20*). In these cases, preparation of extremely thin parallel-plate capacitor structures that can be field cycled either in situ or by implementing a nanoprobe that applies a local bias is common (*20*). Wurtzite ferroelectrics are difficult to analyze with these methods because of the large coercive fields that invariably accelerate surface migration of atomic species across the sample surface and create short-circuit pathways. Alternatively, prior reports demonstrate that the charge accumulation from beam-solid interactions in electron and ion microscopes can create internal fields large enough to reverse ferroelectric polarization (*14*, *15*). By using extended beam exposures during STEM image acquisition, polarization reorientation can be achieved from the large lateral electric fields that emerge from the beam-solid interactions that produce positive sample charging, as described in detail by Cazaux (*12*). For very thin samples, incident electrons do not contribute substantially to charge accumulation because they are fully transmitted. However, some electrons are scattered inelastically, promoting ionization and secondary and Auger electron emission and a net positive charge accumulation for electrically insulating materials. This superimposes additional built-in electric fields, which can reach the megavolt-per-centimeter range needed to switch (Al,B)N. Our primary dataset is an in situ domain switching movie collected on an (Al,B)N film (movie S1). We summarize the in situ data with a set of frames spanning the roughly 7-min experiment (Fig. 3). The images are indexed from top to bottom with row numbers and divided into four regions (I, II, III, and IV), with region I closest to vacuum (the top of the sample), where the charge-induced field is expected to be largest in the vertical direction (and thus capable of inducing switching), and region IV closest to the bottom electrode, which provides a physical path to

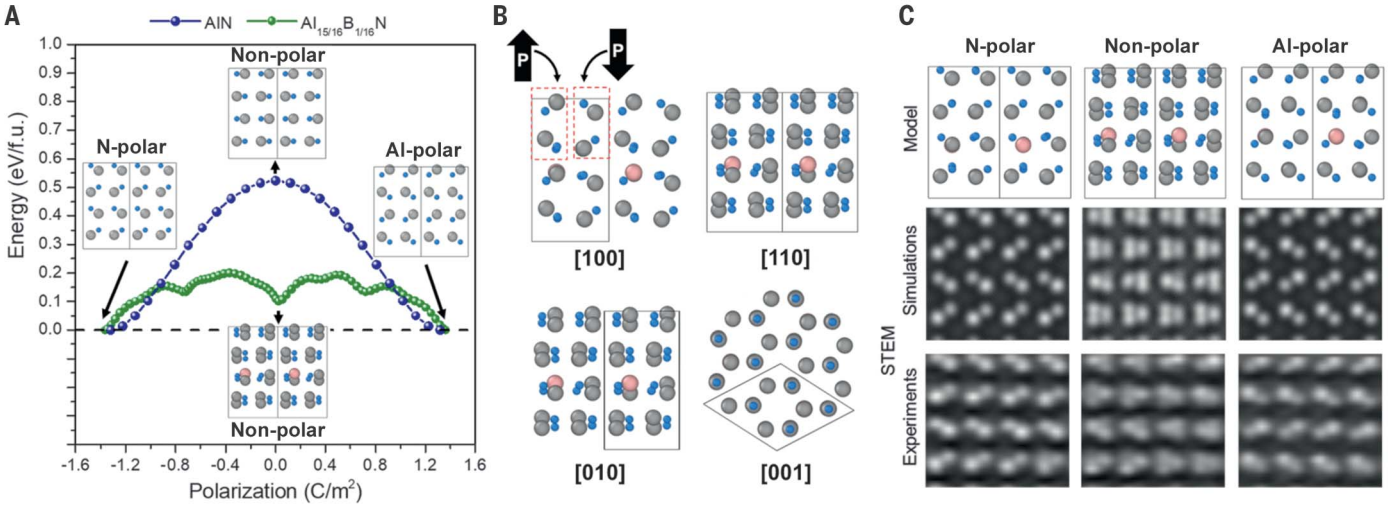


Fig. 4. Nudged-elastic-band simulation of polarization reversal pathways. (**A**) Nudged-elastic-band simulation of polarization reversal pathways for AlN and $Al_{15/16}B_{1/16}N$. (Insets) The structural models at specific stages of the simulation. (**B**) Structural model of the nonpolar transient state calculated for $Al_{15/16}B_{1/16}N$ viewed along different projections. (**C**) Atomic models, STEM image simulations, and experimental images for the N-polar, nonpolar, and Al-polar states.

microscope ground. This distinction is important because the electric field in the experiment will necessarily be spatially heterogeneous in magnitude and evolve over time; nonetheless, it serves as an important mechanism to induce switching in these large-coercive-field samples. Our STEM images are overlayed with red, white, and blue lines, which indicate quantitatively (from image analysis) the dumbbell angles associated with the bond puckering in the wurtzite basal plane; red is positive, blue is negative, and white is 0° on average. We show four graphs that quantify the average dumbbell angles for regions I through IV (Fig. 3B), each one representing a unit-cell-thick layer. We note four observations: (i) In region I, the transition between red and blue is the most clear and uniform and occurs first; this observation is consistent with expectations for maximum charging fields in this zone. (ii) As one progresses from the top zones to the bottom zones, the dumbbell-angle transition is less uniform, and the switching process takes longer; this is again consistent with the anticipated electric-field evolution and gradient direction. (iii) Region IV and below do not completely switch, which is attributed to diminishing electric field toward the bottom of the sample. (iv) The regions of the sample that switch do so through a transient state in which the integrated intensities of all associated scatterers yield an average dumbbell angle of 0° (Fig. 3C).

We also note the 209-s panel in Figure 3A, and in particular, the yellow highlighted rectangular region where the largest electric field is expected. The dumbbell-angle rotation, and thus switching, initiates first at the top of this rectangle and progresses laterally and vertically with time; the structure in this region is identified as a local domain nucleation site with attendant domain walls.

Last, we show the average AlN dumbbell-angle progression for one unit cell in the movie close to the location of maximum anticipated electric field (Fig. 3C). The angle evolution from positive to negative values, and thus polarization down to up, is clearly visible. Figure 3C also contains inset images of the initial N-polar (polarization-down) state, the final Al-polar (polarization-up) state, and the transient intermediate state of this region of the sample.

To further understand the switching pathway and identify the transient state observed experimentally, we carried out first-principles calculations using the nudged-elastic-band method for determining the minimum energy pathway for polarization reversal in both AlN and $Al_{15/16}B_{1/16}N$, which closely matches the experimental composition. After structural optimization, we calculated the polarization reversal pathways (Fig. 4A). The results highlight two distinct mechanisms, in which AlN switches coherently in one step at 0.523 eV/formula unit (f.u.), whereas $Al_{15/16}B_{1/16}N$ switches sequentially in nine steps at 0.200 eV/f.u. The coherent polarization reversal suggests that pure AlN switches through a nonpolar hexagonal (*h*)-BN–like structure, whereas in $Al_{15/16}B_{1/16}N$, we observed an average nonpolar supercell in the middle of the switching process (Fig. 4A, insets). This metastable state is not a *h*-BN–like structure but consists of antipolar arrangements of wurtzite motifs when viewed along the [100] direction, as shown in our atomic models (Fig. 4B). A more convoluted structure is observed when projecting the structure along the [110] or [010] orientation (Fig. 4B), where N-polar and Al-polar unit cells are overlapped in this projection, which agrees qualitatively well with the transient structure observed during the in situ switching experiments. Both in situ data and first-principles calculation independently show that the anion and cation sublattice contribute comparable distortions along the switching path.

To correlate the experimental observations and the first-principles calculations, we carried out dPDC-STEM image simulations using the atomic models of the $Al_{15/16}B_{1/16}N$, at the initial (N-polar), middle (nonpolar), and final (Al-polar) step in the simulation (Fig. 4C). The simulated images correlate well with the experimental STEM images at different stages during the switching process, corroborating the nonpolar state predicted with the nudged-elastic-band simulations. Similar projected local structures have been observed with TEM and STEM images in polarity inversion domain boundaries (IDBs) in other wurtzite structures (*21*–*23*), and the four- and eightfold rings of bonds that were found in simulations of IDBs in GaN (*24*) are present in this metastable $Al_{15/16}B_{1/16}N$ structure (fig. S4). The low-energy IDB in GaN exhibits no interface electronic gap states because the Ga and N atoms can maintain similar local coordination as the parent wurtzite phase.

These results provide insight into the induced ferroelectricity of wurtzite structures such as AlN, where the incorporation of alloying elements, such as B, in the parent wurtzite structure, results in substantial local-bonding and local-structural distortions, as has been pointed out in the (Al,Sc)N system (*25*). We demonstrated that this disorder provides low-energy pathways to nucleate the switching process and that the switching is mediated by a metastable transient nonpolar state. This nonpolar metastable state maintains a local structure similar

to the parent wurtzite structure and analogous to the local structure evidenced in IDBs in numerous nonferroelectric wurtzites. The chemical and structural disorder in the (Al,B)N alloys leads to a relatively flat energy landscape that facilitates switching.

Our work provides detailed atomic-scale structure analysis of ferroelectrically active wurtzite-structured (Al,B)N thin films, revealing that B doping leads to a larger spontaneous polarization relative to pure AlN sputtered films. The study also unambiguously shows the domain nucleation and switching pathway for these emerging ferroelectric materials. The alloying disorder provides a complex but substantially lower-energy-barrier switching pathway to a transient nonpolar state, which engenders ferroelectricity in the class of technologically important polar materials. Such wurtzite-structured materials can be coprocessed with mainstream semiconductors, providing pathways toward CMOS-compatible integrated ferroelectrics, piezoelectrics, and electro-optics. Our insights into the atomic-scale processes of domain switching provide guidance to ongoing and future investigations of wurtzite-structured thin films that can lead to targeted property performance.

REFERENCES AND NOTES

1. S. Fichtner, N. Wolff, F. Lofink, L. Kienle, B. Wagner, *J. Appl. Phys.* **125**, 114103 (2019).
2. J. Hayden *et al*., *Phys. Rev. Mater.* **5**, 044412 (2021).
3. D. Wang, P. Wang, B. Wang, Z. Mi, *Appl. Phys. Lett.* **119**, 111902 (2021).
4. K. Ferri *et al*., *J. Appl. Phys.* **130**, 044101 (2021).
5. S. C. Abrahams, S. K. Kurtz, P. B. Jamieson, *Phys. Rev.* **172**, 551–553 (1968).
6. A. Sebastian, M. Le Gallo, R. Khaddam-Aljameh, E. Eleftheriou, *Nat. Nanotechnol.* **15**, 529–544 (2020).
7. N. Setter *et al*., *J. Appl. Phys.* **100**, 051606 (2006).
8. A. Fernandez *et al*., *Adv. Mater.* **34**, e2108841 (2022).
9. M. Noor-A-Alam, O. Z Olszewski, M. Nolan, *ACS Appl. Mater. Interfaces* **11**, 20482–20490 (2019).
10. S. Clima *et al*., *Appl. Phys. Lett.* **119**, 172905 (2021).
11. W. Zhu *et al*., *Appl. Phys. Lett.* **119**, 062901 (2021).
12. J. Cazaux, *Ultramicroscopy* **60**, 411–425 (1995).
13. R. F. Egerton, P. Li, M. Malac, *Micron* **35**, 399–409 (2004).
14. A. C. G. Nutt, V. Gopalan, M. C. Gupta, *Appl. Phys. Lett.* **60**, 2828–2830 (1992).
15. J. L. Hart *et al*., *Phys. Rev. B* **94**, 174104 (2016).
16. W. Zhu *et al*., *Adv. Electron. Mater.* **8**, 2100931 (2022).
17. S. Calderon, S. D. Funni, E. C. Dickey, *Microsc. Microanal.* **28**, 1–12 (2022).
18. Materials and methods are available as supplementary materials.
19. S. D. Funni *et al*., *APL Mater.* **9**, 091110 (2021).
20. L. Li, L. Xie, X. Pan, *Rep. Prog. Phys.* **82**, 126502 (2019).
21. T. Akiyma *et al*., *Jpn. J. Appl. Phys.* **58** (SC), SCCB30 (2019).
22. N. Stolyarchuk *et al*., *Sci. Rep.* **8**, 14111 (2018).
23. L. T. Romano, J. E. Northrup, M. A. O'Keefe, *Appl. Phys. Lett.* **69**, 2394–2396 (1996).
24. J. E. Northrup, J. Neugebauer, L. T. Romano, *Phys. Rev. Lett.* **77**, 103–106 (1996).
25. K. Yazawa, J. S. Mangum, P. Gorai, G. L. Brennecka, A. Zakutayev, *J. Mater. Chem. C* **10**, 17557–17566 (2022).
26. S. Calderon *et al*., Atomic-scale polarization switching in wurtzite ferroelectrics - dDPC data, Zenodo (2023); https://doi.org/10.5281/zenodo.7916420.
27. S. Calderon *et al*., Atomic-scale polarization switching in wurtzite ferroelectrics - DFT data, Zenodo (2023); https://doi.org/10.5281/zenodo.7916565.

ACKNOWLEDGMENTS

Funding: This material is based on work supported by the Center for 3D Ferroelectric Microelectronics (3DFeM), an Energy Frontier Research Center funded by the US Department of Energy, Office of Science, Office of Basic Energy Sciences Energy Frontier Research Centers program under award DE-SC0021118. E.C.D. and S.C. acknowledge the use of the Materials Characterization Facility at Carnegie Mellon University supported by grant MCF-677785.
Author contributions: Conceptualization: S.C.V. and E.C.D. Material production: J.H. and J.-P.M. Electron microscope characterization: S.C.V, W.T., and E.C.D. First-principles calculations: S.M.B. and I.D. Data interpretation: S.C.V., J.H., S.M.B., E.C.D., J.-P.M., I.D., and S.T.-M. Funding acquisition: E.C.D, J.-P.M., I.D., and S.T.-M. Supervision: E.C.D., J.-P.M., and I.D. Writing – original draft: S.C.V. Writing – review and editing: All authors reviewed and edited the draft. **Competing interests:** The authors declare that they have no competing interests. **Data and materials availability:** TEM data generated in this study are available at Zenodo (*26*). First-principles data and models that support the findings of this study are available at Zenodo (*27*).
License information: Copyright © 2023 the authors, some rights reserved; exclusive licensee American Association for the Advancement of Science. No claim to original US government works. https://www.science.org/about/science-licenses-journal-article-reuse

SUPPLEMENTARY MATERIALS

science.org/doi/10.1126/science.adh7670
Materials and Methods
Figs. S1 to S4
Movie S1
References (*28*–*44*)

Submitted 13 March 2023; accepted 10 May 2023
10.1126/science.adh7670

BIOGEOGRAPHY

Limited climatic space for alternative ecosystem states in Africa

Steven I. Higgins[1]*, Timo Conradi[1], Laurence M. Kruger[2,3], Robert B. O'Hara[4], Jasper A. Slingsby[3,5,6]

One of the foundational premises of ecology is that climate determines ecosystems. This has been challenged by alternative ecosystem state models, which illustrate that internal ecosystem dynamics acting on the initial ecosystem state can overwhelm the influence of climate, and by observations suggesting that climate cannot reliably discriminate forest and savanna ecosystem types. Using a novel phytoclimatic transform, which estimates the ability of climate to support different types of plants, we show that climatic suitability for evergreen trees and C4 grasses are sufficient to discriminate between forest and savanna in Africa. Our findings reassert the dominant influence of climate on ecosystems and suggest that the role of feedbacks causing alternative ecosystem states is less prevalent than has been suggested.

Predicting how global vegetation patterns will be altered by climate change is a fundamental challenge for ecological science (*1*). One particular challenge for prediction models is accommodating the possibility that at any single location in environmental space, alternative ecosystem types may occur. For example, across the global tropics, forest and savanna are both observed between 1000 and 2500 mm of mean annual precipitation (*2*, *3*). The observation that qualitatively different ecosystems (i.e., "ecosystem states") can exist under the same environmental conditions has led to the emergence of the alternative ecosystem state (AES) hypothesis.

The AES hypothesis posits that an AES is a self-maintaining state that cannot be predicted from environmental forcing factors (*4*–*7*). Such self-maintaining states are induced by differences in initial conditions and maintained by positive feedback processes. Strictly, the initial condition or initial ecosystem state refers to the system state at some time zero. In practice, whenever the system state is modified by a historic event (e.g., a stand-replacing fire, windstorm, or drought), this initial condition is reset, conceptually resetting the system to a new time zero. In AES applications such historical events can have a sufficiently large effect to move the ecosystem state into the domain of attraction of an alternative ecosystem state, which is then maintained by positive feedback processes (*8*).

Several lines of evidence are consistent with the AES hypothesis. Theoretical models have demonstrated the possibility that positive feedback processes in the internal system dynamics acting on the initial ecosystem state can allow qualitatively different ecosystem states to persist in the same environmental setting (*9*). Heuristic models (*10*–*12*) and forecasting models (*13*) have supported this interpretation, as have empirical studies using remote sensing (*2*, *3*, *14*, *15*), tree basal area (*16*), and floristic surveys (*17*, *18*). The plausibility of the AES hypothesis is thus not in question. However, the geographical extent of AES regions is unclear.

Attempts to quantify the geographic extent of AES (*2*, *3*, *14*, *15*, *17*, *18*) have done so by identifying regions where environmental drivers cannot predict observed differences in ecosystem states. However, such analyses potentially confound true AES with apparent AES (e.g., fig. S7). True AES is when observed differences in ecosystem state are caused by differences in initial conditions and not by differences in environmental drivers. Apparent AES occurs when differences in observed ecosystem states are erroneously attributed to differences in initial conditions, when in fact they are caused by unmeasured environmental drivers. For example, observed differences in ecosystem state in a landscape exposed to the same climate might be caused by topographic variation or soil differences. This means that prediction uncertainty is not a signature of AES but rather is the outcome of combinations of model, parameter, driver, observation, and initial condition uncertainty (*19*–*21*) (figs. S6, S7, S8).

For predicting global vegetation patterns it is of fundamental importance to know whether the ecosystem state at a particular location in environmental space can be predicted based on external forcing by climate system variables or whether positive feedbacks acting on the initial ecosystem state might determine ecosystem state (*19*, *20*). Here we revisit the challenge posed by the alternative ecosystem state hypothesis for prediction models, by using a recently proposed method for characteri… the influence of climate on vegetation (*22*)… a case study, we use one of the most widely studied examples of alternative ecosystem states: forest and savanna in tropical and subtropical Africa (*2*, *3*, *17*, *23*). Specifically, we test whether a climate-based prediction model can predict forest and savanna from a benchmark dataset of floristically defined savanna and forest sites (*17*) (hereafter the AfroTropTree data). The AfroTropTree data use plant community composition data to unambiguously assign 753 sites to savanna and forest categories and thereby avoids observation uncertainty associated with using remotely sensed data to classify vegetation (*24*, *25*).

Phytoclimatic drivers of forest and savanna

We used a plant growth model (fig. S9), species distribution data, and climate system data (temperature, soil moisture, photosynthetically active radiation, atmospheric CO_2; table S4) to estimate the physiological niches for 4542 African plant species (*21*). The physiological niche as conceptualized by this model (fig. S10) describes how abiotic drivers influence a plant's growth and its assimilation of carbon and nitrogen. We then estimated the climatic suitability of geolocations for major plant growth forms by averaging the niche projections for all species belonging to each growth form (*22*). Conceptually this procedure is a phytoclimatic transform; that is, it uses the plant growth model to transform climate variables into plant suitability variables (*21*). The phytoclimatic transform produced coherent continental projections of the suitability of Africa for different plant growth forms (Fig. 1). The arid parts of the continent were generally unsuitable for all growth forms whereas the warm and moist parts of the continent were suitable for most growth forms, ensuring that correlations between the growth form suitability surfaces (e.g., evergreen trees and climbers) were conspicuous. Differences were also apparent (e.g., annual versus perennial forbs; evergreen versus deciduous trees) and some growth forms (annual forbs and C4 grasses) had broader climatic tolerances than others (evergreen trees, climbers, geophytes, and succulents).

We then used the growth form suitability surfaces (Fig. 1) as explanatory variables in a logistic regression model that predicts ecosystem state (forest or savanna) reported in the AfroTropTree data (*17*, *21*). The logistic regression revealed that the information contained in the phytoclimatic transform (Fig. 1 and table S3) was sufficient to correctly classify 89% of the 678 study sites (table S1). This high prediction accuracy suggests limited overlap in the phytoclimatic spaces occupied by forest and savanna. A similarly high prediction accuracy was found when using standard bioclimatic

[1]Plant Ecology, University of Bayreuth, Universitaetsstrasse 30, 95447 Bayreuth, Germany. [2]Organization for Tropical Studies, P.O. Box 33, Skukuza, 1350, South Africa. [3]Department of Biological Sciences, University of Cape Town, South Africa. [4]Department of Mathematical Sciences, Norwegian University of Science and Technology, Trondheim N-7491 Norway. [5]Centre for Statistics in Ecology, the Environment and Conservation, University of Cape Town, South Africa. [6]Fynbos Node, South African Environmental Observation Network (SAEON), South Africa.
*Corresponding author. Email: steven.higgins@uni-bayreuth.de

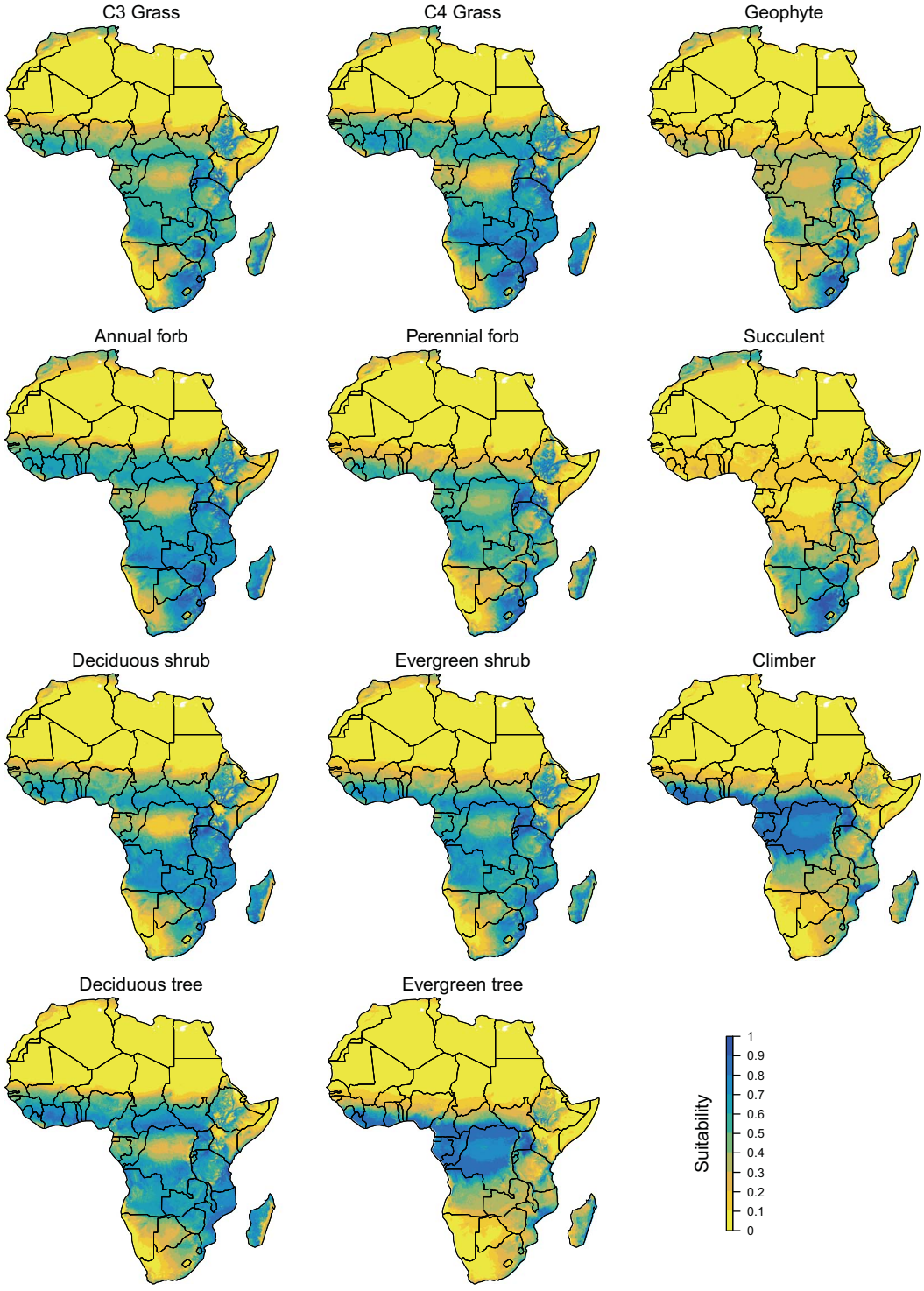


Fig. 1. Climatic suitability surfaces for major plant growth forms. Suitability is the averaged suitability scores of the species belonging to each growth form. See fig. S1 for the standard errors of these surfaces and fig. S2 for relative growth form suitability surfaces.

variables in the logistic regression model (table S2), indicating that our findings are not an artefact of the phytoclimatic variables we used. The phytoclimatic regression model predicted that the probability of forest increases with increasing suitability for evergreen trees and with decreasing suitability for C4 grasses (Fig. 2). This prediction is consistent with work defining forests as systems dominated by shade-tolerant trees and savannas as systems co-dominated by C4 grasses and shade-intolerant trees (*26*) and with older definitions that savannas are systems with a continuous grass layer and a discontinuous tree layer, whereas forests are systems with a continuous tree layer (*27*).

When we inspected the 75 prediction errors (*21*) (Fig. 3) we found that 45 of them could potentially be explained by abiotic factors not included in our analysis (table S3). These abiotic factors included topographic variation,

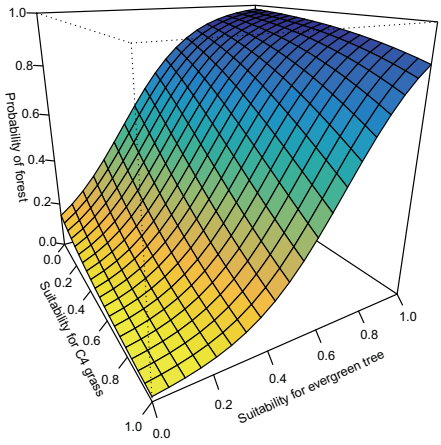


Fig. 2. Probability of forest based on mean annual rainfall. A logistic regression model estimated using penalized maximum likelihood revealed that the probability of forest increases with the suitability for evergreen trees and decreases with the suitability for C4 grasses. The suitability information is shown in Fig. 1. Figure 3 shows this model projected into geographic space. Note that in the logistic regression model the probability of savanna is 1 − the probability of forest.

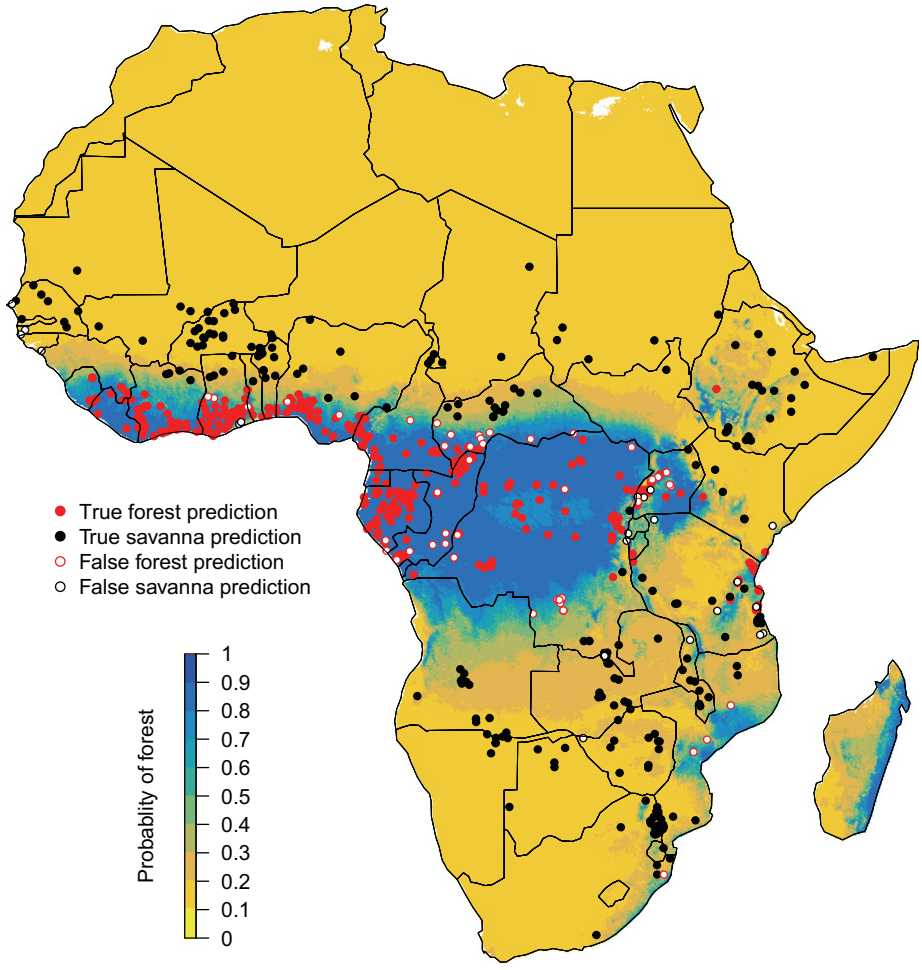


Fig. 3. Probability of forest over Africa. Spatial projection of a logistic regression model for the probability of forest (Fig. 2). The points show that this model correctly identifies 603 of 678 forest and savanna sites (*17*). To enhance visibility of the 75 model errors, the false predictions were plotted on top of true predictions. Zones with intermediate probability of forest are areas where the prediction uncertainty is higher and not necessarily true AES zones.

edaphic constraints such as low soil fertility, the microclimate created by Victoria Falls, floodplains, and estuaries (fig. S3). Moreover, a further 6 prediction errors appeared to have been observation errors. Observation errors were diagnosed when Google Earth imagery of the site clearly contradicted the assignment in the AfroTropTree database, most likely due to errors in site coordinates (*21*). We found no observation errors of this kind in a random sample of 75 correctly predicted sites, indicating that observation errors were more likely in situations where prediction errors were made. Overall, this left 24 of the 678 study sites (3.5%) as potential true AES sites (table S3). The high predictive accuracy of the model (603 of 678, 89%, Fig. 3) combined with suggestions that most (51 of 75, 68%, table S3) prediction errors might be due to factors other than true AES, together challenge the view that true AES are widespread in Africa.

It is notable that topographic effects were associated with 41 of the 75 (55%) model prediction errors (*21*) (table S3). Topography can influence the likelihood of forest or savanna occurrence in many ways. For example, valleys may have moister microclimates that favor forest and repress fires (*6*, *28*, *29*), and elevation change can induce orographic rainfall (favoring forests) and rain shadows (making forests less likely) (*27*) (fig. S5). It is also known that subtle topographic variation associated with catenas and floodplains can be sufficient to create wetter sites that can either promote forests or, when seasonally water logged, exclude trees (*27*, *30*) (fig. S4). That is, prediction uncertainty could be reduced by considering additional topographic drivers, which would further reduce the need to invoke true AES when explaining observed ecosystem states.

Apparent and true AES

Our findings challenge the prevailing view that forest and savanna are true AES over large portions of Africa (*3*, *5*–*7*, *10*, *17*, *31*). The true AES hypothesis proposes that AES occurs on homogenous environmental templates at intermediate resource levels as a result of positive feedbacks acting on initial ecosystem states (Fig. 4A). These feedbacks can involve fire and herbivory being enhanced by grassland states and retarded by forest states (*10*, *11*) or due to spatial dynamics of resource competition acting on a homogenous environmental template (*12*). Our analysis supports an alternative interpretation, which suggests that observations of different ecosystem states at intermediate positions on resource gradients may instead be caused by deterministic factors such as topographic gradients redistributing resources such as moisture in parts of the landscape, thereby creating microenvironments that favor either forests or savannas (Fig. 4B).

Aspects of the true AES hypothesis are supported by field studies conducted in Africa. For example, experiments that excluded fire and grazing in west Africa (*32*–*34*) allowed savanna to transition to forest (for the locations of these and other sites discussed, see fig. S3). Conversely, increases in elephant densities in the Murchison Falls National Park (Uganda) led to forest transitioning into savanna (*35*). Although these studies—by showing that events can shift ecosystems into alternative states—are consistent with AES predictions, they cannot be taken as unequivocal evidence (*36*). Ideally, we need to know that the initial ecosystem state was stable, that an event induced a switch to an

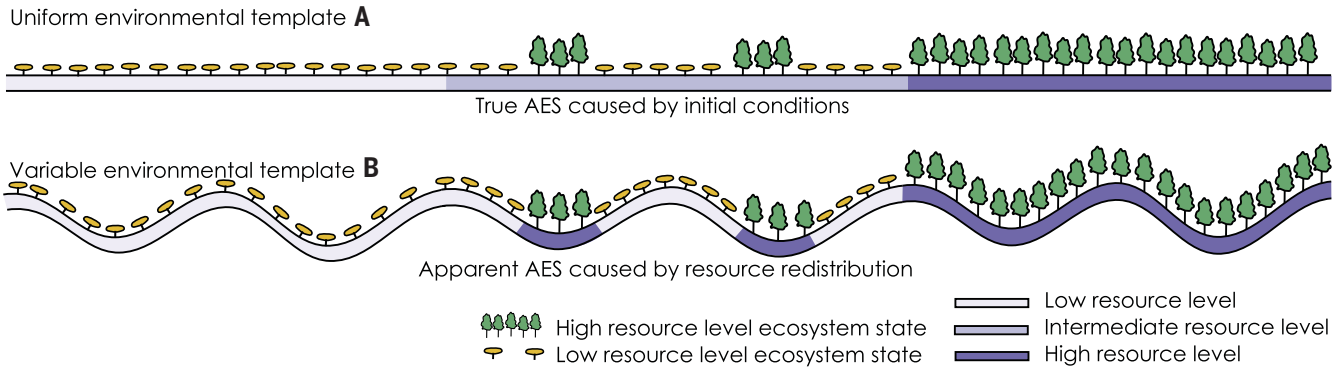


Fig. 4. Alternative ecosystem states along a resource gradient. True alternative ecosystem states may be observed at intermediate resource levels on a uniform environmental template due to positive feedbacks in the internal system dynamics acting on the initial ecosystem state (**A**). Apparent alternative ecosystem states occur when observed differences in ecosystem states are erroneously attributed to differences in initial conditions, when in fact they are caused by environmental drivers not included in the prediction model. For example, variation in the environmental template created by topography can redistribute moisture down slope, thereby creating predictable differences in ecosystem states (**B**). See fig. S7 for an example of how true and apparent AES can be confounded.

alternative ecosystem state, and that the ecosystem subsequently persisted in this alternative state (*8*, *36*). For example, although an extreme fire event consumed a forest and allowed a savanna state to establish in the HluhluweiMfolozi Park (South Africa) (*37*), it is unclear whether the forest patches destroyed by the fire were stable vegetation states and only time will tell whether the savanna will persist as an alternative ecosystem state or whether the forest state will reestablish. That is, we need to expand our observation time windows when evaluating evidence for true AES. For example, even though fire exclusion experiments report increases in fire-sensitive tree species (*36*), they seldom run long enough to demonstrate full canopy closure and exclusion of a flammable grass layer that can retard fires; indeed, fire exclusion treatments can be lost to accidental fires even after decades of fire suppression (*38*). The value of an extended time window is further illustrated by a 45-year time series of forest-savanna mosaics in Cameroon, which showed that forest cover is currently expanding (*39*), meaning that the mosaic is unstable, contrary to what would be expected under the true AES hypothesis (*6*). In summary, observed transitions between savanna and forest ecosystem states are not unequivocal indicators of true AES.

We found that for most locations in Africa (Fig. 3), feedbacks involving fire, herbivory, and light competition do not override the influence of phytoclimatic factors in determining ecosystem state. This is not to say they are unimportant; the role of fire and herbivory in ecosystems is undeniable (*40*, *41*) but they themselves are influenced by climate and vegetation, making it difficult to isolate their role from climatic drivers. Our findings emphasize that it is only at intermediate positions on the phytoclimatic gradient where fire and herbivory feedbacks may be strong enough that the ecosystem state is determined by the initial ecosystem state (Fig. 4A). At such intermediate positions on the gradient it is however also possible that topographic gradients redistribute resources such as soil moisture allowing ecosystem state to be predicted from resource levels irrespective of initial conditions (Fig. 4B). Even though feedbacks may not determine ecosystem states in such situations (Fig. 4B), they may often have sufficient strength to produce an abrupt boundary between forest and savanna states, ensuring that one type does not gradually blend into the other.

Implications of predictable ecosystem states

Our findings have implications for conservation practice and climate change mitigation planning. A concrete example is provided by the uncertainty associated with whether and where to plant trees to mitigate climate change. Previous analyses would suggest that vast parts of Africa are AES regions and by implication climatically suitable for forest (*2*, *3*, *17*) or forest restoration (*42*). The implicit hypothesis is that tree planting and fire suppression in the savannas of AES regions could manipulate the ecosystem state sufficiently to set up positive feedback processes that would allow carbon sequestration on a grand scale in Africa. However, there is well-justified concern that such programs overestimate the potential for carbon sequestration (*43*) and underplay threats to native biodiversity (*44*). Our analysis further suggests that AES regions may be substantially smaller than previously estimated (*2*, *3*, *17*, *31*), greatly reducing the carbon sequestration potential of tree planting in Africa. For example, the region where the prediction uncertainty in our analysis is high is potentially an AES region (Fig. 3). However, this area of heightened prediction uncertainty bundles model, parameter, driver, observation, and initial condition uncertainty. That is, this ecosystem-uncertain region should not be interpreted as a region that could support both forest or savanna (*5*); rather it is a region where we do not know whether it supports forest or savanna (*45*). It is likely that Fig. 3 overestimates the size of the area of high prediction uncertainty because prediction uncertainty could be reduced by, for example, allowing the model to consider topographic effects (e.g., fig. S7) and by reducing observation uncertainty (e.g., fig. S8). This means that significant parts of the environmental template within the area of high prediction uncertainty shown in Fig. 3 would not be suitable for tree planting programs. We therefore caution against using Fig. 3 to plan tree planting activities without isolating uncertainty in the initial ecosystem state from the overall prediction uncertainty (*46*).

Our analyses question the proposition that for a region as large as Australia (7.5 million km^2) (*17*) past climatic conditions or past disturbance events determine whether the vegetation in Africa is savanna or forest (*13*). Previous work appears to have overestimated the geographic extent of AES regions in Africa. For example, although previous work (*15*) presents evidence for the existence of AES in Africa, their data indicate that only 6% of the sites included in their analysis were potentially true AES sites. In conclusion, using a phytoclimatic transform, we were able to predict forest and savanna ecosystem states with substantial accuracy over most of Africa, challenging the view that climate cannot predict ecosystem state over vast regions of Earth (*4*, *7*) and reassuring us that we can develop climate-forced predictions of current and future ecosystem states.

REFERENCES AND NOTES

1. G. B. Bonan, S. C. Doney, *Science* **359**, eaam8328 (2018).
2. M. Hirota, M. Holmgren, E. H. Van Nes, M. Scheffer, *Science* **334**, 232–235 (2011).
3. A. C. Staver, S. Archibald, S. A. Levin, *Science* **334**, 230–232 (2011).

4. W. J. Bond, *J. Veg. Sci.* **16**, 261–266 (2005).
5. W. J. Bond, *Open Ecosystems: Ecology and Evolution Beyond the Forest Edge*. (Oxford Univ. Press, 2019).
6. J. G. Pausas, W. J. Bond, *Trends Plant Sci.* **25**, 250–263 (2020).
7. J. G. Pausas, W. J. Bond, *J. Ecol.* **109**, 3962–3971 (2021).
8. P. Petraitis, *Multiple Stable States in Natural Ecosystems* (Oxford Univ. Press, 2013).
9. I. Noy-Meir, *J. Ecol.* **63**, 459–481 (1975).
10. A. C. Staver, S. A. Levin, *Am. Nat.* **180**, 211–224 (2012).
11. I. Y. Djeumen, Y. Dumont, A. Doizy, P. Couteron, *Ecol. Modell.* **440**, 109381 (2021).
12. M. Rietkerk *et al*., *Science* **374**, eabj0359 (2021).
13. G. R. Moncrieff, S. Scheiter, W. J. Bond, S. I. Higgins, *New Phytol.* **201**, 908–915 (2014).
14. J. C. Aleman, A. C. Staver, T. Gillespie, *Glob. Ecol. Biogeogr.* **27**, 792–803 (2018).
15. D.D'Onofrio, J. von Hardenberg, M. Baudena, *Glob. Ecol. Biogeogr.* **27**, 714–725 (2018).
16. V. de L. Dantas, M. Hirota, R. S. Oliveira, J. G. Pausas, *Ecol. Lett.* **19**, 12–19 (2016).
17. J. C. Aleman *et al*., *Proc. Natl. Acad. Sci. U.S.A.* **117**, 28183–28190 (2020).
18. P. L. Silva de Miranda *et al*., *Glob. Ecol. Biogeogr.* **27**, 899–912 (2018).
19. M. C. Dietze, *Ecol. Appl.* **27**, 2048–2060 (2017).
20. E. G. Simmonds *et al*., *iScience* **25**, 105512 (2022).
21. Materials and methods can be found in the supplementary materials.
22. T. Conradi *et al*., *New Phytol.* **227**, 1294–1306 (2020).
23. S. I. Higgins, S. Scheiter, *Nature* **488**, 209–212 (2012).
24. F. Gerard *et al*., *Glob. Ecol. Biogeogr.* **26**, 854–859 (2017).
25. S. S. Kumar *et al*., *Remote Sens.* **11**, 815 (2019).
26. J. Ratnam *et al*., *Glob. Ecol. Biogeogr.* **20**, 653–660 (2011).
27. H. Walter, *Vegetation of the Earth in relation to climate and the eco-physiological conditions* (Springer, 1973).
28. S. W. Wood, B. P. Murphy, D. M. J. S. Bowman, *J. Biogeogr.* **38**, 1807–1820 (2011).
29. W. Bond, B. van Wilgen, *Fire and Plants* (Population and Community Biology Series, Springer, 2012).
30. M. Fletcher, S. W. Wood, S. G. Haberle, *Ecology* **95**, 2504–2513 (2014).
31. W. J. Bond, F. I. Woodward, G. F. Midgley, *New Phytol.* **165**, 525–537 (2005).
32. R. J. Rose-Innes, "Fire in west African vegetation" in *Proceedings of the Tall Timbers Fire Ecology Conference*, vol. 11, pp. 147 –173, 1972.
33. M. D. Swaine, W. D. Hawthorne, T. K. Orgle, *Biotropica* **24**, 166–172 (1992).
34. D. Louppe, N. Oattara, A. Coulibaly, *Commonw. For. Rev.* **74**, 288–292 (1995).
35. H. K. Buechner, H. C. Dawkins, *Ecology* **42**, 752–766 (1961).
36. E. M. Veenendaal *et al*., *New Phytol.* **218**, 153–166 (2018).
37. H. Beckett, A. C. Staver, T. Charles-Dominique, W. J. Bond, *J. Ecol.* **110**, 902–915 (2022).
38. E. Chidumayo, *Commonw. For. Rev.* **76**, 268–272 (1997).
39. L. B. T. Sagang *et al*., *ISPRS J. Photogramm.* Remote *Sens.* **188**, 142–156 (2022).
40. S. Jia *et al*., *Proc. Natl. Acad. Sci. U.S.A.* **115**, 6237–6242 (2018).
41. A. F. A. Pellegrini *et al*., *Nat. Ecol. Evol.* **5**, 504–512 (2021).
42. J.-F. Bastin *et al*., *Science* **365**, 76–79 (2019).
43. Y. Zhou *et al*., *Nature* **603**, 445–449 (2022).
44. J. W. Veldman *et al*., *Science* **366**, eaay7976 (2019).
45. R. H. Whittaker, *Communities and Ecosystems. Second Edition*. (MacMillan, 1975.
46. J. A. Slingsby, *S. Afr. J. Sci*. **116**, 7684 (2020).
47. S. I. Higgins, pfloek-bt/TTRcodeAESpublic: v1.0.0, Zenodo (2023); https://doi.org/10.5281/zenodo.7854825.

ACKNOWLEDGMENTS

Data sources: We acknowledge the herbaria that contributed data to this work: A, AAS, AAU, ABH, AD, AJOU, AK, AKPM, ALCB, AMNH, ARAN, ARM, AS, ASU, B, BA, BAA, BAB, BABY, BACP, BAF, BAFC, BAI, BC, BCN, BG, BIO, BKF, BM, BOON, BOUM, BR, BRI, BRIT, BRLU, C, CANB, CAS, CATA, CATIE, CBG, CBM, CDA, CDBI, CEN, CHR, CHSC, CIB, CICY, CIMI, CNS, COA, COAH, COFC, COI, COL, CONC, CORD, CP, CS, CSUSB, CTES, CU, CUVC, CVRD, DAV, DBG, DNA, E, EA, ECON, EMMA, ENCB, ERA, F, FCO, FCQ, FLAS, FR, FSU, FTG, FULD, FURB, G, GAT, GB, GENT, GEO, GH, GI, GLM, GMDRC, GMNHJ, GOET, GZU, HAL, HAST, HBG, HBR, HCIB, HGI, HGM, HIB, HO, HSC, HSS, HU, HUAL, HUJ, HUSA, HYO, IAC, IBGE, IBK, IBSC, IBUG, ICEL, ICESI, ICN, IEB, INM, INPA, IPA, IRVC, ISKW, JBAG, JBGP, JCT, JEPS, JOTR, JUA, JYV, K, KMN, KPM, KSTC, KU, KUN, KYO, L, LA, LAE, LAGU, LBG, LCR, LD, LEB, LI, LIL, SC, LP, LPAG, LPB, LPS, LSU, LTB, LW, MA, MAF, MAK, MBK, MBM, MBML, MCNS, MEL, MELU, MERL, MEXU, MGC, MNHM, MNHN, MO, MPN, MSC, MU, MUB, MVJB, NAC, NAS, NCU, ND, NE, NH, NHT, NLH, NMNL, NMSU, NSW, NU, NY, NZFRI, O, OBI, OSA, OSC, P, PAMP, PASA, PE, PERTH, PGM, POM, PY, QMEX, R, RB, RELC, RM, RSA, S, SACT, SALA, SANT, SAV, SBBG, SD, SDSU, SEV, SF, SFV, SI, SJSU, SNM, SP, SPF, SRFA, STL, STU, SVG, SZU, TAI, TAIF, TALL, TAM, TAMU, TAN, TEF, TEX, TI, TKPM, TNS, TOYA, TRH, TROM, TUB, U, UADY, UAM, UAS, UB, UC, UCR, UCS, UCSB, UCSC, UESC, UFG, UFMA, UFMT, UFRN, UFS, UGDA, UJAT, ULM, ULS, UME, UNEX, UNM, UNR, UNSL, UPNA, UPS, US, USF, USP, UT, UTEP, VAL, VEN, VIT, W, WAG, WELT, WII, WIS, WOLL, WU, XAL, YAMA, Z. **Funding:** This work was supported by the following: BMBF SPACES project EMSAfrica, grant 01LL1801A (to S.I.H.); National Research Foundation of South Africa, grant 118593 (to J.A.S.) **Author contributions:** Conceptualization: S.I.H., T.C., R.B.O., L.I.K., and J.S. Methodology: S.I.H., T.C., and R.B.O. Investigation: S.I.H. and T.C. Writing - original draft: S.I.H. Writing - review and editing: S.I.H., T.C., R.B.O., L.M.K., and J.A.S. **Competing interests:** The authors declare that they have no competing interests. **Data and materials availability:** All data are available in the manuscript, the supplementary material or deposited in Zenodo (*47*).
License information: Copyright © 2023 the authors, some rights reserved; exclusive licensee American Association for the Advancement of Science. No claim to original US government works. https://www.sciencemag.org/about/science-licenses-journal-article-reuse

SUPPLEMENTARY MATERIALS

science.org/doi/10.1126/science.add5190
Materials and Methods
Figs. S1 to S10
Tables S1 to S4
References (*48*–*77*)

Submitted 16 June 2022; accepted 12 May 2023
10.1126/science.add5190

INORGANIC CHEMISTRY

Synthesis and isolation of a triplet bismuthinidene with a quenched magnetic response

Yue Pang[1], Nils Nöthling[1], Markus Leutzsch[1], Liqun Kang[2], Eckhard Bill[2], Maurice van Gastel[1], Edward Reijerse[2], Richard Goddard[1], Lucas Wagner[1], Daniel SantaLucia[1], Serena DeBeer[2], Frank Neese[1]*, Josep Cornella[1]*

Large spin-orbit coupling (SOC) is an intrinsic property of the heavy elements that directly affects the electronic structures of the compounds. In this work, we report the synthesis and characterization of a monocoordinate bismuthinidene that features a rigid and bulky ligand. All magnetic measurements [superconducting quantum interference device (SQUID), nuclear magnetic resonance (NMR)] point to a diamagnetic compound. However, multiconfigurational quantum chemical calculations predict the ground state of the compound to be dominated (76%) by a spin triplet. The apparent diamagnetism is explained by an extremely large SOC-induced positive zero-field splitting of more than 4500 wavenumbers that leaves the M_S = 0 magnetic sublevel thermally isolated in the electronic ground state.

Molecular compounds with unpaired electrons typically manifest paramagnetism and enhanced reactivity (*1*, *2*). Transition metals and lanthanides are the prototypical examples of elements that form stable and isolable compounds while accommodating multiple unpaired electrons in their frontier d and f orbitals (Fig. 1A, top) (*3*). Numerous examples of transition metal complexes supporting between 1 and 5 unpaired electrons at the metal site are well known. In the lanthanide series, more than five unpaired electrons can be accommodated, as highlighted by the six unpaired 4f electrons in the lanthanide shift reagent $Eu(dpm)_3$ (dpm is dipivalomethonate) and the seven unpaired 4f electrons in the magnetic resonance imaging contrast agent Gd-DO3A-butrol (gadobutrol). Whereas isolation and characterization of such d- and f-block compounds have become routine, compounds of the p-block elements differ starkly (Fig. 1A, bottom). The discovery of Gomberg's dimer (which equilibrates with the persistent trityl radical) (*4*, *5*), opened the door to the development and isolation of a plethora of persistent or stable radicals with one unpaired electron in the p shell (*6*, *7*). Whereas multicentered diradical species—two unpaired electrons—based on p-block elements are well known (e.g., dioxygen) (*8*), stable and isolable single-centered diradicals still remain elusive. Triplet carbenes, nitrenes, and pnictinidenes are examples of such species, and the long-term quest for their isolation still remains a challenge (*9*–*11*). Initial efforts by Tomioka *et al.* demonstrated the existence of persistent triplet carbenes in solution, although their high reactivity prevented isolation (*12*, *13*). To date, only two stable monocoordinate nitrene and phosphinidene compounds that feature closed-shell ground states have been identified, which were reported by Bertrand *et al.* (Fig. 1B) (*14*, *15*). Recently, a metallonitrene was reported by Schneider and Holthausen *et al.* that has two parallel-spin unpaired electrons mostly centered at the nitrene nitrogen atom (Fig. 1B) (*16*). Owing to its high reactivity, it was structurally characterized in situ by x-ray diffraction analysis as well as in solution at low temperatures. Collectively, these precedents clearly suggest that the synthesis and isolation of a single-centered stable diradical compound based on a main group element are, together, an enormous challenge that, if realized, would open the door to the study of unexplored electronic states of matter. Hence, in the context of our interest in low-valent Bi compounds (*17*), we speculated that bismuthinidenes could serve as an ideal platform to isolate a single-centered p-block diradical. In this work, we present a bismuthinidene that features a single C–Bi(I) bond flanked by rigid, noncoordinating and bulky wing-like substituents that protect the Bi(I) center from decomposition or dimerization. The compound features notable thermal stability both in solution and in the solid state and can be isolated and stored in gram quantities. A range of advanced spectroscopic measurements, combined with an in-depth computational analysis, permitted a complete elucidation of its unusual electronic structure.

[1]Max-Planck-Institut für Kohlenforschung, Kaiser-Wilhelm-Platz 1, 45470 Mülheim an der Ruhr, Germany. [2]Max Planck Institute for Chemical Energy Conversion, Stiftstrasse 34-36, 45470 Mülheim an der Ruhr, Germany.
*Corresponding author. Email: neese@kofo.mpg.de (F.N.); cornella@kofo.mpg.de (J.C.)

Structural characterization

Triplet ground states of Bi(I) species were suggested for gas-phase BiH and BiMe species (*18*–*20*). Yet, in the condensed phase, Bi(I) compounds have a strong tendency to dimerize to form dibismuthenes or to oligome[illegible] (*21*–*23*). However, the presence of additional Lewis-base donors permits isolation of monomeric Bi(I) compounds in the singlet form, such as Dostal's *N*,*C*,*N*-pincer bismuthinidenes (*26*–*24*)). Inspired by the work of Matsuo and Tamao *et al.* (*27*), we reasoned that the rigid, noncoordinating and bulky ^{t}Bu-M^{s}Fluind ligand could serve as a platform to stabilize the monomeric monocoordinate Bi(I) [^{t}Bu, *tert*-butyl; M^{s}Fluind, 3′,3′,5′,5′-tetramethyl-2′,3′,5′,6′-tetrahydrodispiro(fluorene-9,1′-*s*-indacene-7′,9″-fluoren)-8′-yl]. Along these lines, we successfully synthesized the precursor ^{t}Bu-M^{s}Fluind-$BiBr_2$ (**1**) from the parent aryl bromide (**S3**). When **1** was reduced with 2.0 equivalents of cobaltocene in toluene under argon atmosphere at 25°C, ^{t}Bu-M^{s}Fluind-Bi(I) (**2**) was obtained in 81% yield on a gram scale (Fig. 2A). Whereas all reported Bi(I) compounds thus far have a dark color (*21*–*26*), **2** is bright yellow, suggesting a distinctive electronic structure. A single-crystal x-ray diffraction analysis unambiguously supported a monocoordinate bismuthinidene structure (Fig. 2B). Whereas a Bi(I) analog without ^{t}Bu groups in the flanking wings {[M^{s}Fluind-Bi(I)]$_2$, **S2**} possesses a typical Bi=Bi bond of 2.8464(4) Å (see supplementary materials), the shortest Bi•••Bi distance (4.385 Å) in the monomeric structure of **2** is larger than the sum of Bi•••Bi van der Waals radii of 4.14 Å (*28*). Additionally, no solvent molecule is intercalated between the ligand scaffold or in the vicinity of the metal center. The Bi–C(sp^2) bond distance in **2** clearly suggests a single bond [Bi1–C1: 2.2783(10) Å; compare with 2.26 Å (*29*)], which differs from the reported *N*,*C*,*N*-pincer bismuthinidenes, where the Bi–C(sp^2) bond distances indicate partial double-bond character [from 2.138(10) to 2.222(5) Å (*24*, *25*, *30*–*32*)]. The absence of Bi–H bonds was confirmed by infrared (IR) and variable-temperature nuclear magnetic resonance (VT-NMR) data (figs. S11 and S18), combined with reactivity studies (vide infra). In sharp contrast to **1**, the Bi center is centrally situated (C4–C1–Bi1; for **1**, 163.27° and for **2**, 178.78°). The distances between the Bi center and the 9-fluorenyl arms (C9, C14, and their identical atoms; 3.427 to 3.870 Å) lie at the edge of the sum of Bi•••C van der Waals radii of 3.77 Å (*28*, *33*). As suggested by NMR, **2** is symmetric and nondynamic in solution, in the range of −70° to 90°C, in line with the solid-state structure; diffusion-ordered NMR data further support the monomeric form of **2** in solution (table S2).

Although most of the signals of **2** appear in the expected region of the NMR spectrum for diamagnetic compounds, anomalous shifts in certain ^{1}H and ^{13}C NMR signals were clearly observed (Fig. 2C). Among these, H4 and C1 experience the most pronounced influences, shifting to notably shielded positions, from 7.69 and 208.9 parts per million (ppm) in

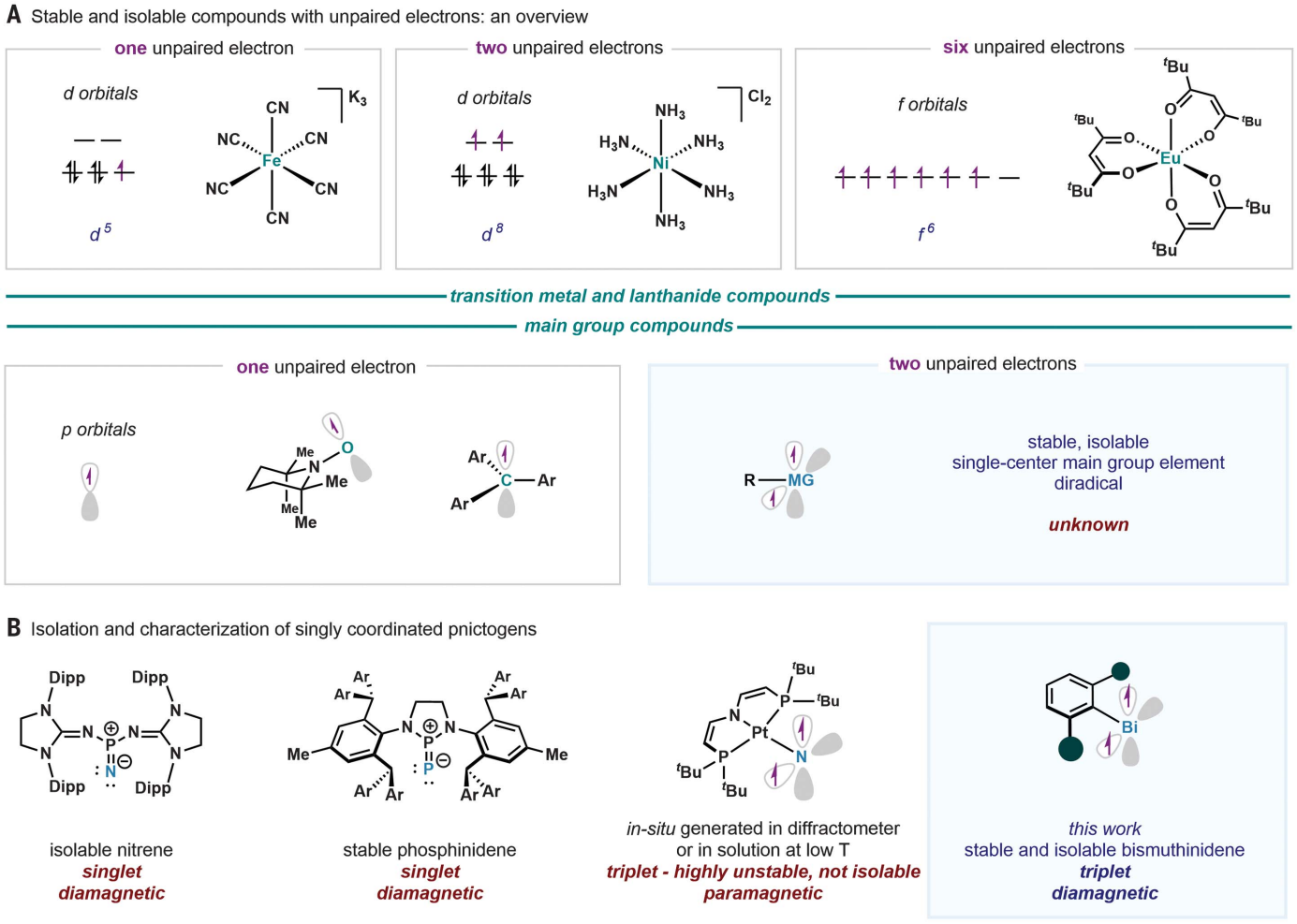


Fig. 1. Electronic structures of molecular compounds with unpaired electrons. (**A**) Examples of stable and isolable transition metal, lanthanide, and main-group (MG) compounds bearing unpaired electrons in the frontier orbitals. Ar, aryl; Me, methyl; R, general substituents. (**B**) State-of-the-art examples of singly coordinated nitrenes and pnictinidenes. Dipp, 2,6-diisopropylphenyl.

the parent Bi(III) **1** to −1.06 and −203.8 ppm in **2**, respectively. In previous reports, several up-field ^{13}C NMR shifts were observed for those nuclei attached to paramagnetic transition metal centers (*34*, *35*). Interestingly, the chemical shifts of the atoms in the central phenyl ring of **2** display an alternating pattern: C1, C3, and H4 are shielded (−203.8, 114.5, and −1.06 ppm, respectively), whereas C2 and C4 are deshielded (234.0 and 160.0 ppm, respectively) (*36*). C9, C14, and their corresponding symmetry-related counterparts are also largely deshielded (177.7 and 176.9 ppm) in spatial proximity to Bi. Unlike common paramagnetic compounds, all NMR signals of **2** are sharp (except C1 because of the line-broadening effects of ^{209}Bi) and nearly temperature independent. The chemical shifts of H4 and C1 only change by 0.20 and 2.8 ppm, over temperature ranges of −70° to 90°C and −40° to 60°C, respectively (figs. S18 and S19). Although **2** is highly air sensitive, it exhibits notable stability in air-free solution and solid state: The solid sample of **2** can be stored at ambient temperature under argon for months, and no noticeable decomposition was observed when a toluene-d_8 solution was heated at 100°C for 24 hours.

The ultraviolet–visible–near-infrared (UV-vis-NIR) spectrum of **2** shows no intense absorption in the visible region. Two weak bands in the visible [wavelength of maximum absorption (λ_{max}) = 490 nm, molar absorption coefficient (ε) ≈ 150 M^{-1} cm^{-1}] and NIR regions (λ_{max} = 1011 nm, ε ≈ 120 M^{-1} cm^{-1}) indicate low-energy, likely spin-forbidden electronic transitions (fig. S10). A strong and unstructured fluorescence spectrum was observed with a maximum at 500 nm when irradiated at 491 nm. Paramagnetic susceptibility was not detected for a powder sample of **2** in the temperature range of 1.8 to 300 K by using a SQUID magnetometer (Fig. 3A). This suggests that only the M_S = 0 magnetic sublevel has any appreciable Boltzmann population up to room temperature (vide infra).

Evidence for +1 oxidation state of 2

Bi L_1-edge x-ray absorption spectroscopy (XAS) data for **2** and a reference complex [Bi(III)Ph_3; Ph, phenyl] are shown in Fig. 3B (see supplementary materials for XAS measurement details), together with the corresponding time-dependent density functional theory (TD-DFT)–calculated spectra. On the basis of the TD-DFT results, the absorption edge peak of **2** is dominated by the two lowest-energy features corresponding to the electric dipole–allowed 2s to 6p transitions. The peak position (16390.1 eV) of **2** is noticeably lower than that of Bi(III)Ph_3 (16392.3 eV), suggesting that the Bi atom is in the +1 oxidation state in **2**. Owing to the large natural width of the 2s core level of Bi (12.4 eV) (*37*), the Bi L_1-edge XAS features are substantially broadened, which is in line with the full width at half maximum of the absorption edge peak obtained in the XAS peak fitting (~15 eV), making it unfeasible to deconvolute the experimental spectra based on theoretical

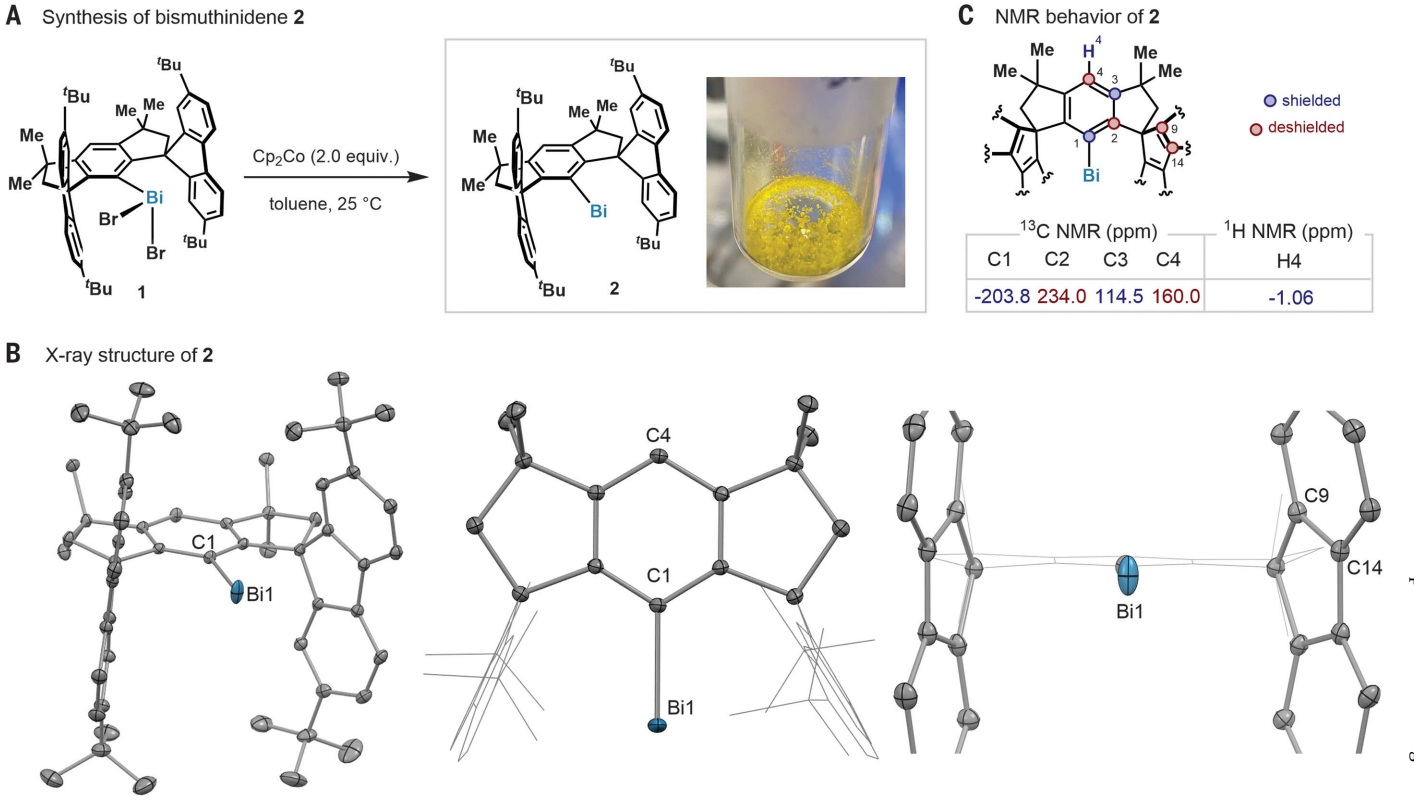


Fig. 2. Synthesis and characterization of a monocoordinate bismuthinidene. (**A**) Synthesis of **2**. [Photo credit: Y.P.] (**B**) Solid-state structure of **2** at 100 K in different orientations (anisotropic displacement ellipsoids are displayed at a probability of 50%, and H atoms were omitted for clarity). (**C**) Unusual shielding-deshielding behavior of the aromatic C and H centers close to Bi in the ^{13}C and ^{1}H NMR spectra (compared with **1** and **S3**).

transitions. Nevertheless, the general experimental trends in the Bi L_I-edge peak positions of known Bi(I) and Bi(III) reference complexes are reasonably reproduced by theory, and more importantly, the experimental XAS data of **2** fit well with the theoretical Bi(I) model. The edge-peak position of **2** (16390.1 eV) is not only lower than that of the Bi(III) atom in $BiPh_3$ but also lower than that of other known Bi(I) complexes, indicating the distinctive electronic structure of the valence 6p orbitals of **2**. However, the 2s-to-6p transition energies determined by TD-DFT calculations of the triplet, closed-shell, and open-shell singlet models of **2** are nearly identical and are not possible to distinguish given the limited experimental resolution.

Additional experimental evidence for the +1 oxidation state of the Bi center of **2** is revealed by its reactivity. Complex **2** reacts with methyl iodide and *N*-methyl maleimide, affording the corresponding oxidative addition complex **3** and the cycloaddition adduct **4**, respectively (Fig. 4). Whereas the former reaction is irreversible and **3** is isolated in high yield, the latter results in a temperature-dependent equilibrium between **2** and **4** (see supplementary materials).

Theoretical analysis

Insights into the intriguing experimental findings were obtained from quantum chemical calculations using the ORCA program package (*38*, *39*). We reasoned that for Bi(I), the Bi 6p shell may contain two electrons in a triplet, closed-shell singlet, or open-shell singlet configuration. Consequently, initial geometry optimizations were performed using scalar relativistic DFT as described in the supplementary materials. Three sets of structures were optimized assuming a closed-shell singlet ground state, a triplet ground state, and a broken-symmetry (BS) open-shell singlet electronic ground state. The triplet and BS geometries turned out to be exceedingly similar and distinctly different from the optimized closed-shell structure. The triplet and BS structures are in good to excellent agreement with experiment, whereas the predicted closed-shell structure shows very large deviations from the x-ray crystal structure (see supplementary materials). From an energetic point of view, DFT predicts the Gibbs free energy of the triplet state to be lowest in energy, with the BS and closed-shell singlets calculated at about 5 and 9 kcal mol^{-1} higher, respectively. The reason for the triplet state being favored by the calculations is readily apparent by examining the singly occupied molecular orbitals (SOMOs) of the triplet state: They represent the in-plane and out-of-plane p orbitals of the central Bi (Fig. 5A). These are dominantly Bi p orbitals with limited admixture of the orbitals of the supporting ligand. However, the analysis of our theoretical results in terms of the atoms-in-molecules (AIM) analysis indicates the presence of bond critical points that connect the bismuth center to the fluorenyl groups. In addition, there is the expected bond-critical point from the single bond between the bismuth and the C(sp^2) of the aryl group (fig. S57).

The absence of paramagnetism for **2** and the theoretical prediction of its lowest electronic state being of triplet parentage may initially appear contradictory. However, given the heavy element nature of bismuth, it is indispensable to treat spin-orbit coupling (SOC) effects in addition to scalar relativity to fully appreciate the electronic structure and physical properties of **2**. This can be achieved by proceeding to a more detailed treatment of the electronic structure offered by relativistic multiconfigurational ab initio methods. Hence, scalar relativistic complete active space self-consistent field (CASSCF) calculations were carried out at the DFT optimized geometries, and dynamic electron correlation was

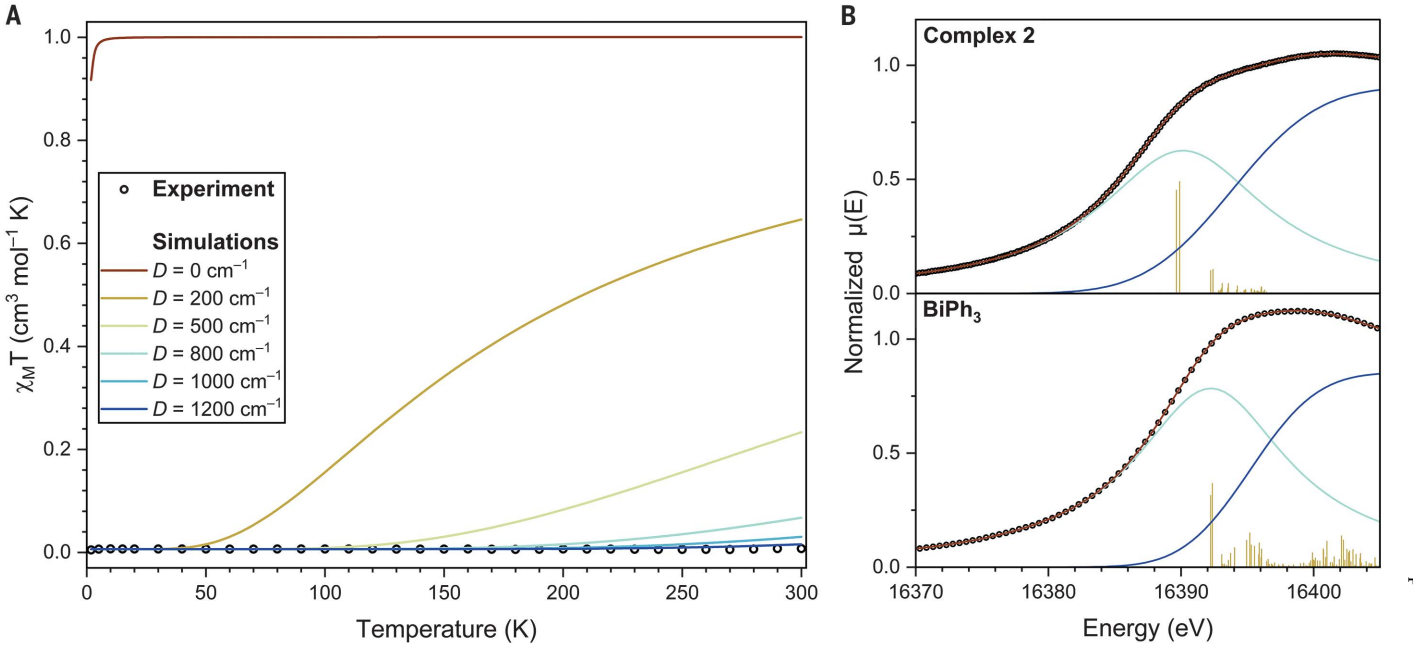


Fig. 3. Susceptibility and XAS measurements of 2. (**A**) Susceptibility. Temperature dependence of the molar magnetic susceptibility, $\chi_M T$, of **2**, measured with a powder sample and magnetic field (B) = 1 T. The experimental data are corrected for a diamagnetic contribution χ_{dia} = −633.2 × 10^{-6} cm^3 mol^{-1}. The simulations accounted for only the z direction of the susceptibility, χ_z, because the contributions of the x and y directions of the susceptibility are negligible in this system. The solid lines represent spin Hamiltonian simulations for a spin S = 1 with g-factor = 2 and different values of the axial zero-field splitting parameter (D). (**B**) XAS. Experimental Bi L_1-edge XAS spectra with peak-fitting results and TD-DFT calculated transitions of **2** (top) and $BiPh_3$ reference (bottom). For each sample, the absorption edge is modeled using a pseudo-Voigt peak (cyan curve) and an error-function background (blue curve) to fit (dark red curve) the experimental XAS spectra (black circles) between 16,370 and 16,405 eV (see table S19 for peak-fitting details). The TD-DFT calculated absorption transitions (plotted as yellow vertical stick spectra) are shifted by a constant value of +312.4 eV based on the calibration established by XAS of the Bi(I) and Bi(III) reference complexes and their corresponding TD-DFT–calculated energies (see table S18 for energy-calibration details). μ(E), absorption coefficient as a function of x-ray energy.

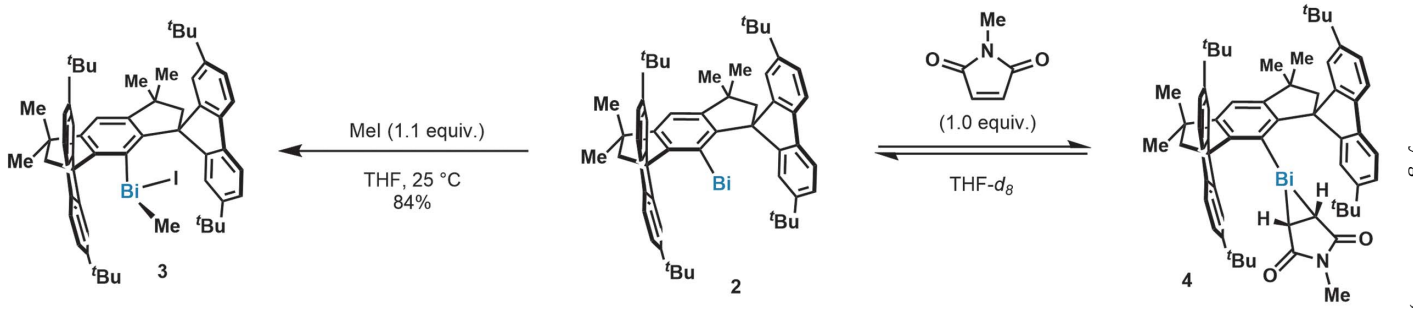


Fig. 4. Reactivity studies of complex 2. THF, tetrahydrofuran.

incorporated using the n-electron valence second-order perturbation theory (NEVPT2). Initially, a minimal active space with two electrons in two orbitals was pursued. The results of these calculations are in broad agreement with the DFT results in that they lead to a triplet ground state with the closed- and open-shell singlet states being higher in energy by about 10 to 15 kcal mol^{-1}. The results of state-averaged CASSCF and NEVPT2 calculations are very similar, suggesting that the effects of dynamic electron correlation are limited for the determination of the ground-state electronic configuration. Subsequently, the active space was extended to include all Bi 6p orbitals as well as the main σ-bonding orbital between the Bi atom and the ligand scaffold leading to a CAS(4,5) description. In these calculations, the scalar relativistic states (six singlet and five triplets were determined to cover the spectrum up to about 50,000 cm^{-1} based on preliminary calculations) were allowed to interact through the SOC. The results provide a concise explanation of the experimental findings. The ground state is still dominated by the spin-triplet state (76%) but contains a large (~24%) admixture of closed- and open-shell singlet states (vide infra). Importantly, the splitting in the magnetic sublevels (the M_S = 0, +1, and −1 components of the triplet state with S = 1) induced by the SOC is so large that a single magnetic sublevel remains thermally isolated; the M_S = ±1 components of the triplet state are of nearly 100% triplet character and are found about 4500 cm^{-1} higher in energy (Fig. 5A). In other words, complex **2** features an extremely large and positive axial zero-field-splitting interaction that splits the M_S = 0 magnetic sublevel away from

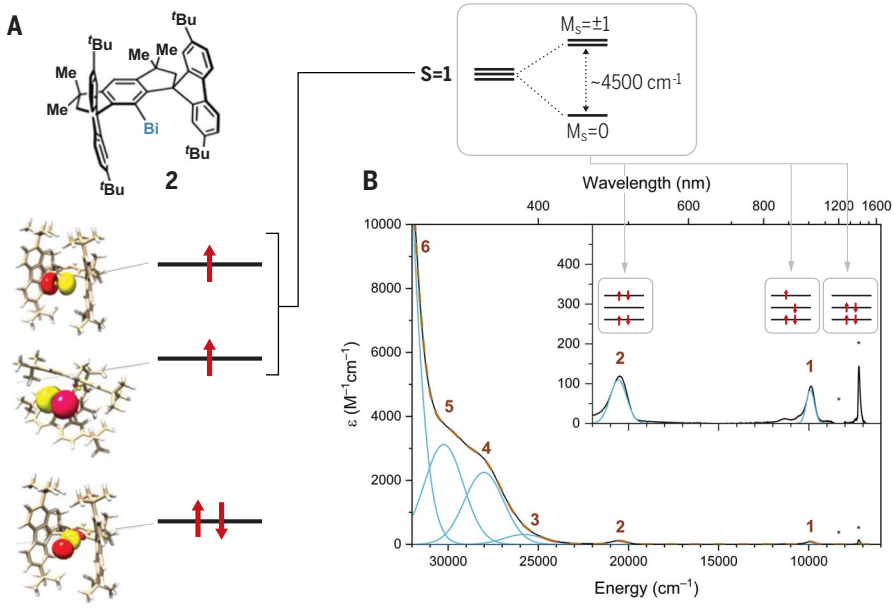


Fig. 5. Theoretical analysis of the electronic structure of 2. (**A**) Electronic structure of **2**. The central Bi (I) features four electrons in the 6p shell. In the electronic ground state, one electron pair forms a Bi–C bond with the ligand scaffold while two nearly degenerate lone pairs are singly occupied with parallel spin electrons. The three magnetic sublevels of the triplet ground state are split by the very large bismuth SOC interaction, which leads to a thermally isolated M_S = 0 level lowest in energy. (**B**) UV-vis-NIR spectrum (0.352 mM of **2** in THF) resolved into individual Gaussian absorption bands labeled 1 to 6 and shown in blue. The arrows indicate our assignment of the UV-vis spectrum in terms of transitions from the lowest magnetic sublevel of the triplet ground state to the singlet configurations indicated by the level scheme above each absorption band. Solvent artifacts are labeled by asterisks in the experimental spectrum. The inset is a zoomed-in view of the UV-vis-NIR spectrum.

the M_S = ±1 states by more than 4500 cm^{-1}, which is equivalent to about 0.55 eV or >15 kcal mol^{-1}. Because the SOC-induced splitting of the magnetic sublevels is so large, the M_S = ±1 magnetic sublevels can never achieve any Boltzmann population in the susceptibility measurement up to room temperature. Moreover, there exists no possible transition that could be triggered by a microwave photon in the electron paramagnetic resonance (EPR) experiments. Thus, given that the lowest three relativistic electronic states are all dominantly of triplet character, we believe that one can legitimately refer to **2** as featuring a "nonmagnetic" triplet ground state.

Based on the results of the relativistic CASSCF and NEVPT2 calculations, band 1 found in the NIR region of the UV-vis-NIR spectrum of **2** at ~10,000 cm^{-1} (Fig. 5B) belongs to transitions from the M_S = 0 magnetic sublevel of the ground state to two states that are almost pure singlets with the leading configurations 2200 (closed-shell singlet) and 2110 (open-shell singlet) in terms of the orbital scheme shown in Fig. 5B (orbital occupation numbers with molecular orbitals read bottom to top). These transitions are calculated at 9940 and 10,011 cm^{-1}, respectively, in very close agreement with experiment. The weak band 2 (Fig. 5B) is assigned to another triplet-singlet transition that becomes allowed by the strong scrambling between singlet and triplet states. It is calculated at 20,596 cm^{-1}, again in excellent agreement with experiment. The excited state corresponds to the configuration 2020 (singlet manifold double excitation).

The low-coordination number of the Bi center leaves two electrons in two nearly degenerate p orbitals, thus resulting in a triplet ground state of **2**. In addition, the intrinsically large SOC constant of Bi substantially stabilizes the M_S = 0 sublevel, leading to an apparent diamagnet.

Note added in proof: During the editing process of this manuscript, a monocoordinate stibinidene appeared in the peer-reviewed literature (*40*).

REFERENCES AND NOTES

1. R. A. Moss, M. S. Platz, M. Jones Jr., Eds., *Reactive Intermediate Chemistry* (Wiley, 2004).
2. J. Stöhr, H. C. Siegmann, Eds., *Magnetism: From Fundamentals to Nanoscale Dynamics* (Springer, 2006).
3. E. König, G. König, Eds., *Magnetic Properties of Coordination and Organometallic Transition-Metal Compounds* (Springer, 1981).
4. M. Gomberg, *Ber. Dtsch. Chem. Ges.* **33**, 3150–3163 (1900).
5. M. Gomberg, *J. Am. Chem. Soc.* **22**, 757–771 (1900).
6. P. P. Power, *Chem. Rev.* **103**, 789–810 (2003).
7. R. G. Hicks, Ed., *Stable Radicals: Fundamentals and Applied Aspects of Odd-Electron Compounds* (Wiley, 2010).
8. M. Abe, *Chem. Rev.* **113**, 7011–7088 (2013).
9. K. Hirai, T. Itoh, H. Tomioka, *Chem. Rev.* **109**, 3275–3332 (2009).
10. C. Wentrup, *Angew. Chem. Int. Ed.* **57**, 11508–11521 (2018).
11. L. Dostál, *Coord. Chem. Rev.* **353**, 142–158 (2017).
12. H. Tomioka, E. Iwamoto, H. Itakura, K. Hirai, *Nature* **412**, 626–628 (2001).
13. E. Iwamoto, K. Hirai, H. Tomioka, *J. Am. Chem. Soc.* **125**, 14664–14665 (2003).
14. F. Dielmann *et al.*, *Science* **337**, 1526–1528 (2012).
15. L. Liu, D. A. Ruiz, D. Munz, G. Bertrand, *Chem* **1**, 147–153 (2016).
16. J. Sun *et al.*, *Nat. Chem.* **12**, 1054–1059 (2020).
17. H. W. Moon, J. Cornella, *ACS Catal.* **12**, 1382–1393 (2022).
18. A. Heimer, E. Hulthén, *Nature* **127**, 557 (1931).
19. G. Herzberg, *Molecular Spectra and Molecular Structure, I. Spectra of Diatomic Molecules* (Van Nostrand, 1950).
20. D. P. Mukhopadhyay *et al.*, *Chem. Sci.* **11**, 7562–7568 (2020).
21. N. Tokitoh, Y. Arai, R. Okazaki, S. Nagase, *Science* **277**, 78–80 (1997).
22. B. Twamley, C. D. Sofield, M. M. Olmstead, P. P. Power, *J. Am. Chem. Soc.* **121**, 3357–3367 (1999).
23. H. J. Breunig, R. Rösler, E. Lork, *Angew. Chem. Int. Ed.* **37**, 3175–3177 (1998).
24. P. Šimon, F. de Proft, R. Jambor, A. Růzicka, L. Dostál, *Angew. Chem. Int. Ed.* **49**, 5468–5471 (2010).
25. G. Wang *et al.*, *Chem. Eur. J.* **25**, 4335–4339 (2019).
26. M. M. Siddiqui *et al.*, *J. Am. Chem. Soc.* **143**, 1301–1306 (2021).
27. T. Matsuo *et al.*, *Bull. Chem. Soc. Jpn.* **84**, 1178–1191 (2011).
28. M. Mantina, A. C. Chamberlin, R. Valero, C. J. Cramer, D. G. Truhlar, *J. Phys. Chem. A* **113**, 5806–5812 (2009).
29. P. Pyykkö, M. Atsumi, *Chem. Eur. J.* **15**, 186–197 (2009).
30. I. Vránová *et al.*, *Chem. Eur. J.* **21**, 16917–16928 (2015).
31. Y. Pang, M. Leutzsch, N. Nöthling, J. Cornella, *J. Am. Chem. Soc.* **142**, 19473–19479 (2020).
32. Y. Pang, M. Leutzsch, N. Nöthling, F. Katzenburg, J. Cornella, *J. Am. Chem. Soc.* **143**, 12487–12493 (2021).
33. J. D. Queen, A. Lehmann, J. C. Fettinger, H. M. Tuononen, P. P. Power, *J. Am. Chem. Soc.* **142**, 20554–20559 (2020).
34. H. Fujii, *J. Am. Chem. Soc.* **124**, 5936–5937 (2002).
35. Y. Hiraoka *et al.*, *Dalton Trans.* **44**, 13439–13443 (2015).
36. J. Ví Cha *et al.*, *Chem. Rev.* **120**, 7065–7103 (2020).
37. M. O. Krause, J. H. Oliver, *J. Phys. Chem. Ref. Data* **8**, 329–338 (1979).
38. F. Neese, F. Wennmohs, U. Becker, C. Riplinger, *J. Chem. Phys.* **152**, 224108 (2020).
39. F. Neese, *Wiley Interdiscip. Rev. Comput. Mol. Sci.* **12**, e1606 (2022).
40. M. Wu *et al.*, *Chem* 10.1016/j.chempr.2023.05.005 (2023).

ACKNOWLEDGMENTS

We acknowledge Deutsches Elektronen-Synchrotron (DESY) (Hamburg, Germany), a member of the Helmholtz Association (HGF), for the provision of experimental facilities. Parts of this research were carried out at PETRA III under proposal I-20220137, and we thank E. Welter for assistance in using the P65 beamline. We acknowledge Diamond Light Source (UK) for experiment time on Beamline I20-scanning under proposal SP30449. We thank F. Mosselmans, S. Hayama, and M. Aramini for their assistance during the beamtime. We thank A. Fürstner for generous support. We also thank the analytical departments at the Max-Planck-Institute für Kohlenfosrchung for support (mass spectrometry, NMR, and x-ray crystallography). **Funding:** Financial support for this work was provided by the Max-Planck-Gesellschaft, Max-Planck-Institut für Kohlenforschung, Max Planck Institute for Chemical Energy Conversion, China Scholarship Council and Förderprogramm des Instituts Stipendium-Gästeprogramm (PhD fellowships to Y.P.), Fonds der Chemischen Industrie (FCI-VCI), and the European Union's Horizon 2020 research and innovation program under agreement no. 850496 (European

Research Council Starting Grant to J.C.). **Author contributions:** Y.P. synthesized and isolated compounds **1** to **3** and **S1** to **S3**. N.N. and R.G. determined the x-ray crystal structures. NMR analysis was conducted by M.L. and Y.P. EPR experiments were conducted by E.R. L.W. helped with synthesizing the ligand. M.v.G. aided in the acquisition and interpretation of the UV-vis data. E.B. and D.S. acquired and analyzed susceptibility data obtained with SQUID magnetometry. L.K. and S.D. acquired and analyzed XAS data. F.N. conducted theoretical calculations on the electronic structure of **2**. The manuscript was written by J.C., F.N., and Y.P. The project was directed by J.C. and F.N.

Competing interests: The authors declare no competing financial interests. **Data and materials availability:** Crystallographic data for structures **1** to **3** and **S1** to **S3** are available free of charge from the Cambridge Crystallographic Data Center under reference numbers 2225004, 2225002, 2225006, 2225003, 2225005, and 2225007, respectively. **License information:** Copyright © 2023 the authors, some rights reserved; exclusive licensee American Association for the Advancement of Science. No claim to original US government works. https://www.science.org/about/science-licenses-journal-article-reuse

SUPPLEMENTARY MATERIALS

science.org/doi/10.1126/science.adg2833
Materials and Methods
Supplementary Text
Figs. S1 to S57
Tables S1 to S27
References (*41*–*67*)

Submitted 14 December 2022; accepted 4 May 2023
Published online 18 May 2023
10.1126/science.adg2833

QUANTUM CHEMISTRY

Quantum simulator to emulate lower-dimensional molecular structure

E. Sierda, X. Huang, D. I. Badrtdinov, B. Kiraly, E. J. Knol, G. C. Groenenboom, M. I. Katsnelson, M. Rösner, D. Wegner*, A. A. Khajetoorians*

Bottom-up quantum simulators have been developed to quantify the role of various interactions, dimensionality, and structure in creating electronic states of matter. Here, we demonstrated a solid-state quantum simulator emulating molecular orbitals, based solely on positioning individual cesium atoms on an indium antimonide surface. Using scanning tunneling microscopy and spectroscopy, combined with ab initio calculations, we showed that artificial atoms could be made from localized states created from patterned cesium rings. These artificial atoms served as building blocks to realize artificial molecular structures with different orbital symmetries. These corresponding molecular orbitals allowed us to simulate two-dimensional structures reminiscent of well-known organic molecules. This platform could further be used to monitor the interplay between atomic structures and the resulting molecular orbital landscape with submolecular precision.

New physical and chemical phenomena can arise when electrons in solids are confined to lower dimensions (*1*, *2*). A prominent example is graphene, in which the motion of electrons becomes relativistic, which has profound consequences on its material properties including chiral (Klein) tunneling, Zitterbewegung, relativistic collapse around charge centers, and emerging pseudomagnetic fields from inhomogeneous deformations (*3*–*6*). Because of confinement, mutual interactions between electrons can furthermore become substantial in lower-dimensional systems, often leading to new and unexpected fragile quantum states of matter such as Mott insulators, superconductivity, or spin-liquid behavior (*7*–*11*). Understanding quantitatively how these exotic quantum states of matter emerge requires understanding the detailed interplay between dimensionality, multiorbital electronic structure, and interactions.

To provide insight into interacting lower dimensional systems and to take advantage of the resultant fragile many-body states of matter, new types of tunable quantum simulators have been developed toward the bottom-up design of many-body Hamiltonians (*12*–*20*). One approach toward this end is the precise atom-by-atom creation of potential landscapes on surfaces based on scanning tunneling microscopy/spectroscopy (STM/STS) (*21*, *22*). With this approach, various artificial two-dimensional (2D) lattices have been created to emulate the single-particle band structure of Dirac and topological materials (*23*–*25*). Although the versatility of this approach is rooted in the countless geometries that can be realized, it often relies on the use of supporting bulk metallic substrates. The latter is a clear drawback in designing atomic and molecular orbitals with tailored symmetry, as well as tuning mutual electron interactions, because of the unwanted influence of the substrate's bulk electronic bands. Therefore, to harness the versatility of this approach, it is vital to develop platforms that use weakly conducting or insulating surfaces (*26*, *27*).

Here, we demonstrated a versatile quantum simulator capable of realizing complex artificial molecular orbitals based solely on patterning individual cesium (Cs) atoms on the surface of semiconducting indium antimonide (InSb). Using STM/STS, we first constructed building blocks from patterned ring structures of Cs atoms, which exhibited a zero-dimensional (0D)–like state, attributable to an artificial atom. This sharply observable bound state in the band gap of the semiconducting substrate was hence strongly decoupled from the bulk and exhibited spatially extended charge density outside the artificial atom. We subsequently showed that two artificial atoms exhibited a long-range distance-dependent coupling, leading to the formation of bonding and antibonding states. Using this as a starting point, we demonstrated the multiorbital nature of the simulator, which was based on creating artificial atomic s, p_x, and p_y orbitals. We used various orbital symmetries and constructed 2D structures with defined geometries that are reminiscent of analogous planar 3D molecular structures. The resultant electronic structure exhibited 2D artificial molecular orbitals, namely molecular σ and π orbitals, with various in-plane symmetries due to orbital hybridization. Using ab initio calculations of the analogous molecules, we compared the resultant and expected molecular orbitals. Because the tailored structures are not restricted by the geometrical relaxation of their molecular analogs, this platform provides an ultimate tool to explore fragile and degenerate states and the interplay of these states with geometr structure. We demonstrated this by explo 2D structures that were reminiscent of various conformations of butadiene molecules.

Institute for Molecules and Materials, Radboud University, Nijmegen, Netherlands.
*Corresponding author. Email: a.khajetoorians@science.ru.nl (A.A.K.); d.wegner@science.ru.nl (D.W.)

Artificial atoms

InSb is a semiconductor with a band gap of 235 meV (*28*). Upon adsorption on its (110) surface, Cs atoms resided at hollow sites of the Sb-terminated surface (supplementary text, section S1, and figs. S1 and S2) (*29*). Concomitantly, charge donation from Cs atoms led to band bending and a dilute 2D electron gas (2DEG), whose dimensionality has also been demonstrated through the quantum Hall effect (*30*–*33*). This 2DEG could be seen by a steplike onset in STS observed in the bulk band gap of the semiconductor (fig. S3), with a carrier density of $N_{2DEG} = 2 \times 10^{12}$ cm^{-2}, where each Cs ion donated approximately 0.4 electrons (supplementary text, section S2, and figs. S4 to S6), depending on the Cs density and doping of the semiconductor (*31*, *32*).

We exploited the ionic nature of individual Cs atoms and patterned them into ring structures (Fig. 1, A and B) to create a potential energy landscape that mimics the $1/r$ potential of an atom in two dimensions. The local concentration of Cs ions created an attractive potential for the electrons of the 2DEG, leading to a bound state within the bulk band gap that could be visualized by STS (Fig. 1, C and D). This bound state manifested as a sharp peak with full width at half maximum of FWHM ≃ 7 mV. Using spatially dependent differential conductance (dI/dV) imaging (see supplementary materials and methods) at the peak energy (Fig. 1C), which we refer to as an orbital map, we found that this bound state was not only located within the ring structure but also symmetrically delocalized up to r = 9.0 ± 0.4 nm outside of the structure (fig. S7). The spatial delocalization of this wave function was due to the interplay of the local-band bending induced by the Cs ring structure and the weak screening of the 2DEG. As a result, we could identify this bound state as an s-like atomic state stemming from the circular potential, which is observable at a sufficiently large distance from the structure. We therefore defined this structure as an artificial atom. For the ring structures that we used in this manuscript, the structural deviations of the Cs atoms from circular symmetry were small compared to the length scale of the associated wave function. Consequently, such deviations led to negligible changes (e.g., anisotropy) in the electronic structure. Previously, it has also been shown that the 2DEG itself is approximately isotropic (*33*). Therefore, the resultant potential was well approximated by a circularly symmetric $1/r$ potential in the xy plane at sufficient separation from the Cs ring structure. We verified this both theoretically and by comparing different artificial Cs

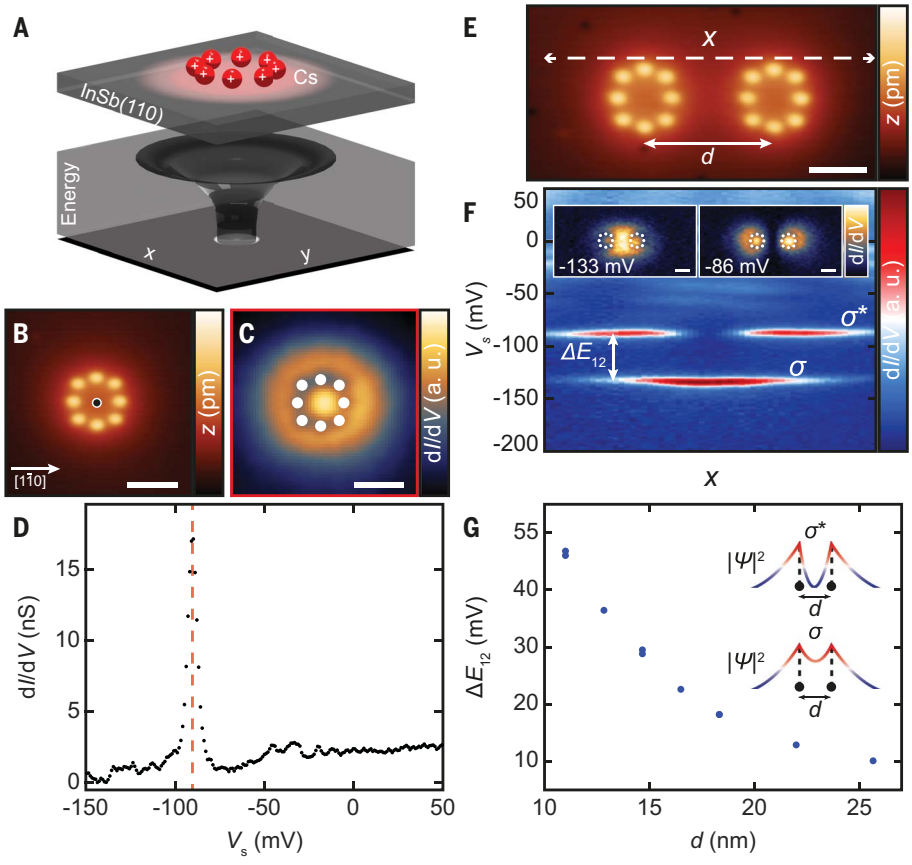


Fig. 1. Formation of an artificial atom from Cs atoms on InSb(110) and bonding/antibonding orbitals of coupled artificial atoms. (**A**) Schematic of the artificial atom created from Cs with a representation of the attractive confinement potential. (**B**) Constant-current STM image of an artificial atom derived from eight Cs atoms arranged in a ring structure (lateral scale, 5 nm; Δz = 300 pm). (**C**) Orbital map of the bound state of the artificial atom in (B), obtained at the voltage marked with a red dashed line in (D) (V_S = −91 mV). The white circles were added to represent the Cs atoms for clarity. (**D**) d*I*/d*V* spectroscopy measured at the indicated black dot in (B), revealing a bound state (red dashed line) within the bulk band gap. (**E**) Constant-current STM image of two artificial atoms separated by $d \approx 11$ nm (lateral scale, 5 nm; Δz = 300 pm). (**F**) d*I*/d*V* spectroscopy measured sequentially along the dashed white line *x* marked in (E). The σ and σ* indicate the bonding and antibonding orbitals, which are separated by ΔE_{12} = 46 mV. Insets in (F) represent spatial distribution of the bonding (σ) and antibonding (σ*) orbitals registered at V_S = −133 mV and V_S = −86 mV, respectively. The white circles were added to represent the positions of the Cs atoms for clarity. (**G**) Distance dependence of the coupling strength $\Delta E_{12}(d)$ between two artificial atoms as a function of separation *d*. The inset shows a textbook schematic representation of squared wave functions of σ and σ* orbitals. a.u., arbitrary units.

structures (supplementary texts, sections S3 and S4; figs. S7, S8, and S9). The calculations showed that the artificial atom also contained orbitals with and p_x and p_y symmetries, which were not observed experimentally because they presumably resided above the Fermi energy (E_F), within the conduction band. Because each Cs atom donated only a fraction of its outer 6*s* electron (*31*, *32*), assigning an integer number of electrons bound to the artificial atom was not possible. As a result, the mesoscopic description of an artificial atom most likely involves many-body effects. However, for distances much larger than the Cs–Cs distance within the artificial atom, we reduced the many-body problem into an effective single-particle Hamiltonian and the aforementioned $1/r$ potential, as shown in the next section.

Coupling artificial dimers

To tailor Hamiltonians that resemble molecular orbitals, it was first necessary to demonstrate that these artificial atoms can couple. We correspondingly created dimers of two artificial atoms separated by $d \approx 11$ nm (Fig. 1E), where *d* is defined as the center-to-center distance. In Fig. 1F, we illustrate a false-color plot of spatially dependent STS taken at points along the line indicated in Fig. 1E. The spectra in Fig. 1F revealed two sharp low-energy states separated by ΔE_{12} = 46.0 ± 0.6 meV. Although the lowest-energy state was most strongly localized in between the two artificial atomic sites, the higher-energy state exhibited a pronounced node with negligible intensity at the same location. Orbital maps (Fig. 1F, inset) confirmed that these energy levels could be identified as bonding (σ) and antibonding (σ*) orbitals resulting from the coupling between the two artificial atomic s orbitals. This behavior persisted for different spacings *d*, where the value of ΔE_{12} monotonically decreased for increasing *d* and was nonzero up to $d \approx 25$ nm (Fig. 1G). This distance dependence could be fitted and well described by a simple tight binding model that considers nearest-neighbor interactions and isotropic atomic orbitals. In comparison with previous observations on other surfaces (*23*–*27*, *34*), our data showed the sharpest peak widths with FWHM ≃ 8 mV, much smaller than ΔE_{12}. For a detailed discussion, see supplementary text (section S5) and fig. S10.

Higher-orbital symmetries in artificial atomic chains

Before simulating molecular orbitals, it was necessary to confirm that the coupling of artificial atomic states also leads to orbitals with distinct symmetry, such as with σ and π characters. Therefore, we fabricated a linear molecular chain composed of six artificial atoms, where each artificial atomic site is separated by $d \approx 12.8$ nm (Fig. 2A). Using d*I*/d*V* spectra taken along a line near the structure as input (fig. S11), we identified more states separated by smaller energies. To uncover the nature of these states, we acquired orbital maps (fig. S12). In the following, we provide a summary and reference supplementary text (section S6) for a more detailed discussion.

The lowest six states resembled a series of σ molecular orbitals derived from a superposition of the artificial atomic s orbitals. Following a textbook example of the linear combination of atomic orbitals (LCAO), an increasing number of nodes was found with increasing energy. We note that a simple tight-binding model using the same parameters as for the dimers and considering only nearest-neighbor hopping was sufficient to reproduce the energies of all σ orbitals. At higher energies (sample bias voltage $V_S \geq -51$ mV), we found three additional states (Fig. 2, D and E, and fig. S12I) that we identified as a series of molecular orbitals derived from LCAO-like superpositions of artificial atomic p_y orbitals, leading to artificial molecular π orbitals with a node plane along the chain axis and increasing local density of states (LDOS) above and below the chain. Again, the number of nodes along the *y* axis increased with increasing energy. Although there should still be

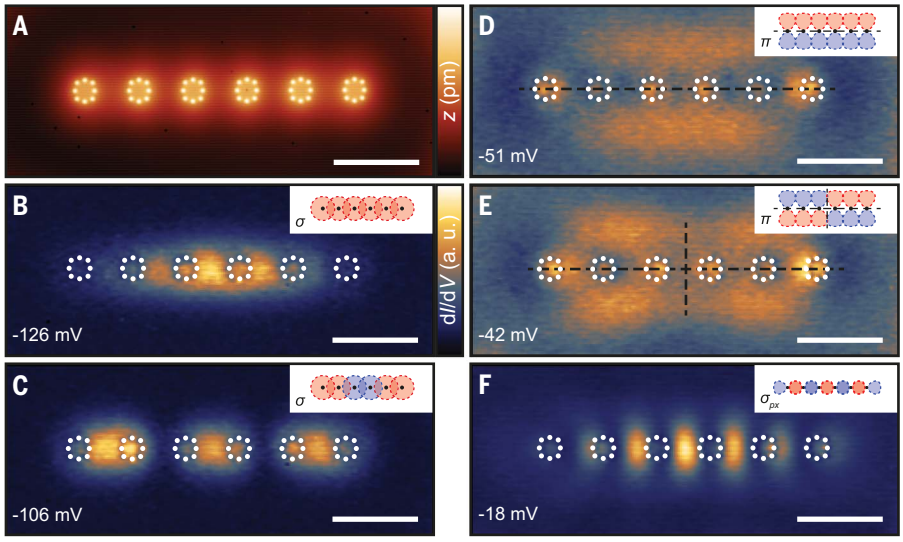


Fig. 2. Multiorbital states in an artificial molecular chain. (**A**) Constant-current STM image of a linear chain composed of six artificial atoms with equal separation $d \approx 12.8$ nm (V_S = 50 mV; lateral scale, 20 nm; Δz = 300 pm). (**B** to **F**) Orbital maps obtained at the voltages indicated in lower-left corner of each image (z_{offset} = −140 pm; V_{mod} = 2 mV; lateral scale, 20 nm). The white circles represent the Cs atomic positions. A schematic representation of atomic-like orbital contributions is provided in the inset of each map, where red and blue colors represent a positive or negative sign of the depicted wave function, respectively. [(B) and (C)] Two σ orbitals: first and third. [(D) and (E)] Set of two π orbitals. Black lines indicate the location of the nodal planes. (F) σ orbital originating from artificial atomic p_x orbitals. a.u., arbitrary units.

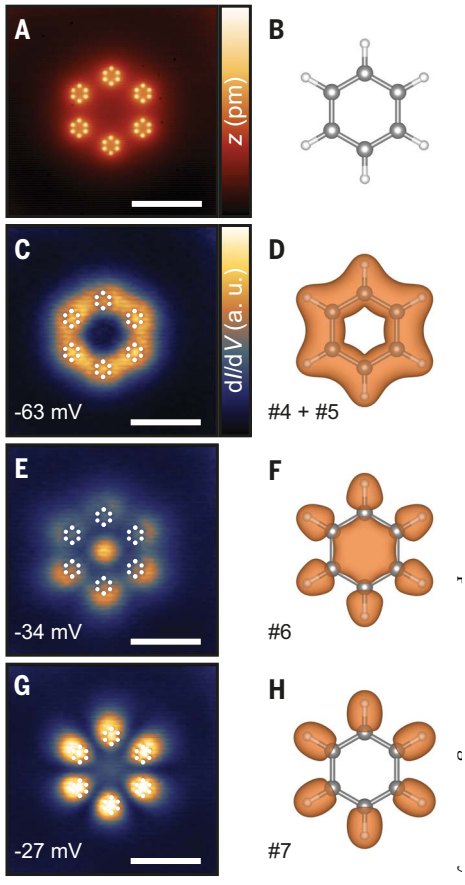


Fig. 3. Artificial benzene and its orbital structure. (**A**) Constant-current STM image of six artificial atoms arranged into a benzene structure with separation of $d \approx 10.5$ nm (lateral scale, 20 nm; Δz = 300 pm). (**B**) The ball-stick model for the benzene molecule in the DFT calculations. (**C**, **E**, **G**) Orbital maps obtained at the voltages indicated in the lower-left corner of each image (z_{offset} = −140 pm;, V_{mod} = 2 mV; lateral scale, 20 nm). The white circles were added to represent the Cs atoms for clarity. (**D**, **F**, **H**) Set of benzene VMOs obtained from the DFT calculations corresponding to orbital maps on the left. The calculations represent the charge density and include the summed charge densities for degenerate orbitals in (D). The orbital order number is indicated in the lower-left corner of each image. a.u., arbitrary units.

three more p_y-derived molecular orbitals at higher sample biases, we did not observe them, presumably because they were located at energies where hybridization with the conduction band may have weakened and broadened their LDOS. However, we found another σ orbital at V_S = −18 mV (Fig. 2F), which perfectly resembled the LCAO of artificial atomic p_x orbitals with bonding character, leading to increased LDOS along the chain axis between each of the artificial atomic sites.

As the form of the potential into the bulk of the InSb can be approximated as a triangular-well potential (*30*), artificial atomic orbitals of p_z-like character cannot be emulated, limiting the dimensionality that can be explored. Accordingly, we did not discover any orbital of p_z-like character in any of our artificial molecular structures. In two dimensions, p_z orbitals project onto s orbitals, which is why many electronic properties of 2D materials originating from p_z-derived bands should also be observable in a pure 2D system. Moreover, evidence for π-like orbitals has previously been reported in an artificial structure (*35*), albeit orbital maps, as done here, are necessary to distinguish different orbital symmetries.

Artificial hybrid molecular orbitals

As a final step toward emulating molecular orbitals, it was necessary to show that artificial atomic orbitals can hybridize. We therefore subsequently created a six-fold symmetric hexagon of artificial atoms, each composed of six Cs atoms, reminiscent of a benzene ring (Fig. 3A; see fig. S14 for structural details). We chose to use a six-Cs structure to permit faster assembly of artificial structures containing many artificial atoms, noting that it also exhibited an *s*-like state and qualitatively did not differ from the eight-Cs structure (supplementary text, sections S4 and S11; figs. S9, S31, and S32). To identify resonance energies, we acquired STS spectra at various locations (fig. S15) and subsequently imaged the resultant orbital maps (*36*). An excerpt of the maps is presented in Fig. 3 and compared with density functional theory (DFT) calculations of the actual benzene molecule. For a detailed identification and discussion of all states, we refer to the supplementary text (section S7) and figs. S13 to S16. In short, for energies below E_F, we could connect all but one of the orbital maps with the first eight calculated benzene valence molecular orbitals (VMOs) by comparing the experimental dI/dV intensities with the calculated charge densities at scaled distances. In cases of degenerate VMOs, we compared their superposition with the experimental maps. The overall qualitative agreement between the orbital maps and the calculated molecular orbitals provided evidence that the artificial atomic s, p_x, and p_y orbitals have undergone sp^2 hybridization to form artificial molecular orbitals.

The versatility of this platform allowed us to create lower-dimensional structures with fragile low-energy states and interrogate the role of geometry on these states. Although the simulated structures are not one-to-one identical to their molecular analogs (e.g., see the discussion regarding p_z orbitals above), studying this interplay is not easily possible in real molecular systems because of other restricting effects, such as relaxation. As an example of this versatility, we built 2D structures which were inspired by real 3D molecules that have nearly degenerate ground states and are hence unstable, and we constructed and compared

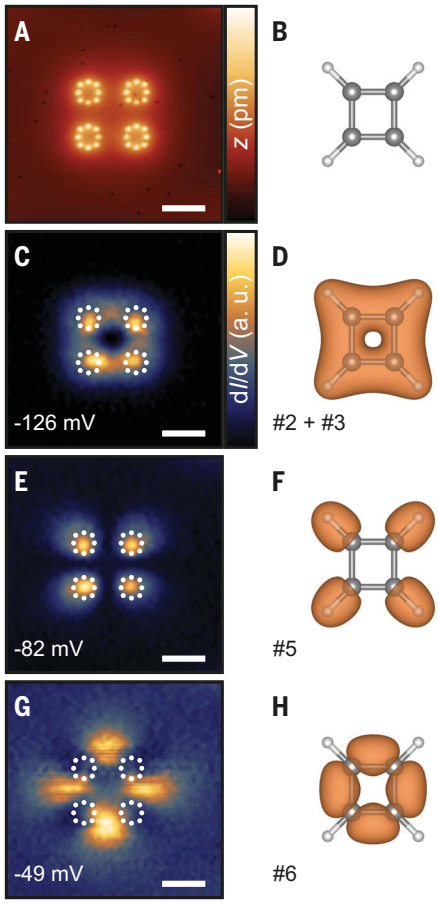


Fig. 4. Artificial cyclobutadiene and its orbital structure. (**A**) Constant-current STM image of four artificial atoms arranged in a cyclobutadiene structure with $d \approx 11$ nm (lateral scale, 10 nm; $\Delta z = 300$ pm). (**B**) The ball-stick model used for the cyclobutadiene molecule in the DFT calculations. (**C**, **E**, **G**) Set of orbital maps obtained at voltages indicated in the lower-left corner of each image. The white circles were added to represent the Cs atoms for clarity ($z_{offset} = -100$ pm; $V_{mod} = 1$ mV; lateral scale, 10 nm). (**D**, **F**, **H**) Set of cyclobutadiene VMOs obtained from the DFT calculations corresponding to orbital maps on the left. The calculations represent the charge density and include the summed charge densities for degenerate orbitals in (D). The orbital order number is indicated in the lower-left corner of each image. a.u., arbitrary units.

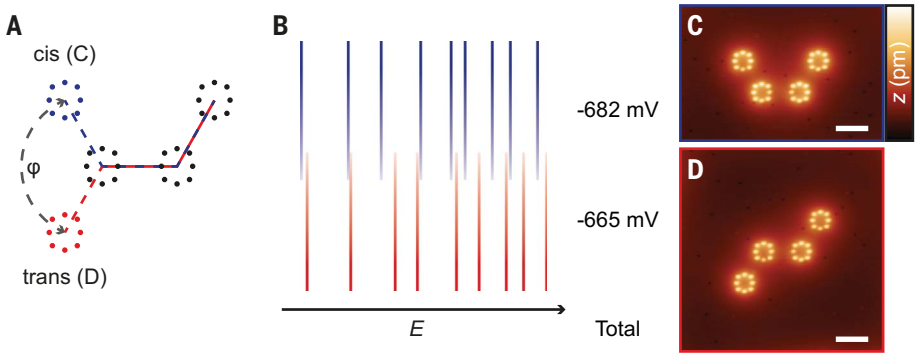


Fig. 5. Comparison of artificial *cis*- and *trans*-butadiene. (**A**) Schematic model of the artificial molecular structure built from four artificial atoms in both cis and trans conformations. (**B**) Schematic comparison of the energies of all nine orbitals from the ground state up to E_F of the cis (blue) and trans conformer (red) as identified from STS. The total energy is the sum of these eigenenergies. (**C** and **D**) Constant-current STM image of (C) the cis and (D) the trans conformer (lateral scale, 10 nm; $\Delta z = 300$ pm).

2D analogs of conformational isomers. We subsequently present examples inspired by various structural realizations of butadiene. For simplicity, we refer to these structures as artificial butadiene.

We started by coupling four artificial atoms separated by $d \approx 11$ nm that form a nearly square arrangement (Fig. 4A; see fig. S19 for details of the structure), resembling the core of cyclobutadiene (Fig. 4B). From simple molecular orbital theory and Hückel's rule, cyclobutadiene in a fourfold symmetric geometry would be antiaromatic and unstable, and it undergoes a Jahn-Teller distortion (*37*, *38*). We applied the same approach as used for artificial benzene above to identify and map the artificial molecular orbitals, which we compared with DFT-calculated orbitals of actual cyclobutadiene in its fourfold-symmetric form (Fig. 4, C and H). For a detailed identification and discussion of all states, we refer to the supplementary text (section S8) and figs. S18 to S22. In short, we were able to assign the first five orbital maps to the first six calculated VMOs of cyclobutadiene. The maps at −67 mV and −49 mV exhibited some deviations, particularly a blurred distribution with reduced intensity. We speculate that this effect can be caused by the orbitals coupling to the 2DEG, which would delocalize the LDOS. Furthermore, small asymmetries were visible, presumably because the structure deviated from a perfect fourfold symmetry (fig. S19), but with no noticeable anisotropy on the orbital levels (fig. S20). Our simulator allows us to explore the interplay of the resultant electronic structure of analogous 2D structures, with or without such distortions.

In a similar fashion as for the cyclobutadiene structure, we also built artificial structures inspired by the cis and trans conformers of 1,3-butadiene, as schematically shown in Fig. 5A (for details, see supplementary text, sections S9 and S10, and figs. S23 to S30). We first built the cis conformer (Fig. 5C) and identified all orbital maps from STS and comparison with calculations. Then, we repositioned the same group of Cs atoms of the left-hand artificial atom to build the trans conformer (Fig. 5D), and we repeated all spectroscopic measurements and calculations. This way, as we built both structures using the same Cs atoms on the same surface with the same local environment, we ensured that the acquired energies are directly comparable. The schematic energy-level diagram of all nine molecular orbitals found below E_F (Fig. 5B) shows that the levels of the cis conformer overall tended to be a bit lower, leading to a reduced sum of the occupied-state energies $E_{total}^{cis} = -682$ meV compared with $E_{total}^{trans} = -665$ meV. In the real 1,3-butadiene molecule, the cis conformer has a higher energy because of steric hindrance, leading to structural bending out of the 2D plane (*39*), which emphasizes both limitations and differences between our lower-dimensional platform and analog 3D molecules. However, as an advantage, this platform would enable to change the angle ϕ quasicontinuously, allowing us to experimentally map the potential landscape against this "reaction coordinate," hence providing a quantitative Walsh diagram for our artificial structure (*40*). Furthermore, equal versus alternating bond lengths can be compared to understand the impact of bond order in this artificial platform.

To showcase the versatility and expandability of our quantum simulator, we also built larger artificial structures representing a transition toward extended lattices. As an example, we manipulated 132 Cs atoms into a network of 22 artificial atoms arranged in a structure that is reminiscent of triangulene (supplementary text, section S12, and figs. S32 to S36), a molecule that is difficult to synthesize and has most recently drawn attention owing to its unusual electron and spin configurations (*41*–*46*).

There are several interesting observations that raise questions about the respective physical origin. For example, there is an uncanny resemblance between VMOs of organic molecules and the 2D orbital maps of the artificial structures built here. Similarly, there is an open question as to which artificial site can be related to an actual element in terms of electron occupation (e.g., C or H) and whether artificial heterostructures (i.e., resembling different elements) can be realized. Related to

this, the link between gating these artificial structures and emulating charge transfer may show exciting prospects. Finally, there are distinct differences related to the dimensionality of the platform, namely that it is below 3D, and comparisons to 3D molecular structure. We discuss these points further in the supplementary text (sections S13 and S14) and in figs. S37 and S38.

Conclusion

We have developed a versatile solid-state quantum simulator based on the use of Cs ions embedded in a 2DEG on the surface of semiconducting InSb(110). We showed that artificial atoms can be created with an electronic signature given by a sharp bound state in the semiconductor band gap. The coupling of the generated electronic states with the bulk is strongly suppressed, leading to charge densities that are spatially delocalized over distances much larger than an expected atomic wave function. This leads to long-range coupling and the ability to create artificial atomic and molecular orbitals with different symmetries. On the basis of this, we created a variety of lower-dimensional structures, from dimers to chains and eventually structures that resemble common organic molecules, and characterized their low-energy electronic structure. We found an uncanny resemblance between the expected in-plane VMOs, as calculated with DFT of the free-standing molecule, and the measured orbital energic order and structure of the artificial molecules. Moreover, we showed that well-known conformational isomers can be artificially simulated, and the geometry perturbed, where the changes in electronic structure as a function of structural change can be monitored. The versatility of the platform is based on being able to create fragile structures with degeneracy, which are often dominated by structural relaxations (e.g., Jahn-Teller distortion), and probe the interplay between geometry and the resultant electronic structure. This approach is distinctly different from that of previous studies of artificial lattices in which utilized states are strongly coupled to the bulk (*21*–*25*, *34*, *47*); for example, the use of scattered quasiparticles from patterned defects on metallic surfaces. At large distance, the attractive potential can be approximated as an atomic-like $1/r$ potential, but locally, the description involving the Cs ions and local 2D carriers most likely involved many-body interactions (*48*). In this way, owing to the interplay of poor screening, lower dimensionality, and low carrier density, this platform may also be suitable for exploring tailored many-body states in designed structures based on strong electron-electron interactions.

REFERENCES AND NOTES

1. D. Deng *et al*., *Nat. Nanotechnol.* **11**, 218–230 (2016).
2. K. S. Novoselov *et al*., *Nature* **438**, 197–200 (2005).
3. M. I. Katsnelson, *The Physics of Graphene* (Cambridge Univ. Press, ed. 2, 2020).
4. M. I. Katsnelson, K. S. Novoselov, A. K. Geim, *Nat. Phys.* **2**, 620–625 (2006).
5. N. Levy *et al*., *Science* **329**, 544–547 (2010).
6. Y. Wang *et al*., *Science* **340**, 734–737 (2013).
7. L. Perfetti *et al*., *Phys. Rev. Lett.* **90**, 166401 (2003).
8. Y. Chen *et al*., *Nat. Phys.* **16**, 218–224 (2020).
9. X. Xi *et al*., *Nat. Nanotechnol.* **10**, 765–769 (2015).
10. P. Dreher *et al*., *ACS Nano* **15**, 19430–19438 (2021).
11. K. T. Law, P. A. Lee, *Proc. Natl. Acad. Sci. U.S.A.* **114**, 6996–7000 (2017).
12. Y. Cao *et al*., *Nature* **556**, 43–50 (2018).
13. Y. Cao *et al*., *Nature* **556**, 80–84 (2018).
14. A. A. Houck, H. E. Türeci, J. Koch, *Nat. Phys.* **8**, 292–299 (2012).
15. I. Bloch, *Nat. Phys.* **1**, 23–30 (2005).
16. I. Bloch, J. Dalibard, S. Nascimbène, *Nat. Phys.* **8**, 267–276 (2012).
17. R. Blatt, C. F. Roos, *Nat. Phys.* **8**, 277–284 (2012).
18. D. S. Lühmann, C. Weitenberg, K. Sengstock, *Phys. Rev. X* **5**, 031016 (2015).
19. C. Gross, I. Bloch, *Science* **357**, 995–1001 (2017).
20. A. Singha *et al*., *Science* **332**, 1176–1179 (2011).
21. A. A. Khajetoorians, D. Wegner, A. F. Otte, I. Swart, *Nat. Rev. Phys.* **1**, 703–715 (2019).
22. M. F. Crommie, C. P. Lutz, D. M. Eigler, *Science* **262**, 218–220 (1993).
23. K. K. Gomes, W. Mar, W. Ko, F. Guinea, H. C. Manoharan, *Nature* **483**, 306–310 (2012).
24. M. R. Slot *et al*., *Nat. Phys.* **13**, 672–676 (2017).
25. R. Drost, T. Ojanen, A. Harju, P. Liljeroth, *Nat. Phys.* **13**, 668–671 (2017).
26. S. Fölsch, J. Martínez-Blanco, J. Yang, K. Kanisawa, S. C. Erwin, *Nat. Nanotechnol.* **9**, 505–508 (2014).
27. Y. Pan, J. Yang, S. C. Erwin, K. Kanisawa, S. Fölsch, *Phys. Rev. Lett.* **115**, 076803 (2015).
28. I. Vurgaftman, J. R. Meyer, L. R. Ram-Mohan, *J. Appl. Phys.* **89**, 5815–5875 (2001).
29. L. J. Whitman, J. A. Stroscio, R. A. Dragoset, R. J. Celotta, *Phys. Rev. Lett.* **66**, 1338–1341 (1991).
30. K. Hashimoto *et al*., *Phys. Rev. Lett.* **101**, 256802 (2008).
31. S. Becker, M. Liebmann, T. Mashoff, M. Pratzer, M. Morgenstern, *Phys. Rev. B Condens. Matter Mater. Phys.* **81**, 155308 (2010).
32. S. Becker *et al*., *Phys. Rev. Lett.* **106**, 156805 (2011).
33. M. Morgenstern *et al*., *Physica E* **44**, 1795–1814 (2012).
34. W. Jolie *et al*., *ACS Nano* **16**, 4876–4883 (2022).
35. V. D. Pham, K. Kanisawa, S. Fölsch, *Phys. Rev. Lett.* **123**, 066801 (2019).
36. J. Repp, G. Meyer, S. M. Stojković, A. Gourdon, C. Joachim, *Phys. Rev. Lett.* **94**, 026803 (2005).
37. T. Bally, S. Masamune, *Tetrahedron* **36**, 343–370 (1980).
38. A. Kostenko *et al*., *Angew. Chem. Int. Ed.* **56**, 10183–10187 (2017).
39. D. Feller, N. C. Craig, *J. Phys. Chem. A* **113**, 1601–1607 (2009).
40. A. D. Walsh, *J. Chem. Soc.* 2260–2266 (1953).
41. E. Clar, D. G. Stewart, *J. Am. Chem. Soc.* **75**, 2667–2672 (1953).
42. J. Inoue *et al*., *J. Am. Chem. Soc.* **123**, 12702–12703 (2001).
43. S. Mishra *et al*., *Angew. Chem. Int. Ed.* **59**, 12041–12047 (2020).
44. S. Mishra *et al*., *Nature* **598**, 287–292 (2021).
45. N. Pavliček *et al*., *Nat. Nanotechnol.* **12**, 308–311 (2017).
46. M. Randić, *Chem. Rev.* **103**, 3449–3605 (2003).
47. M. R. Slot *et al*., *Phys. Rev. X* **9**, 011009 (2019).
48. F. Ma *et al*., *Phys. Rev. X* **10**, 031058 (2020).
49. E. Sierda *et al*., Data for "Quantum simulator to emulate lower dimensional molecular structure." Radboud Data Repository (2023); https://doi.org/10.34973/faps-jp08.

ACKNOWLEDGMENTS

Funding: The experimental part of this project was supported by the European Research Council (ERC) under the European Union's Horizon 2020 research and innovation program (grant no. 818399). We also acknowledge support from the NWO-VIDI project "Manipulating the interplay between superconductivity and chiral magnetism at the single-atom level" with project no. 680-47-534. B.K. acknowledges the NWO-VENI project "Controlling magnetism of single atoms on black phosphorus" with project no. 016.Veni.192.168. The work of M.I.K. was supported by the ERC under the European Union's Horizon 2020 research and innovation program (grant no. 854843-FASTCORR). This publication is part of the project TOPCORE (project no. OCENW.GROOT.2019.048) of the research program Open Competition ENW Groot, which is partly financed by the Dutch Research Council (NWO). **Author contributions:** E.S., X.H., B.K., and E.J.K. performed the experiments. D.I.B., M.I.K., and M.R. performed the DFT and model calculations, with input from G.C.G. including supplemental quantum chemical calculations. E.S., X.H., D.I.B., G.C.G., M.I.K., M.R., D.W., and A.A.K. performed and discussed the data analysis. G.C.G., D.W., and A.A.K. designed the experiments. All authors contributed to the writing of the manuscript and scientific discussion. **Competing interests:** The authors declare no competing interests. **Data and materials availability:** All data needed to evaluate the conclusions in the paper are present in the paper or the supplementary materials. Data for all figures presented in this study are available at Radboud Data Repository (*49*). The following software was used: Gwyddion 2.60 and Matlab R2022a (data processing), VESTA 3.5.7 (visualization of DFT calculations), and Blender 3.3.1 and Adobe Illustrator 27.1 (figure preparation and 3D rendering). **License information:** Copyright © 2023 the authors, some rights reserved; exclusive licensee American Association for the Advancement of Science. No claim to original US government works. https://www.science.org/about/science-licenses-journal-article-reuse. This research was funded in whole or in part by NWO (680-47-534, 016.Veni.192.168, and OCENW.GROOT.2019.048), a cOAlition S organization. The authors will make the Author Accepted Manuscript (AAM) version available under a CC BY public copyright license.

SUPPLEMENTARY MATERIALS

science.org/doi/10.1126/science.adf2685
Materials and Methods
Supplementary Text
Figs. S1 to S38
Table S1
References (*50*–*59*)

Submitted 10 October 2022; resubmitted 22 February 2023
Accepted 10 May 2023
10.1126/science.adf2685

MECHANOCHEMISTRY

Acceleration of Diels-Alder reactions by mechanical distortion

Yerzhan S. Zholdassov[1,2,3], Li Yuan[4], Sergio Romero Garcia[5], Ryan W. Kwok[2,3], Alejandro Boscoboinik[4], Daniel J. Valles[1,2,3], Mateusz Marianski[2,3], Ashlie Martini[5], Robert W. Carpick[4], Adam B. Braunschweig[1,2,3]*

Challenges in quantifying how force affects bond formation have hindered the widespread adoption of mechanochemistry. We used parallel tip-based methods to determine reaction rates, activation energies, and activation volumes of force-accelerated [4+2] Diels-Alder cycloadditions between surface-immobilized anthracene and four dienophiles that differ in electronic and steric demand. The rate dependences on pressure were unexpectedly strong, and substantial differences were observed between the dienophiles. Multiscale modeling demonstrated that in proximity to a surface, mechanochemical trajectories ensued that were distinct from those observed solvothermally or under hydrostatic pressure. These results provide a framework for anticipating how experimental geometry, molecular confinement, and directed force contribute to mechanochemical kinetics.

The great majority of organic reactions carried out in industry and research laboratories rely on strictly solvothermal activation, in which solvent and heat act in concert to drive reactions along a trajectory toward products (*1*). The organic solvents used in these reactions account for >60% of all chemical manufacturing waste (*2*) and are often toxic (*3*), while as a result of the energy demand of solvothermal syntheses, the chemical industry consumes 37% of the total energy used in manufacturing (*4*). As such, there is a critical need to supplement and ideally replace solvothermal chemistry with less wasteful activation approaches. Mechanically activated organic chemistry (*5*)—in which force, rather than heat and solvent or hydrostatic pressure, drives the making and breaking of covalent bonds—can help to ameliorate the waste and energy challenges of organic synthesis because the reactions are run neat or with minimal solvent (*6*), and energy can be provided more efficiently through mechanical rather than thermal means (*7*). Even when solvents are added to mechanochemical reactions, in a process called liquid-assisted grinding, they are added in comparatively small amounts (*8*). Another benefit is that mechanochemically activated conditions often produce stereoisomers and regioisomers that are not favored, or cannot be produced at all, under solvothermal conditions (*9*), although why such mechanically favored products arise is often not well understood.

[1]The Advanced Science Research Center, Graduate Center of the City University of New York, New York, NY 10031, USA. [2]Department of Chemistry, Hunter College, New York, NY 10065, USA. [3]Ph.D. Program in Chemistry, Graduate Center of the City University of New York, New York, NY 10016, USA. [4]Department of Mechanical Engineering and Applied Mechanics, University of Pennsylvania, Philadelphia, PA 19104, USA. [5]Department of Mechanical Engineering, University of California, Merced, CA 95343, USA.
*Corresponding author. Email: abraunschweig@gc.cuny.edu

Despite its many potential advantages, organic mechanochemistry has not been widely adopted in chemical synthesis and manufacturing. This can be attributed in part to substantial remaining gaps in the understanding of reaction kinetics under mechanochemical activation. Until physical models are developed that reliably account for experimental observations, the products of mechanochemical reactions cannot be predicted, and the reactions cannot be easily translated to large scales. Mechanochemical reactions are typically carried out in ball mill (*10*) or planetary mill reactors (*11*) or in twin-screw extruders (*12*), for which it is difficult to determine even the most basic reaction parameters, such as the magnitude of the applied force (F), the reaction time under force (t), or conversion at different time points. Polymer mechanochemistry (*13*–*15*) entails the use of mechanical energy to activate mechanophores (*16*–*18*) embedded within long polymer chains: Sonication (*19*, *20*), atomic force microscopy (AFM) (*21*, *22*), and/or laser pulses (*23*) apply mechanical energy that ruptures the mechanically susceptible bonds in the mechanophores. However, these methods are used to initiate bond rupture, and as a consequence, such studies do not explain bond-formation events in mills and extruders. This difficulty in acquiring quantitative experimental data on bond formation under stress complicates the development and validation of generalizable kinetic models of mechanochemical bond-forming reactions. Furthermore, because mechanochemical reactions are carried out on powders, rather than well-solvated molecules, the kinetics of grinding to expose molecular reactants adds another layer of complexity to kinetic models. For example, the rate of pericyclic [4+2] Diels-Alder cycloadditions in ball (*10*) and planetary (*24*) mills are dependent on particle size (*25*), shaking frequency (*10*), ball mass (*25*), and vessel loading (*26*) in addi to the molecular-scale factors that are kn to affect rates, such as reactant structure and temperature (T) (*27*).

Given all these macroscopic factors, it has been challenging to explain how mechanical energy acts on the reaction potential energy surface. One such explanation is the "hotspot" model (*28*), which postulates that localized heating occurs when milling balls collide with surfaces and with each other, causing the release of kinetic energy. Rate increases in mechanochemical reactions are thus posited to arise because of conventional thermal activation at the collision sites. Although some local heating is observed upon milling, these temperature increases are small and are not commensurate with observed reaction rate increases (*29*). The other dominant kinetic theory of mechanochemistry argues that grinding increases the surface area of powders, increasing the collision probability of reactants, which explains the dependence of rates on powder size (*25*). Ultimately, current kinetic models of organic mechanochemistry—the molecular-scale hotspot theory and the macroscopic model that considers increases in area during grinding—are incomplete because they fail to account for all experimental observations. In particular, they fail to account for the formation of different isomers under mechanochemical activation versus strictly solvothermal activation, which indicates that F can move reactants along a different reaction trajectory than that from heat. As such, any accurate molecular-scale kinetic model of mechanochemical reactions must consider how F distinctly alters reaction trajectories and explain quantitatively how F affects reaction barriers and, in turn, reaction rates. With the physical understanding inherent to an accurate molecular-scale model of mechanical reactivity, the reactions that are susceptible to mechanical activation could be anticipated and their rates and products predicted accurately, leading to the wider adoption of sustainable mechanochemical methods in organic synthesis and chemical manufacturing.

We experimentally and computationally investigated the reaction kinetics of mechanically activated [4+2] Diels-Alder cycloaddition reactions between dienophiles and surface-confined diene monolayers to measure how force affects reaction rates. Pericyclic reactions were chosen because they proceed in concerted fashion without intermediates (*30*), which minimizes challenges in analyzing their kinetics. The reactions were carried out on monolayers so that the complexities associated with grinding powders during milling and reactant availability were not factors in the kinetic analysis, and the effects of F on the free energy of activation ($\Delta G^{\ddagger}$) and reaction trajectories would be isolated. The experiment

(Fig. 1) used elastomeric arrays (figs. S7 and S23) that contained 900 pyramidal tips with heights of 21.9 μm and base edge lengths of 31 μm (*31*, *32*) to bring fluorescently labeled dienophiles into contact with monolayers of the tethered diene, anthracene, that was immobilized covalently onto the surface of a silica (SiO_2) wafer (*33*, *34*). The tip arrays were mounted onto piezoactuators so that they could be pushed into the monolayer with precise control over F and t (*32*, *35*, *36*), resulting in a nanoreactor where the anthracene and dienophile react under mechanical activation. The tips themselves were coated with an ink mixture that consisted of a large excess of the fluorescent dienophiles embedded within a polymer matrix that solubilized the dienophiles and ensured that they were accessible to react with the immobilized anthracene (*37*). We used fluorescence microscopy to track the

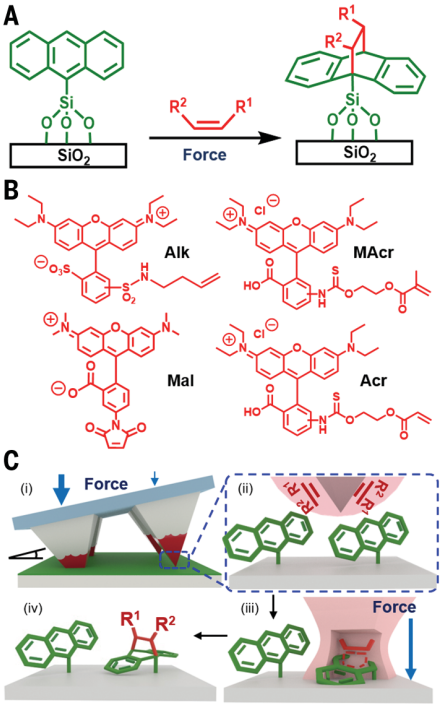


Fig. 1. Force-activated Diels-Alder reactions on anthracene monolayers. (**A**) Diels-Alder cycloaddition reaction between anthracenes immobilized onto SiO_2 surfaces and dienophiles under applied force. (**B**) Structures of dienophiles **Alk**, **Mal**, **MAcr**, and **Acr**. (**C**) (i) Elastomeric tip arrays transfer an ink mixture (red coating), consisting of a dienophile and PEG, onto an anthracene-modified surface. The tip arrays are tilted so that different forces are applied by the tips at different locations across the surface. Thick arrows indicate areas of the tip array that exert high force, and thin arrows indicate areas that exert low force. (ii) Upon contact with the surface, the tips form nanoreactors, (iii) where forces are applied that accelerate the Diels-Alder cycloaddition reactions. (iv) After washing the surface, only covalently bound molecules remain on the surface.

Diels-Alder adduct formation as a function of F and t. We studied the reaction rates of the anthracene monolayer with four different dienophiles—an alkene (**Alk**), a maleimide (**Mal**), a methacrylate (**MAcr**), and an acrylate (**Acr**)—because they differ in the electron demand (*38*) and the steric environment (*39*) around the reactive alkene, factors that affect the reaction rates of Diels-Alder reactions (*27*, *30*) under strictly solvothermal conditions, which allowed us to examine how mechanochemical reactivity trends differ from strictly solvothermal trends. We determined the pressure (p) of the reaction using a scale below the tips and finite element analysis modeling (FEM). The fluorescence data were fit to a first-order kinetic model to determine activation parameters, including the activation energy (E_a), which is the energy difference between the transition state and the initial state in the absence of stress; $\Delta G^{\ddagger}$; and the activation volume ($\Delta V^{\ddagger}$), which is a measure of the sensitivity of a reaction to mechanical activation (*40*, *41*). These data reveal that rate constant (k) increases of a factor of >10× occur at only a few atmospheres of p, and the sensitivity of this experimental approach is such that the effects of subtle differences in dienophile structure on rates could be determined, revealing that mechanochemical reactivity trends are distinct from solvothermal trends. Molecular dynamics (MD) and density functional theory (DFT) modeling of the surface and reaction revealed how molecular distortions account for changes in $\Delta G^{\ddagger}$, providing a generalizable model for mechanochemical reactivity that suggests that the scope of mechanically susceptible reactions may be substantially broader than previously anticipated.

Experimental setup

For the printing experiment, we modified an approach we have developed for studying mechanochemical surface reactions quantitatively (*31*, *32*), in which the reactions occur under a ~1-cm^2 elastomeric polymer tip array (*42*, *43*). The inked 900-tip arrays were mounted onto the z-piezoactuator of an atomic force microscope equipped with a specialized mount for the tip arrays and an x,y–tilting stage. Upon moving the arrays in and out of contact with the surface, each tip in the array prints a two-by-five array of 10 features, in which each feature in a two-by-five array is printed with a different tip-surface contact time t that varies from 1 to 600 s. The substrate is intentionally tilted with respect to the tip-array so that the F applied by individual tips varies systematically across one axis of the surface (*36*). In this experiment, the effect of 30 different values of F, ranging from 1.91 to 89.4 μN (table S1), and 10 different values of t on reaction conversion could all be assessed from a single printed surface. In addition, each two-by-five pattern generated at a given F is repeated 30 times by the tip arrays, resulting in denser data sets that enable higher-fidelity fitting. After printing, the surface was sonicated in ethyl alcohol (EtOH) for 5 min to remove any physisorbed dienophile and polyethylene glycol (PEG) from the substrate, and F, k, E_a, $\Delta V^{\ddagger}$, and $\Delta G^{\ddagger}$ values for the reaction between a fluorescent diene and surface-bound anthracene could be determined from the normalized fluorescence intensity I (fluorescence of feature/fluorescence of background) from images taken from a single printed surface.

Characterization of patterned surfaces

We relied on several complementary analytical techniques to confirm the formation of the anthracene monolayer and, subsequently, the formation of the Diels-Alder adduct. Fluorescence intensity data derived from fluorescence microscopy images (Fig. 2A) confirmed that the immobilization of the fluorophores occurs only where the tips contact the surface, and that I is dependent on both F and t (Fig. 2B). Time-of-flight secondary ion mass spectrometry (ToF-SIMS) data (Fig. 2C) show that fluorescent features of the two-by-three patterns are chemically distinct from unprinted areas, with the spectra of the former containing features consistent with the presence of the dienophile, whereas the latter are consistent with an unreacted anthracene monolayer. X-ray photoelectron spectroscopy (fig. S3), contact angle measurements (fig. S6), and AFM imaging (fig. S13) were carried out, and all data are consistent with the proposed modified surfaces. Control experiments (fig. S12), including patterning of the fluorophores onto a bare SiO_2 surface or the patterning of dyes that lack the reactive alkene onto anthracene surfaces, failed to produce fluorescence patterns, further confirming that the fluorescent patterns are the result of the covalent bond formation that occurs during the Diels-Alder cycloaddition. Although no single surface technique is capable of directly confirming the formation of new covalent bonds in monolayers, the totality of the data makes any explanation of the fluorescent patterns for a reason other than covalent bond formation through a [4+2] Diels-Alder reaction unlikely.

Determination of activation parameters

To analyze the fluorescence data and extract kinetic parameters, we assumed that the Diels-Alder reaction in this system follows a first-order kinetic rate law (eq. S10) and that fluorescence images can be used to quantify conversion as a function of F and t. We adopted the pseudo–first order assumption because at the interface, the dienophile concentration is substantially greater than the anthracene concentration. We have previously applied this same model to the kinetic data of other

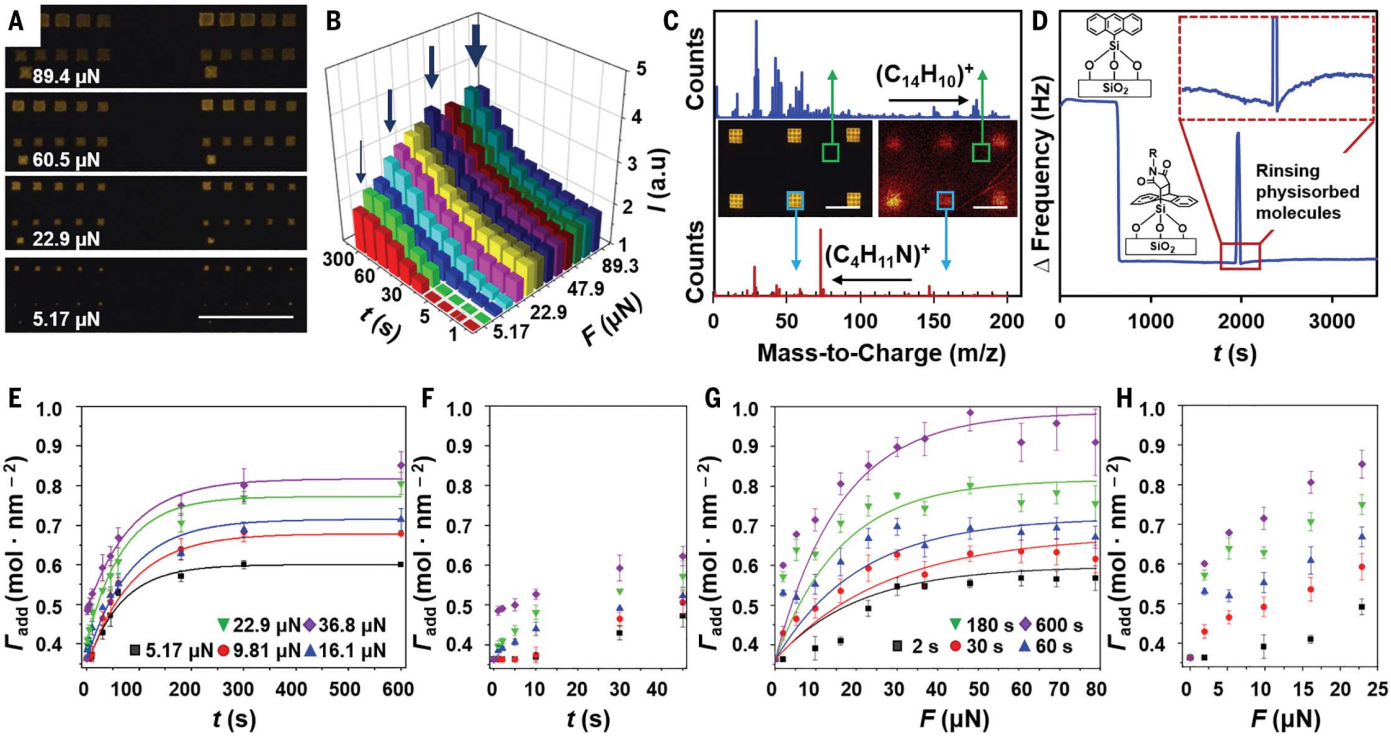


Fig. 2. Experimental data for Diels-Alder reactions on anthracene monolayers with varying force and times. (**A**) Fluorescence image (λ_{ex} = 530 to 550 nm and λ_{em} = 575 to 750 nm, where λ_{ex} is the excitation wavelength and λ_{em} is the emission wavelength), observed after washing and sonication, of surfaces after patterning with fluorescently labeled dienophile **Alk** onto the anthracene-modified SiO_2 surface. The imaged areas vary from high (top) to low (bottom) *F* applied to the substrate during the cycloaddition reaction by the tilted tip arrays. Scale bar, 90 μm. (**B**) Normalized fluorescence intensity (*I* is fluorescence of feature/fluorescence of background) of the printed features of **Alk** as a function of *F* and *t*. Arrows above the bars indicate the data taken from the fluorescent images in (A); the wide arrows indicate high *F*, and narrow arrows indicate low *F*. (**C**) Time-of-flight secondary-ion mass spectrometry (ToF-SIMS) map (positive ion mode) of a surface patterned with **Alk** after sonication and washing. (Middle left) Fluorescent image. (Middle right) Corresponding ToF-SIMS map. Scale bar, 100 μm. Mass spectrometer data were taken from unreacted (top) and reacted (bottom) areas of the surface. The peak at mass/charge ratio (*m/z*) = 178.08 is identified as a $C_{14}H_{10}^{+}$ fragment corresponding to anthracene, and the peak at *m/z* = 73.01 is identified as a $C_4H_{11}N^{+}$ fragment corresponding to the secondary dialkyl amine of the rhodamine dye. (**D**) QCM measurement tracking the formation of the Diels-Alder adduct from the reaction of **Mal** with anthracene-functionalized QCM crystal in PhMe solution. The abrupt drop in the frequency corresponds to the introduction of new solutions into the QCM. The spike in the frequency and inset correspond to the introduction of a solution of EtOH to wash physisorbed molecules from the surface. (**E** and **F**) Plots of surface density of the adduct (Γ_{add}) versus *t* for the reaction of **Alk** with the anthracene surface. (**G** and **H**) Plots of Γ_{add} versus *F* for the reaction of **Alk** with the anthracene surface. Error bars are 1 SD from the mean of three independent measurements. Fits were weighted to the error bars.

pericyclic reactions on monolayers under applied *F* and found good agreement between the model and the experimental data (*32*). To determine the rate constant *k*, it was necessary to track conversion of anthracenes on the surface to adduct by measuring the grafting density of the anthracene (Γ_{anth}) and of the adduct (Γ_{add}) in the fluorescent features. A quartz crystal microbalance (QCM) measurement on a SiO_2 crystal that was subjected to the anthracene monolayer formation protocols provided $\Gamma_{anth,max}$, the concentration of anthracene in the unreacted monolayer, of 1.12 ± 0.33 mol·nm^{-2} (fig. S18), which is in good agreement with the value obtained from MD simulations of $\Gamma_{anth,max}$ = 1.20 ± 0.08 mol·nm^{-2} (figs. S36 and S37). The maximum grafting density of the adduct ($\Gamma_{add,max}$) was determined by monitoring the reaction between an anthracene-modified QCM crystal and a solution of **Mal** within the fluid cell of the QCM (Fig. 2D). This reaction was selected because it occurs rapidly, even in the absence of *F*, so that the reaction would proceed to completion in the QCM. The QCM data were consistent with the formation of the adduct with $\Gamma_{add,max}$ = 0.94 ± 0.14 mol·nm^{-2}, suggesting that only 75 to 84% of the anthracene can react with **Mal**, at which point the surface is saturated with adduct. For the ensuing calculations, we assumed that the adducts that formed with the different dienophiles had similar volumes and, in turn, similar $\Gamma_{add,max}$. An accurate measure of *F* at each feature was needed to understand the relationship between reaction rate and *F*. We determined *F* using a balance below the printed surface and measuring the recorded weight and feature edge length (fig. S22 and table S1) (*35*), and these calculations determined that the *F* across the substrate ranged from 1.91 to 89.4 μN. We conducted FEM of individual pyramidal tips to validate the force measurements, and the relationship between feature length and *z*-displacement matched the experiments and was nearly independent of the assumed elastic constants for polydimethylsiloxane (PDMS). Furthermore, the values of the simulated *F* as a function of *z*-piezo extension could be readily fit to the experimental data by using values of the PDMS elastic constants well within typical measured values (figs. S23 and S24). Last, we considered whether surface roughness could create localized asperities of high force and found that average surface roughness (0.41 nm) (fig. S25) was too low to cause any noteworthy effect.

With these data in hand, the surface density of the adduct ($\Gamma_{t,F}$) could be determined from the fluorescence intensity of the features printed at different *F* and *t* from $I_{t,F}$ using Eq. 1

$$\Gamma_{t,F} = \left[1 - \left(\frac{I_{max} - I_{t,F}}{I_{max}}\right)\right] \cdot \Gamma_{add,max} \quad (1)$$

where I_{max} is the fluorescence intensity of a feature that has reached saturation with the adduct. This equation assumes $\Gamma_{t,F}$ and $I_{t,F}$

are linearly related, an assumption that can be used in organic monolayers when the fluorophores do not couple (*44*). The relationship between $\Gamma_{t,F}$, F, and t for each feature was plotted for all anthracene-dienophile pairs (Fig. 2, E to H, and figs. S27 to S30). In all cases, we observed that $\Gamma_{t,F}$ increased with increasing t and F. **Mal** is the only dienophile that formed adduct in the absence of F, and the rate quickly reached a maximum upon the application of minimal F. This is consistent with known trends for Diels-Alder reactions with normal electron demand, in which the presence of electron withdrawing groups on the dienophile lowers the E_a (*27*, *30*). The plots of $\Gamma_{t,F}$ versus t (Fig. 2, E and F) and $\Gamma_{t,F}$ versus F (Fig. 2, G and H) fit well to a first-order rate model, further validating the pseudo–first order assumption. All fits of kinetic data were weighted to the error bars, and χ^2 analysis showed that the fits were statistically significant at a 95% level of confidence.

A mathematical framework was needed to derive the activation parameters k, E_a, $\Delta V^{\ddagger}$, and $\Delta G^{\ddagger}$ from the experimental data. We adapted the model, developed from examining chemical reactions under hydrostatic pressure (*45*, *46*) and based on the work of Evans and Polanyi (*47*) and Eyring (*48*), that considers how p affects k. Under hydrostatic pressure, cycloaddition reactions have finite and negative $\Delta V^{\ddagger}$, meaning that p will increase k according to Eq. 2

$$\ln(k) = \ln(A) - \frac{E_a}{k_B T} - \frac{p\Delta V^{\ddagger}}{k_B T} \qquad (2)$$

where A is the preexponential factor, T is the temperature, and k_B is Boltzmann's constant. This model, which considers the effects of thermal and mechanical activation on the rate, has $\Delta G^{\ddagger} = E_a + p\Delta V^{\ddagger}$. We follow the convention, used broadly in the study of the effects of p on chemical kinetics, in which a negative $\Delta V^{\ddagger}$ acts to reduce $\Delta G^{\ddagger}$. To apply this model, the mean p in the nanoreactor contacts was determined as a function of F by dividing by the feature area. Our use of mean pressure is consistent with current published work on probe-based mechanochemistry (*32*, *49*, *50*). There was a spatial distribution of that pressure, as seen in our finite element simulations (fig. S23D), but this does not alter the observed trends nor our primary conclusion that nonhydrostatic compression increases reaction rates as a result of molecular distortion, lowering the reaction energy.

With these experimental data, we determined all the activation parameters of interest for each dienophile-anthracene pair. Isothermal first-order Arrhenius plots of $\ln\Gamma_{anth}$ versus t were fitted, and k at each pressure was determined from the best-fit linear correlation (Fig. 3A and fig. S31) that was weighted to the error bars; errors are reported as the standard error of the fit. For **Alk**, k increased from $3.8 \pm 0.25 \times 10^{-3}$ s^{-1} at $p = 0.16$ MPa to $1.55 \pm 0.19 \times 10^{-2}$ s^{-1} at $p = 0.32$ MPa, and this trend of increasing k with increasing p is consistent throughout all the data. The greatest change in k was observed for **MAcr** (from $4.07 \pm 0.58 \times 10^{-3}$ to $1.77 \pm 0.77 \times 10^{-1}$ s^{-1}) and the smallest for **Mal** (from $4.0 \pm 0.050 \times 10^{-2}$ to $1.57 \pm 0.77 \times 10^{-1}$ s^{-1}). The E_a and $\Delta V^{\ddagger}$ were determined from the extrapolated y-intercept and slope, respectively, of the linear fit of the plot of $\ln k$ versus p (Fig. 3B). The E_a follow the trend **MAcr** > **Acr** > **Alk** > **Mal**. The magnitudes of E_a in the anthracene monolayers, 84.5 to 96.4 kJ·mol^{-1}, are similar in magnitude to values for Diels-Alder reactions with anthracene reported in the literature of 63.6 to 83.7 kJ·mol^{-1} (*51*, *52*), and these small differences in magnitude in the E_a between reactions in solution and monolayers can be attributed to differences in molecular structures, reaction geometry, lack of solvent, and the influence of the SiO_2 surface. All $\Delta V^{\ddagger}$ are negative, and the differences in $\Delta V^{\ddagger}$ between the dienophile-anthracene pairs reflect the relative susceptibilities of their rates to mechanically induced pressure. The $\Delta V^{\ddagger}$ range from -60.7×10^3 cm^3·mol^{-1} for **MAcr** to -21.8×10^3 cm^3·mol^{-1} for **Mal** and follow the identical trend of **MAcr** > **Acr** > **Alk** > **Mal**, meaning that the reactions with larger E_a are more sensitive to mechanochemical activation. Also, these $\Delta V^{\ddagger}$ values are substantially greater than the $\Delta V^{\ddagger}$ of −20 to −45 cm^3·mol^{-1} for Diels-Alder reactions observed (*46*) under hydrostatic p in solution, where interfaces do not have a role in the reaction. Last, we calculated the change in free energy of activation $\Delta\Delta G^{\ddagger} = p\Delta V^{\ddagger}$ at every p for each dienophile-anthracene pair (Fig. 3C) and found that $\Delta\Delta G^{\ddagger}$ range from −3.53 to −19.46 kJ·mol^{-1}, with an average value of −8.21 kJ·mol^{-1}, which would cause a ~14-fold rate increase in rate. The relative sensitivity to p shown in Fig. 3B was validated by adding the rhodamine-labeled **Mal** (Fig. 3B, red) and a **MAcr** that was labeled with fluorescein (Fig. 3B, green) to the same tip array (fig. S33) and then printing them simultaneously (fig. S34), which led to the fluorescence intensity of the red dye remaining constant as force was increased, whereas the intensity of the green dye increased with increasing force (fig. S35).

Modeling mechanical distortion

We used DFT calculations to generate a theoretical model for the energetics of the reactants and the transition states (TSs) and to understand mechanistically how F acts on the system to lower the reaction energy (ΔE). Although experiments determined $\Delta G^{\ddagger}$, our calculations and the ensuing theoretical treatment involve ΔE, which is the reaction energy that does not take into account vibrational and entropic effects that are not included in the DFT calculations. Anthracene was simulated as attached to a $Si_4O_9H_3$ cluster to mimic the effect of the surface. DFT calculations predicted the E_a, which is the activation energy for the strictly solvothermal reactions, as defined by Eq. 2, for the Diels-Alder reaction to be between 77.1 (**Mal**) and 90.0 (**Alk**) kJ·mol^{-1} (Fig. 4A and fig. S44). These values are within range of the experimental values. The overestimation of the E_a of **Alk** is likely caused by limiting the reaction system to the anthracene, SiO_2 cluster, and dienophile. In doing so, we neglected the destabilizing effects caused by the interactions between the surrounding SiO_2 surface and the rhodamine fluorophore. This omission led to interactions

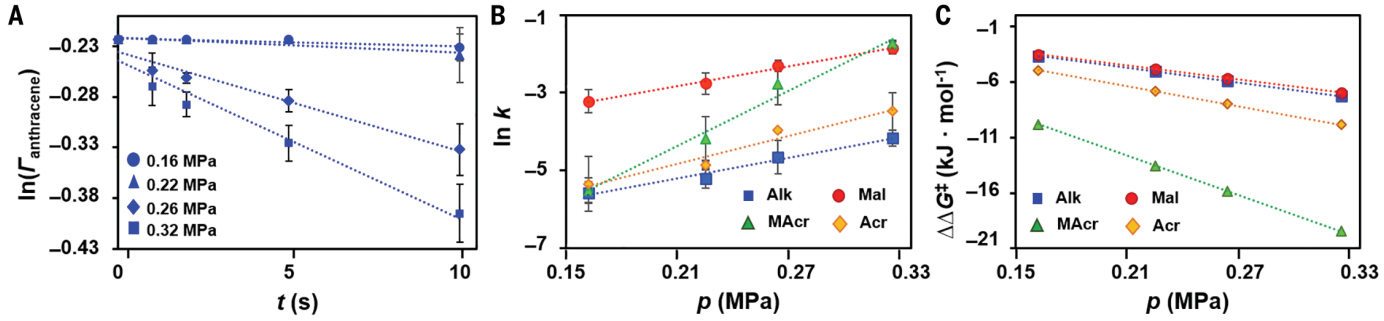


Fig. 3. Activation parameters for the Diels-Alder reactions on anthracene monolayers. (**A**) Isothermal Arrhenius plots of $\ln(\Gamma_{anthracene})$ versus t at different F for the reaction between **Alk** and the anthracene monolayers. Fits are based on eq. S12. The slope of these lines provide k. (**B**) Plot of $\ln k$ versus p for all four dienophiles, the slope of which provides $\Delta V^{\ddagger}$, whereas y-intercept provides E_a. Fits were weighted to the error bars, and coefficients of determination (R^2) are 0.97 to 0.99. (**C**) $\Delta\Delta G^{\ddagger}$ as a function of p.

in the calculations that stabilized the **Alk**-anthracene reactant complex, resulting in a higher reaction barrier than was measured experimentally. MD simulations showed that the anthracene responds to tip-induced compression by bending toward the surface, that the fraction of molecules with distorted CCH angles increases with increasing pressure (fig. S42), and that compression causes deformation of the molecules themselves (figs. S40 to S42). To model the effect of the mechanical distortion caused by uniaxial stress acting on the reactant from the top, we used DFT to distort the anthracene along three angles—OSiC, SiCC, or CCH (Fig. 4A)—and the geometry of the reactant and TS were fully relaxed, while keeping those angles fixed. In this model, we envision that F increases the energy of the reactants by distorting the anthracene in a way that increases its reactivity. The acceleration of the reaction can be then achieved when the distortion energy of the reactants (ΔE_d^R) is larger than the distortion energy of the TS (ΔE_d^{TS}) (*53*). The change in the reaction energy ($\Delta\Delta E$) that occurs during the distortion of the anthracene reactant and TS are shown in Fig. 4B and fig. S45. We observed that distorting the anthracene along OSiC and SiCC angles increases ΔE. However, bending the top H (CCH) toward the dienophile, from the relaxed geometry of between 180° and 190° to 200°, decreases the ΔE of **Alk**, **Acr**, and **MAcr** by 2.6, 4.4, and 5.6 kJ·mol^{-1}, respectively, which is consistent with the experimentally determined $\Delta\Delta G^{\ddagger}$ and follows the identical trend **MAcr** > **Acr** > **Alk** > **Mal**. Only in the case of **Mal** did bending of the CCH angle increase the ΔE, most likely because of repulsive electrostatic interactions between the bulky dienophile and the SiO_2 cluster, although this is still consistent with the smallest $\Delta\Delta G^{\ddagger}$ observed experimentally for **Mal**. Subsequently, we explored the effect of bending of other angles or bending multiple angles simultaneously (fig. S46 and table S14), and these calculations did not result in substantially different values of ΔE. This particular bending motion is productive because it increases asynchronicity—the difference in length ($\Delta r_{C\text{-}C}$) between newly formed C–C bonds—of the TS (Fig. 4C). This deformation from the relaxed, nearly synchronous TS of the **Acr** ($\Delta r_{C-C}^{\mathbf{Acr}} = 0.07$ Å) to the distorted, asynchronous TS ($\Delta r_{C-C}^{\mathbf{Acr}-200} = 0.18$ Å) reduces the destabilizing activation strain and unfavorable Pauli repulsion between the reactants, which results in a lower ΔE (*53*, *54*). Furthermore, the predicted degree of the asynchronicity of the distorted TSs (table S13) is consistent with the increasing acceleration of the reaction, **MAcr** > **Acr** > **Alk** > **Mal**.

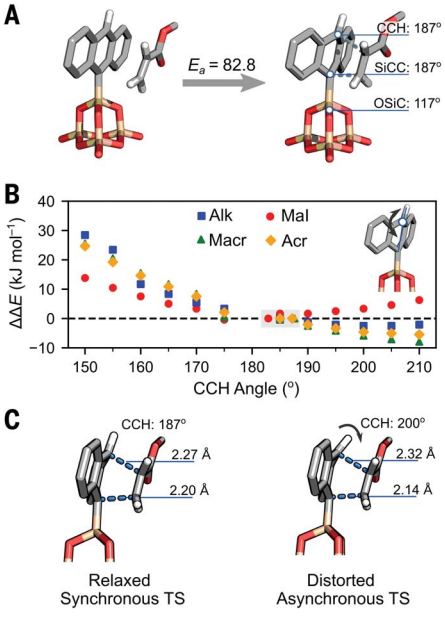


Fig. 4. Mechanical distortion under uniaxial stress. (**A**) The activation energy E_a and the geometry of the relaxed transition state involving **Acr**. Blue lines indicate OSiC, SiCC, and CCH angles, distortion of which by the applied F is explored in (B) and (C). All calculations have been performed at M06-2X/6-311+G(d,p) level of theory (*31*, *32*, *57*, *58*). (**B**) The relative change ($\Delta\Delta E$) to the reaction energy (ΔE) as a function of the CCH angle. The gray box indicates the fully relaxed TS geometry. The bending of the CCH angle leads to the decrease of the ΔE for **MAcr**, **Acr**, and **Alk**. (**C**) The effect of distorting the CCH coordinate on the geometry of the TS. Pushing the H atom toward the dienophile creates an asynchronous TS, which lowers the reaction energy.

Mechanical force, which acts as uniaxial compression, modifies the potential energy surface of the Diels-Alder reaction differently than does hydrostatic pressure. Under strictly solvothermal conditions (Fig. 5A), ΔE is equal to the strictly solvothermal activation energy E_a. Hydrostatic pressure (Fig. 5B) acts along the reaction coordinate by reducing the energy of the transition state (ΔE_H^{TS}), and $\Delta\Delta E = \Delta E_H^{TS} = p\Delta V^{\ddagger}$. $\Delta V^{\ddagger}$ of Diels-Alder reactions under hydrostatic pressure are modest (−20 to −45 cm^3·mol^{-1}) (*46*) because hydrostatic pressure squeezes equally along three axes and does not cause molecular distortion. As such, a p of ~150 MPa is needed for a $\Delta\Delta E$ of −4.4 kJ·mol^{-1}, which is an arbitrarily chosen value of $\Delta\Delta E$ that is in the range of those $\Delta\Delta G^{\ddagger}$ measured here experimentally. Uniaxial compression (Fig. 5C) distorts the reactants, raising their energy by ΔE_d^R, and also distorts the transition state to raise its energy by ΔE_d^{TS}. So, under mechanochemical conditions, in which uniaxial compression can cause distortions to occur, $\Delta\Delta E = \Delta E_d^{TS} - \Delta E_d^R = p\Delta V^{\ddagger}$. Because the magnitudes for the $\Delta V^{\ddagger}$ we observed for mechanically distorted Diels-Alder reactions are large (>10^4 cm^3·mol^{-1}), the same $\Delta\Delta E$ of −4.4 kJ·mol^{-1} can be achieved at p < 1 MPa.

We also found that similarities exist (fig. S47) in how force modifies the potential energy surfaces of mechanochemical bond formation (pushing, which causes uniaxial stress) and mechanochemical bond rupture reactions (pulling, which involves uniaxial stress in the opposite direction). In 2007, Hickenboth *et al.* studied bond rupture in another pericyclic reaction, the ring opening of a benzocyclobutene mechanophore, while using sonication to drive the ring-opening reaction (*20*). Since then, other pericyclic reactions, including the retro Diels-Alder reaction driven by pulling, have also been examined (*17*, *22*). The Diels-Alder reaction (bond forming) and benzocyclobutene ring-opening–retro Diels-Alder reactions (bond rupture) are all pericyclic reactions, meaning that their regioselectivities and stereoselectivities are governed by the Woodward-Hoffmann rules. The studies by Hickenboth *et al.* first revealed that a distorted state also precedes the TS and bond rupture in ring opening, and the result of this distorted state is a decrease in ΔE, where the relationship $\Delta\Delta E = \Delta E_d^{TS} - \Delta E_d^R$, the same relationship that we observed for mechanochemical bond formation, also applies. Thus, the key to understanding regioselectivity and stereoselectivity in mechanochemical pericyclic reactions—and bringing mechanochemically driven pericyclic reactions within the Woodward-Hoffmann manifold—necessitates understanding the distortion that uniaxial mechanical stress induces in the reactants and the TSs. There is, however, an important difference between how pushing and pulling modify the reaction potential energy surface: a Diels-Alder reaction driven by compression will follow a distinct trajectory along the potential energy surface than the retro Diels-Alder reaction of its products. As such, the geometries and energies of the TSs and the distorted states of the Diels-Alder reaction and the retro Diels-Alder reaction will be very different.

We have used elastomeric tip arrays to control precisely the t and F applied between dienes and dienophiles on a surface to determine k, E_a, $\Delta V^{\ddagger}$, $\Delta G^{\ddagger}$, and $\Delta\Delta G^{\ddagger}$ for the Diels-Alder reaction between immobilized anthracene and four dienophiles that differ in steric and electronic demand. We found that $\Delta V^{\ddagger}$ is ~1000-fold greater on surfaces under uniaxial compression than under hydrostatic pressure, indicating that the reactions follow different trajectories. The value of tip-based approaches for measuring the kinetic parameters of mechanochemical bond-breaking reactions is well known, and in this work we show that the techniques are equally valuable for studying bond-forming mechanochemical reactions. These results have important implications for the study, understanding, and wider application and adoption of mechanochemistry. These results also explain that the large $\Delta V^{\ddagger}$ for mechanochemical reactions occur as a result

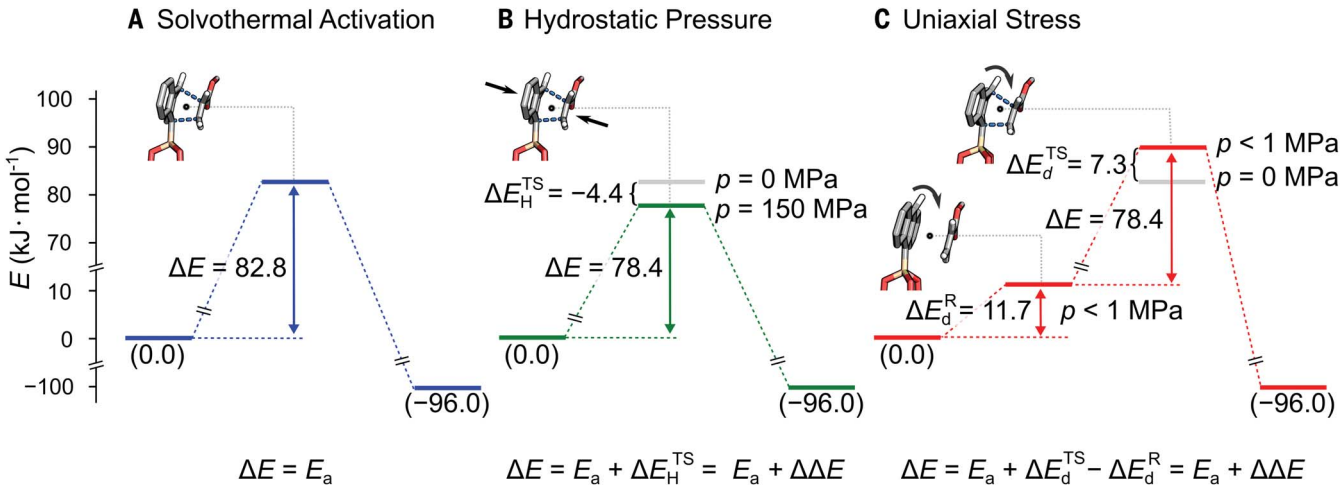


Fig. 5. Comparison of reaction trajectories under strictly solvothermal activation, hydrostatic pressure, and uniaxial stress. (**A**) Reaction potential energy diagram of the Diels-Alder reaction under strictly solvothermal activation. (**B**) Reaction potential energy diagram of the Diels-Alder reaction under hydrostatic pressure. The arrows indicate the hydrostatic forces that accelerate the reaction. ΔE_H^{TS} was calculated by using $\Delta V^{\ddagger}$ of −30 $cm^3 \cdot mol^{-1}$ to predict the change in the ΔE in the hydrostatic mechanism at a p of 150 MPa. (**C**) Reaction potential energy diagram of the Diels-Alder reaction under uniaxial mechanochemical activation. The arrows indicate the deformation of the CCH angle on the diene from the solvothermal TS value of 187° to the arbitrarily chosen distorted TS value of 200° and associated reactant deformation energy (ΔE_d^R) and TS deformation energy (ΔE_d^{TS}). All calculations have been performed at M06-2X/6-311+G(d,p) level of theory. The equations for calculating the reaction energy (ΔE) in each of the three reaction conditions—solvothermal activation, hydrostatic pressure, and mechanical distortion—are provided below the potential energy diagrams.

of the proximity to surfaces and uniaxial stress that cause molecular distortion. This distortion lowers the reaction energy and drives the reaction through a distinct reaction trajectory, which explains why different isomers are often obtained under F than in solvent (*9*, *55*). This phenomenon—the distortion of molecules near surfaces that occurs under F to lower $\Delta G^{\ddagger}$—will be relatively independent of molecular structure and suggests that mechanochemical reactivity is more widespread than previously anticipated. As a consequence, these results should encourage the adoption of mechanochemical methods for sustainable chemical synthesis and for accelerating reactions that are otherwise impractically slow.

REFERENCES AND NOTES

1. S. G. Koenig *et al.*, *ACS Sustain. Chem.& Eng.* **7**, 16937–16951 (2019).
2. R. K. Henderson *et al.*, *Green Chem.* **13**, 854–862 (2011).
3. D. R. Joshi, N. Adhikari, *J. Pharm. Res. Int.* **28**, 1–18 (2019).
4. US Energy Information Administration, "2018 Manufacturing Energy Consumption Survey" (US Energy Information Administration, 2021).
5. G.-W. Wang, *Chem. Soc. Rev.* **42**, 7668–7700 (2013).
6. H. P. DeGroot, T. P. Hanusa, *Organometallics* **40**, 3516–3525 (2021).
7. J.-L. Do, T. Friščić, *ACS Cent. Sci.* **3**, 13–19 (2017).
8. T. Friščić, C. Mottillo, H. M. Titi, *Angew. Chem. Int. Ed.* **59**, 1018–1029 (2020).
9. J. G. Hernández, C. Bolm, *J. Org. Chem.* **82**, 4007–4019 (2017).
10. J. M. Andersen, J. Mack, *Chem. Sci.* **8**, 5447–5453 (2017).
11. F. J. Gotor, M. Achimovicova, C. Real, P. Balaz, *Powder Technol.* **233**, 1–7 (2013).
12. D. Crawford *et al.*, *Chem. Sci.* **6**, 1645–1649 (2015).
13. P. A. May, J. S. Moore, *Chem. Soc. Rev.* **42**, 7497–7506 (2013).
14. J. Li, C. Nagamani, J. S. Moore, *Acc. Chem. Res.* **48**, 2181–2190 (2015).
15. A. L. Black, J. M. Lenhardt, S. L. Craig, *J. Mater. Chem.* **21**, 1655–1663 (2011).
16. J. Li *et al.*, *J. Am. Chem. Soc.* **136**, 15925–15928 (2014).
17. J. Wang *et al.*, *Nat. Chem.* **7**, 323–327 (2015).
18. G. R. Gossweiler *et al.*, *ACS Macro Lett.* **3**, 216–219 (2014).
19. K. L. Berkowski, S. L. Potisek, C. R. Hickenboth, J. S. Moore, *Macromolecules* **38**, 8975–8978 (2005).
20. C. R. Hickenboth *et al.*, *Nature* **446**, 423–427 (2007).
21. M. Horst *et al.*, *J. Am. Chem. Soc.* **143**, 12328–12334 (2021).
22. A. R. Sulkanen *et al.*, *J. Am. Chem. Soc.* **141**, 4080–4085 (2019).
23. J. Sung, M. J. Robb, S. R. White, J. S. Moore, N. R. Sottos, *J. Am. Chem. Soc.* **140**, 5000–5003 (2018).
24. J.-M. Seo, I.-Y. Jeon, J.-B. Baek, *Chem. Sci.* **4**, 4273–4277 (2013).
25. L. Gonnet *et al.*, *ACS Sustain. Chem.& Eng.* **9**, 4453–4462 (2021).
26. K. S. McKissic, J. T. Caruso, R. G. Blair, J. Mack, *Green Chem.* **16**, 1628–1632 (2014).
27. I. Fleming, *Frontier Orbitals and Organic Chemical Reactions* (Wiley, 1976).
28. A. W. Tricker, G. Samaras, K. L. Hebisch, M. J. Realff, C. Sievers, *Chem. Eng. J.* **382**, 122954 (2020).
29. H. Kulla *et al.*, *Chem. Commun.* **53**, 1664–1667 (2017).
30. I. Fleming, *Pericyclic Reactions* (Oxford Univ. Press, 1998).
31. S. Bian *et al.*, *J. Am. Chem. Soc.* **135**, 9240–9243 (2013).
32. X. Han, S. Bian, Y. Liang, K. N. Houk, A. B. Braunschweig, *J. Am. Chem. Soc.* **136**, 10553–10556 (2014).
33. Y. Hong *et al.*, *J. Phys. Chem. C* **123**, 19715–19724 (2019).
34. C. Huang, H. E. Katz, J. E. West, *Langmuir* **23**, 13223–13231 (2007).
35. X. Liao, A. B. Braunschweig, Z. Zheng, C. A. Mirkin, *Small* **6**, 1082–1086 (2010).
36. X. Liao, A. B. Braunschweig, C. A. Mirkin, *Nano Lett.* **10**, 1335–1340 (2010).
37. L. Huang *et al.*, *Small* **6**, 1077–1081 (2010).
38. J. J. Dudkowski, E. I. Becker, *J. Org. Chem.* **17**, 201–206 (1952).
39. W. R. Vaughan, K. S. Andersen, *J. Org. Chem.* **21**, 673–683 (1956).
40. B. Chen, R. Hoffmann, R. Cammi, *Angew. Chem. Int. Ed.* **56**, 11126–11142 (2017).
41. A. Martini, S. H. Kim, *Tribol. Lett.* **69**, 150 (2021).
42. F. Huo *et al.*, *Science* **321**, 1658–1660 (2008).
43. D. J. Eichelsdoerfer *et al.*, *Nat. Protoc.* **8**, 2548–2560 (2013).
44. A. Loyter, V. Citovsky, R. Blumenthal, *Methods Biochem. Anal.* **33**, 129–164 (1988).
45. C. Walling, H. J. Schugar, *J. Am. Chem. Soc.* **85**, 607–612 (1963).
46. T. Asano, W. J. Le Noble, *Chem. Rev.* **78**, 407–489 (1978).
47. M. G. Evans, M. Polanyi, *Trans. Faraday Soc.* **31**, 875–894 (1935).
48. H. Eyring, *J. Chem. Phys.* **3**, 107–115 (1935).
49. H. Spikes, *Friction* **6**, 1–31 (2018).
50. L. Fang, S. Korres, W. A. Lamberti, M. N. Webster, R. W. Carpick, *Faraday Discuss.* **241**, 394–412 (2023).
51. L. J. Andrews, R. M. Keefer, *J. Am. Chem. Soc.* **77**, 6284–6289 (1955).
52. K. E. Wise, R. A. Wheeler, *J. Phys. Chem. A* **103**, 8279–8287 (1999).
53. F. M. Bickelhaupt, K. N. Houk, *Angew. Chem. Int. Ed.* **56**, 10070–10086 (2017).
54. P. Vermeeren, T. A. Hamlin, F. M. Bickelhaupt, *Phys. Chem. Chem. Phys.* **23**, 20095–20106 (2021).
55. S. Biswas *et al.*, *Faraday Discuss.* **241**, 266–277 (2023).
56. Y. Zholdassov *et al.*, Acceleration of Diels-Alder reactions by mechanical distortion. *Dryad* (2023); https://doi.org/10.5061/dryad.0cfxpnw72.
57. Y. Zhao, D. G. Truhlar, *Theor. Chem. Acc.* **119**, 525–525 (2008).
58. M. Linder, T. Brinck, *Phys. Chem. Chem. Phys.* **15**, 5108–5114 (2013).

ACKNOWLEDGMENTS

We thank P. Nautiyal for assistance with acquiring AFM images. We also thank T.-D. Li for assistance with acquiring ToF-SIMS data. **Funding:** A.B.B., R.W.C., and A.M. are grateful to the National Science Foundation Center for the Mechanical Control of Chemistry (CCI CHE-2023644) for generous support. A.B.B. also acknowledges award DBI-2032176 from the National Science Foundation. This work was carried out in part at the Singh Center for Nanotechnology, which is supported by the NSF National Nanotechnology Coordinated Infrastructure Program under grant NNCI-2025608. **Author contributions:** Y.S.Z., A.M., R.W.C., M.M., and A.B.B. conceived the research. Y.S.Z., L.Y., S.R.G., A.B., R.W.K., and D.J.V. carried out the experiments. All authors contributed to the writing of the manuscript. **Competing interests:** The authors declare no competing financial interests. **Data and materials availability:** All data are available in the supplementary materials. Tables S1 to S14 have been uploaded in more reusable tabular format to the Dryad repository (*56*).

License information: Copyright © 2023 the authors, some rights reserved; exclusive licensee American Association for the Advancement of Science. No claim to original US government works. https://www.science.org/about/science-licenses-journal-article-reuse

SUPPLEMENTARY MATERIALS

science.org/doi/10.1126/science.adf5273
Materials and Methods
Figs. S1 to S47
Tables S1 to S14
References (*59*–*78*)

Submitted 27 October 2022; resubmitted 14 February 2023
Accepted 13 April 2023
10.1126/science.adf5273

ANIMAL MOVEMENT

Behavioral responses of terrestrial mammals to COVID-19 lockdowns

Marlee A. Tucker[1]*, Aafke M. Schipper[1], Tempe S. F. Adams[2], Nina Attias[3,4], Tal Avgar[5], Natarsha L. Babic[6], Kristin J. Barker[7], Guillaume Bastille-Rousseau[8], Dominik M. Behr[9,10], Jerrold L. Belant[11], Dean E. Beyer Jr.[11], Niels Blaum[12], J. David Blount[13], Dirk Bockmühl[14], Ricardo Luiz Pires Boulhosa[15], Michael B. Brown[16,17], Bayarbaatar Buuveibaatar[18], Francesca Cagnacci[19], Justin M. Calabrese[20,21], Rok Černe[22], Simon Chamaillé-Jammes[23,24], Aung Nyein Chan[25,17], Michael J. Chase[2], Yannick Chaval[26,27], Yvette Chenaux-Ibrahim[28], Seth G. Cherry[29], Duško Ćirović[30], Emrah Çoban[31], Eric K. Cole[32], Laura Conlee[33], Alyson Courtemanch[34], Gabriele Cozzi[9,10], Sarah C. Davidson[35,36,37], Darren DeBloois[38], Nandintsetseg Dejid[39], Vickie DeNicola[40], Arnaud L. J. Desbiez[3,41,42], Iain Douglas-Hamilton[43,44], David Drake[45], Michael Egan[8,27], Jasper A.J. Eikelboom[46], William F. Fagan[21], Morgan J. Farmer[47], Julian Fennessy[16], Shannon P. Finnegan[48], Christen H. Fleming[21,49], Bonnie Fournier[50], Nicholas L. Fowler[48,51], Mariela G. Gantchoff[52,53], Alexandre Garnier[26,54], Benedikt Gehr[55], Chris Geremia[56], Jacob R. Goheen[57], Morgan L. Hauptfleisch[58], Mark Hebblewhite[59], Morten Heim[60], Anne G. Hertel[61], Marco Heurich[62,63,64], A. J. Mark Hewison[26,27], James Hodson[65], Nicholas Hoffman[66], J. Grant C. Hopcraft[67], Djuro Huber[68], Edmund J. Isaac[28], Karolina Janik[69], Miloš Ježek[70], Örjan Johansson[71,72], Neil R. Jordan[73,74,10], Petra Kaczensky[75,76], Douglas N. Kamaru[57,77], Matthew J. Kauffman[78], Todd M. Kautz[48], Roland Kays[79,80], Allicia P. Kelly[81], Jonas Kindberg[82,83], Miha Krofel[84,85], Josip Kusak[68], Clayton T. Lamb[86], Tayler N. LaSharr[87], Peter Leimgruber[17], Horst Leitner[88], Michael Lierz[89], John D.C. Linnell[60,90], Purevjav Lkhagvaja[91], Ryan A. Long[92], José Vicente López-Bao[93], Matthias-Claudio Loretto[35,94,95], Pascal Marchand[96], Hans Martin[59], Lindsay A. Martinez[97], Roy T. McBride Jr.[98], Ashley A.D. McLaren[99,100], Erling Meisingset[101], Joerg Melzheimer[14], Evelyn H. Merrill[102], Arthur D. Middleton[7], Kevin L. Monteith[87], Seth A. Moore[28], Bram Van Moorter[60], Nicolas Morellet[26,27], Thomas Morrison[67], Rebekka Müller[14], Atle Mysterud[103], Michael J Noonan[104], David O'Connor[105,106,107], Daniel Olson[38], Kirk A. Olson[108], Anna C. Ortega[109,110], Federico Ossi[19], Manuela Panzacchi[60], Robert Patchett[111], Brent R. Patterson[112,113], Rogerio Cunha de Paula[114], John Payne[115], Wibke Peters[116], Tyler R. Petroelje[48], Benjamin J. Pitcher[74,117], Boštjan Pokorny[118,119,120], Kim Poole[121], Hubert Potočnik[122], Marie-Pier Poulin[123], Robert M. Pringle[124], Herbert H.T. Prins[125], Nathan Ranc[19,126,26], Slaven Reljić[68,127], Benjamin Robb[109], Ralf Röder[14], Christer M. Rolandsen[60], Christian Rutz[111], Albert R. Salemgareyev[128], Gustaf Samelius[72,129], Heather Sayine-Crawford[65], Sarah Schooler[48], Çağan H. Şekercioğlu[13,130,31], Nuria Selva[131,132], Paola Semenzato[133,19], Agnieszka Sergiel[131], Koustubh Sharma[134,135,136,137], Avery L. Shawler[7], Johannes Signer[138], Václav Silovský[70], João Paulo Silva[139,140], Richard Simon[141], Rachel A. Smiley[87], Douglas W. Smith[56], Erling J. Solberg[60], Diego Ellis-Soto[142,143,144], Orr Spiegel[145], Jared Stabach[17], Jenna Stacy-Dawes[146], Daniel R. Stahler[56], John Stephenson[147], Cheyenne Stewart[148], Olav Strand[60], Peter Sunde[149], Nathan J. Svoboda[150], Jonathan Swart[151], Jeffrey J. Thompson[152,153], Katrina L. Toal[141], Kenneth Uiseb[154], Meredith C. VanAcker[155,17], Marianela Velilla[152,153,156], Tana L. Verzuh[87], Bettina Wachter[14], Brittany L. Wagler[87], Jesse Whittington[157], Martin Wikelski[35,158], Christopher C. Wilmers[159], George Wittemyer[160,43], Julie K. Young[161,162], Filip Zięba[163], Tomasz Zwijacz-Kozica[163], Mark A. J. Huijbregts[1], Thomas Mueller[39,164,17]

COVID-19 lockdowns in early 2020 reduced human mobility, providing an opportunity to disentangle its effects on animals from those of landscape modifications. Using GPS data, we compared movements and road avoidance of 2300 terrestrial mammals (43 species) during the lockdowns to the same period in 2019. Individual responses were variable with no change in average movements or road avoidance behavior, likely due to variable lockdown conditions. However, under strict lockdowns 10-day 95th percentile displacements increased by 73%, suggesting increased landscape permeability. Animals' 1-hour 95th percentile displacements declined by 12% and animals were 36% closer to roads in areas of high human footprint, indicating reduced avoidance during lockdowns. Overall, lockdowns rapidly altered some spatial behaviors, highlighting variable but substantial impacts of human mobility on wildlife worldwide.

In 2020, governments around the world introduced lockdown measures in an attempt to curb the spread of the novel severe acute respiratory syndrome coronavirus 2 (SARS CoV-2) virus. This resulted in a drastic reduction in human mobility including human confinement to living quarters, closure of recreation and protected areas, and reductions in the movement of vehicles and their associated by-products (e.g., noise and pollutants) (*1*). This "anthropause" provides a unique opportunity to quantify the effects of human mobility on wildlife by decoupling these from landscape modification effects (e.g., roads) (*2*, *3*). It is established that anthropogenic landscape modifications affect how animals use habitats (*4*) and interact with each other (*5*). For example, human infrastructure may induce various behavioral responses in animals, including avoidance (*6*), shifts in movement speed or habitat selection near roads (*7*), and altered diurnal patterns of habitat use (*8*). In addition to these landscape modification effects, animals can react directly to the presence and activity of humans (*9*). These often are perceived as a risk (*10*), which can lead to changes in habitat use due to the avoidance of areas heavily used by humans, increased energetic costs and physiological stress (*11*), and altered demography (e.g., reduced fecundity) (*12*). As large-scale, high-resolution human mobility data are rare, our ability to decouple the effects of landscape modification and human mobility has been limited. In particular, little is known about the overall impact of human mobility on terrestrial mammalian behavior across species and continents. Here, we make use of the quasi-experimental alteration of human mobility during COVID-19 lockdowns in early 2020 to study the effect of human mobility on animal behavior, specifically on movement and road avoidance in terrestrial mammals.

Using animal tracking data to study behavioral changes during lockdowns

We used global positioning system (GPS) tracking data to evaluate how 2300 individual terrestrial mammals, representing 43 species across 76 studies (Fig. 1 and table S1), changed their spatial behavior during the initial 2020 COVID-19 lockdowns compared with the same time period a year earlier. For the initial 2020 lockdown period we included the date of the first government-mandated lockdown in each study area (between 1 February and 28 April, 2020) until 15 May, 2020. We used matching time periods from 2019 as a baseline for comparison. Individuals were tracked for an average of 59 days per observation period (range: 10 to 72 days). We focused on two behaviors: displacement distance (straight-line distance between two consecutive GPS locations) and distance to the nearest road. As changes in displacement might be scale-dependent, we considered displacements at 1-hour and 10-day intervals based on Tucker *et al.* (*13*). Changes in 1-hour displacements reflect immediate responses to altered human mobility (*14*). We expected that reduced human mobility during strict lockdowns would lead to an overall reduction in 1-hour displacements due to fewer avoidance and escape responses, or easier access to foraging areas due to reduced disturbance as has been previously shown for red deer (*14*). For the 10-day displacements, we expected a different response because previous analyses of the effects of land-modifications on mammal movements (*13*) have shown longer displacement distances in areas with low human footprint. Accordingly, displacement distances

Affiliations are listed at the end of this Research Article.
*Corresponding author. Email: marlee.tucker@ru.nl

at the 10-day scale might be longer under lockdown conditions as animals might be able to cross barriers linked to human mobility during such periods (e.g., roads with lower traffic volumes). For each time scale, we evaluated the 50th (median) and 95th percentiles of the displacements. Median displacements represent a suite of behaviors including resting and sleeping (1-hour scale) or residency in the same area (10-day scale). The 95th percentile eliminates stationary behaviors and represents longer and more directed movements such as avoidance behaviors on the 1-hour time scale and long-distance displacements at the 10-day time scale (*13*). Because longer displacements generally have a greater probability of encountering humans or infrastructure, we expected stronger responses for the 95th-percentile displacements.

Although roads may benefit some species by providing foraging opportunities or movement corridors (*15*), their effects are more often negative as they not only create barriers but also increase mortality and facilitate human access to remote areas (*16*). We expected that declines in vehicular traffic during the early 2020 lockdowns (*17*) would reduce the perceived risk level and mammals would therefore be closer to roads.

To evaluate possible changes in displacements or distance to the nearest roads between the lockdown and baseline periods, we calculated log response ratios for each measure (medians and 95th percentiles of the 1-hour and 10-day displacements, and distance to roads) and each individual. Our analyses of the response ratios involved a two-step process following previous work (*18*). First, we used Bayesian mixed-effects models to examine the overall effect of lockdowns on movement distance and distance to the nearest road (i.e., intercept-only model) (*19*). Second, we used Bayesian mixed-effects models to examine possible relationships between the response ratios and various covariates indicative of environmental context (i.e., lockdown strictness, human footprint, and productivity) and species traits (i.e., body mass, diet, activity, and relative brain size) (*19*). For both steps of the analyses, we included random effects for species-study combined to account for nonindependence between effect sizes from the same study and/or species. For the second step of the analysis, we included the Oxford COVID-19 government response tracker stringency index (SI) (*20*) in our models to examine country-level variation in lockdown strictness, ranging from 0 (no lockdown) to 100 (very strict lockdown; e.g., confined to home). We used the human footprint index [(HFI) 1-km resolution] (*21*) as a proxy of direct and indirect human activities including roads, agriculture, and human population density. The HFI values range from 0 to 50, where low values represent areas relatively undisturbed by humans and high values represent areas with high human development levels. We expected stronger behavioral responses to lockdowns in areas with a higher human footprint and in countries with stricter lockdowns for both displacement distances and distance to roads. To account for movement capacity, differences in movements related to diet, activity cycle, and behavioral flexibility, we included body mass (range: 10 to 4000 kg), diet (carnivore, omnivore, herbivore), activity (diurnal or nocturnal), and relative brain size as additional explanatory variables. Finally, we also included the between-year difference in normalized difference vegetation index (NDVI) between 2019 and 2020 to account for potential differences in seasonality and productivity. We fit models for the median and 95th percentile of the 1-hour and 10-day displacements, and for distance to roads including all covariates for lockdown strictness, environmental context, and species traits (*19*). We report our results as the percentage increase or decrease in movement distance or distance to roads by back-transforming the response ratios (*19*) and reporting the 95% credible intervals (CI).

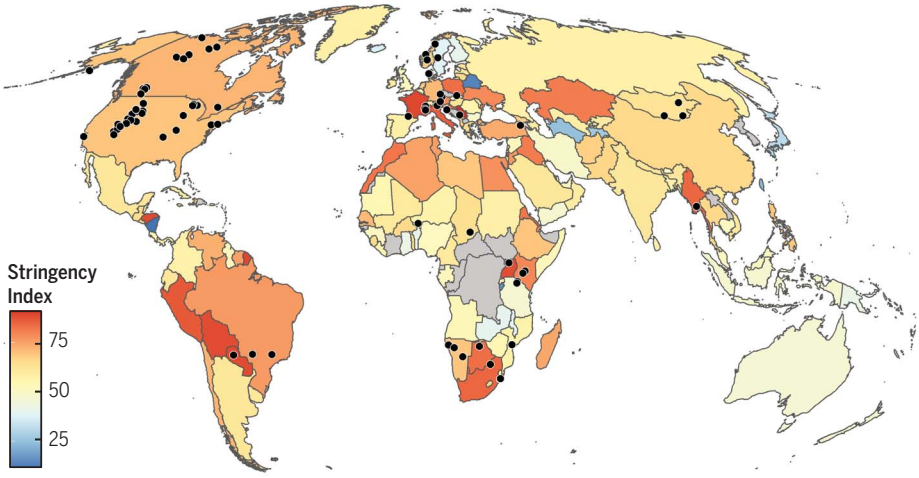


Fig. 1. Distribution of GPS data from 43 terrestrial mammal species. The map represents the mean Oxford COVID-19 government response tracker stringency index (SI) (*20*), which measures lockdown strictness, ranging from 0 (no lockdown) to 100 (very strict lockdown). Values are presented per country during the 2020 study period (i.e., initial lockdown date to 15 May, 2020), where higher values (red) represent countries with a stricter lockdown policy. Light gray represents countries with no SI data. SI values range from 10 to 92. Black points represent the centroids of each study-species combination (n = 90). Map in Mollweide projection.

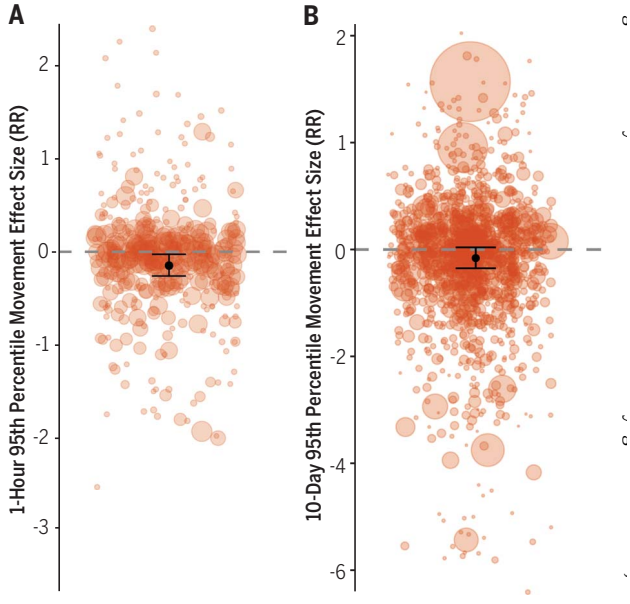


Fig. 2. Changes in 1-hour animal movement during the COVID-19 lockdowns. (**A**) Overall reduction in the 1-hour 95th-percentile displacements (intercept-only model). (**B**) Overall reduction in the 10-day 95th-percentile displacements (intercept-only model). Colored points represent individuals (n = 423 and 1725), with point sizes proportional to the inverse sampling variance of the response ratio for each individual. The black points and error bars indicate the overall effect with 95% CI. The 1-hour 95% CI do not overlap 0 (−0.25 to −0.01) but the 10-day CI did overlap 0 (−0.36 to 0.05). Negative values indicate reduced movement distances during the early 2020 lockdowns whereas positive values indicate increased movement distances during the lockdowns.

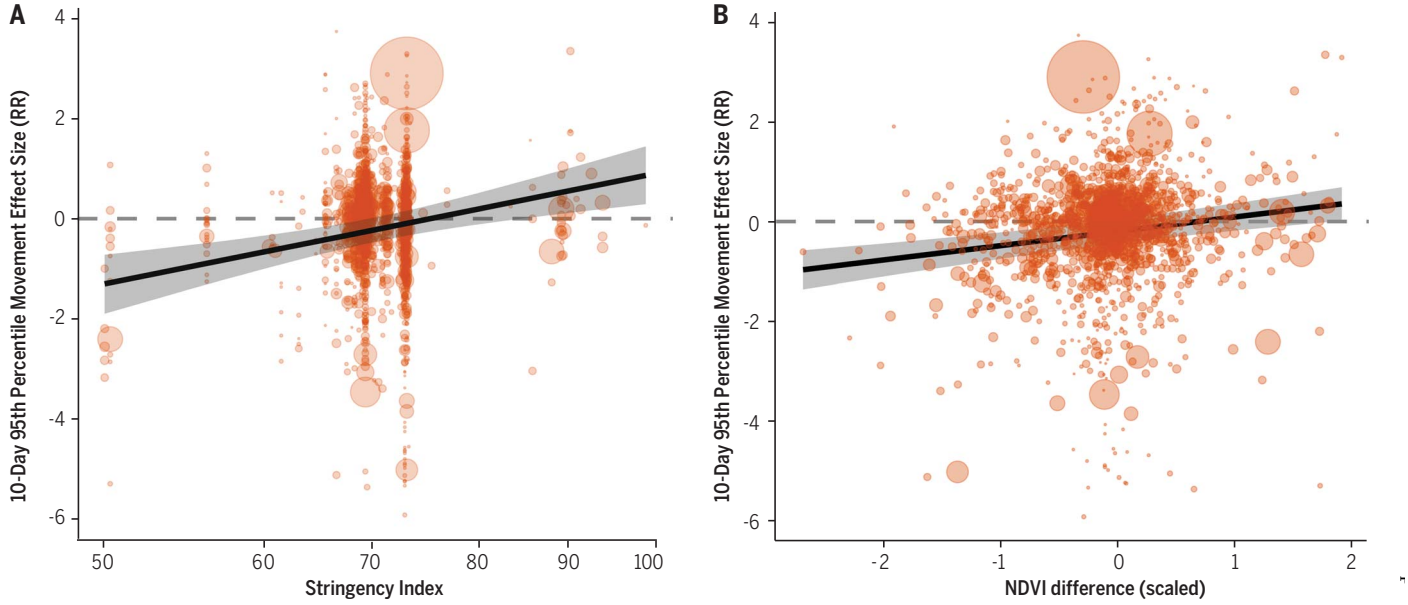


Fig. 3. Changes in 10-day animal movement during the COVID-19 lockdowns. (**A**) Increasing 10-day 95th-percentile displacements in response to the Stringency Index and (**B**) 10-day 95th-percentile displacements were longer during 2020 when we observed higher NDVI values compared with 2019. Colored points represent individuals (n = 1725), with point size proportional to the inverse sampling variance of the response ratio for each individual. The black line is the fitted effect size (response ratio; RR). The shaded area indicates 95% CI, and the dashed gray line at zero illustrates no change. Negative values indicate reduced movement distances during the early 2020 lockdowns whereas positive values indicate increased movement distances during the lockdowns.

Changes in movement displacements during lockdowns

We found an average 12% reduction in 1-hour 95th-percentile displacements when evaluating the impact of only the lockdown itself (intercept-only model, 95% CI: 1 and 22%, Fig. 2 and table S2). This may indicate reduced avoidance and escape behavior of humans (e.g., no need to travel longer distances to avoid humans) (*22*, *23*) as a result of altered human mobility levels during lockdowns. When exploring potential correlates of this response, no covariates had an effect that differed from zero (table S3). For the 1-hour median displacements, we found no overall effect (table S2) and again, no effect of the covariates (table S4). Taken together, these results suggest that responses at the 1-hour scale were highly variable and not dependent on the selected species traits (body mass, diet, activity, or relative brain size) or on the variables describing the local context (lockdown stringency or HFI).

The overall lockdown response was not different from zero for the 10-day 95th-percentile or long-distance displacements (15%, 95% CI; −30 to 5%; Fig. 2B and table S2). However, when exploring the covariates that might explain variation in response ratios the 95% CI of the stringency index did not overlap zero (table S5), with displacements increasing 73% on average in areas of stricter lockdown (i.e., areas with an SI of 90; Fig. 3A). This may indicate that tighter restrictions on human movements, including confinement to living spaces and reduced human mobility in green spaces (e.g., Italy and France; Fig. 1) led to increased landscape permeability for mammals. This effect of human mobility is similar in magnitude to previous work that used the same displacement metric but examined the effect of permanent landscape alterations (land conversion and infrastructure) on terrestrial mammal movements (*13*). Although this work used a spatial comparison rather than comparing changes over time within the same individuals, they found a decline of 67% of the 10-day 95th-percentile displacements in areas where the human footprint is high (*13*). We found no effect of the remaining covariates (HFI, body mass, diet, activity, or relative brain size) (table S5).

We found that the 10-day 95th-percentile displacements in areas with lower lockdown stringency (SI values 50 to 70) were actually shorter (on average 22 to 72%) during the lockdown than in 2019 (Fig. 3A). The reduction in movement may reflect increased human mobility in seminatural areas such as parks and other green spaces (*24*, *25*). In fact, green space use by people in some areas of intermediate lockdown increased up to 350% (*25*). In addition to the lockdown effects, seasonality played a role in determining 10-day movement distances. The 10-day median (fig. S1) and 95th percentile (Fig. 3B) displacements were longer during 2020, when we observed higher NDVI values compared with 2019, which may have led some individuals to begin their spring migration or reproduction earlier in 2020. For the 10-day median displacements, we found no overall lockdown effect (table S2), no effect of lockdown stringency, and no effects of the other covariates (HFI, body mass, diet, activity, or relative brain size) (table S6). This difference in responses between 95% and median movements suggests that lockdown stringency may have affected mainly wide-ranging behavior such as migratory movements, long-distance dispersal, exploratory excursions, or long displacements within individuals' home ranges.

Mammals were closer to roads during lockdowns

We found no overall lockdown response in the distance of individuals to roads (−1%, 95% CI; −5 to 3%, table S2) nor a relationship with the Stringency Index, NDVI difference, or species traits (table S7). However, the response ratios were negatively related to HFI, showing that animals in areas with a high human footprint were on average 36% closer to roads during lockdown (HFI = 36, Fig. 4). In many parts of the world, traffic volume was substantially reduced during lockdowns (*26*, *27*), which in turn lessened the impact of roads on animals, including reduced barrier effects (*15*, *28*) and road-kill numbers (*17*, *29*). Our findings add context to these previous results by demonstrating that not only were road-kill numbers lower during lockdown (*17*, *29*), but also animals were closer on average to roads in human-modified areas, indicating reduced avoidance.

Overall, we detected three main signals of a lockdown effect on terrestrial mammal behavior,

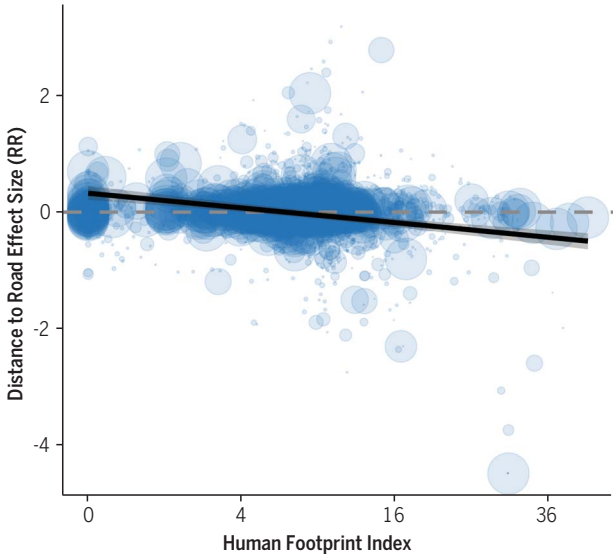


Fig. 4. Changes in animal distance to roads during the COVID-19 lockdowns. Decreasing distance to roads in response to the human footprint index (HFI). Colored points represent individuals (n = 2160), with point size proportional to the inverse sampling variance of the response ratio for each individual. The black line is the predicted effect size (response ratio; RR). The shaded area indicates 95% CI, and the dashed gray line at zero illustrates no change. Negative values indicate closer proximity to roads during the early 2020 lockdowns, whereas positive values indicate increased distance from roads during the lockdowns.

although they were heterogeneously distributed across species and populations. These were (i) reductions in 1-hour 95th-percentile displacements suggesting relaxed avoidance behavior, reduced disturbance, and/or fewer escape responses, (ii) increased 10-day 95th-percentile displacements under strict lockdown conditions, suggesting increased landscape permeability, and (iii) closer proximity to roads in areas heavily used by humans, suggesting a reduction in traffic disturbance. A number of species-specific case studies are consistent with these findings. For example, evidence suggests that during the lockdowns, mountain lions' (*Puma concolor*) usual aversion to urban edges ceased (*9*), crested porcupine (*Hystrix cristata*) abundance increased in urban areas (*30*), diurnal activity of invasive Eastern cottontails (*Sylvilagus floridanus*) increased (*30*), and brown bears (*Ursus arctos*) exploited novel connectivity corridors (*12*).

Despite these three general responses to the lockdowns considerable variation in responses existed across species and study regions (Fig. 2). This variability highlights that lockdown impacts are highly context-dependent. For example, mountain lions explored more urban areas during the lockdown whereas other species including American black bears (*Ursus americanus*), bobcats (*Lynx rufus*), and coyotes (*Canis latrans*) in the same areas did not (*31*). In addition, in our study lockdown stringency was only measured at the country level and did not account for local variability in restrictions. We also note that our data were predominantly from Europe and North America so our results should be interpreted with caution for other regions. Finally, we note that a given movement metric could capture different behaviors in different species, especially at the 10-day scale, whereas displacements could capture behaviors ranging from within home range movements to dispersal.

We show that human mobility is a key driver of some terrestrial mammal behaviors, with a magnitude potentially similar to that of landscape modifications. Therefore, when evaluating human impacts on animal behavior or designing mitigation measures both physical landscape alteration and human mobility should be taken into consideration [see also (*32*)]. Disentangling the effects of human mobility and landscape modification will allow the implementation of conservation measures specifically targeted at mitigating the impacts of human mobility, such as enticements to adjust timing, frequency, and volume of traffic in areas important for animal movement. Mammals have been living with human disturbance for a long time, but we demonstrate that many wildlife populations retain the capacity to respond to changes in human behavior, providing a positive outlook for future mitigation strategies designed to maintain animal movement and the ecosystem functions they provide.

REFERENCES AND NOTES

1. C. Rutz, *Nat. Rev. Earth Environ.* **3**, 157–159 (2022).
2. C. Rutz *et al.*, *Nat. Ecol. Evol.* **4**, 1156–1159 (2020).
3. A. E. Bates *et al.*, *Biol. Conserv.* **263**, 109175 (2021).
4. M. Ciach, Ł. Pęksa, *Curr. Zool.* **65**, 129–137 (2019).
5. C. A. DeMars, S. Boutin, *J. Anim. Ecol.* **87**, 274–284 (2018).
6. M. Howe, M. M. Okello, J. M. Davis, *Afr. Zool.* **48**, 159–166 (2015).
7. M. A. Scrafford, T. Avgar, R. Heeres, M. S. Boyce, *Behav. Ecol.* **29**, 534–542 (2018).
8. W. Neumann, G. Ericsson, H. Dettki, V. C. Radeloff, *Landsc. Urban Plan.* **114**, 9–27 (2013).
9. C. C. Wilmers, A. C. Nisi, N. Ranc, *Curr. Biol.* **31**, 3952–3955.e3 (2021).
10. K. M. Gaynor, J. S. Brown, A. D. Middleton, M. E. Power, J. S. Brashares, *Trends Ecol. Evol.* **34**, 355–368 (2019).
11. B. A. Nickel, J. P. Suraci, A. C. Nisi, C. C. Wilmers, *Proc. Natl. Acad. Sci. U.S.A.* **118**, e2004592118 (2021).
12. A. Corradini *et al.*, *Biol. Conserv.* **253**, 108818 (2021).
13. M. A. Tucker *et al.*, *Science* **359**, 466–469 (2018).
14. P. Sunde, C. R. Olesen, T. L. Madsen, L. Haugaard, *Wildl. Biol.* **15**, 454–460 (2009).
15. J. E. Hill, T. L. DeVault, J. L. Belant, *Mammal Rev.* **51**, 214–227 (2021).
16. A. W. Coffin, *J. Transp. Geogr.* **15**, 396–406 (2007).
17. M. Bíl *et al.*, *Biol. Conserv.* **256**, 109076 (2021).
18. W. Viechtbauer, *J. Stat. Softw.* **36**, 1–48 https://www.jstatsoft.org/v36/i03/ (2010).
19. See Supplementary Materials and Methods.
20. T. Hale *et al.*, *Nat. Hum. Behav.* **5**, 529–538 (2021).
21. B. A. Williams *et al.*, *One Earth* **3**, 371–382 (2020).
22. J. K. Rogala *et al.*, *Ecol. Soc.* **16**, art16 (2011).
23. C. M. Prokopenko, M. S. Boyce, T. Avgar, *J. Appl. Ecol.* **54**, 470–479 (2017).
24. H. Burnett, J. R. Olsen, N. Nicholls, R. Mitchell, *BMJ Open* **11**, e044067 (2021).
25. D. C. Geng, J. Innes, W. Wu, G. Wang, *J. For. Res.* **32**, 553–567 (2021).
26. S. S. Patra, B. R. Chilukuri, L. Vanajakshi, *Transp. Lett.* **13**, 1–9 (2021).
27. Ò. Saladié, E. Bustamante, A. Gutiérrez, *Transp. Res. Interdiscip. Perspect.* **8**, 100218 (2020).
28. G. Shannon, K. R. Crooks, G. Wittemyer, K. M. Fristrup, L. M. Angeloni, *Behav. Ecol.* **27**, 1370–1375 (2016).
29. F. Shilling *et al.*, *Biol. Conserv.* **256**, 109013 (2021).
30. R. Manenti *et al.*, *Biol. Conserv.* **249**, 108728 (2020).
31. R. Vardi, O. Berger-Tal, U. Roll, *Biol. Conserv.* **254**, 108953 (2021).
32. B. A. Nickel, J. P. Suraci, M. L. Allen, C. C. Wilmers, *Biol. Conserv.* **241**, 108383 (2020).
33. M. A. Tucker *et al.*, Supplementary data for Behavioral responses of terrestrial mammals to COVID-19 lockdowns. Dryad (2023); https://doi.org/10.5061/dryad.c59zw3rbd.
34. M. A. Tucker *et al.*, Supplementary code for Behavioral responses of terrestrial mammals to COVID-19 lockdowns. Zenodo (2023); https://doi.org/10.5281/zenodo.6915169.
35. M. A. Tucker *et al.*, Supplementary spatial data for Behavioral responses of terrestrial mammals to COVID-19 lockdowns. Zenodo (2023).

ACKNOWLEDGMENTS

We thank numerous people helping with fieldwork including the Ktunaxa Nation for their support of the Elk Valley grizzly bear collaring project, NP Tara (brown bear research), Tanzania Wildlife Research Institute and Tanzania National Parks, the leadership of Gorongosa National Park for allowing and facilitating research on spiral-horned antelope, the farmers of the Seeis, Hochfeld, and Auas Oanob Conservancies for collaboration and the Namibian Ministry of Environment, Forestry, and Tourism. We also thank all in Madison, WI, USA, who support the UW Urban Canid Project. Collaring of khulan in Mongolia's South Gobi Region was conducted within the framework of the Oyu Tolgoi LLC (OT) Core Biodiversity Monitoring Program, implemented by the Wildlife Conservation Society (WCS) through a cooperative agreement with Sustainability East Asia LLC (SEA). We thank the field team from Tatra National Park (Poland). We want to thank the Mongolian Ministry of Nature, Environment, and Tourism and staff from WCS, OT, SEA, and protected areas for the logistical and practical support during khulan capture. A.K., J.H., B.F., and H.S.C. wish to thank the Indigenous governments and organizations across the Northwest Territories' boreal and barren-ground caribou ranges for their support of caribou monitoring programs. We wish to thank G. Mowat and L. Smit for their support on the Elk Valley grizzly bear collaring project. We thank Save the Elephants and the Welgevonden Game Reserve for their elephant tracking data. We thank the Eastern Shoshone and Northern Arapahoe Fish and Game Department and the Wyoming State Veterinary Laboratory for assistance with the Wyoming bighorn sheep project. The Afognak and Sitkalidak islands elk and bear project was implemented through a cooperative effort of the Alaska Department of Fish and Game, Kodiak Brown Bear Trust, Rocky Mountain Elk Foundation, Koniag Native Corporation, Old Harbor Native Corporation, Afognak Native Corporation, Ouzinkie Native Corporation, Natives of Kodiak Native Corporation and the State University of New York, College of Environmental Science and Forestry. We also thank four anonymous reviewers for comments on the manuscript.
Funding: Supported by the Radboud Excellence Initiative (to M.T.), the German Federal Ministry of Education and Research [MORESTEP, 01LC1710A and 01LC1820A (to T.M. and N.D.)], the National Science Foundation [IIBR 1915347 (to J.M.C., C.H.F., and W.F.F.)], Serbian Ministry of Education, Science and Technological Development [451-03-68/2022-14/ 200178 (to D.C.)], Dutch Research Council NWO program "Advanced Instrumentation for Wildlife Protection" (to H.H.T.P. and J.A.J.E.), Fondation Segré, RZSS, IPE, Greensboro Science Center, Houston Zoo, Jacksonville Zoo and Gardens, Nashville Zoo, Naples Zoo, Reid Park Zoo, Miller Park, WWF, ZCOG, Zoo Miami, Zoo Miami Foundation, Beauval Nature, Greenville Zoo, Riverbanks zoo and

garden, SAC Zoo, La Passarelle Conservation, Parc Animalier d'Auvergne, Disney Conservation Fund, Fresno Chaffee zoo, Play for nature, North Florida Wildlife Center, Abilene Zoo, a Liber Ero Fellowship (to C.T.L.), the Fish and Wildlife Compensation Program, Habitat Conservation Trust Foundation, Teck Coal (to K.P.), and the Grand Teton Association. The collection of Norwegian moose data was funded by the Norwegian Environment Agency, the German Ministry of Education and Research via the SPACES II project ORYCS [FKZ:01LL1804A (to N.B.)], the Wyoming Game and Fish Department, Wyoming Game and Fish Commission, Bureau of Land Management, Muley Fanatic Foundation (including Southwest, Kemmerer, Upper Green, and Blue Ridge Chapters), Boone and Crockett Club, Wyoming Wildlife and Natural Resources Trust, Knobloch Family Foundation, Wyoming Animal Damage Management Board, Wyoming Governor's Big Game License Coalition, Bowhunters of Wyoming, Wyoming Outfitters and Guides Association, Pope and Young Club, US Forest Service, US Fish and Wildlife Service, the Rocky Mountain Elk Foundation, Wyoming Wild Sheep Foundation, Wild Sheep Foundation, Wyoming Wildlife/Livestock Disease Research Partnership, the US National Science Foundation [IOS-1656642 and IOS-1656527 (to R.A.L. and R.M.P.)], the Spanish Ministry of Economy, Industry and Competitiveness [RYC-2015-18932; CGL2017-87528-R AEI/FEDER EU (to J.V.L.B.)], and by a GRUPIN research grant from the Regional Government of Asturias [IDI/2021/000075 (to J.V.L.B.)], Sigrid Rausing Trust, Batubay Özkan, Barbara Watkins, NSERC Discovery Grant [RGPIN-2021-02758 (to M.J.N.)], the Federal Aid in Wildlife Restoration act under Pittman-Robertson project [AKW-12 (to N.J.S.)], the State University of New York, College of Environmental Science and Forestry, the Ministry of Education, Youth and Sport of the Czech Republic [CZ.02.1.01/0.0/0.0/16_019/0000803; CZ.02.2.69/0.0/0.0/19_073/0016944 (to M.J., M.S.P., and V.S.)], the Ministry of Agriculture of the Czech Republic [QK1910462 (to M.J., M.S.P., and V.S.)], Rufford Foundation [grant 29681-1(to D.N.K.)], an American Society of Mammalogists African Graduate Student Research Fund (to D.N.K.), the German Science Foundation [HE 8857/1-1 (to A.G.H.)], the Israeli Science Foundation [grant 396/20 (to O.S.)], the BSF-NSF [2019822 and IOS2015662 (to O.S.)], the Ministry of Agriculture, Forestry and Food and Slovenian Research Agency (CRP V1-1626), the Aage V. Jensen Naturfond (project: Kronvildt - viden, værdier og værktøjer), the Deutsche Forschungsgemeinschaft (DFG, German Research Foundation) under Germany's Excellence Strategy [EXC 2117 – 422037984 (to M.W.)], National Centre for Research and Development in Poland POLNOR/198352/85/2013 (project GLOBE), the Slovenian Research Agency [P4-0059 and N1-0163 (to M.K.)], the David Shepherd Wildlife Foundation, Disney Conservation Fund, Whitley Fund for Nature, Acton Family Giving, Zoo Basel, Columbus, Bioparc de Doué-la-Fontaine, Zoo Dresden, Zoo Idaho, Kolmården Zoo, Korkeasaari Zoo, La Passarelle, Zoo New England, Tierpark Berlin, Tulsa Zoo, the Ministry of Environment and Tourism, Government of Mongolia, the Mongolian Academy of Sciences, the Federal Aid in Wildlife Restoration act and the Illinois Department of Natural Resources, the National Science Foundation [LTREB 1556248 and 2038704 9 (to M.H., E.H.M., and H.M.)], Parks Canada, Natural Sciences and Engineering Research Council, Alberta Environment and Parks, Rocky Mountain Elk Foundation, Safari Club International and Alberta Conservation Association, the Consejo Nacional de Ciencias y Tecnología (CONACYT) of Paraguay [14-INV-208 and PRONII], the Norwegian Environment Agency and the Swedish Environmental Protection Agency, EU funded Interreg SI-HR 410 Carnivora Dinarica project, Paklenica and Plitvice Lakes National Parks, UK Wolf Conservation Trust, EURONATUR and Bernd Thies Foundation, the Messerli Foundation in Switzerland and WWF Germany, the European Union's Horizon 2020 research and innovation program under the Marie Skłodowska-Curie Actions [grant agreement 798091 (to M.-C.L.)], NASA Ecological Forecasting Program [80NSSC21K1182], the Ecotone Telemetry company (to S.C.-J.), the French National Research Agency (to S.C.-J.), LANDTHIRST [ANR-16-CE02-0001-01 (to S.C.-J.)], grant REPOS awarded by the i-Site MUSE thanks to the "Investissements d'avenir" program [ANR-16-IDEX-0006 (to S.C.-J.)], the ANR Mov-It project [ANR-16-CE02-0010 (to A.J.M.H. and N.M.)], the USDA Hatch Act Formula Funding (MSN201473), the Fondation Segre and North American and European Zoos listed at http://www.giantanteater.org/, the Utah Division of Wildlife Resources (to D.O., T.A., and J.K.Y.), the Yellowstone Forever and the National Park Service (to D.R.S, D.W.S., and C.G.), Missouri Department of Conservation, Federal Aid in Wildlife Restoration Grant PROJECT MO W103-R1, and State University of New York, SNSF [31003A_182286 and 310030_204478 (to G.C.)], various donors to the Botswana Predator Conservation Program (to G.C.), data from collared caribou in the Northwest Territories (to A.P.K., J.H., B.F., and H.S.C.) were made available through funds from the Department of Environment and Natural Resources, Government of the Northwest Territories. The European Research Council Horizon2020 [AfricanBioServices 641918], the British Ecological Society, the Paul Jones Family Trust, and the Lord Kelvin Adam Smith fund, the Tanzania Wildlife Research Institute and Tanzania National Parks (to J.G.C.H. and T.M.). The Eastern Shoshone and Northern Arapahoe Fish and Game Department and the Wyoming State Veterinary Laboratory, the Alaska Department of Fish and Game, Kodiak Brown Bear Trust, Rocky Mountain Elk Foundation, Koniag Native Corporation, Old Harbor Native Corporation, Afognak Native Corporation, Ouzinkie Native Corporation, Natives of Kodiak Native Corporation and the State University of New York, College of Environmental Science and Forestry, and the Slovenia Hunters Association and Slovenia Forest Service. F.C. was partly supported by the Resident Visiting Researcher Fellowship, IMéRA/Aix-Marseille Université, Marseille. This work was partially funded by the Center of Advanced Systems Understanding (CASUS), which is financed by Germany's Federal Ministry of Education and Research (BMBF) and by the Saxon Ministry for Science, Culture and Tourism (SMWK) with tax funds on the basis of the budget approved by the Saxon State Parliament. This article is a contribution of the COVID-19 Bio-Logging Initiative, which is funded in part by the Gordon and Betty Moore Foundation (GBMF9881) and the National Geographic Society (NGS-82515R-20) (both grants to C.R.). **Author contributions:** M.A.T. and T.M. conceived the manuscript; M.A.T. conducted the analyses and M.A.T. and T.M. wrote the first manuscript draft. Co-authors contributed data and assisted with writing the final version of the manuscript. **Competing Interests:** H.H.T.P. is a Member of the Welgevonden Scientific Advisory Committee and A.D.M. is a Senior Advisor for Wildlife Conservation for the US Department of Agriculture. C.R. is the President of the International Bio-Logging Society, a member of an expert group providing advice on animal culture and social complexity to the Convention on the Conservation of Migratory Species of Wild Animals (CMS), and member of the advisory committee of a WILDLABS research program aimed at identifying research and funding priorities in movement ecology. **Data and materials availability:** The full dataset used in the final analyses (*33*) and associated code (*34*) are available at Dryad. A subset of the spatial coordinate datasets is available at Zenodo (*35*). Certain datasets of spatial coordinates will be available only through requests made to the authors due to conservation and Indigenous sovereignty concerns (see table S1 for more information on data use restrictions and contact information for data requests). These sensitive data will be made available upon request to qualified researchers for research purposes, provided that the data use will not threaten the study populations, such as by distribution or publication of the coordinates or detailed maps. Some datasets, such as those overseen by government agencies, have additional legal restrictions on data sharing, and researchers may need to formally apply for data access. Collaborations with data holders are generally encouraged, and in cases where data are held by Indigenous groups or institutions from regions that are under-represented in the global science community, collaboration may be required to ensure inclusion. **License information:** Copyright © 2023 the authors, some rights reserved; exclusive licensee American Association for the Advancement of Science. No claim to original US government works. https://www.sciencemag.org/about/science-licenses-journal-article-reuse

[1]Department of Environmental Science, Radboud Institute for Biological and Environmental Sciences, Radboud University, P.O. Box 9010, 6500, GL Nijmegen, Netherlands. [2]Elephants Without Borders, P.O. Box 682, Kasane, Botswana. [3]Instituto de Conservação de Animais Silvestres (ICAS), Campo Grande, Mato Grosso do Sul, Brazil. [4]Department of Wildlife Ecology and Conservation, University of Florida, Gainesville, FL, USA. [5]Department of Wildland Resources and the Ecology Center, Utah State University, Logan, UT 84322, USA. [6]School of Biological Sciences, Monash University, Clayton, Victoria 3800, Australia. [7]Department of Environmental Science, Policy, and Management, University of California, Berkeley, Berkeley, CA 94720, USA. [8]Cooperative Wildlife Research Laboratory, Southern Illinois University, Carbondale, IL, 62901, USA. [9]Department of Evolutionary Biology and Environmental Studies, University of Zurich, Winterthurerstrasse 190, CH - 8057 Zürich, Switzerland. [10]Botswana Predator Conservation, Private Bag 13, Maun, Botswana. [11]Department of Fisheries and Wildlife, Michigan State University, 480 Wilson Road, East Lansing, MI 48824, USA. [12]University of Potsdam, Plant Ecology and Nature Conservation, Am Mühlenberg 3, 14476 Potsdam, Germany. [13]School of Biological Sciences, University of Utah, 257 S 1400 E, Salt Lake City, UT 84112, USA. [14]Department of Evolutionary Ecology, Leibniz Institute for Zoo and Wildlife Research, Alfred-Kowalke-Str. 17, 10315 Berlin, Germany. [15]Instituto Pró-Carnívoros, Atibaia, SP, 12945010 Brazil. [16]Giraffe Conservation Foundation, Eros, PO Box 86099, Windhoek, Namibia. [17]Smithsonian National Zoo and Conservation Biology Institute, Conservation Ecology Center, 1500 Remount Rd, Front Royal, VA, 22630, USA. [18]Wildlife Conservation Society, Mongolia Program, Ulaanbaatar, Mongolia. [19]Animal Ecology Unit, Research and Innovation Centre, Fondazione Edmund Mach, Via E. Mach 1, 38010 San Michele all'Adige, Italy. [20]Center for Advanced Systems Understanding (CASUS), Goerlitz, Germany. [21]Department of Biology, University of Maryland, College Park, 4094 Campus Dr, College Park, MA, USA. [22]Slovenia Forest service, Večna pot 2, 1000 Ljubljana, Slovenia. [23]CEFE, CNRS, Univ Montpellier, EPHE, IRD, Montpellier, France. [24]Mammal Research Institute, Department of Zoology and Entomology, University of Pretoria, South Africa. [25]Dept. Fish, Wildlife and Conservation Biology, Colorado State University, Fort Collins, CO 80525, USA. [26]Université de Toulouse, INRAE, CEFS, F-31326 Castanet-Tolosan, France. [27]LTSER ZA PYRénées GARonne, F-31320 Auzeville-Tolosane, France. [28]Department of Biology and Environment, Grand Portage Band of Lake Superior Chippewa, Grand Portage, MN 55605, USA. [29]Parks Canada Agency, Box 220, Radium Hot Springs, BC, V0A 1M0, Canada. [30]Faculty of Biology, University of Belgrade, Studentski trg 16, 11000 Belgrade, Serbia. [31]KuzeyDoğa Society, Ortakapı Mah. Şehit Yusuf Cad. 69, 36100 Kars, Turkey. [32]U.S. Fish and Wildlfe Service, National Elk Refuge, PO Box 510, Jackson, WY 83001, USA. [33]Missouri Department of Conservation, Columbia, MO, 65201, USA. [34]Wyoming Game and Fish Department, Jackson, WY 83001, USA. [35]Department of Migration, Max Planck Institute of Animal Behavior, 78315 Radolfzell, Germany. [36]Department of Biology, University of Konstanz, 78464 Konstanz, Germany. [37]Department of Civil, Environmental and Geodetic Engineering, The Ohio State University, 43210 Columbus, OH, USA. [38]Utah Division of Wildlife Resources. [39]Senckenberg Biodiversity and Climate Research Centre, Senckenberganlage 25, 60325 Frankfurt am Main, Germany. [40]White Buffalo Inc., 26 Davison Road, Moodus, CT 06469, USA. [41]Royal Zoological Society of Scotland (RZSS), Murrayfield, Edinburgh, UK. [42]Instituto de Pesquisas Ecológicas (IPÊ), Nazaré Paulista, São Paulo, Brazil. [43]Save the Elephants, Marula Manor, Marula Lane, Karen, Nairobi 00200, Kenya. [44]Department of Zoology, Oxford University, Oxford OX1 3PS, UK. [45]Department of Forest and Wildlife Ecology, University of Wisconsin-Madison, Madison, WI 53706, USA. [46]Wildlife Ecology and Conservation Group, Wageningen University and Research, Droevendaalsesteeg 3a, 6708 PB, Wageningen, Netherlands. [47]Department of Forest and Wildlife Ecology, University of Wisconsin, 1630 Linden Drive, Madison, WI 53706, USA. [48]Global Wildlife Conservation Center, State University of New York College of Environmental Science and Forestry, 1 Forestry Drive, Syracuse, NY 13210, USA. [49]Smithsonian Conservation Biology Institute, 1500 Remount Rd, Front Royal, VA, USA. [50]Wildlife and Fish Division, Department of Environment and Natural Resources, Government of the Northwest Territories, P.O. Box 1320, Yellowknife, NT, Canada. [51]Alaska Department of Fish and Game, 43961 Kalifornsky Beach Road, Suite B, Soldotna, AK 99669, USA. [52]State University of New York College of Environmental Science and Forestry, Syracuse, NY 13210, USA. [53]Department of Biology, College of Arts and Sciences, University of Dayton, Dayton, OH 45469, USA. [54]Parc National des Pyrénées, 65000 Tarbes, France. [55]Department of Evolutionary Biology and Environmental Studies, University of Zurich, Winterthurerstrasse 190, 8057 Zurich, Switzerland. [56]Yellowstone Center for Resources, P.O. Box 168, Yellowstone National Park, WY 82190, USA. [57]Department of Zoology and Physiology, University of Wyoming, Laramie, WY 82071, USA. [58]Biodiversity Research Centre, Namibia University of Science and Technnology Pvt bag 13388 Windhoek, Namibia. [59]Wildlife Biology Program, Franke College of Forestry and Conservation, University of Montana, Missoula, MT, 59801, USA. [60]Norwegian Institute for Nature Research, Terrestrial Ecology Department, P.O. Box 5685 Torgarden, 7485 Trondheim, Norway. [61]Behavioural Ecology, Department of Biology, Ludwig Maximilian University of Munich, Großhaderner Str. 2, 82152 Planegg-Martinsried, Germany. [62]Department of Visitor Management and National Park Monitoring, Bavarian Forest National Park, Freyunger Straße 2, 94481 Grafenau, Germany. [63]Chair of Wildlife Ecology and Conservation Biology, Faculty of Environment and Natural Resources, University of Freiburg, Tennenbacher Straße 4, 79106 Freiburg, Germany. [64]Institute for forest and wildlife management, Faculty of Applied Ecology, Agricultural Sciences and Biotechnology, Campus Evenstad, Inland Norway University of Applied Science, NO-2480 Koppang, Norway. [65]Wildlife and Fish Division, Department of Environment and Natural Resources, Government of the Northwest Territories, P.O. Box 1320, Yellowknife, NT X1A 2L9, Canada. [66]Ecological Program,

Pennsylvania Department of Military and Veterans Affairs, Fort Indiantown Gap National Guard Training Center, Annville, PA 17003, USA. [67]Institute of Biodiversity, Animal Health and Comparative Medicine, University of Glasgow, Glasgow G12 8QQ, UK. [68]Veterinary Biology Department, Faculty of Veterinary Medicine, University of Zagreb, Heinzelova 55, HR-10000 Zagreb, Croatia. [69]City of New York Parks and Recreation, Wildlife Unit, 1234 5th Avenue, 5th Floor, NY 10029, USA. [70]Faculty of Forestry and Wood Sciences, Czech University of Life Sciences Prague, Czech Republic. [71]Grimsö Wildlife Research Station, Swedish University of Agricultural Sciences, 739 93 Riddarhyttan, Sweden. [72]Snow Leopard Trust, 4649 Sunnyside Avenue North, Seattle, WA 98103, USA. [73]Centre for Ecosystem Science, School of Biological, Earth and Environmental Sciences, University of New South Wales, Sydney, NSW, 2052, Australia. [74]Taronga Institute of Science and Learning, Taronga Conservation Society, Sydney, NSW, 2088, Australia. [75]Inland Norway University of Applied Sciences, Department of Forestry and Wildlife Management, Norway. [76]University of Veterinary Medicine Vienna, Research Institute of Wildlife Ecology, Austria. [77]Wildlife Department, Ol Pejeta Conservancy, Private Bag-10400, Nanyuki, Kenya. [78]U.S. Geological Survey, Wyoming Cooperative Fish and Wildlife Research Unit, Department of Zoology and Physiology, University of Wyoming, Laramie, WY 82071, USA. [79]North Carolina Museum of Natural Sciences, Raleigh, NC 27601, USA. [80]Department of Forestry and Environmental Resources, North Carolina State University, Raleigh, NC, 27695, USA. [81]Department of Environment and Natural Resources, Government of the Northwest Territories, P.O. Box 2668, Yellowknife, NT X1A 2P9, Canada. [82]Norwegian Institute for Nature Research, NO-7484 Trondheim, Norway. [83]Department of Wildlife, Fish and Environmental studies, Swedish University of Agricultural Sciences, SE- 901 83 Umeå, Sweden. [84]Department of Forestry, Biotechnical Faculty, University of Ljubljana, Jamnikarjeva 101, SI-1000 Ljubljana, Slovenia. [85]Department of Evolutionary Ecology, Leibniz Institute for Zoo and Wildlife Research, Alfred- Kowalke- Str. 17, 10315 Berlin, Germany. [86]Biological Sciences Centre, University of Alberta, Edmonton, Alberta T6G 2E9, Canada. [87]Haub School of Environment and Natural Resources, Wyoming Cooperative Fish and Wildlife Research Unit, Department of Zoology and Physiology, University of Wyoming, 804 East Fremont, Laramie, WY 82072, USA. [88]Büro für Wildökologie und Forstwirtschaft, Klagenfurth, Austria. [89]Clinic for birds, reptiles, amphibians and fish, Justus-Liebig-University Giessen, Germany. [90]Inland Norway University of Applied Sciences, Department of Forestry and Wildlife Management, Anne Evenstads vei 80, 2480 Koppang, Norway. [91]Snow Leopard Conservation Foundation, Ulaanbaatar, Mongolia. [92]Department of Fish and Wildlife Sciences, University of Idaho, Moscow, ID 83844, USA. [93]Biodiversity Research Institute (CSIC - Oviedo University - Principality of Asturias), Oviedo University, E-33600 Mieres, Spain. [94]Technical University of Munich, TUM School of Life Sciences, Ecosystem Dynamics and Forest Management Group, 85354 Freising, Germany. [95]Berchtesgaden National Park, 83471 Berchtesgaden, Germany. [96]Office Français de la Biodiversité, Direction de la Recherche et de l'Expertise, Unité Ongulés Sauvages, Juvignac, France. [97]Wyoming Cooperative Fish and Wildlife Research Unit, Department of Zoology and Physiology, University of Wyoming, Laramie, WY 82071, USA. [98]Faro Moro Eco Research, Estancia Faro Moro, Departmento de Boquerón, Paraguay. [99]Ontario Ministry of Natural Resources and Forestry, Wildlife Research and Monitoring Section, Trent University, 2140 East Bank Drive, Peterborough, Ontario, K9J 7B8, Canada. [100]Department of Environment and Natural Resources, Government of the Northwest Territories, Highway 5, PO Box 900, Fort Smith, Northwest Territories, X0E 0P0, Canada. [101]Department of Forestry and Forestry resources, Norwegian Institute of Bioeconomy Research, Tingvoll gard, NO-6630 Tingvoll, Norway. [102]Department of Biological Sciences, University of Alberta, Edmonton, Alberta T6G 2E9, Canada. [103]Centre for Ecological and Evolutionary Synthesis (CEES), Department of Biosciences, University of Oslo, P.O. Box 1066 Blindern, NO-0316 Oslo, Norway. [104]Department of Biology, University of British Columbia Okanagan, Kelowna, British Columbia, Canada. [105]Save Giraffe Now, 8333 Douglas Avenue, Suite 300, Dallas, Texas 75225, USA. [106]The Faculty of Biological Sciences, Goethe University, Max-von-Laue-Str. 9, 60438 Frankfurt am Main, Germany. [107]National Geographic Partners, 1145 17th Street NW, Washington, DC 20036, USA. [108]Wildlife Conservation Society, Mongolia Program. Post 20A, Box 21, Ulaanbaatar 14200, Mongolia. [109]Wyoming Cooperative Fish and Wildlife Research Unit, Department of Zoology and Physiology, University of Wyoming, Laramie, WY 82071, USA. [110]Program in Ecology, University of Wyoming, Laramie, WY 82071, USA. [111]Centre for Biological Diversity, School of Biology, University of St. Andrews, Sir Harold Mitchell Building, St. Andrews, KY16 9TH, UK. [112]Department of Environmental and Life Sciences, Trent University, 2140 East Bank Drive, Peterborough, Ontario K9J 7B8, Canada. [113]Ontario Ministry of Natural Resources and Forestry, Wildlife Research and Monitoring Section, Trent University, 2140 East Bank Drive, Peterborough, Ontario K9J 7B8, Canada. [114]Centro Nacional de Pesquisa e Conservação de Mamíferos Carnívoros, Instituto Chico Mendes de Conservação da Biodiversidade, Atibaia, SP, 12952011 Brazil. [115]Research Institute of Wildlife Ecology, University of Veterinary Medicine, Vienna, Austria. [116]Department of Biodiversity, Conservation and Wildlife Management, Bavarian State Institute for Forestry, Hans-Carl-von Carlowitz Platz 1, 85354 Freising, Germany. [117]School of Natural Sciences, Faculty of Science and Engineering, Macquarie University, NSW, 2109, Australia. [118]Faculty of Environmental Protection, Trg mladosti 7, 3320 Velenje, Slovenia. [119]Slovenian Forestry Institute, Večna pot 2, 1000 Ljubljana, Slovenia. [120]Department of Biodiversity, Faculty of Mathematics, Natural Sciences and Information Technologies, University of Primorska, Glagoljaška 8, 6000 Koper, Slovenia. [121]Aurora Wildlife Research, 1918 Shannon Point Rd., Nelson, BC, V1L 6K1, Canada. [122]Department of Biology, Biotechnical Faculty, University of Ljubljana, Jamnikarjeva 101, 1000 Ljubljana, Slovenia. [123]Department of Zoology and Physiology, University of Wyoming, Laramie, WY 82071, USA. [124]Department of Ecology and Evolutionary Biology, Princeton University, Princeton, NJ 08544, USA. [125]Department of Animal Sciences, Wageningen University and Research, De Elst 1, 6708 WD, Wageningen, Netherlands. [126]Department of Organismic and Evolutionary Biology, Harvard University, 26 Oxford Street, Cambridge MA 02138, USA. [127]Oikon Ltd, Institute of Applied Ecology, Trg Senjskih uskoka 1-2, HR-10020 Zagreb, Croatia. [128]Association for the Conservation of Biodiversity of Kazakhstan (ACBK), Nur-Sultan, 010000, Kazakhstan. [129]Nordens Ark, 456 93 Hunnebostrand, Sweden. [130]Koç University Department of Molecular Biology and Genetics, Faculty of Sciences, Rumelifeneri, Istanbul, Sarıyer, Turkey. [131]Institute of Nature Conservation Polish Academy of Sciences, Adama Mickiewicza 33, 31-120 Kraków, Poland. [132]Departamento de Ciencias Integradas, Facultad de Ciencias Experimentales, Centro de Estudios Avanzados en Física, Matemáticas y Computación, Universidad de Huelva, 21071 Huelva, Spain. [133]Dimension Research, Ecology and Environment (D.R.E.Am. Italia), Via Garibaldi, 3, 52015 Pratovecchio Stia (AR), Italy. [134]Snow Leopard Trust, Seattle, WA 98103, USA. [135]Global Snow Leopard and Ecosystem Protection Program, Bishkek, Kyrgyzstan. [136]Snow Leopard Foundation, Kyrgyzstan Bishkek, Kyrgyzstan. [137]Nature Conservation Foundation, Mysore 570002, India. [138]Wildlife Sciences, Faculty of Forest Sciences and Forest Ecology, University of Goettingen, Göttingen, Germany. [139]CIBIO, Centro de Investigação em Biodiversidade e Recursos Genéticos, InBIO Laboratório Associado, Campus de Vairão, Universidade do Porto, 4485-661 Vairão, Portugal. [140]BIOPOLIS Program in Genomics, Biodiversity and Land Planning, CIBIO, Campus de Vairão, 4485-661 Vairão, Portugal. [141]City of New York Parks and Recreation, Wildlife Unit, 1234 5th Avenue, 5th Floor, NY, NY 10029, USA. [142]Department of Ecology and Evolutionary Biology, Yale University, New Haven, CT, USA. [143]Center for Biodiversity and Global Change, Yale University, New Haven, CT, USA. [144]Max Planck - Yale Center for Biodiversity Movement and Global Change, Yale University. [145]School of Zoology, Faculty of Life Sciences, Tel Aviv University, Tel Aviv 69978, Israel. [146]San Diego Zoo Wildlife Alliance, 15600 San Pasqual Valley Road, Escondido, CA 92027, USA. [147]Grand Teton National Park, PO Drawer 170, Moose, Wyoming 83012, USA. [148]Wyoming Game and Fish Department, 700 Valley View Dr. Sheridan, WY 82801, USA. [149]Aarhus University, Department of Ecoscience - Wildlife Ecology, C.F. Møllers Allé 4-8, 8000 Aarhus C, Denmark. [150]Alaska Department of Fish and Game, Kodiak, AK 99615, USA. [151]Welgevonden Game Reserve, P.O. Box 433, Vaalwater, South Africa. [152]Guyra Paraguay - CONACYT, Asunción, Paraguay. [153]Instituto Saite, Asunción, Paraguay. [154]Ministry of Environment, Forestry and Tourism, Windhoek, Namibia. [155]Ecology, Evolution and Environmental Biology, Columbia University, NY, NY 10027, USA. [156]School of Natural Resources, University of Arizona, 1064 E Lowell St, Tucson, AZ 85719, USA. [157]Park Canada, Banff National Park Resource Conservation. PO Box 900, Banff, Alberta T1L 1K2, Canada. [158]Centre for the Advanced Study of Collective Behaviour, University of Konstanz, 78457 Konstanz, Germany. [159]Center for Integrated Spatial Research, Environmental Studies Department, University of California, Santa Cruz, CA 95064, USA. [160]Department of Fish, Wildlife and Conservation Biology, Colorado State University, Fort Collins, CO 80523, USA. [161]USDA National Wildlife Research Center, Predator Research Facility, Millville, UT 84326, USA. [162]Department of Wildland Resources, Utah State University, Logan, UT 84322, USA. [163]Tatra National Park, Kuźnice 1, 34-500, Zakopane, Poland. [164]Department of Biological Sciences, Goethe University, Max-von-Laue-Strasse 9, 60438 Frankfurt am Main, Germany.

SUPPLEMENTARY MATERIALS

science.org/doi/10.1126/science.abo6499
Materials and Methods
Fig. S1
Tables S1 to S15
References (*36*–*59*)
MDAR Reproducibility Checklist

Submitted 23 February 2022; accepted 27 April 2023
10.1126/science.abo6499

CLIMATE ECONOMICS

Persistent effect of El Niño on global economic growth

Christopher W. Callahan[1,2]* and Justin S. Mankin[1,2,3,4]

The El Niño–Southern Oscillation (ENSO) shapes extreme weather globally, causing myriad socioeconomic impacts, but whether economies recover from ENSO events and how anthropogenic changes to ENSO will affect the global economy are unknown. Here we show that El Niño persistently reduces country-level economic growth; we attribute $4.1 trillion and $5.7 trillion in global income losses to the 1982–83 and 1997–98 El Niño events, respectively. In an emissions scenario consistent with current mitigation pledges, increased ENSO amplitude and teleconnections from warming are projected to cause $84 trillion in 21st-century economic losses, but these effects are shaped by stochastic variation in the sequence of El Niño and La Niña events. Our results highlight the sensitivity of the economy to climate variability independent of warming and the potential for future losses due to anthropogenic intensification of such variability.

As the leading mode of interannual climate variability, the El Niño–Southern Oscillation (ENSO) integrates a wide range of Earth system processes (*1*). El Niño events shift deep convection from the western to the eastern Pacific, shaping global weather through "teleconnections" (*2*, *3*). Such local responses to remote forcing drive hydroclimate and temperature extremes with many well-documented impacts, including flooding (*4*, *5*), crop losses (*6*, *7*), and civil conflict (*8*). Many climate models project that warming will increase El Niño amplitude (*9*, *10*) and frequency (*11*), with potentially devastating socioeconomic impacts (*12*).

Despite ENSO's global impacts, however, empirical climate-economy studies have generally focused on temperature and rainfall averages (*13*–*16*) or variability (*17*), leaving the costs of changes in modes of climate variability unquantified. While studies have shown that El Niño reduces contemporaneous economic growth (*18*–*20*) and drives commodity price fluctuations (*21*–*23*), it remains unclear if and for how long its impacts persist. Distinguishing between transient and persistent impacts on economic growth is essential. Transient impacts ("level effects") are quickly recovered, as an economy rebounds to its original trajectory. Persistent impacts ("growth effects") reduce an economy's ability to grow, compounding exponentially over time. Poor observational constraints on growth effects limit our understanding of the economic costs of ENSO and climate damages more broadly (*24*–*26*).

[1]Program in Ecology, Evolution, Environment and Society, Dartmouth College, Hanover, NH, USA. [2]Department of Geography, Dartmouth College, Hanover, NH, USA. [3]Department of Earth Sciences, Dartmouth College, Hanover, NH, USA. [4]Ocean and Climate Physics, Lamont-Doherty Earth Observatory of Columbia University, Palisades, NY, USA.
*Corresponding author. Email: christopher.w.callahan.gr@dartmouth.edu

In this study, we estimated the effect of ENSO on past and future economic growth, accounting for the spatiotemporal heterogeneity of ENSO teleconnections. We define ENSO by the E-index and C-index (*27*) (fig. S1). These metrics of El Niño and La Niña, respectively, capture the nonlinear feedbacks that drive ENSO (see methods in the supplementary materials). We defined country-level teleconnections for each index (τ^E and τ^C) using correlations between the indices and country-level temperature and rainfall (methods and fig. S2). Teleconnections are strongest in tropical countries and weaker in the midlatitudes (Fig. 1A), consistent with the physical responses of regional climate to tropical variability (*28*).

We used a distributed lag regression model to quantify the effect of ENSO on growth in national gross domestic product per capita (GDPpc) from 1960 to 2019. Departing from previous work (*8*, *19*, *20*), we interacted the E- and C-indices with teleconnections to allow the economic effect of ENSO to vary smoothly as a function of teleconnection strength (*29*) (methods). Our model compares economic growth before and after El Niño events to assess their cumulative effects over time and distinguish growth effects from level effects (methods). We focused on the 5 years after El Niño events but also evaluated effects for >10 years as well as for La Niña. We then coupled these empirical estimates with climate model projections to assess the future economic effects of changes to ENSO amplitude and teleconnections.

El Niño persistently reduces economic growth

El Niño events persistently decrease economic growth (Fig. 1B). The magnitude of this effect is determined by the strength of each country's E-index teleconnection. In Peru (τ^E = 1.18), for example, a 1–standard deviation El Niño event decreases growth by 1.3 percentage points (pp) in the year of the event [95% confidence interval (CI): 0.9–1.7 pp]. After 5 years, growth in Peru has declined by 6.2 pp (CI: 4.7–8.2) (Fig. 1). By contrast, weakly teleconnected countries experience small and uncertain effects (Fig. 1B). The interaction between El Niño and teleconnections allows us to calculate marginal effects for each country on the basis of their τ^E value (Fig. 1C) and allows statistical significance to be determined by uncertainty in the distributed lag model (Fig. 1C, hatching) rather than prescribing "teleconnected" and "nonteleconnected" countries. Fifty-six percent of countries experience significant declines in growth 5 years after El Niños, averaging 2.3 pp, not simply level effects from which they recover immediately (Fig. 1D).

These negative effects are robust to using alternative ENSO indices, growth data, standard error clustering, or teleconnection metrics, as well as excluding the most strongly teleconnected countries (supplementary text and figs. S3 to S5). They also vary little over the 1960–2019 period, indicating minimal effect heterogeneity across time (fig. S6). ENSO indices vary through time but not space, raising the possibility that our results are confounded by time-varying global economic shocks. However, alternative specifications demonstrate that time-varying confounders are not driving our results: Adding country-specific trends to control for technological or demographic changes has little effect (fig. S4) because ENSO is stochastic (*30*) and measured by detrended indices. Using a spatially varying country-level index of ENSO or discretizing the sample into teleconnected and nonteleconnected groups allowed us to include both country and year fixed effects and yielded results as strong as our main estimates (methods and fig. S7), but we did not use these models in our main analysis because they do not preserve the independent and joint effects of ENSO amplitude and teleconnections (methods). Bootstrap resampling by year or dropping each year or country, ensuring that single years or countries are not driving the results, yielded similar effects (fig. S3). Finally, dropping the 1983 and 1998 El Niño events, which coincided with financial crises, reduced the magnitude of ENSO effects by only ~12% (fig. S4).

Our main observational analysis (Figs. 1 and 2) uses five lags, which reflects a balance between tracing the long-run response to ENSO and a concern for statistical power given the short observational record. Additional lags fit the data better but at the cost of model stability; using five lags balances these effects (fig. S8). Yet models with more lags reveal that El Niño effects can persist for 12 years or beyond, although a rebound begins after ~10 years (figs. S8 and S9), implying that our 5-year results for the historical costs of El Niño are conservative. After >14 years, the effects of ENSO cannot confidently be distinguished from zero. However, data simulations using a perfect model

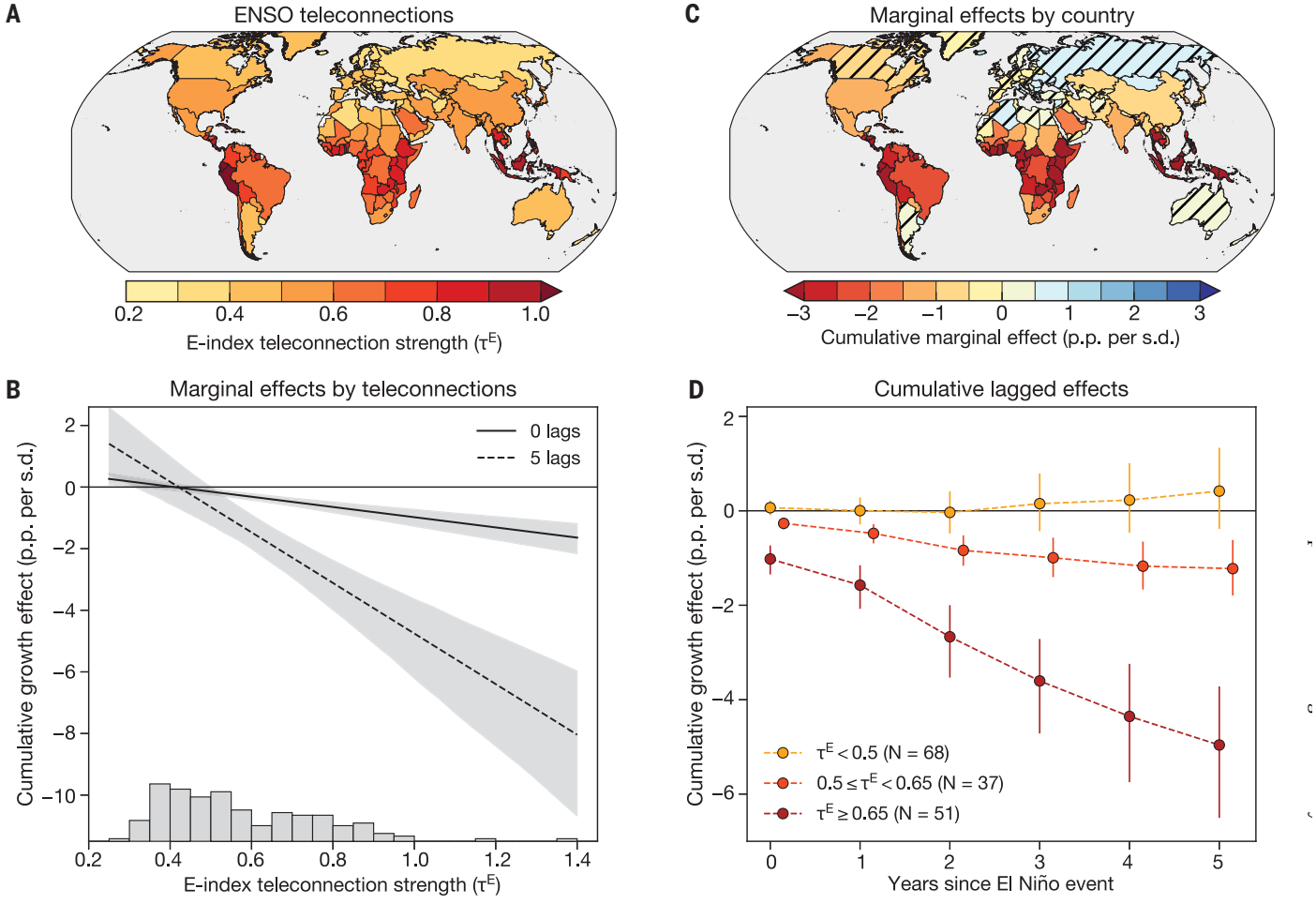


Fig. 1. Teleconnections mediate the effect of El Niño on economic growth. (**A**) Country-level ENSO teleconnections, calculated as the sum of the absolute value of the correlation coefficients between the E-index and monthly country-level temperature and precipitation (methods). (**B**) Marginal effects of El Niño on economic growth across teleconnection values in the year of the event (zero lags, solid line) and the fifth year after the event (five lags, dashed line). Black line shows the mean, and shading shows 95% CIs from bootstrap resampling (methods). The histogram along the bottom shows the density of teleconnection values in the sample. (**C**) Cumulative five-lag effect of El Niño on economic growth for each country. Hatching denotes countries whose effects are not distinguishable from zero [i.e., they fall on a location on the *x* axis in (B) where the shading includes zero]. (**D**) Cumulative effects of El Niño over time, beginning with the year of the event (year 0) and accumulating to the fifth year after the event (year 5). Countries are grouped into three bins according to their teleconnection strength, with "N" denoting the number of countries in each bin. Dots show averages, and bars show 95% CIs. p.p., percentage points; s.d., standard deviation.

framework, where we impute a permanent effect of El Niño to data, demonstrate that models with many lags can yield insignificant coefficients owing to the reduced sample size and large number of parameters (methods and fig. S8). The perfect model framework implies that, even if the real-world effects of ENSO were permanent, we may not be able to detect them given the short observational record. Finally, even if economies do eventually rebound from ENSO, the fact that damages accumulate for more than a decade means that the costs of climate variability are much larger than typically assumed in climate-economy models (*31*).

Our empirical model includes both the E-index and C-index, allowing us to distinguish the effects of eastern Pacific (EP) El Niño and central Pacific (CP) La Niña events (methods). CP La Niña events have beneficial effects (fig. S10), but they are several times weaker than the negative effects of EP El Niño events and statistically insignificant under alternative standard error clustering (table S2). These results reflect the skewness of ENSO itself, whereby EP El Niños tend to be stronger than both La Niñas and CP El Niños, and are consistent with studies showing that La Niña's economic effect is small (*19*, *20*).

The countries most affected by ENSO are generally lower-income, tropical countries (*19*). However, high-income countries also experience significant negative effects (fig. S4), consistent with work showing that these countries are affected by extreme rainfall (*32*) and heat (*33*), both of which ENSO influences. We also identify persistent losses across countries that experience wetting and drying in response to El Niño (fig. S4), as both anomalously low and high rainfall can be damaging (*32*). We emphasize that some regions may experience benefits from El Niño or losses from La Niña. Our goal is to estimate a globally generalizable response to ENSO. That our findings are robust across multiple lines of country heterogeneity provides confidence that they are generalizable, even if individual regions may respond differently.

Losses from historical El Niño events

The persistent effect of ENSO implies that historical El Niño events have altered the income growth of teleconnected countries, potentially generating large economic losses. We quantified the costs of the two largest El Niño events in the past 60 years, in 1982–83 and 1997–98 (Fig. 2). Because an El Niño can

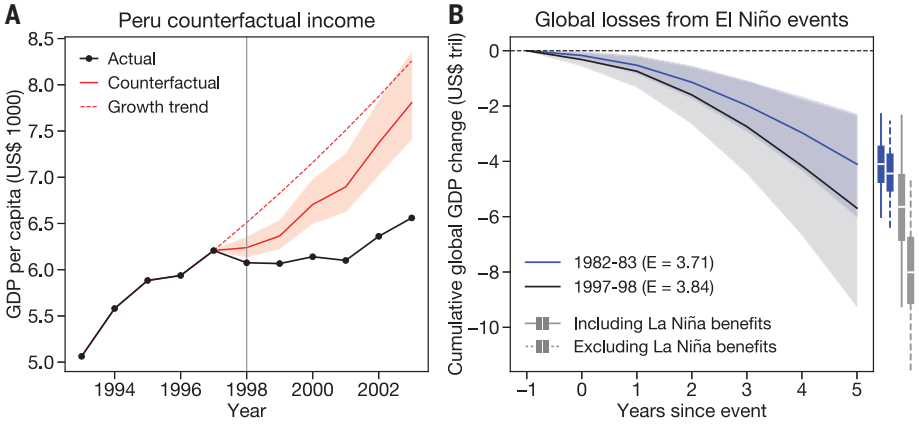


Fig. 2. Damages from extreme El Niño events. (**A**) GDP per capita (GDPpc) in Peru before and after the 1997–98 El Niño event. Black line shows actual GDPpc, red line shows the average counterfactual GDPpc across regression bootstrap samples (methods), and red shading shows 95% CI. Dashed line shows GDPpc if Peru had maintained its average growth rate from the 5 years preceding the event. (**B**) Cumulative global GDP change for the 5 years after the 1982–83 (blue) and 1997–98 (black) El Niño events. Center line shows the mean, and shading shows the 95% CIs across regression bootstrap samples. Global GDP change is only calculated for countries with statistically significant marginal effects (Fig. 1C). "E" in the legend denotes the December-to-February–average E-index in the corresponding years. Boxplots at right show cumulative global GDP change when including the benefits of the following La Niña events (solid lines) and excluding those benefits (dashed lines). All dollar values are in constant 2017 prices.

trigger a subsequent La Niña (*34*), our analysis incorporated both the negative effects of each El Niño and the benefits of the following La Niña (methods). Furthermore, because these events coincided with unrelated currency crises, we used a model excluding these events to more conservatively calculate their impacts (fig. S4).

Consider strongly teleconnected Peru (τ^E = 1.18): Its GDPpc declined in 1998 and stagnated for three more years (Fig. 2A). Given the 1997 financial crisis, Peru's slower growth in 1998 is not entirely attributable to ENSO, but Peru's economy would have grown more quickly had the 1997–98 El Niño not occurred (methods). Income for the average Peruvian would have been some $1,246 greater 5 years later in 2003 absent the event (CI: $853 to $1,793), a 19% increase (Fig. 2A). Other tropical countries such as Ecuador, Brazil, and Indonesia lost anywhere from 5% to 19% of GDPpc (fig. S11).

We estimated global losses from the 1982–83 and 1997–98 events to be trillions of dollars each (Fig. 2B and fig. S11). Our estimates exceed previous ones because we accounted for ENSO's growth effects: One study placed the total costs of the 1997–98 El Niño at $36 billion (*35*). Our accounting has losses from the 1997–98 event rising to two orders of magnitude more than that estimate, some $5.7 trillion by 2003 (CI: $2.3 trillion to $9.2 trillion). The earlier 1982–83 event tallied $4.1 trillion by 1988 (CI: $2.3 trillion to $6 trillion). The greater costs of the 1997–98 event resulted both because it was a stronger El Niño and because the global economy was larger. Absent the compensating benefits of the subsequent La Niñas, the 1983 (1998) event would have produced losses of $4.4 trillion ($8 trillion) (Fig. 2B).

We focused on five lags in this historical analysis to balance the imperatives of tracking the effects of ENSO and maximizing statistical power (fig. S8). Because the effect of El Niño appears to persist for >5 years (fig. S8), the ultimate toll of these events may be even higher than demonstrated here. Regardless, by incorporating growth reductions following the event and including all countries in a single framework, we show that estimates focusing on physical asset losses in low-income countries have strongly underestimated the global economic toll of El Niño.

Climate model projections of ENSO

ENSO's persistent effect raises the question of how it will shape the global economy with further warming. Using climate model simulations from the sixth phase of the Coupled Model Intercomparison Project (CMIP6) that skillfully simulate eastern Pacific sea surface temperatures, we analyzed projected changes to ENSO under four shared socioeconomic pathways (SSPs) (methods).

El Niño amplitude and teleconnections both increase with warming in CMIP6 (Fig. 3). This response is not scenario-dependent, likely owing to the influence of internal climate variability on forced ENSO changes (*36*–*38*). Median amplitude increases by 5 to 21% across scenarios (Fig. 3A), a function of stronger wind–ocean coupling in the eastern Pacific (*9*, *12*). Global mean teleconnections increase by 4 to 15% (Fig. 3B), consistent with a more energetic atmospheric response to El Niño (*39*, *40*). Despite these forced responses, internal variability (proxied by multiple realizations from each model) can vary these responses by >60 pp (Fig. 3, A and B, lower lines).

Beyond amplitude and teleconnection changes, climate projections differ in their E-index time series. Because of ENSO's sensitivity to initial conditions (*36*–*38*) and multidecadal variability (*41*, *42*), a wide range of E-index values across models and scenarios can occur in a given year, even when controlling for amplitude (Fig. 3C and fig. S12). For example, Fig. 3C shows two SSP2-4.5 simulations with similar amplitude changes and E-index skewness but different sequences of EP El Niños and La Niñas. As quantified by the sum of the E-index over the 21st century, MIROC-ES2L r6i1p1f2 experiences strong El Niño events, whereas CESM2-WACCM r3i1p1f1 is dominated by La Niña events. Such differences in the ENSO sequence shape projected damages, as an El Niño–dominated time series yields greater damages than a La Niña–dominated one because of their differential effects (fig. S10). Crucially, because El Niños are stronger than La Niñas, the expectation from increased ENSO amplitude is net losses.

We combined these projections with our empirical estimates to quantify the economic effects of changes in ENSO. We used the SSPs as baselines against which we calculated country-level growth changes on the basis of ENSO amplitude and teleconnection projections (methods). Departing from our historical estimates (Figs. 1 and 2), we projected future ENSO damages with a model that extends damages out to ~14 years because we can confidently detect damage accumulation that long yet cannot identify truly permanent growth effects owing to the short observational record (fig. S8). As such, we made the conservative choice to allow economies to fully recover from future ENSO events after 14 years in our projections (methods). This simplifying choice assumes that the time persistence of ENSO impacts is homogeneous. However, it is possible that different countries recover over different timescales. For example, weakly teleconnected countries may rebound more quickly (Fig. 1D), and the sectoral makeup of an economy (e.g., agriculture-dependent versus manufacturing-dependent) may affect the speed with which it can reinvest in new growth after El Niño events. Further research into whether, how, and over what timescales economies recover from El Niño events would reduce uncertainty in our projections and help economies manage extreme climate events more broadly.

Economic impacts of future ENSO changes

Projected anthropogenic changes to El Niño amplitude and teleconnections will likely cause substantial economic losses over the 21st century (Fig. 4). Under a 2% discount rate (*43*) and a socioeconomic scenario consistent with

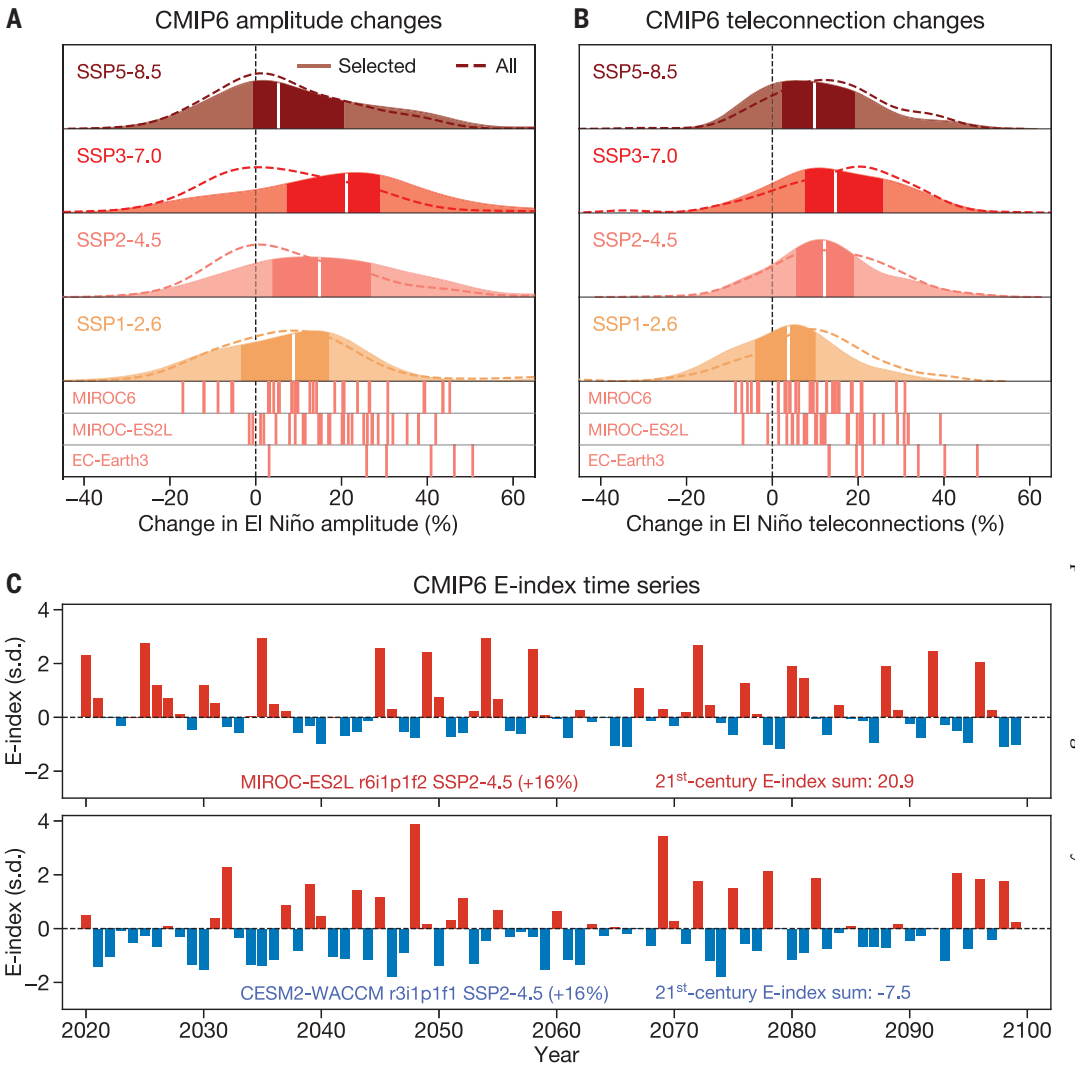


Fig. 3. Climate model projections of ENSO. Change in ENSO amplitude (**A**) and global mean teleconnection strength (**B**) between 1940–2019 and 2020–2099 for an ensemble of CMIP6 simulations from four SSP experiments. In both panels, dashed density lines show changes from all simulations, and solid density plots show amplitude changes from selected high-skill simulations used in the analysis (methods). Vertical lines below the density plots denote amplitude changes from the individual realizations of three models (MIROC6, MIROC-ES2L, and EC-Earth3), all drawn from the SSP2-4.5 experiment, illustrating the wide range of amplitude and teleconnection changes possible from internal variability alone. (**C**) E-index time series from two example simulations with similar amplitude increases: MIROC-ES2L r6i1p1f2 (top) and CESM2-WACCM r3i1p1f1 (bottom), both from the SSP2-4.5 experiment. Red bars denote eastern Pacific El Niño (E > 0), and blue bars denote eastern Pacific La Niña (E < 0). Left inset text in each panel denotes the model information and amplitude change. Right inset text denotes the sum of each E-index time series over the 21st century (2020–2099), with positive values indicating that the time series contains more El Niños than La Niñas and negative values indicating the opposite.

current pledges to reduce greenhouse gas emissions (*44*) (SSP2-4.5), the median cumulative 2020–2099 global losses are projected to be $84 trillion (Fig. 4A), a ~0.9% reduction in global economic output over the 21st century. In all four scenarios, median losses exceed $18 trillion, and damages are negatively skewed, consistent with the asymmetry in ENSO itself.

The range of these projections is large. Under SSP2-4.5, the 95% range spans losses of $453 trillion to benefits of $80 trillion (we write this CI as −$453T to +$80T) across 86,000 combinations of 86 simulations and 1000 regression bootstraps (Fig. 4A). Reducing the discount rate to 1% amplifies median losses under SSP2-4.5 to $131 trillion (−$687T to +$130T), while increasing it to 5% diminishes losses to $26 trillion (−$162T to +$34T). The extreme end of these ranges implies a ~5% reduction in global economic output. In highly teleconnected countries, ENSO changes cause GDPpc reductions of >1% per year, although uncertainty is high even in these countries (fig. S11).

Despite this range across realizations, models, and scenarios, increases in ENSO amplitude and teleconnections are systematically related to greater economic losses (Fig. 4, B and C). Each additional 1 pp in ENSO amplitude increase is associated with $4.1 trillion in additional discounted losses over the 21st century ($P < 0.001$), and each additional 1 pp in teleconnection increase is associated with $6.3 trillion in losses ($P < 0.001$). These findings build on previous projections of changes in ENSO amplitude (*9*, *11*) and teleconnections (*39*, *40*), demonstrating global socioeconomic effects of these physical changes.

These relationships, however, are heterogeneous, as the largely stochastic sequence of El Niños and La Niñas shapes the direction and magnitude of damages. Simulations with E-index sums > 0 (i.e., El Niño–dominated time series) exhibit a negative relationship between ENSO amplitude increases and damages (Fig. 4B, red dots), but the opposite is true for La Niña–dominated time series (blue dots). The same pattern holds for teleconnection changes (Fig. 4C). Critically, because El Niños are stronger than La Niñas, there are many more El Niño– than La Niña–dominated time series. On average, therefore, increases in ENSO amplitude and teleconnections produce large economic losses.

Alternative analytical choices, including incorporating C-index changes or holding teleconnections constant, alter the magnitude of losses but do not change the core result of negative damages with warming (fig. S13). Using only one realization per model increases uncertainty across scenarios (fig. S13B), highlighting the importance of large ensembles to capture ENSO variability (*37*). The assumption that damage persistence is permanent substantially increases the magnitude and uncertainty

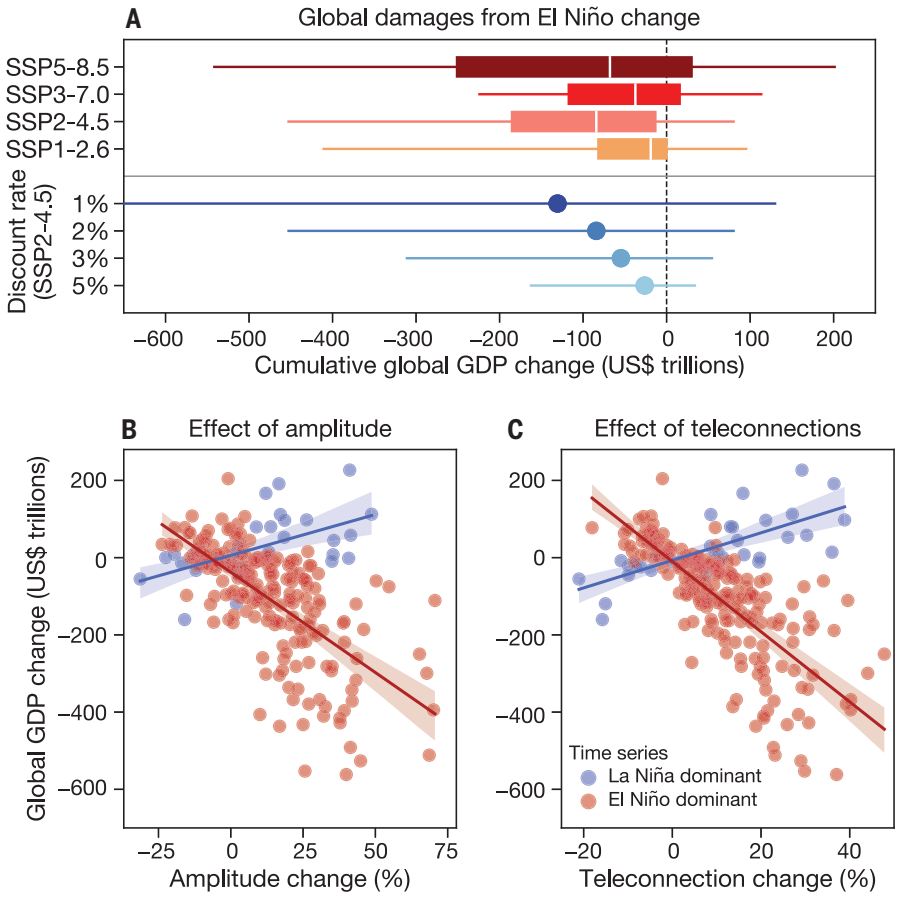


Fig. 4. Global economic impacts of changes in El Niño amplitude and teleconnections. (**A**) Boxplots show the cumulative global GDP change in each scenario under a 2% constant discount rate. Colors correspond to the scenario colors in Fig. 3. In each boxplot, the white vertical line denotes the median, the box spans the first and third quartiles, and the whiskers span the 95% range. The blue lines below the boxplots denote global economic losses under SSP2-4.5 and a range of discount rates. Dots denote the median, and lines span the 95% range. (**B** and **C**) Cumulative global GDP change due to changes in ENSO amplitude (B) and teleconnections (C) with a 2% discount rate, with each dot corresponding to one climate model simulation. Simulations are pooled across all four scenarios. Red dots denote simulations in which the 21st-century E-index sum is greater than 0 (El Niño–dominated time series), while blue dots denote simulations in which the sum is less than 0 (La Niña–dominated time series). Red and blue regression lines and 95% CIs are drawn separately for each subset of simulations.

in projected damages (fig. S13D). Finally, controlling for country-average temperature in our regression does not alter the effect of ENSO (fig. S14), meaning that our results are distinct from temperature-based damage projections (*13*). ENSO affects subnational and subannual extreme heat or rainfall and other hazards, such as drought, all of which have independent impacts (*32*, *45*, *46*).

Our findings have implications for climate mitigation and adaptation. All else being equal, increased ENSO amplitude and teleconnections will generate major economic losses not currently included in assessments of climate damages or mitigation benefits. However, the fact that (i) ENSO-driven damages do not depend strongly on the choice of emissions scenario (Fig. 4A) and that (ii) a range of outcomes are possible given uncertainty in the particular ENSO sequence going forward (Fig. 4, B and C) implies that emissions reductions alone are insufficient to protect economies from El Niño effects. While mitigation remains critical to blunt the catastrophic impacts of anthropogenic warming (*47*), our findings also raise the priority of climate adaptation and resilience efforts. Improved disaster risk management and ENSO early warning could reduce ENSO-driven damages (*48*), and scientific investments in decadal climate prediction could reduce the uncertainty in projections of these damages.

Outlook

Our finding that El Niño has a persistent effect on economic growth has four key implications. Firstly, it demonstrates that growth is highly sensitive to climate variability independent of warming. Our findings demonstrate that the local extreme conditions associated with ENSO integrate into a globally persistent macroeconomic effect, implying large and underestimated costs of historical El Niño events. Secondly, our results demonstrate that future changes to ENSO may increase the macroeconomic costs of warming. Previous climate-economy studies have not incorporated changes in climate variability, and we show that this omission has hidden a potentially major cost of rising temperatures. Thirdly, stochastic variation in ENSO could result in either losses or benefits from warming, emphasizing the importance of investing in ENSO prediction, particularly on decadal timescales (*41*). Lastly, these findings together suggest that while climate mitigation is essential to reduce accumulating damages from warming, it is imperative to devote more resources to adapting to El Niño in the present day.

REFERENCES AND NOTES

1. M. J. McPhaden, S. E. Zebiak, M. H. Glantz, *Science* **314**, 1740–1745 (2006).
2. J. Bjerknes, *Mon. Weather Rev.* **97**, 163–172 (1969).
3. S.-W. Yeh *et al.*, *Rev. Geophys.* **56**, 185–206 (2018).
4. T. W. Corringham, D. R. Cayan, *Weather Clim. Soc.* **11**, 489–504 (2019).
5. F. J. Magilligan, P. S. Goldstein, *Geology* **29**, 431–434 (2001).
6. S. M. Hsiang, K. C. Meng, *Am. Econ. Rev.* **105**, 257–261 (2015).
7. T. Iizumi *et al.*, *Nat. Commun.* **5**, 3712 (2014).
8. S. M. Hsiang, K. C. Meng, M. A. Cane, *Nature* **476**, 438–441 (2011).
9. W. Cai *et al.*, *Nature* **564**, 201–206 (2018).
10. W. Cai *et al.*, *Nat. Clim. Chang.* **12**, 228–231 (2022).
11. W. Cai *et al.*, *Nat. Clim. Chang.* **4**, 111–116 (2014).
12. W. Cai *et al.*, *Nat. Rev. Earth Environ.* **2**, 628–644 (2021).
13. M. Burke, S. M. Hsiang, E. Miguel, *Nature* **527**, 235–239 (2015).
14. M. Burke, V. Tanutama, "Climatic constraints on aggregate economic output" (NBER Working Paper 25779, National Bureau of Economic Research, 2019); http://www.nber.org/papers/w25779.
15. M. Dell, B. F. Jones, B. A. Olken, *Am. Econ. J. Macroecon.* **4**, 66–95 (2012).
16. M. Kalkuhl, L. Wenz, *J. Environ. Econ. Manage.* **103**, 102360 (2020).
17. M. Kotz, L. Wenz, A. Stechemesser, M. Kalkuhl, A. Levermann, *Nat. Clim. Chang.* **11**, 319–325 (2021).
18. P. Cashin, K. Mohaddes, M. Raissi, *J. Int. Econ.* **106**, 37–54 (2017).
19. S. C. Smith, D. Ubilava, *Glob. Environ. Change* **45**, 151–164 (2017).
20. R. Generoso, C. Couharde, O. Damette, K. Mohaddes, *Ann. Econ. Stat.* **140**, 83–126 (2020).
21. A. D. Brunner, *Rev. Econ. Stat.* **84**, 176–183 (2002).
22. D. Ubilava, *Agric. Econ.* **43**, 17–26 (2012).
23. D. Ubilava, *World Dev.* **96**, 490–502 (2017).
24. F. C. Moore, D. B. Diaz, *Nat. Clim. Chang.* **5**, 127–131 (2015).
25. S. Dietz, N. Stern, *Econ. J. (London)* **125**, 574–620 (2015).
26. E. J. Moyer, M. D. Woolley, N. J. Matteson, M. J. Glotter, D. A. Weisbach, *J. Legal Stud.* **43**, 401–425 (2014).
27. K. Takahashi, A. Montecinos, K. Goubanova, B. Dewitte, *Geophys. Res. Lett.* **38**, L10704 (2011).
28. E. M. Rasmusson, T. H. Carpenter, *Mon. Weather Rev.* **110**, 354–384 (1982).
29. D. Ubilava, M. Abdolrahimi, *Environ. Res. Lett.* **14**, 054008 (2019).
30. S. Power, M. Haylock, R. Colman, X. Wang, *J. Clim.* **19**, 4755–4771 (2006).
31. B. A. Bastien-Olvera, F. Granella, F. C. Moore, *Environ. Res. Lett.* **17**, 084038 (2022).
32. M. Kotz, A. Levermann, L. Wenz, *Nature* **601**, 223–227 (2022).

33. N. S. Diffenbaugh, F. V. Davenport, M. Burke, *Environ. Res. Lett.* **16**, 084025 (2021).
34. W. Cai *et al*., *Nat. Clim. Chang.* **5**, 132–137 (2015).
35. M. K. van Aalst, S. Fankhauser, S. M. Kane, K. Sponberg, "Climate information and forecasting for development: lessons from the 1997/98 El Niño" (Environment Department Paper No. 79, Climate Change Series, World Bank Group, 2000); http://documents.worldbank.org/curated/en/451971468739263265/Climate-information-and-forecasting-for-development-lessons-from-the-1997-98-El-Nino.
36. W. Cai *et al*., *Nature* **585**, 68–73 (2020).
37. N. Maher, D. Matei, S. Milinski, J. Marotzke, *Geophys. Res. Lett.* **45**, 11390–11398 (2018).
38. C. Deser, R. Knutti, S. Solomon, A. S. Phillips, *Nat. Clim. Chang.* **2**, 775–779 (2012).
39. K.-S. Yun *et al*., *Commun. Earth Environ.* **2**, 43 (2021).
40. K. Hu, G. Huang, P. Huang, Y. Kosaka, S.-P. Xie, *Nat. Geosci.* **14**, 377–382 (2021).
41. A. T. Wittenberg, A. Rosati, T. L. Delworth, G. A. Vecchi, F. Zeng, *J. Clim.* **27**, 2667–2681 (2014).
42. C. W. Callahan *et al*., *Nat. Clim. Chang.* **11**, 752–757 (2021).
43. Council of Economic Advisers, "Discounting for public policy: Theory and recent evidence on the merits of updating the discount rate," Issue Brief, January 2017; https://obamawhitehouse.archives.gov/sites/default/files/page/files/201701_cea_discounting_issue_brief.pdf.
44. M. Meinshausen *et al*., *Nature* **604**, 304–309 (2022).
45. M. Davis, *Late Victorian Holocausts: El Niño Famines and the Making of the Third World* (Verso Books, 2002).
46. C. W. Callahan, J. S. Mankin, *Sci. Adv.* **8**, eadd3726 (2022).
47. B. O'Neill *et al*., in *Climate Change 2022: Impacts, Adaptation and Vulnerability. Contribution of Working Group II to the Sixth Assessment Report of the Intergovernmental Panel on Climate Change* (Cambridge Univ. Press, 2022), pp. 2411–2538.
48. A. French, R. Mechler, "Managing El Niño risks under uncertainty in Peru" (International Institute for Applied Systems Analysis, 2017); https://pure.iiasa.ac.at/id/eprint/14849/1/French_Mechler_2017_El%20Ni%c3%b1o_Risk_Peru_Report.pdf.

ACKNOWLEDGMENTS

We thank Dartmouth's Research Computing and the Discovery Cluster for computing resources. We thank the World Climate Research Programme, which, through its Working Group on Coupled Modeling, coordinated and promoted CMIP6. **Funding:** This work was supported by National Science Foundation Graduate Research Fellowship 1840344 to C.W.C. and grants from Dartmouth's Neukom Computational Institute, the Wright Center for the Study of Computation and Just Communities, and the Nelson A. Rockefeller Center for Public Policy to J.S.M. **Author contributions:** Both authors designed the analysis. C.W.C. performed the analysis. Both authors interpreted the results and wrote the paper. **Competing interests:** The authors declare no competing interests. **Data and materials availability:** All data and code that support this study are available at https://github.com/ccallahan45/CallahanMankin_ENSOEconomics/. **License information:** Copyright © 2023 the authors, some rights reserved; exclusive licensee American Association for the Advancement of Science. No claim to original US government works. https://www.science.org/about/science-licenses-journal-article-reuse

SUPPLEMENTARY MATERIALS

science.org/doi/10.1126/science.adf2983
Materials and Methods
Supplementary Text
Figs. S1 to S17
Tables S1 to S7
References (*49*–*84*)

Submitted 12 October 2022; accepted 2 May 2023
Published online 18 May 2023
10.1126/science.adf2983

DEVELOPMENTAL BIOLOGY

Linking genome structures to functions by simultaneous single-cell Hi-C and RNA-seq

Zhiyuan Liu[1,2]†, Yujie Chen[1,2]†, Qimin Xia[1,2]†, Menghan Liu[1,2], Heming Xu[1,2], Yi Chi[1,2], Yujing Deng[1,2], Dong Xing[1,2]*

Much progress has been made recently in single-cell chromosome conformation capture technologies. However, a method that allows simultaneous profiling of chromatin architecture and gene expression has not been reported. Here, we developed an assay named "Hi-C and RNA-seq employed simultaneously" (HiRES) and performed it on thousands of single cells from developing mouse embryos. Single-cell three-dimensional genome structures, despite being heavily determined by the cell cycle and developmental stages, gradually diverged in a cell type–specific manner as development progressed. By comparing the pseudotemporal dynamics of chromatin interactions with gene expression, we found a widespread chromatin rewiring that occurred before transcription activation. Our results demonstrate that the establishment of specific chromatin interactions is tightly related to transcriptional control and cell functions during lineage specification.

Different cell types within a multicellular organism share a nearly identical genome but differ substantially in morphology and function. The acquisition of such diverse cellular identities during development requires the regulation of gene expression across multiple layers, including the higher-order spatial organization of chromatin in the nucleus (*1*–*3*). Recently, monomodal single-cell Hi-C and RNA sequencing (RNA-seq) assays were applied to postnatal mouse brains, and cell types identified separately from the two types of data were matched for joint three-dimensional (3D) genome and transcriptome analysis (*4*). However, because 3D genome changes may either precede or follow transcriptome changes during development, the integration of data may incorrectly link a 3D genome state to a transcriptome state if the two types of data are not profiled from the same cells. Recent advances in single-cell multi-omics sequencing technologies have enabled joint profiling of the transcriptome with many other modalities such as DNA methylation, cellular proteins, chromatin accessibility, and histone modifications, and have helped improve our understanding of cell fate commitment at the molecular level (*5*–*8*). However, among these RNA-centric multi-omics technologies, one long-standing gap is the lack of an approach for parallel capture of chromatin conformation. Here, we developed a method called "Hi-C and RNA-seq employed simultaneously" (HiRES) and applied it to explore the functional relationship between the 3D genome and transcriptome during mouse embryonic lineage specification.

[1]Biomedical Pioneering Innovation Center (BIOPIC), School of Life Sciences, Peking University, Beijing, China. [2]Beijing Advanced Innovation Center for Genomics (ICG), Peking University, Beijing, China.
*Corresponding author. Email: dxing@pku.edu.cn
†These authors contributed equally to this work.

Simultaneous single-cell Hi-C and RNA-seq

HiRES begins with an in situ reverse transcription step, followed by an optimized 3C procedure (*9*). Single cells are then flow sorted and preamplified by quasilinear amplification of multiple annealing and looping-based amplification cycles (*10*) in a one-tube reaction. The cDNA reads are extracted in silico through an mRNA-specific tag introduced through reverse transcription (Fig. 1A). This strategy does not involve physical separation of genome and transcriptome, thereby minimizing sample loss and handling time. Thousands of single cells can be processed within a few days using multiwell plates, and the throughput of the assay can be further improved with multiplex single-cell barcodes (*11*).

To validate the efficiency and data quality, we performed HiRES on single nuclei isolated from adult mouse brains. A total of 399 out of 432 nuclei passed quality control filters with consistent performance across replicates (fig. S1, A to C). HiRES detected a median of 27,891 RNA unique molecular identifiers from 6966 genes and 304,124 Hi-C contacts per cell, which outperformed a recent study on the same tissue using monomodal single-cell RNA-seq or Hi-C technology alone (Fig. 1, B and C, and fig. S1D) (*4*). Clustering of single cells on the basis of either gene expression profiles or Hi-C contact maps revealed major brain cell types (Fig. 1D and fig. S1, E to H). Moreover, cell type identities in RNA clusters agreed well with identities in Hi-C clusters (fig. S1I), indicating a functional link between the 3D genome and transcriptome.

Single-cell Hi-C data have been used to reconstruct whole-genome 3D structures from both haploid and diploid cells (*12*–*14*), representing a bona fide snapshot of genome folding at a particular time point rather than a bulk average. With HiRES data, 363 (91%) cells yielded high-quality structures at 20-kb resolution with an imputation-based method [illegible]. The reconstructed structures exhibited [illegible] known chromatin architecture such as chromosome territories, A/B compartments, and radial preference (fig. S2, A to C). Aggregation of the pairwise 3D distance matrices calculated from single-cell structures produced results that were highly concordant with the original contact map and with the previously published data (Fig. 1E).

Similar to single-nucleus RNA-seq, HiRES RNA reads were enriched for nascent transcripts (fig. S2D), which served as a better proxy for transcriptional activity than mature mRNA. We then mapped allelic-resolved gene expression onto the reconstructed 3D genome structure of the same cell (Fig. 1F and fig. S2E) and calculated changes in single-cell chromatin A/B compartments between active and silent transcription sites. We found that transcribing genes were generally located in a more active chromatin environment (fig. S2F), consistent with previous findings using imaging-based methods (*15*). Altogether, these data demonstrate that HiRES is a reliable tool with which to measure 3D genome conformation and gene expression in the same cell with high efficiency, providing an opportunity to directly link genome structures to functions.

3D genome specification during embryogenesis

3D genome conformation has been shown to undergo extensive reorganization during cell differentiation (*16*–*19*). To explore the relationship between genome organization and gene expression during embryonic development, we performed HiRES on 7716 single cells from F_1 hybrid mouse embryos (C57BL/6J × CAST/EiJ) collected between embryonic day 7.0 (E7.0) and E11.5. A total of 7469 cells passed filters for both data types, yielding 2.8 billion DNA contacts and 150 million RNA transcripts (fig. S3A).

To define cell identities, we clustered RNA data after dimensionality reduction and annotated each cluster by projecting single-cell expression profiles to previously published atlas data (fig. S3B) (*20*). Visualization by uniform manifold approximation and projection (UMAP) revealed four major cell populations, including embryonic tissues, extra-embryonic endoderm, extra-embryonic ectoderm, and blood (Fig. 2A and fig. S3C). Within the embryonic population, we captured two differentiation trajectories, the neural trajectory and the mesenchymal trajectory, stemming from epiblast and primitive streak. We identified a cluster of cells exhibiting an overall low transcription level and metaphase chromosomal organization (fig. S3, D to G) (*21*), representing cells undergoing the mitotic phase of the cell cycle.

To resolve the temporal dynamics of 3D genome organization, we clustered single cells using their imputed DNA contact matrices (*22*) and colored each cell according to the RNA

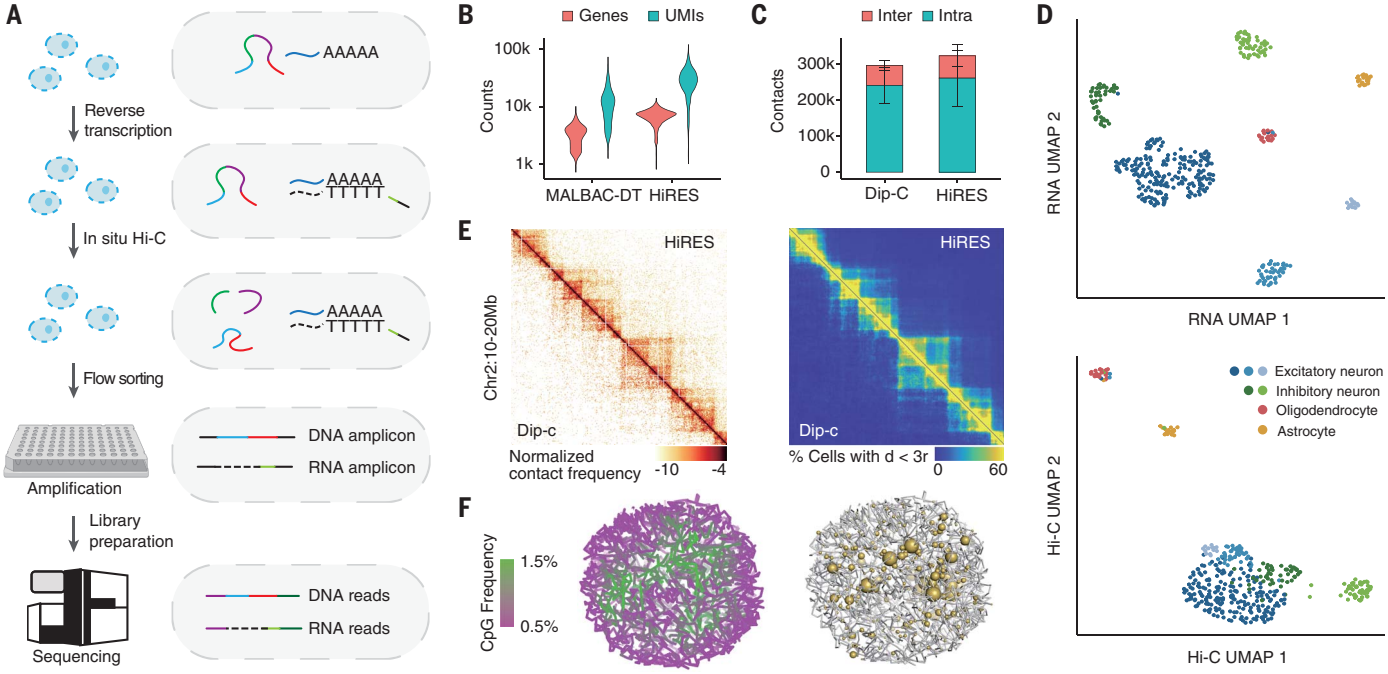


Fig. 1. HiRES simultaneously profiles 3D genome structures and gene expression with high efficiency and accuracy. (**A**) Schematics of the HiRES workflow. (**B**) Number of genes and RNA unique molecular identifiers (UMIs) for HiRES and MALBAC-DT (multiple annealing and looping based amplification cycles for digital transcriptomics). (**C**) Number of chromatin contacts for HiRES and Dip-C. (**D**) Clustering of mouse brain single cells by HiRES RNA data (top) and contact data (bottom). (**E**) Comparison of contact maps (left) and 3D proximity maps [right, shown as the percentage of alleles with 3D distance between two loci fewer than three particle radii (r)] of neurons from HiRES data with published data. (**F**) Example of a single-cell 3D genome structure rendered together with gene expression (right). The size of the yellow balls is proportional to the transcription level. Compartmentalization of euchromatin (green) and heterochromatin (magenta) was visualized by cytosine-phosphate-guanine (CpG) frequency as a proxy (left).

cell type (Fig. 2B). We found that the four cell populations identified by RNA data were also well distinguished on the structural UMAP, suggesting that the first 3D genome specification might have occurred as early as the differentiation of embryonic and extraembryonic lineages. Nevertheless, for the embryonic population, cells originating from the two main germ layers, ectoderm and mesoderm, were largely intermixed before E8.5 and started to diverge from each other gradually afterward, reaching a clear separation at E11.5 (Fig. 2C). We obtained similar results using other single-cell Hi-C clustering methods (fig. S3H). This observation echoes recent findings in *Drosophila* embryos, in which tissues with different cell fates exhibited similar chromatin architecture (*23*, *24*), suggesting that the role of chromatin conformation as a scaffold for gene expression is conserved during early development.

Hierarchically organized chromatin features, such as A/B compartments and topologically associating domains (TADs), have been reported to rearrange extensively in various tissues and cell types (*25*). We characterized A/B compartmentalization at both the bulk and single-cell levels. Consistent with previous reports during neural differentiation (*19*), we observed a gradual increase of interactions between B compartments during development (fig. S4A). Although the changing of compartmentalization correlated with cell type–specific gene expression, a majority (63%) of genomic windows remained invariable during this period of development (fig. S4, B to D). Pairwise comparison of different cell types showed that compartment switches varied from 6% (between oligodendrocyte precursor cells and radial glia) to 18% (between extraembryonic ectoderm and early neurons). We found that two cell types closer in developmental stages exhibited more conserved compartmentalization patterns, which changed gradually with the progress of development (fig. S4, E and F). Similarly, the formation of TAD boundaries also followed this developmental trend (fig. S4, G and H). These results suggested that the establishment of hierarchical chromatin organization depends on not only cell type–specific, but also on developmental stage–specific chromatin features.

We found that well-clustered RNA cell types were often divided into different clusters on the Hi-C UMAP (Fig. 2D and fig. S5A). Differential expression analysis between these Hi-C clusters identified genes highly related to the cell cycle (fig. S5B). Early embryonic development is characterized by a high rate of cell division, during which chromosomes undergo substantial spatial reorganization (*13*, *26*, *27*), so it is necessary to study the 3D genome dynamics during this period in the context of cell cycle.

Cell-cycle dynamics captured by HiRES

For precise cell-cycle phasing at single-cell level, we took advantage of the double-modality data of HiRES and developed a strategy to assign single cells to seven cell-cycle phases on the basis of both DNA and RNA data (*9*). Each phase was characterized by distinct profiles of cell-cycle gene expression, DNA replication, and contact distribution (fig. S6, A and B). The inferred phasing of single cells displayed a continual transition of cell-cycle phases along the vertical axis on the Hi-C UMAP (Fig. 2E). Clusters of G_0 cells, most of which were identified in cell types from later developmental stages such as early neurons and mixed late mesenchyme (fig. S6C), drifted out from the cycling cells without transiting into the S phase. We found that within the embryonic tissues, where RNA-defined clusters were mostly intermixed, contact-defined clusters were more consistent with cell-cycle phases (Fig. 2F), suggesting chromatin conformational changes coordinated by cell cycle as a major contributor to the overall 3D genome structure. This cell-cycle effect also existed in the other three cell populations. Nevertheless, chromatin organization specific to each population must have played a

dominant role in distinguishing them from each other and from the embryonic population. Therefore, cell type–specific and cell cycle–specific chromatin interactions coexist during early development and shape the single-cell 3D genome jointly.

We then investigated whether and how cell-cycle dynamics of chromatin organization change across developmental stages and cell types. We found that interphase cells from later developmental stages showed a more comprehensive establishment of long-range interactions after mitotic exit (fig. S6D). This was possibly caused by the difference in the cell-cycle length, especially the duration of G_1, because a longer cell cycle would allow a more complete chromatin reorganization before the next cell division. Cells from earlier developmental stages are known to have a shorter cell cycle with a truncated G_1 (*28*). As expected, the proportion of G_1 cells was lowest at E7.0, and gradually increased with development (fig. S6E).

To compare the chromatin dynamics associated with the cell-cycle length, we ordered single cells into a "pseudo cell cycle" within each cell type (fig. S7A). This allowed us to align two cell-cycle orders by calculating the minimal distance between pairwise cells using their contact decay profiles (*29*). Alignment of different cell-cycle orders produced many pairings of cells with discordant cell-cycle phases. For instance, the early-S cells of neural ectoderm were aligned to late G_1 cells, instead of early-S cells, of radial glia (Fig. 2G). In general, when aligned to a later developmental stage with a longer G_1, cells from an earlier developmental stage tended to align to a cell-cycle phase preceding its own phase and vice versa (Fig. 2H and fig. S7, B to D). This misalignment of cell-cycle phases was most prominent for early-S cells and attenuated as DNA replication intervened and proceeded (fig. S7E), during which short-range interactions accumulated, in contrast to G_1/G_0 cells. Previous studies have explored the critical role of DNA replication in shaping the 3D genome (*30*–*32*). Our results further indicated that chromatin organization of interphase cells was determined by two independent processes, the spontaneous unfolding of chromosomes after mitotic exit and the replication of the genome. For cell cycles with a short G_1, the two processes overlapped in time and together determined the cell-cycle dynamics of the 3D genome.

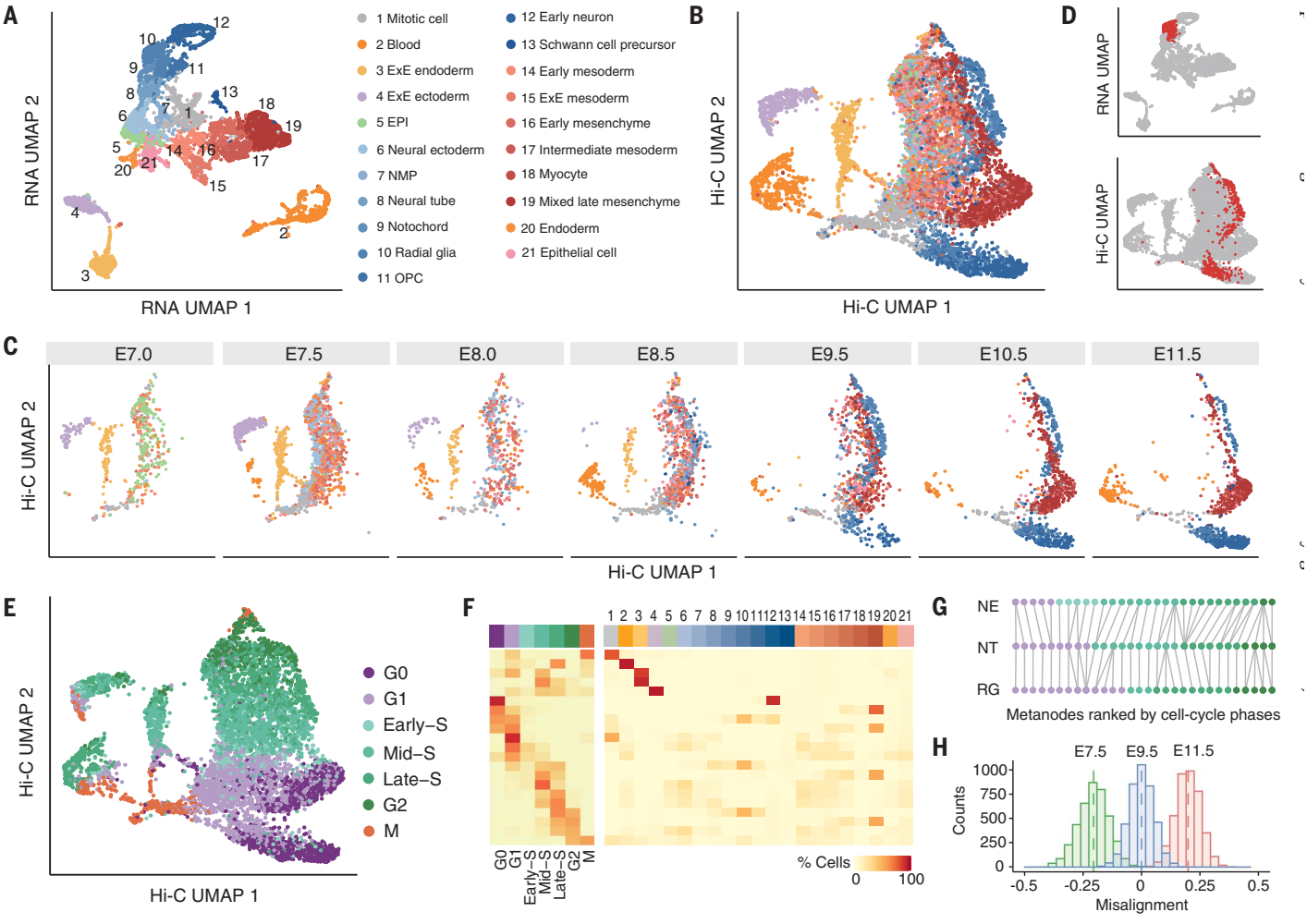


Fig. 2. 3D genome specification during mouse embryonic development. (**A**) UMAP of single-cell transcriptomes of mouse embryos. ExE, extra-embryonic; EPI, epiblast and primitive streak; NMP, neuromesodermal progenitor; OPC, oligodendrocyte precursor cell. (**B**) UMAP of single-cell 3D genomes of mouse embryos. Colors for cell types are the same as in (A). (**C**) UMAPs of single-cell 3D genomes shown by developmental stages. (**D**) Clusters of radial glia highlighted on the RNA (top) and Hi-C (bottom) UMAPs. (**E**) UMAP of single-cell 3D genomes colored by cell-cycle phases. (**F**) Heatmap showing the proportion of cells in the 3D genome clusters that overlapped with clusters defined by the cell cycle or RNA. The numbering for RNA cell types is the same as in (A). (**G**) Alignment of cell-cycle orders among different cell types. NE, neural ectoderm; NT, neural tube; RG, radial glia. (**H**) Misalignment of cell-cycle phases quantified by the difference of cell-cycle ordering for cells from E9.5 versus cells from E7.5, E9.5, and E11.5 (*9*).

Linking differential chromatin interactions to gene expression

Next, we sought to quantitatively investigate cell type–specific differential interactions (DIs) independent of predefined 3D genomic features. The identification of DIs from bulk Hi-C data is challenging because of the high technical noise caused by proximity ligation and the limited number of biological replicates (*33*). We reasoned that using single-cell data could improve the detection sensitivity and accuracy, because each cell could be treated as an independent sample, providing higher statistical power. However, single-cell Hi-C data are extremely sparse at kilobase resolution. To address this issue, we devised the SimpleDiff pipeline (*9*). Instead of using single-cell contact frequencies, SimpleDiff calculates the 3D distance of pairwise genomic loci based on the reconstructed single-cell whole-genome structure and applies a Wilcoxon test to identify DIs between two groups of cells (fig. S8A).

We first tested SimpleDiff on the HiRES dataset between two clusters of excitatory and inhibitory neurons from the adult mouse brains. SimpleDiff identified 123,728 DIs with a false discovery rate (FDR) <5% from 4,849,385 pairs of 20-kb genomic bins. By contrast, no DI was identified with 40 rounds of searching between two groups of cells randomly selected within the same cell type.

The 1D genomic distance between DI anchors peaked around 400 kb, with 24,815 (20%) long-range interactions spanning >1 Mb (fig. S8B). DIs were significantly enriched for cell type–specific marker genes (chi-square test, $P < 2.2 \times 10^{-16}$), especially for top-ranked DIs (fig. S8C). For example, SATB2 is a marker gene with a promoter that was found to form a chromatin loop in human excitatory neurons (*34*). SimpleDiff identified a very similar looping structure specific to excitatory neurons at the mouse Satb2 locus (fig. S8D). DIs overlapping with marker genes tended to show weaker interactions in the corresponding cell type (fig. S8E), which could be partially explained by the recent discovery of "domain melting" in the mouse brain (fig. S8, F to H) (*35*). These results suggested that SimpleDiff identifies DIs at various levels of chromatin organization with high confidence.

We then applied SimpleDiff to the embryonic population of HiRES data. Instead of evaluating DIs between two cell types, we implemented the method in a one-versus-rest manner, similar to the identification of marker genes using single-cell RNA-seq data. A total of 2,861,012 DIs were identified from 17 RNA-defined cell types (Fig. 3, A and B, and fig. S9A), with no significant DI found from a group of randomly selected cells. Early neurons and mixed late mesenchyme showed the highest number of DIs among all cell types, consistent with the distinct clustering of these two cell types on the structural UMAP.

Many DIs were identified from early-stage cell types that were indistinguishable on the structural UMAP. To determine whether these DIs were related to cell functions, we selected the top up-regulated DIs with a cutoff for the difference of interaction strength and performed GREAT analysis. Top up-regulated

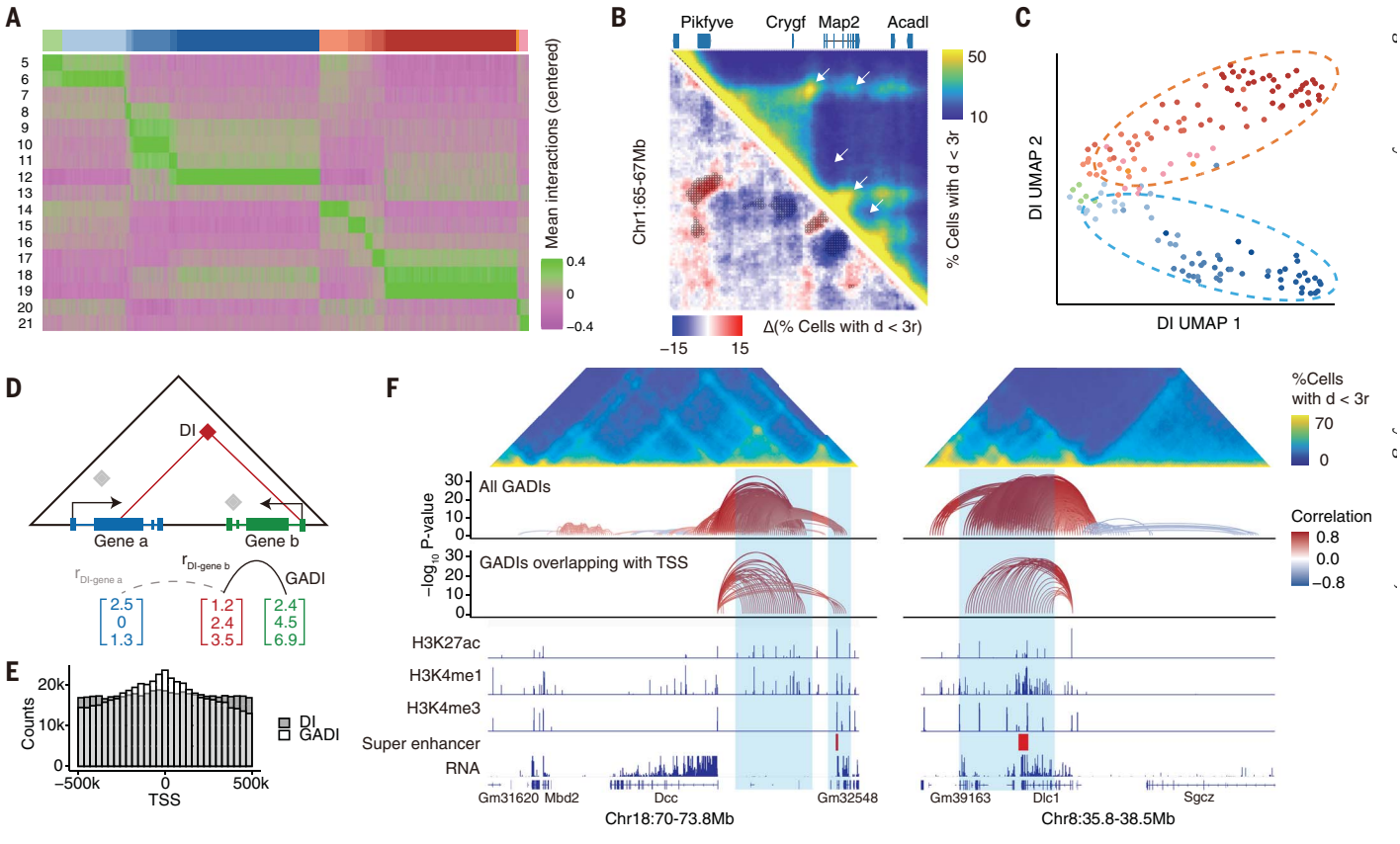


Fig. 3. Linking cell type–specific chromatin interactions to gene expression. (**A**) Heatmap showing representative DIs for mouse embryonic cell types. For visualization purposes, only the top 5% of DIs with increased interaction strength for each cell type are shown. (**B**) Example DIs identified from early neurons. White arrows indicate major regions containing DIs on the 3D proximity map (top). Circles denote top DIs on the 3D difference map (bottom). (**C**) UMAP clustering of metacells based on aggregated DI profiles. Dashed circles indicate the neural ectoderm (blue) and the mesoderm (orange) lineage. (**D**) Schematic depicting the computational framework to link DIs with gene expression. (**E**) Distribution of GADI or DI anchors around TSS regions. GADIs were calculated only on linked genes. DIs were calculated on all genes located within ± 500 kb from either anchor of 100,000 randomly selected DIs. (**F**) Example GADIs linking to Dcc (left) or Dlc1 (right). 3D proximity maps are shown at the top. Each GADI is represented by an arc connecting its two anchors, with the coloring indicating its correlation with gene expression.

DIs were enriched for Gene Ontology terms relevant to the specialized cell types, such as "neuron differentiation" in neural ectoderm and "heart development" in early mesoderm (fig. S9B). This result suggests that despite the fact that chromatin architecture is globally similar for different tissues during early development (*23*, *36*), local rewiring of chromatin interactions is highly cell-type specific and closely related to cell function.

Nevertheless, clustering using the top DI profiles still could not resolve cell types from early developmental lineages (fig. S9C) for two possible reasons: (i) the dynamic nature of the 3D genome made chromatin interactions extremely stochastic in single cells and (ii) the considerable chromatin reorganization associated with the cell cycle predominated the cell type–specific chromatin features, even for G_1 and G_0 cells, most of which were still undergoing continuous chromatin conformational changes after mitosis (fig. S9D). We reasoned that these issues could be solved by combining single cells with similar expression profiles into "metacells," because the cell cycle is much less associated with changes of marker gene expression. Indeed, aggregated metacell DI profiles corresponding to the same cell types clustered together (Fig. 3C), suggesting that co-assay of single-cell RNA-seq can be leveraged to overcome the intrinsic noise of single-cell Hi-C data.

Transcription activity is often accompanied by changing of long-range chromatin interactions that are thousands of base pairs away from the gene (*37*). It is therefore challenging to study the relationship between the formation of chromatin interactions and gene expression. The relatively low noise of metacells enabled us to directly link DIs to their relevant genes on the basis of the covariation of chromatin interactions and gene expression (Fig. 3D). Using the embryonic top DIs and gene expression profiles, we identified 390,252 significant DI-gene associations (FDR <1%), involving 1955 genes and 223,607 DIs, which we refer to as gene-associated DIs (GADIs) (fig. S10A). As a control, only one association was identified using metacells with randomly shuffled expression profiles, suggesting that our method controlled false positives fairly well.

As expected, GADI-linked genes were significantly enriched for cell type–specific marker genes (chi-square test, $P < 2.2 \times 10^{-16}$) (fig. S10B). On average, each gene was associated with a median of 117 GADIs (fig. S10C), and most GADIs (61%) were associated with one single gene. A small portion of GADIs (2.6%) was linked with more than five genes, many of which were from the Hox and Protocadherin gene clusters (fig. S10D). Compared with DIs, GADIs were highly enriched around transcription start sites (TSSs) (Fig. 3E). A majority (69.5%) of GADIs with anchors that overlapped with TSSs showed a positive correlation between interaction strength and gene activity (fig. S10E), consistent with the recent discovery of super-interactive promoters in the developing human brain (*38*). These interactions often linked promoters with distal regulatory elements, including superenhancers (Fig. 3F). As validation, we compared our results with recent reports at two different genetic loci, Zic1/Zic4 and Mir9-2, where functional enhancer-promoter connections were experimentally verified in vivo (*39*). At both loci, we identified GADIs containing enhancer-promoter interactions, which was consistent with other reports (fig. S10F). Therefore, GADIs do not just represent chromatin rewiring in association with transcriptional changes, but also indicate potential enhancer-promoter interactions that underlie cell type–specific gene expression control. Such "gained" enhancer-promoter interactions associated with gene expression have been observed previously (*19*, *40*–*42*); however, it has been challenging to determine their cause-consequence relationship because of the low temporal resolution of bulk studies.

Widespread chromatin interactions rewire before transcription activation

Having linked chromatin interactions to specific genes with GADIs, we were now able to compare the pseudotemporal dynamics of chromatin conformation with transcription at high resolution. We first recovered two embryonic differentiation trajectories, the early neuron trajectory and the mixed late mesenchyme trajectory (fig. S11, A and B) (*43*). We then calculated a "residual" for each GADI-gene pair, defined as the difference of the GADI interaction strength and the expression level from the same metacell, similarly as in the "chromatin potential" approach (*44*), and performed a one-sample *t* test using all metacells along the trajectory to determine whether the residual was significantly deviated from zero (fig. S11C).

From 725 marker genes specifically expressed in early neurons and mixed late mesenchyme, we tested 189,993 GADI-gene pairs. We found that although most chromatin interactions changed concomitantly with gene expression, 40,990 (21.6%) GADI-gene pairs (covering 315 genes) exhibited residuals significantly larger than zero, representing chromatin interactions rewired before transcriptional changes (Fig. 4A and fig. S11D). Most of these prior GADIs (29,858, 72.8%, covering 283 genes) showed positive correlation with gene expression. We also identified a small portion of chromatin interactions (5.1%, covering 9720 GADIs and 98 genes) that changed after transcription (fig. S11E). Genes with nonconcomitant GADIs showed a similar distribution of genetic distance (a median of 300 kb to the closest GADI gene) compared with genes with concomitant GADIs (fig. S11F). In addition, the anchors of nonconcomitant GADIs were not more enriched on other nearby genes (fig. S11G), suggesting that the nonconcomitant changing of chromatin organization and gene expression was unlikely driven by the expression of proximal genes.

To investigate mechanisms leading to the residuals, we analyzed the distribution of tissue-specific ATAC-seq (assay for transposase-accessible chromatin using sequencing) and ChIP-seq (chromatin immunoprecipitation followed by sequencing) signals on these chromatin interactions. In the mixed late mesenchyme lineage, we found that interactions that changed before gene expression were strongly enriched for chromatin signatures of active enhancers regardless of the correlation between GADI interaction strength and gene activity (Fig. 4C and fig. S12A). The negative correlations of prior GADIs could have been caused by a decreased enhancer-promoter proximity upon gene activation, as observed at the mouse Shh locus recently (*45*) and as reflected in our reconstructed single-cell whole-genome structures (fig. S12B). In the early neuron lineage, we observed the opposite result between positive and negative correlations. In particular, only GADIs that were positively correlated with transcription showed similar enrichment of enhancer markers on the interactions that changed before gene expression. By contrast, GADIs that were negatively correlated with transcription were enriched for heterochromatin markers and B-B compartment interactions (Fig. 4C and fig. S13A). These interactions were depleted from TSSs and enriched on gene bodies and flanking regions (fig. S13B). Furthermore, we found that the corresponding neuronal genes (defined as genes with >20 negatively correlated prior GADIs) were generally located in a more silent chromosome environment (fig. S13, C and D). To confirm this observation, we analyzed previously published data obtained during mouse neural differentiation (*19*), and found a similar change of chromatin conformation before gene expression at the same neuronal gene loci (fig. S13, E and F).

Our data suggest different chromatin dynamics underlying the changes of 3D genome before gene expression (Fig. 4D). First, at most genetic loci, chromatin rewiring before gene expression was mainly established between active chromatin, which was possibly driven by the activation of enhancers. Second, for genes located in a repressed chromatin environment, it was the relaxation of the condensed heterochromatin that occurred before transcription activation. These two processes were not mutually exclusive and might coexist on the same genes. Although understanding the detailed molecular mechanisms behind these processes will require further experiments,

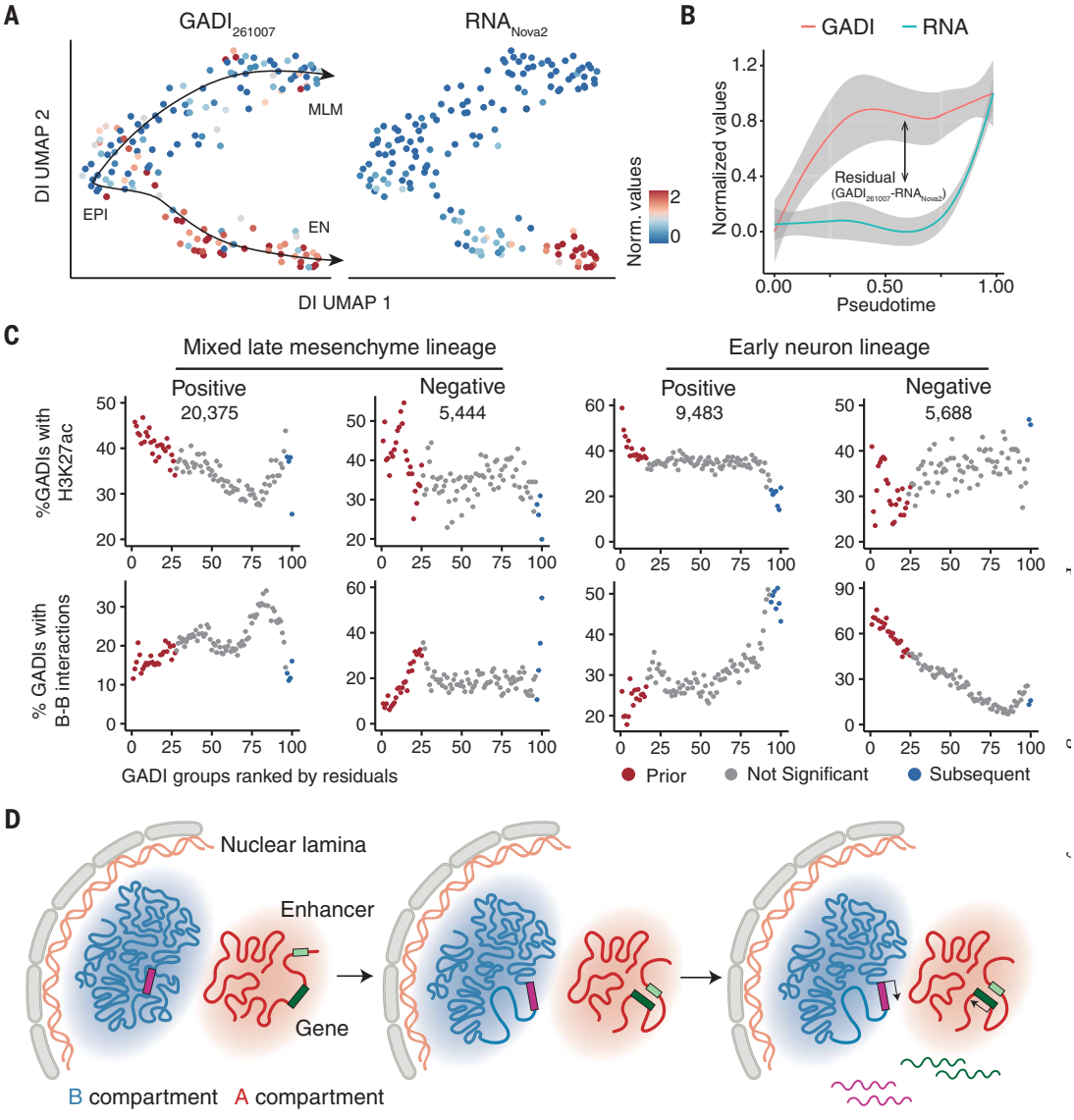


Fig. 4. Widespread chromatin interactions rewired before transcription activation. (**A**) Pseudotemporal dynamics of an individual GADI linked with Nova2 shown on DI UMAP coordinates. EN: early neuron. MLM, mixed late mesenchyme. (**B**) Residuals between $GADI_{261007}$ and Nova2 gene expression along the early neuron trajectory. Shaded areas represent 95% confidence intervals. (**C**) Percentage of GADIs containing H3K27ac signals (top panels) or B-B compartment interactions (bottom panels). GADIs showing positive or negative correlation with mixed late mesenchyme or early neuron marker gene expression were ranked by residuals, respectively, and divided into 100 groups. The numbers of prior GADIs in each group are shown at the top. (**D**) Schematics depicting chromatin reorganizations that occur before transcription activation.

our results have provided strong evidence for the regulatory role of the 3D genome on gene activation.

Discussion

Here, we introduce a highly efficient single-cell multi-omics sequencing method named HiRES for the simultaneous profiling of chromosome conformation and gene expression. Using HiRES, we created a 3D genome and transcriptome atlas of postimplantation mouse embryos and studied the interplay of multiple factors that jointly shape the single-cell 3D genome during development. Our data suggest that the cell cycle is one of the most prominent factors determining the 3D genome of fast-cycling embryonic cells, consistent with previous observations in cell lines (*13*). To characterize chromatin interactions that are differentially established during development, we developed a computational pipeline, SimpleDiff, and identified a large number of DIs closely related to cell functions, even from early developmental lineages in which single-cell contact profiles alone could not resolve cell types. The joint modality data generated by HiRES allow us to perform genome-wide correlation analysis between chromatin interactions and gene expression, which enables a direct linkage between distal genomic loci to their potential target genes. This might be particularly useful for the prediction of enhancer-promoter connections in different cell types when applied together with chromatin state measurements (*46*). Finally, our pseudotemporal analysis reveals that both enhancer-promoter interactions and the decompaction of heterochromatin can contribute to gene expression. Future development of multi-omics approaches incorporating other epigenomic measurements based on HiRES will help to decode the complex processes behind gene activation. Beyond development, we anticipate that our experimental and analytical tools will lead to new insights into the relationship between 3D genome structures and cell functions in both normal and diseased biological samples.

REFERENCES AND NOTES

1. E. E. M. Furlong, M. Levine, *Science* **361**, 1341–1345 (2018).
2. H. Zheng, W. Xie, *Nat. Rev. Mol. Cell Biol.* **20**, 535–550 (2019).
3. A. Hafner, A. Boettiger, *Nat. Rev. Genet.* **24**, 53–68 (2022).
4. L. Tan *et al.*, *Cell* **184**, 741–758.e17 (2021).
5. C. Angermueller *et al.*, *Nat. Methods* **13**, 229–232 (2016).
6. M. Stoeckius *et al.*, *Nat. Methods* **14**, 865–868 (2017).
7. J. Cao *et al.*, *Science* **361**, 1380–1385 (2018).
8. C. Zhu *et al.*, *Nat. Methods* **18**, 283–292 (2021).
9. See the supplementary materials.
10. C. Zong, S. Lu, A. R. Chapman, X. S. Xie, *Science* **338**, 1622–1626 (2012).
11. Y. Zhou *et al.*, *Cancer Cell* **38**, 818–828.e5 (2020).
12. T. J. Stevens *et al.*, *Nature* **544**, 59–64 (2017).
13. T. Nagano *et al.*, *Nature* **547**, 61–67 (2017).
14. L. Tan, D. Xing, C. H. Chang, H. Li, X. S. Xie, *Science* **361**, 924–928 (2018).
15. J. H. Su, P. Zheng, S. S. Kinrot, B. Bintu, X. Zhuang, *Cell* **182**, 1641–1659.e26 (2020).

16. J. E. Phillips-Cremins *et al*., *Cell* **153**, 1281–1295 (2013).
17. J. R. Dixon *et al*., *Nature* **518**, 331–336 (2015).
18. J. Fraser *et al*., *Mol. Syst. Biol.* **11**, 852 (2015).
19. B. Bonev *et al*., *Cell* **171**, 557–572.e24 (2017).
20. T. Stuart *et al*., *Cell* **177**, 1888–1902.e21 (2019).
21. N. Naumova *et al*., *Science* **342**, 948–953 (2013).
22. J. Zhou *et al*., *Proc. Natl. Acad. Sci. U.S.A.* **116**, 14011–14018 (2019).
23. E. Ing-Simmons *et al*., *Nat. Genet.* **53**, 487–499 (2021).
24. S. M. Espinola *et al*., *Nat. Genet.* **53**, 477–486 (2021).
25. A. D. Schmitt *et al*., *Cell Rep.* **17**, 2042–2059 (2016).
26. K. Abramo *et al*., *Nat. Cell Biol.* **21**, 1393–1402 (2019).
27. H. Zhang *et al*., *Nature* **576**, 158–162 (2019).
28. M. A. Ciemerych, P. Sicinski, *Oncogene* **24**, 2877–2898 (2005).
29. A. Alpert, L. S. Moore, T. Dubovik, S. S. Shen-Orr, *Nat. Methods* **15**, 267–270 (2018).
30. B. D. Pope *et al*., *Nature* **515**, 402–405 (2014).
31. V. Dileep *et al*., *Genome Res.* **25**, 1104–1113 (2015).
32. K. N. Klein *et al*., *Science* **372**, 371–378 (2021).
33. A. T. Lun, G. K. Smyth, *BMC Bioinformatics* **16**, 258 (2015).
34. D. S. Lee *et al*., *Nat. Methods* **16**, 999–1006 (2019).
35. W. Winick-Ng *et al*., *Nature* **599**, 684–691 (2021).
36. Y. Zhang *et al*., *Nat. Genet.* **50**, 96–105 (2018).
37. S. Schoenfelder, P. Fraser, *Nat. Rev. Genet.* **20**, 437–455 (2019).
38. M. Song *et al*., *Nature* **587**, 644–649 (2020).
39. Z. Chen *et al*., bioRxiv (2022).
40. A. J. Rubin *et al*., *Nat. Genet.* **49**, 1522–1528 (2017).
41. W. W. Greenwald *et al*., *Nat. Commun.* **10**, 1054 (2019).
42. A. M. Oudelaar *et al*., *Nat. Commun.* **11**, 2722 (2020).
43. M. Setty *et al*., *Nat. Biotechnol.* **37**, 451–460 (2019).
44. S. Ma *et al*., *Cell* **183**, 1103–1116.e20 (2020).
45. N. S. Benabdallah *et al*., *Mol. Cell* **76**, 473–484.e7 (2019).
46. C. P. Fulco *et al*., *Nat. Genet.* **51**, 1664–1669 (2019).
47. Z. Liu, Y. Chi, M. Liu, Custom scripts for: Linking genome structures to functions by simultaneous single-cell Hi-C and RNA-seq, Zenodo (2023); https://doi.org/10.5281/zenodo.7691903.

ACKNOWLEDGMENTS

We thank S. Gao (China Agricultural University) for help with animal experiments, H. Ge (Peking University) for advice on statistical analyses of data, and L. Tan (Stanford University) for helpful discussions regarding the manuscript. **Funding:** This work was supported by the Ministry of Science and Technology of China (grant STI2030-Major Projects 2021ZD0202502), the National Natural Science Foundation of China (grant 92049110), the Fundamental Research Funds for the Central Universities (Clinical Medicine Plus X Young Scholars Project, Peking University), and the Beijing Advanced Innovation Center for Genomics (ICG). **Author contributions:** Z.L., Y.Chen, and D.X. designed the experiments. Y.Chen performed the experiments and collected the data. Z.L. and D.X. analyzed the data. Q.X. harvested the animal tissue. M.L. and Y.Chi helped with data analysis. H.X. and Y.D. helped with the experiments. Z.L., Y.Chen, M.L., and D.X. prepared the manuscript. D.X. managed and supervised the project. **Competing interests:** D.X., Y.Chen, and Z.L. are investors on a patent that covers HiRES. The remaining authors declare no competing interests. **Data and materials availability:** Raw sequencing data have been deposited at the Sequence Read Archive database (BioProject accession no. PRJNA907173). Processed data have been deposited at the Gene Expression Omnibus (accession no. GSE223917). Code is available at Zenodo (*47*). **License information:** Copyright © 2023 the authors, some rights reserved; exclusive licensee American Association for the Advancement of Science. No claim to original US government works. https://www.science.org/about/science-licenses-journal-article-reuse

SUPPLEMENTARY MATERIALS

science.org/doi/10.1126/science.adg3797
Materials and Methods
Figs. S1 to S13
Tables S1 and S2
References (*48*–*59*)
MDAR Reproducibility Checklist

View/request a protocol for this paper from *Bio-protocol*.

Submitted 21 December 2022; accepted 7 May 2023
10.1126/science.adg3797

PALEOECOLOGY

Plio-Pleistocene African megaherbivore losses associated with community biomass restructuring

Faysal Bibi[1]* and Juan L. Cantalapiedra[2]

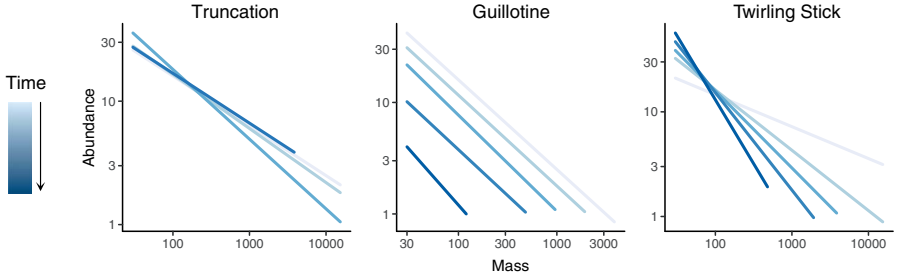
Fossil abundance data can reveal ecological dynamics underpinning taxonomic declines. Using fossil dental metrics, we reconstructed body mass and mass–abundance distributions in Late Miocene to recent African large mammal communities. Despite collection biases, fossil and extant mass–abundance distributions are highly similar, with unimodal distributions likely reflecting savanna environments. Above 45 kilograms, abundance decreases exponentially with mass, with slopes close to −0.75, as predicted by metabolic scaling. Furthermore, communities before ~4 million years ago had considerably more large-sized individuals, with a greater proportion of total biomass allocated in larger size categories, than did later communities. Over time, individuals and biomass were redistributed into smaller size categories, reflecting a gradual loss of large-sized individuals from the fossil record paralleling the long-term decline of Plio-Pleistocene large mammal diversity.

Since at least the early 19th century, the cause of Quaternary megafaunal extinctions has been the subject of much speculation and inquiry (*1*). A strong case for anthropogenic causes has been made on the basis of the coincidence of human arrivals and extinctions in many parts of the world (*2*–*5*). In Africa, hominins and large herbivores coexisted for millions of years, and African megafaunal extinctions were initially thought to have been subdued as a result of coevolution between hominins and their prey (*2*, *3*). However, recent work has shown that the number of large mammal extinctions in Africa did in fact rival that on other continents and that megafaunal losses there began far deeper in the past than previously recognized, starting earlier than 4 million years ago (Ma) (*6*). Because the earliest records of hominin tool use (and presumably butchery) only date back to 3.3 Ma (*7*) and because evidence for active hunting or increased carnivory during the Early or Middle Pleistocene is lacking (*8*, *9*), the early initiation of megafaunal losses argues strongly against an anthropogenic driver for these extinctions. Environmental scenarios, namely a long-term decrease in CO_2 and the expansion of C_4 grasslands, with resulting losses of large-bodied browsers and mixed feeders, have been proposed as causal factors (*6*, *10*). Additionally, genomic evidence has revealed major population declines during the Middle to Late Pleistocene among many extant large mammal species (*11*), indicating that diversity losses were even greater than previously discerned from the fossil record. Questions remain as to the cause and mechanism of these extinctions and extirpations. One limitation to answering such questions is that studies to date have been largely taxonomically based, tabulating species or genus losses with respect to known events in paleoclimate or hominin evolutionary history. In contrast, approaches that tabulate traits at the specimen level require only minimal taxonomic information and provide additional analytical sensitivity by incorporating relative abundance data, which permits the examination of ecological dynamics below the species level.

Fossil mass, abundance, and biomass estimates

We analyzed changes in the body mass structure of late Neogene to recent African large mammal communities using a specimen-based approach. We examined the mass–abundance distributions of individuals in fossil and ex… communities, and compared these to the … tionship, well established across eukaryotes (*12*), of decreasing abundance per unit area (i.e., density) with increasing body size. Damuth (*13*, *14*) observed that average population density (N) scales to body mass (M) as $N = M^{-0.75}$ and that, because individual metabolic rates (MR) scale to body mass as $MR = M^{0.75}$, the energy consumed by a population ($E = N \times MR$) is independent of its body mass ($E = M^0$, also called "energetic equivalence"). In turn, the biomass (B) of a population is $B = N \times M$, which equates to $B = M^{0.25}$. This "metabolic scaling" rule explains why larger species within a single trophic level have exponentially lower population densities in comparison with smaller ones and why larger species can pack more biomass for each unit of energy extracted from the preceding trophic level (fig. S1). More specifically, metabolic scaling predicts that, within a single trophic level or taxonomic scale, abundance should scale to mass raised to an exponent of −0.75 and biomass should scale to mass raised to an exponent of 0.25 (*15*).

Despite extensive examination in ecology, mass–abundance relationships have not been widely investigated in the fossil record. We sought to determine whether the fossil record of African large mammals follows predictions of metabolic scaling and whether changes in mass–abundance distributions have occurred over time in parallel with the long-term decline of megaherbivore diversity (*6*). Specifically, we used fossil community mass–abundance distributions to test among three competing scenarios of megafaunal loss and community



	Truncation	Guillotine	Twirling Stick
Description	Decreasing abundance then loss of largest individuals	Decreasing abundance of all sizes with loss of largest individuals first	Decreasing abundance of larger individuals, increasing abundance of smaller individuals
Possible Cause	Hunting of large individuals	Decrease in primary productivity	Vegetation change causing larger sizes to be relatively less efficient at converting energy to biomass
Expectations	Increasingly negative slope returning to initial value after loss of targeted size category	Constant slope with decreasing y-intercept (if absolute abundance can be measured)	Decreasing slope values

Fig. 1. Three scenarios describing changes in mass–abundance distributions as a result of megaherbivore losses due to different causes. Abundance can be measured as either relative or absolute for the truncation and twirling stick models but must be absolute to observe a decreasing *y*-intercept in the guillotine model. The twirling stick model is the only one that predicts a long-term change in slope.

[1]Museum für Naturkunde, Leibniz Institute for Evolution and Biodiversity Science, 10115 Berlin, Germany. [2]GloCEE–Global Change Ecology and Evolution Research Group, Department of Life Sciences, Universidad de Alcalá, 28805 Alcalá de Henares, Madrid, Spain.
*Corresponding author. Email: faysal.bibi@mfn.berlin

structure alteration (Fig. 1): (i) Under a scenario of human hunters targeting the largest species ("downsizing"), the relationship between mass and abundance becomes more negative as the proportion of large individuals decreases, then the slope rebounds back to its original value when the targeted mass category is extirpated. The result is a community that displays the same mass–abundance slope but a mass–abundance distribution that is truncated at the larger end (Fig. 1A, "truncation model"). (ii) Under a scenario of decreasing resources, the total biomass of a community decreases, affecting species of all sizes equally. Larger species, already less abundant, will be the first to disappear as the carrying capacity shrinks, particularly as their decreasing population densities render them more and more vulnerable to stochastic processes and extinction vortexes (*16*) (Fig. 1B, "guillotine model"). The result is a community with an unchanged mass–abundance slope but decreased total abundance and a loss of the largest individuals. (iii) Under a third scenario, the quality and/or distribution of resources shifts in a way that disrupts the ability of larger individuals to extract energy and provides a competitive advantage to smaller individuals. Biomass is then redistributed toward smaller size categories, and mass–abundance slopes become more negative over time, reflecting progressively decreasing abundance, and eventual extinction, of larger size categories (Fig. 1C, "twirling stick model"). These scenarios are obviously not exhaustive, but they do address three common causal hypotheses—anthropogenic downsizing, productivity loss, and resource reallocation.

To test among these scenarios, we used specimen and metric data from a newly assembled compilation of mammalian dental metrics (*17*). Selecting premolars and molars of extant and fossil Artiodactyla, Perissodactyla, Proboscidea, and Primates, we used the relationship between tooth length and average species mass in extant species (*18*) to estimate body mass for fossil specimens and reconstruct the mass–abundance and mass–biomass distributions of extant and fossil communities (figs. S2 to S4). Our final fossil dataset consisted of 7430 specimens from 61 communities mainly covering Africa but including data from the Arabian subcontinent as well (table S2). Abundance data for 39 extant communities came from Hatton *et al.* (*12*), whose work mainly covers Africa, but also includes a few Indian and South American communities (table S3). These are largely from savanna habitats (e.g., grasslands, shrublands, and woodlands), with a small number of tropical forest habitats as well. Additionally, a compilation of 39 African communities based on census data was made for this study (table S4). Sensitivity analyses were also conducted to assess the robustness of our results to different mass-estimation approaches and to varying data-selection criteria (*19*).

Changing abundance and biomass structure since 4 Ma

We found that mass–abundance distributions in the African fossil record are similar to those of extant communities (Fig. 2 and figs. S5 to S8). Our results indicate that similar fundamental processes underlie mass–abundance relationships in both extant and fossil communities and that these are detectable in the fossil record despite taphonomic, collection, and publication biases. A similar finding was recently demonstrated for species abundances in zoological museum collections (*20*). In comparison with extant communities, however, fossil communities include a greater proportion of large individuals and occasionally individuals estimated to weigh >10 metric tons (the largest African elephants today weigh ~6 tons) (Fig. 2A and fig. S7). Sensitivity tests using different mass-estimation approaches and various subsets of the data gave similar results (figs. S10 to S15) (*19*).

Extant and fossil large herbivore communities are far less abundant, with far less biomass occupied, in the 5 to 45 kg range than predicted by metabolic scaling. Instead of a mass–abundance relationship that is log-linear with a slope around −0.75, communities exhibit unimodal distributions, with peak abundances in the 45 to 405 kg mass range (Fig. 2 and figs. S6 to S8). This reflects the lack of small arboreal primates and forest antelopes in savanna habitats, from which most of our extant and probably all of our fossil

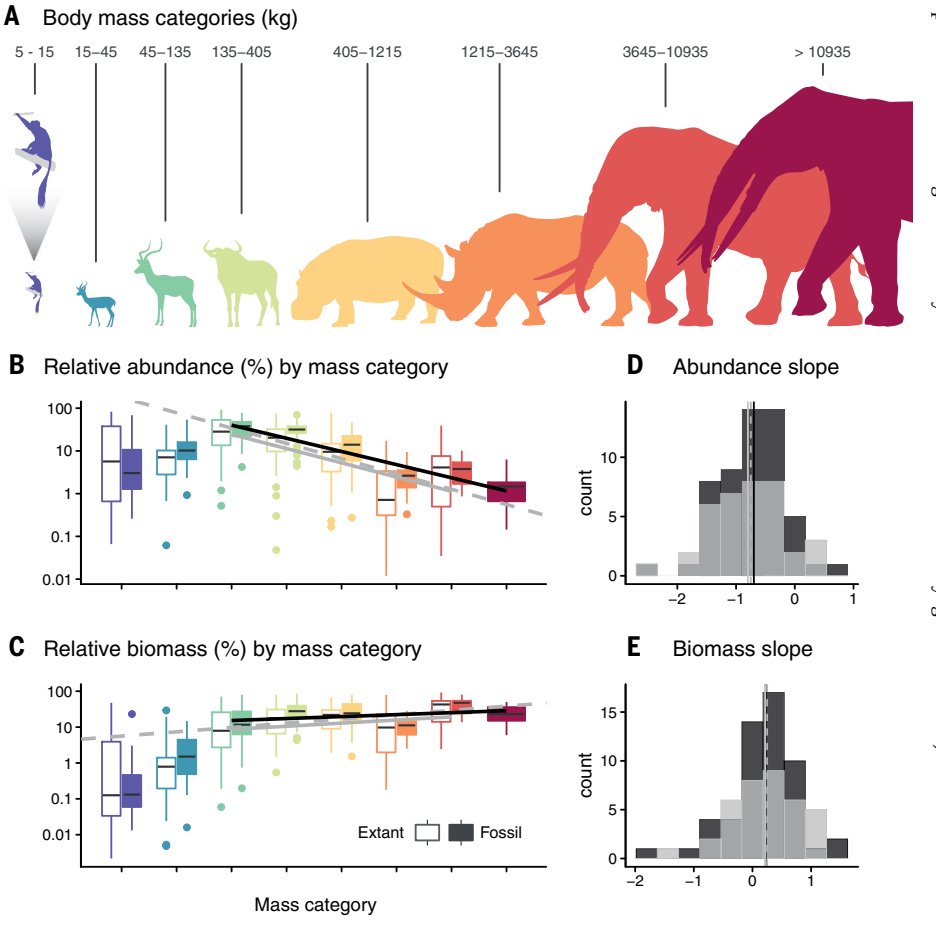


Fig. 2. Individual mass–abundance and mass–biomass distributions in fossil and extant large mammal communities are similar. (**A**) Body mass categories with representative taxa to scale (the monkey is enlarged for clarity). In both fossil and extant communities, mass–abundance (**B**) and mass–biomass (**C**) distributions above 45 kg (solid lines) follow predictions of metabolic scaling [dashed gray lines, slopes of −0.75 (B) and 0.25 (C); *y*-intercept is arbitrary]. Below 45 kg, abundance and biomass are less than predicted by metabolic scaling, likely reflecting savanna habitats. The greater variance of the 5 to 15 kg category in the extant data is due to the inclusion of a few forest communities. Note that *y* axes in (B) and (C) are log-scaled. Boxplot whiskers extend to the value no further than 1.5 times the interquartile range from the box. (**D** and **E**) Distribution of mass–abundance (D) and mass–biomass (E) slope values in fossil and extant communities (>45 kg) are similar, with median values (solid vertical lines) close to expectations of metabolic scaling (dashed vertical lines).

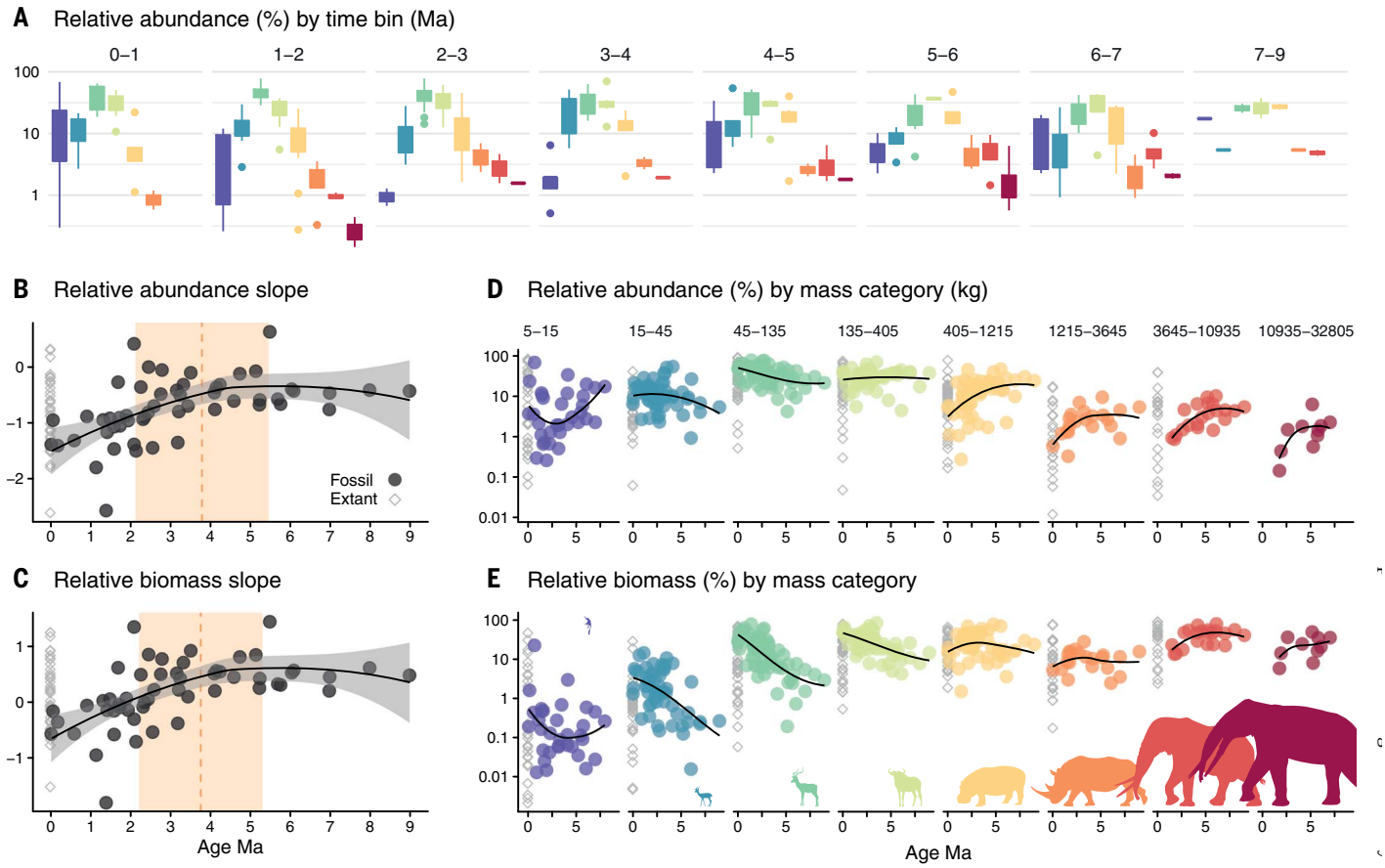


Fig. 3. Changes in mass–abundance and mass–biomass distributions over time. Data points are communities. (**A**) Mass–abundance distributions for fossil communities grouped by time bin. (**B** and **C**) Mass–abundance and mass–biomass slope values in fossil communities (>45 kg) decrease over time, reflecting major changes in community size structure starting ~4 Ma. Orange vertical lines and shaded areas indicate breakpoint medians and their 95% confidence intervals. (**D** and **E**) Relative abundance and biomass occupied by each size class over time [same data as (A)]. Note the decreases in the largest sizes and increases in smaller sizes over time, which explains the steepening slope values in (B) and (C). Lines of fit (loess) are calculated using fossil data only.

communities were sampled. In contrast, extant forest communities show peak abundance at 5 to 45 kg and effectively log-linear relationships (figs. S7 and S9B). When considering only individuals of >45 kg and communities that have at least three size categories occupied (n = 54 fossil and 37 extant communities), mass–abundance relationships abide by predictions of metabolic scaling, with slopes close to −0.75 (medians and 95% quantiles: −0.70, −1.48 to −0.03 for fossil; −0.80, −1.76 to 0.20 for extant), and biomass–abundance slopes of ~0.25 (0.23, −0.62 to 0.88 for fossil; 0.22, −0.69 to 1.20 for extant) (Fig. 2, D and E).

Between the Late Miocene and the Late Pleistocene, there was a reallocation of biomass toward smaller size categories (Fig. 3). Fossil communities experienced a protracted loss of individuals larger than 400 kg starting in the Pliocene, as reflected by increasingly negative mass–abundance and mass–biomass slopes. Akaike information criterion (AIC) values favored a breakpoint at 3.8 Ma for both abundance and biomass (95% confidence intervals: 5.5 to 2.1 Ma and 5.3 to 2.2 Ma, respectively) over a linear model of decrease (difference of >2 AIC units), whereas a Davies test (which tests for a nonconstant regression parameter) was of borderline significance (P = 0.07 and 0.04 for abundance and biomass, respectively). The breakpoint model, however, was neither favored nor significant compared with a linear model in sensitivity analyses (figs. S11 and S15), so the mode of biomass restructuring over time should probably be revisited with a larger dataset. For the time being, our results correspond with the statistically significant 4.6 Ma (5.9 to 3.3 Ma) breakpoint previously identified for megaherbivore diversity decrease (*6*), as well as with Pliocene breakpoints in multiple environmental proxy records (Fig. 4).

Further examination of the temporal trend by mass category revealed major losses of individuals larger than 400 kg since the latest Miocene or Early Pliocene (Fig. 3D). These losses were accompanied by abundance increases or stasis in the 5 to 405 kg mass range (Fig. 3E). A principal components analysis confirms that the increase in the relative abundance of the 45 to 135 kg mass categories, and decrease in all other categories, was a major driver of differences over time (figs. S7 and S8). Our findings confirm the long-term pattern of megafaunal loss and community restructuring previously described by Faith *et al.* (*6*, *21*) and indicate continuous and fundamental changes to the distribution of biomass in African large mammal communities over the past 4 million years or more. This result is robust with regard to different sensitivity analyses (*19*). In terms of our hypothetical scenarios, our results falsify both the truncation and guillotine models, which predict stable mass–abundance slopes, and support the twirling stick model, which predicts progressive changes in slopes over time (Fig. 1).

Extinction accelerated by primary productivity loss

The loss of large-sized individuals in the African fossil record coincided with a decrease in global temperature and, in eastern Africa, with the loss of wooded habitats and the expansion of C_4 grasslands (*22*–*24*), all of which also show statistically significant breakpoints between

~2 and 5 Ma (Fig. 4, C to E). Previous studies have also argued for decreasing atmospheric CO_2 and increasing African aridity at this time, although different proxies have provided conflicting signals in these regards [e.g., (*25*, *26*) and references therein]. Just how paleoenvironmental changes may have led to the observed changes in taxonomic and functional community structure, including those presented here, is still open to debate. Today, interactions between mammalian herbivores and their physical environments are largely mediated through the plants they consume, such that large mammal herbivore biomass is strongly positively correlated with net primary productivity (NPP) (*27*). Major decreases in NPP since the Late Miocene have previously been recorded in both North America and Europe (*28*, *29*), suggesting a global pattern. Such NPP losses could have considerably diminished the total biomass (carrying capacity) of large mammal communities, thereby reducing diversity and causing megafaunal extinctions following the guillotine model. To determine whether African NPP also decreased since the Late Miocene, we used an established correlation between mammalian community dental morphology and NPP in the present day (*30*, *31*) to estimate NPP in African fossil communities. We found that NPP in the African Late Miocene and Early Pliocene was, on average, around three times higher than levels measured today (Fig. 4B). A progressive drop in average NPP began in the Early Pliocene (breakpoint at 4.1 ± 0.78 Ma) and continued to recent times, paralleling the losses in megafaunal abundance and biomass noted above. Although they cannot explain the observed changes in mass–abundance distributions (i.e., slopes), such losses in NPP might have reduced mammalian species richness and accelerated the extinction of the largest size categories (guillotine model) during the Pliocene and Pleistocene [we found no significant relationship between NPP (*32*) and mass–abundance or mass–biomass slopes in extant communities (fig. S16)]. Our finding of decreasing mass–abundance slopes in conjunction with losses in NPP therefore suggests a variant of the twirling stick model that incorporates both biomass reallocation (the exact cause of which remains unknown) and losses in total carrying capacity (i.e., decreasing slope and intercept) over the past ~4 million years.

Several aspects of our conclusions could be further tested. The declines in NPP, for example, are based on the mammalian record, and an independent proxy for paleo-NPP would be welcome to confirm the declining trend. Also needed are improvements of climatic proxy records for global paleo-CO_2 and also regional and local vegetation structure, temperature, seasonality, and aridity indices since Late Miocene times. Finally, further work should attempt to more clearly determine the relationships between NPP and biomass distributions in extant communities, despite wholesale alteration of terrestrial ecosystems by humans (*27*). Through such approaches, the proposed link between climatic changes, decreasing productivity, and the global loss of megafauna during the Plio-Pleistocene may be strengthened, potentially also explaining the large declines in Pleistocene population sizes observed in genomes of surviving large mammal species (*11*). Our study supports a growing body of evidence that the effects of Pleistocene human overkill (well documented in several contexts, especially islands, and especially since 15,000 years ago) (*33*) would have come on top of long-term declines in megafaunal abundance caused by environmental changes. Further work should determine whether the patterns

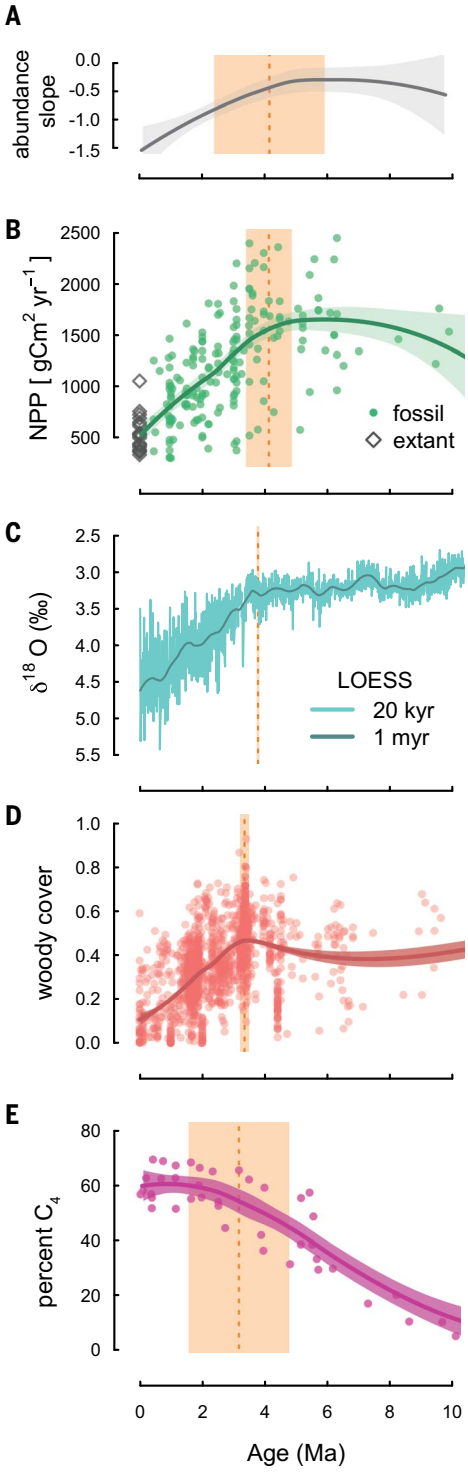


Fig. 4. Environmental context of African megafaunal losses. (**A**) Large mammal community mass–abundance slopes over time (same as Fig. 3C). (**B**) Changes in net primary productivity over time, estimated using dental morphology of mammalian molars from 192 African paleocommunities (*31*) and 23 extant African communities (*12*), assessed at the species level. Data suggest a loss of roughly two-thirds of net primary productivity since ~4 Ma. (**C**) Global marine stable oxygen isotope curves show decreasing global temperatures after ~4 Ma. kyr, thousand years; myr, million years. (**D**) Stable carbon isotope ratios from eastern African paleosol carbonates (*22*) converted to fraction woody cover (*22*, *34*) show decreasing proportions of tree cover after 4 Ma. (**E**) Terrestrial plant wax biomarkers in marine sediments from the Red Sea and Indian Ocean indicate increasing proportions of C_4 grasses since ~10 Ma (*23*). Orange vertical lines and shaded areas indicate breakpoint medians and their 95% confidence intervals. All breakpoints are statistically significant (i.e., preferred over a linear model) and suggest major environmental changes during the Pliocene, coinciding with community biomass restructuring.

revealed by the African record hold up on other continents as well. Mass–abundance distributions could also provide new insights into size-biased extinctions at other times in Earth's history.

REFERENCES AND NOTES

1. D. K. Grayson, in *Quaternary Extinctions: A Prehistoric Revolution*, P. S. Martin, R. G. Klein, Eds. (Univ. of Arizona Press, 1984), pp. 5–39.
2. L. S. Leakey, *Nature* **212**, 1615–1616 (1966).
3. P. S. Martin, in *Quaternary Extinctions: A Prehistoric Revolution*, P. S. Martin, R. G. Klein, Eds. (Univ. of Arizona Press, 1984), pp. 354–403.
4. S. K. Lyons, F. A. Smith, J. H. Brown, *Evol. Ecol. Res.* **6**, 339–358 (2004).
5. C. Sandom, S. Faurby, B. Sandel, J.-C. Svenning, *Proc. R. Soc. London Ser. B* **281**, 20133254 (2014).
6. J. T. Faith, J. Rowan, A. Du, P. L. Koch, *Science* **362**, 938–941 (2018).
7. S. Harmand *et al*., *Nature* **521**, 310–315 (2015).
8. R. J. Blumenschine, B. L. Pobiner, in *Evolution of the Human Diet: The Known, the Unknown, and the Unknowable*, P. S. Ungar, Ed. (Oxford Univ. Press, 2007), pp. 167–190.
9. W. A. Barr, B. Pobiner, J. Rowan, A. Du, J. T. Faith, *Proc. Natl. Acad. Sci. U.S.A.* **119**, e2115540119 (2022).
10. J. L. Cantalapiedra *et al*., *Nat. Ecol. Evol.* **5**, 1266–1272 (2021).
11. L. Chen *et al*., *Science* **364**, eaav6202 (2019).
12. I. A. Hatton, A. P. Dobson, D. Storch, E. D. Galbraith, M. Loreau, *Proc. Natl. Acad. Sci. U.S.A.* **116**, 21616–21622 (2019).
13. J. Damuth, *Nature* **290**, 699–700 (1981).
14. J. Damuth, *Biol. J. Linn. Soc. Lond.* **31**, 193–246 (1987).
15. R. Trebilco, J. K. Baum, A. K. Salomon, N. K. Dulvy, *Trends Ecol. Evol.* **28**, 423–431 (2013).
16. W. F. Fagan, E. E. Holmes, *Ecol. Lett.* **9**, 51–60 (2006).
17. F. Bibi, The Mammal Dental Metrics Database: A compilation of fossil and extant mammal tooth measurements, Dryad (2023); https://doi.org/10.5061/dryad.69p8cz968.
18. K. E. Jones *et al*., *Ecology* **90**, 2648 (2009).
19. See supplementary materials.
20. N. J. Gotelli *et al*., *Methods Ecol. Evol.*, 2041–210X.13705 (2021).
21. J. T. Faith, J. Rowan, A. Du, *Proc. Natl. Acad. Sci. U.S.A.* **116**, 21478–21483 (2019).
22. N. E. Levin, *Annu. Rev. Earth Planet. Sci.* **43**, 405–429 (2015).
23. K. T. Uno, P. J. Polissar, K. E. Jackson, P. B. deMenocal, *Proc. Natl. Acad. Sci. U.S.A.* **113**, 6355–6363 (2016).
24. T. Westerhold *et al*., *Science* **369**, 1383–1387 (2020).
25. S. A. Blumenthal *et al*., *Proc. Natl. Acad. Sci. U.S.A.* **114**, 7331–7336 (2017).
26. Y. Cui, B. A. Schubert, A. H. Jahren, *Geology* **48**, 888–892 (2020).
27. C. Fløjgaard, P. B. M. Pedersen, C. J. Sandom, J. Svenning, R. Ejrnæs, *J. Appl. Ecol.* **59**, 18–24 (2022).
28. S. A. Fritz *et al*., *Proc. Natl. Acad. Sci. U.S.A.* **113**, 10908–10913 (2016).
29. J. Toivonen, M. Fortelius, I. Žliobaitė, *Proc. R. Soc. London Ser. B* **289**, 20212294 (2022).
30. L. Liu *et al*., *Proc. R. Soc. London Ser. B* **279**, 2793–2799 (2012).
31. The NOW Community, NOW — New and Old Worlds Database of Fossil Mammals, version 1, Zenodo (2020); https://doi.org/10.5281/zenodo.4268068.
32. M. L. Imhoff *et al*., *Nature* **429**, 870–873 (2004).
33. A. D. Barnosky, *Proc. Natl. Acad. Sci. U.S.A.* **105** (suppl. 1), 11543–11548 (2008).
34. T. E. Cerling *et al*., *Nature* **476**, 51–56 (2011).

ACKNOWLEDGMENTS

We thank D. Dahrouj, N. Heckeberg, L. Jansen, and L. Rose for data entry, C. Funk for facilitating access to the mammal collections in the Museum für Naturkunde, members of the Amniota Lab at the Museum für Naturkunde and A. Malo for discussions. **Funding:** This work was supported by German Research Foundation grant 282995372 BI 1879 1/1 (F.B.) and Talent Attraction Program of the Madrid Government grant 2017-T1/AMB5298 (J.L.C.). **Author contributions:** Conceptualization: F.B. Methodology: F.B. and J.L.C. Investigation: F.B. and J.L.C. Visualization: J.L.C. and F.B. Funding acquisition: F.B. and J.L.C. Project administration: F.B. Supervision: F.B. Writing – original draft: F.B. Writing – review & editing: F.B. and J.L.C. **Competing interests:** The authors declare that they have no competing interests. **Data and materials availability:** Data and R scripts to replicate all analyses are available in the supplementary materials and additionally in Dryad (*17*). **License information:** Copyright © 2023 the authors, some rights reserved; exclusive licensee American Association for the Advancement of Science. No claim to original US government works. https://www.science.org/about/science-licenses-journal-article-reuse

SUPPLEMENTARY MATERIALS

science.org/doi/10.1126/science.add8366
Materials and Methods
Figs. S1 to S16
Tables S1 to S4
References (*35–271*)
MDAR Reproducibility Checklist
Data S1 to S5

Submitted 7 July 2022; accepted 10 May 2023
10.1126/science.add8366

WORKING LIFE

By **Jeremy Côté**

Taking the lead

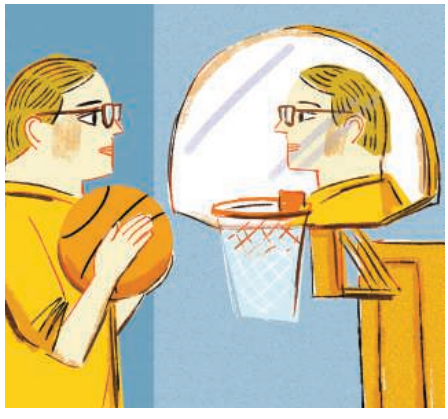
Gazing into the silent, empty gym before practice, I faced reality: I was in charge. Nobody would tell me what to do, and if I failed, nobody would come take over. It was my first practice as a volunteer basketball coach for the local secondary school. I had benefited from volunteer coaches when I was younger, and I was eager to give back to the community. But I worried I had too little experience and knowledge to give the athletes what they would need. What if I taught them nothing useful? What if I was too hard on them? These doubts about my ability to lead were familiar; I had felt them throughout my scientific training.

As an undergraduate research assistant, I carried out meticulous calculations—but with minimal insight into what they meant or how to push the research further. As a master's student, I wrote code for my project—but always within the boundaries of what my supervisor suggested. As an early Ph.D. student, I executed the projects my supervisor gave me—but didn't explore further on my own. At every stage, it was more comfortable to let others lead. I told myself that once I gained more experience and knowledge, I'd be ready to take charge.

That mindset served me well enough through 2 years of my Ph.D. But after wrapping up two research projects, I felt burned out and in need of recharging. I hoped rekindling my love of sports through coaching might help, and I knew the local school was always looking for volunteers who could give a few hours each week. I worried I wouldn't be good enough. But I decided to push past my discomfort, do my best, and learn along the way.

That's how I found myself in that empty gym, excited yet anxious. I had spent hours planning our first practice, reading up on drills to run and thinking about how to create an engaging atmosphere for the athletes. Now, it was time to really put myself to the test.

The athletes trickled in and began shooting around. I watched for a few minutes, collected myself, and began practice with as much energy and enthusiasm as I could muster. Despite my lingering fears, everything went smoothly. The athletes were excited to play and worked hard through the entire session. Afterward, I heard that many of them thought practice was great. That positive feedback—and the fun I had—spurred me on. Maybe I had what it took to lead after all.



"The lessons I was learning as a basketball coach helped me find my footing as a scientific leader."

Around the same time, my Ph.D. supervisor offered me an opportunity to work with a master's student on a project that complemented my work. I would have to be a mentor—and I wasn't sure I could do it. But I decided I couldn't turn down the chance.

My supervisor still supported us, but I had to take more initiative, suggest next steps, and help set the direction for our research, and suggest next steps. These still didn't come naturally. But I found the lessons I was learning as a basketball coach helped me find my footing as a scientific leader, too.

At first, I had thought a coach's job was simply to transfer knowledge. But over time, I realized coaching was so much more. It was how I showed up to each session with a positive outlook, no matter how the rest of my day went. It was how I responded to athletes' feedback, like when one told me I was spending too much time explaining things and not enough time letting them play. And it was how I high-fived each player when they would substitute off during a game, even—or especially—when they were struggling.

I still have to fight the impulse to let those with more experience take charge, particularly in my academic work, and I still struggle to feel confident enough to contribute new directions and ideas to explore. However, I remind myself what coaching showed me: You don't become a leader after crossing a magical threshold of experience and knowledge. Instead, leading is a matter of choice. The key was never in my credentials, but in my willingness to try. ■

Jeremy Côté is a Ph.D. student at the Université de Sherbrooke.
Send your career story to SciCareerEditor@aaas.org.